

Modelling metabolism in the neonatal brain

Tharindi Hapuarachchi

2015

A thesis submitted to University College London
for the Degree of Doctor of Philosophy

CoMPLEX
and
Medical Physics and Biomedical Engineering
Univeristy College London
Gower Street
London WC1E 6BT

Declaration

I, Tharindi Hapuarachchi, confirm that the work presented in this thesis is my own. Where information has been derived from other sources, I confirm that this has been indicated in the thesis.

Abstract

Acute changes in cerebral blood flow and oxygen delivery directly affect brain tissue metabolism, often leading to severe life-long disabilities or death. These events can occur during birth with dire consequences to the infant. In order to identify and monitor these events in the neonatal brain clinicians often use non-invasive techniques such as near-infrared spectroscopy (NIRS) and magnetic resonance spectroscopy (MRS). However, clinical interpretation of these signals is challenging.

This thesis describes a number of mathematical and computational models of cerebral blood flow, oxygenation and metabolism regulation to assist signals integration from multimodal measurements and to investigate brain tissue metabolic activity in neonatal preclinical and clinical studies. The scope of this work is to construct a set of useful computational tools that will illuminate brain tissue and cellular physiology that give rise to changes in clinical measurements, and hence offer information of clinical significance.

The models are composed of differential equations and algebraic relations that mimic the network regulating cellular metabolism. They integrate NIRS and MRS measurements that offer insights into oxygenation and a variety of metabolic products such as ATP and pH. These models are thus able to explore the relation between measured signals and the physiology and biochemistry of the brain.

The first three models presented in this thesis focus on the piglet brain – a preclinical animal model of the human neonatal brain. Previously published models are extended to simulate intracellular pH and used to investigate hypoxia-ischaemia experiments conducted in piglets, predicting NIRS and MRS measurements. The fourth model is an adaptation of the piglet model to the human term neonate, to investigate data from bedside NIRS monitoring of patients with birth asphyxia. Finally a previously published, simpler adult model is adapted to the preterm neonate, simulating data from functional response studies and a functional NIRS study in neonates using a visual stimulus.

Acknowledgements

I would like to thank my supervisors Dr. Ilias Tachtsidis and Prof. Nicola Robertson for their guidance and support throughout this process. This thesis would not have been possible without the help of past and present group members Dr. Tracy Moroz and Dr. Matthew Caldwell whose patience, help, and collaboration have been indispensable. My thanks to Gemma Bale and her pet measurement system CYRIL for collecting neonatal data.

I would also like to thank staff and students at the Centre for Mathematics and Physics in the Life Sciences and Experimental Biology (CoMPLEX). The centre not only funded my study, but also provided access to training and a network of support and advice.

I spent a blissful month in Zurich during my final year collaborating with the Biomedical Optics Research Laboratory in the Neonatology Clinic at University Hospital Zurich. My heartfelt gratitude to Prof. Martin Wolf, Dr. Felix Scholkmann and the team for their hospitality, cooperation and friendship.

I am greatly indebted to my family for their unwavering support and encouragement throughout this journey, and appreciate their attempts to understand my work. I am also fortunate to have wonderful friends, without whom I would have perhaps been more productive, but certainly insane.

Contents

Front Matter	2
Declaration	2
Abstract	3
Acknowledgements	4
Contents	5
List of Figures	10
List of Tables	17
Journal Publications	19
Conference Abstracts	21
Symbols and Abbreviations	23
1 Introduction	25
1.1 Personal statement	28
2 The Brain	29
2.1 Anatomy	29
2.2 Blood flow	31
2.2.1 Autoregulation	32
2.3 Brain cells	33
2.3.1 Neurons	33
2.3.2 Neuroglial cells	33
2.4 Metabolism	34
2.4.1 Glycolysis	34
2.4.2 Tricarboxylic acid cycle	35

2.4.3	Oxidative phosphorylation	35
2.4.4	Malate-aspartate shuttle	36
2.5	Brain pH	40
2.5.1	Regulators of intracellular pH	40
2.6	Hypoxia-ischaemia	42
2.6.1	pH and hypoxia-ischaemia	43
2.7	Adult, neonate and piglet brains	45
3	Clinical Measurements	49
3.1	Methods of measurement	49
3.1.1	Near-infrared spectroscopy	49
3.1.2	Magnetic resonance spectroscopy, MRS	51
3.1.3	Systemic measurements	55
3.1.4	Multimodal measurements	56
3.2	Interpreting measurements	57
3.2.1	Quality of signals	57
3.2.2	Region and frequency of measurement	58
3.3	Animal experiments and neonatal studies	59
3.3.1	Hypoxia-ischaemia studies	59
3.3.2	Functional studies	63
4	Mathematical Models of the Brain	67
4.1	Mathematical modelling	67
4.1.1	The good models	72
4.2	Physiological models of the brain metabolism and circulation	73
4.2.1	The Korzeniewski model	78
4.2.2	The Beard model	78
4.2.3	The Ursino-Lodi model	82
4.2.4	The Cloutier model	83
4.2.5	The Orłowski model	86
4.3	The UCL brain models	89
4.3.1	History of model development at UCL	89
4.4	Modelling principles	93
4.4.1	Chemical reactions	93
4.4.2	Transport	95
4.5	Model optimisation	95
4.5.1	Sensitivity analysis	96

4.5.2	Parameter optimisation	97
4.6	The BrainSignals model	99
4.6.1	Model structure	99
4.6.2	Steady state simulations	108
4.6.3	Simulating hypoxia-ischaemia	111
4.6.4	Simulating functional activation	111
4.7	The BrainPiglet model	115
4.7.1	Model structure	115
4.7.2	Steady state simulations	121
4.7.3	Simulating hypoxia-ischaemia	121
4.7.4	Simulating functional activation	121
4.8	Discussion	124
5	Developing the BrainPiglet model to simulate intracellular pH	130
5.1	Hypoxia-ischaemia piglet experiments	131
5.2	BrainPiglet v2.0	131
5.2.1	Modelling intracellular pH	131
5.2.2	Modelling arterial occlusion	133
5.2.3	Steady state simulations	135
5.2.4	Simulating hypoxia-ischaemia in piglets	139
5.3	BrainPiglet v2.0.1	145
5.3.1	Modelling carbonic acid	145
5.3.2	Steady state simulations	146
5.3.3	Simulating hypoxia-ischaemia in piglets	149
5.4	BrainPiglet v2.1	154
5.4.1	Modelling sodium transporters	154
5.4.2	Steady state simulations	155
5.4.3	Simulating hypoxia-ischaemia in piglets	159
5.5	Discussion	163
6	Simulating hypoxia-ischaemia in the piglet brain	166
6.1	Piglet experiments	167
6.2	Sensitivity analysis of the model	167
6.3	Individual results	171
6.3.1	Good outcomes	172
6.3.2	Poor outcomes	195
6.4	Group results	206

6.4.1	Good outcomes	207
6.4.2	Poor outcomes	210
6.5	Discussion	213
7	Simulating hypoxia-ischaemia in the term neonatal brain	216
7.1	BabyBrain	217
7.2	Simulating hypoxic-ischaemic events	220
7.2.1	Neonate 1	220
7.2.2	Neonate 2	224
7.2.3	Neonate 3	230
7.3	Discussion	234
8	Simulating functional activation in the preterm neonatal brain	237
8.1	BrainSignals preterm neonatal model	237
8.1.1	Sensitivity analysis	240
8.1.2	Simulating functional activation	242
8.2	Discussion	247
9	Conclusions and Future Work	251
9.1	Future work	256
9.1.1	Blood pH	256
9.1.2	Model simplification	256
9.1.3	Model optimisation	257
9.1.4	Simulation of electrical activity	257
9.1.5	Simulations of clinical treatments	257
9.2	Impact	258
	Appendices	258
A	Model definitions	259
A.1	BrainSignals	259
A.1.1	Overview	259
A.1.2	Differential equations	259
A.1.3	Algebraic equations	260
A.1.4	Chemical reactions	260
A.1.5	State variables	261
A.1.6	Intermediate variables	262
A.1.7	Parameters	266

A.2	BrainPiglet v2.0	277
	A.2.1 Overview	277
	A.2.2 Differential equations	277
	A.2.3 Algebraic equations	280
	A.2.4 Chemical reactions	280
	A.2.5 State variables	282
	A.2.6 Intermediate variables	284
	A.2.7 Parameters	291
A.3	BrainPiglet v2.0.1	310
	A.3.1 Overview	310
	A.3.2 Differential equations	310
	A.3.3 Algebraic equations	314
	A.3.4 Chemical reactions	314
	A.3.5 State variables	316
	A.3.6 Intermediate variables	319
	A.3.7 Parameters	326
A.4	BrainPiglet v2.1	347
	A.4.1 Overview	347
	A.4.2 Differential equations	347
	A.4.3 Algebraic equations	351
	A.4.4 Chemical reactions	351
	A.4.5 State variables	354
	A.4.6 Intermediate variables	356
	A.4.7 Parameters	364

Bibliography	386
---------------------	------------

List of Figures

2.1	Anatomy of the brain (Thompson 2000).	30
2.2	The blood-brain barrier (Thompson 2000).	30
2.3	Autoregulation curve for the human adult. The flat section represents the autoregulatory plateau (Edvinsson et al. 1992).	33
2.4	Glycolysis.	37
2.5	The tricarboxylic acid cycle.	38
2.6	Oxidative phosphorylation.	38
2.7	The malate-aspartate shuttle.	39
2.8	Differences in pH among different organelles of the cell. Adapted from Casey et al. (2010) and Uria-Avellanal and Robertson (2014).	40
2.9	Processes regulating intracellular pH.	41
2.10	Sodium-potassium ATPase pump (Thompson 2000).	42
2.11	Variations in the circle of Willis in preterm neonates.	45
2.12	Autoregulation curve for neonates.	46
3.1	Absorption spectra for different chromophores in human tissue. CtOx is cytochrome oxidase (Scholkmann et al. 2014).	50
3.2	MRI images of healthy infants at (A) 30 weeks gestation, (B) term, (C) 6 months and (D) 1 year (Robertson and Wyatt 2004).	52
3.3	MRI images of (A) focal injury in an infant aged 11 days with Sarnat stage II neonatal encephalopathy and (B) global injury in an infant aged 12 days with Sarnat stage III (Robertson and Wyatt 2004).	52
3.4	MRS spectra from a piglet during a hypoxia-ischaemia experiment that subsequently developed severe secondary energy failure	53
3.5	Sample arterial oxygen saturation and blood pressure from a hypoxia-ischaemia experiment in a piglet.	56

3.6	MRS NTP measurements during hypoxia-ischaemia in piglets. Top - representative polynomial fit to NTP/EPP from 6 h after HI.	60
3.7	Correlation between MRS-measured NTP/EPP and NIRS-measured oxidised CCO measurements during hypoxia-ischaemia in piglets. Relationship changes significantly at a threshold point during HI (Bainbridge et al. 2013).	60
3.8	pH maps from 5 coronal brain sections from naive mice or mice exposed to various levels of hypoxia and carotid artery occlusion.	60
3.9	NIRS measurements of CBF and CMRO ₂ during hypoxia-ischaemia in 18 piglets. Solid line - control, dotted line - HI. Grey area represents the HI insult (Tichauer et al. 2006).	63
3.10	Linear regression analysis between ΔoxCCO with ΔHbDiff on the two cerebral hemispheres a neonatal stroke patient in the first 24 hours of life. Point colours and shapes represent different events (Mitra et al. 2015).	63
3.11	Summary of haemodynamic and oxygenation changes typical of a matured brain, stimulated by both neural and systemic activity (Scholkmann 2014).	64
3.12	fNIRS technique applied to infants.	64
4.1	Simulation presented in Korzeniewski and Zoladz (2001) of muscle activation, using an increase in energy demand.	78
4.2	A 50% drop in O ₂ input to the Korzeniewski and Zoladz (2001) model to simulate hypoxia.	79
4.3	Simulation of hypoxia in the Korzeniewski and Zoladz (2001) model with a 50% drop in O ₂	80
4.4	Schematic of the Beard (2005) model	81
4.5	Simulations of the Beard (2005) model following an 80% decrease in O ₂ .	81
4.6	Intracranial dynamics of the Ursino and Lodi (1998) model.	82
4.7	The action of regulatory mechanisms in the Ursino and Lodi (1998) model, on smooth muscle activation factor of large and small pial arteries.	82
4.8	A 50% drop in blood pressure input to the Ursino-Lodi model to simulate ischemia	83
4.9	Simulation of ischemia in the Ursino-Lodi model with a 50% drop in blood pressure.	84

4.10	Schematic diagram of the Cloutier model.(Cloutier et al. 2009)	84
4.11	Simulations of the Cloutier et al. (2009) model of the response to a stimulus	85
4.12	Schematic diagram of the Orłowski model. The additional notation indicates changes made to the Cloutier model. (Orłowski et al. 2011)	86
4.13	Simulations of the Orłowski model following a 80% reduction in CBF (Orłowski et al. 2011)	86
4.14	Simulations of the Orłowski model following a 80% reduction in CBF and O ₂	87
4.15	Simulations of the Orłowski et al. (2013) model	88
4.16	Main processes and compartments of the BrainCirc model(Banaji et al. 2005).	90
4.17	Schematic of the BrainSignals model (Banaji et al. 2008).	90
4.18	The BRAINCIRC and BCMD modelling environments.	93
4.19	Schematic of the BrainSignals model	100
4.20	The autoregulation curve at steady state, with the two extreme values of the autoregulation constant k_{aut} .	102
4.21	Steady state simulations of the BrainSignals model with varying arterial oxygen saturation SaO_2 (a–e) and blood pressure Pa (f–j).	109
4.22	Steady state simulations of the BrainSignals model with varying demand u (a–e) and partial pressure of carbon dioxide $PaCO_2$ (f–j).	110
4.23	Inputs to the BrainSignals model to simulate hypoxia-ischaemia.	111
4.24	Outputs of the BrainSignals model simulation of hypoxia-ischaemia.	112
4.25	Inputs to the BrainSignals model to simulate brain activation.	113
4.26	Outputs of the BrainSignals model simulation of brain activation.	114
4.27	Schematic of the BrainPiglet model v1.0 (Moroz et al. 2012).	115
4.28	Steady state simulations of the BrainPiglet v1.0 model with varying arterial oxygen saturation SaO_2 (a–f) and blood pressure Pa (g–l).	122
4.29	Steady state simulations of the BrainPiglet v1.0 model with varying demand u (a–f) and partial pressure of carbon dioxide $PaCO_2$ (g–l).	123
4.30	Inputs to BrainPiglet v1.0 to simulate hypoxia-ischaemia.	124
4.31	Outputs of BrainPiglet v1.0 simulation of hypoxia-ischaemia.	125
4.32	Inputs to the BrainPiglet v1.0 model to simulate brain activation.	126

4.33	Outputs of the BrainPiglet v1.0 model simulation of brain activation.	127
5.1	Schematic of the BrainPiglet v2.0 model.	132
5.2	Movement of H^+ ions in the BrainPiglet v2.0 model.	133
5.3	Circuit diagram of circulation in the BrainPiglet v2.0 model (Moroz et al. 2012)	135
5.4	Steady state simulations of the BrainPiglet v2.0 model with varying arterial oxygen saturation SaO_2 (a–e) and blood pressure Pa (f–j).	137
5.5	Steady state simulations of the BrainPiglet v2.0 model with varying demand u (a–e) and partial pressure of carbon dioxide P_aCO_2 (f–j).	138
5.6	Simulating hypoxia-ischaemia in Piglet LWP173 using the BrainPiglet v2.0 model.	144
5.7	Steady state simulations of the BrainPiglet v2.0.1 model with varying arterial oxygen saturation SaO_2 (a–e) and blood pressure Pa (f–j).	147
5.8	Steady state simulations of the BrainPiglet v2.0.1 model with varying demand u (a–e) and partial pressure of carbon dioxide P_aCO_2 (f–j).	148
5.9	Simulating hypoxia-ischaemia in Piglet LWP173 using the BrainPiglet v2.0.1 model.	153
5.10	Movement of H^+ ions in the BrainPiglet v2.1 model.	155
5.11	Steady state simulations of the BrainPiglet v2.1 model with varying arterial oxygen saturation SaO_2 (a–e) and blood pressure Pa (f–j).	156
5.12	Steady state simulations of the BrainPiglet v2.1 model with varying demand u (a–e) and partial pressure of carbon dioxide P_aCO_2 (f–j).	157
5.13	Simulating hypoxia-ischaemia in Piglet LWP173 using the BrainPiglet v2.1 model.	162
5.14	Schematic of variables and parameters in the four models.	165
6.1	Experimental protocol for the hypoxia-ischaemia piglet experiments	168

6.2	Morris method sensitivity analysis of the 22 piglet monitoring data sets for the ΔHbO_2 and ΔHhb variables.	169
6.3	Morris method sensitivity analysis of the 22 piglet monitoring data sets for the $\Delta oxCCO$ and cytoplasmic pH pH_o variables. . .	170
6.4	Changes in optimised parameter values for piglets with good outcomes.	179
6.5	Piglet LWP173 measurements and simulations	180
6.6	Piglet LWP175 measurements and simulations	181
6.7	Piglet LWP179 measurements and simulations	182
6.8	Piglet LWP180 measurements and simulations	183
6.9	Piglet LWP186 measurements and simulations	184
6.10	Piglet LWP198 measurements and simulations	185
6.11	Piglet LWP200 measurements and simulations	186
6.12	Piglet LWP201 measurements and simulations	187
6.13	Piglet LWP204 measurements and simulations	188
6.14	Piglet LWP206 measurements and simulations	189
6.15	Piglet LWP209 measurements and simulations	190
6.16	Piglet LWP210 measurements and simulations	191
6.17	Piglet LWP211 measurements and simulations	192
6.18	Piglet LWP213 measurements and simulations	193
6.19	Piglet LWP216 measurements and simulations	194
6.20	Changes in optimised parameter values for piglets with poor outcomes.	198
6.21	Piglet LWP183 measurements and simulations	199
6.22	Piglet LWP185 measurements and simulations	200
6.23	Piglet LWP188 measurements and simulations	201
6.24	Piglet LWP207 measurements and simulations	202
6.25	Piglet LWP208 measurements and simulations	203
6.26	Piglet LWP215 measurements and simulations	204
6.27	Piglet LWP218 measurements and simulations	205
6.28	Group analysis. Measurements are divided into 5 phases, and averaged across the piglets.	206
6.29	Group analysis of 15 piglets with good outcome.	209
6.30	Group analysis of piglets with poor outcome.	212

7.1	Autoregulation curves of the BrainPiglet model, the BabyBrain term neonate model and the BrainSignals preterm neonate model.	218
7.2	Steady state simulations of ΔHbO_2 and $\Delta oxCCO$ in the BabyBrain model with varying arterial oxygen saturation SaO_2	218
7.3	Neonate 1 measurements and simulations	225
7.4	Hypoxia experiments in piglets by Tsuji et al. (1995).	228
7.5	Neonate 2 measurements and simulations	229
7.6	Neonate 3 measurements and simulations	233
7.7	BabyBrain model simulation of $\Delta oxCCO$ in response to changes in the input normal cytoplasmic pH	235
8.1	Autoregulation curves cerebral blood flow (CBF) against blood pressure (Pa) - of the Brainsignals preterm neonate and adult models.	238
8.2	Demand as a model input, using a haemodynamic response function, to simulate functional activation	243
8.3	Model simulated and observed haemodynamic response of the Kozberg et al. study (Kozberg et al. 2013). Changes in deoxy- and oxy- haemoglobin (HHb, HbO ₂) concentrations.	243
8.4	Model simulated and observed haemodynamic response of the Kozberg et al. study (Kozberg et al. 2013). Changes in blood pressure (BP) and total haemoglobin (HbT)	244
8.5	Model simulated and observed haemodynamic response of the Kozberg et al. study (Kozberg et al. 2013). Changes in deoxy- and oxy- haemoglobin (HHb, HbO ₂) concentrations.	244
8.6	Model simulated and observed haemodynamic response of the Kozberg et al. study (Kozberg et al. 2013). Changes in BP and total haemoglobin (HbT).	245
8.7	Model simulated and observed haemodynamic response of the Roche-Labarbe et al. study (Roche-Labarbe et al. 2014). Relative changes in oxy- and deoxy- haemoglobin (rHbO ₂ , rHHb).	245
8.8	Model simulated and observed haemodynamic response of the Roche-Labarbe et al. study (Roche-Labarbe et al. 2014). Relative changes cerebral blood volume (rCBV) and cerebral blood flow (rCBF).	246

8.9	Model simulated and observed haemodynamic response of the Roche-Labarbe et al. study (Roche-Labarbe et al. 2014). Relative changes in cerebral metabolic rate of oxygen consumption (rCMRO ₂).	246
8.10	Model simulation of Neonate 1 of the USZ study.	248
8.11	Model simulation of Neonate 2 of the USZ study.	248
9.1	BrainSignals model simplification. The complete metabolic sub-model with parameters omitted (A), and progressively reduced variants (B,C,D,E) (Caldwell et al. 2015)	256
9.2	BrainSignals model simplification. (A) Steady state simulations for three variants compared with the original metabolic submodel. (B) Simulations of data from human adult hypercapnia experiments. (Caldwell et al. 2015)	257

List of Tables

2.1	A comparison of physiological measurements in healthy preterm, term and adult patients.	48
4.1	Models of cerebral metabolism and blood flow.	74
4.1	Models of cerebral metabolism and blood flow.	75
4.1	Models of cerebral metabolism and blood flow.	76
4.1	Models of cerebral metabolism and blood flow.	77
4.2	A comparison of the three models.	91
4.3	Timeline of models of cerebral metabolism produced at UCL . .	91
4.4	BrainSignals model equations	108
4.5	BrainPiglet v1.0 model equations	120
5.1	New parameters in BrainPiglet v2.0	136
5.2	Sensitivity analysis of BrainPiglet v2.0 using data from Piglet LWP173.	141
5.3	Optimised BrainPiglet v2.0 parameter values for Piglet LWP173 .	142
5.4	New parameters in BrainPiglet v2.1	146
5.5	Sensitivity analysis of BrainPiglet v2.0.1 using data from Piglet LWP173.	150
5.6	Optimised BrainPiglet v2.0.1 parameter values for Piglet LWP173	151
5.7	New parameters in BrainPiglet v2.1	158
5.8	Sensitivity analysis of BrainPiglet v2.1 using data from Piglet LWP173.	160
5.9	Optimised BrainPiglet v2.1 parameter values for Piglet LWP173 .	161
6.1	BrainPiglet v2.0 parameters selected for optimisation to simulate hypoxia-ischaemia piglet experiments	171
6.2	Piglet Outcomes	172
6.3	Optimised parameter values	174

6.4	Optimised parameter values	196
6.5	Optimised parameter values for the good outcome group	208
6.6	Optimised parameter values for the poor outcome group	211
7.1	Altered BrainPiglet parameter values.	219
7.2	Physiological characteristics of the term neonate subjects.	220
7.3	Sensitivity analysis of BabyBrain using data from Neonate 1.	222
7.4	Optimised parameter values for Neonate 1	223
7.5	Sensitivity analysis of BabyBrain using data from Neonate 2.	226
7.6	Optimised parameter values for Neonate 2	227
7.7	Sensitivity analysis of BabyBrain using data from Neonate 3.	231
7.8	Optimised parameter values for Neonate 3	232
8.1	Altered BrainSignals parameter values	239
8.2	Sensitivity analysis of BrainSignals preterm neonate model at steady state.	241
8.3	Physiological characteristics of the two preterm infant subjects.	247

Journal Publications

Tharindi Hapuarachchi, Felix Scholkmann, Matthew Caldwell, Cornelia Haggmann, Stefan Kleiser, Marcin Pastewski, Martin Wolf and Ilias Tachtsidis. Simulation of preterm neonatal brain metabolism during functional neuronal activation using a computational model. *Advances in Experimental Medicine and Biology* (accepted for publication).

Tracy Moroz, Tharindi Hapuarachchi, Matthew Caldwell, Alan Bainbridge, Nicola J Robertson, Chris E Cooper and Ilias Tachtsidis. Modelling blood flow and metabolism in the preclinical neonatal brain during and following hypoxia-ischaemia. *PLOS Computational Biology* (under review).

Matthew Caldwell, Tharindi Hapuarachchi, David Highton, Clare Elwell, Martin Smith and Ilias Tachtsidis. (2015). BrainSignals Revisited: Simplifying a Computational Model of Cerebral Physiology. *PLoS One*, 10(5), e0126695. doi:10.1371/journal.pone.0126695

Tharindi Hapuarachchi, Tracy Moroz, Alan Bainbridge, Stuart Faulkner, David Price, Elizabeth Powell, Tingting Zhu, Esther Baer, Kevin Broad, David Thomas, Ernest Cady, Nicola Robertson, Xavier Golay and Ilias Tachtsidis. (2014). Simulating NIRS and MRS measurements during cerebral hypoxia-ischaemia in piglets using a computational model. *Advances in Experimental Medicine and Biology*, 812, 18793. doi:10.1007/978-1-4939-0620-8_25

Tharindi Hapuarachchi, Tracy Moroz, Alan Bainbridge, David Price, Ernest Cady, Esther Baer, Kevin Broad, Mojgan Ezzati, David Thomas, Xavier Golay, Nicola Robertson and Ilias Tachtsidis. (2013). Modelling blood flow and metabolism in the piglet brain during hypoxia-ischaemia: simulating pH changes. *Advances in Experimental Medicine and Biology*, 789, 3317. doi: 10.1007/978-1-4614-7411-1_44

Tracy Moroz, Tharindi Hapuarachchi, Alan Bainbridge, David Price, Ernest Cady, Esther Baer, Ilias Tachtsidis, Kevin Broad, Mojgan Ezzati, Nicola Robertson, David Thomas, Xavier Golay and Chris Cooper. (2013). Modelling blood flow and metabolism in the piglet brain during hypoxia-ischaemia:

simulating brain energetics. *Advances in Experimental Medicine and Biology*,
789, 33944. doi:10.1007/978-1-4614-7411-1_45

Conference Abstracts

Tharindi Hapuarachchi, Felix Scholkmann, Matthew Caldwell, Cornelia Haggmann, Stefan Kleiser, Andrea J Metz, Marcin Pastewski, Martin Wolf and Ilias Tachtsidis. Simulation of neonatal brain metabolism during functional neuronal activation using a computational model. *ZNZ Symposium 2014, Zurich, Switzerland*. September 2014. Poster.

Felix Scholkmann, Mathew Caldwell, Tharindi Hapuarachchi, Ursula Wolf, Martin Wolf and Ilias Tachtsidis. The significance of systemic changes (blood pressure and PaCO₂) in functional studies using NIRS - An investigation using a mathematical model of brain physiology. *fNIRS 2014, Montreal, Quebec, Canada*. October 2014. Talk.

Tharindi Hapuarachchi, Felix Scholkmann, Matthew Caldwell, Cornelia Haggmann, Stefan Kleiser, Marcin Pastewski, Martin Wolf and Ilias Tachtsidis. Simulation of neonatal brain metabolism using a computational model *International Society on Oxygen Transport to Tissue (ISOTT) Meeting 2014, London*. June 2014. Talk.

Felix Scholkmann, Stefan Kleiser, Marcin Pastewski, Tharindi Hapuarachchi, Cornelia Haggmann, Jean Claude Fauchère, Ilias Tachtsidis and Martin Wolf. Characterizing fluctuations of arterial and cerebral tissue oxygenation in preterm neonates by means of data analysis techniques for nonlinear dynamical systems. *International Society on Oxygen Transport to Tissue (ISOTT) Meeting 2014, London*. June 2014. Talk.

Matthew Caldwell, Tharindi Hapuarachchi, David Highton, Clare Elwell, Ilias Tachtsidis. A family of cerebral physiology models to aid interpretation of clinical data. *UCL Neuroscience Symposium 2014, London* June 2014. Poster.

Tharindi Hapuarachchi, Tracy Moroz, Nicola Robertson and Ilias Tachtsidis. Group Analysis of hypoxia-ischaemia in piglets using a computational model. *International Society on Oxygen Transport to Tissue (ISOTT) Meeting 2013, Hanover, New Hampshire, USA*. June 2013. Talk.

Tharindi Hapuarachchi, Tracy Moroz, Nicola Robertson and Ilias Tachtsidis. Modelling blood flow and metabolism in the preclinical neonatal brain dur-

ing physiological insults. *Computational Life and Medical Sciences (CLMS) Symposium 2013, London*. June 2013. Poster.

Tharindi Hapuarachchi, Tracy Moroz, Alan Bainbridge, Stuart Faulkner, David Price, Elizabeth Powell, Tingting Zhu, Esther Baer, Kevin Broad, David Thomas, Ernest Cady, Nicola Robertson, Xavier Golay and Ilias Tachtsidis. Modelling blood flow and metabolism in the piglet brain during physiological insults: simulating intracellular pH. *Brain 2013, Shanghai, China*. May 2013. Poster.

Tharindi Hapuarachchi, Tracy Moroz, Nicola Robertson and Ilias Tachtsidis. Hypoxia-ischaemia in the neonatal brain: A mathematical and computational model. *id2 conference 2013, London*. May 2013. Poster.

Tharindi Hapuarachchi, Tracy Moroz, Nicola Robertson and Ilias Tachtsidis. Modelling blood flow and metabolism in the preclinical neonatal brain during physiological insults. *Virtual Physiological Human (VPH) Conference 2012, London*. September 2012. Talk.

Tharindi Hapuarachchi, Tracy Moroz, Nicola J. Robertson and Ilias Tachtsidis. Modelling blood flow and metabolism in the piglet brain during hypoxic-ischaemia: simulating pH changes. *International Society on Oxygen Transport to Tissue (ISOTT) Meeting 2012, Bruges, Belgium*. August 2012. Talk.

Tracy Moroz, Tharindi Hapuarachchi, Murad Banaji, Nicola J. Robertson, Chris E. Cooper and Ilias Tachtsidis. Modelling blood flow and metabolism in the piglet brain during hypoxic-ischaemia: simulating brain energetics. *International Society on Oxygen Transport to Tissue (ISOTT) Meeting 2012, Bruges, Belgium*. August 2012. Talk.

Tharindi Hapuarachchi, Tracy Moroz, Nicola Robertson and Ilias Tachtsidis. Modelling blood flow and metabolism in the preclinical neonatal brain during physiological insults. *UCL-NIMR Conference, London*. May 2012. Poster.

Tharindi Hapuarachchi, Tracy Moroz, Nicola Robertson and Ilias Tachtsidis. Modelling blood flow and metabolism in the preclinical neonatal brain during physiological insults. *Joint DTC Life Sciences Conference, Warwick*. May 2012. Poster.

Symbols and Abbreviations

ADP	Adenosine diphosphate
AMP	Adenosine monophosphate
ATP	Adenosine triphosphate
BBB	Blood-brain barrier
CBF	Cerebral blood flow
CCO	Cytochrome-c-oxidase
CMRO ₂	Cerebral metabolic rate of oxygen consumption
CNS	Central nervous system
CO ₂	Carbon dioxide
Cr	Creatine
CSF	Cerebrospinal fluid
HbF	Fetal haemoglobin
HbO ₂	Oxyhaemoglobin
HbT	Total haemoglobin
HHb	Deoxyhaemoglobin
HI	Hypoxia-ischaemia
MCT	Monocarboxylate transporter
MRS	Magnetic resonance spectroscopy
NAA	N-acetyl-aspartate
NAD	Nicotinamide adenine dinucleotide
NIRS	Near infrared spectroscopy
NTP	Nucleoside triphosphate
O ₂	Oxygen
P _a CO ₂	Partial pressure of carbon dioxide
PCr	Phosphocreatine

PMF	Proton motive force
SaO ₂	Arterial oxygen saturation

Chapter 1

Introduction

Neonatal death accounts for approximately 40% of mortality during the first 5 years of life (Lawn et al. 2009). One third of early neonatal deaths, an estimated 904,000 lives, result from birth asphyxia (Lawn et al. 2005). In 2005, a World Health Report estimated that an annual 1 million who survive birth asphyxia may develop cerebral palsy, learning difficulties or other disabilities (WHO 2005). Indeed, the development of neonatal encephalopathy - the disturbance of neurological function - in these infants is strongly predictive of neurodevelopmental disability (Lawn et al. 2009).

Neonatal intensive care is typically informed by a vast array of clinical monitoring measurements, creating the potential for information overload and making it difficult for clinicians to translate relevant information into actionable insights (Ellsworth et al. 2014). Mathematical and computational methods have long been successful in deciphering and solving challenges in the medical domain. In particular, the application of mathematical and computational models provide a powerful mechanism for investigating and understanding biological scenarios. As our knowledge of biology expands and the prevalence of clinical data increases, models will become crucial not only for investigations of elaborate biological dynamics, but also, and perhaps more importantly, for translations and interpretations of value from the abundance of information – to detect the signal from the noise and the light in the data mire.

The work presented in this thesis covers the development of a number of such models, focused on cerebral metabolism in the neonate. Understanding metabolic activity in the brain suffering from neonatal encephalopathy is

vital for the development of neuroprotective strategies that can be used clinically in these circumstances and for identifying patients that are at risk of long-term damage in order to improve outcome. Near infrared spectroscopy (NIRS) and magnetic resonance spectroscopy (MRS) are used to monitor the progress of patients by measuring cerebral oxygenation and the concentrations of certain metabolites such as ATP. These techniques are prominent in neonatal care due to their non-invasive characteristic. Newborn piglets are a common preclinical model of the human neonate. NIRS and MRS have also been employed in investigating cerebral activity in such experimental studies (Springett et al. 2000; Bainbridge et al. 2013; Cooper and Springett 1997).

The Multi-modal Spectroscopy group at University College London combine NIRS and MRS to provide a detailed overview of the metabolic and haemodynamic changes that occur in the brain. The models enable the investigation of cerebral physiology that give rise to these changes, by integrating measurement data from different sources coupled with the known physiology of the brain. The models also provide a predictive capability for entities of clinical significance.

The models are here applied to two clinical scenarios – functional activation and hypoxia-ischaemia. The former refers to the cerebral metabolic changes that occur when the patient is subjected to a stimulus such as sound, light or touch. Hypoxia-ischaemia is the loss of cerebral blood flow and oxygenation, and as a result of birth asphyxia is a major cause of cerebral injury in neonates. Although the numbers are more severe in developing countries, in the developed world asphyxial hypoxic-ischaemic encephalopathy occurs in 1-2 for every 1000 live births (Shah et al. 2007). It is believed that the predominant cause of cerebral damage stems from the deterioration of metabolic processes during the recovery period. Brain activity is often observed to return in the immediate aftermath of the event, only to worsen after several hours (Thoresen et al. 1995; Robertson et al. 2002). The severity of this phenomenon, known as a secondary energy failure, has been found to correlate with outcome (Roth et al. 1992).

The aims and objectives of the work presented in this thesis are to:

- Develop and expand a pre-existing model metabolism in the piglet brain to better simulate intracellular pH

-
- Simulate hypoxia-ischaemia experiments in piglets
 - Adapt a pre-existing model of adult cerebral metabolism to the preterm neonatal brain, and use the model to simulate functional activation studies
 - Adapt the model of piglet cerebral metabolism to the human term neonatal brain, and apply the model to monitoring data from acute brain injury patients
 - Use sensitivity analysis and parameter optimisation in the applications above to gain further insight into physiological changes

In this thesis, Chapter 2 provides an overview of brain anatomy and physiology, with a look at cellular metabolism and pH, and differences between human adult, neonate and piglet brains. Clinical measurement techniques are introduced in Chapter 3. This includes the capacity of NIRS and MRS measurements to detect changes in the brain, and a brief summary of their applications and findings from hypoxia-ischaemia and functional activation studies. Chapter 4 is dedicated to the study of mathematical models, looking at a number of published models of cerebral metabolism and blood flow. Among them are the models produced at UCL, with specific emphasis and detail on the two main models – BrainSignals and BrainPiglet – that were further developed in this thesis. This chapter also describes the model parameter optimisation techniques that were used. Chapter 5 focuses on the development of the BrainPiglet model, completed in three phases, to better simulate intracellular pH. The model is then applied in Chapter 6 to measurement data from hypoxia-ischaemia piglet experiments conducted at UCL. The BrainPiglet model is adapted to the term neonatal brain in Chapter 7, and used to investigate monitoring data from neonates suffering from hypoxic-ischaemic encephalopathy. Chapter 8 outlines the adaptation of the BrainSignals model to the human preterm neonatal brain, and its application to data from functional activation experiments. The final chapter covers conclusions and future work – both a look back at the progress that has been made and a look forward at the challenges and opportunities to come.

1.1 Personal statement

A number of research collaborations have made the work presented in this thesis possible. This section aims to make those collaborations and the author's contributions clear.

The BrainPiglet model was originally developed by Moroz et al. (2012). In this thesis, it is further extended in Chapter 5 to simulate intracellular pH. The hypoxia-ischaemia experiments in piglets, covered in Chapter 6, were carried out by the Preclinical Neonatal Neuroprotection research group, lead by Professor Nicola Robertson at the Institute of Neurology, Queen Square, London. Measurement data from this study was used in this thesis to help build and validate the extended BrainPiglet model.

The development of the human term neonate model in Chapter 7 is followed by its application to monitoring data from neonates suffering from hypoxic-ischaemic encephalopathy at the Neonatal Intensive Care Unit, University College Hospital (UCLH). This data was collected by Gemma Bale of the Multi-modal Spectroscopy group.

Chapter 8 focuses on the adaptation of the BrainSignals model, which was originally developed by Banaji et al. (2005), to the preterm neonate. The model was then applied to data collected during a functional activation study in neonates. This study was conducted by the Biomedical Optics Research Laboratory at University Hospital Zurich and measurement data was subsequently provided to the author.

The computational models developed by the author were compiled and executed in the Brain/Circulation Model Developer (BCMD) interface built by another member of the group – Dr. Matthew Caldwell. The functionality of this interface also enables the creation of the schematic graphs of model variables and parameters presented at the end of Chapter 5.

Chapter 2

The Brain

This work attempts to simulate the behaviour of perhaps the most complex organ of the human body. The brain is a powerhouse, controlling the majority of functions of the body, from hormones to movement and memory to vision - responsible for the existence of life, in both a physical and mental sense.

Any attempt, therefore, to amalgamate every known function of the brain in a single detailed investigation is a near impossible task. Moreover, attempts at creating an all-encompassing computational model, based on the foundations of current knowledge of the brain, would be at best unreliable. The sheer size of such a model involving an infinite number of parameters and variables (with various error margins) would be devoid of accuracy and perhaps also of translatability.

As a consequence, models of the brain must necessarily be focused and limited in scope. With this in mind, this chapter explores those areas and functions of the brain immediately relevant to cerebral oxygenation and cellular metabolism.

2.1 Anatomy

The central nervous system (CNS) consists of the brain, the brainstem and the spinal cord. The cerebral hemispheres are made up of four major lobes: the occipital, parietal, temporal and frontal lobes. The cerebral cortex forms the outer layer of the cerebral hemisphere, and is interconnected over long distances via subcortical pathways. These pathways and those connecting

the cerebral cortex to the spinal cord, brainstem and nuclei deep within the cerebral hemisphere make up the white matter of the cerebral hemisphere.

At the base of the brain, the brainstem is composed of the medulla, pons and midbrain. Also connected to the brainstem is the cerebellum, associated with coordination and movement.

Copyright material removed.

Figure 2.1: Anatomy of the brain (Thompson 2000).

The CNS is surrounded by a series of membranes known as the meninges: the dura mater, the arachnoid mater and the pia mater. Between the latter two lies the subarachnoid space, which is filled with a fluid called the cerebrospinal fluid (CSF) and contains the major arteries. The subarachnoid space expands at specific sites to form cisterns, the largest of which is the cisterna magna found between the cerebellum and medulla.

The blood-brain barrier (BBB) was originally thought of as a single physical barrier stopping the movement of molecules and cells into the brain. However it is now known to be composed of a series of different transport systems selectively facilitating the movement of molecules between the CSF and the blood. This barrier allows small molecules like glucose, although not lipid soluble, to pass through to the CSF but prevents larger protein molecules from entering the brain. The barrier effectively maintains a constant intracerebral chemical environment, and protects against osmotic challenges. By preventing the entrance of cells, it also provides immunological protection. However, this also makes the administration of drugs for the treatment of CNS disorders difficult (Barker and Cicchetti 2012).

Copyright material removed.

Figure 2.2: The blood-brain barrier (Thompson 2000).

Recently, it has been shown that arterial pulsation results in exchanges between the CSF and interstitial fluid (ISF, fluid surround the tissues), in an organised system called the glymphatic system (Ilf et al. 2013). The system uses a network of perivascular tunnels to clear macroscopic waste and facilitate the distribution of compounds such as glucose, lipids and amino acids (Jessen et al. 2015). Experiments in mice have suggested that this glymphatic pathway is also used to clear endogenously produced proteins, including biomarkers of traumatic brain injury (Plog et al. 2015).

2.2 Blood flow

The brain is supplied by four major arteries - the internal carotid and vertebral arteries - that coalesce to form the circle of Willis. This arrangement ensures an adequate distribution of blood to all parts of the brain, even if flow in any one of the arteries is obstructed. This is especially important in the case of the carotid arteries, as they carry approximately 40% each of total blood flow to the brain (Edvinsson et al. 1992). The major branches of the internal carotid arteries form the middle cerebral arteries, which supply the lateral sections of the cerebral hemispheres. The vertebral arteries unite to form the basilar artery, which runs through the pons and connects to the circle of Willis (Edvinsson et al. 1992).

The distribution of capillaries in the brain is heterogeneous, and varies with the number of synapses in the region (Edvinsson et al. 1992). Cerebral grey matter has more than twice the capillary density of white matter. Areas with higher basal levels of glucose use and blood flow such as the cochlear nucleus and cerebral cortex have higher density of capillaries (Edvinsson et al. 1992; Cavaglia et al. 2001). Prolonged periods of hypoxia can also lead to an increase in capillary density (Edvinsson et al. 1992). Ischaemic insults have resulted in more extensive blood-brain barrier leakage in areas of low capillary density (Cavaglia et al. 2001).

The cardiovascular system regulates oxygen transport, vital for cellular metabolism. Blood haemoglobin increases this transport capability approximately 70-fold by binding to oxygen at one of the haemoglobin molecule's 4 binding sites (Polin et al. 2010). The affinity of haemoglobin to oxygen is often described by a sigmoidal equilibrium curve. This shape results from the effect of each haeme group binding to oxygen making it progressively easier for the next,

and is often expressed by the value of P_{50} – the oxygen tension at which 50% of the haemoglobin in blood is saturated (Polin et al. 2010). In both adult and fetal blood, the curve shifts to the right in the event of an increase in the partial pressure of oxygen, or a decrease in pH, or both. This phenomenon is known as the Bohr effect, and can also be induced by CO_2 , either due to pH changes caused by CO_2 or due to CO_2 binding reversibly to amino acid groups in the haemoglobin molecule (Polin et al. 2010).

2.2.1 Autoregulation

Cerebral autoregulation is the function of the brain to maintain constant blood flow despite changes in perfusion pressure (Edvinsson et al. 1992; Polin et al. 2010) - the difference in intravascular pressure between the arterial inflow and the venous outflow (Siesjo 1978). Cerebral blood flow (CBF) is maintained between mean arterial pressures of 60 - 140 mmHg in the adult human, however neither of these limits are fixed points and can change with a variety of intrinsic and extrinsic factors such as arterial carbon dioxide tension and chronic arterial hypertension (Edvinsson et al. 1992). In newborns, this range is less well defined but the lower threshold is known to be approximately 30mmHg (Greisen 2005).

There are three mechanisms by which autoregulation occurs (Edvinsson et al. 1992; Siesjo 1978). The myogenic mechanism suggests that the smooth muscle cells of cerebral vessels respond to changes in transmural pressure by contracting or dilating the vessel wall (Edvinsson et al. 1992). The metabolic hypothesis is that the high neuronal activity causing variations in concentrations of oxygen, carbon dioxide and other metabolites induce an increase in CBF. The third mechanism, described as the neurogenic hypothesis, implies that blood vessel walls are controlled by nerves connected to them (Edvinsson et al. 1992).

Brain injuries, such as those that result from hypercapnia, cranial trauma or hypoxia-ischaemia (see Section 2.6), can impair autoregulation (Greisen 2005; Polin et al. 2010). This is evident in the measurements of the patient's blood pressure, and is a clinical marker of the state of brain.

Copyright material removed.

Figure 2.3: Autoregulation curve for the human adult. The flat section represents the autoregulatory plateau (Edvinsson et al. 1992).

2.3 Brain cells

Neuroglial cells and neurons are the two major types of cells in the nervous system. The adult human brain contains approximately 100 billion nerve cells, however neurons only account for 10-20% of the total population (Barker and Cicchetti 2012).

2.3.1 Neurons

The part of the neuron containing the nucleus and surrounding cytoplasm is called the cell body or soma. It encompasses most of the intracellular organelles such as the mitochondria. Structures called dendrites extend outwards from the soma, increasing the surface area for synapse formation and hence the accumulation of inputs. The axon originates from the soma and conducts information away towards the nerve terminal, and is often insulated by a layer of lipid known as a myelin sheath allowing rapid propagation of signals. The junctions between cells are called synapses.

2.3.2 Neuroglial cells

There are four main types of neuroglial cells in the CNS: oligodendrocytes, astrocytes, microglia and ependymal cells. A large number of oligodendrocytes are found in white matter as they form the myelin insulation of neurons in the CNS.

Microglial cells are the macrophages of the brain, found in both white and grey matter, responsible for mediating immune responses.

Astrocytes are small stellate cells which perform a number of functions throughout the CNS, and account for almost half of the volume of the adult mammalian brain (Agulhon et al. 2008). They form a structural supporting framework for neuronal cells and capillaries (Agulhon et al. 2008). They pro-

mote the formation of high-resistance junctions between capillary endothelial cells to maintain the integrity of the blood-brain barrier (BBB). They also store neurotransmitters and can dispel excessive ion concentrations in the extracellular fluid. Astrocytes may also be involved in response to injury (Barker and Cicchetti 2012).

Ependymal cells are involved in the movement of CBF and work with astrocytes in the blood-brain barrier (Barker and Cicchetti 2012).

2.4 Metabolism

The major metabolic processes of the cell concern the production and use of adenosine triphosphate (ATP) - the energy molecule of the cell. In respiration, glucose and oxygen are converted to carbon dioxide and ATP (Siesjo 1978). Thus measurements of cerebral oxygen consumption can provide an estimate of energy production in the brain (see Chapter 3 for such methods). The cerebral metabolic rate of oxygen consumption $CMRO_2$ can be calculated in vivo using the Fick principle:

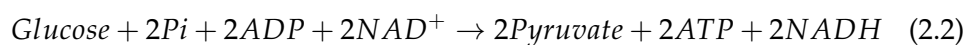
$$CMRO_2 = CBF(A_{O_2} - V_{O_2}) \quad (2.1)$$

where A_{O_2} and V_{O_2} are the arterial and venous concentrations of oxygen across the brain (Polin et al. 2010). Oxygen consumption is varied across the regions of the brain (Polin et al. 2010).

A regional coupling of CBF to metabolism exists in both adult and immature brains – when the rate of cerebral oxidative metabolism is high, so is CBF and vice versa (Polin et al. 2010).

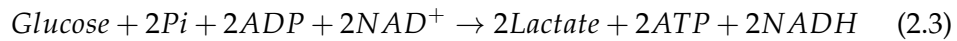
2.4.1 Glycolysis

Glucose can be metabolised either anaerobically or aerobically for the purpose of energy production and is transported from the blood into the cell by GLUT transporters (Siesjo 1978). Figure 2.2 illustrates the many enzyme-driven steps of glycolysis, which are summarised by the equation below (Siesjo 1978). These reactions take place in the cell cytoplasm.



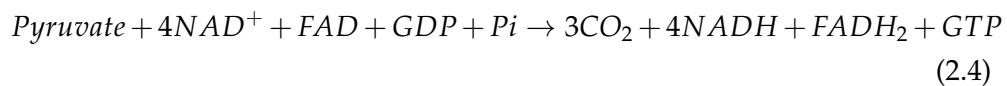
Under aerobic conditions, pyruvate is then oxidised to CO₂ and water by mitochondrial enzymes (Section 2.4.2). The NADH formed is also reoxidised to NAD⁺, through the malate-aspartate shuttle (Section 2.4.4).

In the absence of oxygen, pyruvate is reduced to lactate. This reversible reaction creates two molecules of lactic acid at the end of glycolysis, but still allows the reoxidation of NADH so that the process may continue (Siesjo 1978). The movement of lactate out of the cell into the blood is facilitated by monocarboxylate transporters (Simpson et al. 2007) (see Section 2.5.1).



2.4.2 Tricarboxylic acid cycle

In the mitochondrial matrix, the pyruvate produced by glycolysis is oxidised to carbon dioxide and water. These reactions form the tricarboxylic acid cycle (also known as the citric acid cycle), displayed in Figure 2.3.



2.4.3 Oxidative phosphorylation

Oxidative phosphorylation is the process by which oxygen is used as the final electron acceptor in mitochondria, so that free energy of the pyruvate molecule can be used to phosphorylate adenosine diphosphate (ADP) to ATP (Siesjo 1978). This occurs in the electron transport chain, illustrated in Figure 2.6. The terminal electron acceptor in this series is cytochrome c oxidase (CCO). During the oxidisation of reduced cytochrome c, oxygen is converted to water (Cooper 2002). CCO has three redox centres: the CuA, haeme a and haeme a₃-CuB centres. Electrons pass through these centres in succession before being passed on to oxygen.

As NADH is oxidised, there is a large decrease in energy. This is used to pump protons from the mitochondria into the intermembrane space. The resulting electrochemical gradient creates a proton motive force which in turn drives ATP synthesis.

2.4.4 Malate-aspartate shuttle

As mentioned above, it is important that cytoplasmic NADH is reoxidised in order for respiration to occur repeatedly. However, NADH cannot cross the mitochondrial membrane. The cell instead employs a shuttle system to move other metabolites across as depicted in Figure 2.7, which in turn reduces mitochondrial NAD⁺.

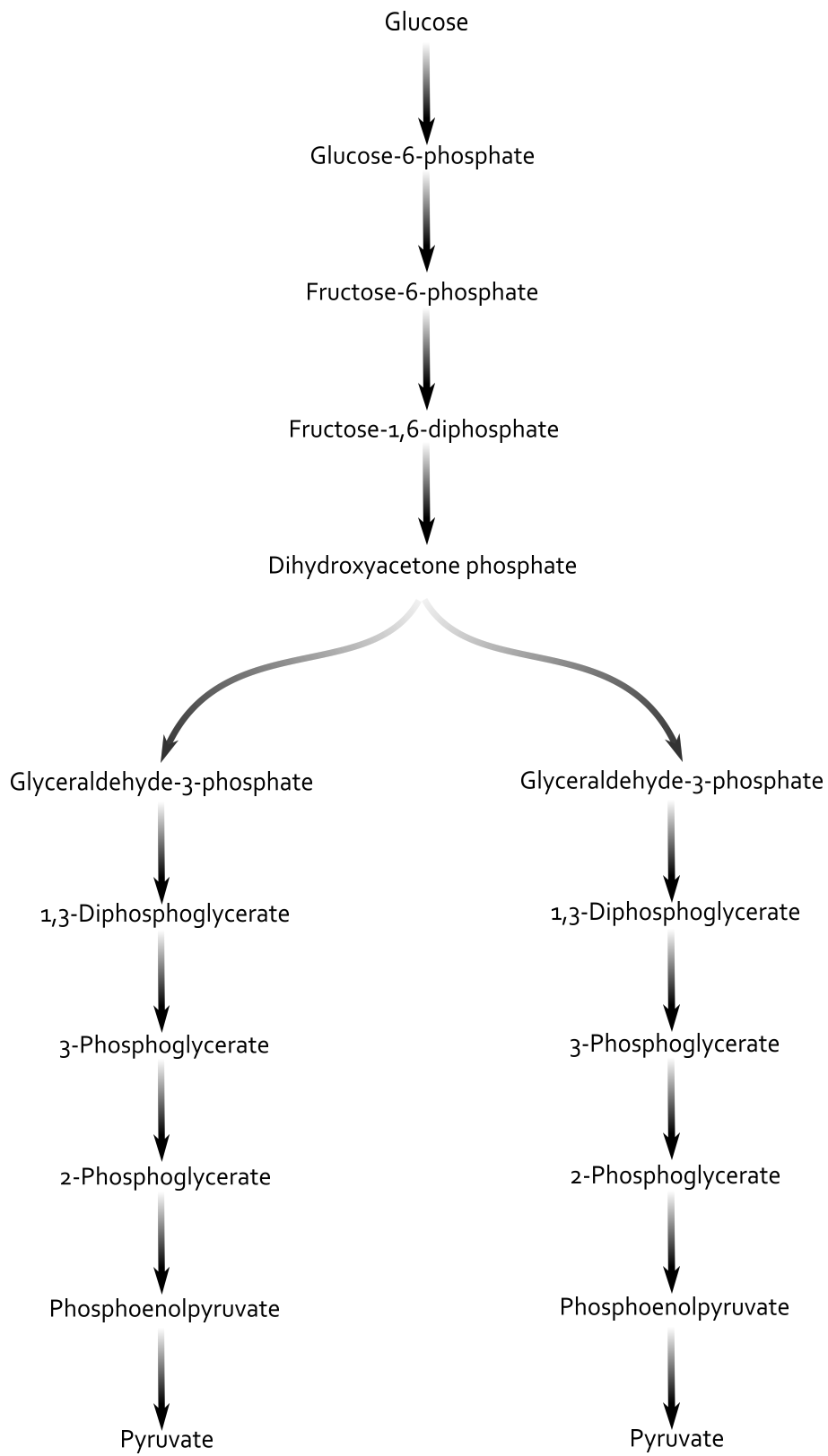


Figure 2.4: Glycolysis.

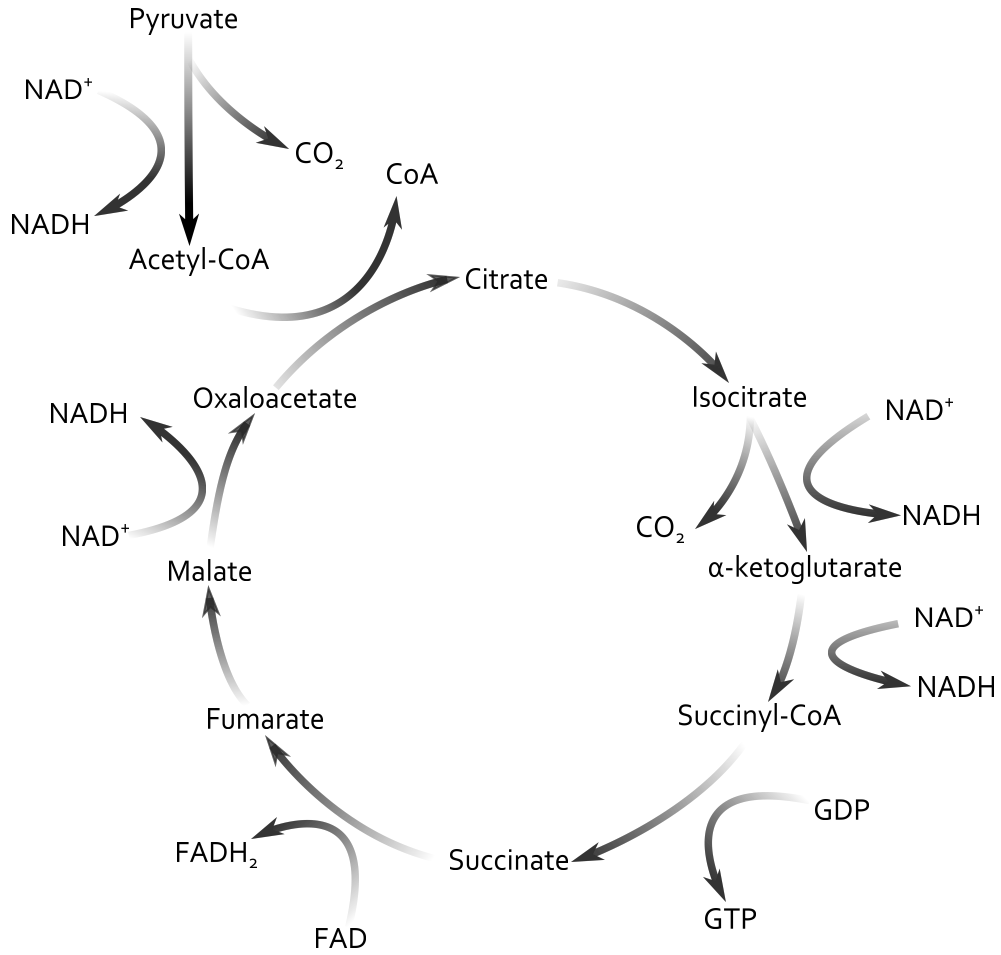


Figure 2.5: The tricarboxylic acid cycle.

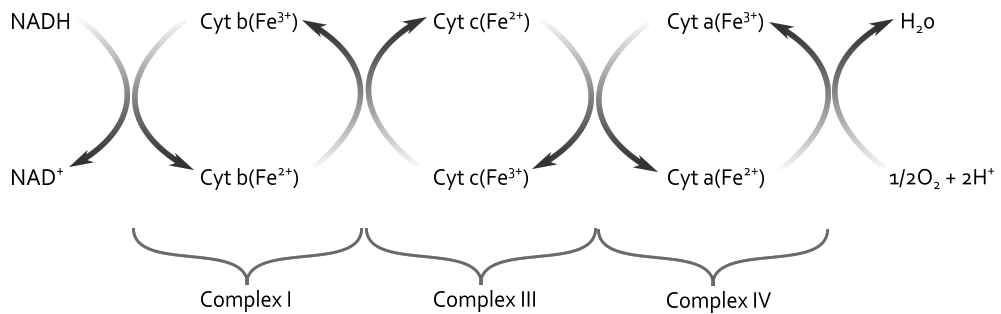


Figure 2.6: Oxidative phosphorylation.

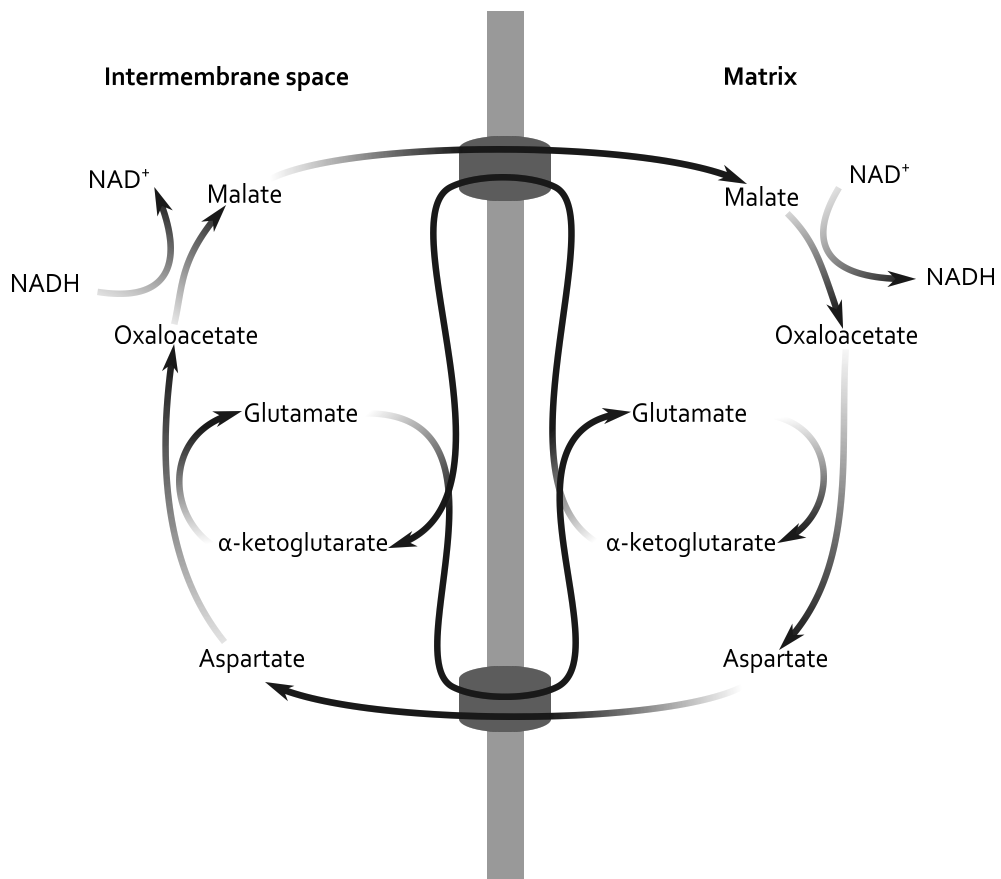


Figure 2.7: The malate-aspartate shuttle.

2.5 Brain pH

pH plays an important role in cellular function, as it maintains the structure (and therefore function) of proteins. Compartmentalisation in eukaryotic cells separates specific functions in membrane-bound organelles, which allows energy to be stored as electrochemical gradients (Casey et al. 2010). The protonation or deprotonation of biological surfaces results in changes in charge, crucial for many metabolic reactions (Casey et al. 2010). The generation of energy in the cell is also dependent on the driving force for proton movement - the proton-motive force (Casey et al. 2010). Intracellular pH is therefore strictly controlled and maintained at approximately 7.03 but varies among different organelles (Kendall et al. 2011; Casey et al. 2010). Extracellular pH lies approximately 0.3-0.4 units above (Kendall et al. 2011). The immature brain is particularly sensitive to shifts in pH, with changes of 0.05pH units significantly affecting network activity (Helmy et al. 2012). Seizures following increases of 0.2pH units have also been observed (Helmy et al. 2012).

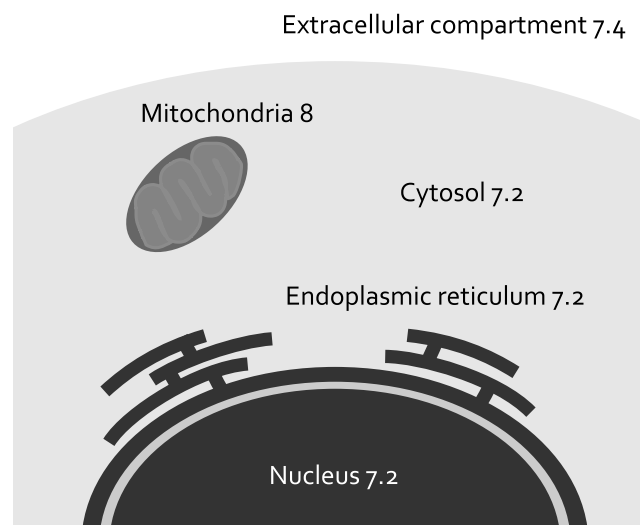


Figure 2.8: Differences in pH among different organelles of the cell. Adapted from Casey et al. (2010) and Uria-Avellanal and Robertson (2014).

2.5.1 Regulators of intracellular pH

A number of different reactions in the cell are known to affect pH. The cell's cytoplasm acidifies due to the actions of a number of metabolic pathways such as glycolysis generating lactate and oxidative phosphorylation in the

mitochondria producing CO_2 . The following are considered to play an important role is regulating pH levels by making the cytoplasm more alkaline.

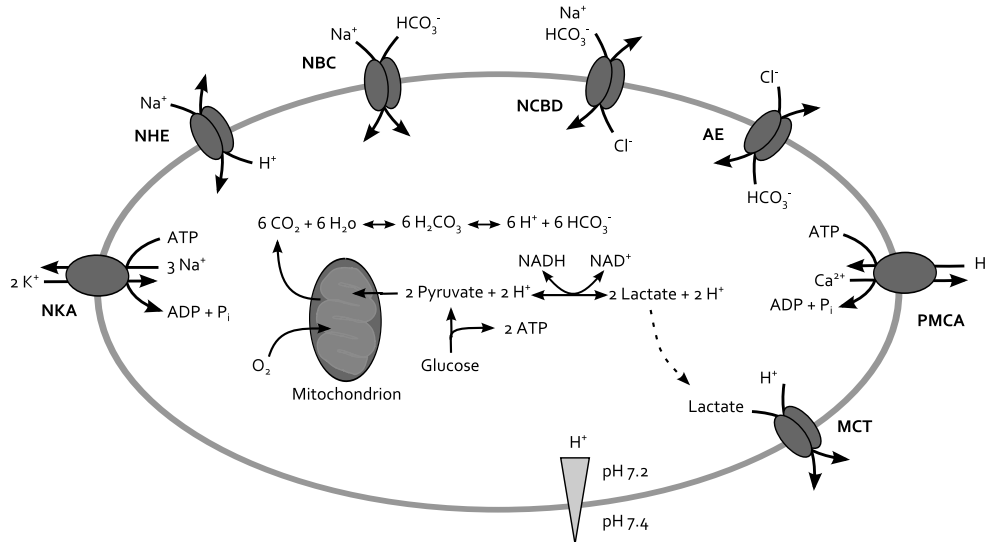


Figure 2.9: Processes regulating intracellular pH. The main transporters on the plasma membrane responsible for alkalinisation are the Na^+/H^+ exchangers (NHEs) and $\text{Na}^+-\text{HCO}_3^-$ transporters (NBCs). Some cell types also have Na^+ -dependent $\text{Cl}^- - \text{HCO}_3^-$ exchangers (NDCBEs). These transporters use the potential energy stored by the Na^+ gradient facilitated by the $\text{Na}^+ - \text{K}^+ - \text{ATPase}$ pumps (NKAs) to drive solute transport. These mechanisms are counterbalanced by the acidifying processes such as the $\text{Cl}^- - \text{HCO}_3^-$ anion exchangers (AEs) and plasma membrane $\text{Ca}^{2+} - \text{ATPases}$ (PMCAs), which transport Ca^{2+} out of the cell in response to stimuli that increase intracellular concentrations. In anaerobic metabolism, monocarboxylate transporters (MCTs) move lactate across the membrane. pH_c cytosolic pH; pH_o extracellular pH. Adapted from Casey et al. (2010).

Sodium/hydrogen exchanger The Na^+/H^+ exchangers (NHEs) are a family of ion integrate membrane transport proteins that maintain intracellular pH in many mammalian cells by transferring Na^+ ions into cells and H^+ ions out in a 1:1 ratio. They are thought to play crucial role in protecting cells from internal acidification (Uria-Avellanal and Robertson 2014).

Sodium-bicarbonate cotransporter As an end product of the process of mitochondrial energy production, eukaryotic cells constantly produce CO_2 . In water, this is a conjugate acid :



Transport proteins on the plasma membrane transfer HCO_3^- across. Of these,

the Na^+ - HCO_3^- transporters (NBCs) are predominant, moving both ions in the same direction, although the stoichiometry is different among its isoforms (Casey et al. 2010).

Sodium-potassium ATPase pump The above sodium transporters use energy stored by the inwardly directed electrochemical Na^+ gradient that is established by Na^+ - K^+ -ATPase pumps (NKAs) to drive solute transport.

Lactate- H^+ cotransporter Monocarboxylate transporters (MCTs) enable the cotransportation of monocarboxylic acids (mainly lactate) and protons out of the cell (Casey et al. 2010). Lactate accumulates in the cytosol following anaerobic respiration (see Section 2.4.1).

Another process known to contribute to alkalization of the cell is Na^+ -dependent $\text{Cl}^-/\text{HCO}_3^-$ exchangers (NDCBEs). Acidification occurs due to $\text{Cl}^-/\text{HCO}_3^-$ or anion exchangers on the plasma membrane as well as calcium-ATPases, exchanging cytosolic Ca^{2+} for extracellular H^+ in response to stimuli that increase intracellular Ca^{2+} (Casey et al. 2010).

Mitochondrial pH is decidedly more alkaline (pH~8) than the cytoplasm, due to the workings of the electron transport chain (see Figure 2.6). In the event of mitochondrial-dependent apoptosis, early changes in mitochondrial pH have been deemed indicative (Casey et al. 2010).

Copyright material removed.

Figure 2.10: Sodium-potassium ATPase pump (Thompson 2000).

2.6 Hypoxia-ischaemia

Asphyxia indicates a global or local decrease in oxygen supply and a concurrent accumulation of end products of energy metabolism such as carbon dioxide and lactate (Helmy et al. 2011). Continued asphyxia, known as *intrapartum asphyxia*, leads to hypoxic and hypercapnic conditions characterised by acidosis (Helmy et al. 2011). Hypoxia describes an environment of low oxygen - the extreme case, the absence of oxygen is referred to as anoxia. Hypercapnia implies a high carbon dioxide environment. In preterm neonates,

poor cerebral oxygenation saturation in the first few weeks after birth is associated with neurodevelopmental outcome (Verhagen et al. 2014).

Ischaemia is a decrease in blood supply to tissue, which then often leads to hypoxic conditions. Ischaemia may be local, affecting part of the brain as in the case of arterial or venous stroke, or global, as in the case of cardiac arrest (Lee et al. 2000).

2.6.1 pH and hypoxia-ischaemia

pH is vital for neuronal survival after trauma (Helmy et al. 2011). Perinatal asphyxia is often characterised by profound acidosis ($\text{pH} < 7$) (Helmy et al. 2011, 2012; Rehncrona et al. 1980). Acidosis in these cases acts as a protective mechanism, and suppresses neuronal activity. Alkalosis, on the other hand, increases the excitability of brain tissue (Helmy et al. 2011). Human infants often display normal cerebral energetics shortly after intrapartum hypoxia-ischemia. Intracellular brain pH neutralises within 5 to 15 minutes of reperfusion (Robertson et al. 2002). However, in those with adverse outcome, even with adequate oxygenation and circulation, phosphocreatine (PCr) and nucleotide triphosphate (NTP, mainly ATP) decrease and Pi rises in the first days of life (Uria-Avellanal and Robertson 2014). An alkaline rise in cerebral intracellular pH has also been observed during this phase. These metabolic changes - called secondary energy failure (SEF) - have been linked to severe neurodevelopmental outcomes in human neonates, with more extensive cerebral injuries exhibiting a more alkaline intracellular pH (Robertson et al. 2002; Uria-Avellanal and Robertson 2014).

Studies using magnetic resonance imaging (MRI) methods found that intracellular brain pH during the first 2 weeks after birth in infants with severely abnormal MRI versus normal MRI was 7.24 versus 7.04. In those infants who died or had a severe neurodevelopmental impairment compared to those with normal outcome was 7.28 to 7.11. In fact, an intracellular pH greater than 7.15 in the first 2 weeks was highly indicative of abnormal (mild, moderate, and severe/dead) neurodevelopmental outcome (Robertson et al. 2002). Brain alkalosis continued for up to 20 weeks in neonates with severe outcome .

There is increasing evidence that following ischaemia, high levels of lactate aid neuronal survival. Lactate takes approximately 30 mins of reperfu-

sion to clear. After 12-24 hours a secondary rise in lactate occurs. Lactate and N-acetyl-aspartate (NAA) – an amino acid found mostly in neurons in the CNS – provide a useful marker of cerebral health in the aftermath of hypoxia-ischaemia. During transient hypoxia-ischaemia, lactate concentration rises whilst NAA falls. After successful resuscitation both return to almost baseline levels, followed however by a secondary increase in lactate and slower decrease in NAA in the next few hours. The Lac/NAA peak area ratio obtained between days 5 and 14 after birth is thought to be an accurate biomarker of long-term neurodevelopmental outcome in patients with neonatal encephalopathy (Uria-Avellanal and Robertson 2014). Brain alkalosis has also been associated with increased cerebral lactate/creatinine ratio (Robertson et al. 2002).

Activation of the Na^+/H^+ exchangers (NHEs) results in a rapid normalisation of intracellular pH (Wakabayashi et al. 1992). Helmy et al. showed that the alkaline pH does not extend to the blood or body, and suggest that alkalosis may be caused by the movement of acid equivalents across the blood-brain barrier (Helmy et al. 2012). Their experiments inhibiting NHEs did not result in brain alkalosis after asphyxia, which supports this hypothesis. Robertson et al. (2013) also conducted a study using NHE inhibitors in piglets which showed a decrease in both Lac/NAA and lactate/creatinine 48 hours after the hypoxic-ischaemic insult. A separate study conducted in mice found that areas of the brain that inhibited severe alkalosis did not necessarily correspond to those areas with the most acidic response during hypoxia-ischaemia, nor the worst tissue damage (Kendall et al. 2011).

Studies in rats have also shown that fast restoration of normal carbon dioxide conditions - normocapnia - leads to brain alkalosis and seizures. However, graduated restoration of normocapnia after asphyxia did not result in alkalosis and nearly no seizures were triggered (Helmy et al. 2011), suggesting a link to pH (Uria-Avellanal and Robertson 2014).

Clinical monitoring and manipulation of intracellular brain pH, especially in preventing rebound brain alkalosis, has been suggested as a potential neuroprotective strategy (Robertson et al. 2002).

2.7 Adult, neonate and piglet brains

There are numerous differences in brain anatomy and function in the various stages of its development, which is also dependant on gestational age. Preterm birth occurs before 37 weeks of gestation and accounts for 6% to 10% of births in the Western world (Polin et al. 2010). The most notable changes in preterm brain development are increases in overall size and cortical folding. The brain has a smooth appearance during early gestation but develops the typical convoluted pattern, increasing the surface area of the brain. From 29 weeks' gestation until term, cortical grey matter volume expands from 60ml to 160ml (Rutherford 2002). The continued process of cortical folding can be observed in the postnatal phase using various imaging techniques (Rutherford 2002).

Development of vascular complexity continues to increase through the postnatal phase (Polin et al. 2010) and variations in the vascular arrangement described in Section 2.2 exist in both humans and animals (Edvinsson et al. 1992). Studies of neonatal preterm brains have discovered variations the development of the circle of Willis at term equivalent age (Malamateniou et al. 2009; van Kooij et al. 2010) (Figure 2.11). The newborn piglet brain has an intact circle of Willis and a blood vessel plexus at the base of the brain. This makes the piglet brain unsuitable for investigating complete cerebral ischaemia, but nevertheless suitable for the study of hypoxia-ischaemia as discussed in Chapter 3, Section 3.3 (Cady et al. 2008).

Copyright material removed.

Figure 2.11: Variations in the circle of Willis in preterm neonates. (a) Normal type, (b) dominant segment on the right indicated with a white arrow and (c) double-sided fetal type posterior cerebral arteries (van Kooij et al. 2010).

Oxygen tension in adult blood is approximately 4 to 5 times that found in fetal blood, however fetal arterial blood oxygen content at term are not much lower than that in the adult. This is due to the higher oxygen affinity of fetal haemoglobin (HbF). Maternal blood is slightly hypocarbic (P_{CO_2} 32mmHg) and alkalotic (pH 7.42). On the other hand fetal blood is slightly hypercarbic

(P_{CO_2} 45mmHg) and acidotic (pH 7.34). Fetal blood releases H^+ and CO_2 as it runs through the exchange vessels causing an increase in pH and decrease in P_{CO_2} while the opposite occurs in maternal exchange vessels (Polin et al. 2010). When pH decreases below 7.2, the Bohr effect is greater for fetal blood than maternal blood. In human neonates, as the dissociation curve also shifts toward the right as the concentration of HbF falls.

Although the higher oxygen affinity of HbF is well adapted for oxygen uptake in the placenta, it is disadvantageous in postnatal life. With adequate lung function, the high oxygen affinity at low oxygen tensions has no benefit as the pulmonary circulation is exposed to oxygen tension around 80 mmHg or higher. At the tissues a lower P_{50} means a lower driving potential for oxygen diffusion, a force of vital importance as oxygen consumption increases by 100-150% in the first few days of life. Thus fetal haemoglobin is gradually replaced by adult haemoglobin, with P_{50} increasing to reach normal adult values in the first 4-6 months of life (Polin et al. 2010).

The autoregulative capacity of the human neonatal brain is unclear at present, mainly due to the difficulty in conducting experimental studies (Vutskits 2014; Greisen 2005). Verma et al. (2000) found a significant relationship with gestational age but not postnatal age. Observations during preterm neonatal intensive care have been inconclusive, with some studies showing a linear relationship between CBF and arterial blood pressure (Lou et al. 1979), while others found no correlation (Tyszczyk et al. 1998). Increasing periods of impaired autoregulation have been linked to bad neurological outcome. Low gestational age and birth weight have also been shown to be a factor (Vutskits 2014). Wong et al. (2008) found that a coherence between cerebral oxygen saturation and mean arterial blood pressure indicated impaired autoregulation in clinically ill preterm infants, and was strongly associated with mortality.

Copyright material removed.

Figure 2.12: Autoregulation curve for neonates. The flat section represents the autoregulatory plateau. The upper threshold is not well estimated (Greisen 2005).

A range of CBF values have been reported in literature of preterm and term neonates, with term neonates thought to have double the CBF of the preterm. These values are presented in Table 2.1 along with piglet and adult values for comparison. Also included in the table are measurements of CCO, which is an invasive procedure and so very little is known about the true concentrations in human neonates. CMRO₂ and blood pressure values vary in literature as well. Mean arterial blood pressure as low as 23 mmHg has been recorded in preterm neonate, while adult healthy human values range close to 100 mmHg. Haemoglobin concentration in blood has been found to increase after birth (Jopling et al. 2009), and subsequently decrease with age. Intracranial pressure is relatively similar in both preterm and term infants, at approximately 5 mmHg, with higher values recorded in adults (7-15 mmHg).

Table 2.1: A comparison of physiological measurements in healthy preterm, term and adult patients.

	Piglet	Preterm neonate	Term neonate	Adult
CBF (ml 100 g ⁻¹ min ⁻¹)	39.7 ± 4.6 – 75.4 ± 15.2 (Springett et al. 2001)	4.9 – 23 (Altman et al. 1988), 12.2 (Meek et al. 1999), 19.8 ± 5.3 (Greisen 1986), 11 – 26 (Edwards et al. 1988)	9.0 – 73 (Altman et al. 1988)	59 ± 21 and 11 ± 4 in high and low compartments (Elwell et al. 1994),
Concentration of cytochrome-c-oxidase (CCO) in tissue (μM)	2.21 ± 0.16 (Springett et al. 2000)	unknown, presumed equivalent to piglet	unknown, presumed equivalent to piglet	approximately 5.5 within range of normal range of HbO ₂ (Cooper et al. 1997)
Cerebral metabolic rate of oxygen consumption (CMRO ₂) (μmol 100 g ⁻¹ min ⁻¹)	89.32 – 134.0 (Brown et al. 2003), 113 ± 12 – 122 ± 19 (Springett et al. 2001)	30.82–68.33 (Elwell et al. 2005)	64.13 (Polin et al. 2010)	142.91 – 147.38 (Polin et al. 2010), 147.38 (Chudler)
Mean arterial blood pressure (mmHg)	50.9 ± 4.4 (Springett et al. 2001)	23.7 – 39.3 (Tyszczuk et al. 1998), 28 – 45 (Pejovic et al. 2007)	45 – 55 (Pejovic et al. 2007), 56.5 – 60.8 (Nascimento et al. 2002)	80 – 100 mmHg (Elwell et al. 1996), 95 (Babbs 2012)
Concentration of haemoglobin in blood (mM)	5.59 – 6.21 (Lossec et al. 1998)	9.75 (Jopling et al. 2009)	11.17 (Jopling et al. 2009)	7.45 – 9.31 (Beutler and Waalen 2006)
Intracranial pressure (mmHg)	4.5 (Soul et al. 2000)	5.1 ± 0.9 (Easa 1983)	5.3 ± 1.3 (Easa 1983), 1.5 – 6 (Steiner and Andrews 2006)	7 – 15 (Steiner and Andrews 2006)

Chapter 3

Clinical Measurements

One of the primary aims of the models presented in this thesis is to aid in the interpretation of clinical measurements. There exist various technologies to examine a living body, via the quantification of specific chemicals or its translation to imagery. However, the fundamental biological processes and structure that give rise to the changes observed in these signals is not always clear. The technology is often limited in the detail it can offer – namely it can indicate *when* a change occurs but not necessarily *how* or *why*. Therefore in order to maintain clinical utility of these signals, it is important to be able to obtain meaningful inferences beyond simple correlations with outcome.

3.1 Methods of measurement

The data used in this thesis has been obtained largely from non-invasive techniques employed to monitor subjects in neonatal intensive care and in experiments conducted in piglets. Non-invasive methods are advantageous both in the clinic and in experimentation as results are less subject to external noise and unwanted side effects. These methods and the quantities they monitor are briefly described below.

3.1.1 Near-infrared spectroscopy

Colour-inducing compounds called chromophores in tissue absorb light as it passes through the body. Visible light has high absorption and scattering in the body, making it unsuitable for measurement. However, near-infrared light (wavelength 650 - 1000nm) is less absorbed by water and so penetrates

further. In addition, the only compounds in the mammalian brain that affect absorption signals with changes in oxygen concentration are cytochrome aa3 and haemoglobin. For these reasons near-infrared spectroscopy is a good method for the measurement of cerebral haemodynamics and oxygenation (Wray et al. 1988). NIRS is often used to investigate task-evoked responses in the brain, using for example somatosensory or visual stimuli. This technique is known as functional NIRS (fNIRS).

Copyright material removed.

Figure 3.1: Absorption spectra for different chromophores in human tissue. CtOx is cytochrome oxidase (Scholkmann et al. 2014).

Haemoglobin

NIRS can be used to estimate changes in the concentrations of oxygenated haemoglobin (ΔHbO_2) and deoxygenated haemoglobin (ΔHHb) (see Section 2.2). The total haemoglobin concentration (ΔHbT) gained by adding the two can reflect changes in cerebral blood volume. The difference between the two values (ΔHb_{diff}) may however be a more reliable measurement, as some of the signal noise is removed in the subtraction.

Cytochrome-C-Oxidase, CCO

The difference spectrum between oxidised and reduced CCO can be detected in-vivo using NIRS (Tisdall et al. 2007; Cooper et al. 1997) (see Section 2.4.3 for explanation of CCO). The enzyme contains four redox active metal centres, one of which – the binuclear CuA centre – absorbs near-infrared light well. However, the concentration of this centre is less than 10% that of haemoglobin, making detection quite difficult (Cooper and Springett 1997). Given that the total concentration of CCO in tissue remains constant, the NIRS CCO signal represents changes in the redox state of CCO (ΔoxCCO).

The importance of this signal lies in its mitochondrial origin, giving a valuable measure of cellular mitochondrial oxygen consumption in comparison with ΔHbO_2 and ΔHHb which are intravascular concentrations. In particular, in the observation of the brain, the haemoglobin signal is prone to

detecting concentrations in skin as well, while concentrations of CCO in skin are lower than in the brain and nonexistent in red blood cells (Tisdall et al. 2007).

Tissue Oxygenation Index, TOI

A measure of oxygen saturation recorded by NIRS, TOI is calculated as a ratio of oxyhaemoglobin to the total haemoglobin concentration:

$$TOI = \frac{[HbO_2]}{[HbO_2] + [HHb]} \times 100\% \quad (3.1)$$

TOI is sometimes referred to as the tissue oxygen saturation (TOS), depending on the instrumentation used.

3.1.2 Magnetic resonance spectroscopy, MRS

This technique uses the principle of nuclear magnetic resonance (NMR). Nuclei with an odd number of protons and/or neutrons have magnetic properties (eg. ^1H , ^{31}P , ^{13}C), and when placed in a magnetic field tend to align and rotate - 'precess' - to be parallel with the field. This precession occurs at a frequency known as the Larmor frequency. If a pulse of radiofrequency (RF) energy is applied at the Larmor frequency, the alignment of the nuclei is disrupted. When the pulse is removed the nuclei move back into alignment, emitting a RF signal at the Larmor frequency. By measuring this emitted frequency it is possible to determine the type of atom present in a sample. In the case of a biological sample, composed of various different atoms, it is possible to use a Fourier transform to analyse the contributing compounds. MRS has been invaluable in investigating neonatal cerebral disorders (Robertson and Wyatt 2004).

A more popular use of this technique is in imaging. MRI can provide a valuable visual indication of the state of the brain, especially in neonatal development. The maturation of white matter and the progression of cortical folding can be observed and quantified by this method (Rutherford 2002; Paus et al. 2001). Functional MRI (fMRI) is often used to detect regional activation of the brain, mapping brain function in both the developing young and in adults (Robertson and Wyatt 2004; Logothetis 2008; DeCharms 2008). The blood-oxygenation level dependent (BOLD) fMRI signal detects changes

in blood oxygenation, where an increase in BOLD is consistent with a drop in venous deoxyhemoglobin concentration (Hyder et al. 2001).

Copyright material removed.

Figure 3.2: MRI images of healthy infants at (A) 30 weeks gestation, (B) term, (C) 6 months and (D) 1 year (Robertson and Wyatt 2004).

Copyright material removed.

Figure 3.3: MRI images of (A) focal injury in an infant aged 11 days with Sarnat stage II neonatal encephalopathy and (B) global injury in an infant aged 12 days with Sarnat stage III (Robertson and Wyatt 2004).

Lactate

Found in almost undetectable concentrations in normal healthy tissue, the presence of lactate implies the failure of aerobic respiration, and the occurrence anaerobic glycolysis (Gujar 2005; Bertholdo et al. 1980; Soares and Law 2009) (see Section 2.4.1). Therefore, lactate is expected to rise under anoxic and hypoxic conditions. However, a small peak may be seen in the newborn brain during the first few hours of life (Bertholdo et al. 1980). Acute inflammation leading to activation of macrophages may also cause an increase in lactate (Soares and Law 2009; Currie et al. 2013).

Creatine, Cr

The peak associated with creatine originates from at least two compounds: creatine (Cr) and phosphocreatine (PCr). Since both these molecules are associated with ATP, the creatine peak is viewed as a marker of brain energy metabolism (Gujar 2005; Bertholdo et al. 1980; Soares and Law 2009; Currie et al. 2013). Cr concentration is relatively stable, and often used as an internal reference for calculating metabolite ratios (Gujar 2005; Bertholdo et al. 1980; Soares and Law 2009; Currie et al. 2013). However, variation has been

observed between individuals and regions of the brain (Bertholdo et al. 1980; Soares and Law 2009; Currie et al. 2013). Also, as Cr does not originate in the brain, the concentration can be affected by systemic diseases (Bertholdo et al. 1980; Soares and Law 2009; Currie et al. 2013). Tissue death may also cause a loss of Cr (Gujar 2005; Currie et al. 2013).

N-acetyl Aspartate, NAA

Specific to the brain, NAA is produced in neuron mitochondria before being transported to the neuronal cytoplasm and along axons (Bertholdo et al. 1980; Soares and Law 2009). NAA is thus present in both white and grey matter and is used as a marker of neuronal and axonal viability and density (Bertholdo et al. 1980; Soares and Law 2009). The role of NAA has not yet been clearly deciphered, however a loss of NAA is seen in many white matter diseases such as hypoxic encephalopathy and is generally a sign of neuronal loss (Gujar 2005; Bertholdo et al. 1980; Soares and Law 2009). The lactate/NAA peak area ratio is an accurate magnetic resonance biomarker of outcome after neonatal encephalopathy (Thayyil et al. 2010). There is a natural rise in NAA in the developing brain, and concentrations in grey matter and have been found to be higher than in white matter in the adult brain (Currie et al. 2013).

Copyright material removed.

Figure 3.4: MRS spectra from a piglet during a hypoxia-ischaemia experiment that subsequently developed severe secondary energy failure; (a) before HI, (b) 1.6 h after HI, and (c) during secondary energy failure 23.4 h after HI. (Cady et al. 2008)

Nucleotide triphosphate, NTP

The nucleotide triphosphate (NTP) measurement arises predominantly from ATP, which accounts for approximately 70% of the signal (Bainbridge et al. 2013). Hence, changes in the NTP signal can be used to indicate changes in ATP. NTP is often compared against the exchangeable phosphate pool (EPP), as the ratio is considered as a more stable indicator of ATP, where

$$EPP = Pi + PCr + 2\gamma\text{-NTP} + \beta\text{-NTP} \quad (3.2)$$

as in Cady et al. (2008). α -, β - and γ -NTP peaks can be viewed on the MRS spectrum, which can be used also to calculate pH (see below).

Intracellular pH

Two methods of estimating the value of intracellular pH in the brain have been used here. The first is based on inorganic phosphate (Pi) and phosphoethanolamine (PEt), and the second on ATP shifts.

Pi-Pet Measurement Petroff et al. used the chemical shift difference between the Pi resonance and, as a reference, PCr resonance to determine intracellular pH (Petroff et al. 1985). This was done using the Henderson-Hasselbalch equation and a suitable calibration curve:

$$pH_{Pi} = 6.77 + \log_{10} \left(\frac{\delta_{Pi} - 3.29}{5.68 - \delta_{Pi}} \right) \quad (3.3)$$

where δ_{Pi} is the amplitude weighted mean of the Pi components (Cady et al. 2008).

Phosphoethanolamine (PEt) is a compound involved in the construction of cell membranes (Azzopardi et al. 1989). Together with phosphocholine, forms the majority of the phosphomonoester (PME) peak in the MRS spectrum. PEt has been also been used to estimate intracellular pH (Corbett et al. 1987; Pettegrew and Withers 1988), using the following titration curve:

$$pH_{PEt} = 5.625 + \log_{10} \left(\frac{\delta_{PEt} - 3.190}{6.946 - \delta_{PEt}} \right) \quad (3.4)$$

where we used the PME peak for δ_{PEt} . The average of the two measures can be used to obtain a Pi-Pet measurement (pH_{Pi-Pet}).

ATP Measurement Williams and Smith presented a method for assessing intracellular pH from ATP shifts, via a software named MAGPAC (MAGnesium and PH from ATP Calculation) (Williams and Smith 1995). This tool was created by numerically modelling the three MRS shift differences of NTP (mainly ATP) ($\delta(\gamma - \alpha)$, $\delta(\alpha - \beta)$, $\delta(\gamma - \beta)$) using model calibration solutions, prepared as a function of total $[Mg]/[ATP]$ and pH. To obtain pH

estimates from our experiments, the mean of each of the three α -, β - and γ -NTP shifts are input into the MAGPAC program.

Comparisons Differences have been detected in the pH measurement techniques above. Even with similar titration conditions, in one case, the baseline value of pH_{PEt} was observed to be more acidic than pH_{Pi} and pH_{ATP} , with the former slightly more alkaline than the latter (Cady et al. 2008). However, baseline values of pH_{PEt} below pH_{Pi} and pH_{ATP} have also been reported. These results may arise because pH_{Pi} originates from not only intracellular Pi but extracellular Pi as well. Also PEt may be more prominent in more acid intracellular compartments or tissues, such as in immature cerebral tissue (Cady et al. 2008).

Pi is also present in dead cells. On the other hand, pH_{ATP} is particular to the intracellular space of viable cells. PEt is also thought to be essentially intracellular.

In the aftermath of hypoxia, pH_{Pi} and pH_{PEt} were observed to attain baseline values in piglets after approximately 2 hours (Cady et al. 2008). However, in newborn infants more than 48h old with very severe injuries, pH_{Pi} was more alkaline (Robertson et al. 2002). Similarly, in both piglet and rat brains pH_{ATP} and other intracellular pH measures have indicated alkalosis after hypoxia-ischaemia and ischaemia (Cady et al. 2008; Williams and Smith 1995) (see Section 2.6.1).

3.1.3 Systemic measurements

As part of normal clinical practice, systemic measurements are often recorded simultaneously with other measurements. A sample of piglet arterial oxygen saturation and blood pressure during a hypoxic-ischemic phase is illustrated in Figure 3.5.

Arterial Oxygen Saturation

Pulse oximetry, like NIRS, uses light to measure blood oxygenation. Two wavelengths of light are used to calculate the oxygen concentration of haemoglobin in pulsating blood (SpO_2) and non pulsating blood separately (Aoyagi 2003). The pulsatile volume changes are assumed to be caused by changes in arterial volume. Hence, SpO_2 is a measure of arterial oxygen saturation (SaO_2).

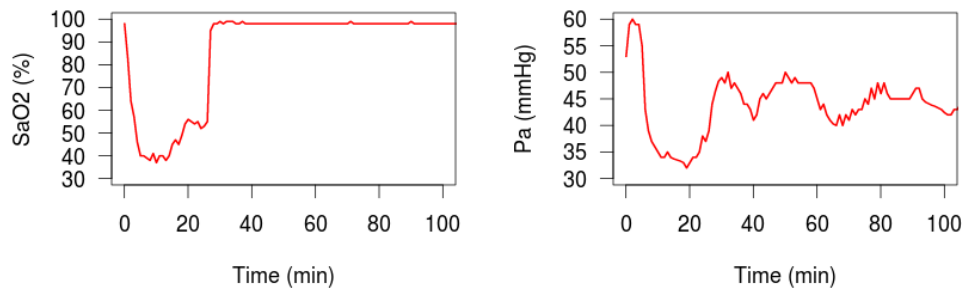


Figure 3.5: Sample arterial oxygen saturation and blood pressure from a hypoxia-ischaemia experiment in a piglet.

Blood Pressure

A sphygmomanometer is the most common device for measuring blood pressure. It consists of an inflatable cuff, usually placed on the upper arm. Measurements are quoted as the diastolic (maximum) and systolic (minimum) arterial pressures, and are for a normal patient on average 120 and 80mmHg respectively.

Partial Pressure of Carbon Dioxide

End tidal CO_2 (EtCO_2) is the partial pressure of carbon dioxide (PCO_2) breathed out during respiration. This carbon dioxide diffuses out of the blood in the capillaries to the air in the alveoli of the lungs. Under normal conditions there is an equilibrium between the blood and the air, and so EtCO_2 is equivalent to the arterial partial pressure of carbon dioxide, $P_a\text{CO}_2$ (Ward and Yealy 1998).

An infrared capnometer, often used to measure ventilation during anaesthesia, can be used to measure EtCO_2 (Kodali 2013). The normal measurement is approximately 35-40mmHg.

3.1.4 Multimodal measurements

Recent studies have utilised combinations of the above measurement techniques to provide a comprehensive approach to investigating changes in the living body (Tachtsidis et al. 2012; Worley et al. 2012; Tisdall and Smith 2007; Bainbridge et al. 2013). This has facilitated the focus away from rigid physiological target setting to the possibilities of more individual and patient-specific approaches (Tisdall and Smith 2007). Section 3.3 details some of the

multimodal hypoxia-ischaemia and functional studies conducted in animals and neonates.

3.2 Interpreting measurements

"But there are also unknown unknowns – the ones we don't know we don't know."

— Donald Rumsfeld

Measurements from clinical instrumentation and patient history provide us with a wealth of information, that much is true, and as technologies advance we will doubtless be, if not already, in the midst of a clinical data quagmire. However, we are still far from gaining the complete knowledge of the human body at every possible scale. There are thus "*unknown unknowns*", things that we do not yet know exist. While methods of mathematical modelling may facilitate suggestions of the existence of such structures/processes, it is impossible to model the unknown outright. Hence it is important to bear in mind that the picture painted by measurements available (and therefore the model) is far from complete.

3.2.1 Quality of signals

The measurement techniques above carry a varying degree of instrumental noise, apart from that gained from the handling probes or due to patient movement. The NIRS signals obtained for this thesis did not exhibit much noise, whereas the MRS signals did, especially those measuring NTP. Most of the signals have been preprocessed and smoothed, either using an algorithm or manually. Where this has been done, it has been indicated in the accompanying text.

It is often difficult to ascertain whether an abrupt change in the signal is the result of unwanted noise or that of a 'valid' physiological change that has been recorded. While time periods and concurrence with simultaneous recordings in other signals can provide clues, the end decision is clearly subjective. Therefore, I have made a particular effort to keep the use of smoothing methods at a minimum.

3.2.2 Region and frequency of measurement

The measurements are limited by the region of the brain that they cover. Near infrared can penetrate biological tissue relatively well, but is hampered by extracerebral structures such as the skull and scalp which detract light (Brown et al. 2003). Hence it is more effective in younger subjects such as in neonates and piglets, where the skull is not as thick. Indeed in piglet experiments the NIRS source and detector probes can be placed on either side of the head, thus enabling a measurement of the region in between. However, in adult patients, this is not possible and instead the probes are often placed a few centimetres apart from each other. It must also be noted that measurements gained from examining a single voxel of the cerebral space is not necessarily reflective of the brain as a whole.

Superficial fluctuations in oxygenation and blood flow in the skin are also known to contribute to noise. This is especially problematic in fNIRS experiments investigating task-evoked responses, where the emotional response of 'blushing' can often cause false positives (Kirilina et al. 2012).

NIRS instrumentation however does have the advantage of being a portable device that can be installed at the bedside and hence provide continuous commentary on the clinical state of patient. MRS on the other hand requires the patient to be exposed to an electromagnetic field, at present produced by a bulky expensive device. The effects of long term exposure to such fields is also unclear (Hartwig et al. 2009). It is therefore not feasible at present to record MRS at the bedside. While continuous recordings are obtained in the case of animal experimentation, long term MRS recordings of the human neonatal brain are rare.

Systemic measurement techniques such as the pulse oximeter are often applied far from the brain, and are employed in determining an overall measurement for the body. Thus they are not necessarily reflective of the exact values in the brain itself, but are assumed to provide a good indication.

The frequency of the various measurement techniques and instrumentation varies greatly. Some measurements are recorded per minute, and others per second. Higher frequencies naturally facilitate better resolution, but are more prone to noise.

3.3 Animal experiments and neonatal studies

Animal models are a vital resource of clinical knowledge, especially in the investigation of life-threatening events and conditions, such as hypoxia-ischaemia (HI), where carrying out controlled experiments on human subjects is not feasible. Several species have been used for both in-vivo and in-vitro experiments, including rats, mice, sheep, lambs, monkeys and piglets (Lodygensky et al. 2008; Yager and Ashwal 2009; Northington 2006; Longo and Packianathan 1997). The use of piglet in particular has increased in recent decades (Lind et al. 2007). However, animal experiments have the disadvantages of first, the possibility that findings in animals may not be applicable to humans, and second, the unwanted effects of the anaesthetics used. These can often interact with the body, and sometimes with each other if used in association. Anaesthetics can have different effects on different organs and thus influence the results (Bazin et al. 2004).

3.3.1 Hypoxia-ischaemia studies

Numerous groups have conducted hypoxia-ischaemia studies in piglets. Lorek et al. (1994) used ^{31}P -MRS to investigate secondary energy failure following HI in twelve piglets, induced by temporary hypoxemia (low blood oxygen) and occlusion of the carotid arteries. [PCr]/Pi and NTP/EPP ratios dropped to near zero during the HI phase and returned to baseline following reperfusion and reoxygenation. At 24 hours, although blood oxygen, glucose and pressure were normal, both ratios were observed to decrease again, while intracellular pH remained unchanged. The severity of the secondary energy failure was directly related to the magnitude of the energy depletion. Mehmet et al. (1994) used the same technique to observe that the extent of cell death due to apoptosis was directly related to the degree of high-energy phosphate depletion during HI. Penrice et al. (1997) employed both ^{31}P and ^1H -MRS alternately to detect the Lac/Cr ratio rise during HI, fall towards baseline, and then rise again by the 48 hour mark. Cady et al. (2008) used ^{31}P -MRS to determine early injury-severity biomarkers. NTP/EPP correlated linearly with severity, and alkaline intracellular pH approximately 2 hours after the insult indicated a severe injury as well. Bainbridge et al. (2013) using both ^{31}P -MRS and NIRS found oxidised CCO, PCr/EPP and NTP/EPP dropped during HI, and significant correlations

between oxidised CCO and ^{31}P -MRS ratios. Figure 3.7 shows the correlation between MRS-measured NTP/EPP and NIRS-measured oxidised CCO. Double-linear model was fitted, meeting at a threshold point, to show the change in the relationship. However, it is likely that in reality this change is more gradual. A study in neonatal rats found brain alkalosis following recovery from birth asphyxia to play a role in triggering seizures (Helmy et al. 2011). Another study in mice recorded the distribution of pH changes in the brain following the insult (Kendall et al. 2011) (Figure 3.8).

Copyright material removed.

Figure 3.6: MRS NTP measurements during hypoxia-ischaemia in piglets. Top - representative polynomial fit to NTP/EPP from 6 h after HI. NTP_{\min} is the minimum and used as the secondary energy failure index. Bottom - Linear regression of NTP/EPP at approximately 2 h after HI against NTP_{\min} (Cady et al. 2008).

Copyright material removed.

Figure 3.7: Correlation between MRS-measured NTP/EPP and NIRS-measured oxidised CCO measurements during hypoxia-ischaemia in piglets. Relationship changes significantly at a threshold point during HI (Bainbridge et al. 2013).

Copyright material removed.

Figure 3.8: pH maps (a-n) from 5 coronal brain sections from naive mice (b) or mice exposed to 60 min of 8% O_2 (hypoxia alone, H, c), carotid occlusion alone (CROC, d), carotid occlusion with additional 15- to 90-min hypoxia (e-h), and re-exposure (Reox) to normal room air after carotid occlusion and 90 min of hypoxia (i-n). Carotid occlusion with additional hypoxia (e-h) results in rapid onset of brain acidosis. Re-exposure to normal room air after occlusion and hypoxia results in rapid disappearance of acidosis and culminates with a global alkaline overshoot at 4-6 h. OB = Olfactory bulb; Ctx = cortex; Str = striatum; Hip = hippocampus; Thal = thalamus (Kendall et al. 2011).

3.3. Animal experiments and neonatal studies

These studies paved the way for neuroprotective strategies to be administered within hours of a perinatal insult to stop the cascade of irreversible injury (Robertson and Wyatt 2004). In particular, hypothermia – cooling the brain by 3-4°C was found to be effective in inhibiting apoptosis (Edwards et al. 1995; Trescher et al. 1997; Edwards et al. 1998) and reduced lactate accumulation (Amess et al. 1997). Drugs such as melatonin have been suggested as additional therapies that could further improve outcome (Levene 2010).

One of the first studies using MRS to investigate cerebral metabolism in neonates was conducted by Cady et al. (1983). Since then many have followed, involving both preterm and term infants. Azzopardi et al. (1989) investigated in both preterm and term infants (27-42 weeks) using ³¹P-MRS and found reduced values of the PCr/Pi ratio correlated with unfavourable outcome (severe impairments or death). Where losses in NTP/EPP were recorded, 'death was almost inevitable'. Robertson et al. (1999) studied persistent lactate after neonatal encephalopathy in infants aged less than 2 weeks to over 30 weeks. Increased Lac/Cr ratio and PCr was associated with an alkaline intracellular pH and increased Pi/PCr. This was found to be irrespective of outcome or age. A follow up studies of 78 infants (151 studies in total) found intracellular pH more alkaline in those with unfavourable outcome during the first 2 weeks after birth. In infants with severely abnormal versus normal MRI pH was recorded to be 7.24 versus 7.04 and in those who subsequently developed cerebral atrophy versus those who did not, 7.23 versus 7.06. Infants who died or had a severe neurodevelopmental impairment versus normal outcome, pH was recorded at 7.28 versus 7.11. Alkalosis was associated with higher Lac/Cr, and intracellular pH remained more alkaline in the severe outcome group up to 20 weeks after birth.

Studies in the effectiveness of hypothermia in treating hypoxic-ischaemic encephalopathy have been conducted in neonates following the animal experiments detailed above. In a randomised trial, Azzopardi et al. (2009) found in infants who had perinatal asphyxia, moderate hypothermia for 72 hours did not reduce the combined rate of death or severe disability significantly but improved neurologic outcomes in infants who did survive. Another study by Shah et al. (2007) found systemic or selective head cooling reduced death and moderate to severe neurodevelopmental disability.

NIRS and ³¹P-MRS were combined in Tsuji et al. (1995), investigating corre-

lations of cerebral changes in HbO₂, HHb and oxCCO with PCr and NTP depletion during HI in four-week old piglets. The animals were subjected to brief sequential episodes of increasingly severe hypoxia, with inspired oxygen reduced to 12, 8, 6, 4 and 0%. An HbO₂ decrease and HHb increase were observed at all levels of hypoxia, however a loss in PCr and NTP was only observed when inspired oxygen was less than 12% and was increasingly severe. Intracellular acidosis also increased similarly at lower oxygen levels. The main finding of this study was a high correlation between Δ oxCCO and NTP and PCr, suggesting decreases in Δ oxCCO as a marker for brain energy depletion. No correlation was observed however between Δ HHb or Δ HbO₂ and NTP or PCr, which may be, as the authors suggest, due to changes in blood pressure, affecting CBF.

Tichauer et al. (2006) used NIRS to follow changes in CBF and CMRO₂ during an HI study in newborn piglets. They observed that CBF increased approximately 70% immediately after HI while CMRO₂ decreased approximately 30% and remained lower than baseline throughout the 6 hour period post-insult. A follow-up study by the same group using ³¹P-MRS and ¹H-MRS in conjunction with NIRS periodically before and after HI. While they detected a significant decrease in CMRO₂, it did not correlate with other metabolite concentrations during the last 3 hours of the recovery period and no significant changes were observed in PCr and lactate concentrations. The authors thus conclude that the fall in CMRO₂ may be due to mitochondrial dysfunction and reduced energy demands during the acute phase. Similar studies in neonatal animals also observed decreased CMRO₂ after HI (Shadid et al. 1998; Rosenberg 1986), however others reported no changes in CMRO₂ (Solas et al. 2004). CMRO₂ has also been quantified in human neonates using NIRS (Elwell et al. 2005), and increased values have been observed in infants with brain injuries (such as HI) compared to healthy subjects in the first days of life (Grant et al. 2009).

Bale et al. (2014) used NIRS to monitor changes in haemodynamics and CCO in newborn infants with encephalopathy during the first few days of life. Spontaneous oxygen desaturations lead to consistent decreases in Δ HbDiff (= HbO₂ - HHb) and Δ oxCCO, and increases in Δ HbT. Mitra et al. (2015) also used NIRS to investigate cerebral changes following neonatal stroke in a term infant at 24 hours of life. During a 3-hour period, repeated transient changes were recorded, with decreases in HbO₂, HHb and oxCCO

Copyright material removed.

Figure 3.9: NIRS measurements of CBF and CMRO₂ during hypoxia-ischaemia in 18 piglets. Solid line - control, dotted line - HI. Grey area represents the HI insult (Tichauer et al. 2006).

in both cerebral hemispheres without significant changes in systemic variables. However, changes in HbDiff and oxCCO in the injured hemisphere were highly coupled (Figure 3.10).

Copyright material removed.

Figure 3.10: Linear regression analysis between ΔoxCCO with ΔHbDiff on the two cerebral hemispheres a neonatal stroke patient in the first 24 hours of life. Point colours and shapes represent different events (Mitra et al. 2015).

3.3.2 Functional studies

Brain activation in the young is of considerable interest in developmental science. Numerous studies have been conducted in the awareness and processing of auditory, visual, olfactory and somatosensory stimuli and both fNIRS and fMRI have been informative in mapping the onset of autism (Lloyd-Fox et al. 2013; Courchesne et al. 2007). However, functional studies in current literature report disparate results in the haemodynamic responses observed, most notably in the characteristics – magnitude and sign – of stimulus-evoked changes in HbO₂ and HHb. In particular, some studies have reported a increase in HHb, while others report an decrease as is typically observed in adults, resulting from an increase in CBF that overcompensates for the increased CMRO₂.

Anderson et al. (2001) used fMRI to to investigate responses to an auditory stimulus in healthy preterm and term neonates, and observed decreases in the BOLD signal in 9 of the 14 neonates with BOLD response. A fNIRS study also in preterm and term infants, aged between 1 and 49 days, observed var-

3.3. Animal experiments and neonatal studies

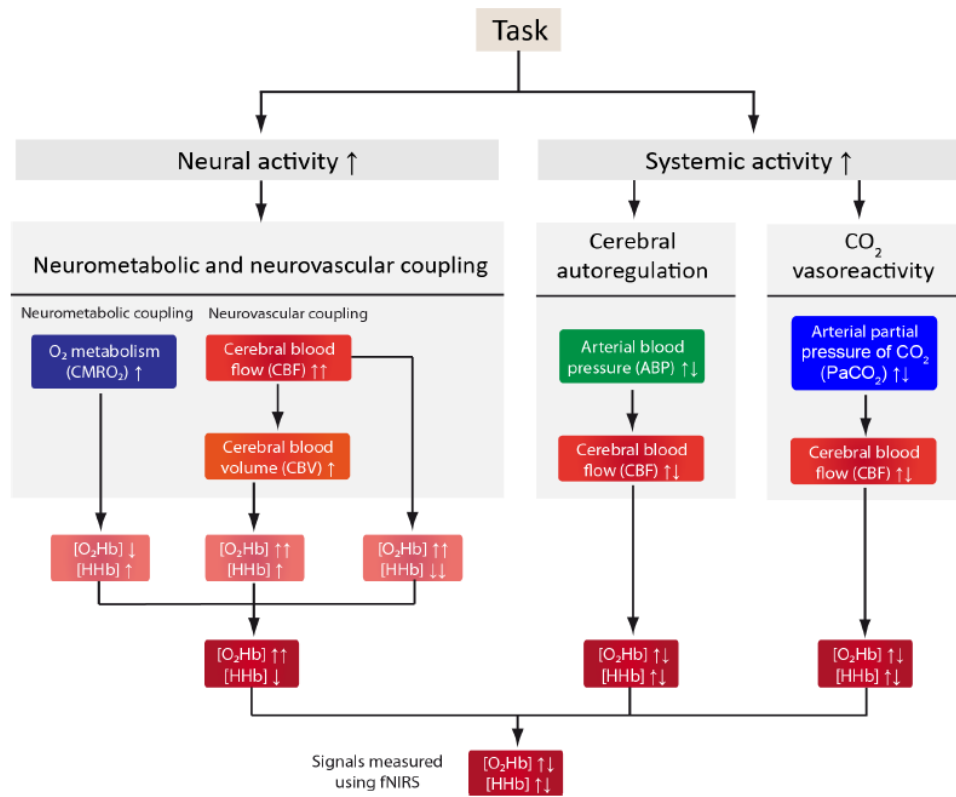


Figure 3.11: Summary of haemodynamic and oxygenation changes typical of a matured brain, stimulated by both neural and systemic activity (Scholkmann 2014).

Copyright material removed.

Figure 3.12: fNIRS technique applied to infants. (a) typical haemodynamic response from cortical activation showing an increase in HbO₂ and a decrease in HHb (b) NIRS probes arranged in headgear on an infant (c) spatial changes in HbO₂ in response to an experimental stimulus and (d) the corresponding NIRS source-detector arrangement (Lloyd-Fox et al. 2010).

ied reponses in ΔCBV , ΔHbO_2 and ΔHHb to an auditory stimulus (Zaramella et al. 2001). Of those infants that responded with an increase in ΔCBV and ΔHbO_2 , approximately 60% also showed an increase in ΔHHb while 40% showed a decrease. In yet another auditory study, Zimmermann et al. (2012) found a correlation between total haemoglobin concentration and the nega-

tive BOLD response in preterm neonates, suggesting that the period of low haematocrit during the transition from fetal to adult haemoglobin may be responsible.

Bartocci et al. (2000) investigated the response to olfactory stimuli in newborn infants using NIRS. In neonates 6 hours to 8 days after birth, an increase in HbO₂ was observed in the left orbito-frontal region in response to vanilla scent, with the magnitude of the increase inversely related to post-natal age.

Meek et al. (1998) conducted an fNIRS study to observe regional haemodynamic responses to a visual stimulus in infants ages 3 days to 14 weeks. They observed out of 10 infants, 9 showed an Δ HbO₂ increase and 9 showed a Δ HHb increase. A similar study in newborn term infants by Biallas et al. (2012) concluded that the sensitivity of NIRS to detect haemodynamic responses and their reproducibility on an individual level needed to be improved for clinical applications. Seghier et al. (2004) used fMRI in a 3-month old infant with ischaemic brain injury. A negative BOLD response was observed in the visual cortex of the intact right hemisphere, while no activation was observed in the injured hemisphere. Another fNIRS study in term neonates, conducted in the first 10 days of life, a marked increase in HbO₂ and/or marked decrease in HHb was detected in the occipital cortex (Karen et al. 2008).

Heep et al. (2009) used fMRI to observe responses in preterm neonates to a somatosensory stimulation of each forearm at term-equivalent age (median gestational age: 26.5 weeks; median postconceptional age: 39 weeks). In 7 of the 10 experiments, a negative BOLD signal was recorded. The 3 experiments which saw positive BOLD responses were observed in patients with aberrant structural and behavioural indices, and is thought likely to be an early indicator of abnormal development. Kozberg et al. (2013) also demonstrated a negative BOLD response in postnatal rats, age equivalent to human newborns, and development of the positive BOLD response with maturation towards adulthood. The authors also noted that increases in blood pressure lead to hyperemia resembling the adult positive BOLD responses, which may account for the variability observed in studies. Another fNIRS study by Roche-Labarbe et al. (2014) also in preterm neonates using stimulation of the hand was first to report local increases in CBF and CMRO₂, in addition to increases in HbO₂ and decreases in HHb.

3.3. Animal experiments and neonatal studies

Both the Kozberg et al. (2013) and Roche-Labarbe et al. (2014) studies are investigated in more detail in this thesis in Chapter 7, where the BrainSignals model is used to simulate these observations.

Chapter 4

Mathematical Models of the Brain

Mathematical models have been used in scientific research for centuries. Current literature provides a number of models of cellular metabolism, including several produced at UCL. This chapter offers an overview of the nature of mathematical modelling, a brief look at a few models published by external groups and a more detailed look at two recent models developed at UCL that are used in this thesis.

4.1 Mathematical modelling

Essentially, all models are wrong, but some are useful.

— Box and Draper (1987), *Empirical Model-Building and Response Surfaces*

The first models are thought to have been created around 30,000BC; numbers – counting and writing or marking them – were followed by models in astronomy and architecture several millennia later. In that sense, mathematical models have a great history, and have been very effective torches in the journey of scientific understanding. Yet it seems in many ways as though the field is still in its infancy, especially in its application to biology.

In 1960, Eugene Wigner expressed his apprehension of the use of mathematics in other disciplines in his essay titled *The Unreasonable Effectiveness of Mathematics in the Natural Sciences* (Wigner 1960). More than half a cen-

ture later, his ideas still resonate. Granted Wigner was concerned about application of mathematics to physics, and this was back in the day when disciplines were thought of in the traditional sense as having quite strict boundaries. Wigner was scratching the tip of a largely ignored iceberg of the inability to comprehend how interdisciplinary science could possibly work.

The understanding of the associations between disciplines has since advanced to become more acceptable, and more recently trendy. Mathematics in particular is considered vital for the advancement of other sciences – an acknowledgement of the power of quantitative evidence and proof. Mathematical models are used in various fields from architecture and astrophysics to finance and security. Its application in the the field of biology, although hardly new, is still a prime candidate for Wigner’s concerns. Mathematics prides itself on its undoubtable shatter-proof theorems, established on clear foundations that hold true for all time. It’s a discipline where rigorousness and exactness are basic standards of working. Biology on the other hand stands on ever changing foundations that alter with frequent acquisitions of new knowledge. The nature of this alliance is conflicting. The function and authority of a mathematical model is undermined by what biological knowledge is *considered to be known* and is *purported to be true*.

Regardless, this alliance is perceived to be mutually beneficial by some. Biology can influence and inspire new mathematical theorems (Sturmfels 2005). However it cannot be denied that the lion’s share of work conducted in mathematical biology is in applying predetermined mathematical concepts to biological problems. This work spans from nanoscale processes to phenomena that occur across the globe. Recent work has focused on amalgamating multiscale models. For example, the Virtual Physiological Human (VPH) initiative aims to provide a framework for developing computational models of the human body, integrating protein, cellular, tissue, organ and organ-system scales (Hunter and Borg 2003; Gavaghan et al. 2009). This field of work is often referred to as being a part of *systems biology*. While the exact definition of the term is still contested, it is generally thought to encompass mathematical and computational models of biological systems.

Mathematical models encompass a wide range of different methods, from purely statistical approaches to dynamic time dependent models. Certain approaches can provide an analytical insight, not accessible through merely

computational or experimental methods. Many models are built upon others, expanding and refining to suit the needs of the biological problem at hand. Different logical strategies can be employed in the building of a model. They can be mechanistic, simulating the specific biological processes being investigated, or phenomenological, starting with the data in order to recreate the relationships that gave rise to it. Many other terms are used to describe these two basic ideas: bottom-up and top-down approaches, white-box and black-box modelling and forward and reverse modelling (Gunawardena 2014). Regardless of the strategy chosen, the fundamental structure of a model remains the same. Any mathematical model consists of a set of assumptions from which a set of conclusions can be derived.

However, in some cases biology offers no realistic justifications for the assumptions being made, making so-called mechanistic models less purely so. For example in the modelling of biochemistry, the equations which are often used to represent reactions (such as the law of mass action or the Hill function) don't follow a chemist's or physicist's rationale. They are formulations based on phenomenology, not on fundamental laws (Gunawardena 2014):

The point here is not that we should not guess; we often have no choice but to do so. The point is to acknowledge the consequences of phenomenology and guessing for the kinds of models we make. They are no longer objective descriptions of reality.

The title for Gunawardena's article *Models in biology: 'accurate descriptions of our pathetic thinking'* comes from the Nobel Prize lecture delivered by the pharmacologist James Black (Black 2005), who argued:

Models in analytical pharmacology are not meant to be descriptions, pathetic descriptions, of nature; they are designed to be accurate descriptions of our pathetic thinking about nature...They are meant to expose assumptions, define expectations and help us to devise new tests.

Gunawardena goes on to say that in forward models based on such guesswork, if the model is not predictive and assumptions not certain, its only *raison d'être* is to test those pathetic assumptions by being falsifiable.

An initial impulse of modelling a biological problem is often to include as much detail as possible in order to produce the most accurate predictions. This may be because of the historical paucity of information in biology. However, as the number of model parameters increases so does the complexity and the uncertainty. The model exists in a multidimensional space, determined by the number of parameters it carries, and the range of values deemed plausible for each parameter. Each range of biological values is burdened with uncertainty, and through the model's relationships translate into uncertainties in model output that are difficult to disentangle. The usefulness of a model is therefore governed as much by what is left out as it is by what is included.

*With four parameters I can fit an elephant, and with
five I can make him wiggle his trunk*

— *John von Neumann*

Many systems biology models call for a large number of free parameters due to the nature of what is being simulated. Waterfall et al. (2006) identify what they call 'sloppy' models, where behaviour is mainly determined by a small number 'stiff' parameter combinations which translate into constrained directions in the model space. Other directions of model behaviour are less constrained or 'sloppy'. In effect, the model behaviour space has fewer dimensions than that of the parameter space it is mapped from, and therefore changes in single parameters can have very little effect (Transtrum et al. 2010, 2011). Gutenkunst et al. (2007) found that the 17 systems biology models they studied had the characteristic sloppy pattern, concluding that 'these results argue that focusing on parameter values may be a very inefficient route to useful models' (Gutenkunst et al. 2007).

Biological models, especially mechanistic models which emanate from biological structure, with very accurate and efficient parameters is not a realistic enterprise. First, because the underlying biological foundation is often ridden with uncertainty the model applied on top is poorly supported. Second, it is often quite difficult to determine what biological structures or activity, translated into parameters, will be more influential in a model before it is actually built. Thus, it is usually an exercise of trial and error, where detail is added and tested for efficacy (if at all). Gunawardena also discusses

this, noting that model building often involves some level of simplification, adding that 'this is as true for the experimentalists informal model – the cartoon that is sketched on the whiteboard – as it is for the mathematicians formal model' (Gunawardena 2014) .

The utility of a mathematical model also rests on its approval and recognition by those it is intended to benefit. In the clinical sphere such quantitative models, burdened with assumptions and confined by numerical parameters, present complex and questionable reasoning that is perhaps (and rightly so) a more difficult pill to swallow. This is obviously and understandably true in the science of intensive care, where the models of this thesis apply, as lives are constantly at risk.

However, quantitative models with assumptions and abstractions are already widely used in these fields, but are often hidden from view. They escape notice when they are either packaged in such a way that conveys an air of authority – for example within a clinical device, where the results are conveniently displayed graphically – or if they have entered into the realm of tradition – have always been used, and so have become part of the furniture. Research trends and the emergence of umbrella terms such as systems biology have spotlighted quantitative models in recent times, laying them bare to more scrutiny and targeted scepticism. This is nonetheless good for the field of quantitative modelling in biology, as it forces a more thorough inspection of its fundamental behaviour and encourages more principled and credible endeavours.

We must take a guarded approach in the endorsement of quantitative models. It is important to understand whether the model being used is appropriate and suitable for the problem being investigated. This is especially true when applying existing models to new problems. In data-driven modelling, it is necessary to examine whether the data can answer the question being asked. The scope of the model is inevitably constrained by the limitations of the original environment or experiment from which the data was obtained. One must also refrain from generalising the results obtained from the model, keeping in mind the original assumptions that were made in the building process.

4.1.1 The good models

*There are three simple rules for creating a model.
Unfortunately, nobody knows what they are.*

— James Haefner, in *Modelling Biological Systems*
Haefner (2005)

The characteristics of an ideal model can vary from one application and field to another. However, there are a number of common attributes that are desirable in a mathematical model. Some of these are listed below, inspired by Smye and Clayton (2002).

Accuracy – Model validation is task more difficult in practice than may seem, and more commonly and ideally done by comparing predicted values with measured ones. Cloutier et al. (2009) go so far as to claim that mathematical models are only credible when calibrated with relevant experimental data. However, this is not always possible - a forward model may be purely theoretical, an investigation of scenario for which experimental data is not available, such as is likely in astrophysics. The model may be the only source of information at all. Where it *is* possible, care must be taken to ensure that the methods used to improve the accuracy of the predictions reflect the accuracy of the data itself (Smye and Clayton 2002). It is also important to understand that a model is by definition *not the real thing* and *will never be*.

*The best model of a cat is another cat, or preferably the
same cat.*

— Arturo Rosenblueth

Prediction – Good models will not simply describe what has already been observed (Smye and Clayton 2002), but will further current knowledge by either adding detail to the unseen processes that gave rise to what has been observed, or predict that which has not (as discussed briefly above). Although stochastic processes are common in biology, models can be predictive of processes on a larger scale (Smye and Clayton 2002).

Economy – It is advisable to follow the Occam's razor principle – *entities should not be multiplied unnecessarily* or in more applicable terms *when you have two competing theories that make exactly the same predictions, the simpler one*

4.2. Physiological models of the brain metabolism and circulation

is the better. This is what Smye and Clayton (2002) refer to as *"the real skill of the model builder – the ability to identify and describe the essential elements of a biological process."*

Utility – Perhaps obvious, but a model should be, if anything, useful. This is an attribute that can be easily overlooked by those creating models especially if they normally reside outside the field of application. If a mathematical model in a medical context cannot provide information of use to the clinician it is intended to benefit, then the model would it have failed its purpose.

As to where the models presented in this thesis lie in the spectrum of usefulness, goodness and applicability – I leave this to the discussion at the end of this thesis (Chapter 9). For now, we move to consider a number of existing physiological models of the brain.

4.2 Physiological models of the brain metabolism and circulation

Creating a mathematical model to predict the complex behaviour of the brain is both a daunting and interesting challenge. A number of different approaches have been used to investigate various areas and functions of the brain. An exhaustive list of all the different varieties of models is beyond the realm of this thesis. However, a selection of physiological models is listed in Table 4.1. Some of these models either focus only on metabolism or circulation whilst others combine both.

Table 4.1: Models of cerebral metabolism and blood flow.

Model	Focus	Simulation	Clinical Application
Korzeniewski and Froncisz (1991)	Oxidative phosphorylation	Respiration in isolated cells – CCO, ATP synthesis and use	Comparison with experimental results
Czosnyka et al. (1993)	Circulation	Arterial CO ₂ – PaCO ₂ – cerebral perfusion pressure, cerebral blood flow, blood pressure, cerebrovascular resistance and autoregulation	Interhemispheric asymmetry of CBF reactivity to changes in PaCO ₂ in patients with carotid artery stenosis
Ursino and Lodi (1998)	Circulation	Intracranial pressure, cerebral blood flow, autoregulation and CO ₂	
Hyder et al. (1998)	Oxygen delivery	CMRO ₂ , CBF, haemoglobin concentrations and oxygenation	Proportionality between CBF and CMRO ₂ , in graded anesthesia in rats and humans and for functional activations in humans
Korzeniewski and Zoladz (2001)	Oxidative phosphorylation	Extension of previous models to include creatine kinase system	To demonstrate that in skeletal muscle, the creatine kinase system has no significant influence on kinetic properties of oxidative phosphorylation.

Table 4.1: Models of cerebral metabolism and blood flow.

Model	Focus	Simulation	Clinical Application
Aubert et al. (2001)	Oxygen delivery and metabolism	CBF, oxygenation, metabolites – NAD, NADH, lactate, ATP ADP, AMP, creatine, phosphocreatine, glucose, glycogen, pyruvate and sodium membrane transport	Interpretation of MRS and fMRI data obtained during prolonged simulations
Gjedde (2002)	Oxygen delivery	CBF, oxygenation and oxygen consumption (CMRO ₂)	Investigate the mismatch between increased blood flow and oxygen consumption during neuronal excitation
Aubert and Costalat (2005)	Oxygen delivery and metabolism in astrocytes and neurons	covers quantities in previous model above, now compartmentalised in astrocytes and neurons	Test the astrocyte-neuron lactate shuttle hypothesis

Table 4.1: Models of cerebral metabolism and blood flow.

Model	Focus	Simulation	Clinical Application
Jung et al. (2005)	Circulation	Cerebral blood flow, blood pressure, cerebrospinal fluid, autoregulation, and oxygenation,	Connection between arterial blood pressure and the production of cerebrospinal fluid. Correlation of partial oxygen pressure of brain tissue to the mean arterial blood pressure in the case of an impaired autoregulation mechanism
Beard (2006)	Oxygen transport and metabolism	ATP, ADP, creatine phosphate, inorganic phosphate, NAD, NADH, oxygenation and blood flow	Reproduce experimental observations of ATP, ADP, CrP, and inorganic phosphate levels in canine hearts. Quantitative predictions of changes in phosphate metabolites during cardiac ischemia.
Vatov et al. (2006)	Metabolism	CBF, partial oxygen pressure, mitochondrial NADH redox state and extracellular potassium	Complete and partial ischemia, cortical spreading depression under normoxic and partial ischemic conditions. Real-time computation of variables during clinical or experimental procedures

Table 4.1: Models of cerebral metabolism and blood flow.

Model	Focus	Simulation	Clinical Application
Simpson et al. (2007)	Metabolism in astrocytes and neurons	glucose, glucose transporter proteins, lactate and monocarboxylate transporters	Investigate the astrocyte-neuron lactate shuttle hypothesis
Alastruey et al. (2008)	Circulation	Cerebral blood flow, autoregulation, arterial haemodynamics	Effect of anatomical variations in the circle of Willis, following carotid artery occlusion
Cloutier et al. (2009)	Metabolism in astrocytes and neurons	Based on Aubert and Costalat (2005), includes glutamate cycling and glycogen	Simulations compared with data from a sensory stimulation (restraint) in rats
Linninger et al. (2009)	Circulation	Blood, cerebrospinal fluid, brain parenchyma, spinal canal and intracranial pressure	Cerebrospinal fluid flow differences in patients with hydrocephalus (fluid build-up inside the skull)
Orlowski et al. (2011)	Metabolism in astrocytes and neurons	Based on Cloutier et al. (2009), extended to simulate pH response during ischaemia	Understand pH dynamics in damaged and vulnerable brain tissue after stroke
Orlowski et al. (2013)	Metabolism in astrocytes and neurons	Extension of previous model to include extracellular concentrations	Oedema and propagation of stroke across the brain

A few good models of brain metabolism and blood flow relevant to this thesis have been summarised below. These models have been implemented and run in different modelling environments, the results of which are presented here.

4.2.1 The Korzeniewski model

A model of oxidative phosphorylation in mammalian skeletal muscle, the Korzeniewski and Zoladz (2001) model was also built upon earlier work (Korzeniewski 1998). It includes substrate dehydrogenation, complex I, III and IV, cytochrome c oxidase, proton concentration in both cytosol and mitochondria and the proton leak. The model also incorporates ATP synthase, ATP/ADP carrier, phosphate carrier, the use of ATP, adenylate kinase, and creatine kinase (see Chapter 2, Section 2.4.3 for an overview of oxidative phosphorylation). Figure 4.1 displays a simulation of muscle activation (and increased energy demand).

Copyright material removed.

Figure 4.1: Simulation presented in Korzeniewski and Zoladz (2001) of muscle activation, using an increase in energy demand.

A hypoxia simulation was run using the model with the Braincirc interface (see Section 4.3.1), instigated by a 50% drop in O_2 concentration (Figure 4.2). The model predicts a drop in oxidised cytochrome and a rise in reduced cytochrome, as might be expected with low metabolism. A drop is also observed in both mitochondrial and cytosolic ATP concentration and a consequent drop in PCr and rise in Cr concentration.

4.2.2 The Beard model

Beard (2005) introduced a model of mitochondrial respiration, including the electron transport chain and ATP synthesis, based on data from cardiac mitochondria. In order to simulate cardiac energetics, the model is focused on the chemical and electrical components of the proton motive force. It also

4.2. Physiological models of the brain metabolism and circulation

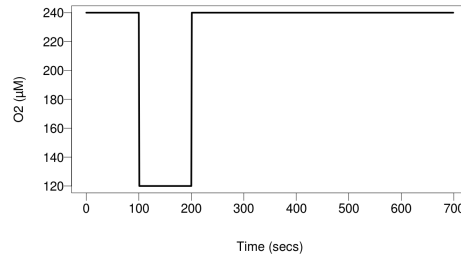


Figure 4.2: A 50% drop in O₂ input to the Korzeniewski and Zoladz (2001) model to simulate hypoxia.

incorporates cytochrome c concentration and consists of two mitochondrial compartments - the matrix and intermembrane space.

This model was made available on the CellML repository (Yu et al. 2011). Figure 4.5 illustrates hypoxia simulations from this model, stimulated by a 80% decrease in O₂ and compiled using the OpenCell environment (Ope 2009). This environment allows the user to state parameter values before the model is run, but is not set up in such a way that allows time-dependent changes, unless a new time-dependent function is declared for that parameter. Predicted value of reduced cytochrome c is similar to that presented in the Beard (2005). There is a decrease in mitochondrial NAD and pH while a slightly higher than normal value of free mitochondrial ATP.

The model of cellular energetics was extended to simulate oxygen transport in cardiac tissue in Beard (2006). It simulates capillary, interstitial and cellular space (in this case myocyte). The concentration of oxygen and other metabolites primarily vary along the length of the capillary, incorporating an axially distributed blood-tissue oxygen exchange model. The interstitial and cellular spaces are assumed to be stagnant. Cytoplasmic and mitochondrial compartments compose the cellular region. This model was not available online but the published model analysis with data on blood flow and oxygen consumption showed a linear relationship between whole-heart perfusion and the rate of ATP consumption (Beard 2006). However, the authors note that ATP hydrolysis is likely to vary across the regions of the heart. The model also predicted inorganic phosphate to be a key regulator of oxidative phosphorylation.

4.2. Physiological models of the brain metabolism and circulation

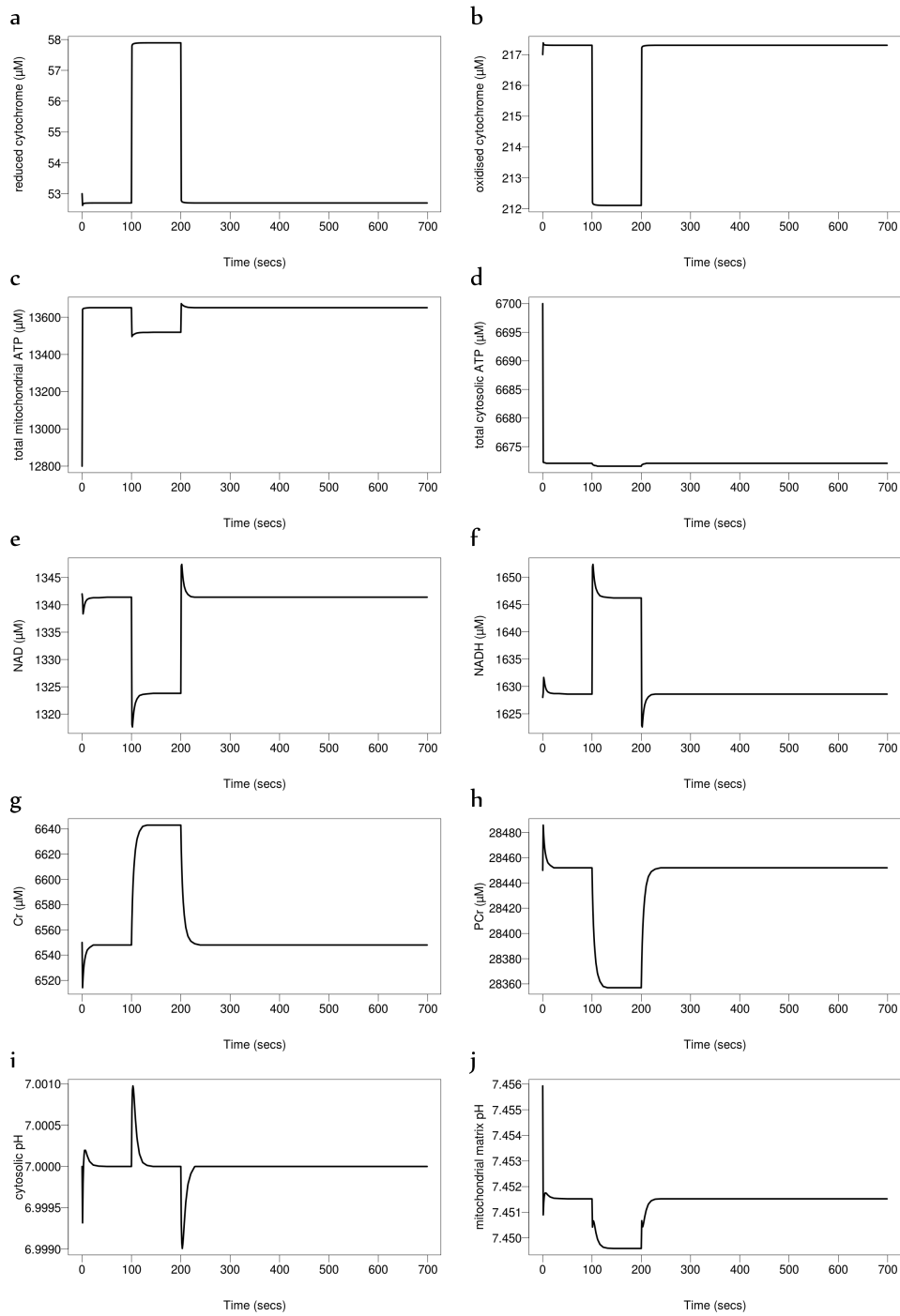


Figure 4.3: Simulation of hypoxia in the Korzeniewski and Zoladz (2001) model with a 50% drop in O_2

4.2. Physiological models of the brain metabolism and circulation

Copyright material removed.

Figure 4.4: Schematic of the Beard (2005) model

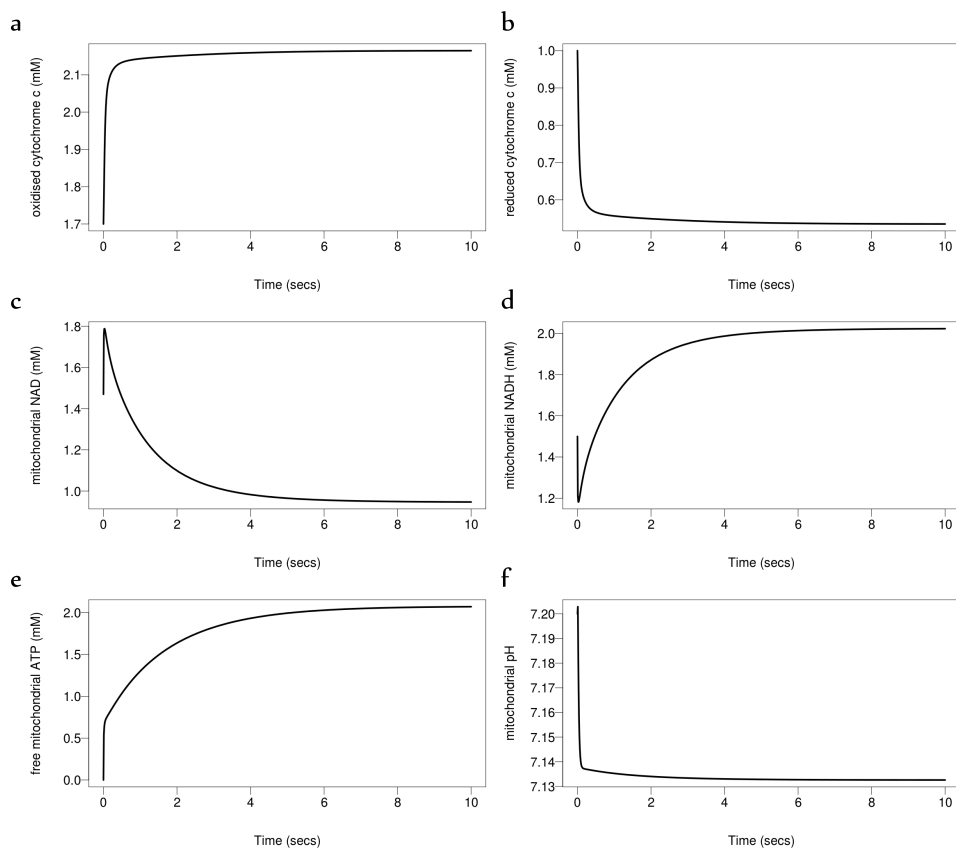


Figure 4.5: Simulations of the Beard (2005) model following an 80% decrease in O_2 .

4.2.3 The Ursino-Lodi model

Copyright material removed.

Figure 4.6: Intracranial dynamics of the Ursino and Lodi (1998) model. G_1, G_2 and C_1, C_2 are the hydraulic conductances and compliances of the proximal and distal cerebral arteries respectively. P_a, P_1 and P_2 represent systemic arterial pressure and pressure in large pial and smaller arteries. P_{ic} and C_{ic} are intracranial pressure and compliance. G_{pv}, G_{ve} and C_{vi}, C_{ve} are the conductances and compliances of large cerebral veins and extracranial pathways. G_{vs}, G_f, G_o are conductances of terminal intracranial veins, cerebrospinal fluid formation and CSF outflow. q, q_f, q_o, I_i represent cerebral blood flow and CSF formation, outflow and injection rate respectively.

Copyright material removed.

Figure 4.7: The action of regulatory mechanisms in the Ursino and Lodi (1998) model, on smooth muscle activation factor M_j of large and small pial arteries ($j = 1, 2$). The top branch represents the autoregulation mechanism and the bottom branch the CO_2 response. The inputs for the autoregulation branch are different in the two segments – large pial arteries respond actively to variations in cerebral perfusion pressure, whereas small pial arteries are sensitive to CBF changes. Dynamics are simulated by a gain factor G and a first-order low-pass filter with time constant τ . A_{CO_2} is a corrective factor which lowers CO_2 reactivity at low levels of CBF as a consequence of ischemia. The two regulatory mechanisms interact nonlinearly through a sigmoidal static relationship.

A model of cerebral haemodynamics and pressure was published by Ursino and Lodi (1998), following earlier similar work (Ursino and Lodi 1997). The model investigates the relationship between cerebral blood flow, blood volume, intracranial pressure and the regulatory mechanisms – autoregulation and CO_2 reactivity. Figure 4.6 illustrates the intracranial dynamics in the form of an electric analog diagram. Cerebrovascular regulation is controlled by the radius and tension of smooth muscle. The autoregulation and CO_2 reactivity mechanisms are displayed in Figure 4.7.

The model was run on the in-house interface Braincirc (see Section 4.3.1). Ischemia was simulated by a 50% drop in blood pressure (Figure 4.8). The

4.2. Physiological models of the brain metabolism and circulation

results are displayed in Figure 4.9. The model predicts a drop in CBF, and a drop in the radius of the middle cerebral artery, as it attempts to compensate. Intracranial and venous pressure is observed to rise whilst blood velocity is maintained relatively constant.

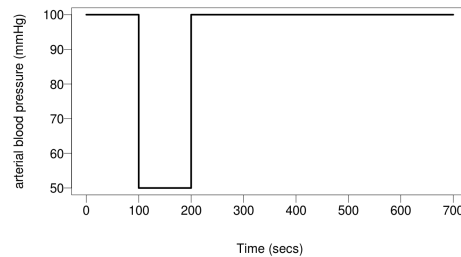


Figure 4.8: A 50% drop in blood pressure input to the Ursino-Lodi model to simulate ischemia

4.2.4 The Cloutier model

Focused on energy metabolism, this model was based on an earlier model by Aubert et al. (Aubert and Costalat 2005, 2007; Cloutier et al. 2009). An important aspect of these models is that they simulate neurons and astrocytes as separate compartments.

The model includes the exchange of glucose, lactate, oxygen carbon dioxide between the capillaries and the cells. Reactions involved in energy metabolism, including glycolysis and the production and consumption of ATP are modelled. Also incorporated is an astrocyte-neuron lactate shuttle. The main distinction in the metabolic activity of neurons and astrocytes comes into play in the simulation of neural stimulation. Maintaining ionic gradients in these cells is considered to be a major energy consumer. The coordination of neuronal and astrocytic responses to stimuli is controlled by the cycling of glutamate between the two cells. This activates the sodium pump in astrocytes to maintain the sodium gradient.

Figure 4.11 displays simulations of the model run using an in-house compiler BCMD (see Section 4.3.1). The model incorporates stimulus functions that affect sodium and glutamate concentrations, so no additional input parameters are required to model the stimulus on execution.

4.2. Physiological models of the brain metabolism and circulation

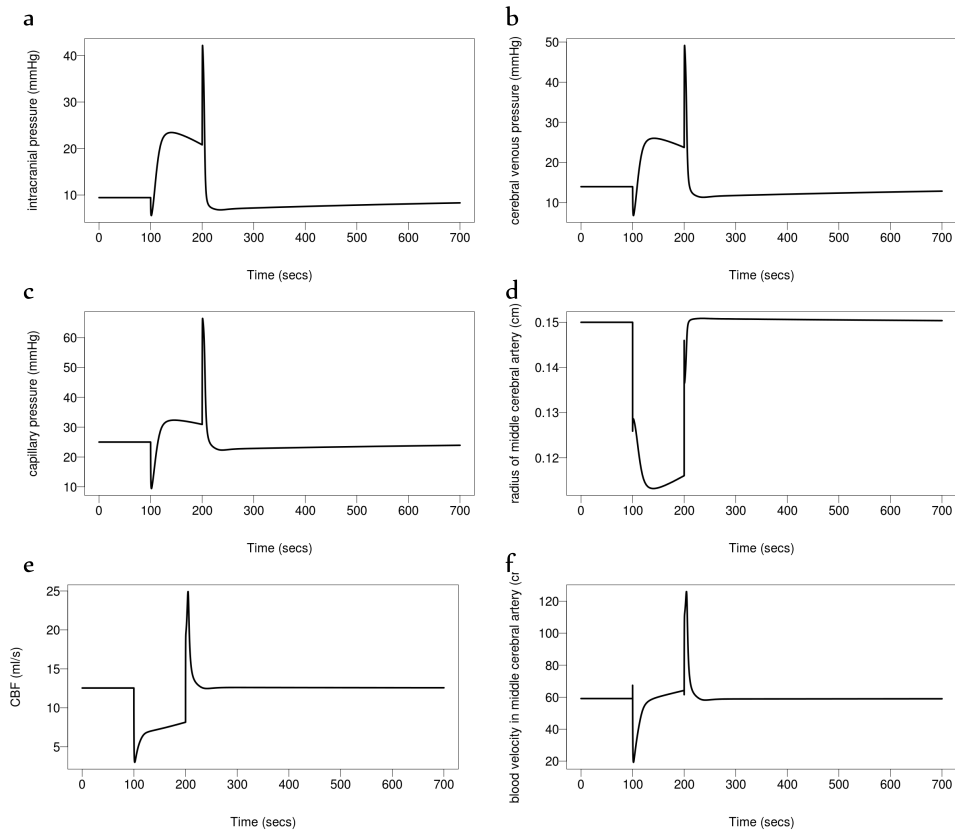


Figure 4.9: Simulation of ischemia in the Ursino-Lodi model with a 50% drop in blood pressure.

Copyright material removed.

Figure 4.10: Schematic diagram of the Cloutier model.(Cloutier et al. 2009)

4.2. Physiological models of the brain metabolism and circulation

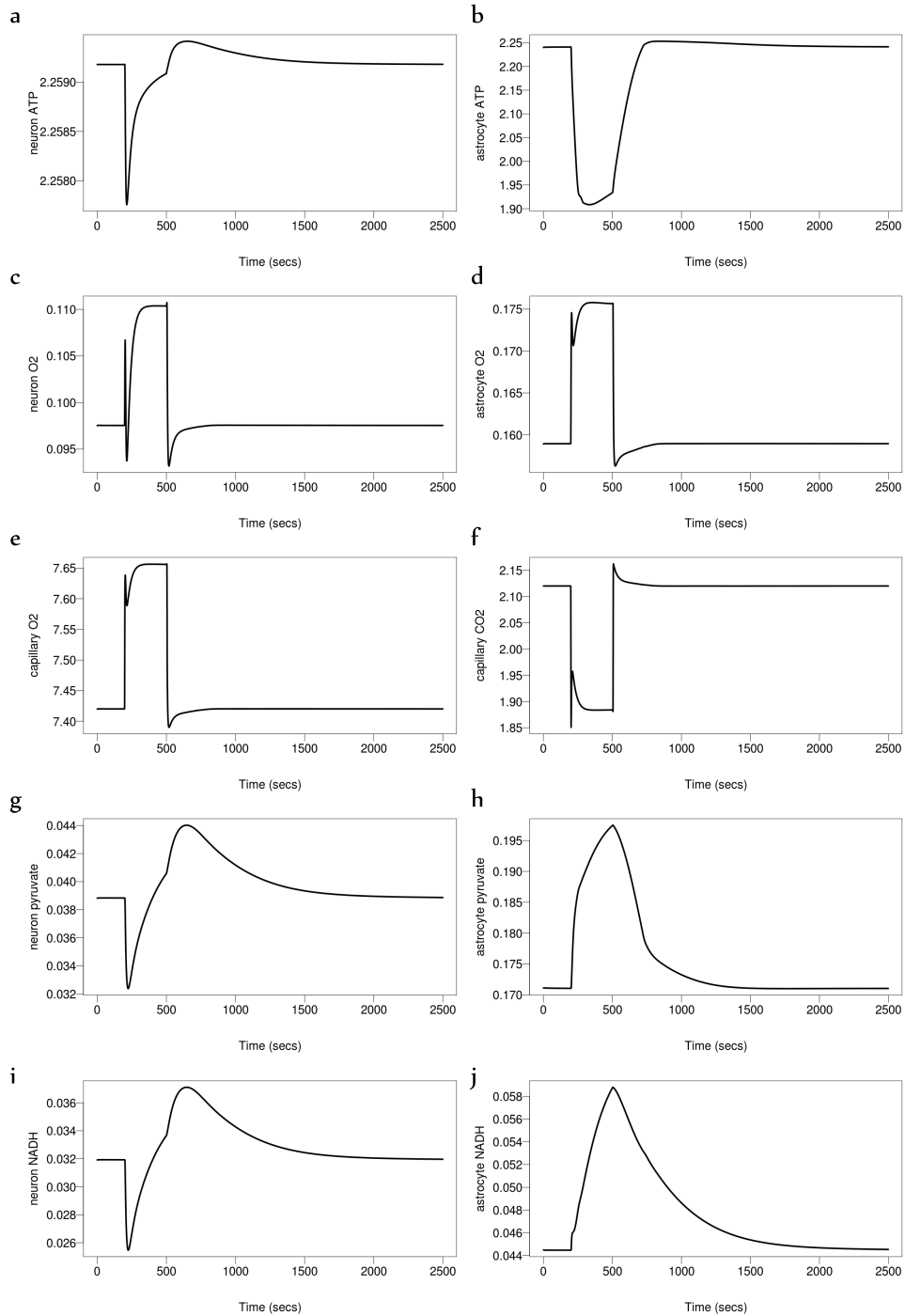


Figure 4.11: Simulations of the Cloutier et al. (2009) model of the response to a stimulus

4.2.5 The Orłowski model

Copyright material removed.

Figure 4.12: Schematic diagram of the Orłowski model. The additional notation indicates changes made to the Cloutier model. (Orłowski et al. 2011)

Orłowski et. al extended the Cloutier model to simulate pH dynamics under ischaemia (Orłowski et al. 2011). The authors here assume a linear relationship between the concentration of H^+ ions and the concentration of ATP, the production of lactate and the concentration of phosphocreatine (PCr).

Changes in glycogen concentration are made sensitive to changes in AMP concentration in the astrocyte. pH is regulated in the model by an intracellular buffer solution of carbonic acid and the products of its dissociation and the movement of H^+ ions to the extracellular space. Carbon dioxide dynamics are also investigated by simulating its concentration in the capillaries and the extracellular space. ATP consumption is linked to the rate of the sodium-potassium pump. Figure 4.13 illustrates results from the model during ischaemia, simulated by an 80% drop in cerebral blood flow. Especially notable here is the drop in pH in both neurons and astrocytes.

Copyright material removed.

Figure 4.13: Simulations of the Orłowski model following a 80% reduction in CBF (Orłowski et al. 2011)

The model was made available on the CellML platform (Yu et al. 2011). It was downloaded and run using the OpenCell environment (Ope 2009), as was used in the original publication. A simulation of ischemia using an 80% drop in cerebral blood flow confirmed the results in Orłowski et al. (2011). Figure 4.14 displays a simulation of hypoxia-ischaemia, caused by an 80% drop in cerebral blood flow and arterial oxygen. These simulations actually show a smaller drop in pH in both neurons and astrocytes, and a

4.2. Physiological models of the brain metabolism and circulation

quicker recovery, than that observed in the ischaemia simulation presented in the authors' paper. Lactate increases throughout, possibly due to anaerobic metabolism. Both intracellular Na and ATP showed a more linear increase and decrease respectively. The changes in ATP is not as marked either. The simulations do not seem to be successful beyond the 6000 seconds time period in this environment.

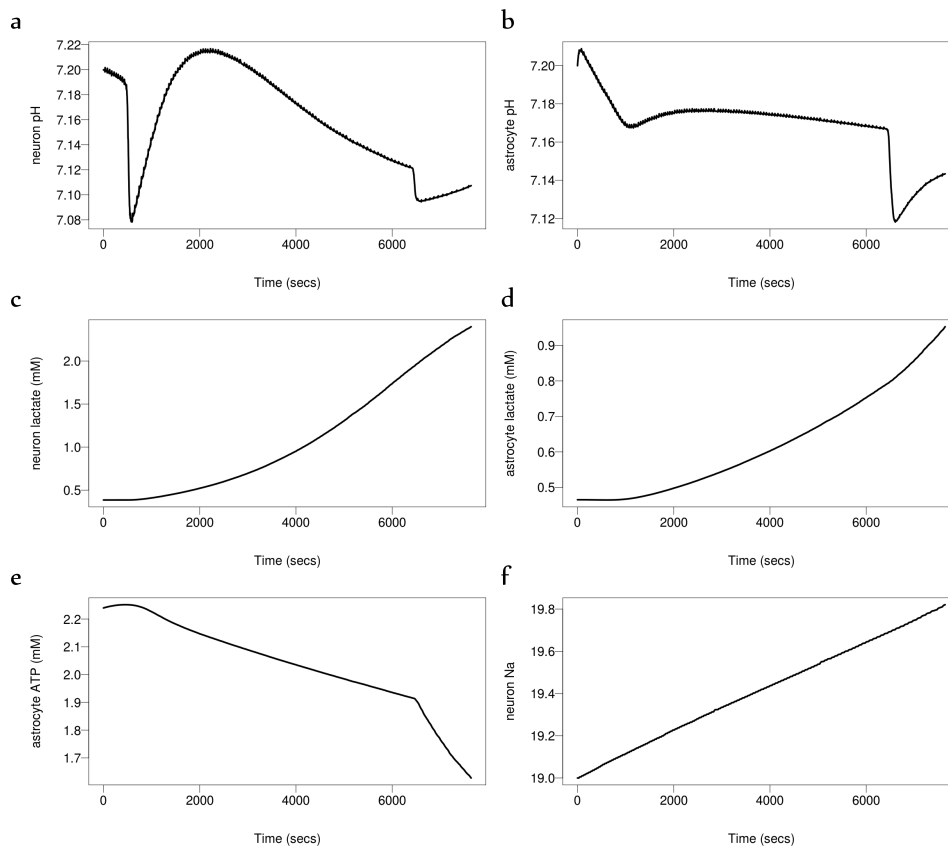


Figure 4.14: Simulations of the Orlowski model following a 80% reduction in CBF and O_2

The model was further extended in Orlowski et al. (2013) to investigate tissue damage caused by oedema following ischemic stroke, by incorporating simulations of cell volume change and diffusion of ions in the extracellular space. Figure 4.15B displays their results from simulations of the size of the extracellular and cellular space and Na^+ ion concentration after a 90% decrease in blood flow, with and without diffusion of Na^+ ions to the extracellular space. Figure 4.15C shows a simulation of a cubic mesh of 1000

4.2. Physiological models of the brain metabolism and circulation

cubic cells representing tissue, where blood flow is decreased to 90% in cells 2cm away from the left surface. Also displayed is the CO₂ levels across the front surface of the tissue model, showing a higher concentration closer to the stroke area.

Copyright material removed.

Figure 4.15: Simulations of the Orłowski et al. (2013) model

4.3 The UCL brain models

The Biomedical Optics Research Laboratory (BORL) at UCL's department of Medical Physics lays claim to a number of mathematical and computational models of brain metabolism and circulation. This work spans almost a decade to date, and runs alongside an extensive research effort into non-invasive clinical measurement techniques, including near infrared spectroscopy. These measurement techniques are detailed more thoroughly in the next chapter.

4.3.1 History of model development at UCL

The models presented in this thesis are derived from a number of previously published brain models – a timeline of which is illustrated in Table 4.3. A brief history and description of these models is summarised below.

BrainCirc

The first model, an elaborate adult brain model, was published in 2005 by Banaji et al (Banaji et al. 2005). Three preexisting models of circulation, brain biochemistry and vascular smooth muscle function were united in one. Thus, a physiological approach was used and the model was constructed in a modular way so as to enable easy modification.

The model encompasses three 'sites': blood vessels, brain tissue and vascular smooth muscle. Each of these are further divided into different components: arteries, arterioles, capillaries and veins in the vascular system, extracellular, intracellular, cytoplasmic and mitochondrial compartments in brain tissue, and vascular smooth muscle in the proximal and distal arterial segments. Biochemical reactions are represented as mass action or Michaelis Menten equations. Other equations included are those representing the biomechanics of vessel walls and circulation, and volume balance equations between different compartments derived from conservation laws.

BrainCirc is the largest of all the models in this series, including a vast number of variables and parameters. In order to manage and run such a large and complex model, the BRAINCIRC modelling environment was built. This software focuses on the biological processes (eg. chemical reactions) that are central to the model. These can be input into the interface

Copyright material removed.

Figure 4.16: Main processes and compartments of the BrainCirc model (Banaji et al. 2005).

and the environment then converts them into differential equations (Banaji 2005).

BrainSignals

Technical developments allowed the measurement of oxidised CCO concentration using NIRS. In order to better understand and interpret these measurements, the model was extended to simulate them. The BrainCirc model was first greatly simplified in order to maintain the possibility of optimising parameters for each individual patient. The BrainSignals model was then used to successfully simulate ΔoxCCO and tissue oxygen saturation (TOS) measurements from patients undergoing hypoxia and hypercapnia challenges (Banaji et al. 2008). The model was later also shown to predict data from a hypoxemia challenge (low blood oxygen levels) (Jelfs et al. 2012).

Copyright material removed.

Figure 4.17: Schematic of the BrainSignals model (Banaji et al. 2008).

BrainPiglet

Following the commencement of hypoxia-ischaemia experiments in piglets by a collaborating research group, in 2012 Moroz et al. published the first version of the BrainPiglet model. This is an adaptation and extension of the BrainSignals model (Moroz et al. 2012). 11 of the 107 parameters were altered to suit the piglet brain. The model was also extended to simulate magnetic resonance spectroscopy (MRS) measurements - ATP, PCr, Pi and

lactate - which were recorded simultaneously during the experiments. The next section details this model.

Comparison

The general differences between the BrainCirc, BrainSignals and BrainPiglet v1.0 models are detailed in Table 4.2. Compartments included are volume compartments in reactions and do not include blood compartments. The number of parameters include those that are explicitly set as well as those that are derived from other parameters.

Table 4.2: A comparison of the three models.

	BrainCirc	BrainSignals	BrainPiglet v1.0
Compartments	4	1	2
Reactions	81	5	16
Differential equations	5	5	5
Algebraic relations	72	3	3
Variables	168	12	30
Parameters	697	196	270

Computational environments

With the development of the first model BrainCirc, the team also created a similarly named interface BRAINCIRC to compile the model. The models are encoded as a combination of reactions, differential equations and algebraic relations. However, this interface was ridden with many issues - exasperated further by a lack of proper documentation. A new simpler interface has been recently developed by Matthew Caldwell, called BCMD –

TABLE 4.3 Timeline of models of cerebral metabolism produced at UCL

2005	•	BrainCirc
2008	•	BrainSignals
2012	•	BrainPiglet v1.0
2013	•	BrainPiglet v2.0
2014	•	BrainPiglet v2.1
	•	BrainSignals neonatal
	•	Baby Brain

Brain/Circulation Model Developer (Figure 4.18). BCMD retains the same logical basis of model construction – the model is described in reactions and differential equations – and uses the same RADAU5 solver, but offers a much better understanding of model behaviour. The interface software and all model definitions are freely available from <http://tinyurl.com/ucl-bcmd>. Unlike BRAINCIRC which only runs in a Linux environment, BCMD is also compatible with Windows and Mac environments.

BCMD is mainly written in Python 2.7, however models are translated into C and linked against a Fortran library. It uses the RADAU 5 DAE solver by Hairer and Wanner (1996) – an implicit Runge-Kutta method of order 5 for integrating stiff systems of differential-algebraic equations. BCMD offers a number of functions. In model compilation and running, the graphical user interface (GUI) is able to outline any errors. Initial values of model parameters can be altered, artificial inputs can be generated (including noise), and outputs can be plotted. The software enables sensitivity analysis (including the morris method used in this thesis) and can generate relevant heatmaps. It also allows for optimisation of parameter values to better simulate known outputs, using the particle swarming method used in this thesis. BCMD can further be used to create dependency graphs of model variables and parameters such as those presented in the discussion in Chapter 5.

As discussed earlier in this chapter, several other modelling environments are used in systems biology. The systems biology markup language (SBML) (Hucka et al. 2003) and CellML (Cuellar et al. 2003) are the most popular languages for model specification. Both are based on XML and enable the computational representation of biological processes, which must be compiled using suitable software. Commonly, these software environments do not support the use of time series data, and we have not identified one that does. The models encoded are often perturbed from steady state by altering parameter values, the effect of which may be observed over time. These environments are hence not compatible with the objective of the UCL metabolism models.

The early BRAINCIRC interface does facilitate the import and export of SBML models. The metabolism models are thus available in SBML format, although their functionality is significantly reduced by the environment. The BCMD interface may also include a similar feature in the future. MATLAB is another popular environment for systems biology models. While

it useful (and has been used) for signal processing of measurements and plotting results, confining the model to MATLAB restricts access to those who have license to use the software. BRAINCIRC and BCMD on the other hand are open-source, and freely available. They also compile the model first before it is run, unlike MATLAB, and so have a lower computational cost.

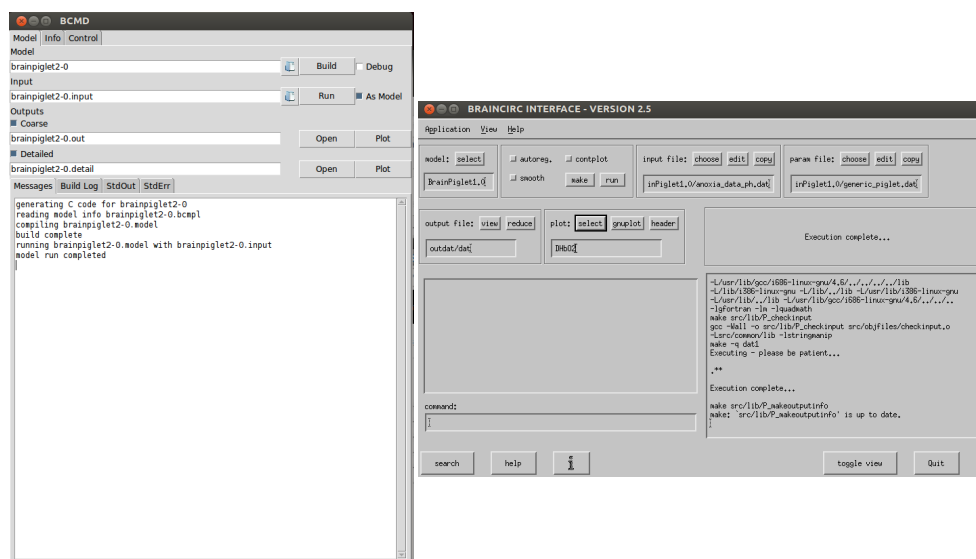


Figure 4.18: The BRAINCIRC and BCMD modelling environments.

4.4 Modelling principles

Although the UCL group have produced a number of different models, they all follow the same general principles. This section is an overview of the modelling approach taken to simulate chemical reactions and transport processes. These methods are widely used in quantitative biology – a good review can be found in Haefner (2005).

4.4.1 Chemical reactions

Mathematical models represent chemical reactions in different ways, depending on the type of reaction and the information the model aims to convey. The BrainPiglet model uses the same technique that was conceptualised in the BrainCirc model. The types of reactions encoded in these models, and how they are constructed is described below.

Mass Action

These reactions can be reversible or irreversible, with two rate constants or just one in the latter case. For example, take the reversible reaction involving substrates A and B to produce C and D. This reaction is represented by



where n_a, n_b, n_c and n_d represent the quantities of each substrate and k_1 and k_{-1} represent the rates of the forward and backward reactions respectively. The rate of formation of any product can be calculated. For example, for product C;

$$[\dot{C}] = k_1 [A]^{n_a} [B]^{n_b} - k_{-1} [C]^{n_c} [D]^{n_d} \quad (4.2)$$

At equilibrium, the forward and backward rates are equal and so the equilibrium constant K_{eq} is thus

$$K_{eq} = \frac{k_1}{k_{-1}} = \frac{[A]^{n_a} [B]^{n_b}}{[C]^{n_c} [D]^{n_d}} \quad (4.3)$$

The Gibbs free energy change for the reaction is zero at equilibrium, but at other times is given by

$$\Delta G = RT \left[-\ln K_{eq} + \ln \left(\frac{[A]^{n_a} [B]^{n_b}}{[C]^{n_c} [D]^{n_d}} \right) \right] \quad (4.4)$$

Michaelis Menten

Reactions catalysed by enzymes are represented mathematically as Michaelis Menten equations, which capture the following kinetics between a substrate S, enzyme E and product P:



The first reaction forming the substrate complex (ES) is reversible but the second creating the product is not. The total concentration of enzyme is assumed constant. For example, take the simple enzyme-catalysed reaction



where V_{max} is the maximum rate of reaction and Km_A is the Michaelis constant for A - the concentration of A at which the reaction rate is half the maximum. We assume that the concentration of the ES complex also remains constant i.e. $[\dot{E}S] = 0$. This leads to

$$V_{max} = k_2[E_T] \quad (4.7)$$

$$Km_A = \frac{k_{-1} + k_2}{k_{-1}} \quad (4.8)$$

where $[E_T]$ is the total concentration of enzyme ($= [E] + [ES]$). The rate of formation of product is represented by

$$[\dot{A}] = -\frac{V_{max}[A]}{Km_A + [A]} \quad (4.9)$$

4.4.2 Transport

Passive diffusion across a barrier is simulated in the model as a mass action process.

$$\frac{\delta c_1}{\delta t} = -D(c_1 - c_2) \quad (4.10)$$

where c_1 and c_2 are the concentrations in the two compartments, and D is the diffusion coefficient. Active or carrier-mediated transport of substances, such as those instigated by membrane proteins, are represented in a more complex format such as Michaelis-Menten equations.

4.5 Model optimisation

There are two main approaches to model optimisation - first the optimisation of the model itself to develop, for example, a faster, simpler and more accurate model, and second the optimisation of model parameters to produce a better simulation. The first approach is discussed in Chapter 9. This section focuses on the latter.

It is often advantageous and sometimes necessary to optimise a model to the particular event or environment being simulated. This is especially true for data driven models, where the results are so dependent on the individual data set being used.

The models presented in this thesis aim to be patient- and state-specific. That is, they simulate a clinical scenario in a particular patient and at a particular moment in time when their cerebral health maybe changing. Thus for accurate simulations it is vital that the model parameters are optimised to the greatest possible extent.

4.5.1 Sensitivity analysis

Some models, such as those presented in this thesis, incorporate a large number of parameters which can be computationally exhaustive to optimise. Thus, methods of sensitivity analysis can be used to determine the most influential parameters for the variables that we are investigating. This initial selection greatly reduces the computational cost and complexity of optimisation, allowing a smaller set of parameters to be optimised to achieve significantly more accurate simulations.

A very simple form of this analysis would be to increment each parameter x by Δx in turn and measure the effect on the model output. While this maybe sufficient for small, simple models, when working with a large number of parameters it is essential to take into account the interaction between parameters as well.

The Morris method

The Morris method is one of the most popular sensitivity analysis methods for models with a large number of parameters. It aims to determine the factors with effects that are (i) negligible, (ii) linear and additive and (iii) non-linear or involved in interactions with other factors. These effects are calculated by changing one factor at a time (Saltelli et al. 2004).

For a k -dimensional vector of parameters X , with components X_i , each can assume integer values in the set $0, 1/(p-1), 2/(p-1), \dots, 1$. The parameter space is then a k -dimensional p -level grid. Let Δ be a predetermined multiple of $1/(p-1)$. For a given value x of X , the elementary effect for the i th input factor is

$$d_i(x) = \frac{[y(x_1, \dots, x_{i-1}, x_i + \Delta, x_{i+1}, \dots, x_k) - y(x)]}{\Delta} \quad (4.11)$$

where $x = (x_1, x_2, \dots, x_k)$ is any selected value in the parameter space such that for all $i = 1, \dots, k$, $(x + e_i\Delta)$ is still in the parameter space, where e_i is a vector of zeros with a unit as its i th component (Saltelli et al. 2004; Morris 1991).

A distribution of elementary effects F_i for each i th input factor is calculated by randomly sampling different x from the parameter space. The number of effects of each F_i is $p^{k-1}[p - \Delta(p - 1)]$. The mean μ of the distribution F_i , or more commonly to allow for non-linear effects, the mean of the absolutes μ^* , and the standard deviation σ , is calculated for each parameter. Thus parameters with a greater influence have a larger value of μ^* . A greater standard deviation σ indicates that the parameter's influence on the output depends on its interaction with other parameters.

4.5.2 Parameter optimisation

There are a number of different methods of optimising parameter values to suit different models and modelling approaches.

The Powell method

The Powell's conjugate direction method locates a minimum of a function of several variables, without calculating derivatives. The best known approximation of the minimum is used as a starting point. On each iteration, the algorithm selects a new direction to search for a minimum. However, it is possible that the minimum calculated in this manner may be a local minimum and not a global one (Powell 1964).

This method was used as an initial optimisation technique (via SciPy (Jones et al.)). However, locating local minimums is not sufficient for a parameter space as complex as this one. Therefore, a global minimum method was used instead.

The PSwarm method

The particle swarm or PSwarm method, also derivative-free, is a global optimisation algorithm for variables that have specific lower and upper bounds

(Vaz and Vicente 2007, 2009). Each iteration is divided into two steps. The first, the poll step, applies a pattern search method (more specifically a coordinate search). The second, the search step, uses particle swarming to generate points in the feasible region, in order to find a global minimum. Generating a population in the search step allows the algorithm to then poll around the best particle, and so improves the overall robustness of the algorithm (Vaz and Vicente 2009). This method was used to optimise the models in this thesis.

4.6 The BrainSignals model

This section introduces the first of two previously published models that have been used and extended in this thesis. The BrainSignals model presented here was published by Banaji et al. (2008) and simulates circulation and metabolism in the *adult* human brain. Following another much larger model of brain metabolism (Banaji et al. 2005), it was distinct in its ability to predict changes in CCO and simulate brain activation.

4.6.1 Model structure

This was the first model to simulate and predict the state of the CuA centre in cytochrome-c-oxidase in an *in vivo* setting. The model also incorporates functional activation, and so respond to four stimuli: changes in blood pressure, arterial oxygenation, arterial carbon dioxide and functional activation. Figure 4.19 illustrates the processes included in the model.

Functional activation is simulated by a parameter u which represents energy demand in the brain. The normal value for this parameter is set as 1. Increasing this value represents activation.

Circulation

A simplified version of the circulatory model published by Ursino and Lodi (1998) has been incorporated in to the model. It includes a proximal and distal arterial compartment which regulates flow by responding to stimuli differently. It is divided into three compartments: the arteries (and arterioles), capillaries and veins with volumes V_a , V_c and V_v respectively. V_c is assumed to be negligible. V_a is proportional to the square of the arterial radius. On the other hand, V_v is constant. CBF – the volume of blood which flows through a unit volume of tissue in unit time – is defined by the following:

$$CBF = (P_a - P_v)G \quad (4.12)$$

where P_a and P_v are the arterial and venous blood pressures. G is the conductance, determined by:

$$G = K_G r^4 \quad (4.13)$$

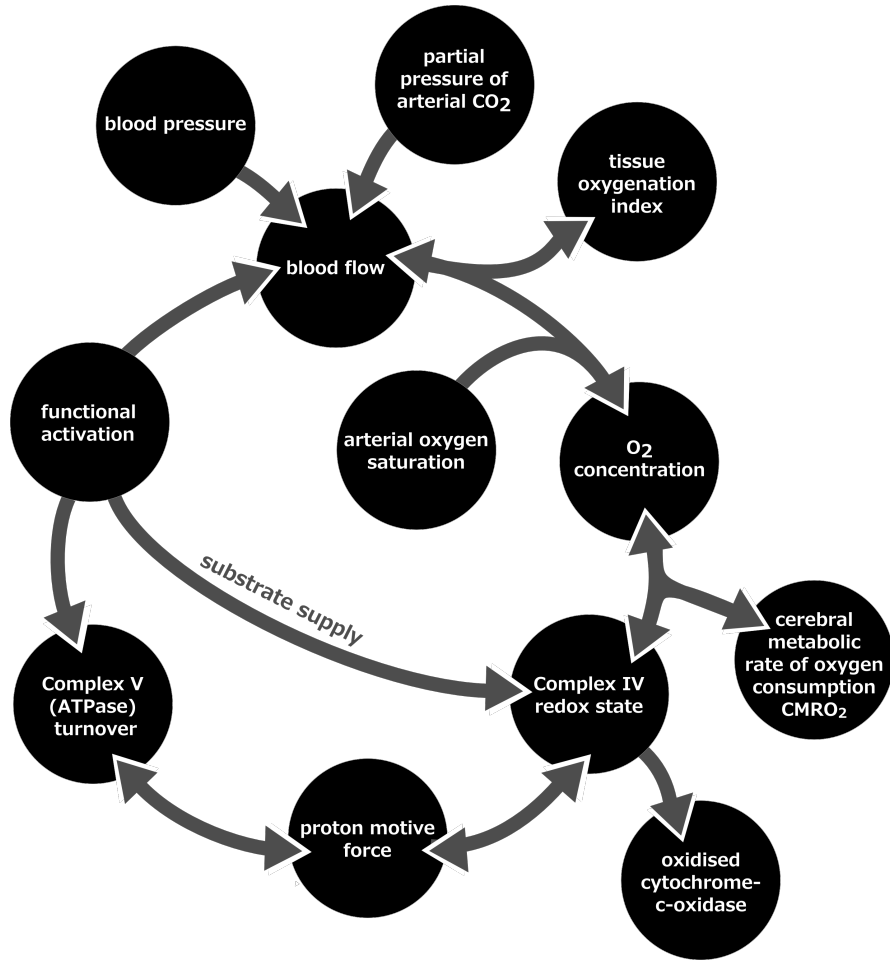


Figure 4.19: Schematic of the BrainSignals model

where K_G is a constant and r is the typical radius of the blood vessel according to the Poiseuille law. The radius is governed by its relationship with the elastic and muscular forces of the vessel wall, T_e and T_m respectively:

$$T_e + T_m = \left(\frac{P_a + P_v}{2} - P_{ic} \right) r \quad (4.14)$$

where P_{ic} is the intracranial pressure (assumed constant).

$$T_e = \left(\sigma_{e0} \left(e^{K_\sigma(r-r_0)/r_0} - 1 \right) - \sigma_{coll} \right) h \quad (4.15)$$

where σ_{e0} , K_σ , r_0 and σ_{coll} are constants. h is thickness of the thickness of the vessel wall, determined by the following which conserves wall volume:

$$(r + h)^2 - r^2 = (r_0 + h_0)^2 - r_0^2 \quad (4.16)$$

h_0 and r_0 are the normal thickness and radius of the vessel wall.

$$T_m = T_{max} \exp\left(-\left|\frac{r + r_m}{r_1 - r_m}\right|^{n_m}\right) \quad (4.17)$$

where T_{max} is the maximum tension, r_m is the radius at T_{max} and r_t and n_m are parameters which control the shape of the curve. T_{max} determines the influence of stimuli on tension, and hence is controlled by SaO_2 , P_aCO_2 , P_a and the energy demand (u). η represents this influence,

$$\eta = \sum_x R_x \left(\frac{v_x}{v_{x_n}} - 1\right) \quad (4.18)$$

where x represents one of the four quantities above. R_x represents the sensitivity to the stimulus and v_x is time filtered x

$$\frac{dv_x}{dt} = \frac{1}{\tau_x}(x - v_x) \quad (4.19)$$

where τ_x is constant that determines how long it takes for the stimulus to have a vasoactive effect. T_{max} relates to η

$$T_{max} = T_{max}(1 + k_{aut}\mu) \quad (4.20)$$

where k_{aut} is a constant that simulates the autoregulation capacity of the brain, normally set to 1. μ represents the level of regulatory input, which depends on η via a sigmoidal function and is defined by

$$\mu = \frac{\mu_{min} + \mu_{max}e^\eta}{1 + e^\eta} \quad (4.21)$$

where μ_{min} and μ_{max} are the bounds of μ . Figure 4.20 illustrates the effect of k_{aut} on autoregulation in the model.

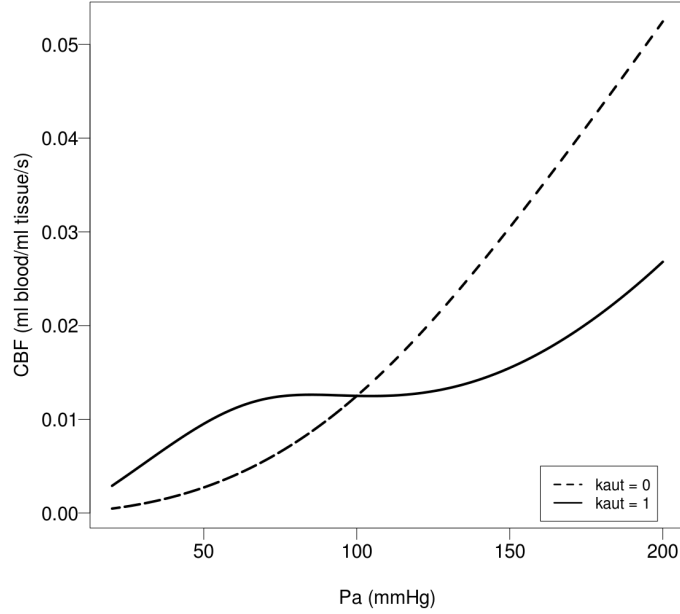


Figure 4.20: The autoregulation curve at steady state, with the two extreme values of the autoregulation constant k_{aut} .

Oxygen Transport

The model simulates oxyhaemoglobin (HbO_2) and deoxyhaemoglobin (HHb) concentrations in blood. The total concentration of haemoglobin ($[Hbtot]$) is assumed to remain constant;

$$[HbO_{2,a}] + [HHb_a] = [HbO_{2,v}] + [HHb_v] = [Hbtot] \quad (4.22)$$

where subscripts a and v denote arterial and venous compartments respectively. Arterial oxygenation can be determined using arterial oxygen saturation (SaO_2), which is often measured;

$$[HbO_{2,a}] = SaO_2[Hbtot] \quad (4.23)$$

SvO_2 is venous oxygen saturation and is similarly calculated:

$$[HbO_{2,v}] = SvO_2[Hbtot] \quad (4.24)$$

Oxygen concentration in the capillaries ($[O_{2,c}]$) depends on capillary saturation ScO_2 .

$$[O_{2,c}] = \phi \left(\frac{ScO_2}{1 - ScO_2} \right)^{\frac{1}{n_h}} \quad (4.25)$$

where ϕ is the concentration of oxygen at half the maximum saturation and n_h is the Hill coefficient for the dissociation of oxygen from haemoglobin. This model does not incorporate the Bohr effect and so this value remains a constant.

$$ScO_2 = \frac{SaO_2 + SvO_2}{2} \quad (4.26)$$

Oxygen is transported from the capillaries to the mitochondria at rate $J_{O_2,min}$, where

$$J_{O_2,min} = D_{O_2}([O_{2,c}] - [O_2]) \quad (4.27)$$

where D_{O_2} is the diffusion coefficient and $[O_2]$ and $[O_{2,c}]$ are oxygen concentrations in the mitochondria and the capillary respectively. Under normal conditions, D_{O_2} is such that the rate of use of oxygen ($CMRO_2$) is equal to the rate of delivery. Further, we assume

$$J_{O_2,min} = CBF([HbO_{2,a}] - [HbO_{2,v}]). \quad (4.28)$$

Thus combining the above equations provide the means of calculating oxygen saturations in the veins and capillaries and $J_{O_2,min}$.

The tissue oxygenation saturation (TOS) is calculated by the following:

$$TOS = \frac{Vol_{art}[HbO_{2,a}] + Vol_{ven}[HbO_{2,v}]}{(Vol_{art} + Vol_{ven})[Hbtot]} \quad (4.29)$$

Vol_{art} is assumed proportional to r^2 , so

$$Vol_{art} = Vol_{art,n} r^2 / r_n^2 \quad (4.30)$$

where $Vol_{art,n}$ and r_n are the corresponding normal values. With normal arterio-venous volume ratio AVR_n ,

$$AVR_n = Vol_{art,n} / Vol_{ven} \quad (4.31)$$

TOS can be defined as :

$$TOS = \frac{(r/r_n)^2 [HbO_{2,a}] + [HbO_{2,v}] / AVR_n}{((r/r_n)^2 + \frac{1}{AVR_n}) [Hbtot]} \quad (4.32)$$

$Vol_{blood,n}$ is defined as an estimate of blood volume in tissue. Hence the concentration of total, oxy- and deoxy-haemoglobin can be calculated by:

$$HbT = \frac{1000}{4} (Vol_{art} + Vol_{ven}) [Hbtot] Vol_{blood,n} \quad (4.33)$$

$$HbO2 = \frac{1000}{4} (Vol_{art} [HbO_{2,a}] + Vol_{ven} [HbO_{2,v}]) Vol_{blood,n} \quad (4.34)$$

$$HHb = HbT - HbO2 \quad (4.35)$$

The values are multiplied by $Vol_{blood,n}$ to convert hem to tissue concentrations and the factor of 1000/4 arises from the conversion of units (mM to μ M) and the 4 binding sites on haemoglobin. The NIRS quantities of ΔHbT , $\Delta HbO2$ and ΔHHb are thus

$$\Delta HbO2 = HbO2 - HbO2_n \quad (4.36)$$

$$\Delta HHb = HHb - HHb_n \quad (4.37)$$

$$\Delta HbT = HbT - HbT_n \quad (4.38)$$

Metabolism

A mitochondrial submodel is used here as an approximation of the more detailed processes, inspired by earlier models Korzeniewski and Zoladz (2001), Beard (2005) and Banaji (2006), and focuses on oxidative phosphorylation. Protons are pumped into the mitochondria creating a proton motive force, Δp . Protons then return back to the cytoplasm via ATP synthase, and thus

drive the production of ATP. The proton motive force Δp has a chemical and an electrical component:

$$\Delta p = \Delta\Psi + Z\Delta pH_n \quad (4.39)$$

where $\Delta\Psi$ is the membrane potential and ΔpH_n is the difference between cytoplasmic pH, pH_o , and mitochondrial pH, pH_m . Z is a constant defined by

$$Z = \frac{RT}{\log_{10}(e)F} \quad (4.40)$$

where R is the ideal gas constant, T is temperature and F is the Faraday constant. Cytoplasmic pH is constant in the model but mitochondrial pH is related to the concentration of protons. The mitochondrial volume of protons is $R_{Hi}V_{mit}$, where V_{mit} is the mitochondrial volume and R_{Hi} is a scaling factor given by

$$R_{Hi} = \frac{C_{buffi}}{(10^{-pH_m} - 10^{(-pH_m - dpH)})/dpH} \quad (4.41)$$

where C_{buffi} and dpH are constants.

The model simulates oxidative phosphorylation by way of two redox centres in cytochrome c oxidase – Cu_A and the terminal electron acceptor cytochrome a_3 . These centres can be in either oxidised or reduced state. The electron transport chain is modelled as three reactions. The first combines Complexes I-III and involves the transfer of four electrons from NADH to the Cu_A centre and $p1$ protons across the mitochondrial membrane. This reversible reaction has rate f_1 ;

$$f_1 = k_1Cu_{A,o} - k_{-1}Cu_{A,r} \quad (4.42)$$

where k_1 and k_{-1} are the forward and backward rates respectively.

$$k_1 = k_{1,0} \exp(-c_{k1}(\Delta p - \Delta p_n)) \quad (4.43)$$

where $k_{1,0}$ is related to $NAD/NADH$, c_{k1} is a constant and Δp_n is the normal value of Δp . The ratio of the forward and backward rates is given by

$$\frac{k_1}{k_{1,0}} = Keq_1 = \frac{Cu_{A,oeq}}{Cu_{A,req}} \quad (4.44)$$

The free energy produced by this reaction is represented as ΔG_1 :

$$\Delta G_1 = -4 \left(E_1 + Z \log \left(\frac{Cu_{A,o}}{Cu_{A,r}} \right) \right) + p_1 \Delta p \quad (4.45)$$

where E_1 is defined by:

$$E_1 = \varepsilon_0(Cu_A) - \varepsilon_0(NADH) + \frac{Z}{2} \log \left(\frac{1}{[NAD]/[NADH]} \right) \quad (4.46)$$

where ε_0 is a standard redox potential. $\Delta G_1 = 0$ at equilibrium, so the equilibrium constant can be calculated as

$$Keq_1 = 10^{-(p_1 \Delta p / 4 - E_1) / Z} \quad (4.47)$$

The second reaction involved the transfer of four electrons to the haemoglobin a_3/Cu_B centre and the movement of p_2 protons across the membrane. The reversible reaction has rate

$$f_2 = k_2 Cu_{A,r} cyta_{3,o} - k_{-2} Cu_{A,o} cyta_{3,r} \quad (4.48)$$

where k_2 and k_{-2} are the forward and backward rates respectively.

$$k_2 = k_{2,n} \exp(-c_{k2}(\Delta p - \Delta p_n)) \quad (4.49)$$

where $k_{2,n}$ and c_{k2} are constants. As with the first reaction, the free energy is given by

$$\Delta G_2 = -4 \left(E_2 + Z \left(\log \left(\frac{Cu_{A,r}}{Cu_{A,o}} \right) + \log \left(\frac{cyta_{3,o}}{cyta_{3,r}} \right) \right) \right) + p_2 \Delta p \quad (4.50)$$

which gives equilibrium constant

$$\frac{k_2}{k_{-2}} = Keq_2 = 10^{(p_2 \Delta p / 4 - E_2) / Z} \quad (4.51)$$

In the last reaction, oxygen is reduced and p_3 protons are moved across the membrane. The rate is given by

$$f_3 = k_3 [O_2] c_{yta_{3,0}} \left(\frac{e^{c_3(\Delta p - \Delta p_{30})}}{1 + e^{c_3(\Delta p - \Delta p_{30})}} \right) \quad (4.52)$$

where Δp_{30} , c_3 and k_3 are constants. The rate of oxygen consumption ($CMRO_2$) is determined by the rate of this reaction:

$$CMRO_2 = V_{mit} f_3 \quad (4.53)$$

Under normal conditions, $f_1 \equiv f_2 \equiv f_3$. The membrane potential $\Delta\Psi$ is proportional to the rates of these reactions:

$$\frac{d\Delta\Psi}{dt} = \frac{p_1 f_1 + p_2 f_2 + p_3 f_3}{C_{im}} \quad (4.54)$$

where C_{im} is the capacitance of the inner mitochondrial membrane. The flow rate of protons through Complex V, through the membrane, L_{CV} is simulated as

$$L_{CV} = L_{CV,max} \left(\frac{1 - e^{-\theta}}{1 + r_{CV} e^{-\theta}} \right) \quad (4.55)$$

where $L_{CV,max}$ is the maximum flow rate and r_{CV} is a constant that accounts for the difference between forward and backward rates.

$$\theta = k_{CV}(\Delta p + Z \log(u) - \Delta p_{CV0}) \quad (4.56)$$

where Δp_{CV0} is the proton motive force at which no movement of protons would be induced. Normal conditions see 25 % of protons return through leak channels. This percentage varies with the proton motive force Δp .

$$L_{lk} = k_{unc} L_{lk0} (\exp(k_{lk2} \Delta p) - 1) \quad (4.57)$$

where L_{lk0} and k_{lk2} are constants. k_{unc} represents uncouplers - under normal conditions this value is set as 1.

Table 4.4: BrainSignals model equations. These reactions are modelled as simple diffusion, and take place in the mitochondrial compartment.

Reaction	Equation
Oxidative phosphorylation	$14H_{mit}^+ + 4Cu_{A,o} \rightarrow$ $4H_{mit}^+ \rightarrow 4Cu_{A,o} + 4cyta_{3,r}$ $O_2 + 4H_{mit}^+ + 4cyta_{3,r} \rightarrow$
Protons re-enter mitochondrial matrix (via leak and complex V)	$\rightarrow H_{mit}^+$
Oxygen in	$\rightarrow O_2$

4.6.2 Steady state simulations

Figures 4.21 and 4.22 illustrate the BrainSignals adult model at steady state within a range of input values in SaO_2 , P_a , P_aCO_2 and demand u . Increasing SaO_2 sees decreasing CBF and blood volume as less blood is required to oxygenate the tissue (Figure 4.21). Correspondingly, increased oxygenation and metabolic activity are observed (TOI, $\Delta oxCCO$ and $\Delta CMRO_2$). These relationships are largely almost linear. Increasing blood pressure is followed by increasing oxygenation and metabolic activity. CBF displays the typical autoregulation curve, with a steady phase around the normal blood pressure value of 100 mmHg. Normalised blood volume reaches a maximum higher than 1 around 50mmHg before returning to normal around 100mmHg, as blood volume rises to compensate for low pressure.

Model behaviour at very low values of SaO_2 and P_a (for example below 50% and 40 mmHg respectively) are unreliable as these values are quite unlikely in an adult patient. While these functions in this range may be of mathematical interest, care must be taken in interpreting model results beyond the range commonly observed in clinical data.

Increases in demand cause an almost linear increase in CBF, blood volume, $\Delta oxCCO$ and $\Delta CMRO_2$ (Figure 4.22). Note that at demand lower than normal ($0 < u < 1$), these values are below normal as well. TOI also displays low values at demand less than normal, but increases as demand rises. P_aCO_2 also shows almost linear relationships with each of the variables, increasing with higher metabolic activity.

4.6. The BrainSignals model

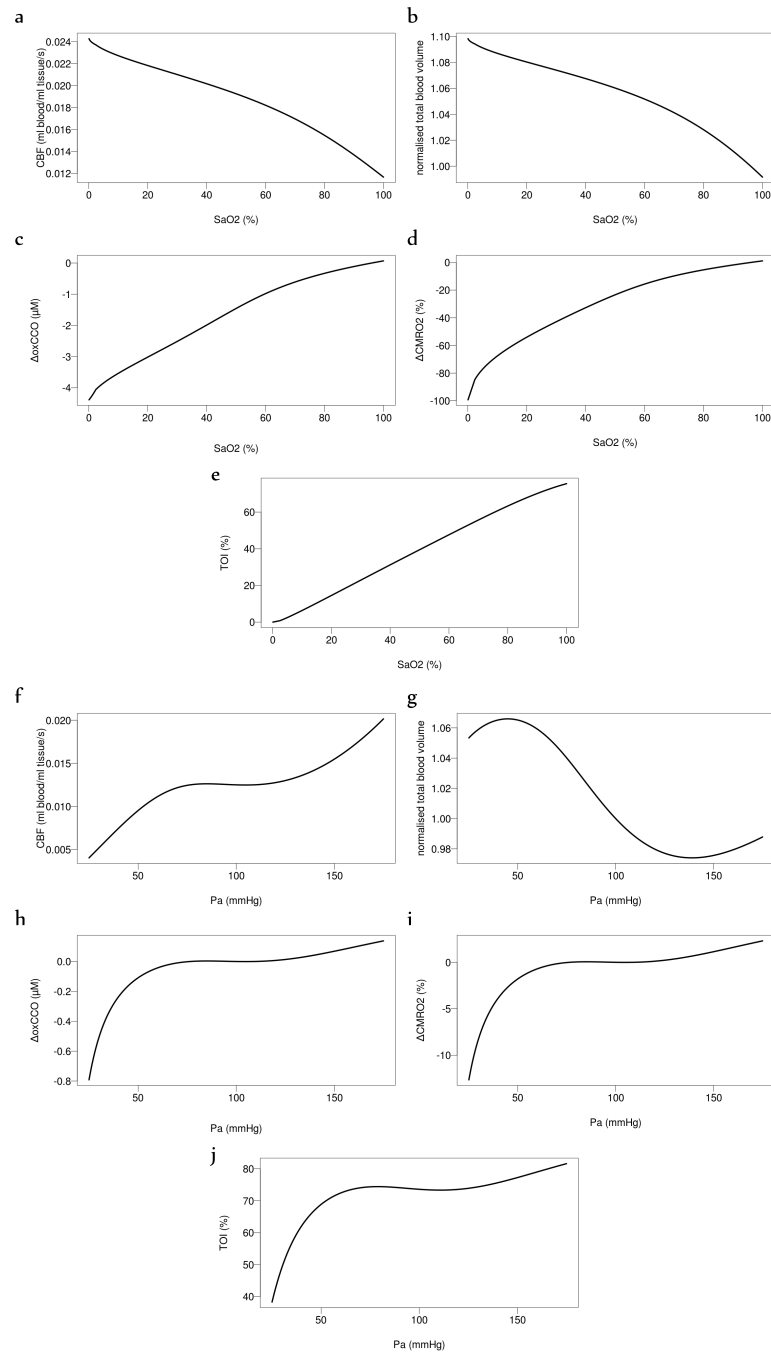


Figure 4.21: Steady state simulations of the BrainSignals model with varying arterial oxygen saturation SaO_2 (a–e) and blood pressure Pa (f–j).

4.6. The BrainSignals model

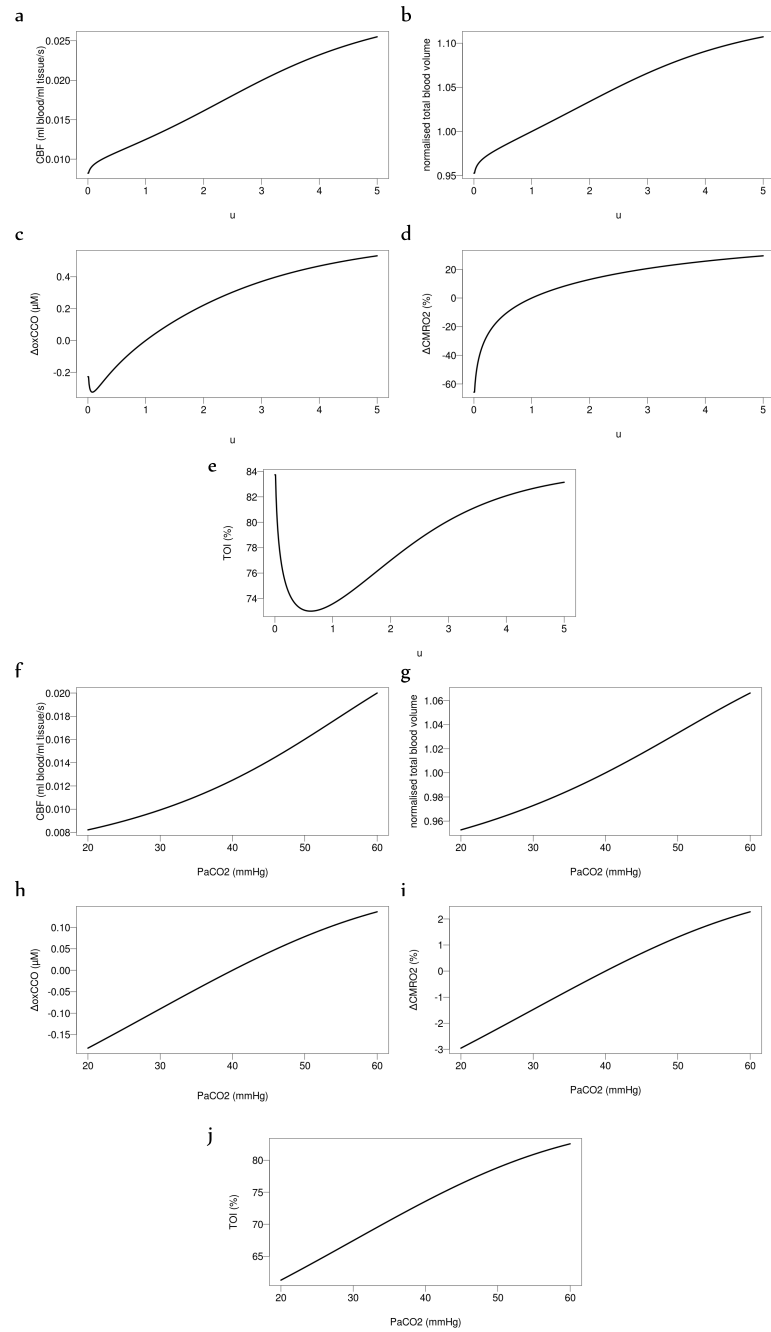


Figure 4.22: Steady state simulations of the BrainSignals model with varying demand u (a–e) and partial pressure of carbon dioxide P_aCO_2 (f–j).

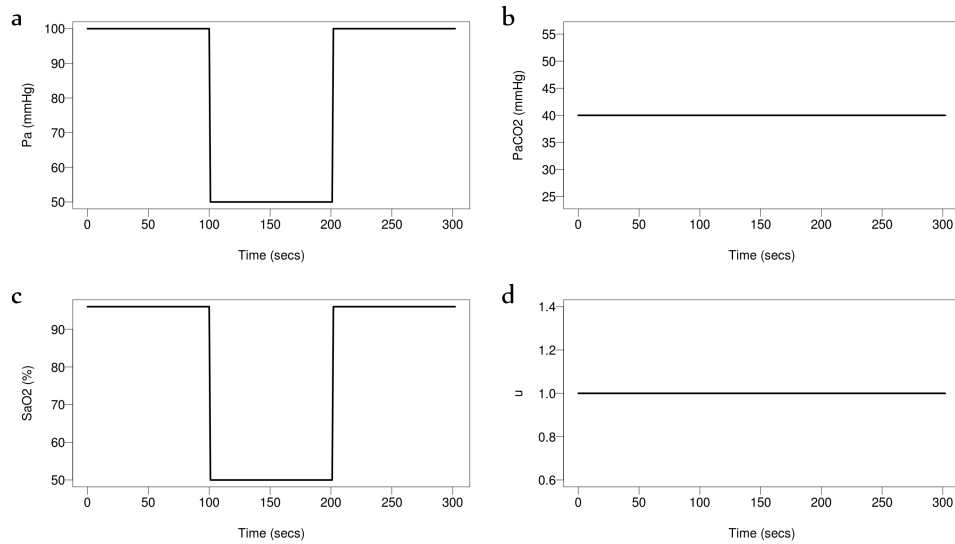


Figure 4.23: Inputs to the BrainSignals model to simulate hypoxia-ischaemia. (a) Blood pressure, P_a , and (c) arterial oxygen saturation, SaO_2 are reduced temporarily while (b) partial pressure of carbon dioxide, P_aCO_2 and (d) the energy demand, u are kept constant.

4.6.3 Simulating hypoxia-ischaemia

The BrainSignals model is used here to simulate the response to a temporary decrease in oxygenation and blood flow, to illustrate the model's capability. Blood pressure and SaO_2 are reduced by approximately half, to 50mmHg and 50% respectively (Figure 4.23). The model predicts a decrease in ΔHbO_2 and rise in ΔHHb , together with a rise in ΔHbT . The model also simulates a drop in metabolic activity; $\Delta oxCCO$ and $CMRO_2$ drops due to the low availability of oxygen, as seen in the TOI (Figure 4.24).

4.6.4 Simulating functional activation

A simple simulation is carried out here, by increasing the energy demand u by in the model 20% to 1.2. Figure 4.25 displays the model inputs. The model then predicts a corresponding rise in ΔHbO_2 and fall in ΔHHb (Figure 4.26). $\Delta oxCCO$ also rises, as does $CMRO_2$ indicating an increase in metabolism. The increase in ΔHbT and CBF suggest an increase in flow to the tissue which also shows an increase in oxygenation via TOI. Thus, this is the overcompensation of flow that is typically observed in adults, with an

4.6. The BrainSignals model

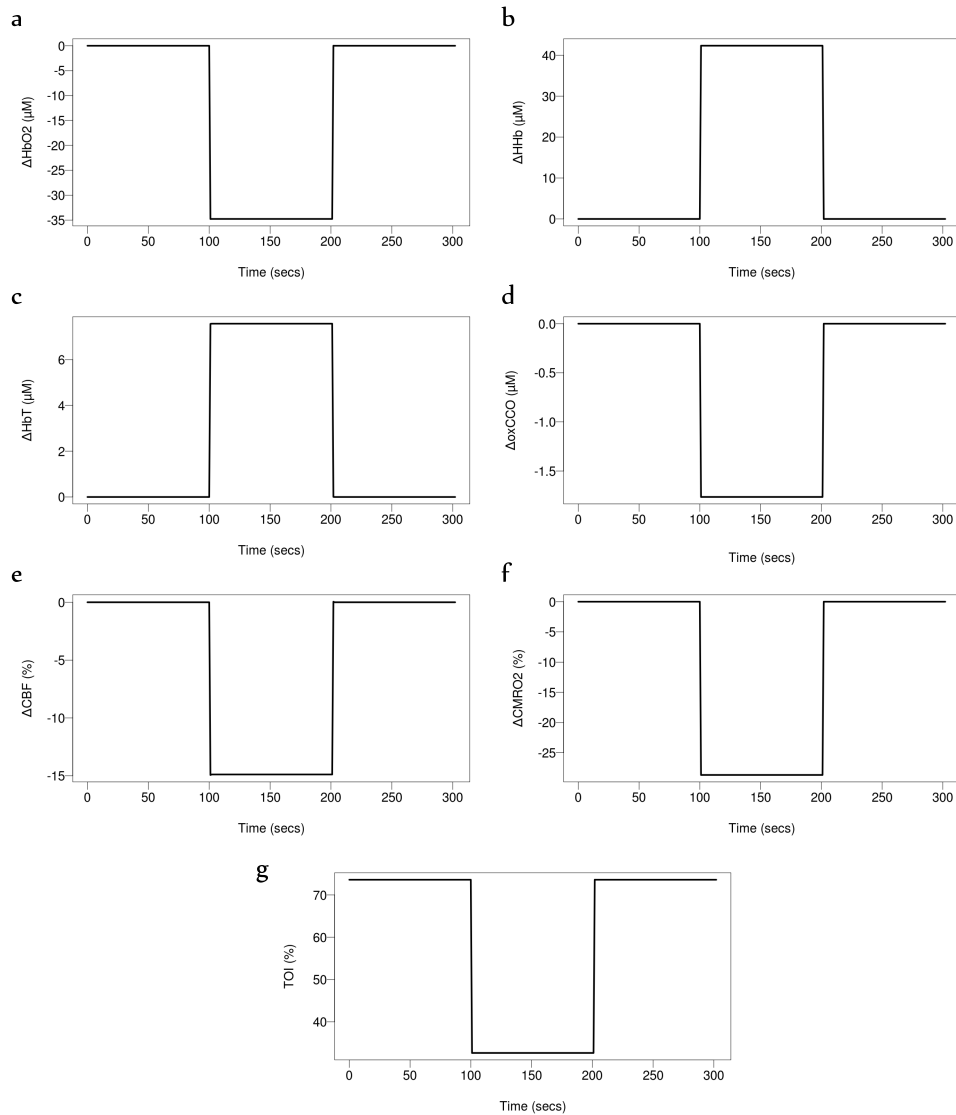


Figure 4.24: Outputs of the BrainSignals model simulation of hypoxia-ischaemia. Changes in (a,b,c) oxy-haemoglobin deoxy-haemoglobin and total haemoglobin, ΔHbO_2 , ΔHHb , ΔHbT and (d) oxidised cytochrome-c-oxidase $\Delta oxCCO$. Percentage change in (e) cerebral blood flow, CBF, (f) cerebral metabolic rate of oxygen consumption $CMRO_2$ and (g) tissue oxygenation index, TOI

increase in blood flow overcompensating the increased demand for oxygen, and hence leading to a decrease in ΔHHb .

When the energy demand returns to baseline, so do the variables above.

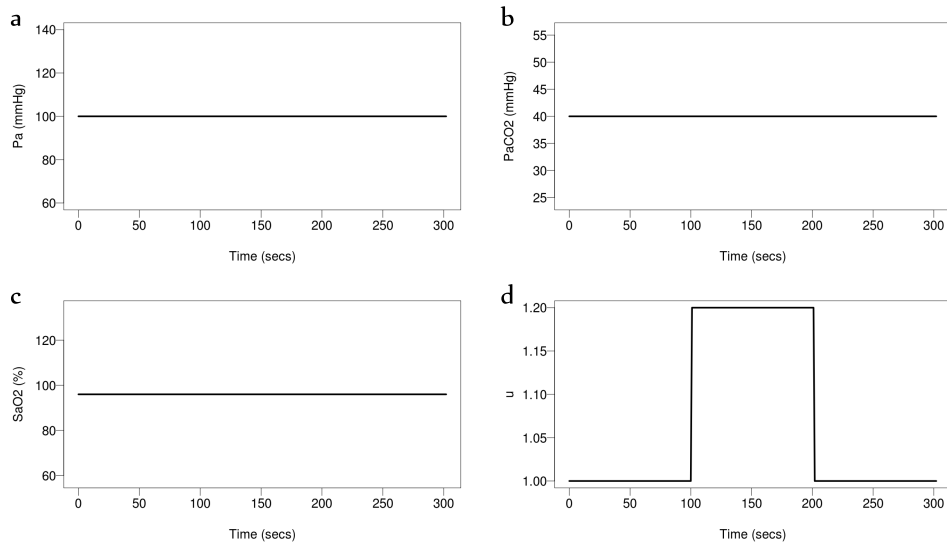


Figure 4.25: Inputs to the BrainSignals model to simulate brain activation. (a) Blood pressure, P_a , (b) partial pressure of carbon dioxide, $P_a\text{CO}_2$ and (c) arterial oxygen saturation, SaO_2 are kept constant while (d) the energy demand, u is increased temporarily.

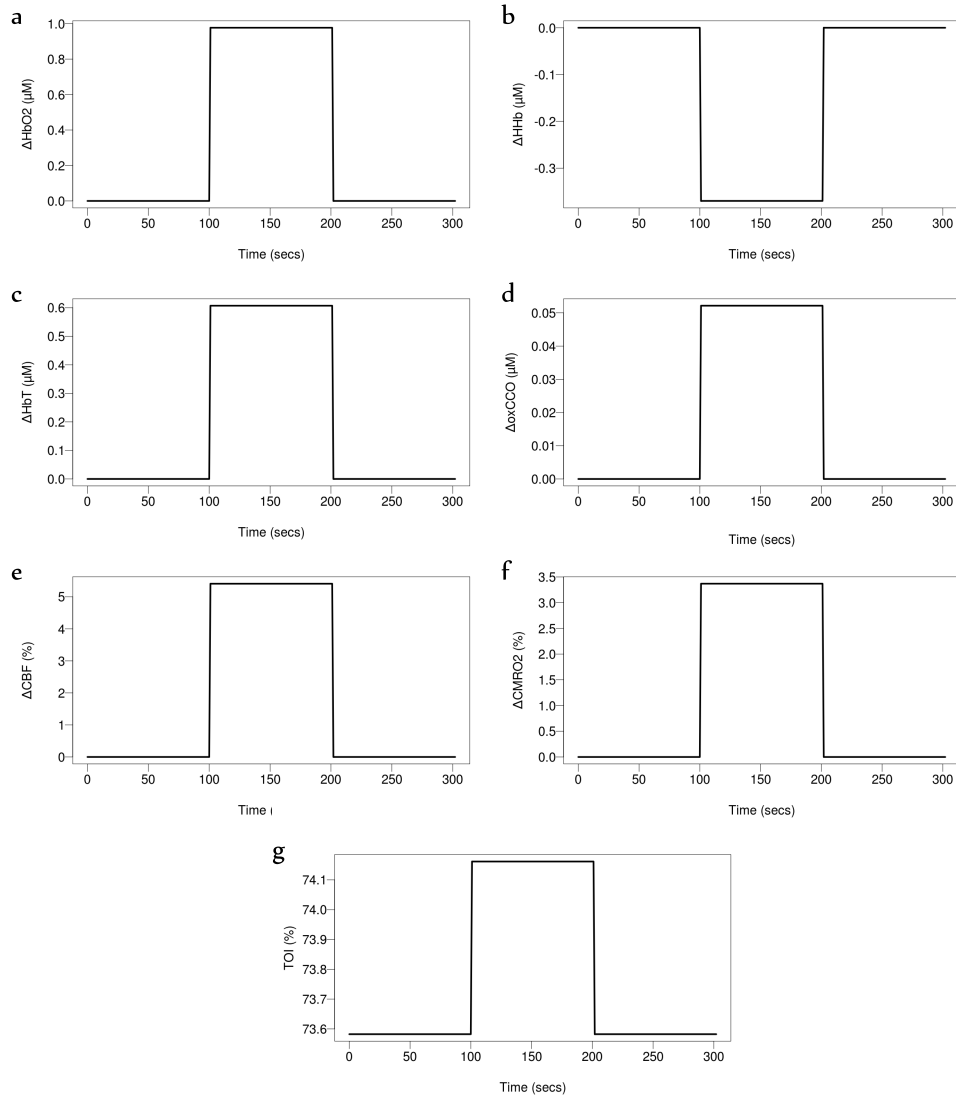


Figure 4.26: Outputs of the BrainSignals model simulation of brain activation. Changes in (a,b,c) oxy-haemoglobin deoxy-haemoglobin and total haemoglobin, ΔHbO_2 , ΔHb , ΔHbT and (d) oxidised cytochrome-c-oxidase $\Delta oxCCO$. Percentage change in (e) cerebral blood flow, CBF, (f) cerebral metabolic rate of oxygen consumption $CMRO_2$ and (g) tissue oxygenation index, TOI

4.7 The BrainPiglet model

Following the commencement of hypoxia-ischaemia experiments in piglets by a collaborating research group, in 2012 Moroz et al. published the first version of the BrainPiglet model. This is an adaptation and extension of the BrainSignals model (Moroz et al. 2012). 11 of the 107 parameters were altered to suit the piglet brain. The model was also extended to simulate magnetic resonance spectroscopy (MRS) measurements - ATP, PCr, Pi and lactate - which were recorded simultaneously during the experiments. This section details this model.

4.7.1 Model structure

The model is focused on simulating cerebral NIRS and MRS measurements in piglets during anoxic, hypoxic and ischaemic insults. Figure 3.6 illustrates a simple schematic of the model.

Copyright material removed.

Figure 4.27: Schematic of the BrainPiglet model v1.0 (Moroz et al. 2012).

Circulation

The circulatory part of BrainPiglet1.0 is an extended form of the circulation model in BrainSignals. Venous volume is no longer constant, and is determined by the change of venous pressure P_v from its normal value $P_{v,n}$:

$$V_v = V_{v,n} + C_v(P_v - P_{v,n}) \quad (4.58)$$

where $V_{v,n}$ is the normal value and C_v is the compliance of the venous compartment, which remains constant. P_v is determined by

$$P_v = \frac{G_v P_{vs} + G_n P_{an}}{G_n + G_v} \quad (4.59)$$

Arterial volume V_a is defined by the arterial radius r :

$$V_a = V_{a,n} \left(\frac{r}{r_n} \right)^2 \quad (4.60)$$

where $V_{a,n}$ is the arterial volume and r_n is the arterial radius under normal conditions. The radius is also controlled by the following relation with the elastic tensions:

$$T_e + T_m - (P_1 - P_{ic})r = 0 \quad (4.61)$$

P_1 is the average pressure in arteries and veins:

$$P_1 = \frac{P_a + P_v}{2} \quad (4.62)$$

Metabolism

A number of additions have been made to the metabolic component of the BrainSignals model. ATP synthesis is simulated in the mitochondrial compartment. However, the movement of ADP and ATP out of the mitochondria is not explicitly modelled. The rate of return of protons through Complex V is altered from BrainSignals to include protons required to phosphorylate ATP.

$$\theta = k_{CV} \left(\Delta p + \frac{Z}{n_a} \log \left(\frac{g_p}{g_{p,n}} \right) - \Delta p_{CV0} \right) \quad (4.63)$$

where n_a is the number of protons required to phosphorylate one ATP molecule and Δp_{CV0} is the proton motive force at which no movement of protons would be induced. g_p is the phosphorylation potential.

$$g_p = \frac{([ADP]/c^\theta)([P_i]/c^\theta)}{[ATP]/c^\theta} \quad (4.64)$$

which is the equilibrium constant for the hydrolysis of ATP. As the concentration of solute is low, the activity is represented by the solute concentration divided by the standard concentration c^θ (1M). Therefore, g_p , like other equilibrium constants is a dimensionless quantity, defined by

$$g_p = \frac{[ADP][P_i]}{(1000mM)[ATP]} \quad (4.65)$$

The Gibb free energy of ATP hydrolysis is given by

$$\Delta G = \Delta G^o + ZF \log(g_p) \quad (4.66)$$

where ΔG^o is the standard Gibbs free energy of hydrolysis and F is the Faraday's constant. Given the above, the proton motive force at which there is no net flow of protons, Δp_{CV0} , is calculated as

$$\Delta p_{CV0} = \frac{-\Delta G_n}{n_a F} \quad (4.67)$$

where ΔG_n is the normal value of ΔG . ATP synthesis occurs in the mitochondria by Complex V at a rate

$$\frac{L_{CV} V_{mit}}{n_a} \quad (4.68)$$

The entirety of the TCA cycle is simulated as a single simple diffusion reaction in the model. The rate of this reaction is given by

$$\frac{v_{TCA} [Py] [NAD]}{(k_{m,tcaN} + [NAD]) (k_{m,tcaP} + [Py])} \quad (4.69)$$

The k_m value for pyruvate is small, suggesting that pyruvate concentration does not greatly influence the TCA cycle unless it is very low. The rate is also influenced by [ATP] and [ADP], but mainly by the NAD/NADH ratio.

Glycolysis is simplified as a single Michaelis Menten reaction, with maximum rate v_{glyc}

$$v_{glyc} = \frac{v_{glyc,n} (I + 1)}{1 + I \frac{[ATP]}{[ATP]_n} \frac{[AMP]_n}{[AMP]}} \quad (4.70)$$

where $v_{glyc,n}$ is the normal maximum rate, I relates to the dependency on AMP and ATP concentrations. Under normal conditions, the rate of glycolysis is set equivalent to the rate of glucose consumption ($CMR_{gluc,n}$). The net rate of glucose transport between capillaries and the cell is

$$v_{glut} \left(\frac{[gluc_c]}{[gluc_c] + k_{glut}} - \frac{[gluc]}{[gluc] + k_{glut}} \right) \quad (4.71)$$

where $[gluc_c]$ and $[gluc]$ are the capillary and cytoplasm glucose concentrations respectively. $[gluc_c]$ is assumed to be constant. k_{glut} is an average of different GLUT transporters found in the brain. The maximum rate v_{glut} is set so that this net rate is equivalent to the normal rate of glucose consumption, $CMR_{gluc,n}$.

The transport of lactate in and out of the cell is simulated similarly. The net rate of transport is thus

$$v_{MCT} \left(\frac{[lac_c]}{[lac_c] + k_{MCT}} - \frac{[lac]}{[lac] + k_{MCT}} \right) \quad (4.72)$$

where $[lac_c]$ and $[lac]$ are the capillary and cytoplasm lactate concentrations respectively, and $[lac_c]$ is assumed constant. The maximum rate v_{MCT} is calculated from the normal rate of lactate consumption, $CMR_{lac,n}$.

Under normal conditions,

$$\frac{1}{6}CMRO_{2,n} - CMR_{gluc,n} = \frac{1}{2}CMR_{lac,n} \quad (4.73)$$

Pyruvate-lactate conversion is simulated as a mass action reaction. This occurs very fast and so effectively the interchange is at equilibrium. The rate of this reaction is given by

$$k_{pl}[Py][H_{cyt}^+] - k_{pl}^- [lac][NAD_{cyt}] \quad (4.74)$$

where k_{pl}^- is a constant and k_{pl} is related to $[NADH_{cyt}]$. Under normal conditions, the ratio k_{pl}/k_{pl}^- is such that the net rate of the reaction is equivalent to $CMR_{lac,n}$.

ATP hydrolysis is simulated as a Michaelis Menten reaction, the maximum rate of which is dependent on a demand parameter, u . Creatine kinase uses phosphocreatine, PCr, to produce ATP. Adenylate kinase convert ADP to AMP and ATP. These mass action reactions have rates

$$k_{PCr}[PCr][ADP][H_{cyt}^+] - k_{PCr}^- [ATP][Cr] \quad (4.75)$$

$$k_{AK}[ADP]^2 - k_{AK}^- [ATP][AMP] \quad (4.76)$$

respectively. These reactions occur at a rate much faster than the others and so are effectively at equilibrium.

Table 4.5: BrainPiglet v1.0 model equations

Reaction	Equation	Type of reaction	Compartments involved
ADP to ATP	$ADP + Pi \rightarrow ATP$	Simple diffusion	Cytoplasm
ATP to ADP	$ATP \rightarrow ADP + Pi$	Michaelis Menten	Cytoplasm
ADP to AMP and ATP	$2ADP \rightarrow AMP + ATP$	Reversible mass action	Cytoplasm
Oxidative phosphorylation	$14H_{mit}^+ + 4CytC_{ox} \rightarrow 2NAD^+$	Simple diffusion	Mitochondria
	$4H_{mit}^+ \rightarrow 4CytC_{ox} + 4a_{3r}$	Simple diffusion	Mitochondria
	$O_2 + 4H_{mit}^+ + 4a_{3r} \rightarrow$	Simple diffusion	Mitochondria
Glycolysis	$2ADP + 2Pi + gluc \rightarrow 2ATP + 2Py$	Michaelis Menten	Cytoplasm
Pyruvate to Lactate	$Py \leftrightarrow lac$	Reversible mass action	Cytoplasm
TCA cycle	$Py + 6NAD \rightarrow$	Simple diffusion	Mitochondria, Cytoplasm
Phosphocreatine to ATP	$PCr + ADP \leftrightarrow ATP + Cr$	Reversible mass action	Mitochondria
Protons re-enter mitochondrial matrix (via leak and complex V)	$\rightarrow H_{mit}^+$	Simple diffusion	Mitochondria
Lactate in	$\rightarrow lac$	Rate term	Cytoplasm
Lactate out	$lac \rightarrow$	Michaelis Menten	Cytoplasm
Glucose in	$\rightarrow gluc$	Rate term	Cytoplasm
Glucose out	$gluc \rightarrow$	Michaelis Menten	Cytoplasm
Oxygen in	$\rightarrow O_2$	Simple diffusion	Mitochondria

4.7.2 Steady state simulations

Steady state simulations in the BrainPiglet model with varying SaO_2 show similar results to BrainSignals (Figure 4.28). Mitochondrial pH also increases with SaO_2 , which indicates acidosis caused by hypoxia. Pa also displays similar results to BrainSignals, including the typical autoregulation curve with CBF, here with the steady phase around the normal pressure value of 50mmHg.

The effect of demand on the model seems to plateau by $u = 2$, unlike BrainSignals (Figure 4.29). Mitochondrial pH is observed to decrease with increased metabolic activity. Variables increase almost linearly with $PaCO_2$.

4.7.3 Simulating hypoxia-ischaemia

As in the previous section, the BrainPiglet v1.0 model is used here to simulate the effect of a decrease in oxygen and blood flow (Figures 4.30 and 4.31). Blood pressure was reduced by 40% and SaO_2 by approximately 30%. Although baseline parameter values such as blood pressure are different between the adult human BrainSignals model and the BrainPiglet model, there is a significant difference in the response of the model to the hypoxic-ischaemic stimulus. The predicted changes suggest more complex behaviour. Mitochondrial pH is also simulated here, showing a slight drop during HI as might be expected. NTP/EPP also decreased during HI, following a decrease in metabolism.

4.7.4 Simulating functional activation

The model was also used to produce a functional response, by increasing the demand parameter u by 20%. Figures 4.32 and 4.33 illustrate the inputs and predicted changes. The haemoglobin variables, CBF, $CMRO_2$, and TOI display a slower return to baseline than the others. NTP/EPP decreases due to the increased use of ATP, and mitochondrial pH decreases as more protons re-enter the mitochondria through leak channels following increased oxidative phosphorylation.

4.7. The BrainPiglet model

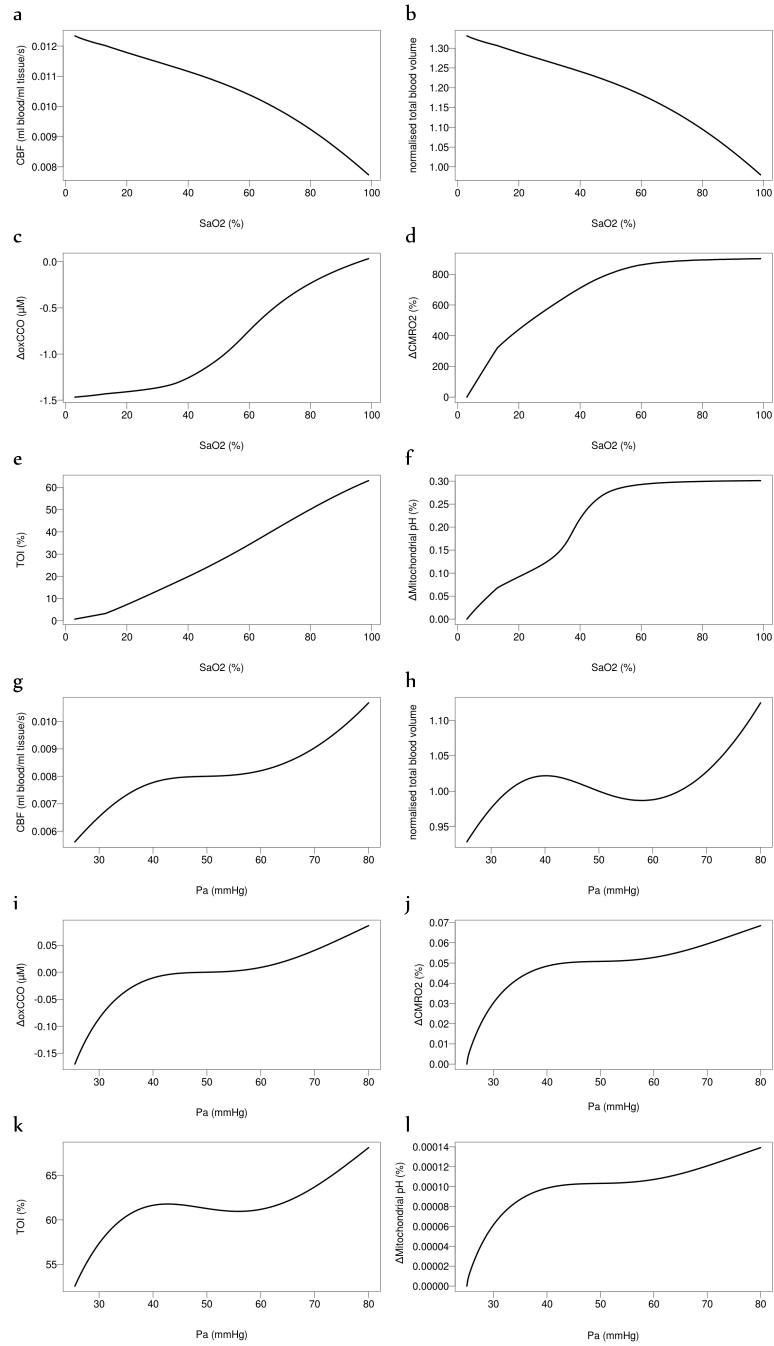


Figure 4.28: Steady state simulations of the BrainPiglet v1.0 model with varying arterial oxygen saturation SaO_2 (a–f) and blood pressure Pa (g–l).

4.7. The BrainPiglet model

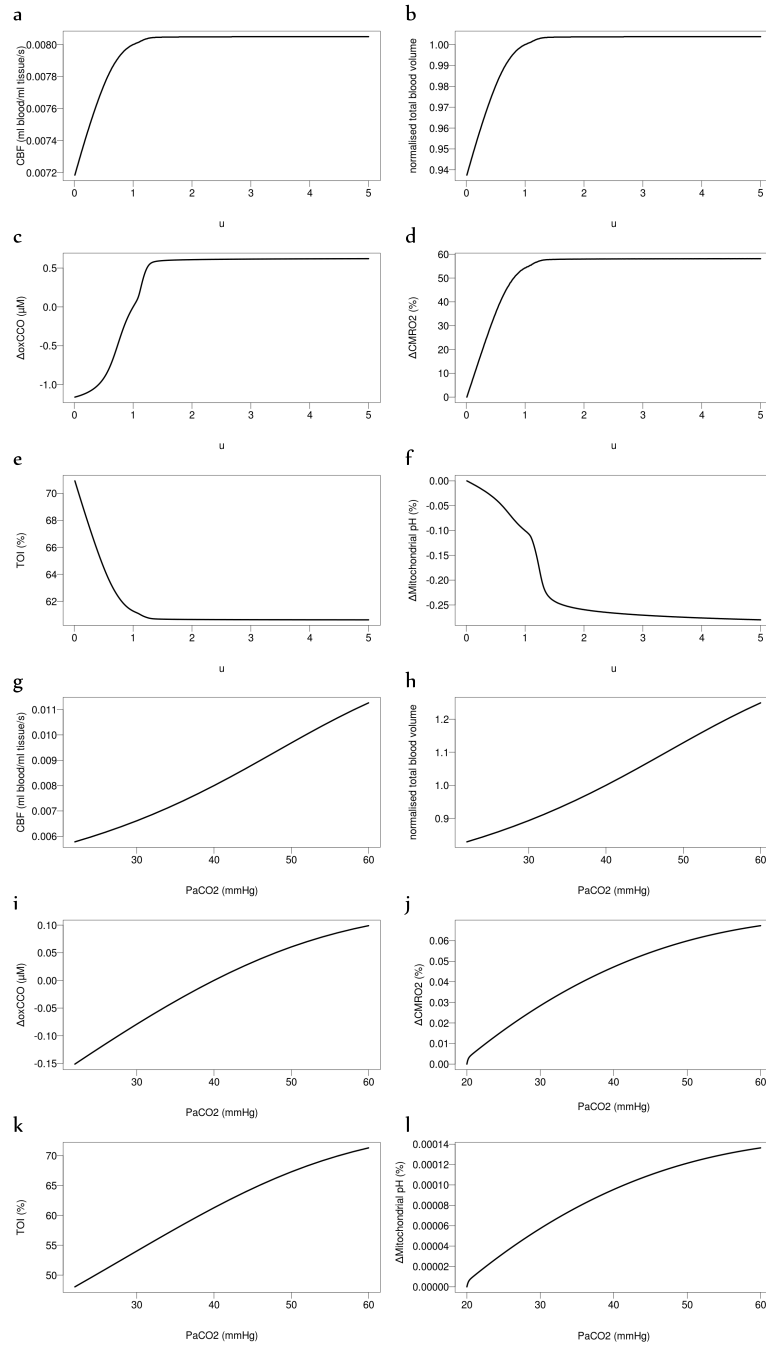


Figure 4.29: Steady state simulations of the BrainPiglet v1.0 model with varying demand u (a–f) and partial pressure of carbon dioxide P_aCO_2 (g–l).

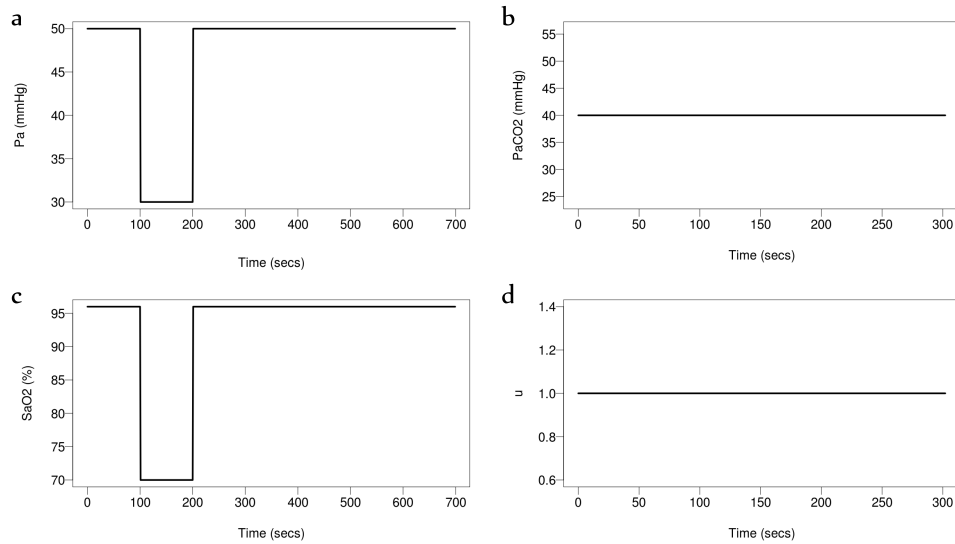


Figure 4.30: Inputs to BrainPiglet v1.0 to simulate hypoxia-ischaemia. (a) Blood pressure, P_a , and (c) arterial oxygen saturation, SaO_2 are reduced temporarily while (b) partial pressure of carbon dioxide, P_aCO_2 and (d) the energy demand, u are kept constant.

4.8 Discussion

Mathematical models are a valuable medium to further our understanding of complex behaviour. As discussed at the start of this chapter, there are a number of considerations to be taken into account in the construction and application of models in biology. There exist discrepancies between the nature of functioning in and advancement of the two fields. Biological models incorporate significantly more guesswork than a strict mathematician would like to admit and be comfortable with. However, this very balance of detail and often plausible but subjective assumptions is one of the most important skills of a good modeller.

It is sometimes necessary to clarify the value of systems biology models such as those presented in this thesis. Models provide a method for bringing pieces of information together, to understand the relationships between them, and to derive and translate the cumulative reasoning. These models are not meant to be stand-alone directors of intelligence, but are meant to be used in conjunction with other sources of information – such as measurement data – to aid overall understanding. They aim to add value, not to be

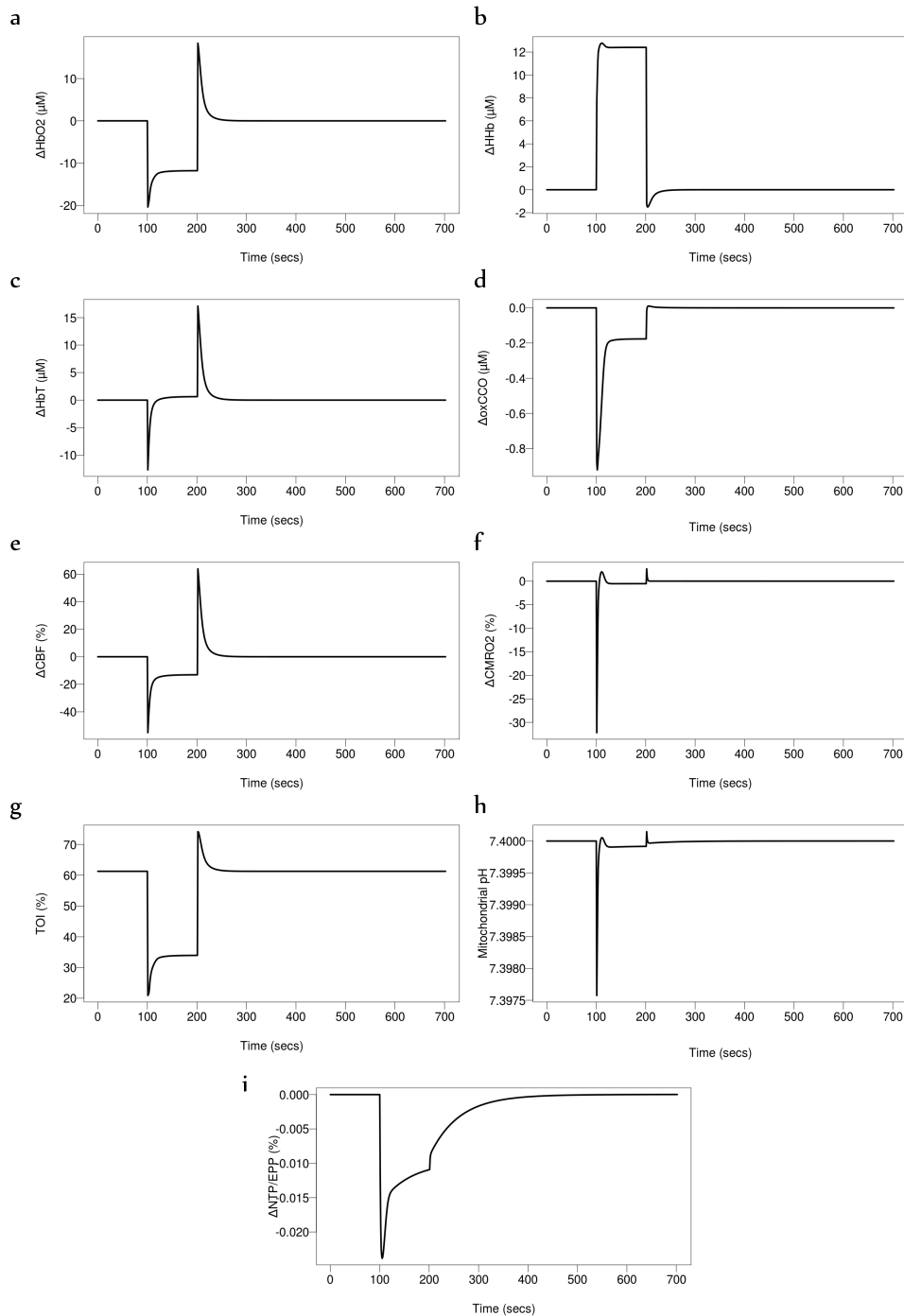


Figure 4.31: Outputs of BrainPiglet v1.0 simulation of hypoxia-ischaemia. Changes in (a,b,c) oxy-haemoglobin deoxy-haemoglobin and total haemoglobin, ΔHbO_2 , ΔHHb , ΔHbT and (d) oxidised cytochrome-c-oxidase $\Delta oxCCO$. Percentage change in (e) cerebral blood flow, CBF, (f) cerebral metabolic rate of oxygen consumption $CMRO_2$ and (g) tissue oxygenation index, TOI. (h) Mitochondrial pH and (i) percentage change in NTP/EPP.

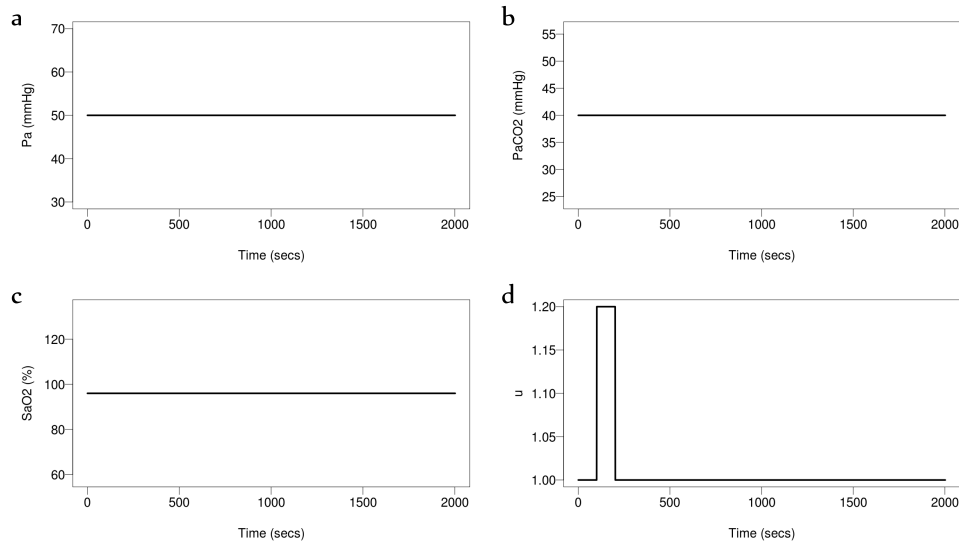


Figure 4.32: Inputs to the BrainPiglet v1.0 model to simulate brain activation. (a) Blood pressure, P_a , (b) partial pressure of carbon dioxide, $P_a\text{CO}_2$ and (c) arterial oxygen saturation, SaO_2 are kept constant while (d) the energy demand, u is increased temporarily.

the sole perpetrators of it.

A mathematical model's core characteristic can also be its greatest downfall. Parameter values govern model behaviour, but in a biological world, these values are often vague or non-existent. This is a powerful argument for model simplicity.

There are a number of good models of cellular metabolism. Both the Cloutier and Orłowski models, being related, have very similar mechanisms but their implementation is focused on different applications and hence different model behaviours. The Cloutier model was created primarily to investigate the effect of neuronal stimulation, and so can provide interesting results of short-term changes in ATP and other metabolites in astrocytes and neurons. The Orłowski model is primarily used to investigate stroke, and so focuses more on the long-term changes. Its simulation of hypoxia-ischaemia in particular showed interestingly different results compared to the ischaemia only simulation.

The Beard and Korzeniewski models are focused on mitochondrial activity and hence necessarily limited in the simulations they offer. However, both

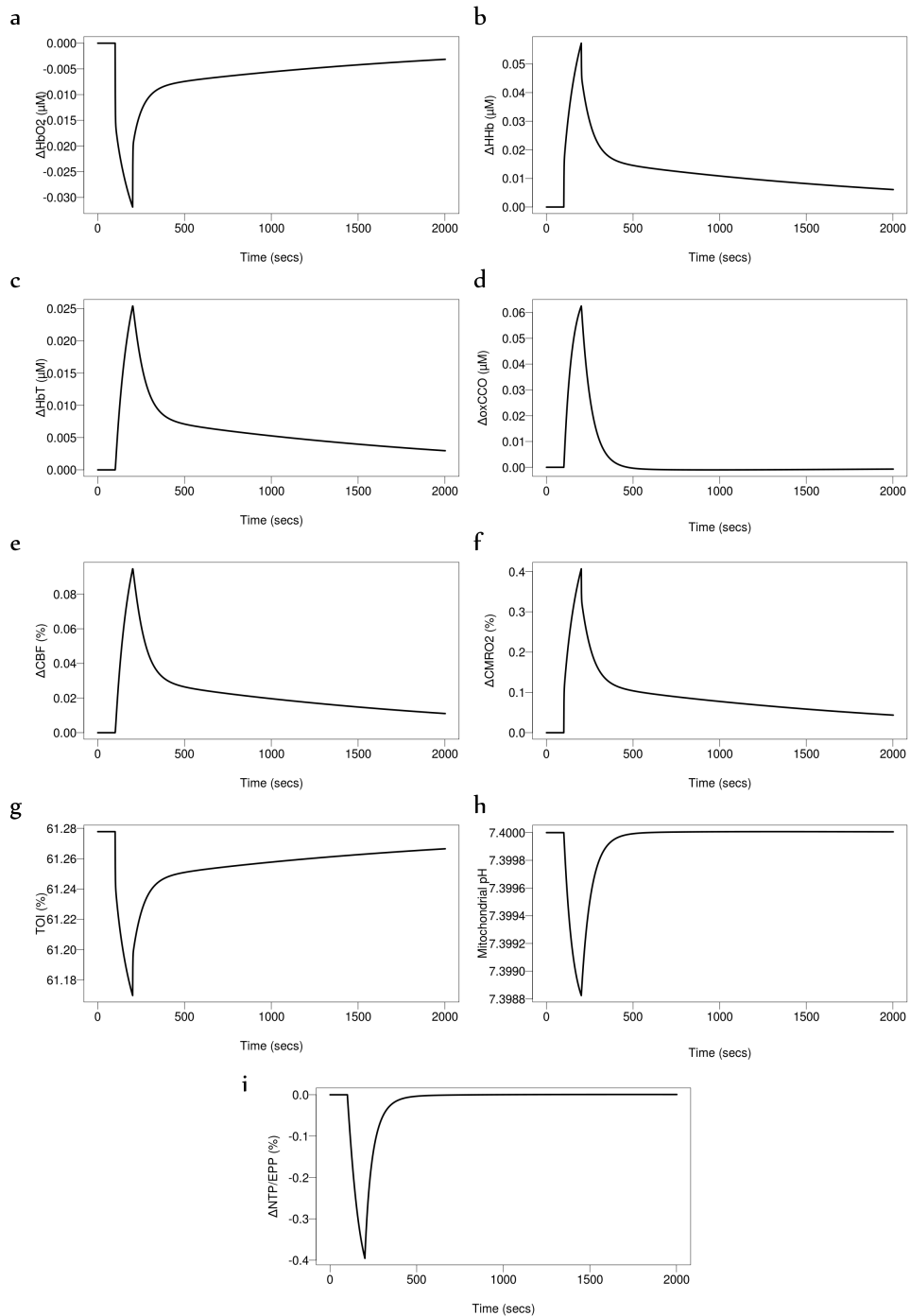


Figure 4.33: Outputs of the BrainPiglet v1.0 model simulation of brain activation. Changes in (a,b,c) oxy-haemoglobin deoxy-haemoglobin and total haemoglobin, ΔHbO_2 , ΔHHb , ΔHbT and (d) oxidised cytochrome-c-oxidase $\Delta oxCCO$. Percentage change in (e) cerebral blood flow, CBF, (f) cerebral metabolic rate of oxygen consumption $CMRO_2$ and (g) tissue oxygenation index, TOI. (h) Mitochondrial pH and (i) percentage change in NTP/EPP.

models exhibit similar behaviour during hypoxia. The circulatory Ursino-Lodi model also displays interesting vascular behaviour during ischaemia.

In running and implementing these models the role of the model environment was quite evident. The Orłowski model was run in the OpenCell environment and set up in such a way that allowed the user to observe the effect of disrupting parameter values from their norm. On the other hand the Cloutier model, run on our in-house interface BCMD, could be run on a series of input data. This enables a greater ability to probe the model, using complex, time-dependent inputs. Similar observations were made with the hypoxia simulations run on the Beard (OpenCell) and Korzeniewski (Brain-circ) models. Therefore, the value of a model can sometimes be constrained simply by the computational environment in which it exists.

The UCL models have been developed with a definitive scope in mind – to investigate data produced by clinical systems that have also been developed by the group. They are hence at an advantage, by having real clinical data to ground the model throughout the building process. BrainCirc, BrainSingals and BrainPiglet have all been driven by data collected during various clinical experiments conducted by the group. BrainSignals is the simplest of the three, and a very effective predictor of haemodynamics in the adult brain, simulating ΔHbT , ΔHbO_2 , ΔHHb , ΔCCO , CBF and CMRO_2 . BrainPiglet on the other hand incorporates more of the metabolic activity in the cell and therefore can display, in addition to more predictions, more complex results. BrainPiglet v1.0 adds predictions of mitochondrial pH and ATP (or NTP). Both models are able to simulate changes that occur during functional activation and hypoxia-ischaemia as illustrated in this chapter, however it must be noted that this is not exhaustive of the model's capabilities.

It is difficult to categorise the UCL models within the phenomenological and mechanistic characteristic framework. They are phenomenological by their nature of being data-driven, but also mechanistic by incorporation of the biochemistry that gives rise to the changes observed. Indeed this characterisation depends on the modelling process rather than solely on the stand-alone model itself. If model results are compared to experimental or clinical data and this feeds back into the model building process, then the model could be said to have phenomenological or top-down characteristics. The amount of detail incorporated in these models also depends heavily on the application. For example the Cloutier and Orłowski models differ between

astrocytes and neurons, whereas in the UCL models this is not an important differentiation to make, because the measurement techniques don't either (among other reasons).

Nearly all of the models mentioned in this chapter have been based on others and since publication have inspired even more models. Thus many systems biology models are often connected by a hidden underlying framework, and the design choices made in one are easily transferred to another regardless of the intended applications. It is hard to determine whether this has any real detrimental effect on the new application of the model, but it is important to be mindful of this in the implementation.

The optimisation of large systems biology models is a difficult task. The models presented in this thesis have been optimised using the PSwarm algorithm to select the best value for each of the parameters considered to be influential in the model (as suggested by the sensitivity analysis Morris method). It is necessary in this context to define the range of values for each parameter. However, this is more easily said than done. Where parameter values can be determined from literature, they vary greatly from one source to another. In cases where the values are not available, the range is at best an educated guess. This process determines the boundaries of the multidimensional space in which a model exists. There is no guarantee however, that the combination of parameter values selected by the algorithm, and hence the trajectory of model behaviour within the space, is biologically feasible. These important considerations must be taken into account in the translation of model results.

The next chapter describes the extension and further development of the BrainPiglet model to simulate intracellular pH.

Chapter 5

Developing the BrainPiglet model to simulate intracellular pH

The role of pH in brain injury is of considerable clinical interest. Changes in pH can alter protein structure, vital to many cellular processes. Brain acidosis is thought to augment cell death under certain conditions. pH is also known to become more acidic in hypoxic-ischaemic environments, while alkalosis following hypoxia-ischaemia has been correlated with adverse outcome (often leading to secondary energy failure) (Robertson et al. 2002). Recent hypoxia-ischaemia experiments conducted in piglets collected both NIRS and MRS measurements of metabolites during and in the aftermath of the insult. The MRS measurements also provided an estimate of cerebral pH. In order to investigate these further, the simulation of pH in the BrainPiglet model was improved.

This chapter details the extension of the BrainPiglet model for its application to measurement data from the piglet experiments. The model was developed incrementally in three phases, by incorporating biochemical processes known to influence pH in the cell. The effects of these additions are analysed at each stage.

5.1 Hypoxia-ischaemia piglet experiments

A novel multi-modal measurement technique, combining both near-infrared spectroscopy and magnetic resonance spectroscopy, was used to monitor cerebral metabolism and haemodynamics in newborn piglets undergoing a hypoxia-ischaemia insult. This data provides a valuable insight into the changes that occur during and in the aftermath of a hypoxia-ischaemia event in the neonatal brain. The protocol is detailed in the next chapter, which covers simulations of the experiments. To summarise briefly here, both blood flow to brain and inspired oxygen were reduced during the insult phase and subsequently returned to normal. Both NIRS and MRS measurements were continuously recorded during the experiment.

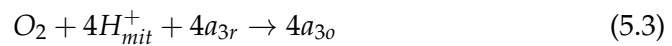
5.2 BrainPiglet v2.0

The development of the model was carried out in three phases, all focused on the capacity of the model to simulate intracellular pH. This section details the first phase.

5.2.1 Modelling intracellular pH

The BrainPiglet model was extended to improve the simulation of mitochondrial pH and to simulate a varying cytoplasmic pH. A number of pre-existing reactions in the model were altered to include the main H^+ dynamics in the cell - these are listed below. The water produced by these reactions was ignored as water is not currently simulated in the model and its addition would complicate it further, requiring more complex revision.

Oxidative phosphorylation



Glycolysis

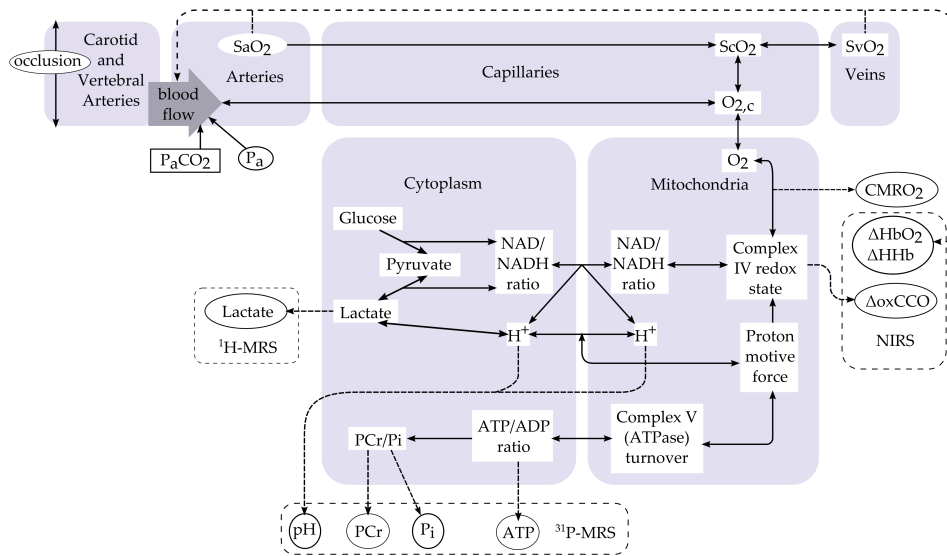
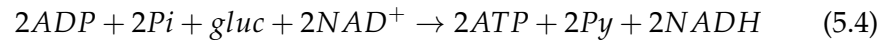


Figure 5.1: Schematic of the BrainPiglet v2.0 model.



Tricarboxylic acid cycle



Pyruvate to lactate



Lactate transport in and out of the cell



The corresponding rates of reactions have also been modified to include protons.

Malate-aspartate shuttle

The malate-aspartate shuttle facilitates the movement of electrons across the mitochondrial membrane and involves the interconversion of NAD and NADH on either side (see Section 2.4.4 and Figure 2.7). A simplified representation of this process was also incorporated into the model:



The malate-aspartate shuttle is simulated as a mass action process. The rate of this reaction is given by

$$k_{MAshut}[H_{cyt}^+][NAD] - k_{MAshut}^-[NAD_{cyt}][H_{mit}^+] \quad (5.10)$$

The buffering of H^+ ions in the cytoplasm is simulated in a similar way to those in the mitochondria, with an identical value for dpH and a slightly higher value of $C_{buff,c}$ as in Korzeniewski and Zoladz (2001).

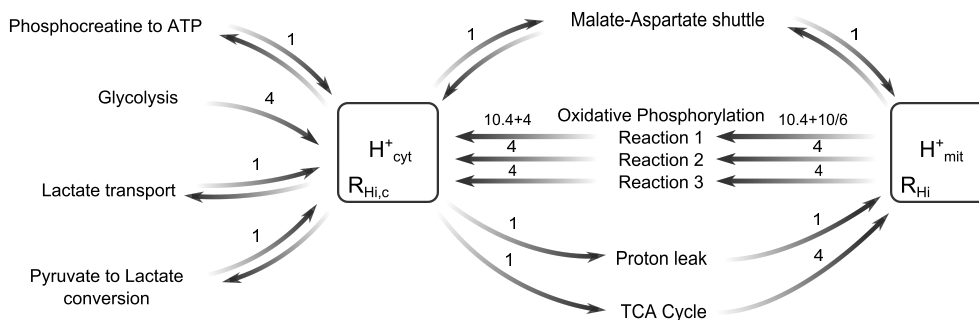


Figure 5.2: Movement of H^+ ions in the BrainPiglet v2.0 model.

The normal value of pH in the cytoplasm was set at 7.00. The normal mitochondrial pH was increased to 8.00 (from the previous value of 7.40) to reflect values found in Casey et al. (2010).

5.2.2 Modelling arterial occlusion

In order to accurately simulate hypoxia-ischemia, the model was also extended to simulate occlusion of the carotid arteries. This work detailed below, and included in this version of the model, was carried out by Tracy Moroz (Moroz et al. 2012, 2013).

An additional arterial compartment, simulating the carotid and vertebral arteries was introduced. This compartment directly supplies the main arterial compartment and has a conductance G_0 . Consequently, simply reducing G_0 simulates occlusion of the arteries, and decreases the pressure of blood supplied to the brain. The pressure of the carotid and vertebral arteries is denoted by P_a while this pressure of the cerebral arteries is now denoted as P_{a2} , and can be calculated by equating the blood flow in the two compartments;

$$G_0(P_a - P_{a2}) = 2G(P_{a2} - P_1) \quad (5.11)$$

where P_1 is the average pressure. V_v is now dependent on pressure;

$$V_v = V_{v,n} + C_v(P_v - P_{v,n}) \quad (5.12)$$

where P_v and $P_{v,n}$ represent venous blood pressure at the start of the compartment, with the latter under normal conditions. C_v is the compliance of the venous compartment, which remains constant. P_v can be calculated from the conductance of the veins G_v as a fraction of the total conductance G_t ;

$$P_v = \frac{G_t}{G_v}(P_a - P_{vs}) + P_{vs} \quad (5.13)$$

where P_{vs} is the constant pressure at the venous sinuses and

$$G_t = \frac{GG_0G_v}{GG_0 + GG_v + G_vG_0} \quad (5.14)$$

The radius in the elastic tension relationship r_0 (see equation 4.15) is now determined by

$$r_0 = (1 - r_{frac}r_{occ}) \quad (5.15)$$

where r_{occ} and r_{frac} are the fractions by which the radius of the carotid arteries and the supplying artery compartment respectively has been reduced. r_{frac} is given by

$$1 - c_{frac} = (1 - r_{frac})^4 \quad (5.16)$$

where c_{frac} is the fraction of arterial blood which flows through the carotid arteries under normal conditions. To simulate occlusion, G_0 is determined by

$$G_0 = G_{0,n}(1 - c_{frac}) \quad (5.17)$$

where $G_{0,n}$ is the conductance when there is no occlusion, which can be calculated by

$$G_{0,n} = G_{0,rat}G_n \quad (5.18)$$

G_n is the normal conductance of the cerebral arterial compartment. The ratio $G_{0,rat}$ was set by observing the results of model simulations. With a high $G_{0,rat}$, CBF remains high until the conductance is only a small fraction of its normal value. When $G_{0,rat}$ is low, the relationship is more linear. A value of 10.0 was thus chosen for $G_{0,rat}$.

Copyright material removed.

Figure 5.3: Circuit diagram of circulation in the BrainPiglet v2.0 model (Moroz et al. 2012)

5.2.3 Steady state simulations

The model behaviour at steady state is quite similar to that in BrainPiglet v1.0 for CBF, blood volume and TOI (Figures 5.4 and 5.5). Acidosis in the mitochondria at low values of SaO_2 is much more pronounced in BrainPiglet v2.0 than in v1.0. Cytoplasmic pH is also similarly affected. Very little change in pH is observed with changes in blood pressure. pH is seen to decrease with increasing demand u . However mitochondrial pH is observed to reach a maximum around $u = 1$, the normal value of demand, and decrease as u drops below 1. This may be due to the low metabolic rate, and the movement of protons from cytoplasm to the mitochondria. Indeed cytoplasmic pH rises slightly above the normal value of 7.00 for $u < 1$. pH increases with P_aCO_2 in both mitochondria and cytoplasm.

Table 5.1: New parameters in BrainPiglet v2.0

Parameter	Description	Value	Source
Km_{glucNN}	Km for NAD in the carriage of glycolysis	1.0	Banaji et al. (2005)
Keq_{MAshut}	Equilibrium constant for the malate-aspartate shuttle	10.0	Banaji et al. (2005)
NAD_{cytn}	Normal concentration of NAD in the cytoplasm	359 mM	Williamson et al. (1967)
$NADH_{cytn}$	Normal concentration of NADH in the cytoplasm	50 mM	Williamson et al. (1967)
$G_{0,rat}$	Ratio between the conductance of the cerebral arteries and the supplying artery compartment	10.0	Determined from model simulations

It must be noted here that the simulation of demand in the model has been implemented with the intension of investigating increases in demand beyond the normal - at a resting state. Hence, the effect of a lower than normal demand ($u < 1$) has not been investigated or tested, and it not a focus of the group's current research. It is nevertheless interesting to observe these changes.

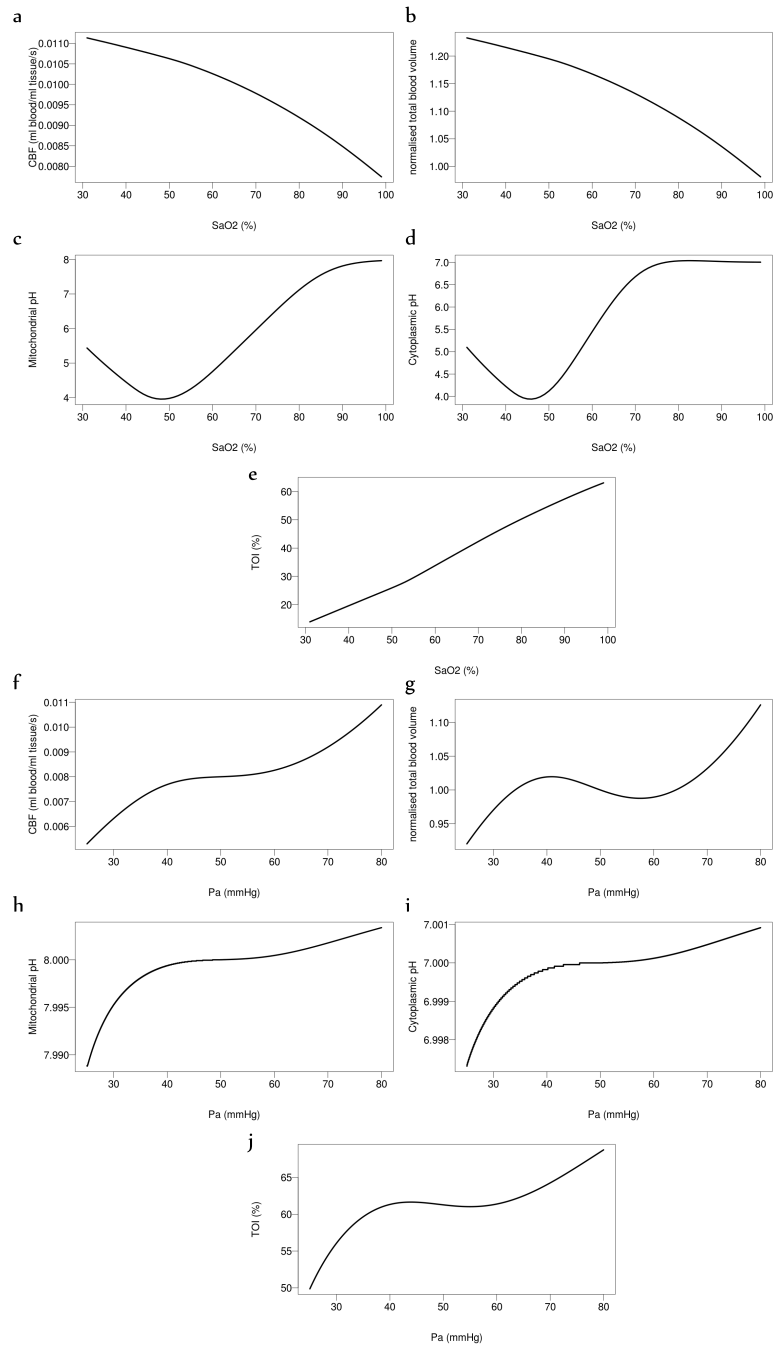


Figure 5.4: Steady state simulations of the BrainPiglet v2.0 model with varying arterial oxygen saturation SaO_2 (a–e) and blood pressure P_a (f–j).

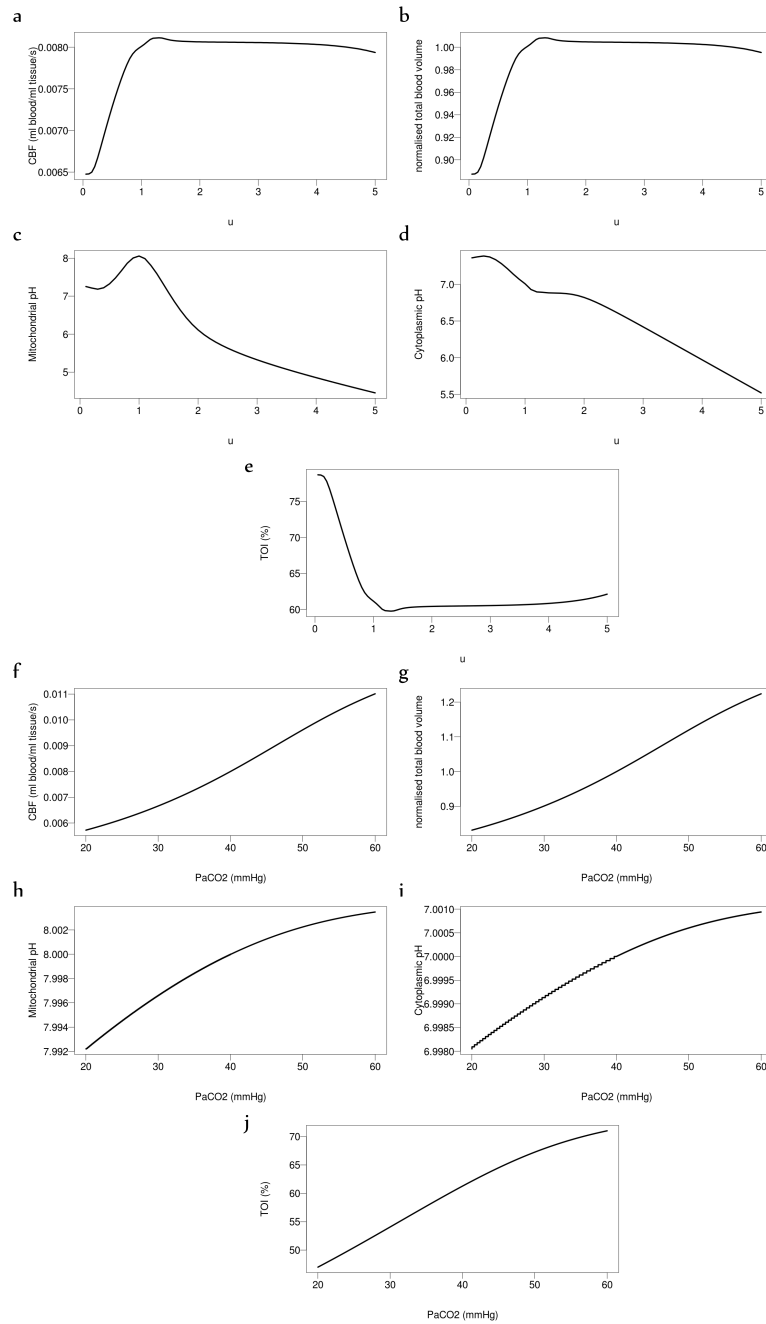


Figure 5.5: Steady state simulations of the BrainPiglet v2.0 model with varying demand u (a–e) and partial pressure of carbon dioxide P_aCO_2 (f–j).

5.2.4 Simulating hypoxia-ischaemia in piglets

In order to test the performance of the new model, it was run using a data set from the piglet experiments (Piglet LWP173).

Sensitivity analysis and optimisation

First the model parameters need to be optimised to the data set, so a sensitivity analysis using the Morris method was conducted. Table 5.2 displays the results - parameters ranked by importance for each of the variables that we are interested in optimising (ΔHbO_2 , ΔHb , $\Delta oxCCO$ and cytoplasmic pH, pH_o). For brevity, the table only includes the 10 top parameters for each variable. Based on this ranking, 6 parameters were selected to be optimised. These are indicated by an asterisk in Table 5.2. Parameters related to the regulation of blood flow feature heavily for ΔHbO_2 and ΔHb . Although the parameter controlling the sensitivity of autoregulatory stimuli to demand R_{autu} ranks first for cytoplasmic pH pH_o , it was not selected to be optimised as demand is not thought to change in this experiment. The concentration of cytochrome in tissue $[CCO]_{tis}$ is not very well defined in literature. Thus this parameter was also selected, to gain a better understanding of how it may vary in piglets before and after hypoxia-ischaemia.

Measurements were divided into two sections, with the start of titration as the dividing point (see protocol in Figure 6.1). This is done in an attempt to represent the state of the brain before and after the insult, so that the parameter optimisation process may expose the specific cerebral physiology that has been altered during the hypoxic-ischaemic insult. The division here is obviously not definitive – it is hard to pinpoint the exact moment when injury or irreversible change occurs. As this period of uncertainty is relatively small compared to the rest of the signal, it is conceivable that the optimisation will not be greatly affected. There are a number of continuous processes that occur in the brain, regardless of health. The aim here is to gauge average overall changes during the experiment.

Simulations of ΔHbO_2 , ΔHb and $\Delta oxCCO$ were compared with their counterpart NIRS measurements. Simulated cytoplasmic pH pH_o was compared with the phosphate-derived pH measurement. The ATP-derived pH measurement was not used for optimisation as the measurement was significantly more noisy. The optimised parameter values are presented in Table

5.3. Before the insult, the autoregulation constant has been reduced significantly from the normal value. This could be due to an abnormality in the piglet, or an underdeveloped autoregulative capacity. The concentration of CCO has been significantly increased compared to normal (0.00566 mM vs. 0.0022 mM). The normal mitochondrial pH is also slightly higher (7.81 vs. 7.4). The largest change in value over the course of the insult was in the *NADpool* parameter (+50%). The autoregulation constant also reduced by approximately 30%.

Table 5.2: Sensitivity analysis of BrainPiglet v2.0 using data from Piglet LWP173. Parameters ranked in order of influence in optimising selected output variables. Asterisks indicate parameters selected for optimisation.

Variable				Parameter	Description
HbO ₂	HHb	Δ oxCCO	pH _o		
1	1			k_{aut}^*	Autoregulation constant
2	2			$P_{a,n}^*$	Normal arterial blood pressure
3	3		7	r_m^*	Value of vessel radius giving maximum muscular tension
4	4			P_a	Arterial blood pressure
5	5			$P_{aCO_2,n}$	Normal arterial partial pressure of CO ₂
6	6	8	5	σ_{coll}	Value of pressure at which vessels collapse
7	7			h_0	Vascular wall thickness when radius is r_0
8	8			Vol_{mit}	Fraction of brain water which is mitochondria
9	9	11		$SaO_{2,n}$	Normal saturation of the arterial haemoglobin
10	10	7	19	r_n	Normal radius of blood vessels
11	11	6	4	r_t	Parameter in the muscular tension relationship
13		9	2	$NAD_{cyt,n}^*$	Normal concentration of NAD in the cytoplasm
	13		10	$NADH_{cyt,n}$	Normal concentration of NADH in the cytoplasm
		1	9	pH_{mn}^*	Normal mitochondrial pH
		2		$Km_{glucNgl}$	Km for glucose in the caricature of glycolysis
		3		$ck2$	Controls sensitivity of forward rate of the second oxidative phosphorylation reaction to the proton motive force
		4		$CVinh$	Control parameter representing the action of complex V inhibitors
		5		k_{lk2}	Controls rate at which protons reenter the mitochondrial matrix through leak channels
		10		$a_{frac,n}$	Normal oxidised fraction of Cu _A
			1	R_{autu}	Controls sensitivity of autoregulatory stimuli to demand
			3	$NADpool^*$	Total mitochondrial NAD and NADH concentration
			6	n_m	Exponent in the muscular tension relationship
			8	pH_{on}	Normal cytoplasmic pH

Table 5.3: Optimised BrainPiglet v2.0 parameter values for Piglet LWP173

Parameter	Description	Normal Value	Before Insult	After Insult	% Change
k_{aut}	Autoregulation constant	1.0	0.582	0.404	-30.6
$P_{a,n}$	Normal arterial blood pressure	50 mmHg	45.0	46.4	3.11
$pH_{m,n}$	Normal mitochondrial pH	7.4	7.81	8.15	4.35
NAD_{cytn}	Normal concentration of NAD in the cytoplasm	359.0 mM	318.0	400.0	25.8
NAD_{pool}	Total mitochondrial NAD and NADH concentration	3.0 mM	2.4	3.60	50.0
r_m	Value of vessel radius giving maximum muscular tension	0.027 cm	0.0304	0.0324	6.58
$[CCO]_{tis}$	Concentration of cytochrome in tissue	0.0022 mM	0.00566	0.00620	9.54

Model simulation

SaO_2 and blood pressure P_a measurements from the piglet were used as model inputs (Figure 5.6). During occlusion, a sharp drop is observed in SaO_2 and P_a , leading to a hypoxic-ishaemic environment. Following removal of the occlusion, blood flow and oxygenation recover back to near-baseline levels. The fraction r_{occ} was also increased to 1.0 during the occlusion phase to simulate complete occlusion of the carotid arteries.

The optimised parameter values for the section before the insult were used at the start of the run, and were gradually changed to the optimised values for the section after the insult. This change occurs over a period of 1 minute, from the start of titration.

Figure 5.6 illustrates the model simulations of ΔHbO_2 , $\Delta HHHb$, ΔHbT , $\Delta oxCCO$ plotted against corresponding measurements from the piglet experiment for comparison. Both optimised and non-optimised simulations are presented here. The model is able to simulate the drop in ΔHbO_2 , ΔHbT and $\Delta oxCCO$, and the rise in $\Delta HHHb$. In particular, model optimisation has greatly improved the simulation $\Delta oxCCO$.

Simulations of ΔCBF and $\Delta CMRO_2$ indicate a drop, as may be expected, during the insult phase. The model simulation of cytoplasmic pH is com-

pared with the the two pH measurements - that calculated from phosphate and ATP. Both measurements indicate a more acidic pH during the insult phase, although the ATP measurement is very noisy. Simulated mitochondrial pH indicates an alkaline rise in pH towards the end the insult. However the optimised simulation differs significantly, with a much more pronounced acidic drop immediately afterwards followed by a slow recovery.

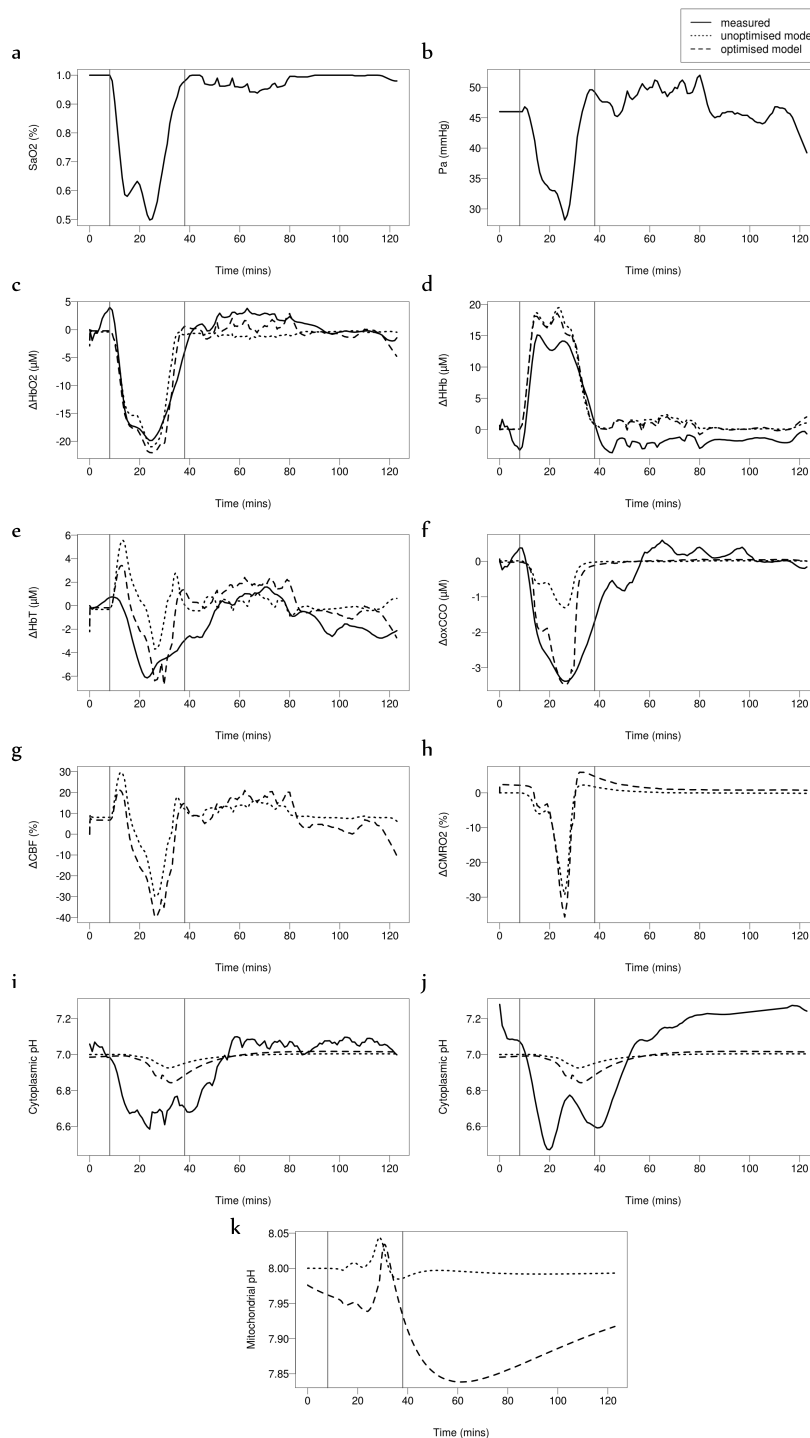
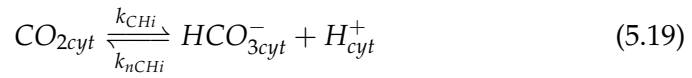


Figure 5.6: Simulating hypoxia-ischaemia in Piglet LWP173 using the BrainPiglet v2.0 model. Vertical lines indicate the start and end of occlusion of the carotid arteries. (a) SaO_2 and (b) blood pressure P_a measurements are model inputs. (c,d,e, f) Simulations and measurements of ΔHbO_2 , ΔHHb , ΔHbT and $\Delta oxCCO$. (g,h) Simulations of ΔCBF and $\Delta CMRO_2$. Simulated cytoplasmic pH compared with measured (i) phosphate-derived pH and (j) ATP-derived pH. (k) Simulated mitochondrial pH.

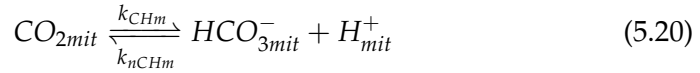
5.3 BrainPiglet v2.0.1

5.3.1 Modelling carbonic acid

The association and dissociation of intracellular carbonic acid is expected to significantly affect intracellular proton concentration. The following equation models the dissolution of CO₂ and the dissociation of carbonic acid H₂CO₃ in the cytoplasm as a mass action reaction:



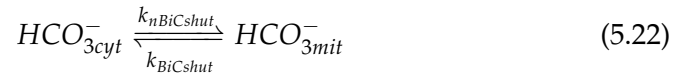
where k_{nCHI} and k_{CHI} are calculated from the half time value. Similarly in the mitochondria:



CO₂ diffuses into and out of the mitochondria:



where $k_{CO2shut}$ is set so that when there exists a concentration gradient, the net rate is equivalent to CMRO₂. Carbonic acid H₂CO₃ also moves into and out of the mitochondria:



The rate of this mass action reaction is determined by half-time and equilibrium data. Diffusion of CO₂ out of the cell is simulated by:



The rate k_{CO2out} is set so that at equilibrium the rate is equivalent to CMRO₂.

Tricarboxylic acid cycle

The TCA cycle was also updated to include the production of CO_2 :



Table 5.4: New parameters in BrainPiglet v2.1

Parameter	Description	Value	Source
k_{CHmht}	halftime for the production of carbonic acid in mitochondria	25 mM	Banaji et al. (2005)
k_{CHiht}	halftime for the production of carbonic acid in cell cytoplasm	3.2 mM	Banaji et al. (2005)
k_{CHEq}	equilibrium constant for the production and dissociation of carbonic acid	7.9e-4 mM	Banaji et al. (2005)
k_{BiCshtht}	the rate of transfer of bicarbonate ions from cytoplasm to mitochondria	2.2e3 mM	Banaji et al. (2005)
$P_t\text{CO}_2$	partial pressure of CO_2 in tissue	54 mmHg	Banaji et al. (2005)
$henry_{\text{CO}_2t}$	solubility of CO_2 in tissue	0.038 mM/mmHg	Banaji et al. (2005)

5.3.2 Steady state simulations

The behaviour of the BrainPiglet v2.0.1 model at steady state for $S_a\text{O}_2$ and blood pressure P_a are very similar to that of v2.0 (Figure 5.7). However, the addition of carbonic acid has affected the behaviour of the model at lower than normal demand ($u < 1$), with pH rising to become more alkaline at lower demand (Figure 5.8). Cytoplasmic pH also drops much faster as demand increases in the new model, even beyond feasibility into negative numbers around ($u = 3$).

With $P_a\text{CO}_2$, model behaviour remain similar to v2.0 (Figure 5.8). There is a slight difference in sensitivity of Cytoplasmic pH, with a slower decrease as $P_a\text{CO}_2$ decreases. Mitochondrial pH at $P_a\text{CO}_2$ values below normal (less than 40) shows irregular behaviour, which is an indication of increased complexity of the model.

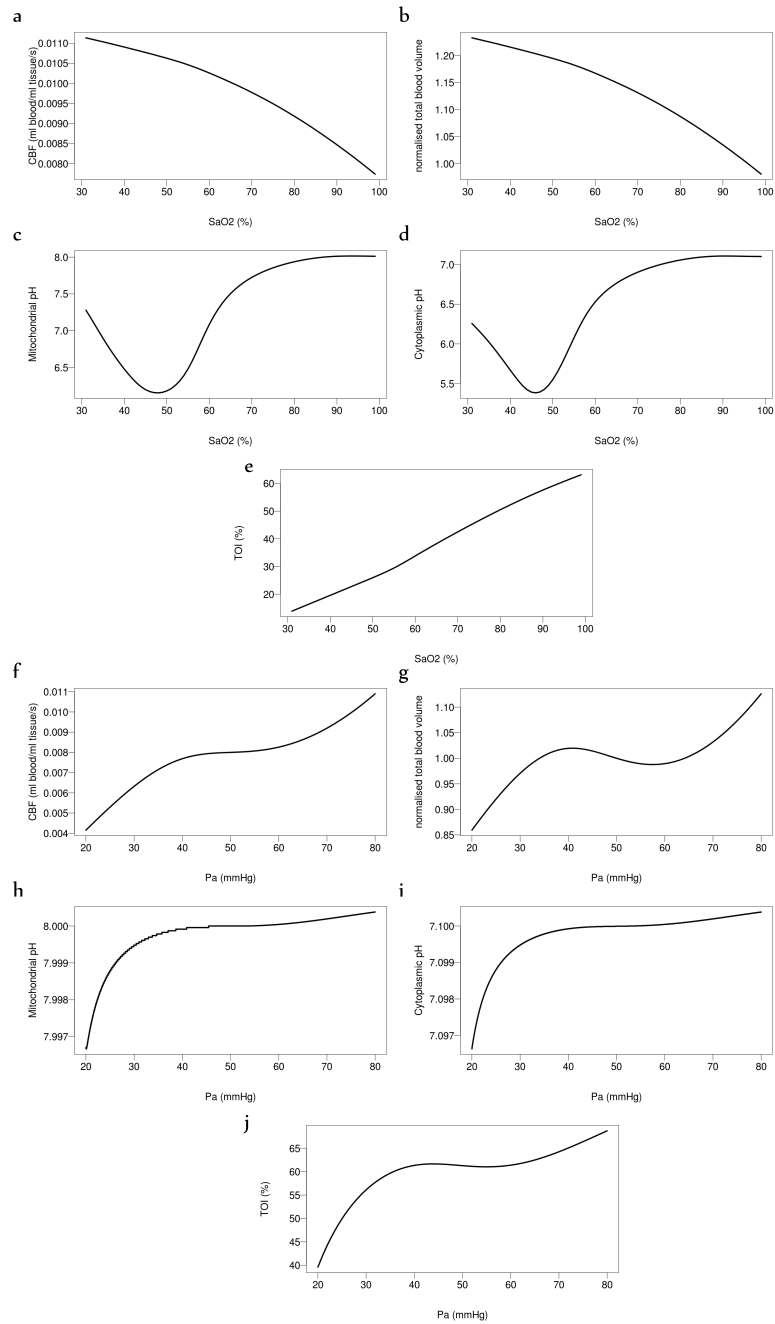


Figure 5.7: Steady state simulations of the BrainPiglet v2.0.1 model with varying arterial oxygen saturation SaO_2 (a–e) and blood pressure Pa (f–j).

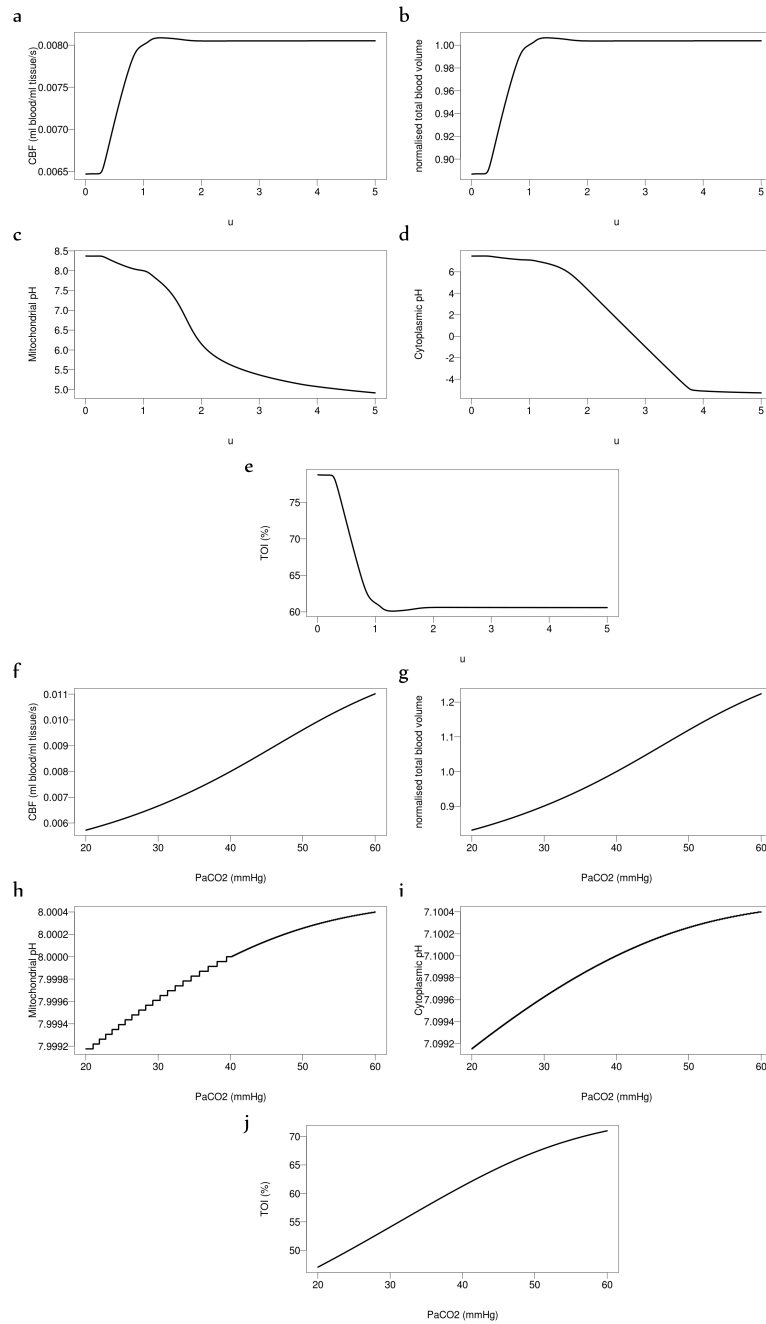


Figure 5.8: Steady state simulations of the BrainPiglet v2.0.1 model with varying demand u (a–e) and partial pressure of carbon dioxide P_aCO_2 (f–j).

5.3.3 Simulating hypoxia-ischaemia in piglets

The model was applied to measurement data from Piglet LWP173, as before, to test the performance of the new additions.

Sensitivity analysis and optimisation

Table 5.5 displays the sensitivity analysis results for the altered model, using data from Piglet LWP173. The 10 most influential parameters are shown here for each of the four variables. Consequently, 6 parameters (indicated by an asterisk in Table 5.5) were selected to be optimised, along with the concentration of cytochrome in tissue $[CCO]_{tis}$ as before and the autoregulation constant k_{aut} , to gauge the autoregulative capacity of the piglet. It is noticeable here that parameter influence is more convoluted than in BrainPiglet v2.0.1.

As with BrainPigletv2.0, the optimised autoregulation constant was lower than normal, and decreased after the insult. The optimised concentration of CCO was again higher than the normal value in the model and increased during the insult. The largest changes were in $NADpool$ and Vol_{mit} which both increased by 50%.

Table 5.5: Sensitivity analysis of BrainPiglet v2.0.1 using data from Piglet LWP173. Parameters ranked in order of influence in optimising selected output variables. Asterisks indicate parameters selected for optimisation.

Variable				Parameter	Description
HbO ₂	HHb	Δ oxCCO	pH _o		
1	1			P_{vs}^*	Pressure in the venous sinuses
2	2	18	13	SaO_{2n}	Normal saturation of the arterial haemoglobin
3	7	9	3	n_m^*	Exponent in the muscular tension relationship
4	9	13	18	$k_{nADPATP}$	Backward rate for conversion of two molecules of ADP to one of ATP and one of AMP
5	3	16	10	σ_{coll}^*	Value of pressure at which vessels collapse
6	4			Inh_{glucN}	Controls how strongly the AMP/ATP ratio inhibits the conversion of glucose to pyruvate
7	5			r_{CV}	Controls ratio of maximal to minimal rates of oxidative phosphorylation
8	6			C_{buffi}	Buffering capacity for protons in mitochondria
9	8	6	5	P_a	Arterial blood pressure
10	17			K_σ	Controls sensitivity of elastic stress in vessel walls to radius
12	15	5	9	r_0	A special radius in the elastic tension relationship
13	20	10	4	P_{ic}	Intracranial blood pressure
14	14	3	7	$c3^*$	Controls the sensitivity of the third oxidative phosphorylation reaction to the proton motive force
15	10			$blood_{frac}$	Normal blood volume as a fraction of brain tissue volume
16	18	17	8	k_{aut}^*	Autoregulation constant
17	12	7	6	phi	Value of O ₂ at half maximal saturation
	13	2	1	NAD_{pool}^*	Total mitochondrial NAD and NADH concentration
	16	8	2	u	Demand
		1		Vol_{mit}^*	Fraction of brain water which is mitochondria
		4	11	n_a	Number of protons passing through Complex V for each ATP synthesised

Table 5.6: Optimised BrainPiglet v2.0.1 parameter values for Piglet LWP173

Parameter	Description	Normal Value	Before Insult	After Insult	% Change
$P_{v,s}$	Pressure in the venous sinuses	1.5 mmHg	1.22	1.20	-1.64
n_m	Exponent in the muscular tension relationship	1.83	1.46	2.20	50.7
Vol_{mit}	Fraction of brain water which is mitochondria	0.067	0.0536	0.0804	50.0
NAD_{pool}	Total mitochondrial NAD and NADH concentration	3.0 mM	2.4	3.60	50.0
$c3$	Controls the sensitivity of the third oxidative phosphorylation reaction to the proton motive force	0.11 m/V	0.0880	0.0880	0
σ_{coll}	Value of pressure at which vessels collapse	62.79 mmHg	75.3	75.3	0
k_{aut}	Autoregulation constant	1.0	0.687	0.567	-17.5
$[CCO]_{tis}$	Concentration of cytochrome in tissue	0.0022 mM	0.00593	0.007	18.0

Model simulation

As before, SaO_2 and blood pressure P_a measurements from the piglet were used as model inputs, and the fraction r_{occ} was used to simulate occlusion. Optimised parameters were used before and after the insult.

Model simulations of the unoptimised model are very similar to that of BrainPigletv2.0, including the simulation of cytoplasmic and mitochondrial pH. However, optimisation of the model has not been as successful here. In both ΔHbO_2 and ΔHHb , the baseline of the optimised simulation after the insult has a significant error compared to the measurements. $\Delta oxCCO$ simulation does not reach the magnitude of the drop measured. The $\Delta CMRO_2$ optimised simulation shows a large rise following the insult. Cytoplasmic pH differs very little after optimisation, and thus does not show an improvement. Mitochondrial pH simulation has again changed significantly after optimisation, with a stronger alkaline rise during the insult, followed by an acidic drop afterwards.

It appears that the addition of carbonic acid has not improved the simulation of cytoplasmic pH. For mitochondrial pH, as there is no measurement data for comparison, the simulation is difficult to validate. Indeed, it seems that

with these additions, the efficiency of the optimisation process has been weakened, most notably for $\Delta oxCCO$.

5.3. BrainPiglet v2.0.1

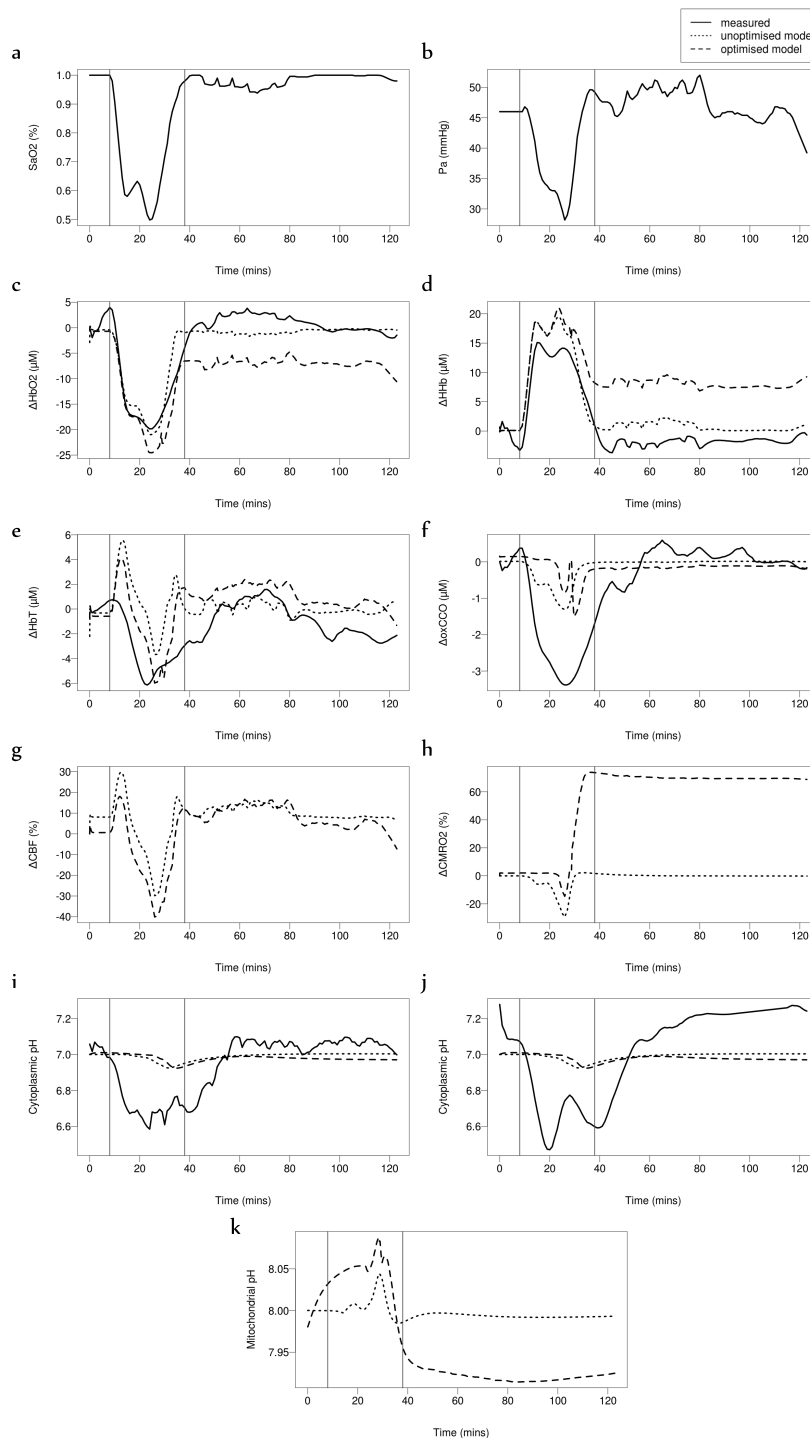


Figure 5.9: Simulating hypoxia-ischaemia in Piglet LWP173 using the BrainPiglet v2.0.1 model. (a) SaO_2 and (b) blood pressure P_a measurements are model inputs. (c,d,e, f) Simulations and measurements of ΔHbO_2 , ΔHHb , ΔHbT and $\Delta \alpha CCO$. (g,h) Simulations of ΔCBF and $\Delta CMRO_2$. Simulated cytoplasmic pH compared with measured (i) phosphate-derived pH and (j) ATP-derived pH. (k) Simulated mitochondrial pH.

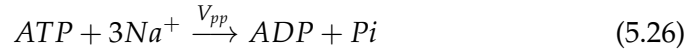
5.4 BrainPiglet v2.1

5.4.1 Modelling sodium transporters

Sodium-driven transporters are thought to play an important role in regulating intracellular pH by co-transporting H^+ ions across the cell membrane (see Chapter 2, Section 2.5.1). In order to simulate these, the concentration of sodium was introduced as a new variable in the model. Transport of sodium ions into the cell is governed by:



where k_{NA} depends on deviations from the normal intracellular sodium concentration Na_n . The sodium-potassium pump on the plasma membrane helps maintain a Na^+ gradient to drive solute transport:



This Michaelis-Menten reaction has the rate V_{pp} :

$$V_{pp} = \frac{V_{maxKATPm}(ATP - ATP_n)(Na - Na_n)^3}{(Km_{kATPA} + (ATP - ATP_n))(Km_{kATPNa}^3 + (Na - Na_n)^3)} \quad (5.27)$$

The Sodium-hydrogen exchanger (NHE) on the membrane is simulated by the following reaction;



where the rate i_{NHE} is adapted from Orłowski et al. (2011). The rate is pH-dependent – NHE is inactive for a pH above 7.2 and reaches a maximum at 6.2 (Orłowski et al. 2011; Helbig et al. 1988; Fuster et al. 2008). It also follows MichaelisMenten kinetics with respect to the Na^+ gradient. Thus,

$$i_{NHE} = \frac{V_{maxNHE}(Na_n^+ - Na^+)}{Km_{NHE} + (Na_n^+ - Na^+)} \times \frac{1}{1 + e^{NapH(pH_o - 6.7)}} \quad (5.29)$$

where $NapH$ is a constant. The Sodium bicarbonate cotransporter is modelled by another Michaelis-Menten equation:



where the rate is defined by

$$V_{NaBiC} = \frac{V_{maxKATPm}(Na_n^+ - Na^+)(HCO_{3cytn}^- - HCO_{3cyt}^-)}{(Km_{NaBiC} + (Na_n^+ - Na^+))(Km_{NaBiC} + (HCO_{3cytn}^- - HCO_{3cyt}^-))} \quad (5.31)$$

Figure 5.10 illustrates the proton dynamics in the new model.

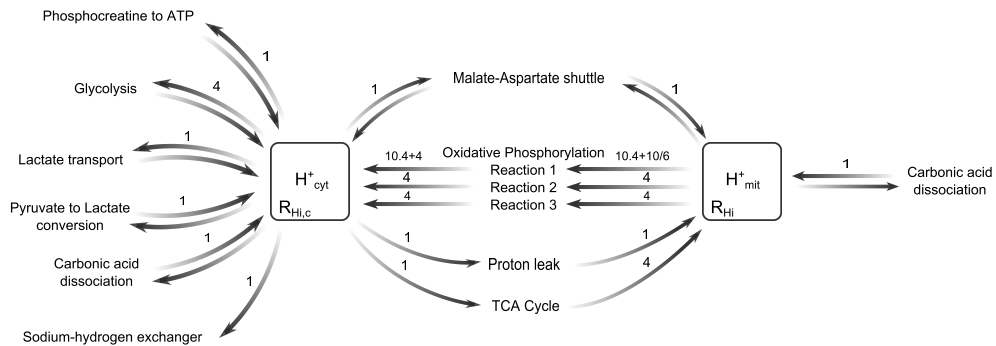


Figure 5.10: Movement of H^+ ions in the BrainPiglet v2.1 model.

5.4.2 Steady state simulations

As in BrainPiglet v2.0, the steady state behaviour of modelled CBF, blood volume and TOI are quite similar in v2.1 (Figures 5.11 and 5.12). However, pH drops less appreciably at low saO_2 and mitochondrial pH exhibits more linear behaviour at demand $u < 1$.

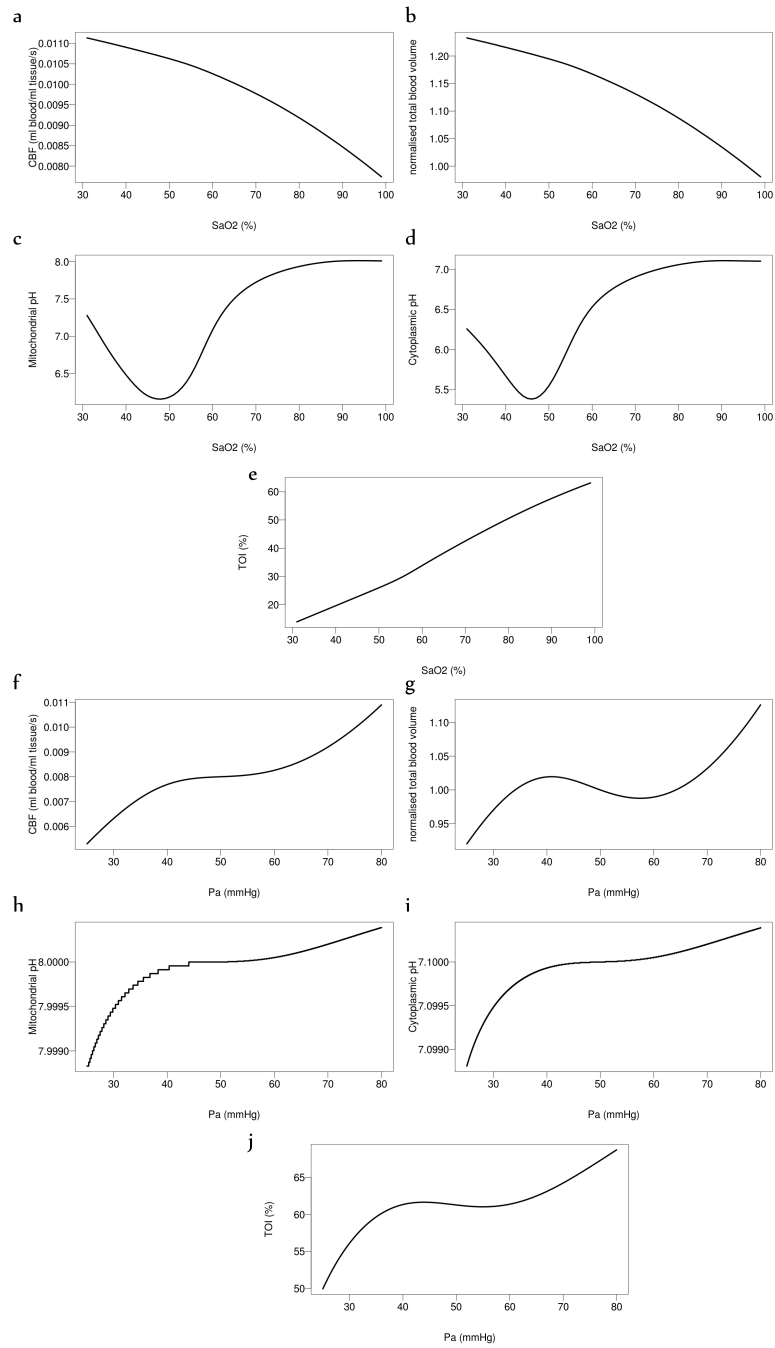


Figure 5.11: Steady state simulations of the BrainPiglet v2.1 model with varying arterial oxygen saturation SaO_2 (a–e) and blood pressure Pa (f–j).

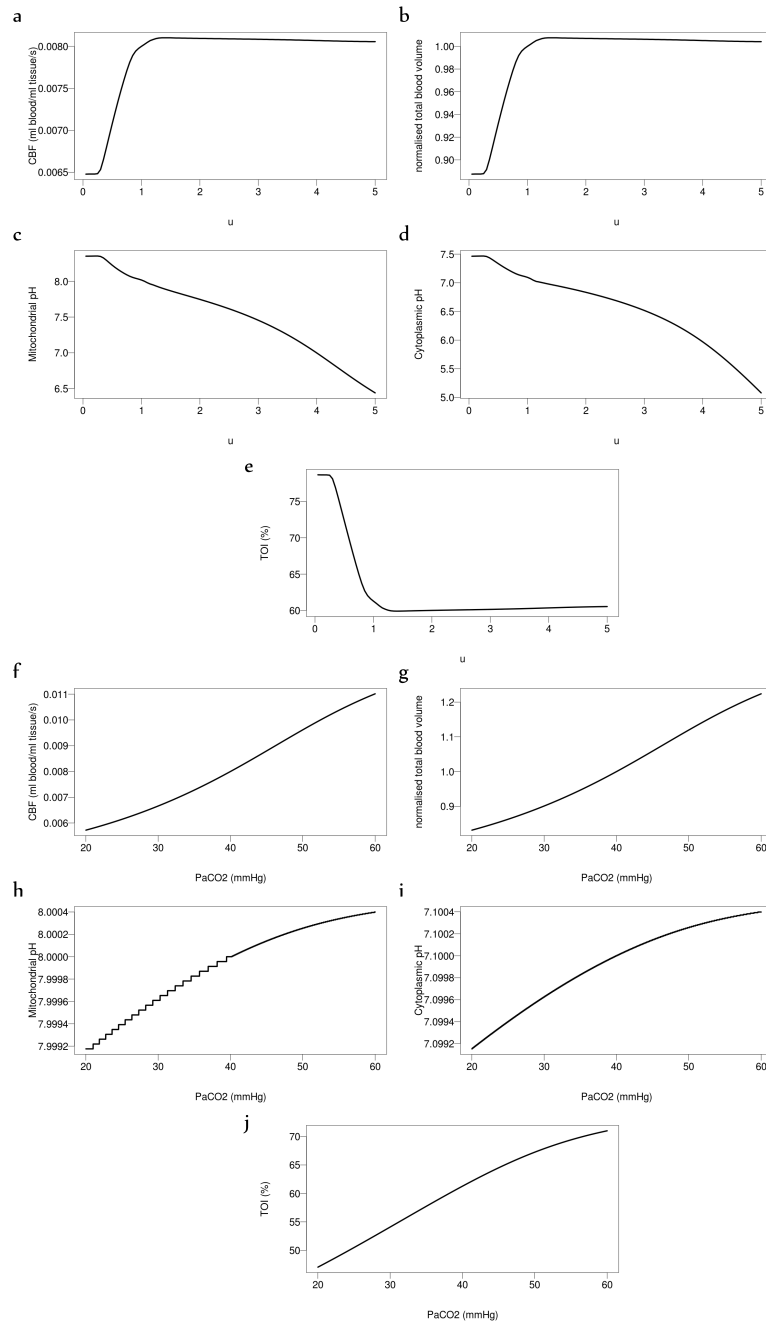


Figure 5.12: Steady state simulations of the BrainPiglet v2.1 model with varying demand u (a–e) and partial pressure of carbon dioxide P_aCO_2 (f–j).

Table 5.7: New parameters in BrainPiglet v2.1

Parameter	Description	Value	Source
Km_{KATPA}	Km for intracellular ATP for the sodium-potassium pump	1.4 mM	de Lima Santos and Ciancaglini (2003)
Km_{KATPNa}	Km for intracellular sodium for the sodium potassium pump	20 mM	12–44 mM Zahler et al. (1997), 8.3–24.7 mM Crambert et al. (2000), 11 mM de Lima Santos and Ciancaglini (2003)
Km_{NaBiC}	Km for the sodium-bicarbonate transporter	10.4 mM	Akiba et al. (1986)
Km_{NHE}	Km for the sodium-hydrogen exchanger	33 mM	Helbig et al. (1988)
Na_n	normal concentration of intracellular sodium	15 mM	15 mM Aubert and Costalat (2002) 5–14 mM Lo et al. (2006)
Na_pH	constant in the rate of the sodium-hydrogen exchanger	1.0	Orlowski et al. (2011)
$Vmax_{kATPm}$	Vmax for the sodium-potassium pump	94.2 mM	38.4–150 mM Zahler et al. (1997)
$Vmax_{NaBiC}$	Vmax for the sodium-bicarbonate transporter	0.001 mM	An estimate. 1.84–2.07 nmol/mg protein/2s Akiba et al. (1987)
$Vmax_{NHE}$	Vmax for the sodium-hydrogen exchanger	0.01 mM	An estimate. 9.2 nmol/mg protein/min Narins et al. (2004), 1.62 nmol/cm ² sample/min Helbig et al. (1988)

5.4.3 Simulating hypoxia-ischaemia in piglets

The model was run with measurement data from Piglet LWP173.

Sensitivity analysis and optimisation

Sensitivity analysis results are displayed in Table 5.8. 5 parameters (indicated by an asterisk) were selected to be optimised, along with the concentration of cytochrome in tissue $[CCO]_{tis}$ and the autoregulation constant k_{aut} , as with the previous model. It is apparent here that the new parameter representing normal sodium concentration Na_n has a significant influence on the four variables.

Table 5.8: Sensitivity analysis of BrainPiglet v2.1 using data from Piglet LWP173. Parameters ranked in order of influence in optimising selected output variables. Asterisks indicate parameters selected for optimisation.

Variable				Parameter	Description
HbO ₂	HHb	Δ oxCCO	pH _o		
1	1			$blood_{frac}^*$	Normal blood volume as a fraction of brain tissue volume
2	2	1	1	Na_n^*	Normal concentration of sodium
3	3	3	9	Vol_{mit}^*	Fraction of brain water which is mitochondria
4	5	16	7	r_t	Parameter in the muscular tension relationship
5	4	12		σ_{e0}	Parameter in relationship determining elastic stress in vessel walls
6	14			n_m	Exponent in the muscular tension relationship
7	11			$[lac]_n$	Normal concentration of lactate in the cytoplasm
8	10	17	6	$NADH_{cyt,n}$	Normal concentration of NADH in the cytoplasm
9	6	2	3	NAD_{pool}^*	Total mitochondrial NAD and NADH concentration
10	18			r_n	Normal radius of blood vessels
11	7			P_{ic}	Intracranial blood pressure
12	16	20	10	r_0	A special radius in the elastic tension relationship
13	9	4	5	r_{occ}	Controls occlusion of the carotid arteries
14	8			C_v	Compliance of the veins (normalised)
18	13	9	4	u	Demand
		5	2	$NAD_{cyt,n}^*$	Normal concentration of NAD in the cytoplasm
		6		$ck2$	Controls sensitivity of forward rate of the second oxidative phosphorylation reaction to the proton motive force
		7	12	$C_{buf fi}$	Buffering capacity for protons in mitochondria
		8		E_{N0}	NADH standard redox potential
		10	18	n_a	Number of protons passing through Complex V for each ATP synthesised
		15	8	$CMRO_{2,n}$	Resting cerebral metabolic rate of oxygen consumption

Table 5.9: Optimised BrainPiglet v2.1 parameter values for Piglet LWP173

Parameter	Description	Normal Value	Before Insult	After Insult	% Change
NAD_{cyt}	Normal concentration of NAD in the cytoplasm	359.0 mM	318.0	318.0	0
$blood_{frac}$	Normal blood volume as a fraction of brain tissue volume	0.0325	0.0304	0.0336	10.5
NAD_{pool}	Total mitochondrial NAD and NADH concentration	3.0 mM	2.4	3.60	50.0
Vol_{mit}	Fraction of brain water which is mitochondria	0.067	0.0536	0.0804	50.0
$[CCO]_{tis}$	Concentration of cytochrome in tissue	0.0022 mM	0.00584	0.007	19.9
k_{aut}	Autoregulation constant	1.0	0.689	0.596	-13.5
Na_n	Normal concentration of sodium	15.0 mM	15.7	15.1	-3.82

Model simulation

As before, SaO_2 and blood pressure measurements from the piglet were used as model inputs, and the fraction r_{occ} was used to simulate occlusion. Optimised parameters were used before and after the insult.

The results are very similar to BrainPigletv2.0.1, except in the optimised simulation of ΔHbT , where the error margin after the insult is much larger in this model. In short, there has been no visible improvement in the simulation of pH which the addition of the sodium transporters. Instead it has only further weakened the capacity of the optimisation process.

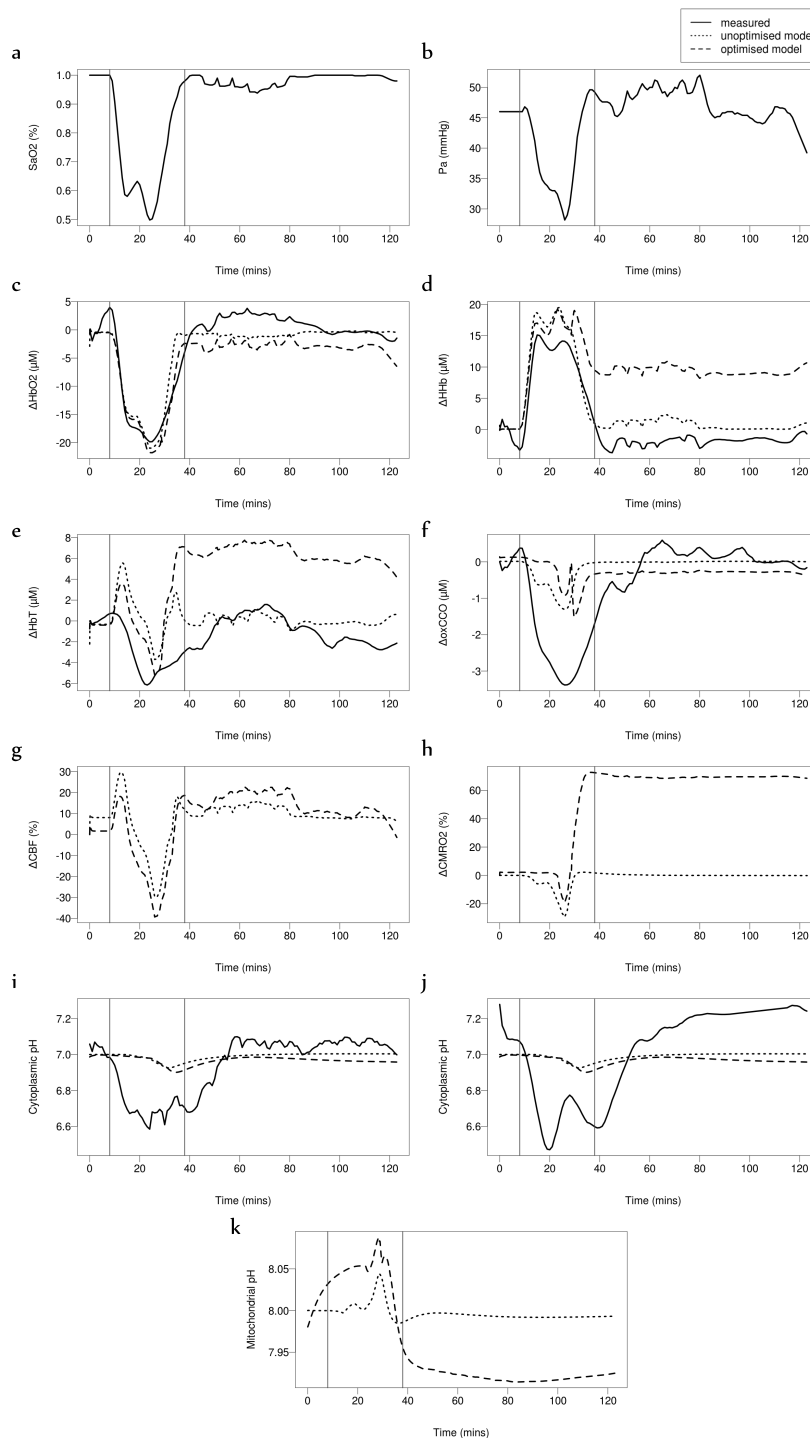


Figure 5.13: Simulating hypoxia-ischaemia in Piglet LWP173 using the BrainPiglet v2.1 model. (a) SaO_2 and (b) blood pressure P_a measurements are model inputs. (c,d,e, f) Simulations and measurements of ΔHbO_2 , ΔHHb , ΔHbT and $\Delta \alpha CCO$. (g,h) Simulations of ΔCBF and $\Delta CMRO_2$. Simulated cytoplasmic pH compared with measured (i) phosphate-derived pH and (j) ATP-derived pH. (k) Simulated mitochondrial pH.

5.5 Discussion

The BrainPiglet v2.0 model incorporates a significant representation of the movement, use and production of protons within the cell to simulate cytoplasmic and mitochondrial pH. The model was able to replicate the steady state simulations seen in BrainPiglet v1.0, with the addition here of pH. Both simulations had responses which might have been expected – more acidic pH at lower oxygenation, blood pressure and P_aCO_2 and at higher demand. In the simulation of hypoxia-ischaemia in the piglet, the optimisation of parameters was necessary to obtain a good prediction of $\Delta oxCCO$, and a better simulation of the acidic drop in cytoplasmic pH. The optimisation also significantly altered the simulation of mitochondrial pH, displaying a more acidic pH following the insult phase.

BrainPiglet v2.0.1 added the dynamics of carbonic acid, however it was found that these developments did not result in an improvement in model predictions. Steady state simulation were overall similar to v2.0, but it is in the simulations of data from the piglet experiments that the true complexity of the model starts to emerge. First in the sensitivity analysis suggested a much more complex model than that in v2.0. The optimised model behaved less accurately in relation to $\Delta oxCCO$ and cytoplasmic pH in particular. It also resulted in larger errors in post-insult values of ΔHbO_2 and ΔHHb , and an unusually large increase in $\Delta CMRO_2$ compared to the normal unoptimised model. These results and the sensitivity analysis suggest that the increase in model parameters, variables and complexity have made it more difficult to optimise, and therefore less effective in simulating individual patients and precise events.

The further development of the model to include sodium transporters – BrainPiglet v2.1 – did not prove more successful in simulating cytoplasmic pH during the piglet experiment. The optimised model did not perform better than BrainPiglet v2.0.1 or BrainPiglet v2.0. Therefore, in moving forward to accurately simulate the complete piglet experiments, BrainPiglet v2.0 was selected. These simulations are presented in the next chapter.

It is reassuring, in some ways, to see that the unoptimised model is capable of producing good simulations of the measurements. Firstly, this implies that the underlying physiology of the cell produces the changes observed in the measurements – a validation of the techniques used to measure clinically

important metabolites. Secondly, the model with its normal parameters is a better defined and known system. Optimisation of these variables also takes a considerable amount of processing power at the moment. For each piglet data set, the morris sensitivity analysis takes approximately a day and a half to run on a better than average PC and the parameter value optimisations take approximately half an hour. These time scales are not conducive to the possibility of an online system.

The validity of such optimisations of biological parameters are undermined by the lack of knowledge about how they vary in relation to one another. Although the optimisations can take into account the individual ranges for each parameter, it is unknown whether the optimised combination is biologically plausible. This is likely to augment the differences observed between optimised simulations and measurements. The ranges prescribed to the parameters are also constrained by available literature (if any). Furthermore, the progression of parameters from the optimised values before the insult to those after the insult may not be compatible with the physiological network of the cell.

The extensions of BrainPiglet embody the significantly increasing complexity of the models. Figure 5.14 illustrates schematics of v2.1, v2.0.1 and v2.0 showing all variables and parameters in the model, along with that for BrainSignals for comparison. These were created using the in-house bcmd software and GraphViz. What looks like an increasingly artless mess is representative of the divergence from the more modular and simpler format of the BrainSignals model to the more interconnected, intricate and detailed BrainPiglet model. These differences are naturally a consequence of the biology the models aim to simulate. In order to increase the capacity of the model to predict changes in clinically important variables, the models must become more elaborate. However, as discussed earlier in Chapter 4, a balance should be achieved between the volume of information that is included and the complexity and therefore accuracy of the model itself. This is a very fine theoretical line. Indeed, although BrainPiglet v2.0.1 and v2.1 includes more of the dynamics thought to be influential in cellular metabolism, especially in pH dynamics, in practice, the optimised model simulations of the v2.0 model were overall far more effective and accurate than that observed in v2.0.1 and v2.1. This is indicative of the greater instability of of the larger models.

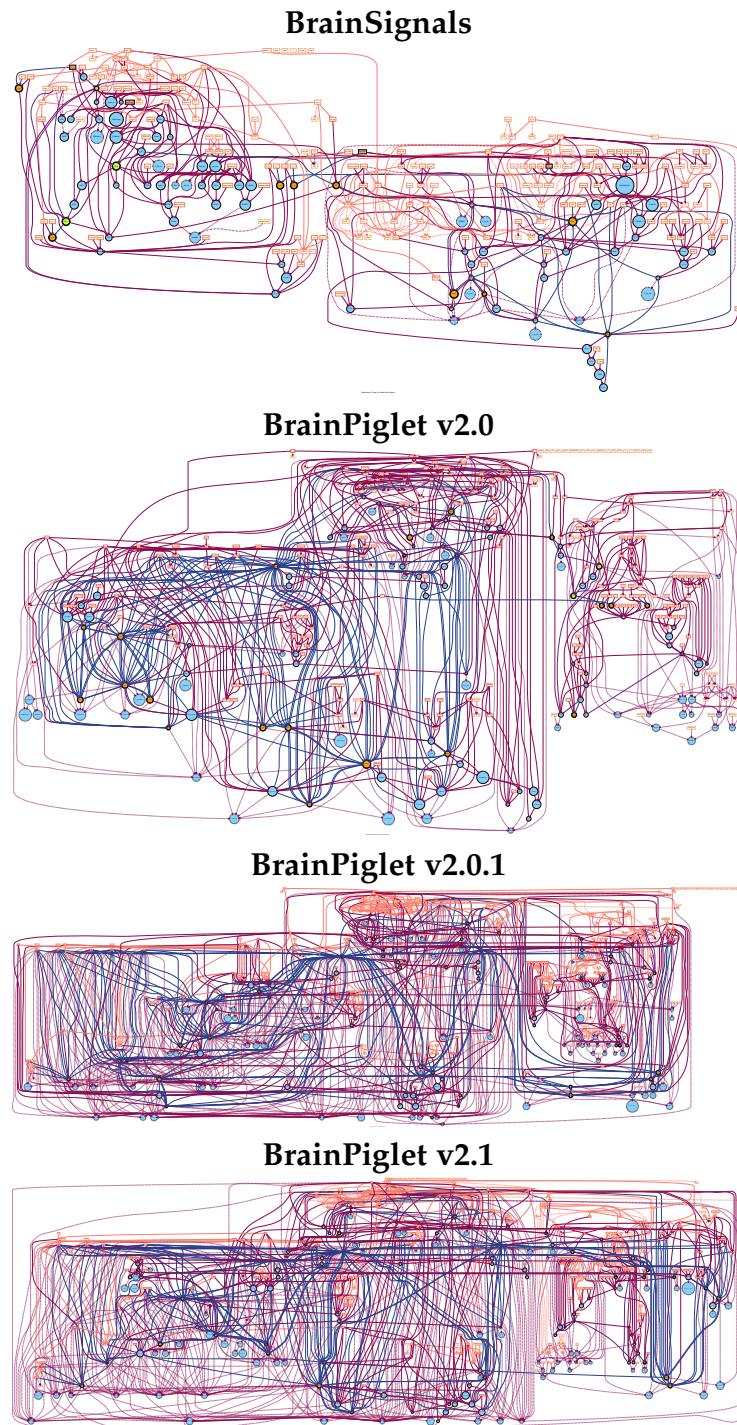


Figure 5.14: Schematic of variables and parameters in the four models. Rectangles and circles indicate parameters and variables respectively. Lines represent dependencies.

Chapter 6

Simulating hypoxia-ischaemia in the piglet brain

A study in newborn piglets used NIRS and MRS measurements to investigate the metabolic changes that occur in the brain in response to a hypoxia-ischaemia insult. Although the protocol remained the same, some of these piglets recovered well immediately following the insult whilst others did not. The recovery of ΔoxCCO was notably lacking in piglets with poor outcomes. The underlying differences between these piglets is not entirely clear. The BrainPiglet model v2.0 was used to investigate the discrepancies in the recovery of signals in piglets with different outcomes, by simulating the measurements to better understand the biological network of the cell that gives rise to the changes observed. Measurement data from 22 piglets were obtained for this investigation.

In this chapter, the model is first used to simulate measurements from piglets on an individual basis, initially from 15 piglets with good outcomes and subsequently from 7 with poor outcomes. The measurements for each group are then averaged and simulated by the model to examine overall changes and variations. Model parameters were optimised for each simulation to obtain the best possible fit of the model to the observed measurements, and to gain an insight into possible physiological changes caused by the insult.

6.1 Piglet experiments

Experiments were under UK Home Office Guidelines (Animals [Scientific Procedures] Act, 1986) and approved by the Institute of Neurology, University College London. In this study, 1-day-old piglets were mechanically ventilated and anaesthetised. Inflatable occluders were surgically inserted around the carotid arteries. Normal levels of arterial oxygen and carbon dioxide, blood glucose and heart rate were maintained. Changes (Δ) in concentrations of oxyhaemoglobin and deoxyhaemoglobin (ΔHbO_2 , ΔHHb) and brain oxidised CCO (ΔoxCCO) were monitored using broadband NIRS. ^{31}P -MRS was used to measure changes in concentrations of metabolites such as inorganic phosphate (Pi), phosphocreatine (PCr) and nucleotide triphosphate (NTP – mainly adenosine triphosphate (ATP)). Comparable with normal clinical practice, systemic variables - arterial blood pressure (P_a), arterial oxygen saturation (SaO_2), breathing rate and heart rate - were continuously recorded. Firstly baseline ^{31}P -MRS and NIRS were recorded. Transient hypoxia-ischaemia was then induced (over approximately 1 hour) by inflating the carotid artery occluders and reducing fractional inspired oxygen (FiO_2) to 12% from a normal value of 21%. Once β -NTP (mainly adenosine triphosphate; ATP) had reduced to approximately 40% of baseline, FiO_2 was gradually brought back to normal. This titration was completed over 10-20 minutes and the carotid occluders were then released. ^{31}P -MRS and broadband NIRS were acquired every 1 minute throughout hypoxia-ischaemia and for approximately a further 2 hours to monitor recovery.

The above protocol is illustrated in Figure 6.1. Intracellular pH was calculated from MRS measurements via two methods, the first using inorganic phosphate (Pi) and phosphoethanolamine (PEt), and the second using NTP concentrations. These methods are detailed in Section 3.1.2.

6.2 Sensitivity analysis of the model

As the Morris method of sensitivity analysis is dependent on the input data used to run the model, each of the 22 data sets was analysed using the BrainPiglet v2.0 model to investigate the most influential parameters for each data set. Figures 6.2, and 6.3 detail these results.

For the haemodynamic variables ΔHbO_2 and ΔHHb , the results are quite

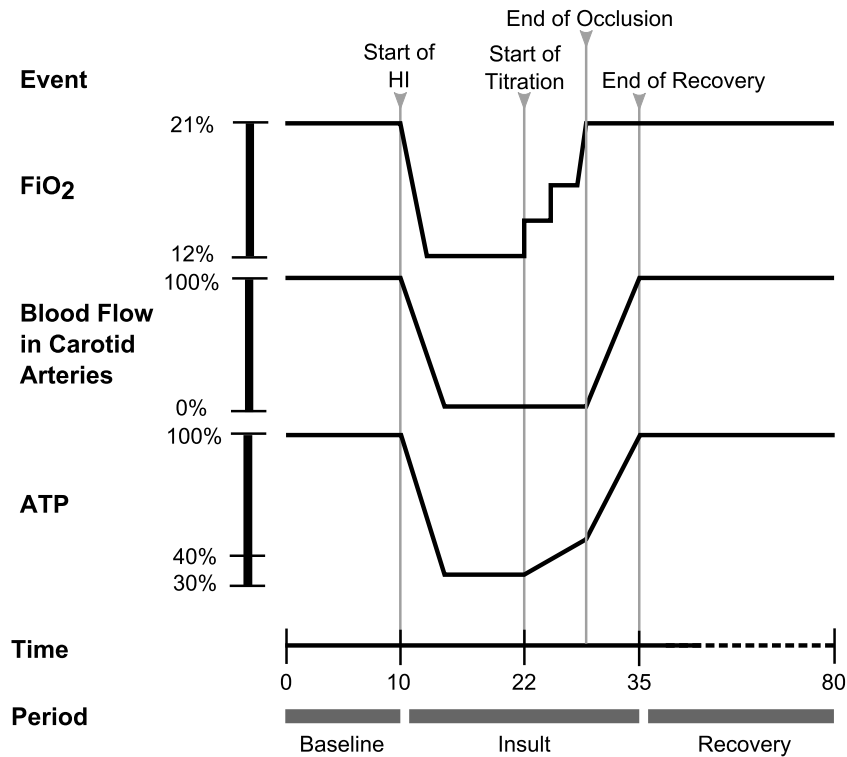


Figure 6.1: Experimental protocol for the hypoxia-ischaemia piglet experiments

similar. The exponent in the muscular tension relationship n_m , normal concentration of oxygen in the mitochondria $[O_2]_n$, sensitivity of elastic stress in vessel walls to radius K_σ , and sensitivity of autoregulatory stimuli to demand R_{autu} ranked most important among the data sets.

$\Delta\alpha CCO$ is more influenced by the normal mitochondrial inner membrane potential, $\Delta\psi_n$, normal concentration of oxygen in the mitochondria, $[O_2]_n$, demand u and normal oxidised fraction of Cu_A , $Cu_{A,frac,n}$. In comparison to the other three variables, Cytoplasmic pH, pH_o , is strongly influenced by a larger subset of parameters. At the top of these are the normal value of pH in the cytoplasm $pH_{o,n}$, normal concentration of NAD in the cytoplasm NAD_{cytn} , normal arterial oxygen saturation $SaO_{2,n}$ and total mitochondrial NAD and NADH concentration NAD_{pool} .

Following this analysis, 8 parameters were chosen to be optimised, including the autoregulation constant k_{aut} and the concentration of cytochrome in tissue $[CCO]_{tis}$. These parameters are listed in Table 6.1.

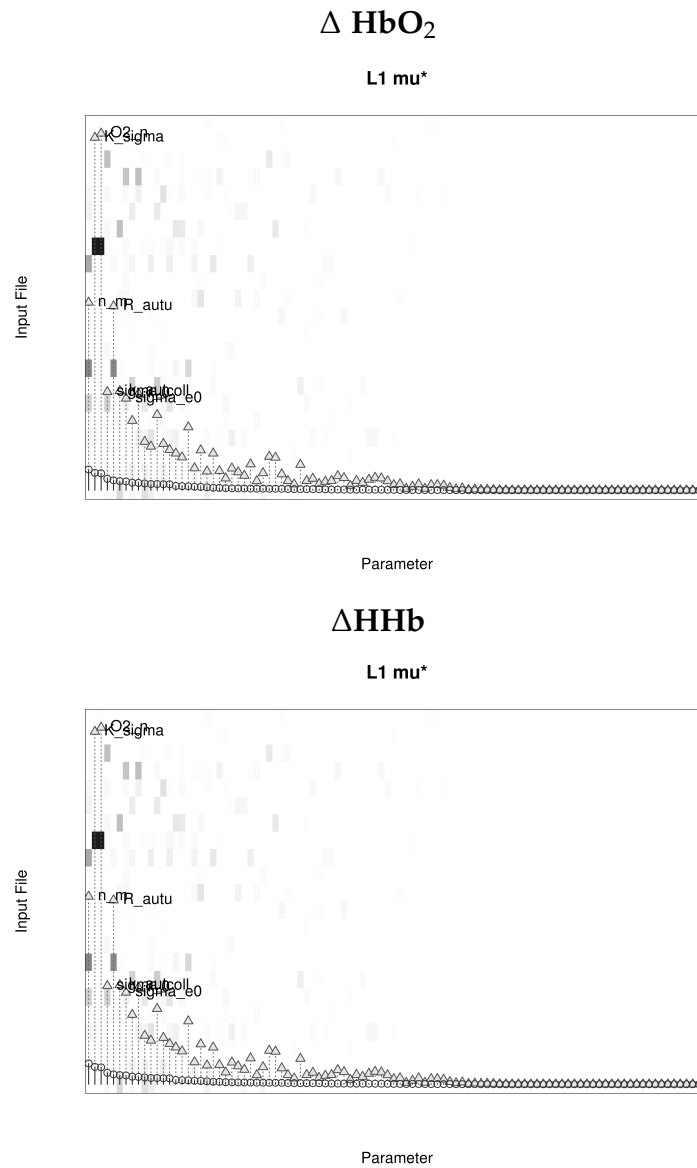


Figure 6.2: Morris method sensitivity analysis of the 22 piglet monitoring data sets for the ΔHbO_2 and ΔHHb variables. Darker shading against an input file indicates greater sensitivity. Circles and triangles indicate mean and maximum μ^* values respectively for each parameter. The top 25% of most influential parameters are labelled.

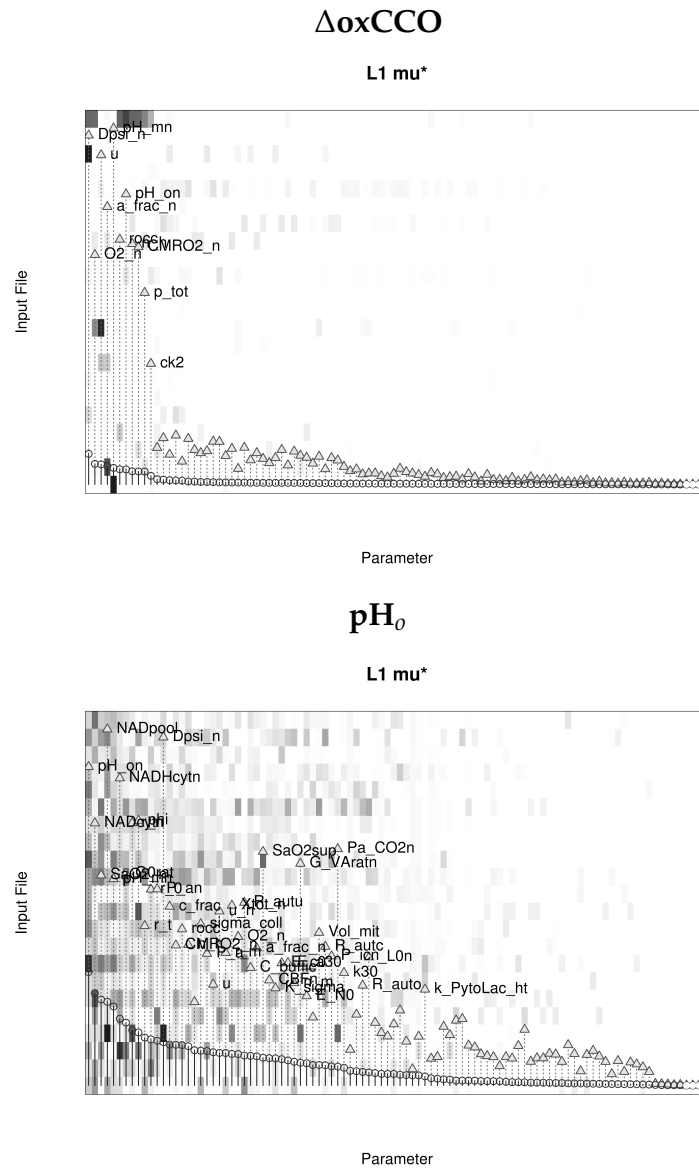


Figure 6.3: Morris method sensitivity analysis of the 22 piglet monitoring data sets for the $\Delta oxCCO$ and cytoplasmic pH pH_0 variables. Darker shading against an input file indicates greater sensitivity. Circles and triangles indicate mean and maximum μ^* values respectively for each parameter. The top 25% of most influential parameters are labelled.

Table 6.1: BrainPiglet v2.0 parameters selected for optimisation to simulate hypoxia-ischaemia piglet experiments

Parameter	Description
$\Delta\psi_n$	Normal mitochondrial inner membrane potential
$[O_2]_n$	Normal concentration of oxygen in the mitochondria
n_m	Exponent in the muscular tension relationship
K_σ	Controls sensitivity of elastic stress in vessel walls to radius
$NAD_{cyt,n}$	Normal concentration of NAD in the cytoplasm
$[CCO]_{tis}$	Concentration of cytochrome in tissue
k_{aut}	Autoregulation constant
$pH_{o,n}$	Normal value of pH in the cytoplasm

6.3 Individual results

This section details the analysis of data from each of the 22 piglets. NIRS and MRS data were synchronised and each data set was smoothed using the MATLAB *smooth* function (Mat 2013) and some very large spikes most likely caused by mechanical movements were manually removed. The MRS data was especially noisy during the insult phase. Signals were then re-sampled to a resolution of 1 Hz.

Measurements of arterial oxygen saturation (SaO_2) and blood pressure (P_a) from the 22 piglets were input into the model. P_aCO_2 was not recorded during these experiments, however the fraction of inspired carbon dioxide was maintained constant throughout. Therefore, we have assumed that P_aCO_2 remains constant at 40mmHg. The times of occlusion of the carotid arteries (r_{occ}) was also input. At the moment when occlusion of the carotid arteries takes place, the value of the occlusion parameter r_{occ} increases from 0 to 1 over the time period of one minute, returning back to zero when the occlusion is removed.

In order to investigate potential differences in the metabolic activity, the 22 piglets were divided into two groups according to their recovery immediately following the hypoxia-ischaemia insult, predominantly in $\Delta oxCCO$. This approach aims to provide some insight into how the haemodynamic and metabolic events during hypoxia-ischaemia relate to injury severity. Outcomes were classified as 'good' or 'poor' according to the recovery of the piglet immediately following the insult. Note that it does not take into account the overall health of the piglet at the end of the 48-hour monitoring

period. Table 6.2 details these outcomes.

Table 6.2: Piglet Outcomes

Good	Poor
LWP173	LWP183
LWP175	LWP185
LWP179	LWP188
LWP180	LWP207
LWP186	LWP208
LWP198	LWP215
LWP200	LWP218
LWP201	
LWP202	
LWP204	
LWP206	
LWP210	
LWP211	
LWP213	
LWP216	

6.3.1 Good outcomes

15 piglets exhibited a good recovery immediately following the insult. The parameters listed in Table 6.1 were optimised for each data set for the baseline and recovery periods separately as indicated in Figure 6.1 (before and after the insult). Table 6.3 lists the optimised values for each data set.

The BrainPiglet v2.0 model was run using SaO_2 and P_a measurements as inputs, with optimised parameters gradually changing from baseline to recovery values over a period of 3 minutes from the start of titration (see Figure 6.1). This period of time was selected to minimise fluctuations in variables caused by sudden changes in parameter values. Figures 6.5 to 6.19 show the 15 data sets compared with model simulations.

Although the same protocol was followed, and these 15 piglets had good outcomes, there is considerable variation observed in these measurements. This is perhaps to be expected as with most clinical recordings. These variations will be revisited in the next section on group analysis where they are quantified. Considering individual piglets, the parameter optimisations show changes in pre-insult and post-insult values (Figure 6.4). Normal

cytoplasmic pH pH_{on} was slightly increased following the insult in most piglets. The concentration of cytochrome in tissue $[CCO]_{tis}$ showed considerable variation, increasing in some piglets but decreasing in others. The autoregulation constant k_{aut} decreased following the insult, which may be expected and is perhaps characteristic of possible injury. The normal concentration of oxygen in the mitochondria $[O_2]_n$ and the normal concentration of NAD in the cytoplasm $NAD_{cyt,n}$ were both decreased in the majority of the piglets, most likely due to the decrease in oxygen delivery and thus in oxidative phosphorylation. Similarly, the normal mitochondrial inner membrane potential, $\Delta\psi_n$ reduced in the majority of piglets, but increased in some. This affects the proton motive force which the rate of the oxidative phosphorylation reactions are sensitive to (greater $\Delta\psi_n$ leads to faster rates). The parameter controlling the sensitivity of elastic stress in vessel walls to the radius K_σ increased in most piglets but decreased in others (hence respectively increasing and decreasing elastic stress). The effect of decreases in the exponent in the muscular tension relationship n_m is however less straightforward. n_m has a positive or negative effect on the muscular tension depending on whether the radius is less than or greater than the value of the constant r_t (see Chapter 4, Section 4.6, Equation 4.17). The value of the radius does change during the simulation, but largely remains higher than r_t . Thus, on average, decreases in n_m result in a higher muscular tension. Increases in elastic and muscular tension in vessel walls result in a larger radius (see Chapter 4, Section 4.7, Equation 4.61)

In the measurements, the general drop and recovery can be detected in most piglets, except in LWP200 and LWP210 where although oxygenation recovers, P_a does not. The changes in haemoglobin variables are fairly consistent across the piglets, with a drop in ΔHbO_2 during the insult accompanied by a rise in $\Delta H Hb$. These changes are well simulated by the model, except in LWP216, where the magnitude of the change is not replicated in the simulation. The decrease in ΔHbT was not well predicted in some piglets (LWP175, LWP179, LWP180, LWP198). On the other hand two piglets showed a rise in ΔHbT (LWP209 and LWP216) which as not well replicated in the simulations. In LWP200, the model predicts a poorer recovery than that observed in $\Delta H Hb$ and ΔHbT .

The magnitude of the drop in $\Delta oxCCO$ is relatively well simulated across the piglets. In LWP206 and LWP209 the model predicts a smaller drop and

better recovery than that observed. Simulated ΔCBF and $\Delta CMRO_2$ also showed a drop during the insult in most piglets. In four piglets, CBF did not recover quite so well (LWP180, LWP198, LWP200 and LWP206).

There were considerable differences in the two pH measurements, although both generally displayed more acidic values in response to the insult. There was a wider variation in the measured pH values than that simulated. The nadir of the drop in modelled pH was often reached at the end of the insult, whereas the measurement nadir was not always thus defined. The magnitude of the drop in pH was well simulated in some piglets (such as LWP173, LWP200, LWP201, LWP206) while in some the drop of simulated pH was insufficient (LWP 198, LWP204). In some cases the simulation better suited one measurement and not the other (such as in LWP175) or the measurements were very noisy making it difficult to compare with simulations and optimise simulations against them (LWP204, LWP216). Note here that only the phosphate-derived pH measurement was used for optimisation, the ATP-derived measurement was not.

Simulated mitochondrial pH also displayed a lot of variation between the piglets, generally registering a small rise during the insult phase and a subsequent drop immediately afterwards. It remained more acidic in the period following the insult phase in most piglets, except in LWP173, which displayed a slow recovery back to baseline values.

Table 6.3: Optimised parameter values

Normal mitochondrial inner membrane potential, $\Delta\psi_n$			
Normal value: 145			
Piglet	Before Insult	After Insult	% Change
173	150	150	0
175	150	128.2890	-14.4740
179	150	129.5580	-13.6280
180	150	145.5670	-2.9553
186	127.8410	150	17.3332
198	127.3560	137.0320	7.5976
200	150	141.4520	-5.6987
201	150	150	0
204	150	150	0
206	150	148.4290	-1.0473

6.3. Individual results

209	150	150	0
210	149.9990	125	-16.6661
211	150	150	0
213	150	150	0
216	125	136.7530	9.4024
Average	145.3464	142.8053	-1.7483

Concentration of cytochrome in tissue, $[CCO]_{tis}$

Normal value: 0.0022

Piglet	Before Insult	After Insult	% Change
173	0.0050	0.0064	26.6460
175	0.0066	0.0070	5.9660
179	0.0070	0.0070	-0.0334
180	0.0053	0.0065	23.3449
186	0.0052	0.0010	-80.6733
198	0.0070	0.0013	-81.0393
200	0.0061	0.0070	13.8807
201	0.0030	0.0022	-25.6047
204	0.0062	0.0070	13.7381
206	0.0070	0.0070	-0.0021
209	0.0070	0.0070	-0.0021
210	0.0047	0.0070	49.8721
211	0.0062	0.0070	12.5242
213	0.0070	0.0070	-0.0021
216	0.0050	0.0046	-8.1048
Average	0.0059	0.0057	-3.6854

Autoregulation constant, k_{aut}

Normal value: 1.0

Piglet	Before Insult	After Insult	% Change
173	1	0.9298	-7.0151
175	1	0.4466	-55.3438
179	1	1	0
180	0.9475	0	-99.9999
186	1	1	-0.0012
198	0.6857	0.6857	0
200	0.6191	0.4798	-22.4911
201	1	0.6245	-37.5534
204	1	0.4272	-57.2782
206	1	0.4809	-51.9149

6.3. Individual results

209	1	0.9262	-7.3822
210	0.7235	0.7235	0
211	1	0.8402	-15.9788
213	1	0.7705	-22.9520
216	1	1	0
Average	0.9317	0.7284	-25.1940

Sensitivity of elastic stress in vessel walls to radius, K_σ

Normal value: 10

Piglet	Before Insult	After Insult	% Change
173	11.0391	12	8.7045
175	10.3736	9.4173	-9.2184
179	8	10.2671	28.3388
180	8.3231	11.9222	43.2421
186	11.3765	11.3699	-0.0580
198	12	8	-33.3333
200	12	12	0
201	8	8	0
204	10.1555	8	-21.2250
206	8	12	50
209	8	8	0
210	12	8	-33.3333
211	9.9259	11.0382	11.2060
213	10.3814	12	15.5913
216	8	10.6646	33.3075
Average	9.8383	10.1786	3.4587

Normal concentration of oxygen in the mitochondria, $[O_2]_n$

Normal value: 0.024

Piglet	Before Insult	After Insult	% Change
173	0.0202	0.0192	-4.8011
175	0.0284	0.0192	-32.3813
179	0.0288	0.0278	-3.4319
180	0.0288	0.0203	-29.3962
186	0.0263	0.0192	-26.9981
198	0.0281	0.0192	-31.6595
200	0.0228	0.0192	-15.7107
201	0.0192	0.0192	0
204	0.0271	0.0194	-28.3554
206	0.0248	0.0192	-22.4396

6.3. Individual results

209	0.0247	0.0192	-22.1500
210	0.0192	0.0288	49.9995
211	0.0268	0.0200	-25.5549
213	0.0248	0.0192	-22.7333
216	0.0288	0.0286	-0.5885
Average	0.0253	0.0212	-16.0973

Exponent in the muscular tension relationship, n_m

Normal value: 1.0

Piglet	Before Insult	After Insult	% Change
173	1.4640	2.1960	50
175	2.1960	1.4796	-32.6248
179	2.1960	1.4640	-33.3333
180	2.1960	2.1783	-0.8078
186	1.4641	1.4640	-0.0082
198	2.1953	1.4640	-33.3118
200	2.1942	2.1960	0.0811
201	2.0886	2.1960	5.1427
204	2.1960	1.4640	-33.3333
206	2.1960	2.1960	0
209	2.1960	2.1960	0
210	2.1960	1.4640	-33.3330
211	2.1960	1.6053	-26.8975
213	2.1960	1.4640	-33.3333
216	2.1960	2.1450	-2.3210
Average	2.0911	1.8115	-13.3712

Normal concentration of NAD in the cytoplasm, $NAD_{cyt,n}$

Normal value: 359

Piglet	Before Insult	After Insult	% Change
173	400	399.9990	-0.0002
175	400	318	-20.5000
179	318	318	0
180	400	318.0070	-20.4983
186	399.9930	318	-20.4986
198	399.8830	318.0010	-20.4765
200	400	318.0010	-20.4998
201	399.9990	318.0010	-20.4996
204	400	318.0220	-20.4945
206	399.9990	318	-20.4998

6.3. Individual results

209	318.0010	400	25.7858
210	400	396.3180	-0.9205
211	318	400	25.7862
213	400	318	-20.5000
216	400	328.7620	-17.8095
Average	383.5917	340.3407	-11.2753

Normal value of pH in the cytoplasm, $pH_{o,n}$

Normal value: 7

Piglet	Before Insult	After Insult	% Change
173	6.8920	6.9385	0.6746
175	6.8957	7.1765	4.0719
179	7.2564	7.1988	-0.7927
180	6.8920	7.2789	5.6135
186	7.1698	7.1363	-0.4678
198	7.1126	7.1061	-0.0914
200	6.8933	7.1537	3.7770
201	6.9840	7.0580	1.0593
204	7.1604	6.8999	-3.6379
206	6.9114	7.1489	3.4362
209	6.9938	7.1565	2.3259
210	7.1699	6.9663	-2.8395
211	6.9049	7.2031	4.3179
213	6.9509	7.1708	3.1642
216	6.9631	7.2836	4.6036
Average	7.010	7.1250	1.6411

6.3. Individual results

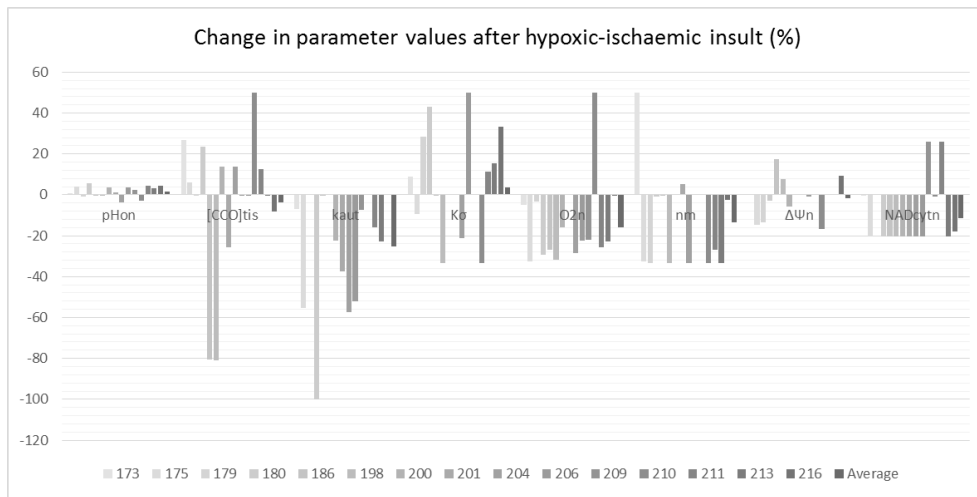


Figure 6.4: Changes in optimised parameter values for piglets with good outcomes. Recovery values after the insult compared to values before the insult

6.3. Individual results

LWP173

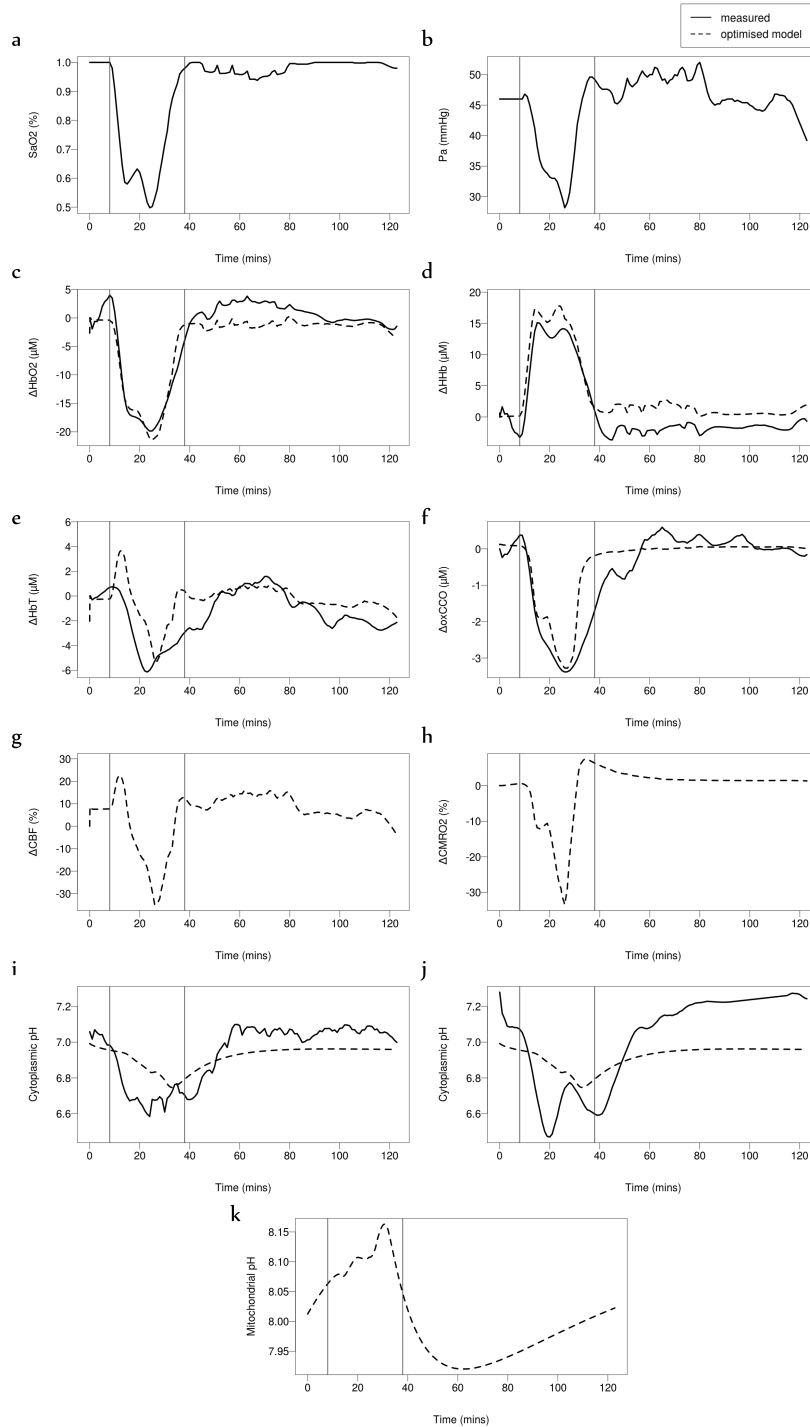


Figure 6.5: Piglet LWP173. (a) SaO_2 and (b) blood pressure P_a measurements are model inputs. (c,d,e,f) Simulations and measurements of ΔHbO_2 , ΔHHb , ΔHbT and $\Delta oxCCO$. (g,h) Simulations of ΔCBF and $\Delta CMRO_2$. Simulated cytoplasmic pH compared with measured (i) phosphate-derived pH and (j) ATP-derived pH. (k) Simulated mitochondrial pH.

LWP175

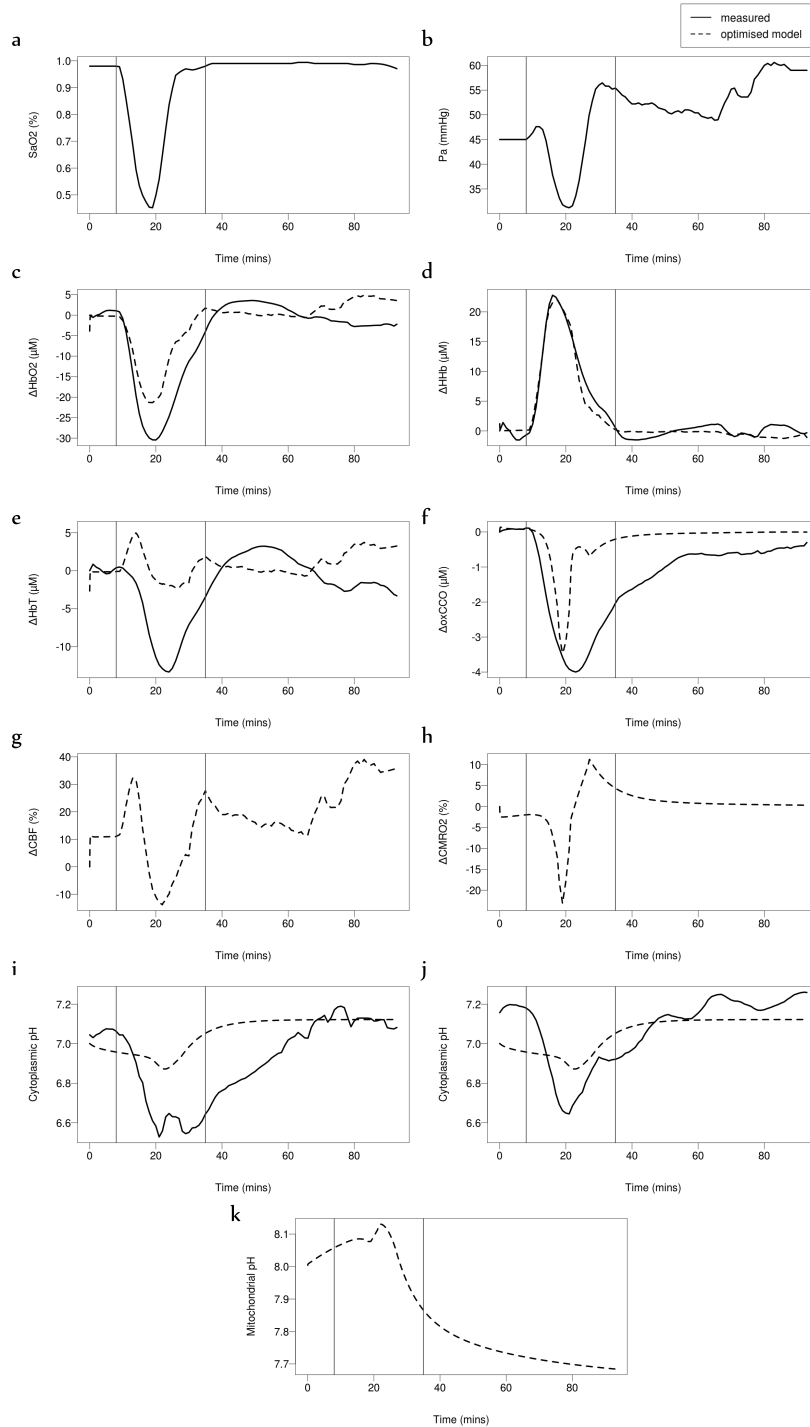


Figure 6.6: Piglet LWP175. (a) SaO_2 and (b) blood pressure P_a measurements are model inputs. (c,d,e,f) Simulations and measurements of ΔHbO_2 , ΔHHb , ΔHbT and $\Delta oxCCO$. (g,h) Simulations of ΔCBF and $\Delta CMRO_2$. Simulated cytoplasmic pH compared with measured (i) phosphate-derived pH and (j) ATP-derived pH. (k) Simulated mitochondrial pH.

LWP179

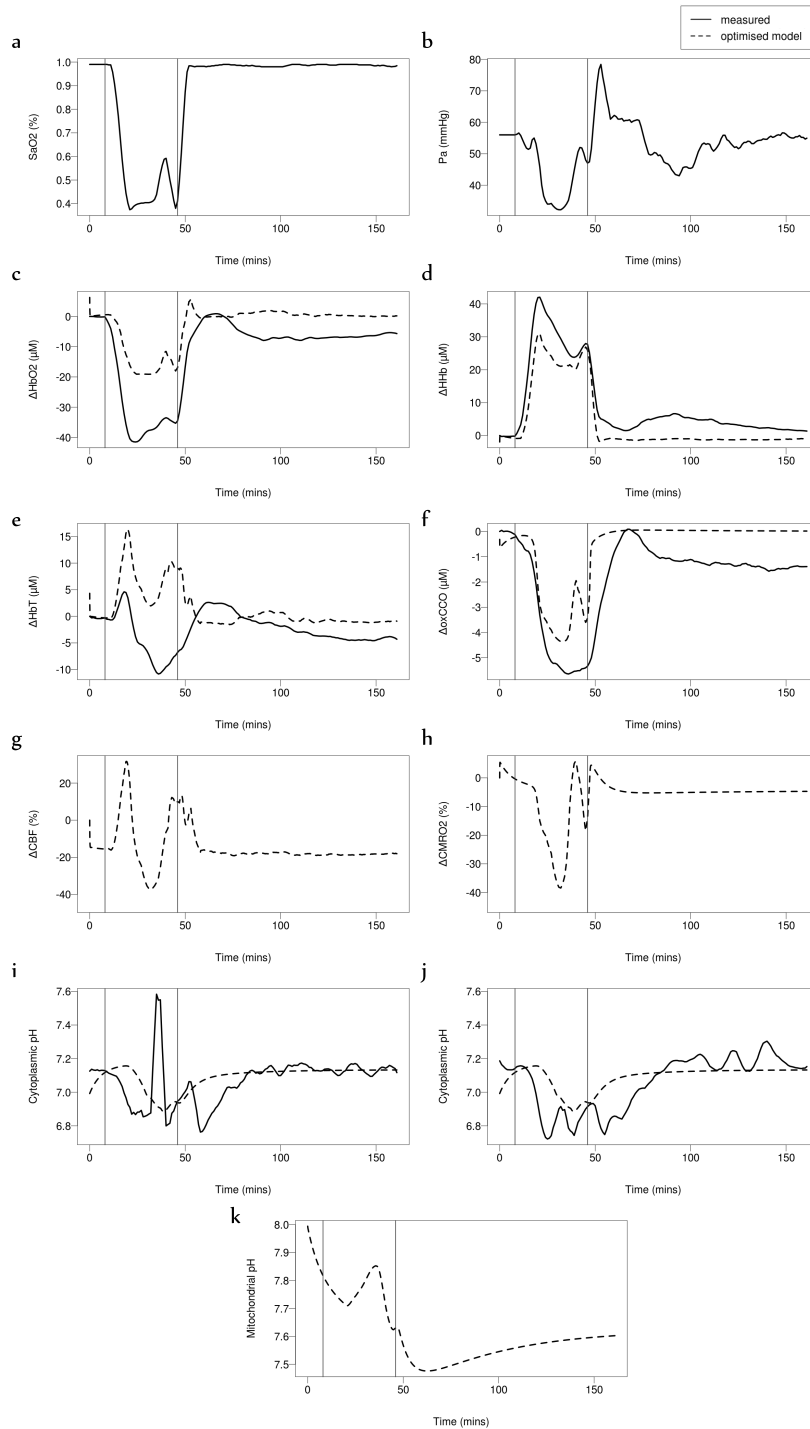


Figure 6.7: Piglet LWP179. (a) SaO_2 and (b) blood pressure P_a measurements are model inputs. (c,d,e,f) Simulations and measurements of ΔHbO_2 , ΔHHb , ΔHbT and $\Delta oxCCO$. (g,h) Simulations of ΔCBF and $\Delta CMRO_2$. Simulated cytoplasmic pH compared with measured (i) phosphate-derived pH and (j) ATP-derived pH. (k) Simulated mitochondrial pH.

LWP180

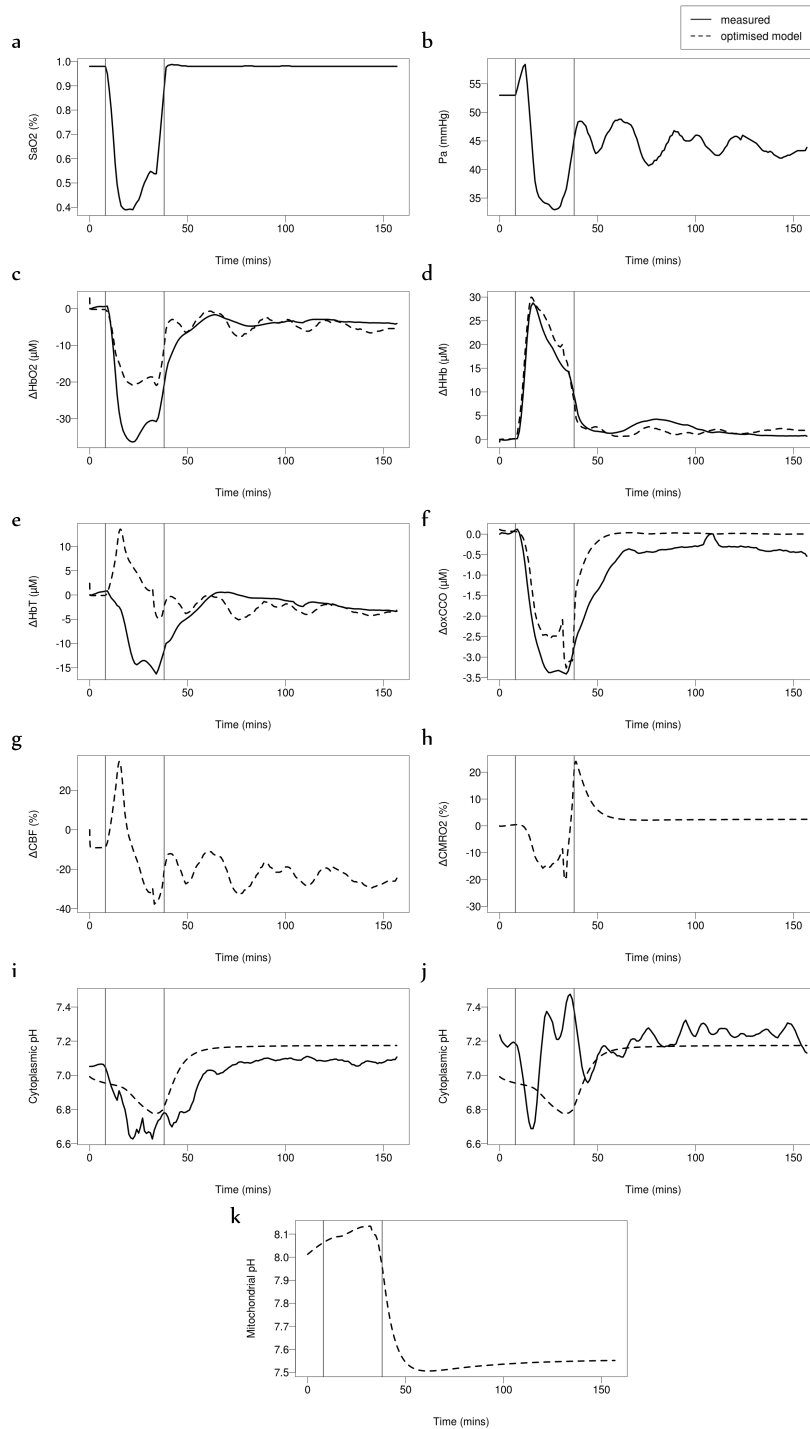


Figure 6.8: Piglet LWP180. (a) SaO_2 and (b) blood pressure P_a measurements are model inputs. (c,d,e,f) Simulations and measurements of ΔHbO_2 , ΔHHb , ΔHbT and $\Delta oxCCO$. (g,h) Simulations of ΔCBF and $\Delta CMRO_2$. Simulated cytoplasmic pH compared with measured (i) phosphate-derived pH and (j) ATP-derived pH. (k) Simulated mitochondrial pH.

LWP186

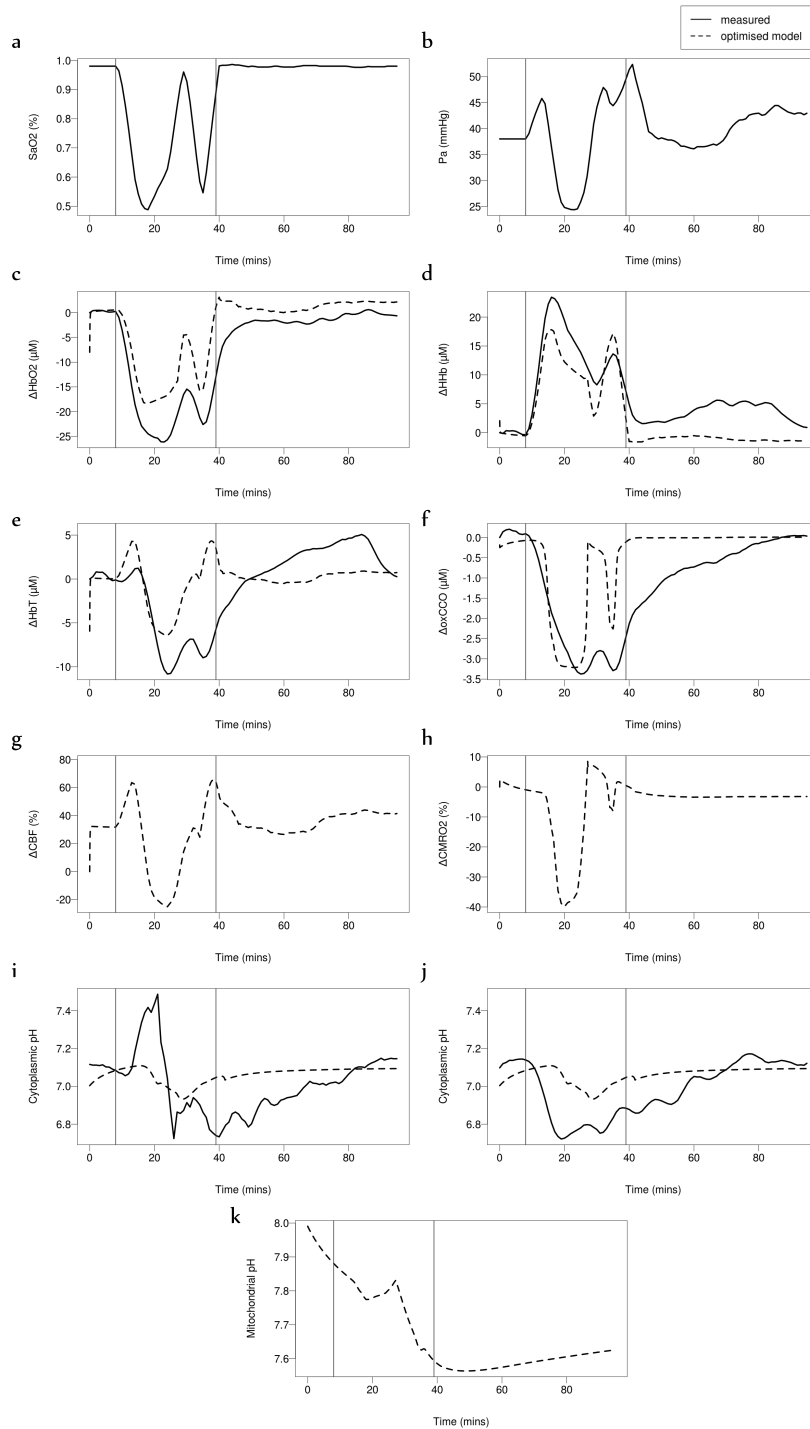


Figure 6.9: Piglet LWP186. (a) SaO_2 and (b) blood pressure P_a measurements are model inputs. (c,d,e,f) Simulations and measurements of ΔHbO_2 , ΔHHb , ΔHbT and $\Delta oxCCO$. (g,h) Simulations of ΔCBF and $\Delta CMRO_2$. Simulated cytoplasmic pH compared with measured (i) phosphate-derived pH and (j) ATP-derived pH. (k) Simulated mitochondrial pH.

LWP198

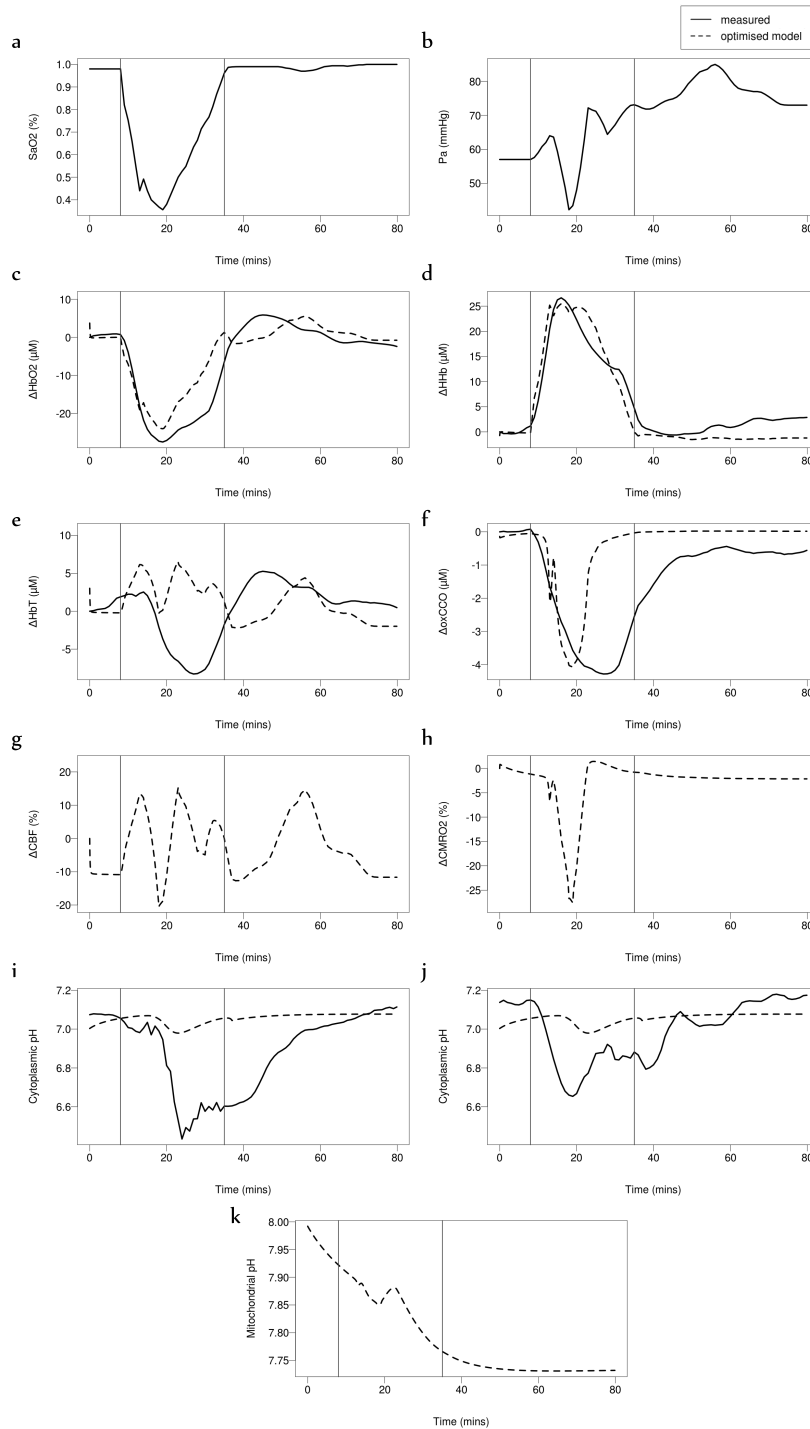


Figure 6.10: Piglet LWP198. (a) SaO_2 and (b) blood pressure P_a measurements are model inputs. (c,d,e,f) Simulations and measurements of ΔHbO_2 , ΔHHb , ΔHbT and $\Delta oxCCO$. (g,h) Simulations of ΔCBF and $\Delta CMRO_2$. Simulated cytoplasmic pH compared with measured (i) phosphate-derived pH and (j) ATP-derived pH. (k) Simulated mitochondrial pH.

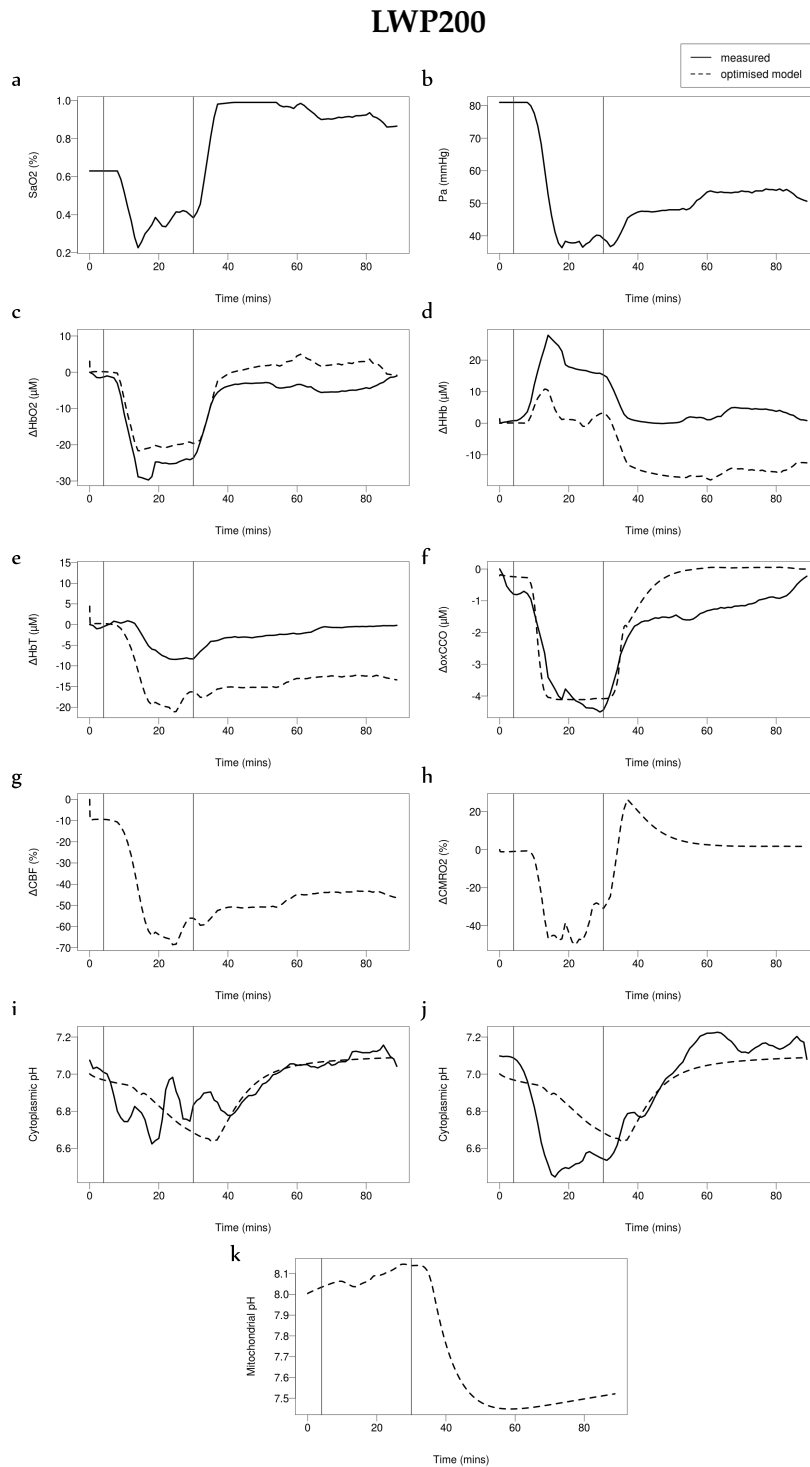


Figure 6.11: Piglet LWP200. (a) SaO_2 and (b) blood pressure P_a measurements are model inputs. (c,d,e,f) Simulations and measurements of ΔHbO_2 , ΔHHb , ΔHbT and $\Delta oxCCO$. (g,h) Simulations of ΔCBF and $\Delta CMRO_2$. Simulated cytoplasmic pH compared with measured (i) phosphate-derived pH and (j) ATP-derived pH. (k) Simulated mitochondrial pH.

LWP201

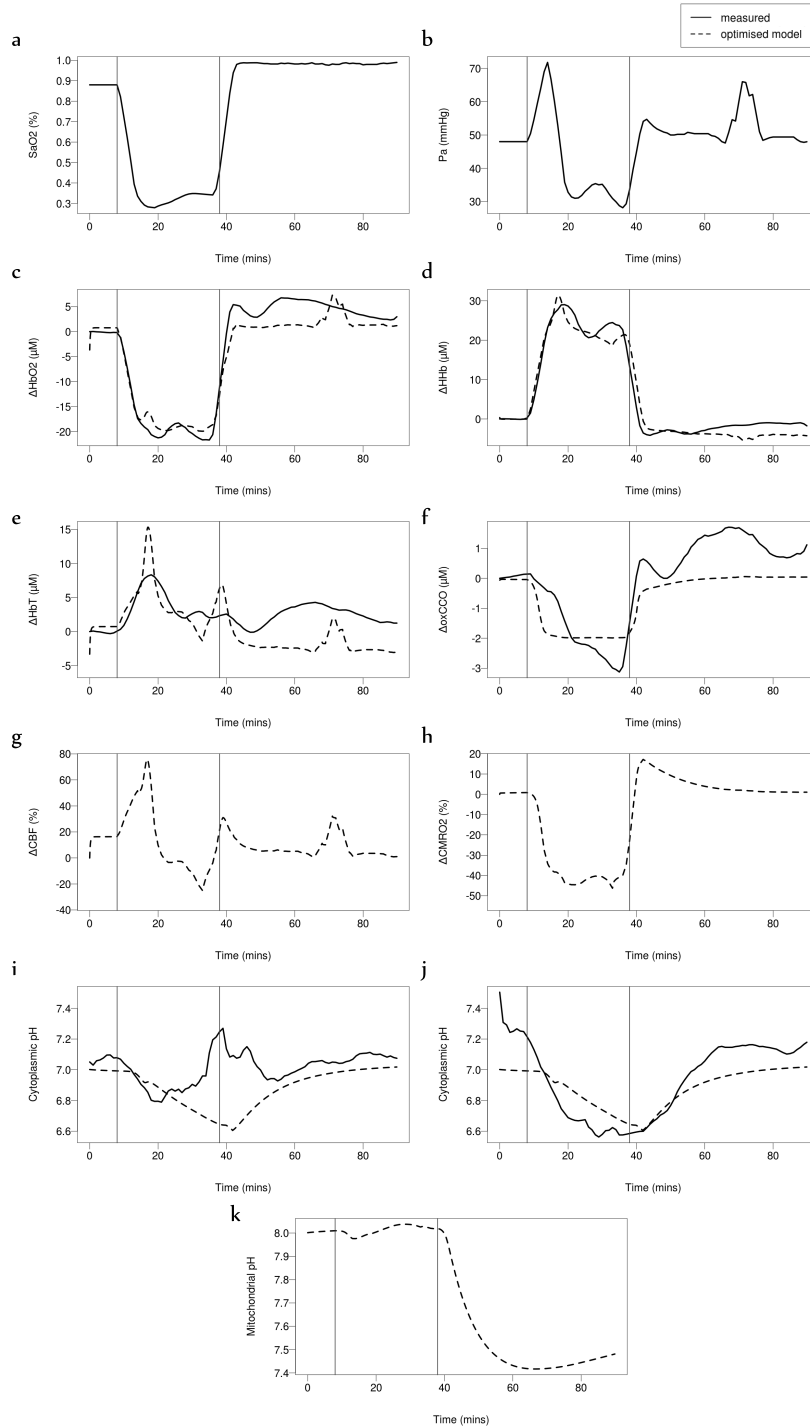


Figure 6.12: Piglet LWP201. (a) SaO_2 and (b) blood pressure P_a measurements are model inputs. (c,d,e,f) Simulations and measurements of ΔHbO_2 , ΔHHb , ΔHbT and $\Delta oxCCO$. (g,h) Simulations of ΔCBF and $\Delta CMRO_2$. Simulated cytoplasmic pH compared with measured (i) phosphate-derived pH and (j) ATP-derived pH. (k) Simulated mitochondrial pH.

6.3. Individual results

LWP204

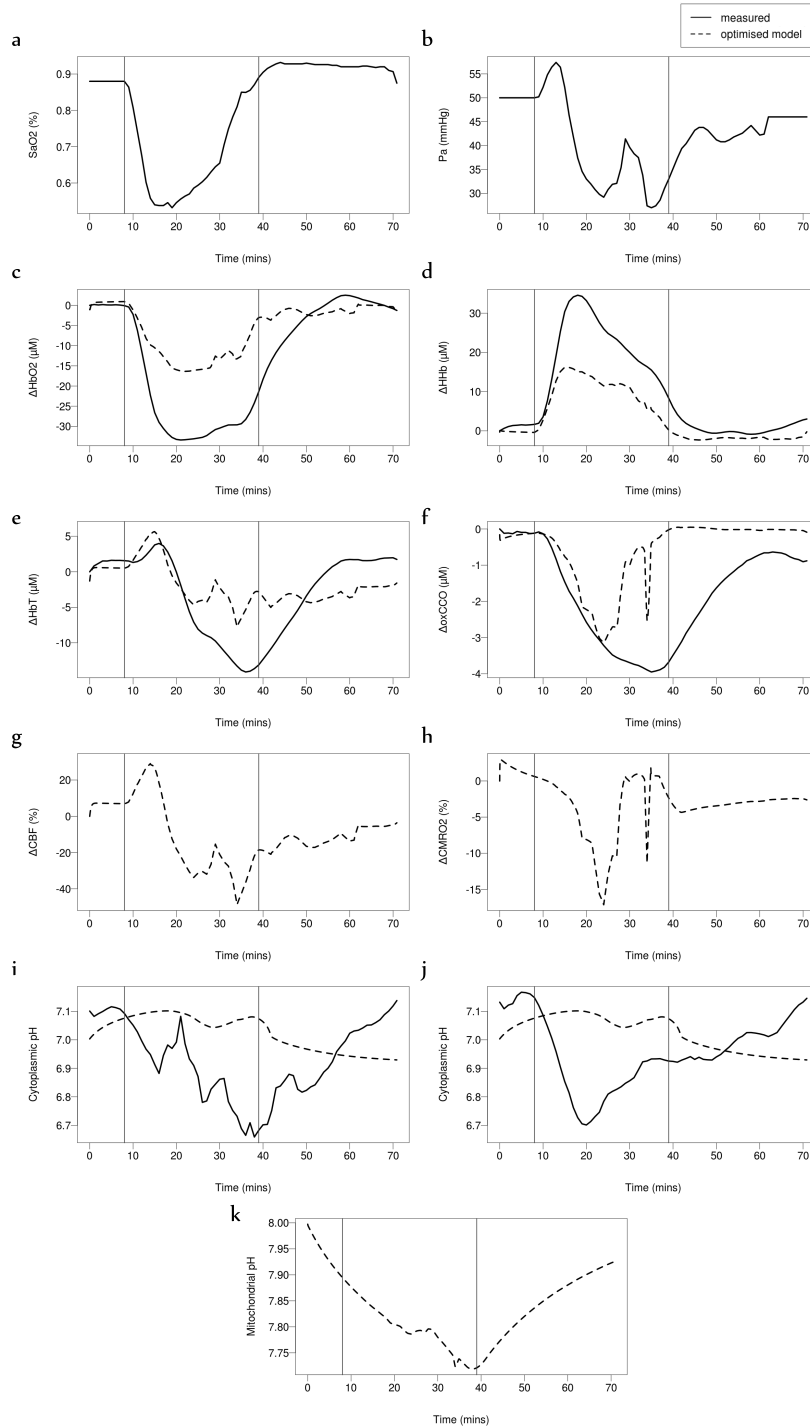


Figure 6.13: Piglet LWP204. (a) SaO_2 and (b) blood pressure P_a measurements are model inputs. (c,d,e,f) Simulations and measurements of ΔHbO_2 , ΔHHb , ΔHbT and $\Delta oxCCO$. (g,h) Simulations of ΔCBF and $\Delta CMRO_2$. Simulated cytoplasmic pH compared with measured (i) phosphate-derived pH and (j) ATP-derived pH. (k) Simulated mitochondrial pH.

LWP206

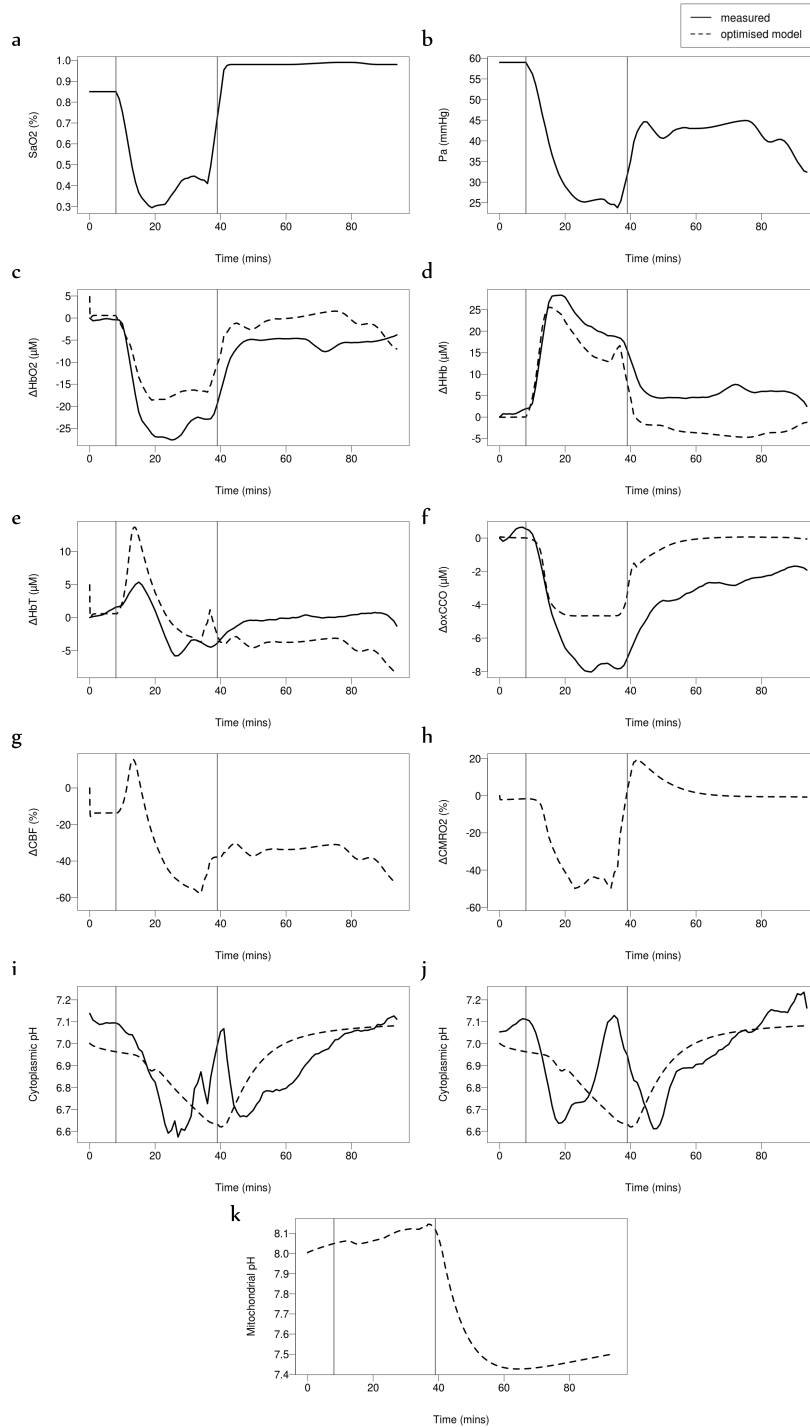


Figure 6.14: Piglet LWP206. (a) SaO_2 and (b) blood pressure P_a measurements are model inputs. (c,d,e,f) Simulations and measurements of ΔHbO_2 , ΔHHb , ΔHbT and $\Delta oxCCO$. (g,h) Simulations of ΔCBF and $\Delta CMRO_2$. Simulated cytoplasmic pH compared with measured (i) phosphate-derived pH and (j) ATP-derived pH. (k) Simulated mitochondrial pH.

6.3. Individual results

LWP209

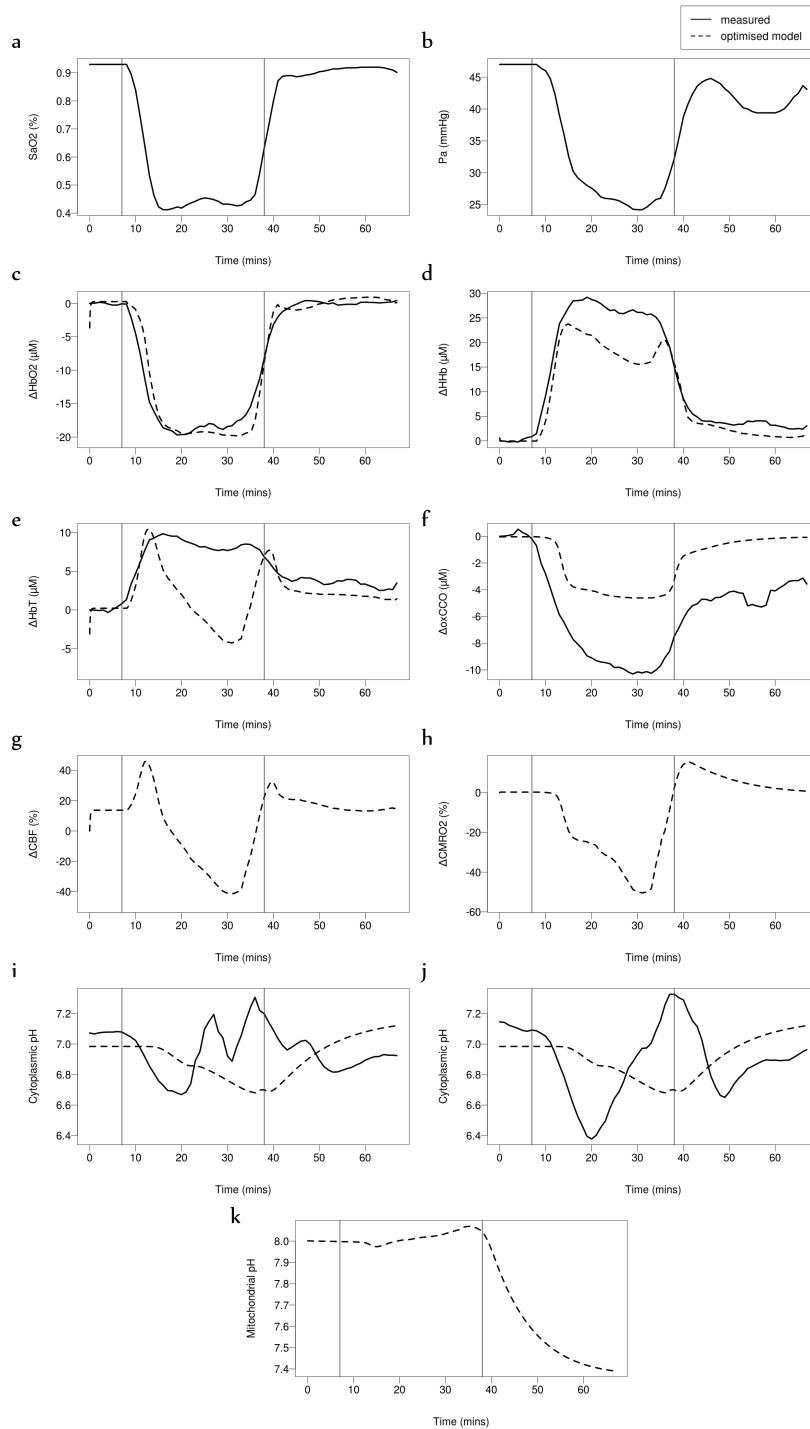


Figure 6.15: Piglet LWP209. (a) SaO_2 and (b) blood pressure P_a measurements are model inputs. (c,d,e,f) Simulations and measurements of ΔHbO_2 , ΔHHb , ΔHbT and $\Delta oxCCO$. (g,h) Simulations of ΔCBF and $\Delta CMRO_2$. Simulated cytoplasmic pH compared with measured (i) phosphate-derived pH and (j) ATP-derived pH. (k) Simulated mitochondrial pH.

LWP210

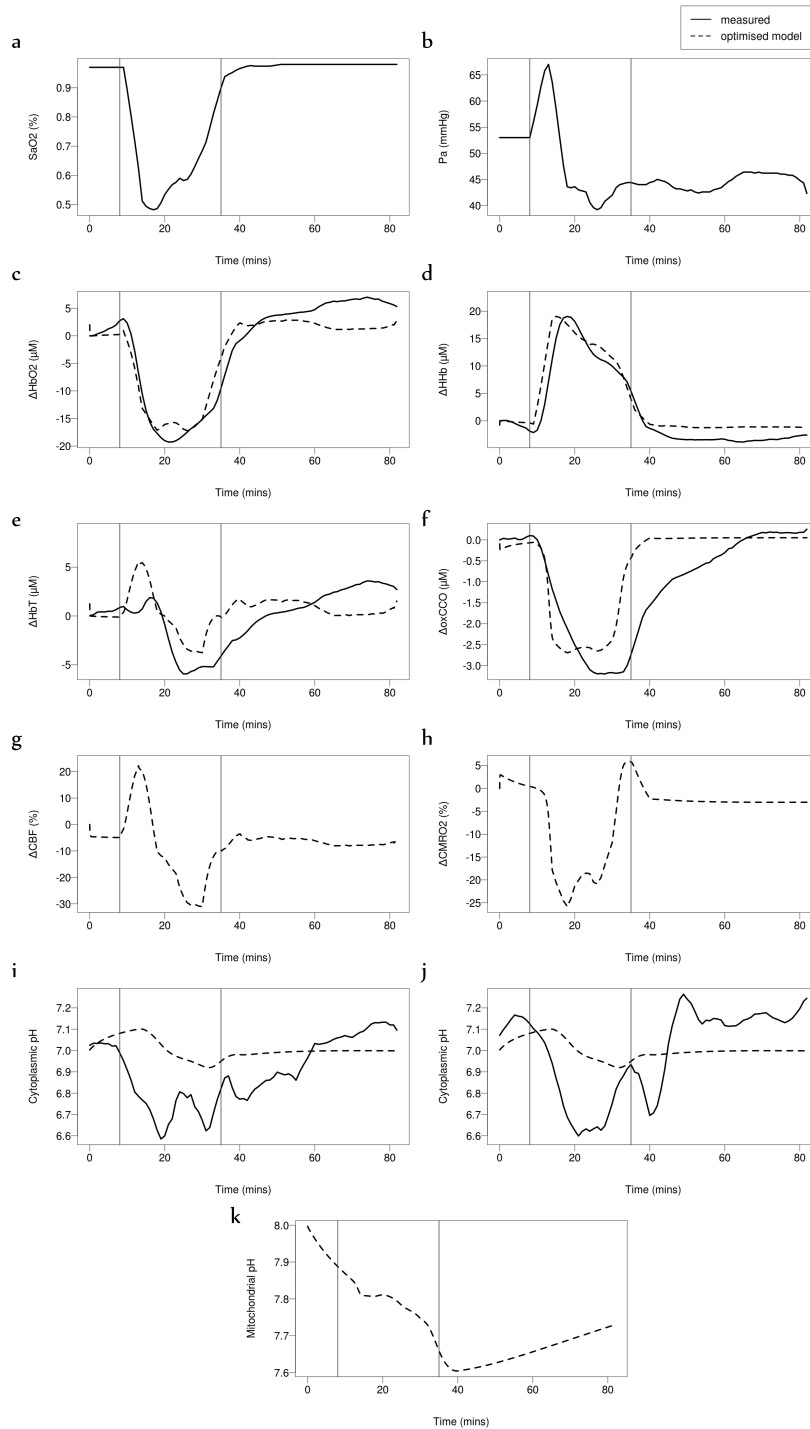


Figure 6.16: Piglet LWP210. (a) SaO_2 and (b) blood pressure P_a measurements are model inputs. (c,d,e,f) Simulations and measurements of ΔHbO_2 , ΔHHb , ΔHbT and $\Delta oxCCO$. (g,h) Simulations of ΔCBF and $\Delta CMRO_2$. Simulated cytoplasmic pH compared with measured (i) phosphate-derived pH and (j) ATP-derived pH. (k) Simulated mitochondrial pH.

LWP211

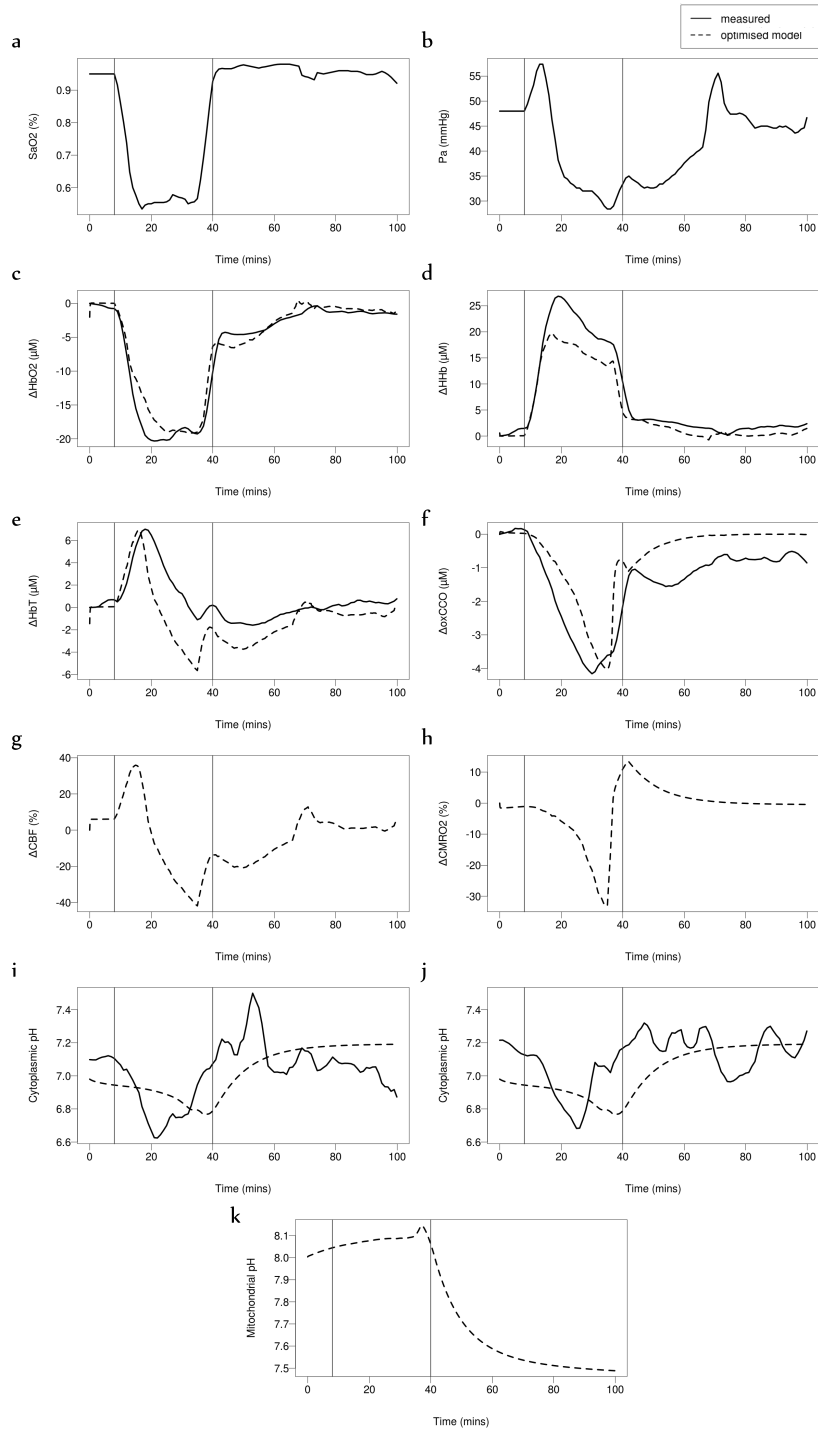


Figure 6.17: Piglet LWP211. (a) SaO_2 and (b) blood pressure P_a measurements are model inputs. (c,d,e,f) Simulations and measurements of ΔHbO_2 , ΔHHb , ΔHbT and $\Delta oxCCO$. (g,h) Simulations of ΔCBF and $\Delta CMRO_2$. Simulated cytoplasmic pH compared with measured (i) phosphate-derived pH and (j) ATP-derived pH. (k) Simulated mitochondrial pH.

LWP213

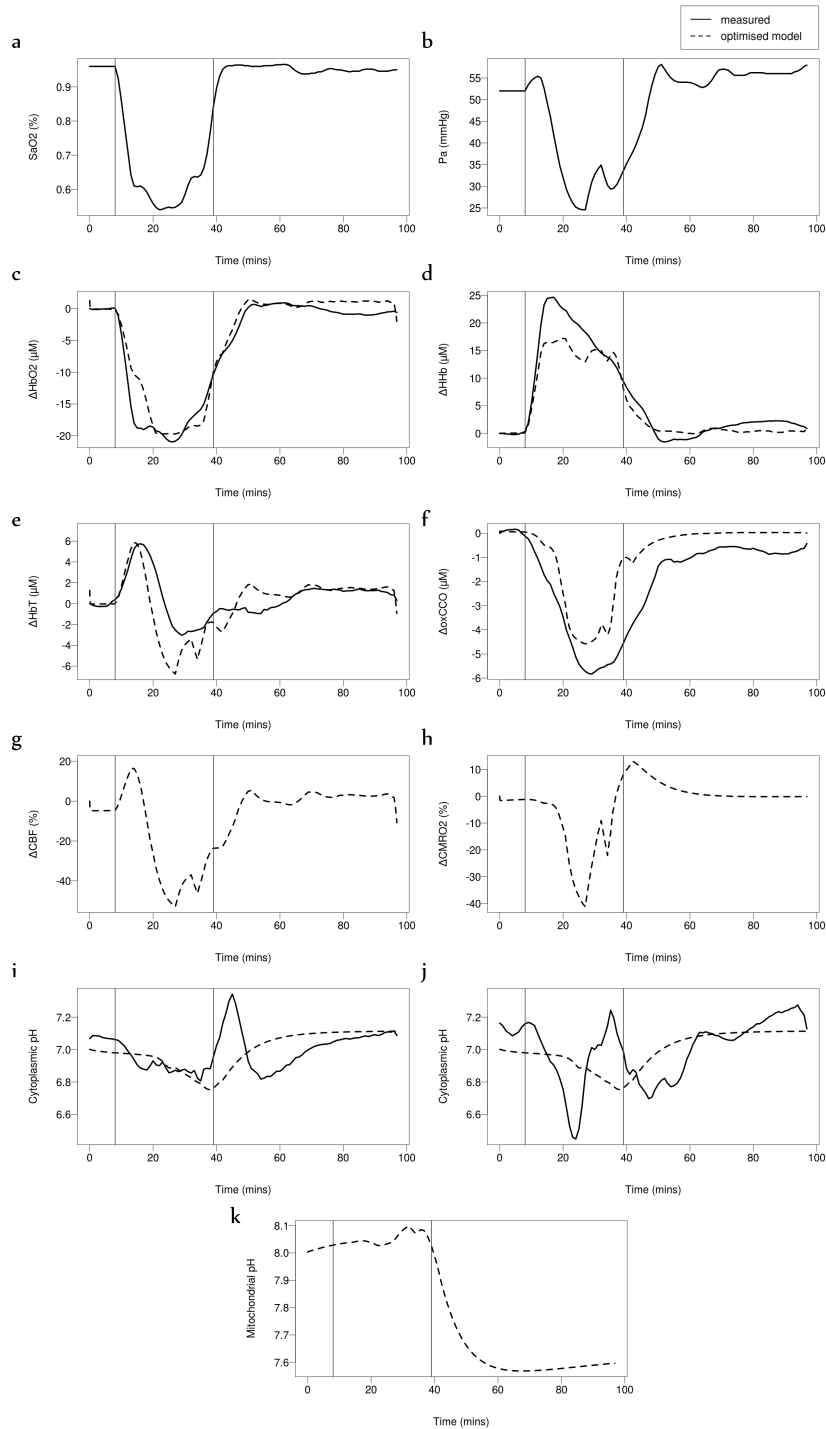


Figure 6.18: Piglet LWP213. (a) SaO_2 and (b) blood pressure P_a measurements are model inputs. (c,d,e,f) Simulations and measurements of ΔHbO_2 , ΔHHb , ΔHbT and $\Delta oxCCO$. (g,h) Simulations of ΔCBF and $\Delta CMRO_2$. Simulated cytoplasmic pH compared with measured (i) phosphate-derived pH and (j) ATP-derived pH. (k) Simulated mitochondrial pH.

LWP216

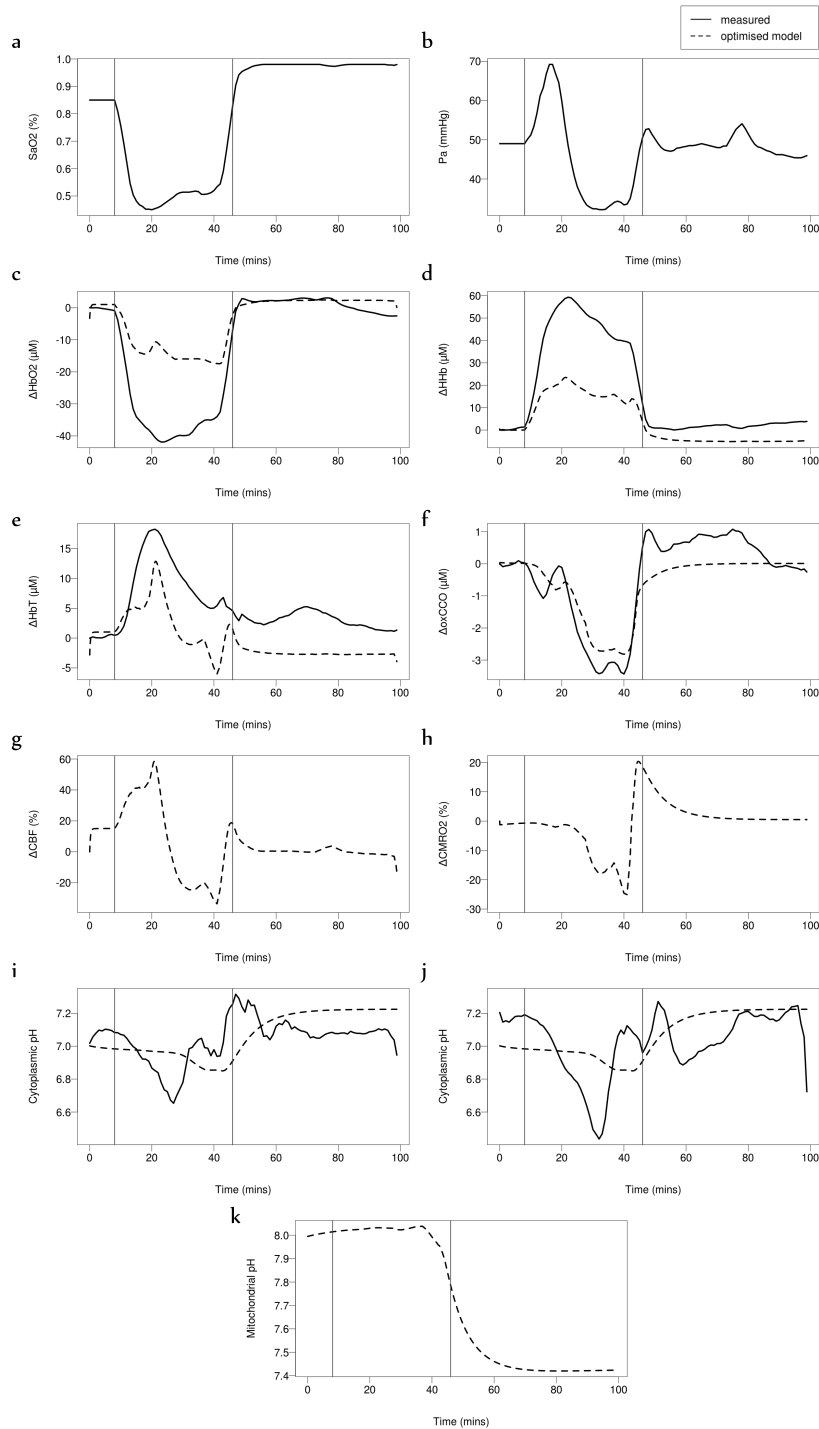


Figure 6.19: Piglet LWP216. (a) SaO_2 and (b) blood pressure P_a measurements are model inputs. (c,d,e,f) Simulations and measurements of ΔHbO_2 , ΔHHb , ΔHbT and $\Delta oxCCO$. (g,h) Simulations of ΔCBF and $\Delta CMRO_2$. Simulated cytoplasmic pH compared with measured (i) phosphate-derived pH and (j) ATP-derived pH. (k) Simulated mitochondrial pH.

6.3.2 Poor outcomes

This section presents results from 7 piglets that did not recover well after the hypoxic-ischaemic insult. This is evidenced by a lower than baseline value of the oxygenation measurements, especially ΔHbO_2 , in the aftermath of the insult. Table 6.4 lists the optimised values. Figures 6.21 to 6.27 illustrate the data compared with optimised model simulations.

The changes in optimised parameters before and after the insults are quite similar to that of the good outcome group (Table 6.3). Normal cytoplasmic pH was slightly increased post-insult in most piglets. Concentration of cytochrome $[CCO]_{tis}$ increased in three piglets, decreased in one and remained near constant in the others. Autoregulation constant k_{aut} remained constant in some piglets, and decreased in others. The normal concentration of oxygen in the mitochondria $[O_2]_n$ and the normal concentration of NAD in the cytoplasm $NAD_{cyt,n}$ both reduced in the majority of the piglets. The parameter controlling the sensitivity of elastic stress in vessel walls to the radius K_σ increased in most piglets but decreased in two. The normal mitochondrial inner membrane potential $\Delta\psi_n$ decreased in some piglets but stayed near constant in others. However, the main difference in the poor outcome group is the lack of change in exponent of the muscular tension relationship n_m , which suggests that the muscular tension of vessel walls did not alter significantly after the insult.

The piglets in the poor outcome group displayed a drop in SaO_2 and P_a during the insult, except in LWP215, where an increase in P_a was recorded, and in LWP218 where P_a did not recover following the insult. Consequently, model simulation of ΔHbT in LWP215 suggested an increase, although a decrease in ΔHbT was measured. The model simulates ΔHbO_2 and ΔHHb relatively well, except in LWP185 and LWP218 where the magnitude of the change observed during the insult is not reached. In many piglets, the $\Delta oxCCO$ measurement did not recover to baseline values following the insult, however this was not reflected in the simulations. It is feasible therefore that some level of injury may have occurred leading to an impairment of metabolic function, that is not reflected in the model.

Simulated CBF and $CMRO_2$ showed a drop during the insult. pH measurements again displayed a lot of variation. Although less discernible, values become more acidic during the insult. The cytoplasmic pH simulations

achieve a good estimate of the measurements overall. Simulated mitochondrial pH displays a similar rise and drop trend to that observed in the good outcome group, except in LWP188 and LWP218 where it drops fairly continuously from the start.

Table 6.4: Optimised parameter values

Normal mitochondrial inner membrane potential, $\Delta\psi_n$			
Normal value: 145			
Piglet	Before Insult	After Insult	% Change
183	133.215	127.311	-4.4319
185	150	150	0
188	150	150	0
207	150	150	0
208	150	125.001	-16.6660
215	150	150	0
218	125	125.687	0.5496
Average	144.0307	139.7141	-2.9970

Concentration of cytochrome in tissue, $[CCO]_{tis}$			
Normal value: 0.0022			
Piglet	Before Insult	After Insult	% Change
183	0.0047	0.0070	48.6935
185	0.0040	0.0070	76.2522
188	0.0057	0.0038	-33.6448
207	0.007	0.0070	-0.0006
208	0.007	0.007	0
215	0.0070	0.007	0.0021
218	0.007	0.007	0
Average	0.0061	0.0065	8.0466

Autoregulation constant, k_{aut}			
Normal value: 1.0			
Piglet	Before Insult	After Insult	% Change
183	1	1	0
185	0	0	0
188	1	0.6042	-39.5840
207	1	1	0
208	1	0.1659	-83.4066
215	1	1	0

6.3. Individual results

218	1	0	-100
Average	0.8571	0.6814	-20.4983

Sensitivity of elastic stress in vessel walls to radius, K_σ

Normal value: 10

Piglet	Before Insult	After Insult	% Change
183	11.5692	9.2094	-20.3971
185	12	8.9600	-25.3343
188	8	12	50
207	9.3711	11.3263	20.8645
208	8	12	50
215	9.8345	8.7615	-10.9105
218	9.3059	11.9999	28.9490
Average	9.725814286	10.60814429	9.0720

Normal concentration of oxygen in the mitochondria, $[O_2]_n$

Normal value: 0.024

Piglet	Before Insult	After Insult	% Change
183	0.02135	0.0288	34.9142
185	0.0192	0.0192	0
188	0.02808	0.0192	-31.6236
207	0.0243	0.0192	-20.9766
208	0.0259	0.0212	-17.9390
215	0.0192	0.0192	0.0005
218	0.0288	0.0219	-23.8531
Average	0.0238	0.0213	-10.8122

Exponent in the muscular tension relationship, n_m

Normal value: 1.0

Piglet	Before Insult	After Insult	% Change
183	1.464	1.464	0
185	1.464	1.464	0
188	2.196	2.196	0
207	2.196	2.196	0
208	2.196	2.196	0
215	2.196	2.196	0
218	1.4947	1.464	-2.0533
Average	1.8867	1.8823	-0.2324

Normal concentration of NAD in the cytoplasm, $NAD_{cyt,n}$

6.3. Individual results

Normal value: 359

Piglet	Before Insult	After Insult	% Change
183	400	318.001	-20.4998
185	400	318	-20.5
188	396.11	318.001	-19.7190
207	400	318.001	-20.4998
208	400	318	-20.5
215	318	318	0
218	336.45	318.003	-5.4828
Average	378.6514	318.0009	-16.0175

Normal value of pH in the cytoplasm, $pH_{o,n}$

Normal value: 7

Piglet	Before Insult	After Insult	% Change
183	6.9199	7.1594	3.4609
185	6.892	7.2656	5.4201
188	7.1984	7.1368	-0.8559
207	6.892	7.1538	3.7992
208	7.0526	7.1168	0.9112
215	6.892	7.1306	3.4614
218	7.1126	7.1272	0.2047
Average	6.9942	7.1557	2.3094

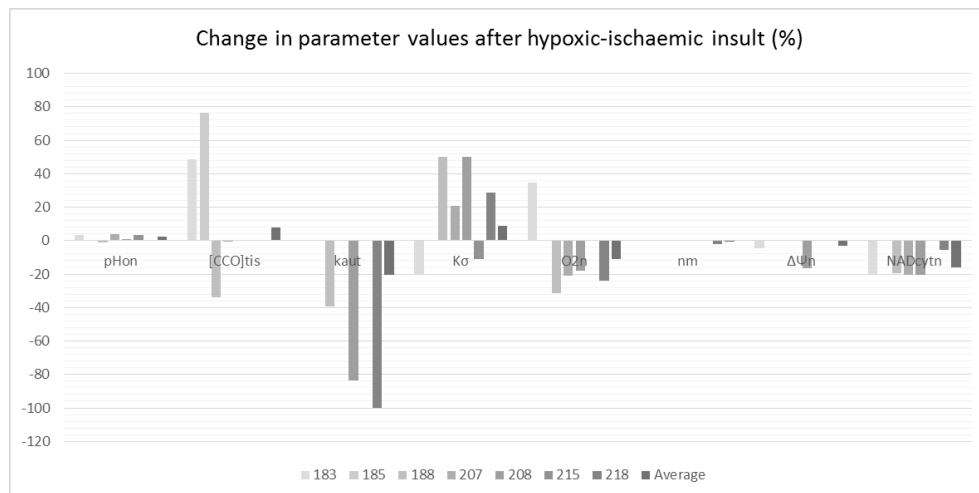


Figure 6.20: Changes in optimised parameter values for piglets with poor outcomes. Recovery values after the insult compared to values before the insult

LWP183

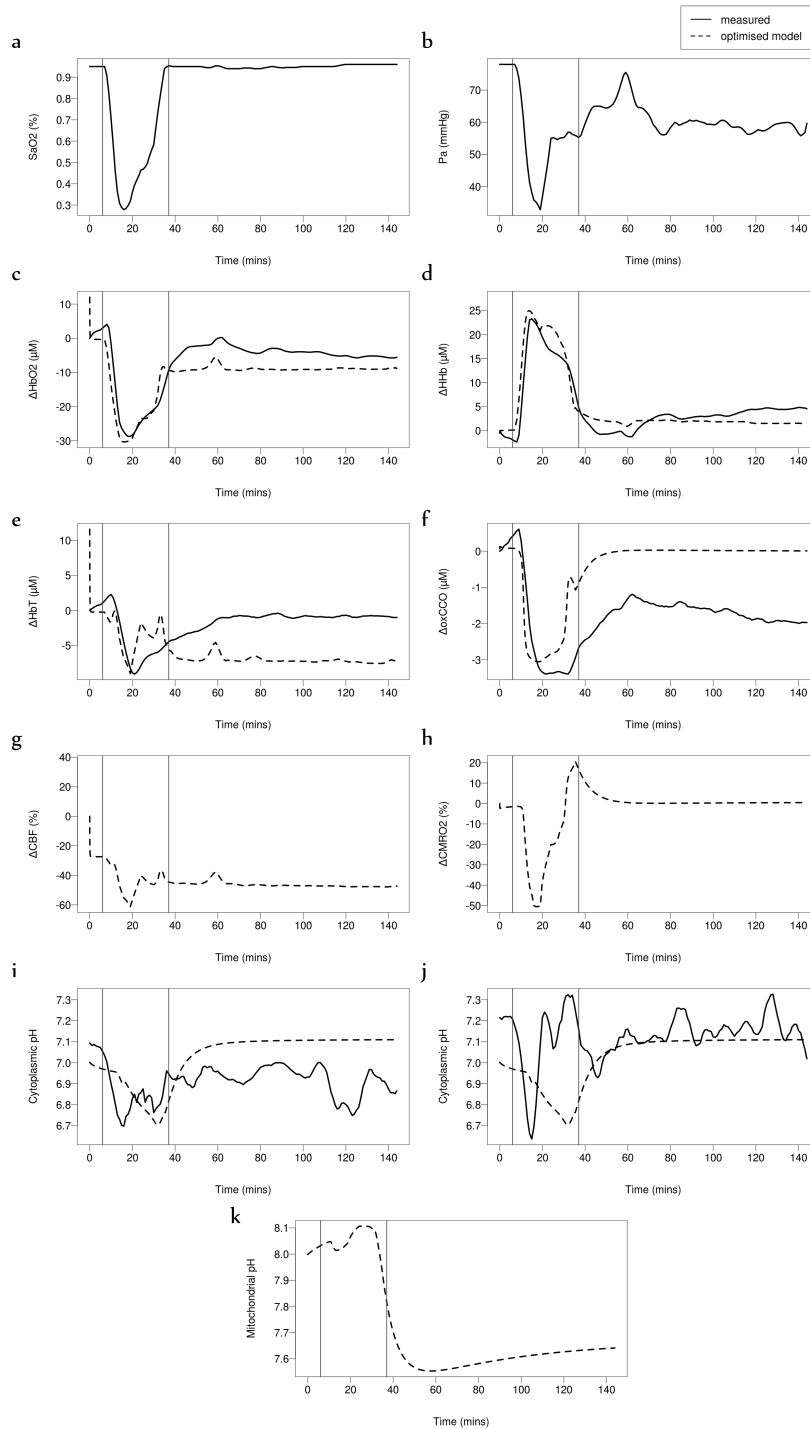


Figure 6.21: Piglet LWP183. (a) SaO_2 and (b) blood pressure P_a measurements are model inputs. (c,d,e,f) Simulations and measurements of ΔHbO_2 , ΔHHb , ΔHbT and $\Delta oxCCO$. (g,h) Simulations of ΔCBF and $\Delta CMRO_2$. Simulated cytoplasmic pH compared with measured (i) phosphate-derived pH and (j) ATP-derived pH. (k) Simulated mitochondrial pH.

LWP185

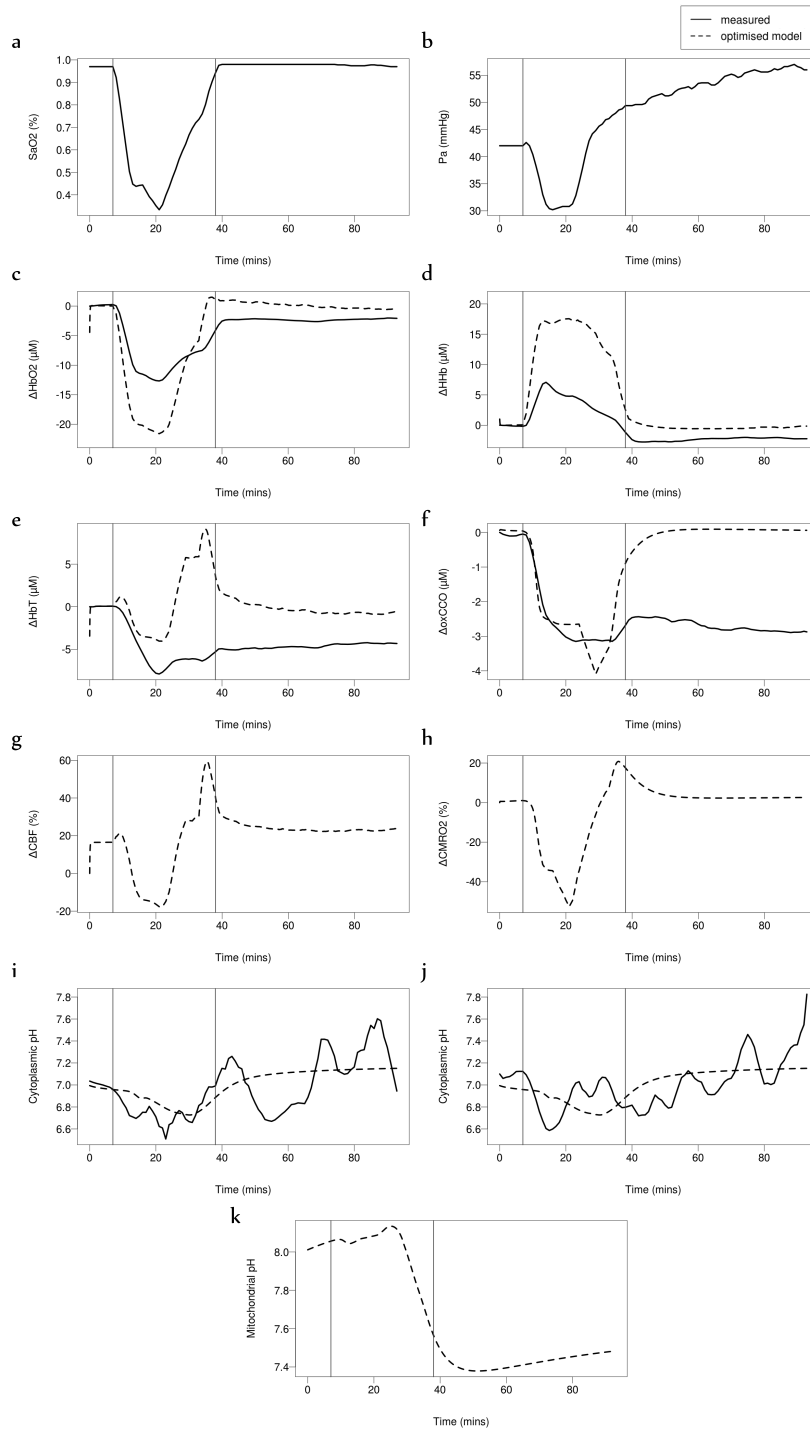


Figure 6.22: Piglet LWP185. (a) SaO_2 and (b) blood pressure P_a measurements are model inputs. (c,d,e,f) Simulations and measurements of ΔHbO_2 , ΔHHb , ΔHbT and $\Delta oxCCO$. (g,h) Simulations of ΔCBF and $\Delta CMRO_2$. Simulated cytoplasmic pH compared with measured (i) phosphate-derived pH and (j) ATP-derived pH. (k) Simulated mitochondrial pH.

LWP188

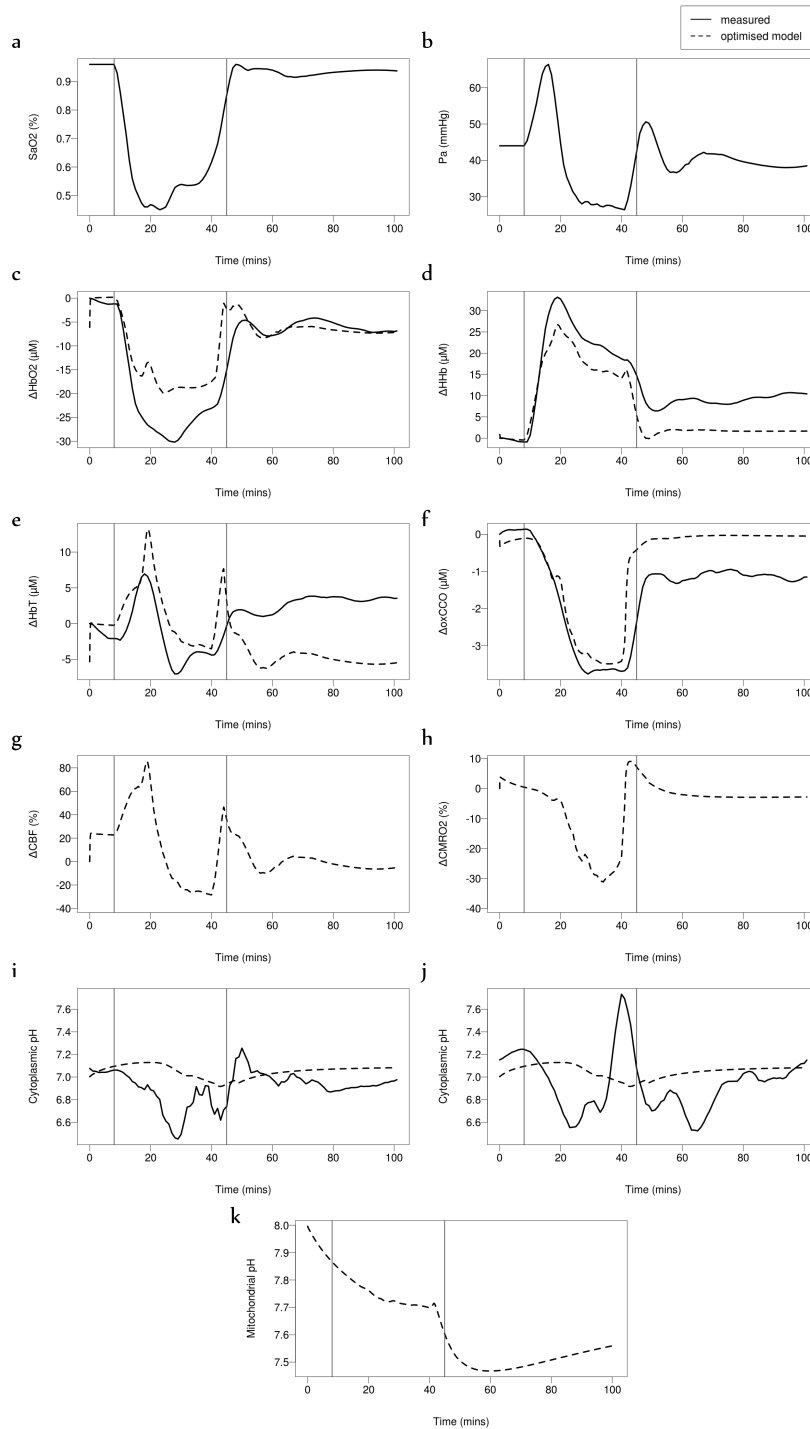


Figure 6.23: Piglet LWP188. (a) SaO_2 and (b) blood pressure P_a measurements are model inputs. (c,d,e,f) Simulations and measurements of ΔHbO_2 , ΔHHb , ΔHbT and $\Delta oxCCO$. (g,h) Simulations of ΔCBF and $\Delta CMRO_2$. Simulated cytoplasmic pH compared with measured (i) phosphate-derived pH and (j) ATP-derived pH. (k) Simulated mitochondrial pH.

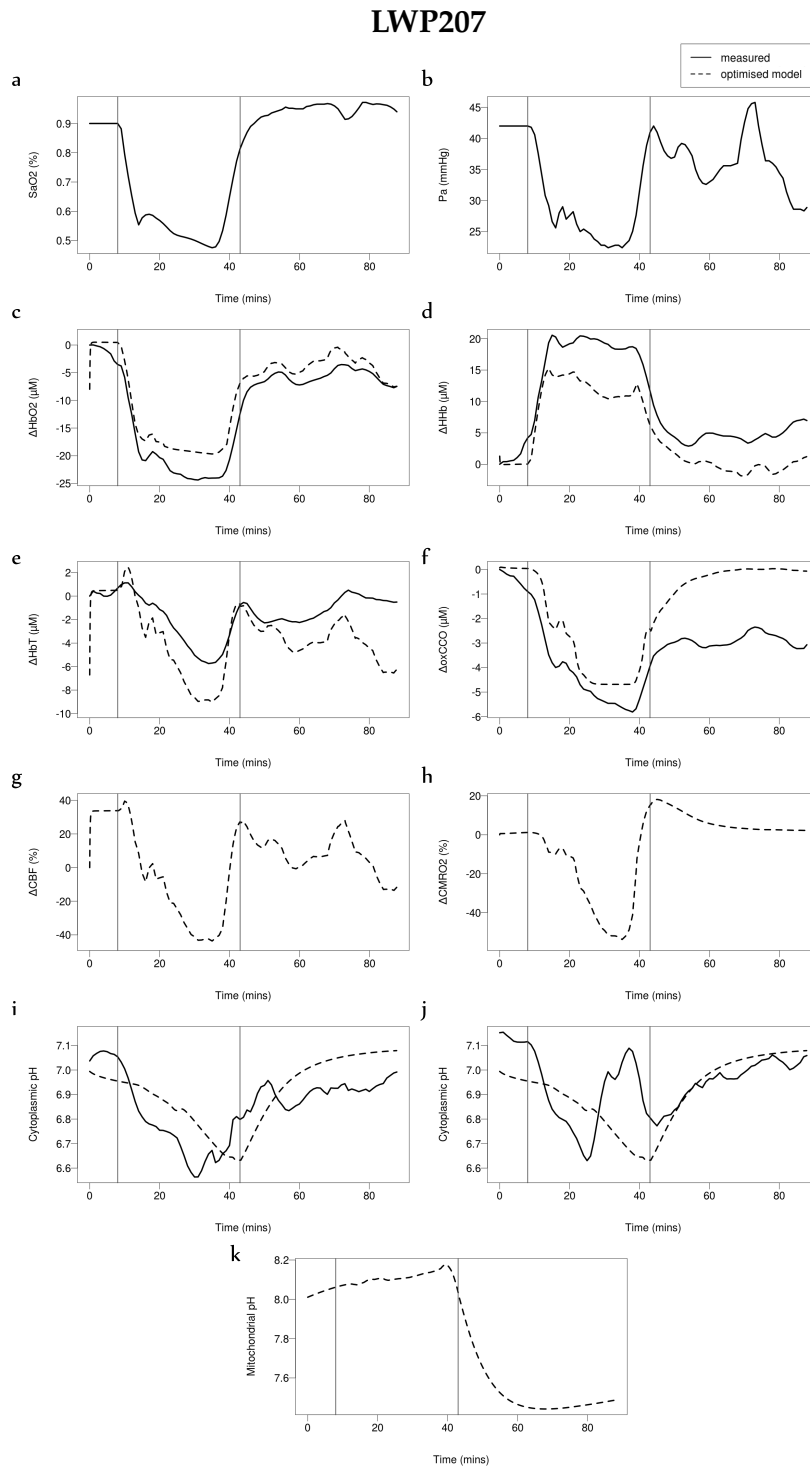


Figure 6.24: Piglet LWP207. (a) SaO_2 and (b) blood pressure P_a measurements are model inputs. (c,d,e,f) Simulations and measurements of ΔHbO_2 , ΔHHb , ΔHbT and $\Delta oxCCO$. (g,h) Simulations of ΔCBF and $\Delta CMRO_2$. Simulated cytoplasmic pH compared with measured (i) phosphate-derived pH and (j) ATP-derived pH. (k) Simulated mitochondrial pH.

LWP208

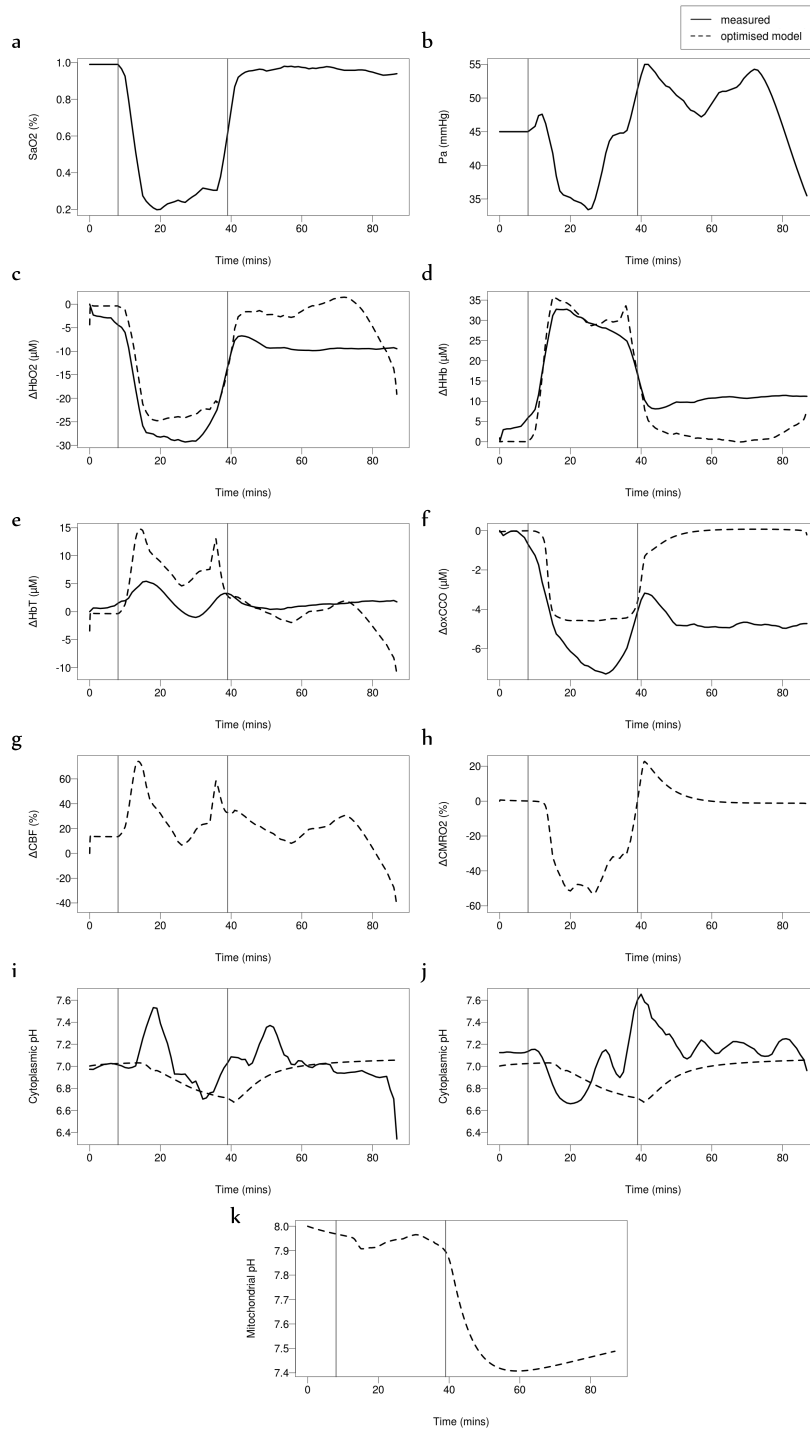


Figure 6.25: Piglet LWP208. (a) SaO_2 and (b) blood pressure P_a measurements are model inputs. (c,d,e,f) Simulations and measurements of ΔHbO_2 , ΔHHb , ΔHbT and $\Delta oxCCO$. (g,h) Simulations of ΔCBF and $\Delta CMRO_2$. Simulated cytoplasmic pH compared with measured (i) phosphate-derived pH and (j) ATP-derived pH. (k) Simulated mitochondrial pH.

LWP215

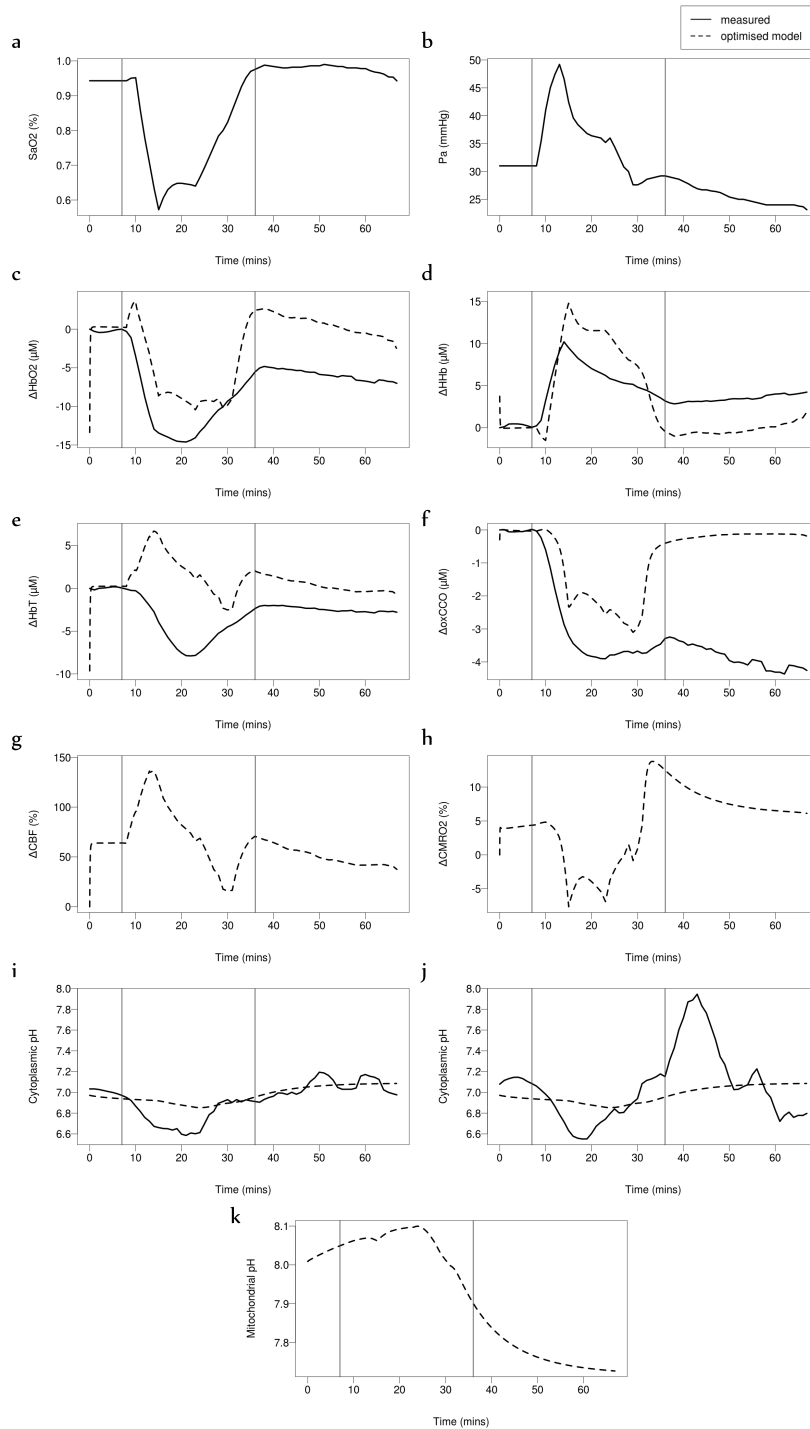


Figure 6.26: Piglet LWP215. (a) SaO_2 and (b) blood pressure P_a measurements are model inputs. (c,d,e,f) Simulations and measurements of ΔHbO_2 , ΔHHb , ΔHbT and $\Delta oxCCO$. (g,h) Simulations of ΔCBF and $\Delta CMRO_2$. Simulated cytoplasmic pH compared with measured (i) phosphate-derived pH and (j) ATP-derived pH. (k) Simulated mitochondrial pH.

LWP218

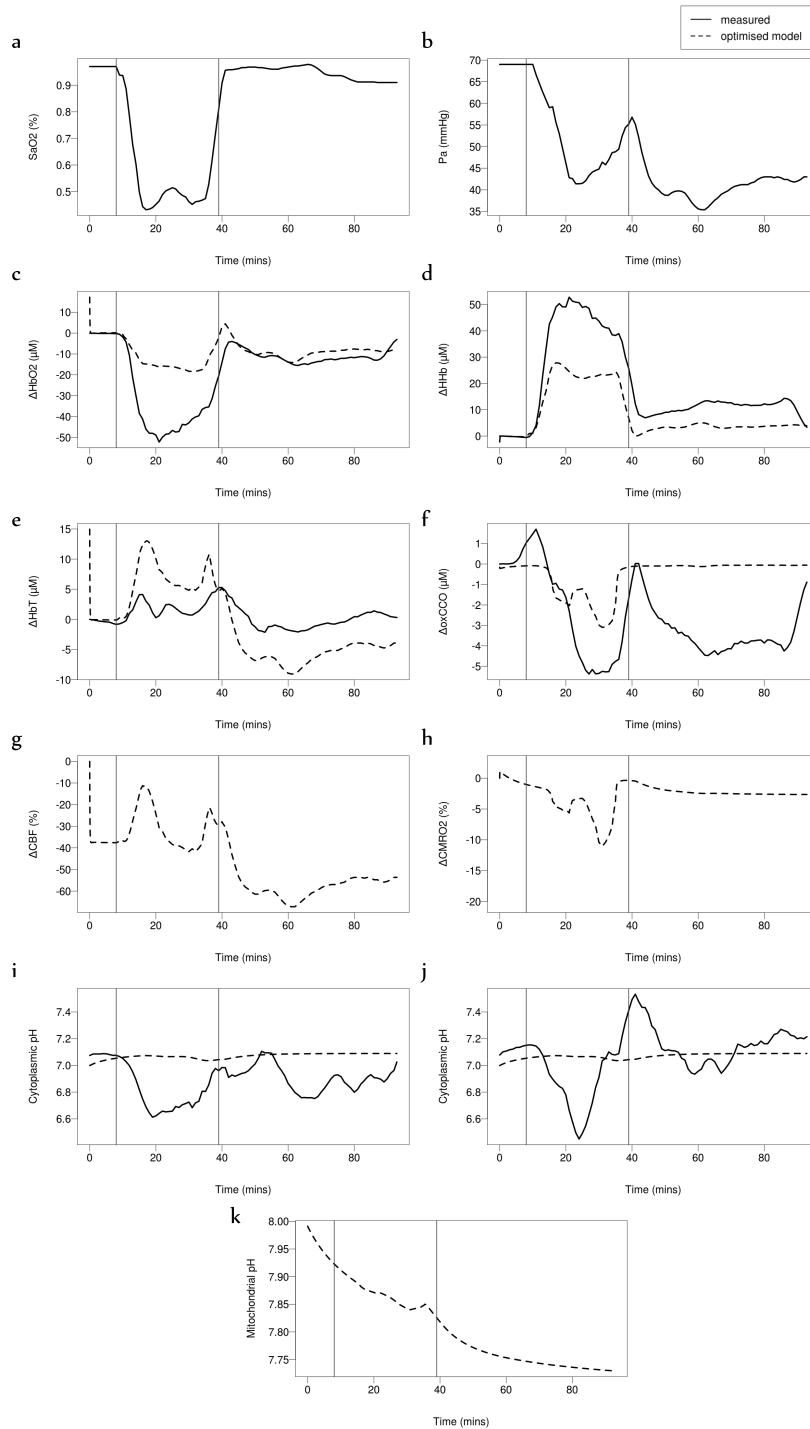


Figure 6.27: Piglet LWP218. (a) SaO_2 and (b) blood pressure P_a measurements are model inputs. (c,d,e,f) Simulations and measurements of ΔHbO_2 , ΔHHb , ΔHbT and $\Delta oxCCO$. (g,h) Simulations of ΔCBF and $\Delta CMRO_2$. Simulated cytoplasmic pH compared with measured (i) phosphate-derived pH and (j) ATP-derived pH. (k) Simulated mitochondrial pH.

6.4 Group results

By combining data from a number of piglets, we can get a much better overview of the metabolic and haemodynamic events that occur during the experiments. This averaging also reduces the effect of arbitrary noise in the signals. As the duration of each piglet experiment varied slightly, in order to average the signals effectively the data was manually divided into five time periods:

Phase 1: The baseline from the start of recording to the start of the insult, when the vascular occluders are applied and fraction of inspired oxygen is reduced.

Phase 2: Start of the hypoxic-ischaemic insult to the nadir, when ATP drops to approximately 40%.

Phase 3: The nadir of the insult to the moment when the occluders are released. During this period the fraction of inspired oxygen, FiO_2 is gradually increased.

Phase 4: The restoration of blood flow to the end of recovery.

Phase 5: Post recovery from hypoxia-ischaemia.

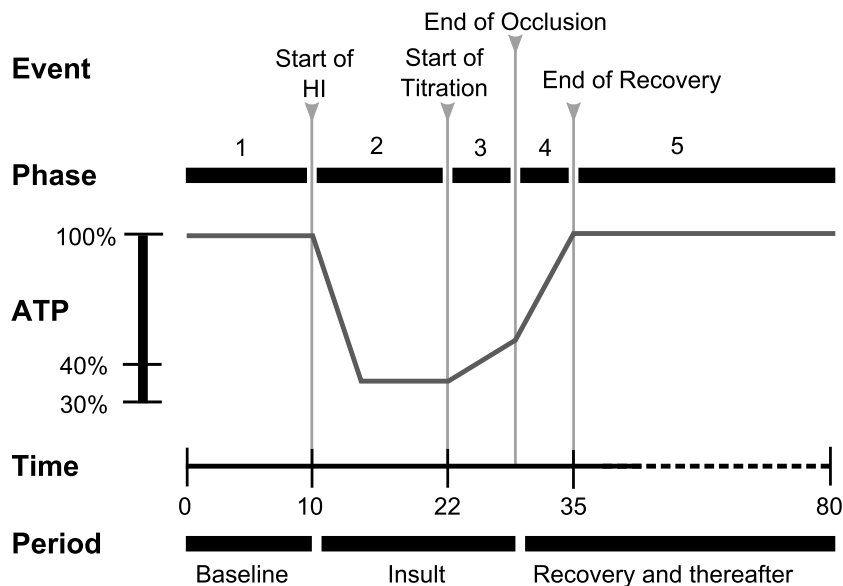


Figure 6.28: Group analysis. Measurements are divided into 5 phases, and averaged across the piglets.

Each phase was divided into 10 sections which were then averaged individually using a Python script. The mean of each section across all piglets was

then calculated. The mean time for each phase across all piglets was also calculated and an average signal produced. This allows an investigation both in the variations of concentration and the relative time at which these events occur. Figure 6.28 illustrates this process. This procedure was done for each measurement and for each of the two groups - those with good and poor outcomes.

6.4.1 Good outcomes

Table 6.5 lists the optimised BrainPiglet v2.0 parameter values for averaged data from the 15 piglets with good outcomes. Baseline cytochrome concentration $[CCO]_{tis}$ was much higher than the normal value in the model, and increased slightly following the insult. The autoregulation constant k_{aut} was 1 at baseline and decreased to 0 following the insult. Other significant changes during the insult were decreases in the normal concentration of oxygen in the mitochondria $[O_2]_n$ and the exponent of the muscular tension relationship n_m . The first is a likely result of hypoxia, and the second possibly due to ischemia as the muscular tension in the vessel increases to compensate for low blood flow.

Averaged measurements and optimised simulations are presented in Figure 6.29. A lot of variation was observed in P_a and pH throughout the measurements. ΔHbT and $\Delta oxCCO$ displayed more variation during the insult and in the recovery phase, while SaO_2 , ΔHbO_2 and ΔHhb displayed most variation during the insult. The time of recovery in the $\Delta oxCCO$ and pH measurements is also notably different among the piglets.

ΔHhb was well simulated here, while the simulated drop in ΔHbO_2 fell just outside the error margins of the measurements. Simulated ΔHbT showed a higher rise at the start of the insult than that observed. $\Delta oxCCO$ was well predicted, and simulated ΔCBF and $\Delta CMRO_2$ decreased considerably during the insult. $\Delta CMRO_2$ was predicted to recover well following the insult, while ΔCBF showed a slower recovery. These last four simulated signals displayed a spike at the end of the insult phase – at the point where parameter values changed to those optimised for the region after the insult. This is further discussed in the discussion section at the end of this chapter.

Cytoplasmic pH simulations did not replicate the magnitude of the drop during the insult, but did simulate an acidic change. Simulated mitochon-

drial pH dropped from the start of the experiment to lower than baseline values, with a slow recovery after the insult.

Table 6.5: Optimised parameter values for the good outcome group

Parameter	Description, Unit	Normal Value	Before insult	After insult	% Change
$\Delta\psi_n$	Normal mitochondrial inner membrane potential, mV	145	149.965	150	0.0233
$[O_2]_n$	Normal concentration of oxygen in the mitochondria, mM	0.024	0.0288	0.0198	-31.25
n_m	Exponent in the muscular tension relationship, None	1.83	2.1858	1.464	-33.0222
K_σ	Controls sensitivity of elastic stress in vessel walls to radius, None	10	8	9.5600	19.5
$NAD_{cyt,n}$	Normal concentration of NAD in the cytoplasm, mM	359	400	318	-20.5
$[CCO]_{tis}$	Concentration of cytochrome in tissue, mM	0.0022	0.0066	0.0070	0.0061
k_{aut}	Autoregulation constant, None	1	1	0	-100
$pH_{o,n}$	Normal value of pH in the cytoplasm, None	7.0	7.1879	7.1944	0.0904

6.4. Group results

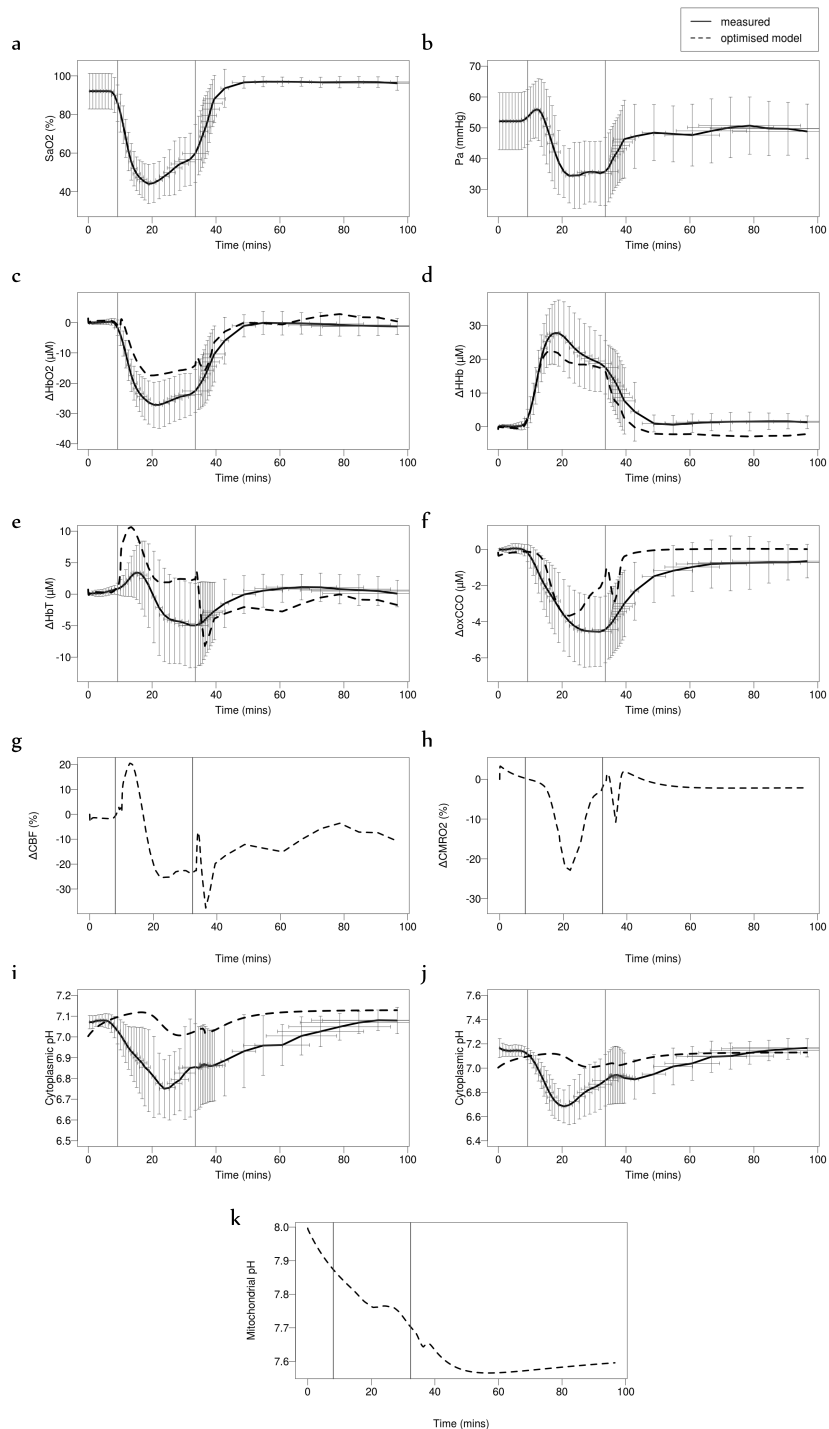


Figure 6.29: Group analysis of 15 piglets with good outcome. Vertical and horizontal standard deviation of measurements shown. (a) SaO_2 and (b) blood pressure P_a measurements are model inputs. (c,d,e,f) Simulations and measurements of ΔHbO_2 , ΔHhb , ΔHbT and $\Delta oxCCO$. (g,h) Simulations of ΔCBF and $\Delta CMRO_2$. Simulated cytoplasmic pH compared with measured (i) phosphate-derived pH and (j) ATP-derived pH. (k) Simulated mitochondrial pH.

6.4.2 Poor outcomes

The process was repeated for the 7 piglets with poor outcomes. Table 6.6 lists the optimised parameter values, which again suggest a higher baseline value of cytochrome $[CCO]_{tis}$ than the normal value in the model. Over the insult phase there is a larger increase in $[CCO]_{tis}$ and the parameter controlling the sensitivity of elastic stress to the vessel radius K_σ than that calculated from the good outcome group. The autoregulation constant also changes similarly, dropping to a near 0 value. The normal concentration of oxygen in the mitochondria $[O_2]_n$ also decreased as before. However, in this case there was no change in the exponent of the muscular tension relationship n_m , which may suggest a more significant impairment of the piglets' autoregulative capacities and the ability of the vessels to compensate for the lack of blood flow. Normal cytoplasmic pH value was calculated to be slightly lower in this case before the insult, and rising after.

Figure 6.30 illustrates the measurements and optimised model simulations. The variations in measurements are similar here, with P_a and pH displaying a lot of deviations from the mean throughout. Both ΔHbO_2 and ΔHHb were fairly well simulated here. Simulated ΔHbT displays a rise at the start of the insult, not observed in the measurements.

Compared to the good outcomes group, the most notable difference in the measurements here is the lack of recovery in the measured $\Delta\alpha CCO$ values which achieve lower than baseline levels following the insult. However, this is not reflected in the simulation which shows a good recovery following the insult, suggesting either irreversible impairment that has not been simulated, or other un-modelled processes may play a role.

pH measurements achieve similar values to that observed in the good outcome group during the insult, and are simulated relatively well by the model's cytoplasmic pH. Mitochondrial pH simulation increases slightly towards the end of the insult phase, and drops immediately afterwards to more acidic values. The acidic pH reached after the insult in this simulation is similar to that in the good outcome group.

Table 6.6: Optimised parameter values for the poor outcome group

Parameter	Description, Unit	Normal Value	Before insult	After insult	% Change
$\Delta\psi_n$	Normal mitochondrial inner membrane potential, mV	145	150	150	0
$[O_2]_n$	Normal concentration of oxygen in the mitochondria, mM	0.024	0.0253	0.0192	-24.1107
n_m	Exponent in the muscular tension relationship, None	1.83	2.196	2.1960	0
K_σ	Controls sensitivity of elastic stress in vessel walls to radius, None	10	8	12	50
$NAD_{cyt,n}$	Normal concentration of NAD in the cytoplasm, mM	359	400	318.001	-20.4998
$[CCO]_{tis}$	Concentration of cytochrome in tissue, mM	0.0022	0.0065	0.0070	7.6923
k_{aut}	Autoregulation constant, None	1	1	0.1195	-88.05
$pH_{o,n}$	Normal value of pH in the cytoplasm, None	7.0	6.895	7.1404	3.5591

6.4. Group results

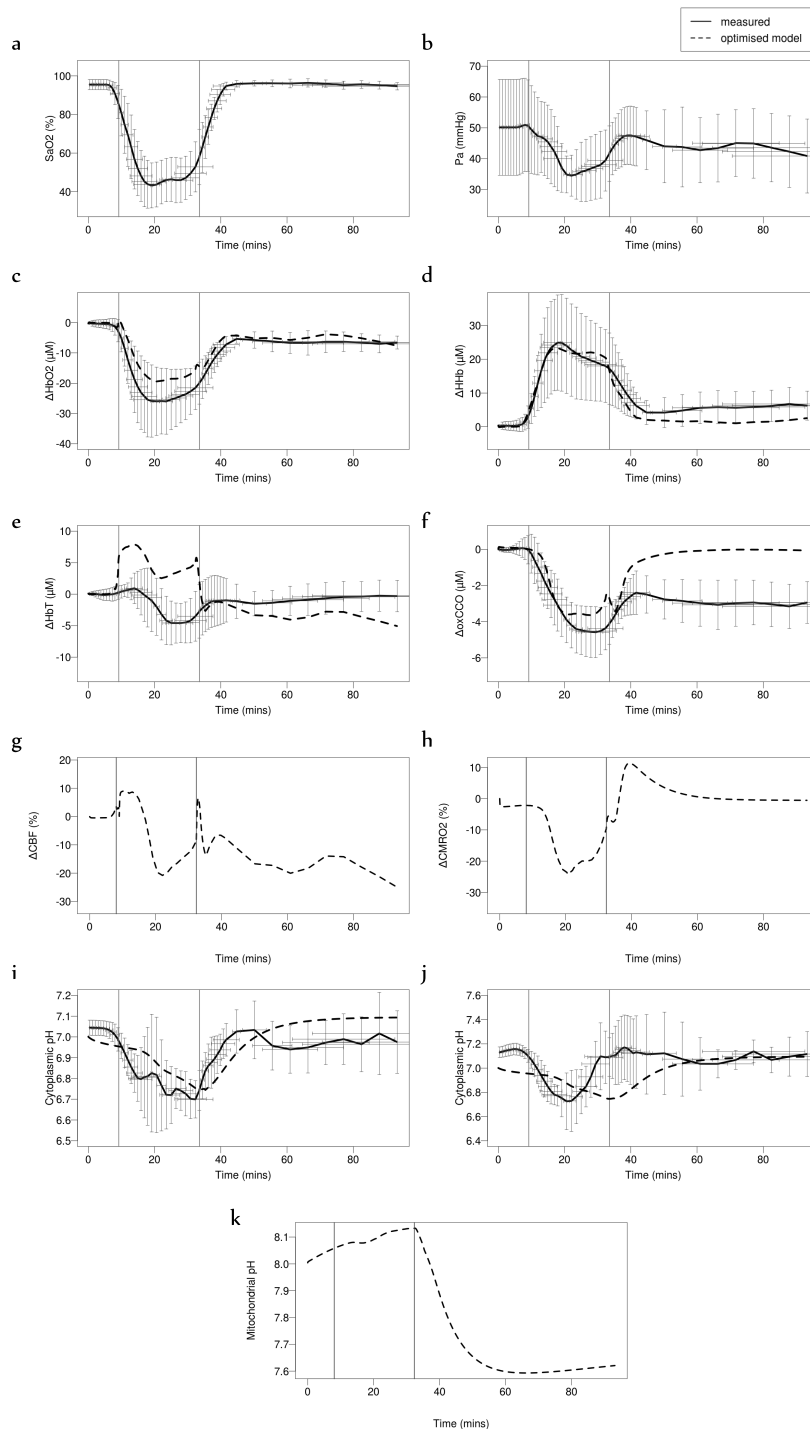


Figure 6.30: Group analysis of piglets with poor outcome. Vertical and horizontal standard deviation of measurements shown. (a) SaO_2 and (b) blood pressure P_a measurements are model inputs. (c,d,e,f) Simulations and measurements of ΔHbO_2 , ΔHb , ΔHbT and $\Delta oxCCO$. (g,h) Simulations of ΔCBF and $\Delta CMRO_2$. Simulated cytoplasmic pH compared with measured (i) phosphate-derived pH and (j) ATP-derived pH. (k) Simulated mitochondrial pH.

6.5 Discussion

The BrainPiglet v2.0 model performed quite well in predicting the changes observed during hypoxia-ischaemia in piglets. The model is able to simulate most of the changes observed in the individual NIRS and MRS measurements. It replicated the typical haemodynamic response observed in the piglets during the insult (drop in ΔHbO_2 and rise in ΔHbT), the decline in oxidative phosphorylation (drop in $\Delta oxCCO$) and the acidic changes observed in intracellular pH measurements. The change in ΔHbT was less consistent, with some experiments showing a rise while other dropped during the insult. Simulations were similarly different, and not always successful in predicting the change. The lack of recovery in $\Delta oxCCO$ following the insult was indicative of poor outcome. However, the model simulated a complete recovery of $\Delta oxCCO$ in these piglets as well. This suggests that the cellular physiology included in the model may not be the driving force behind the differences in $\Delta oxCCO$ recovery values in the poor outcome group. It is feasible that this may result from cell death caused by the insult. Although the model has in the past been used to simulate cell death by introducing a simple linear function (Moroz et al. 2013), simulating cell death in relation to pH dynamics is a more complicated affair, as acidosis is known to have differing effects on apoptosis during and in the aftermath of oxygen and glucose deprivation (Almaas et al. 2003).

Optimisation of model parameters showed that the model was able to detect a change in autoregulatory capacity, by suggesting a lower value of the autoregulation constant k_{aut} following the insult. This was true of piglets with both good and poor outcome (Figures 6.4 and 6.20). Optimisation of the normal concentration of cytochrome in tissue $[CCO]_{tis}$ suggests higher values at baseline than that found in current literature ($\sim 0.006\text{mM}$ vs. $\sim 0.002\text{mM}$). The main difference in between the good and poor outcome piglets was in the optimised values of the exponent of the muscular tension relationship n_m , which decreased following the insult – leading to higher tension – in the good outcome group, but did not change noticeably in the poor outcome group. This may be suggestive of a decreased ability in the poor outcome piglets to regulate blood flow.

It must be understood that the model's scope is limited by the chosen inputs – SaO_2 and blood pressure. The model is only able to translate changes

observed in these two measurements. Optimisation of model parameters attempts to incorporate other variations, however it cannot infer the multitude of other possible influences. It is also important to reiterate which variables the model has been optimised to predict – ΔHbO_2 , ΔHHb , $\Delta oxCCO$ and cytoplasmic pH pH_o . In particular, cytoplasmic pH is optimised to the phosphate-derived pH measurement, and not the ATP-derived one, mainly due to noise issues. However, the phosphate-derived pH measurement was considerably noisier than the NIRS measurements. Optimising to noisy signals inevitably lessens the efficacy of the optimisation process. ΔHbT was not optimised, and so it is not surprising to obtain simulations that better predict the other variables in comparison.

The pH measurements were compared against simulated cytoplasmic pH as the measurements were more likely to be representative of this variable rather than mitochondrial pH. Little is known of the pH changes in mitochondria, mainly due to the difficulty in obtaining measurements of pH in them, isolated from changes in other cellular compartments. Overall, the model suggests a drop in mitochondrial pH, although the timing of this decrease varies in the simulations. In some, the drop occurs only after the occlusion is released, while in others it occurs from the start of the experiment. There is no discernible difference in this change between the good and poor outcome piglets. It must be noted here that blood pH is not simulated in this model. This may have a significant effect on intracellular pH, and in particular ties in with haemoglobin affinity for oxygen.

The group analysis figures display the significant differences in measurements observed in the individual piglets, although the general trends remain similar (Figures 6.29 and 6.30). There is a notable lack of recovery in $\Delta oxCCO$ in the poor outcome group. Although this particular change was again not simulated, overall the simulations did well to replicate the measurements. As before, in the optimised parameter values, the exponent of the muscular tension relationship n_m decreased following the insult in the good outcome group, but did not change in the poor outcome group.

The gradual transition of optimised parameter values, from those optimised for the measurements before the insult and after, does have a noticeable effect on the simulations, sometimes resulting in a spike, as the model adjusts itself to the new set of parameters. Care has been taken to employ a selective period of time over which this transition occurs (3 mins), in order to

minimise such noise.

The BrainPiglet model has been shown to be capable of simulating changes in metabolic activity of the piglet brain during hypoxia-ischaemia. These experiments and simulations occur over a relatively short period of time (approximately 1 hour). It remains to be seen whether long term changes, such as secondary energy failure, can be similarly simulated.

Chapter 7

Simulating hypoxia-ischaemia in the term neonatal brain

The well-being of the developing neonatal brain can be particularly difficult to ascertain. This is partly due to the lack of clinical information surrounding brain injury and the stages of development in such vulnerable patients. There are a great many factors that contribute to differences in cerebral metabolism and behaviour in neonates as they develop. For example, significant changes in cortical folding are visible in magnetic resonance images from the 23rd week of gestation. Substantial increases in surface area and tissue volume occur between 24 and 42 weeks (Rutherford 2002). Blood flow is affected by changes in development of the vascular system while white matter development and myelination enable better transmission of neural impulses. These changes also vary with gestational age, current age and sex among numerous other factors. Therefore, the application of mathematical and computational techniques in the field of neonatology to decipher the amalgamation of these factors is especially potent.

Newborn infants who have sustained a hypoxic-ischaemic insult may be at risk for evolving brain injury. While some cell death occurs during hypoxia-ischaemia, considerable cell death may occur hours or days later (Edwards et al. 1998). For those suffering from hypoxic-ischaemic encephalopathy, effective management and treatment is critical to mitigate severe consequences (Perlman 2006). Understanding the underlying mechanisms responsible for these cascading events is vital for the development of suitable interventions.

The BrainPiglet model was adapted to the term human neonate to inves-

tigate hypoxic-ischaemic events in monitoring measurements from patients with acute brain injury. The model is applied to data from three neonates with mild, moderate and severe hypoxic-ischaemic encephalopathy. As the neonates have abnormal cerebral health, model parameters were optimised to better predict the changes observed and to gain some insight into the differences between the neonates.

7.1 BabyBrain

Recent developments by our research group in the application of a new clinical measurement system (CYRIL) in the neonatal intensive care unit at UCLH lead to the collection of monitoring data from term neonates suffering from hypoxic-ischaemic encephalopathy (Bale et al. 2014). In order to investigate this data, the BrainPiglet v2.0 model was adapted to the term neonatal brain.

Model parameters were altered as shown in Table 7.1. Normal brain blood fraction $V_{blood,n}$ remains the same as for preterm neonates as the source measurement was conducted in both preterm and term neonates (Wyatt et al. 1990).

Figure 7.1 illustrates the autoregulation curve of the BabyBrain term neonate model, compared with that of the BrainPiglet model and the BrainSignals preterm model. Steady state simulations of ΔHbO_2 and $\Delta oxCCO$ are displayed in Figure 7.2. Desaturations which drop to between 85% to 75% produce much more significant changes in $\Delta oxCCO$.

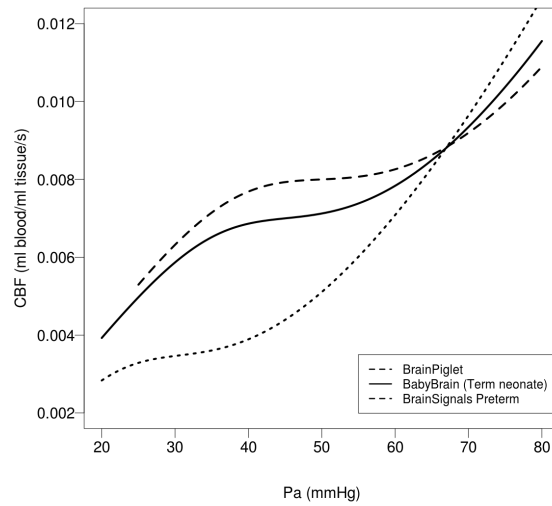


Figure 7.1: Autoregulation curves of the BrainPiglet model, the BabyBrain term neonate model and the BrainSignals preterm neonate model.

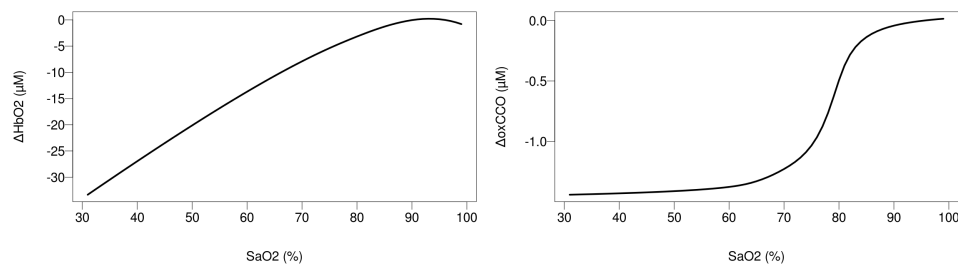


Figure 7.2: Steady state simulations of ΔHbO_2 and $\Delta oxCCO$ in the BabyBrain model with varying arterial oxygen saturation SaO_2 .

Table 7.1: Altered BrainPiglet parameter values.

Parameter	Description	Units	BrainPiglet	Term neonate	Source
CBF_n	Normal cerebral blood flow (CBF)	ml 100 g ⁻¹ min ⁻¹	46	40	Altman et al. (1988)
$CMRO_{2,n}$	Normal cerebral metabolic rate of oxygen consumption (CMRO2)	μ mol 100 g ⁻¹ min ⁻¹	114	64.13	Polin et al. (2010)
P_a and $P_{a,n}$	Mean arterial blood pressure	mmHg	50	45	Vutskits (2014); Polin et al. (2010)
$[Hbtot]$ and $[Hbtot]_n$	Total concentration of haemoglobin in blood	mM	5.4	11.17	Polin et al. (2010)
$V_{blood,n}$	Normal blood volume as a fraction of brain tissue volume		0.0325	0.0233	Wyatt et al. (1990)
P_{ic} and $P_{ic,n}$	Intracranial pressure	mmHg	4.5	5.3	Easa (1983)

7.2 Simulating hypoxic-ischaemic events

Term neonates undergoing treatment for acute brain injury at the Neonatal Intensive Care Unit at UCLH were monitored over the first 6 days of life. Each neonate was graded using the Sarnat system which considers the severity of neonatal encephalopathy. They were scored as mild (Stage I), moderate (Stage II) or severe (Stage III) based on clinical and EEG observations. Also measured was the Lac/NAA ratio, known to be a better predictor of outcome than the Sarnat Grade (Barkovich 2006; Thayyil et al. 2010), and so was used to classify the neonates. Higher ratios are indicative of poorer outcomes (Thayyil et al. 2010). A novel multi-distance broadband NIRS system, the Cytochrome Research Instrument and appLication (CYRIL) was used to measure ΔHbO_2 , ΔHHb and ΔoxCCO at a sampling frequency of 1 Hz. SaO_2 was measured by pulse oximetry and mean arterial blood pressure by an intra-arterial catheter. Neonates were continuously monitored using NIRS, with some interruptions due to clinical procedures.

Hypoxic-ischaemic events in three of these term neonates were selected to be investigated by the BabyBrain model. Details of these three neonates are presented in Table 7.2.

Table 7.2: Physiological characteristics of the term neonate subjects.

	Gestational age (weeks)	Actual age (hours)	Weight (g)	Gender	Sarnat Grade	Lac/NAA
Neonate 1	38.9	48.6	2850	Male	Moderate	0.16
Neonate 2	37.7	35.6	3750	Male	Mild	0.25
Neonate 3	40.3	51.7	3110	Male	Severe	0.39

7.2.1 Neonate 1

A significant hypoxic event was recorded in Neonate 1, with the smallest Lac/NAA ratio.

Sensitivity analysis and optimisation

Sensitivity analysis results are displayed in Table 7.3. 6 parameters were chosen to be optimised, indicated in the table with an asterisk, along with the normal cytochrome concentration in tissue $[\text{CCO}]_{tis}$. Table 7.4 lists the optimised values. The exponent in the muscular tension relationship n_m ,

was optimised to be higher than normal at baseline, but decreased following the event. In general, this increases muscular tension in the vessel walls (see Chapter 4, Section 4.7, Equation 4.61 for dependencies). Baseline cytoplasmic pH was remained close to the normal value throughout. The rate of the third oxidative phosphorylation reaction (which uses O_2) $k_{3,0}$ increased following the event. The largest change was in the cytochrome concentration $[CCO]_{tis}$, which was optimised to be higher than normal and decreased during the event.

Table 7.3: Sensitivity analysis of BabyBrain using data from Neonate 1. Parameters ranked in order of influence in optimising selected output variables. Asterisks indicate parameters selected for optimisation.

Variable				Parameter	Description
ΔHbO_2	ΔHHb	ΔHbT	ΔoxCCO		
1	1		20	r_0^*	A special radius in the elastic tension relationship
2	2	20		$rocc$	Arterial occlusion constant
3	3	5		n_m^*	Exponent in the muscular tension relationship
4	4	17	9	CBF_n	Normal cerebral blood flow
5	5	12		h_0	Vascular wall thickness when radius is r_0
6	6	9	4	r_n	Normal radius of blood vessels
7	7	19		$[Py]_n$	Normal concentration of pyruvate ions in the cytoplasm
8	8	18		k_{pl}	Rate of forward reaction in the pyruvate lactate equilibrium
9	9			$P_{ic,n}$	Normal intracranial blood pressure
10	10		19	C_{buffic}	Buffering capacity for protons in cytoplasm
14	14	10		NAD_{pool}	Total mitochondrial NAD and NADH concentration
		1		$[Hbtot]_n^*$	Normal total haemoglobin concentration in the arteries and veins.
		2		k_{aut}^*	Autoregulation constant
		3		ϕ	Value of $[O_2]$ at half maximal saturation
		4	13	$[CCO]_{tis}^*$	Concentration of cytochrome in tissue
		6		P_{vs}	Pressure in the venous sinuses
		7		r_t	Parameter in the muscular tension relationship
		8		σ_{coll}	Value of pressure at which vessels collapse
		14	6	CV_{inh}	Control parameter representing the action of complex V inhibitors
			1	pH_{on}^*	Normal cytoplasmic pH
			2	$k_{3,0}^*$	Rate constant for third oxidative phosphorylation reaction at zero PMF
			3	k_{Ik2}	Controls rate at which protons reenter the mitochondrial matrix through leak channels
			5	$L_{CV,0}$	Normal complex V flux as a fraction of maximum possible flux
			7	$[gluc]_n$	Normal cellular concentration of glucose
			8	k_{AK}	Forward rate constant for the conversion of ADP to ATP and AMP
			10	$G_{0,rat}$	Ratio between conductance of cerebral arteries and supplying artery compartment

7.2. Simulating hypoxic-ischaemic events

Table 7.4: Optimised parameter values for Neonate 1

Parameter	Description	Normal Value	Before Event	After Event	% Change
r_0	A special radius in the elastic tension relationship	0.0126 cm	0.0151	0.0151	0
n_m	Exponent in the muscular tension relationship	1.83	2.1954	1.464	-33.3151
pH_{on}	Normal cytoplasmic pH	7	7.0219	7.0518	0.4258
$[Hbtot]_n$	Total concentration of haemoglobin in blood	11.17 mM	4.0606	3.5004	-13.7960
$k_{3,0}$	Rate constant for third oxidative phosphorylation reaction at zero PMF	250000 $\text{mM}^{-1} \text{s}^{-1}$	200000	272523	36.2615
k_{aut}	Autoregulation constant	1	1	1	0
$[CCO]_{tis}$	Concentration of cytochrome in tissue	0.0022 mM	0.007	0.001	-85.7143

Model simulation

SaO_2 was observed to decrease by 27% although P_a varied throughout and no significant change was visible during the event (Figure 7.3). Changes in haemoglobin concentrations are well predicted, with an increase in $\Delta H H b$ and $\Delta H b T$. However, the significant decrease in $\Delta oxCCO$ was not predicted. Looking more closely at the change in $\Delta oxCCO$ shows that the drop here does not coincide with the decrease in oxygenation or the other variables. Hence it is possible that some other mechanism or significant injury maybe responsible for this decline, which is not encapsulated by the input variables used here by the model – SaO_2 and P_a .

Simulated CBF shows a significant increase during the event, which seems to correspond to the changes observed in the haemoglobin concentrations. Simulated $CMRO_2$ decreases very little during the event. The simulation here also shows a spike at the end of the event, caused by the change in model parameter values. The simulated pH values change slightly during the event, however cytoplasmic pH becomes increasingly alkaline and mitochondrial pH acidic with time. To reiterate, these changes in simulated variables are only in response to variations in the the input parameters SaO_2 and P_a . While the haemodynamic changes appear to be consistent with the measurements, the metabolic changes are not (evidenced by the lack of accuracy in the prediction of $\Delta oxCCO$). Thus the model prediction of $CMRO_2$

and pH are less likely to be accurate. In fact, a significant drop in $\Delta oxCCO$ would normally be accompanied by a drop in $CMRO_2$ as less oxygen is being used.

7.2.2 Neonate 2

The youngest of the three subjects, Neonate 2 had a mild hypoxic-ischaemic event. Figure 7.5 illustrates the measured SaO_2 and P_a values which dropped approximately 10% and 8% respectively during the event, although P_a varied significantly throughout.

Sensitivity analysis and optimisation

The morris method was used to determine the most influential parameters for ΔHbO_2 , ΔHHb , ΔHbT and $\Delta oxCCO$. Results are displayed in Table 7.5. 6 parameters were chosen to be optimised, indicated in the table with an asterisk, along with the normal cytochrome concentration in tissue $[CCO]_{tis}$ and the autoregulation constant k_{aut} .

Each parameter was optimised at baseline before the hypoxic-ischaemic event and after, to investigate any potential physiological changes. Optimised values are presented in Table 7.6. The ratio between the conductance of the cerebral arteries and the supplying artery compartment $G_{0,rat}$ was decreased from its normal model value at baseline, perhaps suggesting reduced blood delivery in the neonate. It was increased following the event, and was the largest change in the optimised parameters. However, the autoregulation constant remained at the maximum throughout, suggesting good autoregulative capacity. Cytoplasmic pH was slightly decreased from the normal model value, while baseline cytochrome concentration $[CCO]_{tis}$ was approximately half the normal model value. Optimised $[CCO]_{tis}$ did not change during the event.

7.2. Simulating hypoxic-ischaemic events

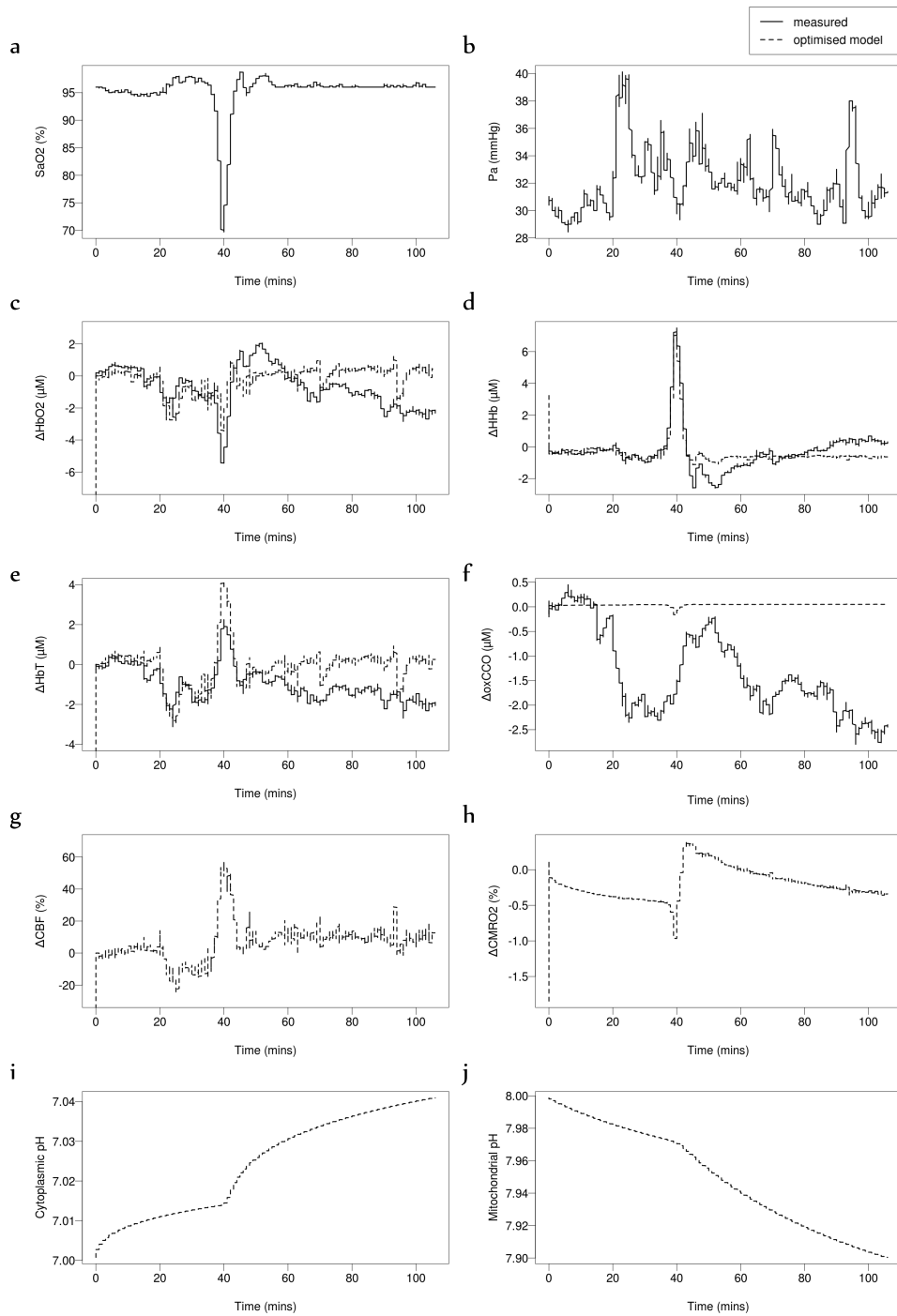


Figure 7.3: Neonate 1: (a) SaO_2 and (b) blood pressure P_a measurements are model inputs. (c,d,e,f) Simulations and measurements of ΔHbO_2 , ΔHHb , ΔHbT and $\Delta oxCCO$. (g,h) Simulations of ΔCBF and $\Delta CMRO_2$. (i, k) Simulated cytoplasmic pH and mitochondrial pH.

Table 7.5: Sensitivity analysis of BabyBrain using data from Neonate 2. Parameters ranked in order of influence in optimising selected output variables. Asterisks indicate parameters selected for optimisation.

Variable				Parameter	Description
ΔHbO_2	ΔHHb	ΔHbT	ΔoxCCO		
1	1			$G_{0,rat}^*$	Ratio between the conductance of the cerebral arteries and the supplying artery compartment
2	2			CBF_n^*	Normal cerebral blood flow
3	3	3		σ_{e0}^*	Parameter in relationship determining elastic stress in vessel walls
4	4	2		h_0^*	Vascular wall thickness when radius is r_0
5	5	10		$[Hb_{tot}]_n$	Normal total haemoglobin concentration in the arteries and veins.
6	6	1		P_a	Arterial blood pressure
7	7	11		K_σ	Controls sensitivity of elastic stress in vessel walls to radius
8	8	6		$NAD_{cyt,n}$	Normal concentration of NAD in the cytoplasm
9	9	8	10	$SaO_{2,n}$	Normal arterial oxygen saturation
10	10	7	2	SaO_2	Arterial oxygen saturation
17	17		1	pH_{on}^*	Normal cytoplasmic pH
		4	15	r_m	Value of vessel radius giving maximum muscular tension
		5		σ_{coll}	Value of pressure at which vessels collapse
		9		r_n	Normal radius of blood vessels
			3	$ck2^*$	Controls sensitivity of forward rate of the second oxidative phosphorylation reaction to the proton motive force
			4	$k_{3,0}$	Rate constant for third oxidative phosphorylation reaction at zero PMF
			5	$k_{m,tcaN,f}$	k_m for NAD in the TCA cycle as a fraction of normal NAD concentration
			6	R_{autop}	Controls sensitivity of autoregulatory stimuli to arterial blood pressure
			7	n_h	Hill coefficient for haemoglobin saturation
			8	na	Number of protons passing through Complex V for each ATP synthesised
			9	ϕ	Value of $[O_2]$ at half maximal saturation

Table 7.6: Optimised parameter values for Neonate 2

Parameter	Description	Normal Value	Before Event	After Event	% Change
$G_{0,rat}$	Ratio between the conductance of the cerebral arteries and the supplying artery compartment	10.0	4	5.9973	49.9325
CBF_n	Normal cerebral blood flow	0.007 ml/m-l/s	0.0064	0.0064	0
σ_{e0}	Parameter in relationship determining elastic stress in vessel walls	0.1425 mmHg	0.114	0.114	0
h_0	Vascular wall thickness when radius is r_0	0.003 cm	0.0036	0.0036	0
pH_{on}	Normal cytoplasmic pH	7	6.8247	6.8255	0.1802
$ck2$	Controls sensitivity of forward rate of the second oxidative phosphorylation reaction to the proton motive force	0.02 m/V	0.016	0.016	0
k_{aut}	Autoregulation constant	1	1	1	0
$[CCO]_{tis}$	Concentration of cytochrome in tissue	0.0022 mM	0.001	0.001	0

Model simulation

Figure 7.5 displays ΔHbO_2 , ΔHHb , ΔHbT and $\Delta oxCCO$ simulations from the model compared with measurements from Neonate 2. ΔHHb and ΔHbT are observed to increase during the event while ΔHbO_2 decreases. All three return to baseline. These changes are well simulated by the model. However, the magnitude of the simulated change in ΔHbT is much larger than observed.

There is a rise in $\Delta oxCCO$ observed during this phase. This is an unusual response to the decrease in oxygenation and blood flow, which is often predicted to result in lower levels of aerobic metabolism. The model thus predicts a slight decrease in $\Delta oxCCO$. A study in piglets conducted by Tsuji et al. (1995) recorded a slight increase in $\Delta oxCCO$ during hypoxia brought about by reducing the inspired oxygen concentration to 12% (from 25%), but recorded a decrease at 8% and lower (Figure 7.4). Although they offered no explanation for this change, it is currently hypothesised that at these slight reductions of oxygen delivery, the anesthetic or analgesic may have an effect

on the response in $\Delta oxCCO$.

Copyright material removed.

Figure 7.4: Hypoxia experiments in piglets by Tsuji et al. (1995), brought about by reducing inspired oxygen concentration to 12% , 8%, 6%, 4% and 0%. Measurements in HbO_2 , HHb (Hb) and oxidised cytochrome ($CytO_2$) from one piglet displayed at the top. Average values from 8 piglets are shown in the table. A slight increase in $\Delta oxCCO$ is observed at 12%.

Also presented in Figure 7.5 are the predicted changes in CBF and $CMRO_2$. ΔCBF increases during the event while $\Delta CMRO_2$ decreases. However, as the model does not predict the increase in $\Delta oxCCO$, the change here in $\Delta CMRO_2$ is put in question since the rate of use of O_2 is so directly dependent on oxidative phosphorylation. pH simulations show a slight change during the event, however cytoplasmic pH becomes increasingly acidic, while mitochondrial pH becomes increasingly alkaline.

7.2. Simulating hypoxic-ischaemic events

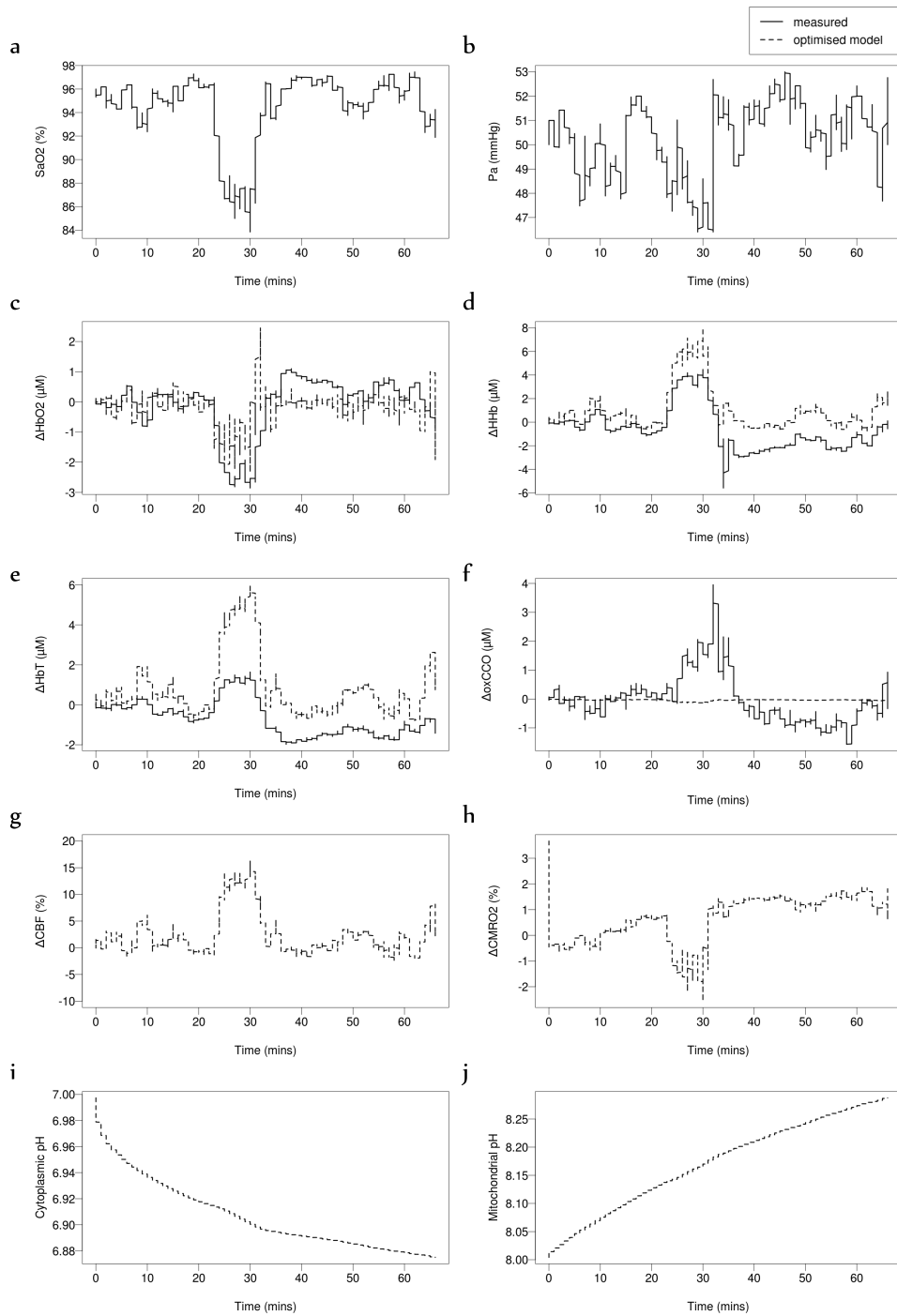


Figure 7.5: Neonate 2: (a) SaO_2 and (b) blood pressure P_a measurements are model inputs. (c,d,e,f) Simulations and measurements of ΔHbO_2 , ΔHHb , ΔHbT and $\Delta oxCCO$. (g,h) Simulations of ΔCBF and $\Delta CMRO_2$. (i, k) Simulated cytoplasmic pH and mitochondrial pH.

7.2.3 Neonate 3

Neonate 3 suffered from severe encephalopathy and was the oldest of the group.

Sensitivity analysis and optimisation

Sensitivity analysis results are displayed in Table 7.7. 6 parameters were chosen to be optimised, indicated in the table with an asterisk, along with the autoregulation constant k_{aut} . The buffering capacity for protons in the cytoplasm C_{buffic} was reduced during the event, leading to a slower change in cytoplasmic proton concentration. The sensitivity of autoregulatory stimuli to oxygen in the capillary R_{auto} was increased at baseline and dropped again after the event by more than 90%. Although the autoregulatory constant remained at maximum throughout, this perhaps signals a loss in the capacity to regulate oxygen delivery. The sensitivity of elastic stress in vessel walls to the radius K_σ was decreased at baseline, but remained constant thereafter. The normal radius of the blood vessels r_0 also decreased during the event, perhaps in response to the lack of oxygen.

Baseline cytochrome values $[CCO]_{tis}$ were again higher than normal model values and remained approximately the same throughout. The oxidised fraction of cytochrome $a_{frac,n}$ was very high at baseline (close to 1) and dropped to a 0.4 after the event. This combination signals a high concentration of oxidised cytochrome before the event and a substantial loss afterwards.

Table 7.7: Sensitivity analysis of BabyBrain using data from Neonate 3. Parameters ranked in order of influence in optimising selected output variables. Asterisks indicate parameters selected for optimisation.

Variable				Parameter	Description
ΔHbO_2	ΔHHb	ΔHbT	ΔoxCCO		
1	1			R_{autu}	Controls sensitivity of autoregulatory stimuli to demand
2	2			R_{auto}^*	Controls sensitivity of autoregulatory stimuli to oxygen in the capillary
3	3		15	C_{buffic}^*	Buffering capacity for protons in cytoplasm
4	4	7		$P_{a,n}$	Normal arterial blood pressure
5	5			P_a	Arterial blood pressure
6	6	14		$[NAD]_n / NADH_n$	Normal NAD/NADH ratio
7	7		2	$a_{frac,n}^*$	Normal oxidised fraction of Cu_A
8	8			c_3	Controls sensitivity of third oxidative phosphorylation reaction to PMF
9	9			r_0	A special radius in the elastic tension relationship
10	10	8		SaO_2	Arterial oxygen saturation
15	15	11	7	h_0	Vascular wall thickness when radius is r_0
18	18	2	9	K_σ^*	Controls sensitivity of elastic stress in vessel walls to radius
		1		r_n^*	Normal radius of blood vessels
		3		$V_{olt,n}$	Normal total blood volume
		4		$blood_{frac}$	Normal blood volume as a fraction of brain tissue volume
		5		$[Hbtot]_n$	Normal total haemoglobin concentration in the arteries and veins.
		6		c_{frac}	Fraction of arterial blood which flows through the carotid arteries
		9		NAD_{pool}	Total mitochondrial NAD and NADH concentration
		10	20	σ_{coll}	Value of pressure at which vessels collapse
		15	10	ϕ	Value of $[\text{O}_2]$ at half maximal saturation
			1	$[\text{CCO}]_{tis}^*$	Concentration of cytochrome in tissue
			3	$G_{VArat,n}$	Normal ratio of conductances between arteries and veins G_v / G_n (determines venous pressure)
			4	n_h	Hill coefficient for haemoglobin saturation
			5	$NAD_{cyt,n}$	Normal concentration of NAD in the cytoplasm
			6	$NADH_{cyt,n}$	Normal concentration of NADH in the cytoplasm
			8	pH_{on}	Normal cytoplasmic pH

7.2. Simulating hypoxic-ischaemic events

Table 7.8: Optimised parameter values for Neonate 3

Parameter	Description	Normal Value	Before Event	After Event	% Change
C_{buffic}	Buffering capacity for protons in cytoplasm	0.025	0.0200	0.0300	50
R_{auto}	Controls sensitivity of autoregulatory stimuli to oxygen in the capillary	1.5	10	0.7875	-92.125
$a_{frac,n}$	Normal oxidised fraction of Cu_A	0.67	0.9730	0.4	-58.89
K_σ	Controls sensitivity of elastic stress in vessel walls to radius	10	8	8	0
r_n	Normal radius of blood vessels	0.0187 cm	0.0218	0.0150	-31.1927
k_{aut}	Autoregulation constant	1	1	1	0
$[CCO]_{tis}$	Concentration of cytochrome in tissue	0.0022 mM	0.0069	0.0068	-1.4493

Model simulation

This neonate exhibited the most severe hypoxic-ischaemic event, with SaO_2 dropping by 80% and P_a also significantly decreasing by 50% (Figure 7.6). Simulated changes in haemoglobin – ΔHbO_2 , $\Delta HHHb$ and ΔHbT – were greater than that observed. All three returned to baseline following the event.

$\Delta oxCCO$ was well predicted in this case, showing a considerable drop during the event. The simulation returned to baseline immediately after, although the measurement did not. Significant reductions in CBF and $CMRO_2$ were predicted during the event. In this case, simulated cytoplasmic and mitochondrial pH decreased, becoming more acidic during the event and subsequently returned to baseline values. Mitochondrial pH decreased again immediately afterwards.

7.2. Simulating hypoxic-ischaemic events

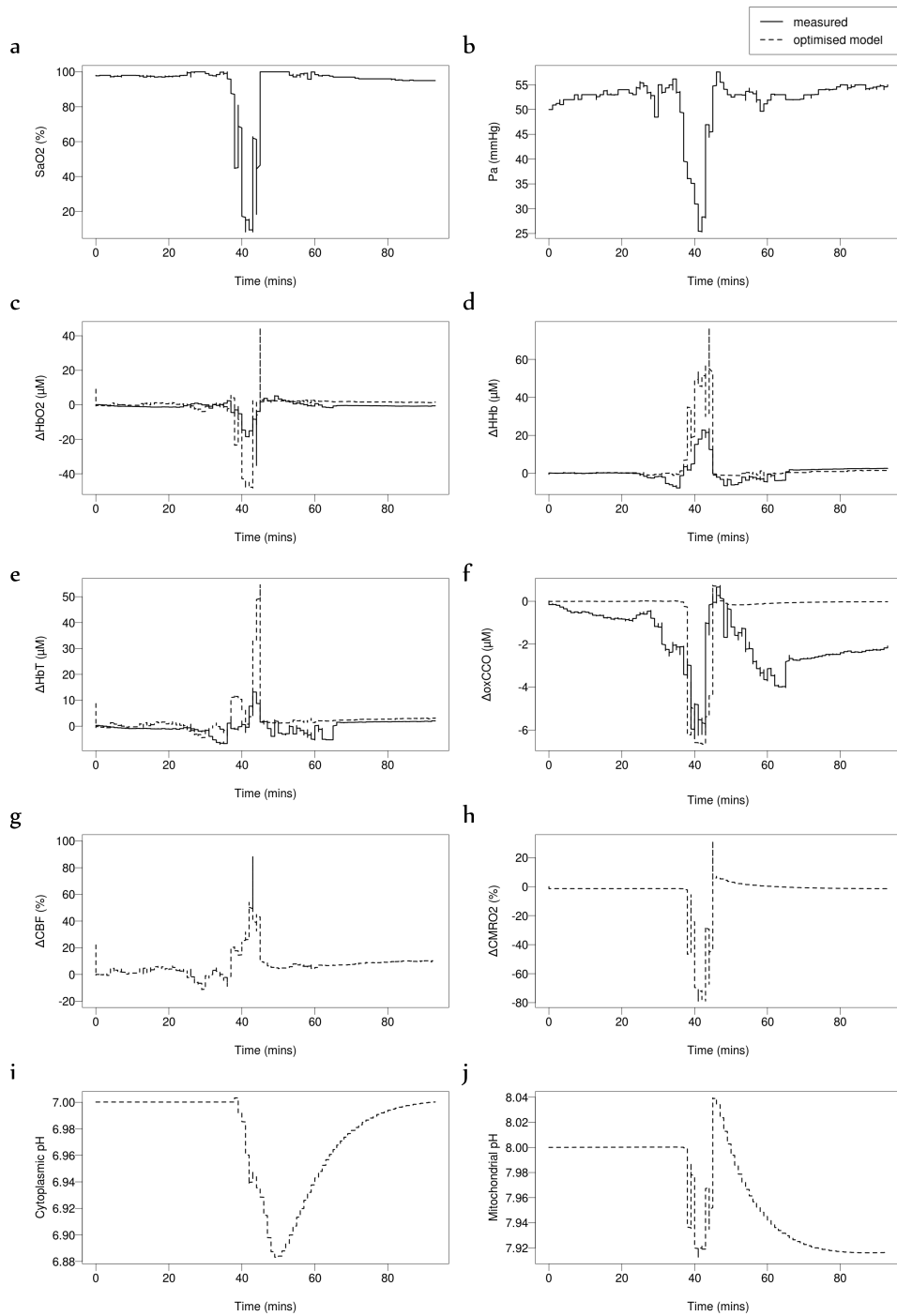


Figure 7.6: Neonate 3: (a) SaO_2 and (b) blood pressure P_a measurements are model inputs. (c,d,e,f) Simulations and measurements of ΔHbO_2 , ΔHHb , ΔHbT and $\Delta oxCCO$. (g,h) Simulations of ΔCBF and $\Delta CMRO_2$. (i, k) Simulated cytoplasmic pH and mitochondrial pH.

7.3 Discussion

The BabyBrain term neonate model was created by altering parameter values in BrainPiglet v2.0 to suit the human term neonate. The autoregulation curves of the two models are fairly similar, but shifted in BabyBrain due to the lower normal blood pressure and CBF values (Figure 7.1). Sensitivity analysis suggests that the concentration of sodium in the model is influential.

The BabyBrain term model was used to investigate monitoring data of term neonates suffering from hypoxic-ischaemic encephalopathy of different levels of severity. Neonates 1 and 3, with the lowest and highest Lac/NAA ratios respectively, went through more severe hypoxic-ischaemic events compared to Neonate 2. The model was able to simulate changes in haemoglobin relatively well. All three neonates exhibited a decrease in ΔHbO_2 and an increase in ΔHHb and ΔHbT . The magnitude of the change was in some cases not well represented (such as in Neonate 3).

The neonates showed varied responses in $\Delta oxCCO$. In Neonate 1 $\Delta oxCCO$ decreased significantly, although this decrease did not coincide with the hypoxic event. While the model predicted a small drop in $\Delta oxCCO$ in response to hypoxic conditions, it did not predict the changes observed. It is likely that these changes were caused by some other mechanism(s) not incorporated into the model or in the input signals. Indeed at steady state, the drop in $\Delta oxCCO$ caused by varying SaO_2 is not large (Figure 7.2).

In Neonate 2 $\Delta oxCCO$ rose during the event. Although slight increases have been recorded with small decreases in oxygenation in piglet experiments (Tsuji et al. 1995), the mechanism responsible is unclear. The model predicts a small drop in $\Delta oxCCO$ as would be expected during hypoxic conditions. At the time of writing, similar increases in $\Delta oxCCO$ have been observed during desaturations in 3 other term neonates in the same study. These neonates vary in injury severity. Details of treatment have been requested but yet to be acquired at the time of writing.

Changes in P_aCO_2 are known to affect $\Delta oxCCO$. While P_aCO_2 was measured in these neonates, the measurement was unreliable and incomplete, with significant sections missing from the recordings, and so was not used as an input to the model. However, the measurements during the events in Neonate 1 and 2 showed no significant change in P_aCO_2 .

The sensitivity analysis results from Neonate 1 and 2 both suggest that the concentration and movement of protons has a heavy influence on variations in $\Delta\alpha\text{CCO}$ (Tables 7.5 and 7.3). Indeed, altering the normal cytoplasmic pH in the model shows a strong response in the $\Delta\alpha\text{CCO}$ simulation (Figure 7.7). As there is no continuous measurement of pH in these subjects, it is not possible to determine whether the brain pH was close to normal at the start of the measurement.

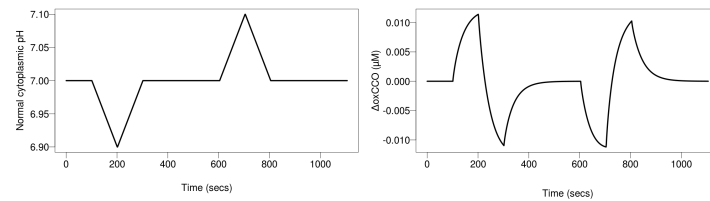


Figure 7.7: BabyBrain model simulation of $\Delta\alpha\text{CCO}$ in response to changes in the input normal cytoplasmic pH

Simulations of Neonate 1 and 2 were repeated with the BrainPiglet v2.1 model adapted to the term neonate, to test whether the more detailed model of pH dynamics, including carbonic acid and sodium transporters, would be capable of simulating the observed changes. The simulation of $\Delta\alpha\text{CCO}$ was no better than in v2.0. Other factors such as blood pH are likely to have an important role. However, this addition would further increase the complexity of the model and the difficulty in optimising it.

In the more severe case, Neonate 3, the drop in $\Delta\alpha\text{CCO}$ was quite clearly a product of the drastic loss of SaO_2 . Here, the model was able to simulate the change very well.

Model simulations of CBF, CMRO_2 , and pH also give an insight into changes not observed by the monitoring systems. CBF is predicted to increase in Neonates 1 and 2, where blood pressure does not change significantly during the event. In contrast, in the more severe case (Neonate 3) CBF drops significantly, mirroring the decrease blood pressure during the event.

CMRO_2 is predicted to drop slightly in mild and moderate cases and much more significantly in the severe case as might be expected. However, in mild and moderate cases (Neonates 1 and 2) where the observed change in $\Delta\alpha\text{CCO}$ is not well simulated, these predictions in CMRO_2 are those expected to arise simply in conjunction with the simulated $\Delta\alpha\text{CCO}$. As it

appears that other mechanisms are at play effecting oxidative phosphorylation, it is likely that the actual change in $CMRO_2$ will be different.

The simulation of pH in Neonates 1 and 2 did not yield significant event-related responses. However, in Neonate 3 the model predicted an acidic change in both cytoplasmic and mitochondrial pH. Both values subsequently returned to baseline, although mitochondrial pH decreased again immediately afterwards. There are two key observations here - the first is that the hypoxic-ischaemic stimulus need to be of significant magnitude for a sizeable change in pH to be simulated. Second, mitochondrial pH may vary differently from cytoplasmic pH. In the current model, cytoplasmic pH appears to have a stronger capacity for recovery than the mitochondrial pH.

As discussed before, the model's capacity for prediction is limited not only by the scope of the select biological mechanisms that have been incorporated into the model, but also by the model inputs. The model translates the variations it detects in SaO_2 and blood pressure into the simulations of NIRS and MRS variables via a network of reactions considered relevant. The optimisation of model parameters is able to incorporate other changes or differences to some degree. However, it largely ignores (as it must) other possible influences, which the observed measurements are subject to. Therefore, the differences between simulated and measured variables can be indicative of processes not incorporated into the model.

Chapter 8

Simulating functional activation in the preterm neonatal brain

This chapter describes the adaptation of the human adult BrainSignals model to the human preterm neonatal brain, and its application to clinical data to investigate different functional haemodynamic responses observed in healthy subjects in two published studies. The first was conducted by Kozberg et al. (2013) in rats using a somatosensory stimulus, and reported an increase in HHb in some rats and a decrease in others. The second study by Roche-Labarbe et al. (2014) also using a somatosensory stimulus observed a decrease in HHb in preterm human neonates. The model is also applied to data from a recent functional study in preterm neonates using a visual stimulus. This study also observed both increases and decreases in HHb. The model was used to replicate these responses, to explore possible explanations for these differences.

8.1 BrainSignals preterm neonatal model

The BrainSignals model of human adult cerebral metabolism was published by Banaji et al. (2008). The model is described in detail in Chapter 4, Section 4.6. In order to adapt the model to the human preterm neonate, a number of parameters, known to be significantly different in the young, were altered (Table 8.1). This is a similar process to that taken in the creation of the

8.1. BrainSignals preterm neonatal model

BrainPiglet model (Moroz et al. 2012). The cytochrome parameters $[CCO]_{tis}$ and $Cu_{A,frac,n}$ have been measured in piglets as this technique is invasive. All other parameters in the table have been obtained from human subjects.

Figure 8.1 displays the autoregulation curves for the adult and neonatal BrainSignals models, comparable to approximations in literature (Volpe 2008).

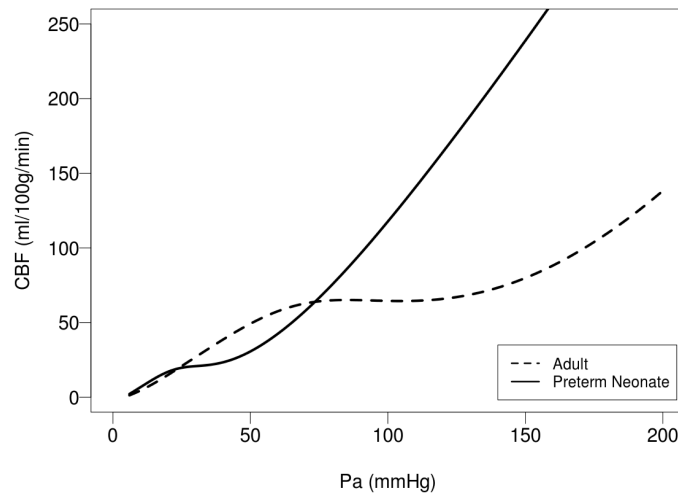


Figure 8.1: Autoregulation curves cerebral blood flow (CBF) against blood pressure (Pa) - of the BrainSignals preterm neonate and adult models.

Table 8.1: Altered BrainSignals parameter values

Parameter	Description	Units	BrainSignals	Preterm neonate	Source
CBF_n	Normal cerebral blood flow (CBF)	ml 100 g ⁻¹ min ⁻¹	49	19.8	Greisen (1986)
$[CCO]_{tis}$	Total concentration of cytochrome-c-oxidase (CCO) in tissue	μ M	5.5	2.2	Cooper et al. (1997), Springett et al. (2000)
$Cu_{A,frac,n}$	Normal fraction of oxidised CCO		0.8	0.67	Springett et al. (2000)
$CMRO_{2,n}$	Normal cerebral metabolic rate of oxygen consumption (CMRO2)	μ mol 100 g ⁻¹ min ⁻¹	155	40.865	Elwell et al. (2005)
P_a and $P_{a,n}$	Mean arterial blood pressure	mmHg	100	30	Polin et al. (2010)
$[Hbtot]$ and $[Hbtot]_n$	Total concentration of haemoglobin in blood	mM	9.1	9.75	Polin et al. (2010), Jopling et al. (2009)
$V_{blood,n}$	Normal blood volume as a fraction of brain tissue volume		0.04	0.0233	Wyatt et al. (1990)
P_{ic} and $P_{ic,n}$	Intracranial pressure	mmHg	9.5	5.1	Easa (1983)

8.1.1 Sensitivity analysis

Table 8.2 illustrates results of the morris method analysis. Results show that the most influential parameters are related to the characteristics of blood flow and vessel walls (σ_{e0} , K_{σ} , r_0 , r_t , r_m , h_0), related to the rate of which protons re-enter the mitochondrial matrix (k_{tk2}) and normal model inputs SaO_2 , Pa , and $PaCO_{2n}$.

Table 8.2: Sensitivity analysis of BrainSignals preterm neonate model at steady state. Parameters ranked in order of influence in optimising selected output variables.

Variable				Parameter	Description
ΔHHb	ΔHbO_2	ΔHbT	ΔoxCCO		
1	1	15	6	r_0	A special radius in the elastic tension relationship
2	2		7	σ_{e0}	Parameter in relationship determining elastic stress in vessel walls
3	3		10	SaO_2	Arterial oxygen saturation
4	4	9	2	P_a	Arterial blood pressure
5	5	12	5	r_t	Parameter in the muscular tension relationship
6	6			Vol_{mit}	Normal mitochondrial volume
7	7	2		$P_aCO_{2,n}$	Normal arterial partial pressure of CO_2
8	8	17	8	$P_{ic,n}$	Normal intracranial blood pressure
9	9	8	1	r_m	Value of vessel radius giving maximum muscular tension
10	10	4	4	h_0	Vascular wall thickness when radius is r_0
11	11	6		$blood_{frac}$	Normal blood volume as a fraction of brain tissue volume
12	12	10	9	$[Hbtot]_n$	Normal total haemoglobin concentration in the arteries and veins.
15	15	5	11	P_{vs}	Pressure in the venous sinuses
17	16	3	3	K_σ	Controls sensitivity of elastic stress in vessel walls to radius
		1	18	k_{lk2}	Controls rate at which protons reenter the mitochondrial matrix through leak channels
		7	16	$[CCO]_{tis}$	Concentration of cytochrome in tissue

8.1.2 Simulating functional activation

The BrainSignals preterm neonatal model was used to investigate the varied observations in the neonatal brain responses to functional activation, namely the changes in HHb and HbO₂ recorded (see Chapter 3, Section 3.3.2). Observations as reported in Kozberg et al. (2013) and Roche-Labarbe et al. (2014) were simulated. The model was further applied to data collected from a recent stimulus-evoked haemodynamic response study in preterm neonates.

The Kozberg study

Kozberg et al. (2013) is a functional study conducted in postnatal rats, age-equivalent to human newborns, subjected to a somatosensory stimulus. Although our model is focused on the human neonate, we were interested in replicating the qualitative response observed in these animals. The results were divided into two groups – rats which exhibited a rise in blood pressure in response to the stimulus and those which did not.

Rats that exhibited a rise in blood pressure also showed an increase in HbO₂ and HbT and a decrease in HHb, where the increase in HbO₂ was greater than the decrease in HHb (functional hyperemia). In the rats that showed a slight decrease or no change in blood pressure, the opposite results were observed – a decrease in HbO₂ and HbT and a rise in HHb. These conflicting results were attributed to a lack of functional hyperemia and an overarching effect of arterial vasoconstriction in the latter group.

In order to simulate these results, we increased the models demand parameter u to simulate functional activation with the shape of a steep rising haemodynamic response function (HRF):

$$u = 1.0 + \alpha HRF \tag{8.1}$$

where α is a real number (Figure 8.2). We simulated blood pressure also using the function

$$P_a = P_{a,n} + \beta HRF. \tag{8.2}$$

8.1. BrainSignals preterm neonatal model

where β is a real number. The values for α and β were optimised to obtain the best fit of model simulations to the observed results. SaO_2 and P_aCO_2 were assumed to remain constant. The model was used to predict changes HbO_2 , HHb and HbT which were compared against the observations.

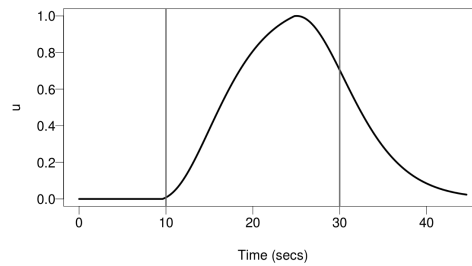


Figure 8.2: Demand as a model input, using a haemodynamic response function, to simulate functional activation

For the first group of animals who showed an increase in blood pressure, the values $\alpha = 2$ and $\beta = 1.5$ were used. Figures 8.3 and 8.4 show the results of the model simulations superimposed with that observed in the study.¹ Although vasoconstriction was observed in the study, preventing the dilation of the vessels in the model actually reversed these results.

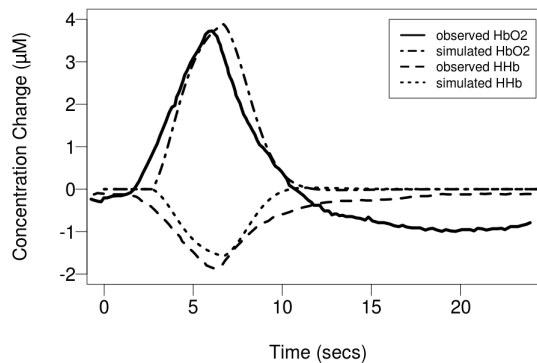


Figure 8.3: Model simulated and observed haemodynamic response of the Kozberg et al. study (Kozberg et al. 2013), investigating functional response in rats, with an increase in demand and blood pressure (BP). Changes in deoxy- and oxy-haemoglobin (HHb, HbO_2) concentrations.

For the second group of rats, which exhibited no rise in blood pressure, we reduced the arterial radius by 1% and used $\beta = -0.18$.

¹Plot Digitizer software was used to extract data from the published figures (Huwaldt and Steinhorst)

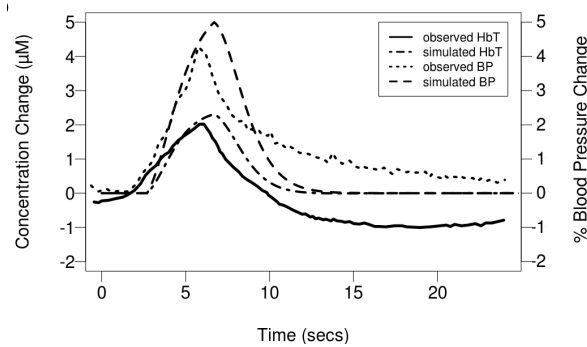


Figure 8.4: Model simulated and observed haemodynamic response of the Kozberg et al. study (Kozberg et al. 2013), investigating functional response in rats, with an increase in demand and blood pressure (BP). Changes in blood pressure (BP) and total haemoglobin (HbT).

$$r = r_n(1 - 0.01HRF) \quad (8.3)$$

We did not need to increase the demand u , suggesting that an increase in oxygen consumption was not required to produce this response. Figures 8.5 and 8.6 illustrate these results, which are very closely comparable to the original data obtained by Kozberg et al. (2013).

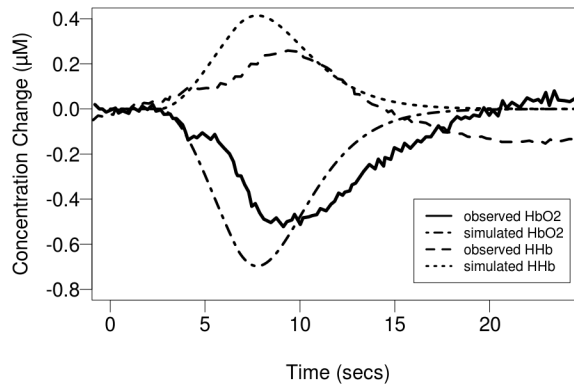


Figure 8.5: Model simulated and observed haemodynamic response of the Kozberg et al. study (Kozberg et al. 2013), investigating functional response in rats, with a slight decrease in arterial radius and blood pressure (BP). Changes in deoxy- and oxy- haemoglobin (HHb, HbO₂) concentrations.

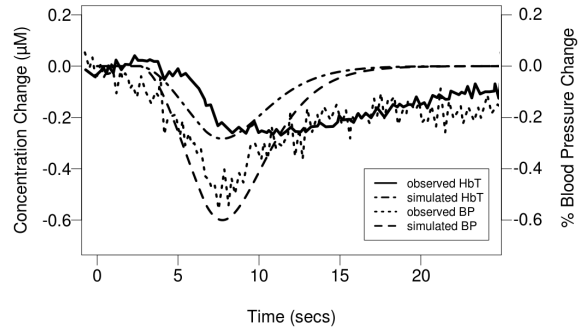


Figure 8.6: Model simulated and observed haemodynamic response of the Kozberg et al. study (Kozberg et al. 2013), investigating functional response in rats, with a slight decrease in arterial radius and blood pressure (BP). Changes in BP and total haemoglobin (HbT).

The Roche-Labarbe study

The second study investigated was conducted in preterm human neonates by Roche-Labarbe et al. (2014). They observed a decrease in HHb and an increase in HbO₂, CBF, CMRO₂ and cerebral blood volume (CBV) in response to a somatosensory stimulus. These results were replicated relatively well by simply increasing the models demand ($\alpha = 0.5$) (Figure 8.7, 8.8 and 8.9). However our predicted CBF and CMRO₂ was higher and HHb slightly lower than that observed.

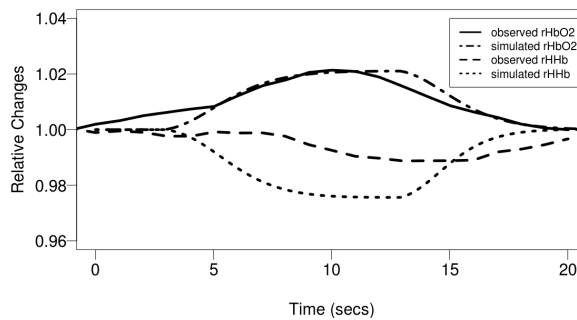


Figure 8.7: Model simulated and observed haemodynamic response of the Roche-Labarbe et al. study (Roche-Labarbe et al. 2014), investigating functional response in human preterm neonates, with an increase in demand. Relative changes in oxy- and deoxy- haemoglobin (rHbO₂, rHHb)

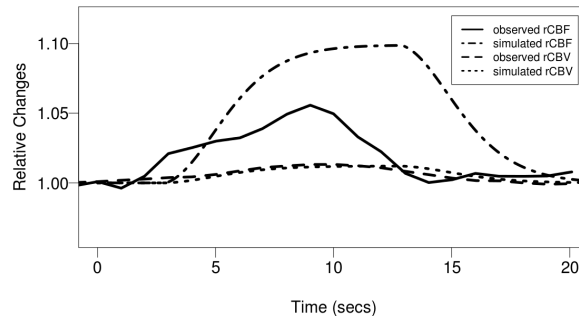


Figure 8.8: Model simulated and observed haemodynamic response of the Roche-Labarbe et al. study (Roche-Labarbe et al. 2014), investigating functional response in human preterm neonates, with an increase in demand. Relative changes cerebral blood volume (rCBV) and cerebral blood flow (rCBF)

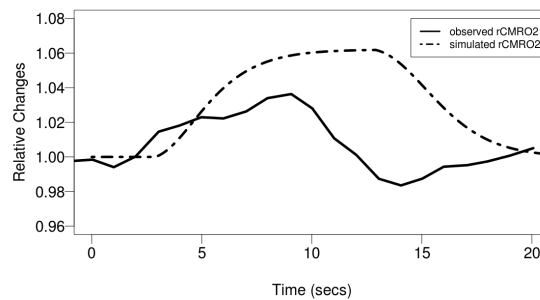


Figure 8.9: Model simulated and observed haemodynamic response of the Roche-Labarbe et al. study (Roche-Labarbe et al. 2014), investigating functional response in human preterm neonates, with an increase in demand. Relative changes in cerebral metabolic rate of oxygen consumption (rCMRO2).

The USZ study

A functional near infrared spectroscopy (fNIRS) study was recently conducted at University Hospital Zurich (USZ), investigating the functional response in the preterm brain evoked by a visual stimulus. A blinking pocket LCD display was used as the stimulus and changes in tissue oxygenation and haemodynamics were measured over the prefrontal cortex using a novel spatially-resolved NIRS device (OxyPrem). Measurements of changes in HbO₂, HHb and HbT were averaged over repeated stimuli. Characteristics of two preterm subjects are detailed in Table 8.3.

SaO₂ and PaCO₂ were unlikely to vary greatly in these infants and so were

Table 8.3: Physiological characteristics of the two preterm infant subjects.

	Gestational age (weeks)	Actual (weeks)	age	Weight (g)	Hematocrit (%)
Neonate 1	33.3	33.4		2380	52.5
Neonate 2	25.9	39.0		3460	30.0
	Haemoglobin (g/dL)	FiO₂ (%)		Baseline SpO₂ (%)	Baseline heart rate (BPM)
Neonate 1	17.08	21.0		95	148
Neonate 2	9.70	28.0		92-95	165

kept constant. P_a was also assumed to remain constant in the first instance. In Neonate 1, the measurements showed an increase in ΔHbO_2 and ΔHbT during the stimulus, and a decrease in ΔHHb (Figure 8.10). This response was simulated in the model by a simple increase in demand ($\alpha = 0.7$). Modelled CBF and CMRO_2 showed a corresponding rise during the stimulus.

In Neonate 2, a similar increase in CMRO_2 , ΔHbO_2 and ΔHbT was observed during the stimulus. However, an increase in ΔHHb was also observed (Figure 8.11). This response was simulated in ΔHHb by an increase in demand ($\alpha = 0.7$) while maintaining CBF constant at its normal value throughout the stimulus. Better predictions of ΔHbO_2 and ΔHbT were obtained by adding a decrease in blood pressure during the stimulus (Equation 8.2 with $\beta = -7$) to match the magnitude of ΔHbO_2 and ΔHbT . However this decrease was too large to be physiologically likely within this timeframe (-7 mmHg).

8.2 Discussion

The BrainSignals model was successfully adapted to the preterm neonatal brain by changing a number of parameters. The autoregulatory capacity of the preterm brain remains unclear. However, as our model simulation suggests, preterm neonates may be able to maintain constant blood flow only within a very narrow range of blood pressure values (Figure 8.1). Sensitivity analysis suggests that the parameters related to the functioning of blood vessel walls are influential in this model. These were not altered from the BrainPiglet values, but it is unlikely that such values in the human neonate can be accurately sourced owing to the difficulty in obtaining them, and to the changes in these vessels brought about by vascular development.

A number of studies have observed that the response of HHb to a functional

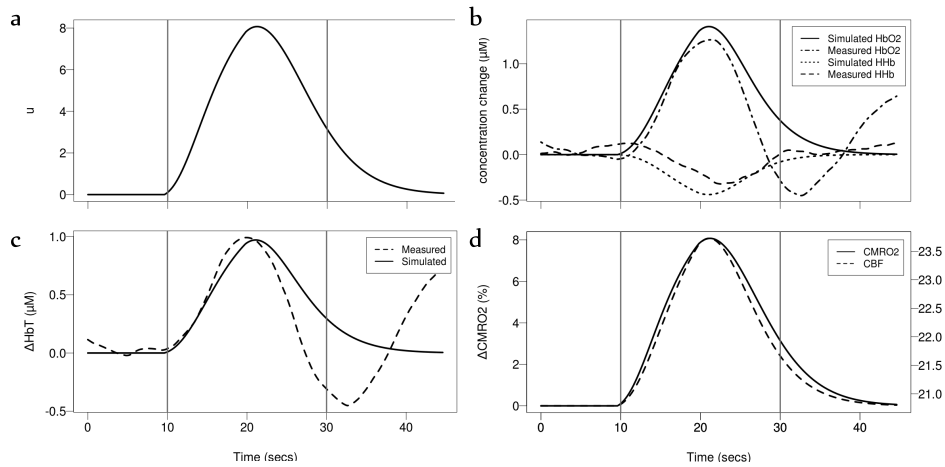


Figure 8.10: Model simulation of Neonate 1 of the USZ study. Simulated haemodynamic response with an increase in demand u (a). Vertical lines indicate stimulus period. Measured and simulated changes in (b) oxy- and deoxy- haemoglobin (HbO₂, HHb) and (c) total haemoglobin (HbT). (d) Simulated cerebral metabolic rate of oxygen consumption (CMRO₂) cerebral blood flow (CBF).

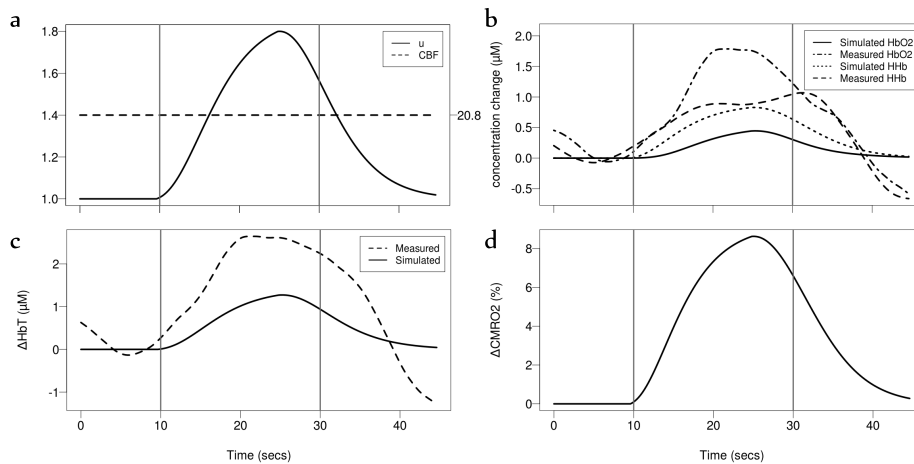


Figure 8.11: Model simulation of Neonate 2 of the USZ study. Simulated haemodynamic response with an increase in demand u and CBF maintained constant (a). Vertical lines indicate stimulus period. Measured and simulated changes in (b) oxy- and deoxy- haemoglobin (HbO₂, HHb) and (c) total haemoglobin (HbT). (d) Simulated cerebral metabolic rate of oxygen consumption (CMRO₂).

stimulus is sometimes inverted in healthy preterm neonates as compared to adults. The preterm model is capable of simulating the varied haemodynamic responses observed in studies performed by Kozberg et al. (2013) and

Roche-Labarbe et al. (2014). The model predicted an HHb decrease in response to the stimulus unless vasoconstriction was imposed as observed by Kozberg et al. (2013). Decreasing the radius of the blood vessel resulted in the inverted response.

The BrainSignals preterm model was also able to simulate fNIRS data from the USZ study relatively well. In Neonate 1 a similar response of hyperemia was observed as in the Roche-Labarbe et al. (2014) study. In Neonate 2, the observed rise in ΔHHb was simulated here by a constant CBF. However, the magnitude of ΔHbO_2 and ΔHbT response was not sufficiently simulated. Neonates 1 and 2 are markedly different in both gestational and actual age. The former, being older, is more likely to have a developed autoregulatory capacity although both subjects showed an increased HbT response. Their differences in haematocrit and haemoglobin are also notable. Indeed it has been suggested previously that HbT may have an effect on the haemodynamic response in newborns (Zimmermann et al. 2012). However, by changing baseline HbT, no effect was seen on the magnitude or shape of the model's simulations. These initial results suggest that the interaction of many variables affect the functional haemodynamic response including CBF, blood pressure and the varied stages of development. This makes it very difficult to define a normal functional response for all neonates.

It is important here to discuss the scope of the model presented in this chapter. It is perhaps obvious that the BrainSignals model is much more limited in its capacity to simulate metabolites than the BrainPiglet models (presented in previous chapters). The BrainSignals model was created with a focus on functional activation and predicting $\Delta xCCO$, whilst the BrainPiglet model was produced to investigate hypoxia-ischaemia and developed to examine intracellular pH. Although adapted to neonatal parameters, the preterm model does not take into account the effects of fetal haemoglobin which is present in significant concentrations at birth (see Chapter 2, Section 2.7). It is also likely that many model parameters will be affected by the stage of development of the neonate. As mentioned in this chapter, preterm neonates have significant differences in physiology. The stage of development of healthy preterm neonates at term-equivalent age is also unclear at present. Possible genetic differences introduce further variability. In the application of these models, this complexity becomes more convoluted when the subjects being investigated are suffering from brain injury or exhibiting

non-normal symptoms. Indeed the majority of literature on the physiological characteristics of human neonates are studies of infants who are or have been ill. This is not very surprising, as most neonates are unlikely to be kept for monitoring in their first days of life unless their health necessitates their stay.

Simulating functional activation, and the measurements obtained during such experiments, is a more challenging task than simulating hypoxia ischaemia. The latter is gross global insult and produces a more significant change in cerebral metabolism and health, which is in turn more easily and clearly detected. During functional activation, the variations in the input signals – blood pressure and SaO_2 – are less marked, leading to smaller perturbations from the norm in the model. Thus, functional activation models may require much more data for development and validation.

The work presented in these last two chapters is the realisation of an important goal in the continuous progress of a series of computational models. This adaptation of the models to simulate metabolism in the human neonate marks the beginning of what is likely to be a series of neonatal models to investigate clinical data from young patients in intensive care.

Chapter 9

Conclusions and Future Work

In this thesis, five new models of cerebral metabolism are presented. They are all adaptations and extensions of previously published models, and are focused on simulating and interpreting cerebral NIRS and MRS measurements during hypoxia-ischaemia and functional activation events. The models also provide a predictive capability for parameters that are indicative of mechanisms of metabolic activity, such as the redox state of cytochrome, autoregulation and cerebral oxygen consumption.

Mathematical and computational models are powerful mechanisms for investigating biological complexity. However, their authority is hindered by the dichotomy between the nature of the method and that of the subject it is being applied to. Quantitative concepts employ specific and concrete structures and values, which are seldom identifiable in biological environments.

The creation of exact or completely accurate models of cerebral metabolism is an extremely difficult task in the current scientific sphere, with the exception of those producing very broad, general predictions. The accuracy and complexity of a model are strongly related to the question that is being asked. It is often easier to understand *if* there is a cerebral response than to understand *what* the response is. In order to answer the more complex questions, as discussed in Chapter 4, the impulse in model building to include as much detail as possible can be a risky fault. The aim is the creation of a model that is on the one hand accurate enough to suit the needs of the application, and on the other simple enough to be translated and understood.

The cerebral metabolism models built at UCL add to a growing collection

of such models that are based on brain physiology. Many of these are built upon others, extending, adapting and refining to suit the needs of the application at hand. The UCL BrainSignals and BrainPiglet models are great examples of this approach – both are derived from earlier models and were created specific to a particular clinical application. BrainSignals was reduced and extended from the earlier much more convoluted BrainCirc model, focused on human adult cerebral metabolism and simulating NIRS measurements ($\Delta oxCCO$ in particular). BrainPiglet is an adapted and extended form of BrainSignals to suit cerebral metabolism in the piglet, and to simulate both NIRS and MRS measurements. These models aim to aid in the investigation of cerebral activity by relating changes observed in clinical measurements to the physiology that gives rise to them.

The BrainPiglet model was extended in this thesis in an effort to better simulate intracellular pH dynamics, by incorporating cellular mechanisms known to govern intracellular proton concentrations. The first version of the model improved the representation of proton use and production in pre-existing reactions, in addition to the introduction of the malate-aspartate shuttle. These changes allowed a more authoritative simulation of cytoplasmic pH and the new modelling of mitochondrial pH, and were coupled with parallel work on improving the simulation of artery occlusion. The second version, BrainPiglet v2.0.1, integrates the simulation of carbonic acid in both mitochondrial and cytoplasmic compartments. The third, BrainPiglet v2.1, adds the workings of the sodium transporters on the cellular membrane – the sodium-potassium pump and the sodium-hydrogen exchanger. These new models therefore required the introduction of a significant number of new variables and parameters.

The improved BrainPiglet models have been shown to be capable of simulating changes observed during cerebral hypoxia-ischaemia in piglets. In an initial investigation using data from one piglet, the models accurately predict the observed increases in ΔHbO_2 and ΔHbT and decrease in ΔHHb during the insult. The models also simulate the decreases observed in $\Delta oxCCO$, albeit with less precision in v2.0.1 and v2.1, mainly due to a weaker performance by the optimisation process. This relates to increased complexity in v2.0.1 and v2.1, and back to the arguments around, and need for, a balance between model efficacy and detail.

Indeed the developments in BrainPiglet v2.0.1 and v2.1 did not noticeably

improve the simulation of cytoplasmic pH compared to BrainPiglet v2.0, which predicts quite well the acidic pH observed in the MRS measurements during the insult. More interesting perhaps is the model's prediction of mitochondrial pH, which had a varied response during the hypoxic-ischaemic insult, but became more acidic following the release of blood occlusion. These results suggest that intracellular pH dynamics maybe considerably more intricate than may seem. However, the known regulators of intracellular pH thought to be biologically important did not have a considerable effect on the model's capacity to simulate it. It could be argued that the effect of these additions fall short simply because of the increased difficulty in optimisation.

Following this initial trial of the three models, BrainPiglet v2.0 was chosen to investigate the full set of experiments of piglets with both poor and good outcomes. The model simulated the observed acidic drop in cytoplasmic pH relatively well. Mitochondrial pH again displayed varying changes during the insult phase, but became more acidic in all piglets following the release of blood occlusion. There was no particular pattern in good or poor outcome groups. It remains to be seen whether changes in mitochondrial pH can have significant effects on intracellular pH as a whole, and whether these changes lead to complex dynamics post-insult, resulting in secondary energy failure.

Chapter 7 presented the adaptation of the BrainPiglet v2.0 model to the term neonate (and hence named the BabyBrain model). This involved changes in the normal range of values for parameters known to be significantly different in the young. These changes worked surprisingly well, even though the parameters were chosen for their biological importance (as was done with earlier adaptations) and not necessarily for their calculated influence. The model was employed in simulating events in NIRS measurements from term neonates with hypoxic-ischaemic encephalopathy. Three neonates with different severities of encephalopathy were investigated. The neonates displayed different variations in $\Delta oxCCO$. Neonate 1 displayed a decrease in $\Delta oxCCO$ not corresponding to the event, which was not well predicted by the model, as it simulated event-related responses. Neonate 2 showed a slight increase in $\Delta oxCCO$, an unusual response to a drop in oxygenation. Neonate 3, the most severe case, displayed a significant drop in response to the event, which was well simulated by the model. Event-related changes in intracellular pH in Neonate 2 are also predicted, suggesting an acidic

drop in both cytoplasmic and mitochondrial pH, followed by an acidic drop in the mitochondrial pH while cytoplasmic pH returns to baseline. Taking into account the earlier results from the piglet experiments, this indicates that mitochondrial pH may indeed fluctuate very differently to that in the cytoplasm, and that its role in influential cellular mechanisms must be scrutinised in more detail.

The next chapter covered the adaptation of the adult BrainSignals model to the human preterm neonate brain. Preterm neonate physiology is slightly different to the term, with values further away from adult values in most cases. The adapted BrainSignals model was subsequently used to simulate NIRS data from two published functional activation studies that reported different responses in the preterm brain. Roche-Labarbe et al. (2014) observed a decrease in $\Delta H H b$ in preterm neonates in response to a somatosensory stimulus, contrary to the established normal response in the adult which involves an increase in $\Delta H H b$. Kozberg et al. (2013) conducted the study in age-equivalent rats and observed an increase in $\Delta H H b$ in some and a decrease in others. The model was able to simulate a decrease in $\Delta H H b$, except in the presence of vasoconstriction as was observed in Kozberg et al. (2013). The BrainSignals preterm model was also used to simulate changes observed in a neonatal NIRS study conducted by a collaborating group at University Hospital Zurich, using a visual stimulus. Here the two subjects displayed opposite responses, and the model was able to simulate the increase in $\Delta H H b$ by keeping CBF constant. These results collectively point to the differing role of autoregulation in developing infants, the extent of which has not yet been determined. The physiology of preterm infants varies greatly. The development of preterm neonates is also not synonymous with that of term neonates, even though their actual ages may be equivalent. This makes it more difficult to characterise preterm neonatal health.

The models presented in this thesis are quite large, complex models, necessarily so because of the physiological approach taken in building them. Each development and extension was born from the emergence of new research interests in different aspects of cerebral physiology, and not from the mathematical or computational bearings of such additions. That is, model development has so far given priority and importance to the biological phenomena, while the mathematical and computational implications of such

developments, such as increases in complexity and possible error, were secondary and/or considered unavoidable.

As is typical for systems biology models, many of the model parameters are poorly defined in literature, often due to technical limitations, while some do not represent a measurable physical property. In the case of neonatal patients, many of these values are also based on studies of infants who are not in their best health. Sensitivity analysis results have consistently shown that for most model variables, the majority of parameters exert very little influence on model output. The upside here is that these inaccuracies have little impact on model behaviour. If so, however, what then is the parameter's function? Such parameters therefore form part of *physiological window dressing* - parameters which do not offer much function other than to ornament for apparent biological validation. Thus the supposed biological complexity here is simply a smokescreen, masking the real drivers of a dynamical system. Model simplification is therefore paramount to the continued effectiveness and applicability of such models. However, in physiological models it is difficult to contrive a simplified, estimated system, without first considering the more detailed, complex one. Hence, the path to model simplification must inevitably be a two step process, that starts with the formulation of an unsimplified model, more concerned with biological relevance and less with efficiency.

The current models do not incorporate the ability to simulate irreversible injury such as cell death. Thus, in patients with severe injuries, or where the time course being simulated includes a severe insult (such as the hypoxia-ischaemia insults), this must be taken into account. The model also has no spatial characteristics at present. However, it is feasible that several units of the model could be connected in a three-dimensional mesh to create a spatial representation of the brain, such as in Orłowski et al. (2013).

The models presented in this thesis have provided an insight into the physiological basis of cerebral activity observed in a number of different studies, conducted in both humans and animals. They have facilitated a look into the workings of a complex cellular network that generates changes observed in clinical measurements and ultimately governs patient health. The models are thus instruments that assist by aggregating and augmenting clinical data, for improved understanding and therefore a clearer resolution on patient treatment and outcome.

9.1 Future work

9.1.1 Blood pH

The model extensions focused on improving intracellular pH. However, changes in blood pH are more commonly measured in clinical settings and also affect cerebral metabolism. Changes in pH alter the affinity of haemoglobin to bind oxygen, with a higher affinity at more acidic levels (Bohr effect). This is likely to have an impact on intracellular metabolism, but does require a significant model extension, leading to more variables and parameters and the issues of increased complexity.

9.1.2 Model simplification

The group's recent work in the modelling domain has turned to model simplification, starting with the BrainSignals model (Caldwell et al. 2015). To start the process with the simplest model in the series may not perhaps seem to be an intuitive choice, however it is therefore also the easiest to tackle. This effort has focused on reducing the model, by removing superfluous elements and substituting model relationships with approximate functions.

Figures 9.1 and 9.2 illustrate the simplification of the metabolic submodel, and the results of simulating data from adult hypercapnia experiments using the simplified model variations and the original submodel. It is clear that the simplification has preserved the capacity of the model to simulate such variations very well (Caldwell et al. 2015).

Copyright material removed.

Figure 9.1: BrainSignals model simplification. The complete metabolic submodel with parameters omitted (A), and progressively reduced variants (B,C,D,E) (Caldwell et al. 2015)

This work has so far been tested with clinical data from healthy patients. However, it is the physiology of critically ill patients that will be a much greater challenge for the reduced model.

Copyright material removed.

Figure 9.2: BrainSignals model simplification. (A) Steady state simulations for three variants compared with the original metabolic submodel. (B) Simulations of data from human adult hypercapnia experiments. (Caldwell et al. 2015)

9.1.3 Model optimisation

Biological parameters must be optimised for each patient, especially in a simplified model system. While a couple of sensitivity analysis and optimisation methods have been explored in this thesis and in the group's past work, it is apparent that better, more efficient methods would be beneficial. For example, a variance-based global sensitivity analysis method – Extended Fourier Amplitude Sensitivity Test (eFAST) – has been suggested as a possible alternative to the Morris method that is currently used by the group (Saltelli et al. 1999). It is suggested that eFAST maybe more capable of handling the large number of model parameters.

9.1.4 Simulation of electrical activity

Electroencephalography (EEG) measurements are often recorded alongside NIRS at the bedside. This combination of measurement techniques has recently been used to investigate neonatal seizures, which are currently poorly classified and associated with poor neurodevelopmental outcomes. Changes in blood volume and oxygenation have been found to correlate with electrographic events (Singh et al. 2014; Cooper et al. 2011).

The current UCL cerebral metabolism models do not incorporate the electrical activity of the cell. Such additions would allow the simulation of neonatal seizures, further enhancing the capacity of the model. However, as discussed above, some simplifications maybe required to make these developments feasible.

9.1.5 Simulations of clinical treatments

Many of the clinical procedures used to alleviate the effects of brain injury aim to inhibit select metabolic activity. For example, therapeutic hypother-

mia has been proven to be an effective treatment to better the outcomes of hypoxia-ischaemia in certain cases, when administered in the first 24 h to reduce cerebral metabolic activity (Austin et al. 2013; Lobo et al. 2013; Robertson et al. 2008). However, the physiological underpinnings of this process are not well understood. It is quite feasible that the model could be applied to investigate such treatments, by using long-term continuous data from the patient.

9.2 Impact

The newborn is a delicate and vulnerable patient. Injury to the brain can be life-threatening or have severe life-long consequences. The impact on the individual is immense, and on their families immeasurable. The wider impact on society, both socially and economically, is extensive.

Therefore, therapies that can improve the quality of life, to any degree, are of vital importance. Mathematical and computational modelling are avenues to explore and assess the mechanisms of such injuries, and the response to clinical interventions. They help shape our understanding of experimental results and by simulating possible treatments, improve our likelihood of success. In a world where the amount of clinical data collected becomes unmanageable, such models can bring together a wide range of linked information and translate them into actionable insights. Today, they are an almost necessary precursor to the development of effective evidence-based clinical strategies that can be introduced at the bedside.

Appendix A

Model definitions

A.1 BrainSignals

A.1.1 Overview

- 9 differential state variables
- 3 algebraic state variables
- 52 intermediate variables
- 213 parameters

A.1.2 Differential equations

$$\frac{d\text{Cu}_{A,o}}{dt} = 4f_2 - 4f_1 \quad (\text{A.1})$$

$$\frac{d\text{a}3_r}{dt} = 4f_2 - 4f_3 \quad (\text{A.2})$$

$$\frac{d\Delta\Psi}{dt} = \frac{p_2 f_2 + p_1 f_1 + p_3 f_3 - L}{C_{im}} \quad (\text{A.3})$$

$$\frac{d\text{H}_m^+}{dt} = \frac{1}{R_{Hi}} L - \frac{p_3}{R_{Hi}} f_3 - \frac{p_1}{R_{Hi}} f_1 - \frac{p_2}{R_{Hi}} f_2 \quad (\text{A.4})$$

$$\frac{d[\text{O}_2]}{dt} = \frac{1}{\text{CBF}_n} J_{\text{O}_2} - f_3 \quad (\text{A.5})$$

$$\frac{dv_c}{dt} = \frac{1}{v_{u,n}} (\text{PaCO}_2 - v_c) \quad (\text{A.6})$$

$$\frac{dv_o}{dt} = \frac{1}{v_{u,n}} ([\text{O}_{2,c}] - v_o) \quad (\text{A.7})$$

$$\frac{dv_p}{dt} = \frac{1}{v_{u,n}} (P_a - v_p) \quad (\text{A.8})$$

$$\frac{dv_u}{dt} = \frac{1}{v_{u,n}} (\text{CBF} - v_u) \quad (\text{A.9})$$

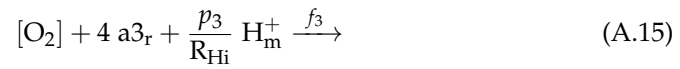
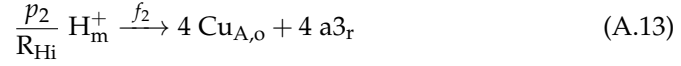
A.1.3 Algebraic equations

$$[\text{O}_{2,c,\text{init}}] \left(\frac{\text{ScO}_2}{1 - \text{ScO}_2} \right)^{\frac{1}{n_h}} - [\text{O}_{2,c}] = 0 \quad (\text{A.10})$$

$$T_e + T_m - (P_1 - P_{ic}) r = 0 \quad (\text{A.11})$$

$$\text{CBF} ([\text{HbO}_{2,a}] - [\text{HbO}_{2,v}]) - J_{\text{O}_2} = 0 \quad (\text{A.12})$$

A.1.4 Chemical reactions



A.1.5 State variables

Symbol	Units	Initialiser	Notes
$\text{Cu}_{A,o}$	mM l^{-1}	$\text{Cu}_{A,o,init}$	The concentration of oxidised cytochrome-c-oxidase
$a3_r$	mM l^{-1}	$a3_{r,init}$	Concentration of reduced cyt a3 in mitochondria
$\Delta\Psi$	mV	$\Delta\Psi_{init}$	Mitochondrial inner membrane potential
H_m^+	mM l^{-1}	$\text{H}_{m,init}^+$	Concentration of hydrogen ions in mitochondria
$[\text{O}_2]$	mM l^{-1}	$\text{O}_{2,init}$	The concentration of oxygen in the mitochondria
$[\text{O}_{2,c}]$	mM l^{-1}	$[\text{O}_{2,c,init}]$	The concentration of oxygen in the capillary.
r	cm	r_{init}	Typical radius of cerebral vessels
v_c	mM l^{-1}	$v_{\text{CO}_2,n}$	CO_2 passed through a first order filter.
v_o	mM l^{-1}	$v_{\text{O}_2,n}$	capillary O_2 passed through a first order filter.
v_p	mmHg	$v_{P_a,n}$	Arterial blood pressure passed through a first order filter.
v_u	dimensionless	$v_{u,n}$	The demand parameter u passed through a first order filter.
$[\text{HbO}_{2,v}]$	mM l^{-1}	$[\text{HbO}_{2,v,init}]$	The concentration of bound oxygen in the veins.

A.1.6 Intermediate variables

Symbol	Units	Expression	Notes
$\text{Cu}_{A,o}$	mM l^{-1}	$\mathcal{E}_0(\text{cyt } a_3) - \text{Cu}_{A,o}$	The concentration of reduced cytochrome-c-oxidase in the mitochondria.
AVR	dimensionless	$\frac{\text{Vol}_{\text{art}}}{\text{Vol}_{\text{ven}}}$	Arterio-venous volume ratio
a_3_o	mM l^{-1}	$\mathcal{E}_0(\text{cyt } a_3) - a_3_r$	Concentration of oxidised cyt a3 in mitochondria
C_{0i}	dimensionless	$\frac{10^{-\text{pH}_m} - 10^{-\text{pH}_m - \text{dpH}}}{\text{dpH}}$	Natural buffering capacity for protons in mitochondria
CBF	m l blood^{-1} $\text{m l tissue}^{-1} \text{ s}^{-1}$	$G (P_a - P_v)$	Cerebral blood flow
CBF_{norm}	dimensionless	$\frac{\text{CBF}}{\text{CBF}_n}$	
Δ_{oxCCO}	$\mu\text{M l}^{-1}$ (brain tissue)	$\Delta_{\text{oxCCO}}_{\text{offset}} + 1000\text{CBF}_n (\text{Cu}_{A,o} - \text{VArat}_n)$	The expected CCO signal (as measured by NIRS)
CMRO_2	mM O_2 l^{-1} (brain tissue) s^{-1}	$f_3 \text{CBF}_n$	Cerebral metabolic rate for oxygen
ΔG_1	mV	$p_1 \Delta p - 4 \left(E_1 + \mathcal{E}_0(\text{cyt } a_3) \log_{10} \left(\frac{\text{Cu}_{A,o}}{\text{Cu}_{A,o}} \right) \right)$	Free energy associated with reaction 1
ΔG_2	mV	$p_2 \Delta p - 4 \left(E_2 + \mathcal{E}_0(\text{cyt } a_3) \left(\log_{10} \left(\frac{\text{Cu}_{A,o}}{\text{Cu}_{A,o}} \right) - \log_{10} \left(\frac{a_3_r}{a_3_o} \right) \right) \right)$	Free energy associated with reaction 2
DHbdiff	dimensionless	$\text{DHbdiff}_{\text{offset}} + \Delta \text{HbO}_2 - \Delta \text{HHb}$	

ΔHbO_2	μMl^{-1} (brain tissue)	$DHbO_{2,offset} + \text{HbO}_2 - \text{HbO}_{2n}$	Change in total oxygenated haemoglobin (NIRS)
ΔHbt	μMl^{-1} (brain tissue)	$DHbT_{offset} + \text{Hbt} - \text{Hbt}_n$	Change in total haemoglobin (NIRS)
ΔHHb	μMl^{-1} (brain tissue)	$DHHb_{offset} + \text{HHb} - \text{HHb}_n$	Change in total deoxygenated haemoglobin (NIRS)
Δp	mV	$\Delta\Psi + \mathcal{E}_0(\text{cyt } a_3) (\text{pH}_m - \text{pH}_o)$	The proton motive force across the mitochondrial inner membrane.
η	dimensionless	$R_P \left(\frac{v_p}{v_{P_{a,n}}} - 1 \right) + R_O \left(\frac{v_o}{v_{O_{2,n}}} - 1 \right) + R_u \left(1 - \frac{v_u}{v_{u,n}} \right) + R_C \left(1 - \frac{v_c}{v_{CO_{2,n}}} \right)$	Total autoregulatory stimuli
f_1	$\text{mMl}^{-1} \text{s}^{-1}$	$k_1 \text{Cu}_{A,o} - k_{-1} \text{Cu}_{A,o}$	The rate at which CuA is reduced
f_2	$\text{mMl}^{-1} \text{s}^{-1}$	$k_2 \text{Cu}_{A,o} a_{3o} - k_{-2} \text{Cu}_{A,o} a_{3r}$	The rate at which CuA is oxidised and cyt a3 reduced.
f_3	$\text{mMl}^{-1} \text{s}^{-1}$	$\frac{k_{3,0} [\text{O}_2] a_{3r} \exp(-c_3 (\Delta p - \Delta p_{30}))}{1 + \exp(-c_3 (\Delta p - \Delta p_{30}))}$	The rate at which cyt a3 is oxidised
G	mmHg	$R_u r^4$	Resistance of cerebral circulation
h	cm	$(r r + 2r_0 h_0 + h_0 h_0)^{\frac{1}{2}} - r$	Wall thickness of cerebral vessels
HbO_2	μMl^{-1} (brain tissue)	$\frac{\text{Vol}_{art} [\text{HbO}_{2,a}] + \text{Vol}_{ven} [\text{HbO}_{2,v}]}{4} \text{Vol}_{blood,n} \times 1000$	Total oxygenated haemoglobin (NIRS)
Hbt	μMl^{-1} (brain tissue)	$\frac{(\text{Vol}_{art} + \text{Vol}_{ven}) [\text{HbO}_{2,a,n}]}{4} \text{Vol}_{blood,n} \times 1000$	Total haemoglobin (NIRS)
HHb	μMl^{-1} (brain tissue)	$\frac{\text{Vol}_{art} [\text{Hb}_a] + \text{Vol}_{ven} [\text{Hb}_v]}{4} \text{Vol}_{blood,n} \times 1000$	Total deoxygenated haemoglobin (NIRS)

J_{O_2}	m MO_2 $\text{l}^{-1}(\text{brain tissue}) \text{ s}^{-1}$	$(1 - J_{O_2,swtch}) J_{O_2} + J_{O_2,swtch} J_{O_2smth}$	The rate at which oxygen is supplied to the mitochondria.
J_{O_2}	dimensionless	$f_{\min}(D_{O_2} ([O_{2,c}] - [O_2]), \text{CBF} [\text{HbO}_{2,a}])$	
J_{O_2smth}	dimensionless	$-\frac{1}{2} \left((D_{O_2} ([O_{2,c}] - [O_2]) - \text{CBF} [\text{HbO}_{2,a}])^2 + e p s^2 \right)^{\frac{1}{2}}$ $-\frac{1}{2} D_{O_2} ([O_{2,c}] - [O_2]) + \frac{3}{2} \text{CBF} [\text{HbO}_{2,a}]$	
k_1	s^{-1}	$k_{1,0} \exp(-c_{k1} (\Delta p - \text{SaO}_{2n}))$	Forward rate constant for reaction 1
k_2	$\text{m}^{-1} \text{M s}^{-1}$	$k_{2,n} \exp(-c_{k2} (\Delta p - \text{SaO}_{2n}))$	Forward rate constant for reaction 2
Keq_1	dimensionless	$10^{\frac{-1}{\varepsilon_0(\text{cyta}_3)} \left(\frac{p_1 \Delta p}{4} - E_1 \right)}$	Equilibrium constant for reaction 1
Keq_2	dimensionless	$10^{\frac{-1}{\varepsilon_0(\text{cyta}_3)} \left(\frac{p_2 \Delta p}{4} - E_2 \right)}$	Equilibrium constant for reaction 2
k_{-1}	s^{-1}	$\frac{k_1}{\text{Keq}_1}$	Backward rate constant for reaction 1
k_{-2}	$\text{m}^{-1} \text{M s}^{-1}$	$\frac{k_2}{\text{Keq}_2}$	Backward rate constant for reaction 2
L	$\text{m M l}^{-1} \text{ s}^{-1}$	$L_{CV} + L_{lk}$	The rate at which protons reenter the mitochondrial matrix
L_{CV}	$\text{m M l}^{-1} \text{ s}^{-1}$	$\frac{L_{CV,frac} L_{CV,max} (1 - \exp(-\theta))}{1 + r_{CV} \exp(-\theta)}$	The rate at which protons reenter the mitochondrial matrix associated with ADP phosphorylation
L_{lk}	$\text{m M l}^{-1} \text{ s}^{-1}$	$\Delta p_{3,corr} f_n (\exp(\Delta p f_n) - 1)$	The rate at which protons reenter the mitochondrial matrix through leak channels
μ	dimensionless	$\frac{\mu_{\min} + \mu_{\max} \exp(\eta)}{1 + \exp(\eta)}$	Total autoregulatory stimuli filtered through sigmoidal function

pH_m	<i>pH units</i>	$-\log_{10} \left(\frac{H_m^+}{1000} \right)$	Mitochondrial pH
$r_{buf fi}$	dimensionless	$\frac{C_{buf fi}}{C_{0i}}$	Buffering capacity for protons in mitochondria
R_{Hi}	dimensionless	$\frac{r_{buf fi}}{S_aO_2 + S_vO_2}$	Relative mitochondrial volume for protons
S_{CO_2}	dimensionless	$\frac{2}{\sigma_e} \left(\exp \left(\frac{K_\sigma (r - r_0)}{r_0} \right) - 1 \right) - \sigma_{coll}$	Capillary oxygen saturation
σ_e	mmHg	$\frac{[HbO_{2,v}]}{[HbO_{2,a,n}]}$	Elastic stress in vessel walls
S_vO_2	dimensionless	$\sigma_e h$	Venous oxygen saturation
T_e	mmHg cm	$T_{max} \exp \left(- \left \frac{r - r_m}{r_t - r_m} \right ^{n_m} \right)$	Elastic tension in vessel walls
T_m	mmHg cm	$T_{max0} (1 + T_{e,n} \mu)$	Muscular tension in vessel walls
T_{max}	mmHg cm	$k_{CV} (\Delta p + \mathcal{E}_0(\text{cyt a}_3) \log_{10}(\text{CBF}) - L_{CV,max})$	Maximum muscular tension developed by circulation
θ	dimensionless	$100 \left(\frac{\left(\frac{r}{[Hbtot_c]} \right)^2 [HbO_{2,a}] + \frac{Vol_{ven}}{Vol_{art,n}} [HbO_{2,v}]}{\left(\frac{r}{[Hbtot_c]} \right)^2 + \frac{Vol_{ven}}{Vol_{art,n}}} \right)$	Driving force for complex V
TOS	dimensionless	$\frac{[HbO_{2,a,n}]}{[HbO_{2,a,n}]}$	Tissue Oxygenation index.
V_{mca}	$m \text{ l blood}^{-1}$ $m \text{ l tissue}^{-1} s^{-1}$	$CBF CBF_{scale}$	Blood velocity in the middle cerebral artery
Vol_{art}	dimensionless	$Vol_{art,n} \left(\frac{r}{[Hbtot_c]} \right)^2$	Arterial blood volume as a fraction of normal total blood volume
Vol_{tot}	dimensionless	$Vol_{art} + Vol_{ven}$	Normalised total blood volume

$[\text{Hb}_v]$	m M l^{-1}	$[\text{HbO}_{2,a,n}] - [\text{HbO}_{2,v}]$	The concentration of deoxyhaemoglobin in the veins.
-----------------	---------------------	---	---

A.1.7 Parameters

Symbol	Units	Initialiser	Notes
VARat_n	dimensionless	0.8	Normal oxidised fraction of CuA
$\text{CuA}_{o,\text{init}}$	m M l^{-1}	VARat_n	Initial oxidized CuA
VARat_n	m M l^{-1}	$\mathcal{E}_0(\text{cyt a}_3) \text{VARat}_n$	Normal oxidized CuA
$\text{CuA}_{a,o,n}$	m M l^{-1}	$\mathcal{E}_0(\text{cyt a}_3) - \text{VARat}_n$	The resting amount of reduced cytochrome-c-oxidase
$\text{a3}_{\text{frac},n}$	dimensionless	$1 - \frac{\text{a3}_{r,n}}{\mathcal{E}_0(\text{cyt a}_3)}$	Normal oxidised fraction of cyt a3
$\text{a3}_{o,\text{init}}$	m M l^{-1}	$\text{a3}_{o,n}$	Initial oxidised cytochrome a3
$\text{a3}_{o,n}$	m M l^{-1}	$\mathcal{E}_0(\text{cyt a}_3) - \text{a3}_{r,n}$	Normal oxidised cytochrome a3
$\text{Vol}_{\text{blood},n}$	dimensionless	0.04	Normal blood volume as a fraction of brain tissue volume
$\text{a3}_{r,\text{init}}$	m M l^{-1}	$\text{a3}_{r,n}$	Initial reduced cytochrome a3
$\text{a3}_{r,n}$	m M l^{-1}	$\frac{\frac{f_n}{k_{3,0}}}{\text{PaCO}_{2n}} \frac{\exp(-c3(\text{SaO}_{2n} - \Delta p_{30}))}{1 + \exp(-c3(\text{SaO}_{2n} - \Delta p_{30}))}$	Normal reduced cytochrome a3
$c3$	dimensionless	0.11	Parameter controlling the sensitivity of reaction 3 to PMF
$C_{\text{buf}fi}$	dimensionless	0.022	Buffering capacity for protons in mitochondria

C_{im}	$mmol/L/mV$	0.00675	Capacitance of mitochondrial inner membrane
C_{NADH}	mV	$C_{NADH,n}$	Redox potential minus standard redox potential for NADH at normal demand
$C_{NADH,n}$	mV	$\frac{\mathcal{E}_0(\text{cyt } a_3)}{2} \log_{10} \left(\frac{1}{N_{rat,n}} \right)$	Normal value of C_{NADH}
CBF_n	$m \text{ l blood}^{-1}$ $m \text{ l tissue}^{-1} s^{-1}$	0.0125	Normal cerebral blood flow
CBF_{scale}	dimensionless	5000	
$\Delta \text{oxCCO}_{offset}$	$m M^{-1}$	0	An arbitrary baseline offset to the CCO signal
c_{k1}	dimensionless	0.01	Parameter controlling sensitivity of k1 to PMF
c_{k2}	dimensionless	0.02	Parameter controlling sensitivity of k2 to PMF
$CMRO2_n$	$m \text{ l blood}^{-1}$ $m \text{ l tissue}^{-1} s^{-1}$	0.034	The resting CMRO2.
$L_{CV,frac}$	dimensionless	1	A control parameter representing the action of complex V inhibitors
$[CCO]_{mit}$	$m M^{-1}$	0	Concentration of cytochrome c oxidase in mitochondria
cytox_{tis}	$m M^{-1}$	0.0055	Concentration of cytochrome c oxidase in tissue
D_{NADH}	dimensionless	0.01	$D_{NADH} * Z$ is the change in NADH redox potential for a ten-fold increase in u

D_{O_2}	s^{-1}	$\frac{R_u}{[O_{2,c,n}] - PaCO_{2n}}$	Diffusion rate between capillaries and mitochondria.
$\Delta G_{1,n}$	m V	$p_1 SaO_{2n} - 4 \left(E_{1,n} + \mathcal{E}_0(\text{cyt } a_3) \log_{10} \left(\frac{VA_{rat_n}}{Cu_{A,o,n}} \right) \right)$	Normal free energy associated with reaction 1
$\Delta G_{2,n}$	m V	$p_2 SaO_{2n} - 4 \left(E_2 + \mathcal{E}_0(\text{cyt } a_3) \left(\log_{10} \left(\frac{Cu_{A,o,n}}{VA_{rat_n}} \right) + \log_{10} \left(\frac{a_{3o,n}^3}{a_{3r,n}^3} \right) \right) \right)$	Normal free energy associated with reaction 2
$DHbdiff_{offset}$	dimensionless	0	An arbitrary baseline offset to the signal
$DHbO_{2,offset}$	dimensionless	0	An arbitrary baseline offset to the signal
$DHbT_{offset}$	dimensionless	0	An arbitrary baseline offset to the signal
$DHHb_{offset}$	dimensionless	0	An arbitrary baseline offset to the signal
$\Delta p_{3,corr}$	m V	-25	Dp_{30} minus normal PMF
Δp_{30}	m V	$\Delta p_n + \Delta p_{3,corr}$	Value of PMF at which reaction 3 is maximally sensitive to PMF
$L_{CV,max}$	m V	90	A constant in the rate of complex V
Δp_n	m V	$\Delta \Psi_n + \mathcal{E}_0(\text{cyt } a_3) \Delta pH_n$	The resting value of the proton motive force.
dpH	dimensionless	0.001	A constant in the buffering relationship
ΔpH_n	dimensionless	$pH_{m,n} - pH_{o,n}$	The resting value of pH difference across mitochondrial inner membrane
$\Delta \Psi_{init}$	m V	$\Delta \Psi_n$	Initial value of mitochondrial inner membrane potential
$\Delta \Psi_n$	m V	145	Normal mitochondrial inner membrane potential
$E_{1,NADH}$	m V	$\mathcal{E}_0(Cu_A) - \mathcal{E}_0(NADH) + C_{NADH}$	E_1 when the reducing substrate is NADH
$E_{1,NADH,n}$	m V	$\mathcal{E}_0(Cu_A) - \mathcal{E}_0(NADH) + C_{NADH,n}$	Normal value of E_{1NADH}

E_1	m V	$E_{1,NADH}$	The energy provided by electron transfer to CuA
$E_{1,n}$	m V	$E_{1,NADH,n}$	The normal energy provided by electron transfer to CuA
E_2	m V	$\mathcal{E}_0(\text{cyt a}_3) - \mathcal{E}_0(\text{Cu}_A)$	The energy provided by transfer of four electrons from CuA to to cyt a3
$\mathcal{E}_0(\text{cyt a}_3)$	m V	350	Cyt a3 standard redox potential
$\mathcal{E}_0(\text{Cu}_A)$	m V	247	CuA standard redox potential
$\mathcal{E}_0(\text{NADH})$	m V	-320	NADH standard redox potential
f_n	$\text{m M l}^{-1} \text{ s}^{-1}$	$\frac{\text{CBF}_n}{\text{CBF}_n}$	Normal resting rate of f1 and f2.
G_n	/mmHg/s	$\frac{\text{CBF}_n}{P_a - P_{v,n}}$	Normal resistance of cerebral circulation
h_0	cm	0.003	Vascular wall thickness when radius is r_0
$\text{H}_{m,\text{init}}^+$	m M l^{-1}	$\text{H}_{m,n}^+$	Initial hydrogen ion concentration in mitochondria
h_n	cm	$([\text{Hbtot}_c] [\text{Hbtot}_c] + 2r_0 h_0 + h_0 h_0)^{\frac{1}{2}} - [\text{Hbtot}_c]$	Normal wall thickness of cerebral vessels
$\text{H}_{m,n}^+$	m M l^{-1}	$10^{3-p\text{H}_{m,n}}$	Normal hydrogen ion concentration in mitochondria
$\text{HbO}_{2,n}$	$\mu\text{M l}^{-1}$ (brain tissue)	$\frac{\text{Vol}_{\text{art},n} [\text{HbO}_{2,a}] + \text{Vol}_{\text{ven}} [\text{HbO}_{2,v,n}]}{4} \text{Vol}_{\text{blood},n} \times 1000$	Normal total oxygenated haemoglobin (NIRS)
Hbt_n	$\mu\text{M l}^{-1}$ (brain tissue)	$\frac{(\text{Vol}_{\text{art},n} + \text{Vol}_{\text{ven}}) [\text{Hbtot}_n]}{4} \text{Vol}_{\text{blood},n} \times 1000$	Normal total haemoglobin (NIRS)
HHb_n	$\mu\text{M l}^{-1}$ (brain tissue)	$\frac{\text{Vol}_{\text{art},n} [\text{Hb}_a] + \text{Vol}_{\text{ven}} [\text{Hb}_{v,n}]}{4} \text{Vol}_{\text{blood},n} \times 1000$	Normal total deoxygenated haemoglobin (NIRS)

$k_{1,0}$	s^{-1}	$\frac{k_{1,n}NADH}{NADH_n}$	Forward rate constant for reaction 1 at normal PMF
$k_{1,n}$	s^{-1}	$\frac{f_n}{VArat_n - \frac{1}{K_{eq1,n}} Cu_{A,o,n}}$	The value of k_1 at normal Δp and NADH
$k_{2,n}$	$m^{-1} Ms^{-1}$	$\frac{f_n}{Cu_{A,o,n} a_{3o,n} - \frac{1}{K_{eq2,n}} VArat_n a_{3r,n}}$	Normal forward rate constant for reaction 2
$k_{3,0}$	$m^{-1} Ms^{-1}$	$2.5E + 5$	An apparent second-order rate constant for reaction 3 at zero PMF
$T_{e,n}$	dimensionless	1	Control parameter allowing destruction of autoregulation
K_G	dimensionless	$\frac{G_n}{[Hbtot_c]^4}$	Constant of proportionality relating pressure drop to flow
f_n	mV	0.038	Second constant controlling rate of L_{lk} of Dp.
K_σ	mmHg	10	Parameter controlling sensitivity of σ_e to radius
$\Delta p_{3,corr}$	dimensionless	1	Parameter representing the action of uncouplers
k_{CV}	mV	$\frac{-1}{Dp_n - Dp_C V0} \log\left(\frac{1 - L_C V0}{1 + r_C V L_C V0}\right)$	Parameter controlling the sensitivity of complex V flux to driving force
$K_{eq1,n}$	dimensionless	$10^{\frac{-1}{E_0(cyt a_3)} \left(\frac{p_1 SaO_{2n}}{4} - E_{1,n}\right)}$	Normal equilibrium constant for reaction 1
$K_{eq2,n}$	dimensionless	$10^{\frac{-1}{E_0(cyt a_3)} \left(\frac{p_2 SaO_{2n}}{4} - E_2\right)}$	Normal equilibrium constant for reaction 2
$k_{-1,0}$	s^{-1}	$\frac{f_n}{K_{eq1,n} VArat_n - Cu_{A,o,n}}$	Backward rate constant for reaction 1 at normal PMF

$k_{-2,n}$	$m^{-1} Ms^{-1}$	$\frac{f_n}{K_{eq2,n} Cu_{A,o,n} a_{3o,n} - V_{Arat_n} a_{3r,n}}$	Normal backward rate constant for reaction 2
$L_{CV,0}$	dimensionless	0.4	Normal complex V flux as a fraction of maximum possible flux
$L_{CV,frac}$	dimensionless	$1 - L_{lk,frac}$	Normal fraction of proton entry into mitochondria associated with ADP phosphorylation
$L_{CV,max}$	$mM^{-1} s^{-1}$	$\frac{L_C V_n}{L_C V_0}$	The maximum rate of proton flow through complex V.
$L_{CV,n}$	mV/s	$L_n L_{CV,frac}$	The resting flow of protons into the matrix through complex V
f_n	mV/s	$\frac{CBF_n}{\exp(SaO_{2n} f_n) - 1}$	First constant controlling rate of L_{lk} of Dp.
$L_{lk,frac}$	dimensionless	0.25	Normal fraction of proton entry into mitochondria which is via leak channels
$L_{lk,n}$	mV/s	$L_n L_{lk,frac}$	The resting flow of protons into the matrix via leak channels.
L_n	mV/s	$p_{tot} f_n$	The total flow of protons back into mitochondria
μ_{max}	dimensionless	1	Maximum value of mu
μ_{min}	dimensionless	-1	Minimum value of mu
μ_n	dimensionless	0	Normal value of mu
n_h	dimensionless	2.5	Hill coefficient for haemoglobin saturation
n_m	dimensionless	1.83	Exponent in the muscular tension relationship

$NADH_n$	$m M l^{-1}$	$\frac{N_t}{1 + N_{rat,n}}$	Normal mitochondrial NADH concentration
$N_{rat,n}$	dimensionless	9	Normal NAD/NADH ratio
N_t	$m M l^{-1}$	3	Total mitochondrial NAD + NADH concentration
$O_{2,init}$	$m M l^{-1}$	0.024	Normal oxygen concentration in mitochondria.
$[O_{2,a}]$	$m M l^{-1}$	$\phi \left(\frac{SaO_2sup}{1 - SaO_2sup} \right)^{\frac{1}{n_h}}$	Arterial dissolved oxygen concentration
$[O_{2,c,init}]$	$m M l^{-1}$	$[O_{2,c,n}]$	Initial concentration of dissolved oxygen in the capillary.
$[O_{2,c,n}]$	$m M l^{-1}$	$[O_{2,c,init}] \left(\frac{ScO_2n}{1 - ScO_2n} \right)^{\frac{1}{n_h}}$	Normal concentration of dissolved oxygen in the capillary.
p_1	dimensionless	$p_{tot} - p_{23}$	The number of protons pumped by a_{red} (reduction reaction)
p_2	dimensionless	4	Total protons pumped by reaction 2
p_{23}	dimensionless	8	Total protons pumped by reactions 2 and 3
p_3	dimensionless	$p_{23} - p_2$	Total protons pumped by reaction 3
P_1	mmHg	$\frac{P_a + P_v}{2}$	Average blood pressure in vessels
$P_{1,n}$	mmHg	$\frac{P_{a,n} + P_{v,n}}{2}$	Normal average blood pressure in vessels
P_a	mmHg	100	Arterial blood pressure
p_{C1}	dimensionless	8	Total protons pumped by complex 1
p_{C3}	dimensionless	4	Total protons pumped by complex 3
P_{ic}	mmHg	9.5	Intracranial blood pressure

$P_{ic,n}$	mmHg	9.5	Normal intracranial blood pressure
p_{tot}	dimensionless	20	Total protons pumped by reactions 1, 2 and 3
P_v	mmHg	4	Venous blood pressure
$P_{v,n}$	mmHg	4	Normal venous blood pressure
PaCO ₂	mmHg	40	Arterial partial pressure of CO ₂
PaCO _{2,n}	mmHg	40	Normal arterial partial pressure of CO ₂
pH _{m,n}	<i>pHunits</i>	7.4	Normal mitochondrial pH
pH _o	<i>pHunits</i>	7	Extra-mitochondrial pH
pH _{o,n}	<i>pHunits</i>	7	Normal extra-mitochondrial pH
ϕ	m M ⁻¹	0.036	Value of O ₂ at half maximal saturation
r_0	cm	0.0126	A special radius in the elastic tension relationship
R_C	dimensionless	2.2	Parameter controlling sensitivity of eta to arterial CO ₂
R_O	dimensionless	1.5	Parameter controlling sensitivity of eta to arterial O ₂
R_P	dimensionless	4	Parameter controlling sensitivity of eta to arterial pressure
R_u	dimensionless	0.5	Parameter controlling sensitivity of eta to u
r_{CV}	dimensionless	5	Parameter controlling the ratio of maximal to minimal rates of oxidative phosphorylation
r_m	cm	0.027	Value of vessel radius giving maximum muscular tension

r_n	cm	0.0187	Normal radius of blood vessels normal radius of blood vessels
r_t	cm	0.018	Parameter in the muscular tension relationship
SaO_{2n}	dimensionless	0.96	Normal saturation of the arterial haemoglobin
SaO_2	dimensionless	0.96	Saturation of the arterial haemoglobin
ScO_{2n}	dimensionless	$\frac{SaO_{2n} + SvO_{2n}}{2}$	Normal capillary oxygen saturation
σ_{coll}	mmHg	62.79	Value of pressure at which vessels collapse
σ_{e0}	mmHg	0.1425	Parameter in relationship determining σ_e
$\sigma_{e,n}$	mmHg	$\sigma_{e0} \left(\exp \left(\frac{K_\sigma ([Hbtot_c] - r_0)}{r_0} \right) - 1 \right) - \sigma_{coll}$	Normal elastic stress in vessel walls
SvO_{2n}	dimensionless	$\frac{[HbO_{2,v,n}]}{[Hbtot_n]}$	Normal venous oxygen saturation
$v_{u,n}$	dimensionless	5	The time constant associated with v_c
$T_{e,n}$	mmHg cm	$\frac{\sigma_{e,n} h_n}{T_{max,n}}$	Normal elastic tension in vessel walls
T_{max0}	mmHg cm	$1 + T_{e,n} \mu_n$	T_{max} at normal μ
$T_{max,n}$	mmHg cm	$\frac{T_{m,n}}{\exp \left(- \left \frac{[Hbtot_c] - r_m}{r_t - r_m} \right ^{n_m} \right)}$	Normal maximum muscular tension developed by circulation
$T_{m,n}$	mmHg cm	$(P_{1,n} - P_{ic,n}) [Hbtot_c] - T_{e,n}$	Normal muscular tension in vessel walls
$v_{o,n}$	dimensionless	20	The time constant associated with v_o
$v_{p,n}$	dimensionless	5	The time constant associated with v_p
$v_{u,n}$	dimensionless	0.5	the time constant associated with v_u

u	dimensionless	$L_{CV,frac} + (PaCO_2 - PaCO_{2n}) uf$	The representation of "demand" in the model.
u_n	dimensionless	1	Resting "demand"
$u_{\Delta p}$	dimensionless	$\frac{\Delta\Psi_n}{SaO_{2n}}$	Membrane potential as a fraction of total PMF
uf	dimensionless	0	Parameter controlling the effect of $PaCO_{2n}$ on demand
$v_{CO_2,n}$	$m Ml^{-1}$	$PaCO_{2n}$	Normal value of v_c (CO2 passed through a first order filter)
$v_{O_2,n}$	$m Ml^{-1}$	$[O_{2,c,n}]$	Normal value of v_o (capillary O2 passed through a first order filter)
$v_{P_a,n}$	mmHg	P_a	Normal value of v_p (ABP passed through a first order filter)
$v_{u,n}$	dimensionless	u_n	Normal value of v_u (u passed through a first order filter)
$VARat_n$	dimensionless	3	The normal ratio of the volume of the veins to the volume of the arteries
$Vol_{art,n}$	dimensionless	$\frac{Vol_{tot,n}}{1 + VARat_n}$	Normal arterial blood volume as a fraction of total blood volume
Vol_{mit}	dimensionless	0.067	Fraction of brain water which is mitochondria
$Vol_{tot,n}$	dimensionless	1	Normal total blood volume
Vol_{ven}	dimensionless	$Vol_{tot,n} \frac{VARat_n}{1 + VARat_n}$	Venous blood volume as a fraction of total blood volume

$[\text{HbO}_{2,a,n}]$	m M l^{-1}	$[\text{Hbtot}_n] \text{ SaO}_{2n}$	Normal concentration of arterial oxy-haemoglobin.
$[\text{HbO}_{2,v,init}]$	m M l^{-1}	$[\text{HbO}_{2,v,n}]$	Initial concentration of venous oxy-haemoglobin.
$[\text{HbO}_{2,v,n}]$	m M l^{-1}	$\frac{\text{CBF}_n [\text{HbO}_{2,a,n}] - R_u}{\text{CBF}_n}$	Normal concentration of venous oxy-haemoglobin.
$[\text{Hbtot}_n]$	m M l^{-1}	9.1	Normal total haemoglobin concentration in the arteries and veins.
$[\text{Hb}_{v,n}]$	m M l^{-1}	$[\text{Hbtot}_n] - [\text{HbO}_{2,v,n}]$	Normal unsaturated venous haemoglobin
Z	m V	59.028	$2.303 \cdot \text{RT}/\text{F}$

A.2 BrainPiglet v2.0

A.2.1 Overview

- 21 differential state variables
- 3 algebraic state variables
- 95 intermediate variables
- 295 parameters

A.2.2 Differential equations

$$\begin{aligned} \frac{d[\text{ADP}]}{dt} = & (k_{\text{PCr}}^- + [\text{ATP}] [\text{Cr}]) - 2 (k_{\text{AK}} + [\text{ADP}]^2) - (k_{\text{PCr}} + [\text{PCr}] [\text{ADP}] [\text{H}^+]) \\ & + \frac{V_{\text{max,ATP}} [\text{ATP}]}{k_m + [\text{ATP}]} + 2 (k_{\text{AK}}^- + [\text{ATP}] [\text{AMP}]) - k_{\text{ATP,Cv}} \\ & - 2 \frac{v_{\text{glyc}} [\text{ADP}]^2 [\text{Pi}]^2 [\text{gluc}] \text{NAD}_{\text{cyt}}^2}{(k_{m,\text{glycA}}^2 + [\text{ADP}]^2) (k_{m,\text{glycP}}^2 + [\text{Pi}]^2) (k_{m,\text{glycG}} + [\text{gluc}]) (k_{m,\text{glycN}}^2 + \text{NAD}_{\text{cyt}}^2)} \end{aligned} \quad (\text{A.18})$$

$$\frac{d[\text{AMP}]}{dt} = (k_{\text{AK}} + [\text{ADP}]^2) - (k_{\text{AK}}^- + [\text{ATP}] [\text{AMP}]) \quad (\text{A.19})$$

$$\begin{aligned} \frac{d[\text{ATP}]}{dt} = & (k_{\text{AK}} + [\text{ADP}]^2) - (k_{\text{PCr}}^- + [\text{ATP}] [\text{Cr}]) + (k_{\text{PCr}} + [\text{PCr}] [\text{ADP}] [\text{H}^+]) \\ & - \frac{V_{\text{max,ATP}} [\text{ATP}]}{k_m + [\text{ATP}]} - (k_{\text{AK}}^- + [\text{ATP}] [\text{AMP}]) + k_{\text{ATP,Cv}} \\ & + 2 \frac{v_{\text{glyc}} [\text{ADP}]^2 [\text{Pi}]^2 [\text{gluc}] \text{NAD}_{\text{cyt}}^2}{(k_{m,\text{glycA}}^2 + [\text{ADP}]^2) (k_{m,\text{glycP}}^2 + [\text{Pi}]^2) (k_{m,\text{glycG}} + [\text{gluc}]) (k_{m,\text{glycN}}^2 + \text{NAD}_{\text{cyt}}^2)} \end{aligned} \quad (\text{A.20})$$

$$\frac{d[\text{Cr}]}{dt} = (k_{\text{PCr}} + [\text{PCr}] [\text{ADP}] [\text{H}^+]) - (k_{\text{PCr}}^- + [\text{ATP}] [\text{Cr}]) \quad (\text{A.21})$$

$$\begin{aligned} \frac{d[\text{gluc}]}{dt} &= V_{\text{glucosein}} v_{\text{glut}} \\ &- \frac{v_{\text{glyc}} [\text{ADP}]^2 [\text{P}_i]^2 [\text{gluc}] \text{NAD}_{\text{cyt}}^2}{\left(k_{m,\text{glycA}}^2 + [\text{ADP}]^2\right) \left(k_{m,\text{glycP}}^2 + [\text{P}_i]^2\right) \left(k_{m,\text{glycG}} + [\text{gluc}]\right) \left(k_{m,\text{glycN}}^2 + \text{NAD}_{\text{cyt}}^2\right)} \\ &\quad - \frac{v_{\text{glut}} [\text{gluc}]}{k_{\text{glut}} + [\text{gluc}]} \quad (\text{A.22}) \end{aligned}$$

$$\begin{aligned} \frac{d[\text{H}^+]}{dt} &= \frac{1}{R_{\text{Hic}}} (k_{\text{PCr}}^- + [\text{ATP}] [\text{Cr}]) - \frac{1}{R_{\text{Hic}}} (k_{\text{PCr}} + [\text{PCr}] [\text{ADP}] [\text{H}^+]) + \frac{p_1 + 4}{\frac{R_{\text{Hic}}}{\text{CBF}_n}} f_1 \\ &- \frac{1}{R_{\text{Hic}}} \frac{v_{\text{MCT}} [\text{lac}] [\text{H}^+]}{(k_{\text{MCT}} + [\text{lac}]) (k_{\text{MCT}} + [\text{H}^+])} + \frac{1}{R_{\text{Hic}}} (k_{\text{pl}}^- + [\text{lac}] \text{NAD}_{\text{cyt}}) + \frac{1}{R_{\text{Hic}}} V_{\text{lacin}} v_{\text{MCT}} \\ &+ \frac{1}{R_{\text{Hic}}} (k_{\text{MAshut}}^- + \text{NAD}_{\text{cyt}} \text{H}_m^+) + \frac{p_2}{\frac{R_{\text{Hic}}}{\text{CBF}_n}} f_2 - \frac{1}{R_{\text{Hic}}} (k_{\text{MAshut}} + [\text{H}^+] [\text{NAD}]) - \frac{1}{\frac{R_{\text{Hic}}}{\text{CBF}_n}} L \\ &\quad - \frac{1}{R_{\text{Hic}}} (k_{\text{pl}} + [\text{Py}] [\text{H}^+]) - \frac{1}{\frac{R_{\text{Hic}}}{\text{CBF}_n}} k_{\text{TCA}} \\ &+ \frac{4}{R_{\text{Hic}}} \frac{v_{\text{glyc}} [\text{ADP}]^2 [\text{P}_i]^2 [\text{gluc}] \text{NAD}_{\text{cyt}}^2}{\left(k_{m,\text{glycA}}^2 + [\text{ADP}]^2\right) \left(k_{m,\text{glycP}}^2 + [\text{P}_i]^2\right) \left(k_{m,\text{glycG}} + [\text{gluc}]\right) \left(k_{m,\text{glycN}}^2 + \text{NAD}_{\text{cyt}}^2\right)} \quad (\text{A.23}) \end{aligned}$$

$$\begin{aligned} \frac{d[\text{lac}]}{dt} &= V_{\text{lacin}} v_{\text{MCT}} - \frac{v_{\text{MCT}} [\text{lac}] [\text{H}^+]}{(k_{\text{MCT}} + [\text{lac}]) (k_{\text{MCT}} + [\text{H}^+])} \\ &\quad - (k_{\text{pl}}^- + [\text{lac}] \text{NAD}_{\text{cyt}}) + (k_{\text{pl}} + [\text{Py}] [\text{H}^+]) \quad (\text{A.24}) \end{aligned}$$

$$\begin{aligned} \frac{d[\text{P}_i]}{dt} &= \frac{V_{\text{max,ATP}} [\text{ATP}]}{k_m + [\text{ATP}]} - k_{\text{ATP,Cv}} \\ &- 2 \frac{v_{\text{glyc}} [\text{ADP}]^2 [\text{P}_i]^2 [\text{gluc}] \text{NAD}_{\text{cyt}}^2}{\left(k_{m,\text{glycA}}^2 + [\text{ADP}]^2\right) \left(k_{m,\text{glycP}}^2 + [\text{P}_i]^2\right) \left(k_{m,\text{glycG}} + [\text{gluc}]\right) \left(k_{m,\text{glycN}}^2 + \text{NAD}_{\text{cyt}}^2\right)} \quad (\text{A.25}) \end{aligned}$$

$$\frac{d[\text{PCr}]}{dt} = (k_{\text{PCr}}^- + [\text{ATP}] [\text{Cr}]) - (k_{\text{PCr}} + [\text{PCr}] [\text{ADP}] [\text{H}^+]) \quad (\text{A.26})$$

$$\begin{aligned} \frac{d[\text{Py}]}{dt} &= (k_{\text{pl}}^- + [\text{lac}] \text{NAD}_{\text{cyt}}) - (k_{\text{pl}} + [\text{Py}] [\text{H}^+]) - \frac{1}{\text{CBF}_n} k_{\text{TCA}} \\ &+ 2 \frac{v_{\text{glyc}} [\text{ADP}]^2 [\text{P}_i]^2 [\text{gluc}] \text{NAD}_{\text{cyt}}^2}{(k_{m,\text{glycA}}^2 + [\text{ADP}]^2) (k_{m,\text{glycP}}^2 + [\text{P}_i]^2) (k_{m,\text{glycG}} + [\text{gluc}]) (k_{m,\text{glycN}}^2 + \text{NAD}_{\text{cyt}}^2)} \end{aligned} \quad (\text{A.27})$$

$$\frac{d\text{Cu}_{\text{A},o}}{dt} = 4f_2 - 4f_1 \quad (\text{A.28})$$

$$\frac{d\text{cyta3}_r}{dt} = 4f_2 - 4f_3 \quad (\text{A.29})$$

$$\frac{d\Delta\Psi}{dt} = \frac{p_2 f_2 + p_1 f_1 + p_3 f_3 - L}{C_{im}} \quad (\text{A.30})$$

$$\begin{aligned} \frac{d\text{H}_m^+}{dt} &= \frac{1}{\text{R}_{\text{Hi}} \text{CBF}_n} (k_{\text{MAshut}} + [\text{H}^+] [\text{NAD}]) - \frac{p_1 + \frac{5}{3}}{\text{R}_{\text{Hi}}} f_1 \\ &- \frac{1}{\text{R}_{\text{Hi}} \text{CBF}_n} (k_{\text{MAshut}}^- + \text{NAD}_{\text{cyt}} \text{H}_m^+) - \frac{p_2}{\text{R}_{\text{Hi}}} f_2 - \frac{p_3}{\text{R}_{\text{Hi}}} f_3 + \frac{1}{\text{R}_{\text{Hi}}} L + \frac{4}{\text{R}_{\text{Hi}}} k_{\text{TCA}} \end{aligned} \quad (\text{A.31})$$

$$\begin{aligned} \frac{d[\text{NAD}]}{dt} &= 2f_1 + \frac{1}{\text{CBF}_n} (k_{\text{MAshut}}^- + \text{NAD}_{\text{cyt}} \text{H}_m^+) \\ &- \frac{1}{\text{CBF}_n} (k_{\text{MAshut}} + [\text{H}^+] [\text{NAD}]) - 5k_{\text{TCA}} \end{aligned} \quad (\text{A.32})$$

$$\begin{aligned} \frac{d\text{NAD}_{\text{cyt}}}{dt} &= (k_{\text{MAshut}} + [\text{H}^+] [\text{NAD}]) - (k_{\text{pl}}^- + [\text{lac}] \text{NAD}_{\text{cyt}}) \\ &\quad - (k_{\text{MAshut}}^- + \text{NAD}_{\text{cyt}} \text{H}_m^+) + (k_{\text{pl}} + [\text{Py}] [\text{H}^+]) \\ &\quad - 2 \frac{v_{\text{glyc}} [\text{ADP}]^2 [\text{Pi}]^2 [\text{gluc}] \text{NAD}_{\text{cyt}}^2}{(k_{m,\text{glycA}}^2 + [\text{ADP}]^2) (k_{m,\text{glycP}}^2 + [\text{Pi}]^2) (k_{m,\text{glycG}} + [\text{gluc}]) (k_{m,\text{glycN}}^2 + \text{NAD}_{\text{cyt}}^2)} \end{aligned} \quad (\text{A.33})$$

$$\frac{d[\text{O}_2]}{dt} = \frac{1}{\text{CBF}_n} J_{\text{O}_2} - f_3 \quad (\text{A.34})$$

$$\frac{dv_{\text{CO}_2}}{dt} = \frac{1}{v_{u,n}} (P_a \text{CO}_2 - v_{\text{CO}_2}) \quad (\text{A.35})$$

$$\frac{dv_{\text{O}_2}}{dt} = \frac{1}{v_{u,n}} ([\text{O}_{2,c}] - v_{\text{O}_2}) \quad (\text{A.36})$$

$$\frac{dv_{P_a}}{dt} = \frac{1}{v_{u,n}} (P_{a2} - v_{P_a}) \quad (\text{A.37})$$

$$\frac{dv_u}{dt} = \frac{1}{v_{u,n}} (\text{CBF} - v_u) \quad (\text{A.38})$$

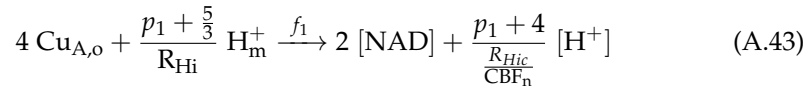
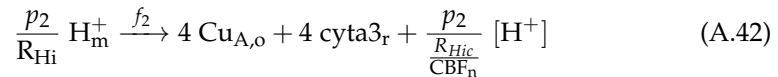
A.2.3 Algebraic equations

$$[\text{O}_{2,c}]_{\text{init}} \left(\frac{\text{ScO}_2}{1 - \text{ScO}_2} \right)^{\frac{1}{n}} - [\text{O}_{2,c}] = 0 \quad (\text{A.39})$$

$$T_e + T_m - (P_1 - P_{ic}) r = 0 \quad (\text{A.40})$$

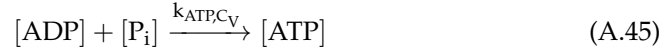
$$\text{CBF} ([\text{HbO}_{2,a}] - [\text{HbO}_{2,v}]) - J_{\text{O}_2} = 0 \quad (\text{A.41})$$

A.2.4 Chemical reactions

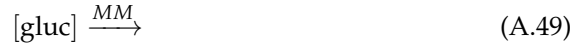
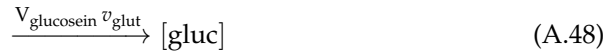
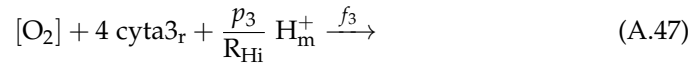




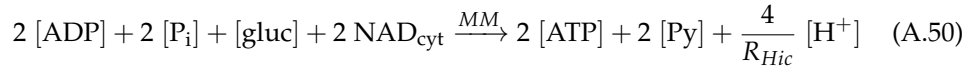
Mass Action kinetics are assumed for the forward reaction, with calculated rate term $k_{\text{AK}} + [\text{ADP}]^2$. Mass Action kinetics are assumed for the reverse reaction, with calculated rate term $k_{\text{AK}}^- + [\text{ATP}] [\text{AMP}]$.



Michaelis-Menten kinetics are assumed, with calculated rate term $\frac{V_{\text{max,ATP}} [\text{ATP}]}{k_m + [\text{ATP}]}$.

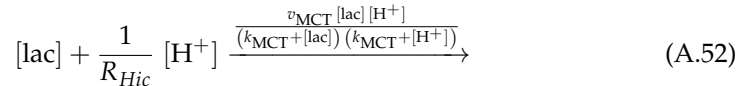
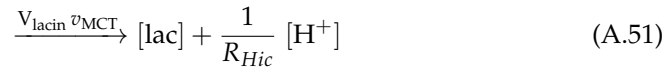


Michaelis-Menten kinetics are assumed, with calculated rate term $\frac{v_{\text{glut}} [\text{gluc}]}{k_{\text{glut}} + [\text{gluc}]}$.



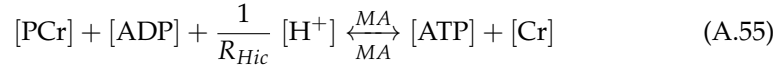
Michaelis-Menten kinetics are assumed, with calculated rate term

$$\frac{v_{\text{glyc}} [\text{ADP}]^2 [\text{P}_i]^2 [\text{gluc}] \text{NAD}_{\text{cyt}}^2}{\left(k_{m,\text{glycA}}^2 + [\text{ADP}]^2\right) \left(k_{m,\text{glycP}}^2 + [\text{P}_i]^2\right) \left(k_{m,\text{glycG}} + [\text{gluc}]\right) \left(k_{m,\text{glycN}}^2 + \text{NAD}_{\text{cyt}}^2\right)}$$



Mass Action kinetics are assumed for the forward reaction, with calculated rate term $k_{MAshut} + [H^+] [NAD]$. Mass Action kinetics are assumed for the reverse reaction, with calculated rate term $k_{MAshut}^- + NAD_{cyt} H_m^+$.

$$\xrightarrow{J_{O_2}} \frac{1}{CBF_n} [O_2] \quad (A.54)$$



Mass Action kinetics are assumed for the forward reaction, with calculated rate term $k_{PCr} + [PCr] [ADP] [H^+]$. Mass Action kinetics are assumed for the reverse reaction, with calculated rate term $k_{PCr}^- + [ATP] [Cr]$.

$$\frac{1}{\frac{R_{Hic}}{CBF_n}} [H^+] \xrightarrow{L} \frac{1}{R_{Hi}} H_m^+ \quad (A.56)$$



Mass Action kinetics are assumed for the forward reaction, with calculated rate term $k_{pl} + [Py] [H^+]$. Mass Action kinetics are assumed for the reverse reaction, with calculated rate term $k_{pl}^- + [lac] NAD_{cyt}$.

$$\frac{1}{\frac{1}{CBF_n}} [Py] + 5 [NAD] + \frac{1}{\frac{R_{Hic}}{CBF_n}} [H^+] \xrightarrow{k_{TCA}} \frac{4}{R_{Hi}} H_m^+ \quad (A.58)$$

A.2.5 State variables

Symbol	Units	Initialiser	Notes
[ADP]	mM	[ADP] _n	ADP concentration in cytoplasm and mitochondria
[AMP]	mM	[AMP] _n	AMP concentration in cytoplasm
[ATP]	mM	[ATP] _n	ATP concentration in cytoplasm and mitochondria
[Cr]	mM	[Cr] _n	Creatine concentration in cytoplasm
[gluc]	mM	[gluc] _n	Concentration of glucose in the cytoplasm
[H ⁺]	mM	[H ⁺] _n	Concentration of hydrogen ions in the cytoplasm
[lac]	mM	[lac] _n	Concentration of lactate in the cytoplasm

$[P_i]$	mM	$[P]_n$	Inorganic phosphate concentration in cytoplasm and mitochondria
$[PCr]$	mM	$[PCr]_n$	Phosphocreatine concentration in cytoplasm
$[Py]$	mM	$[Py]_n$	Concentration of pyruvate in the cytoplasm
$Cu_{A,o}$	mM	$Cu_{A,o,init}$	The concentration of oxidised cytochrome-c-oxidase
$cyta3_r$	mM	$[a3r]_{init}$	Concentration of reduced cyt a3 in mitochondria
$\Delta\Psi$	mV	$\Delta\Psi_{init}$	Mitochondrial inner membrane potential
H_m^+	mM	$H_{m,init}^+$	Concentration of hydrogen ions in mitochondria
$[NAD]$	mM	$[NAD]_n$	Concentration of NAD in the mitochondria
NAD_{cyt}	mM	NAD_{cytn}	Concentration of NAD in the cytoplasm
$[O_2]$	mM	$[O_2]_{init}$	The concentration of oxygen in the mitochondria
$[O_{2,c}]$	mM	$[O_{2,c}]_{init}$	The concentration of oxygen in the capillary.
r	cm	r_{init}	Typical radius of cerebral vessels
ν_{CO_2}	mmHg	$\nu_{CO_2,n}$	CO2 passed through a first order filter.
ν_{O_2}	mM	$\nu_{O_2,n}$	capillary O2 passed through a first order filter.
ν_{P_a}	mmHg	$\nu_{P_a,n}$	Arterial blood pressure passed through a first order filter.
ν_u	dimensionless	$\nu_{u,n}$	The demand parameter u passed through a first order filter.
$[HbO_{2,v}]$	mM	$[HbO_{2,v}]_{init}$	The concentration of bound oxygen in the veins.

A.2.6 Intermediate variables

Symbol	Units	Expression	Notes
$\text{Cu}_{A,o}$	mM	$\mathcal{E}_0(\text{cyt } a_3) - \text{Cu}_{A,o}$	The concentration of reduced cytochrome-c-oxidase in the mitochondria.
AVR	dimensionless	$\frac{V_a}{V_v}$	Arterio-venous volume ratio
cyta_3_o	mM	$\mathcal{E}_0(\text{cyt } a_3) - \text{cyta}_3_r$	Concentration of oxidised cyt a3 in mitochondria
C_{0i}	dimensionless	$\frac{10^{-pH_m} - 10^{-pH_m - dpH}}{dpH}$	Natural buffering capacity for protons in mitochondria
C_{0ic}	dimensionless	$\frac{10^{-pH_o} - 10^{-pH_o - dpH}}{dpH}$	Natural buffering capacity for protons in cytoplasm
C_{NADH}	mV	$\frac{\mathcal{E}_0(\text{cyt } a_3)}{2} \log_{10} \left(\frac{1}{[\text{NAD}]/[\text{NADH}]} \right)$	Redox potential minus standard redox potential for NADH at normal demand
CBF	$\text{ml m}^{-1} \text{s}^{-1}$	$G (P_{a2} - P_v)$	Cerebral blood flow
ΔoxCCO	μM	$\Delta \text{oxCCO}_{\text{offset}} + 1000 \text{CBF}_n (\text{Cu}_{A,o} - \text{VArat}_n)$	The expected CCO signal (as measured by NIRS)
CMRO_2	mM s^{-1}	$f_3 \text{CBF}_n$	Cerebral metabolic rate for oxygen
ΔG_1	mV	$p_1 \Delta p - 4 \left(E_1 + \mathcal{E}_0(\text{cyt } a_3) \log_{10} \left(\frac{\text{Cu}_{A,o}}{\text{Cu}_{A,o}} \right) \right)$	Free energy associated with reaction 1
ΔG_2	mV	$p_2 \Delta p - 4 \left(E_2 + \mathcal{E}_0(\text{cyt } a_3) \left(\log_{10} \left(\frac{\text{Cu}_{A,o}}{\text{Cu}_{A,o}} \right) - \log_{10} \left(\frac{\text{cyta}_3_r}{\text{cyta}_3_o} \right) \right) \right)$	Free energy associated with reaction 2

ΔG	J mol^{-1}	$\Delta G^\circ + \mathcal{E}_0(\text{cyt a}_3) F \log_{10}(g_p)$	Gibbs free energy of ATP hydrolysis
ΔHbdiff	μM	$\Delta \text{Hbdiff}_{\text{offset}} + \Delta \text{HbO}_2 - \Delta \text{HHb}$	Change in Hbdiff (NIRS)
ΔHbO_2	μM	$\Delta \text{HbO}_{2,\text{offset}} + \text{HbO}_2 - \text{HbO}_{2n}$	Change in total oxygenated haemoglobin (NIRS)
ΔHbt	μM	$\Delta \text{HbT}_{\text{offset}} + \text{Hbt} - \text{Hbt}_n$	Change in total haemoglobin (NIRS)
ΔHHb	μM	$\Delta \text{HHb}_{\text{offset}} + \text{HHb} - \text{Hbt}_n$	Change in total deoxygenated haemoglobin (NIRS)
Δp	mV	$\Delta \Psi + \mathcal{E}_0(\text{cyt a}_3) \Delta \text{pH}$	The proton motive force across the mitochondrial inner membrane.
ΔpH	dimensionless	$\text{pH}_m - \text{pH}_o$	The pH difference across mitochondrial inner membrane
$E_{1,NADH}$	mV	$\mathcal{E}_0(\text{Cu}_A) - \mathcal{E}_0(\text{NADH}) + C_{\text{NADH}}$	E1 when the reducing substrate is NADH
E_1	mV	$E_{1,NADH}$	The energy provided by electron transfer to Cu_A
η	dimensionless	$R_P \left(\frac{v_{P_a}}{v_{P_a,n}} - 1 \right) + R_O \left(\frac{v_{O_2}}{v_{O_2,n}} - 1 \right) + R_u \left(1 - \frac{v_u}{v_{u,n}} \right) + R_C \left(1 - \frac{v_{\text{CO}_2}}{v_{\text{CO}_2,n}} \right)$	Total autoregulatory stimuli
f_1	mM s^{-1}	$k_1 \text{Cu}_{A,o} - k_{-1} \text{Cu}_{A,o}$	The rate at which Cu_A is reduced
f_2	mM s^{-1}	$k_2 \text{Cu}_{A,o} \text{cyt a}_3 - k_{-2} \text{Cu}_{A,o} \text{cyt a}_3$	The rate at which Cu_A is oxidised and cyt a3 reduced.
f_3	mM s^{-1}	$\frac{c_{k2} [\text{O}_2] \text{cyt a}_3 \exp(-c_3 (\Delta p - \Delta p_{30}))}{1 + \exp(-c_3 (\Delta p - \Delta p_{30}))}$	The rate at which cyt a3 is oxidised
G	$\text{mmHg}^{-1} \text{s}^{-1}$	$R_u r^4$	Resistance of cerebral circulation

g_p	dimensionless	$\frac{[\text{ADP}] [\text{P}_i]}{[\text{ATP}] \times 1000}$	(Normalised) phosphorylation potential (or ADP/ATP ratio)
G_t	$\text{mmHg}^{-1} \text{s}^{-1}$	$\frac{G G_0 G_v}{G G_0 + G G_v + G_v G_0}$	The total conductance of the cerebral blood vessels
h	cm	$\left(r^2 + 2r_0 h_0 + h_0 h_0 \right)^{\frac{1}{2}} - r$	Wall thickness of cerebral vessels
HbO_2	μM	$\frac{V_a [\text{HbO}_{2,a}] + V_v [\text{HbO}_{2,v}]}{V_a [\text{HbO}_{2,a}] + V_v [\text{HbO}_{2,v}]} V_{\text{blood},n} \times 1000$	Total oxygenated haemoglobin (NIRS)
Hbt	μM	$\frac{(V_a + V_v) [\text{HbO}_{2,a}]_n}{(V_a + V_v) [\text{HbO}_{2,a}]_n} V_{\text{blood},n} \times 1000$	total haemoglobin (NIRS)
HHb	μM	$\frac{V_a [\text{HHb}_a] + V_v [\text{HHb}_v]}{4} V_{\text{blood},n} \times 1000$	Total deoxygenated haemoglobin (NIRS)
J_{O_2}	mM s^{-1}	$J_{\text{O}_2,\text{min}}$	The rate at which oxygen is supplied to the mitochondria.
$J_{\text{O}_2,\text{min}}$	mM s^{-1}	$f_{\text{min}} (D_{\text{O}_2} ([\text{O}_{2,c}] - [\text{O}_2]), \text{CBF} [\text{HbO}_{2,a}])$	Rate at which oxygen is supplied to the mitochondria, minimum of diffusion rate and delivery rate
k_1	s^{-1}	$k_{1,0} \exp(-c_{k1} (\Delta p - \text{SaO}_{2,n}))$	Forward rate constant for reaction 1
$k_{1,0}$	s^{-1}	$\frac{k_{1,n} \frac{N_t}{1 + [\text{NAD}]/[\text{NADH}]}}{[\text{NADH}]_n}$	Forward rate constant for reaction 1 at normal PMF
k_2	$\text{m}^{-1} \text{M s}^{-1}$	$k_{2,n} \exp(-c_{k2} (\Delta p - \text{SaO}_{2,n}))$	Forward rate constant for reaction 2
k_{MAshut}	s^{-1}	$\frac{\text{CBF}_n \text{NADH}_{\text{cyt}}}{3} \frac{1}{K_{\text{eqMAshut}} [\text{NAD}]_n [\text{H}^+]_n \text{NADH}_{\text{cyt}} - \text{NAD}_{\text{cytn}} \text{H}_{\text{m},n}^+ \text{NADH}}$	Rate of forward reaction in the malate-aspartate shuttle

k_{MAshut}^-	s^{-1}	$\frac{k_{MAshut} NADH}{NADH_{cyt} Keq_{MAshut}}$	Rate of backward reaction in the malate-aspartate shuttle
k_{PCr}^-	$m^{-1} M s^{-1}$	$\frac{\log(2)}{\left(Keq_{PCr} \left([PCr]_n + [ADP]_n + \frac{[H^+]_n}{R_{Hic}} \right) + [Cr]_n + [ATP]_n \right) t_{1/2,PCr}}$	The backward rate of reaction for the reaction in which phosphocreatine combines with ADP to give creatine and ATP
k_{PCr}	$m^{-1} M s^{-1}$	$\frac{\log(2)}{\left([PCr]_n + [ADP]_n + \frac{[H^+]_n}{R_{Hic}} + \frac{[Cr]_n + [ATP]_n}{Keq_{PCr}} \right) t_{1/2,PCr}}$	The forward rate of reaction for the reaction in which phosphocreatine combines with ADP to give creatine and ATP
k_{pl}	s^{-1}	$\frac{2CMR_{gluc,n} - \frac{CBF_n}{3} + k_{pl}^- [lac]_n NAD_{cytn}}{[Py]_n [H^+]_n} \frac{NADH_{cytn}}{NADH_{cytn}}$	Rate of forward reaction in the pyruvate lactate equilibrium
k_{TCA}	$m M s^{-1}$	$\frac{v_{TCA} [Py] [NAD]}{(k_{m,tcaN} + [NAD]) (k_{m,tcaP} + [Py])}$	Rate of the TCA cycle
$k_{ATP,CV}$	$m M s^{-1}$	$\frac{L_{CV} CBF_n}{n_a}$	Rate of ATP synthesis by Complex V
Keq_1	dimensionless	$10^{\frac{-1}{\varepsilon_0(cyt a_3)} \left(\frac{p_1 \Delta p}{4} - E_1 \right)}$	Equilibrium constant for reaction 1
Keq_2	dimensionless	$10^{\frac{-1}{\varepsilon_0(cyt a_3)} \left(\frac{p_2 \Delta p}{4} - E_2 \right)}$	Equilibrium constant for reaction 2
k_{-1}	s^{-1}	$\frac{k_1}{Keq_1}$	Backward rate constant for reaction 1
k_{-2}	$m^{-1} M s^{-1}$	$\frac{k_2}{Keq_2}$	Backward rate constant for reaction 2
L	$m M s^{-1}$	$L_{CV} + L_{lk}$	The rate at which protons reenter the mitochondrial matrix

L_{CV}	mM s^{-1}	$\frac{L_{CV, \text{frac}} L_{CV, \text{max}} (1 - \exp(-\theta))}{1 + r_{CV} \exp(-\theta)}$	The rate at which protons reenter the mitochondrial matrix associated with ADP phosphorylation
L_{lk}	mM s^{-1}	$\Delta p_{3, \text{corr}} f_n (\exp(\Delta p f_n) - 1)$	The rate at which protons reenter the mitochondrial matrix through leak channels
μ	dimensionless	$\frac{\mu_{\text{min}} + \mu_{\text{max}} \exp(\eta)}{1 + \exp(\eta)}$	Total autoregulatory stimuli filtered through sigmoidal function
NADH	mM	$N_t - [\text{NAD}]$	Concentration of NADH in the mitochondria mitochondrial NADH concentration
NADH_{cyt}	mM	$\text{NAD}_{\text{cytn}} + \text{NADH}_{\text{cytn}} - \text{NAD}_{\text{cyt}}$	Concentration of NADH in the cytoplasm
$[\text{NAD}]/[\text{NADH}]$	dimensionless	N_{rat}	NAD/NADH ratio in the mitochondria
NTP/EPP	dimensionless	$\frac{[\text{ATP}]}{\frac{EPP}{P_{a2} + P_v}}$	NTP/EPP calculation
P_1	mmHg	$\frac{2}{P_{a2} + P_v}$	Average blood pressure in vessels
P_{a2}	mmHg	$\frac{G_0 P_a + G P_v}{G + G_0}$	The pressure at the start of the cerebral artery compartment
P_v	mmHg	$\frac{G_t}{G_v} (P_a - P_{vs}) + P_{vs}$	Venous blood pressure
pH_m	dimensionless	$-\log_{10} \left(\frac{[\text{H}_m^+]}{1000} \right)$	Mitochondrial pH
pH_o	dimensionless	$-\log_{10} \left(\frac{[\text{H}^+]}{1000} \right)$	Extra-mitochondrial pH

r_{buffi}	dimensionless	$\frac{C_{\text{buffi}}}{C_{0i}}$	Buffering capacity for protons in mitochondria
r_{buffic}	dimensionless	$\frac{C_{\text{buffic}}}{C_{0ic}}$	Buffering capacity for protons in cytoplasm
R_{Hi}	dimensionless	r_{buffi}	Relative mitochondrial volume for protons
R_{Hic}	dimensionless	r_{buffic}	Relative cytoplasmic volume for protons
S_{cO_2}	dimensionless	$\frac{S_{\text{aO}_2} + S_{\text{vO}_2}}{2}$	Capillary oxygen saturation
σ_e	mmHg	$\sigma_{e0} \left(\exp \left(\frac{K_\sigma (r - r_0)}{r_0} \right) - 1 \right) - \sigma_{\text{coll}}$	Elastic stress in vessel walls
S_{vO_2}	dimensionless	$\frac{[\text{HbO}_{2,v}]}{[\text{HbO}_{2,a}]_n}$	Venous oxygen saturation
T_e	mmHg cm	$\sigma_e h$	Elastic tension in vessel walls
T_m	mmHg cm	$T_{\text{max}} \exp \left(- \left \frac{r - r_m}{r_t - r_m} \right ^{n_m} \right)$	Muscular tension in vessel walls
T_{max}	mmHg cm	$T_{\text{max}0} (1 + T_{e,n} \mu)$	Maximum muscular tension developed by circulation
θ	dimensionless	$k_{\text{CV}} \left(\Delta p + \frac{\mathcal{E}_0(\text{cyt a}_3)}{n_a} \log_{10} \left(\frac{g_p}{g_{p,n}} \right) - L_{\text{CV,max}} \right)$	Driving force for complex V
TOS	dimensionless	$\frac{100 \left(\frac{\left(\frac{r}{[\text{Hb}_{\text{totc}}} \right]^2}{\left(\frac{r}{[\text{Hb}_{\text{totc}}} \right]^2 + \frac{V_v}{V_{a,n}}} \right) [\text{HbO}_{2,a}] + \frac{\frac{V_v}{V_{a,n}}}{\left(\frac{r}{[\text{Hb}_{\text{totc}}} \right]^2 + \frac{V_v}{V_{a,n}}} \right) [\text{HbO}_{2,v}]}{[\text{HbO}_{2,a}]_n}$	Tissue Oxygenation index.
v_{glyc}	m M s^{-1}	$\frac{v_{\text{glyc},n} (I + 1)}{1 + I \frac{[\text{ATP}]_n}{[\text{ATP}]_n} \frac{[\text{AMP}]_n}{[\text{AMP}]_n}}$	Vmax for glycolysis

V_{mca}	cm s^{-1}	$\text{CBF}/\text{CBF}_{\text{scale}}$	The velocity of blood in the middle cerebral artery
V_a	dimensionless	$V_{a,n} \left(\frac{r}{[\text{Hbtot}_c]} \right)^2$	Arterial blood volume as a fraction of normal total blood volume
V_t	dimensionless	$V_a + V_v$	Normalised total blood volume
V_v	dimensionless	$V_{v,n} + C_v (P_v - P_{v,n})$	Venous blood volume as a fraction of total blood volume
$[\text{HHb}_v]$	m M	$[\text{HbO}_{2,a}]_n - [\text{HbO}_{2,v}]$	The concentration of deoxy-haemoglobin in the veins.

A.2.7 Parameters

Symbol	Units	Initialiser	Notes
$[\text{ADP}]_n$	m M	0.012	The normal concentration of ADP in the cytoplasm
$[\text{AMP}]_n$	m M	$\frac{K_{\text{eq,ADPATP}} [\text{ADP}]_n^2}{[\text{ATP}]_n}$	Normal AMP concentration in cytoplasm
$[\text{ATP}]_n$	m M	1.2	The normal concentration of ATP in the cytoplasm
$[\text{Cr}]_n$	m M	$\frac{K_{\text{eq,PCr}}^* [\text{ADP}]_n [\text{PCr}]_n}{[\text{ATP}]_n}$	Normal concentration of creatine in cytoplasm
$[\text{gluc}]_n$	m M	1.2	Normal cellular concentration of glucose
$[\text{H}^+]_n$	m M	$1000 \left(10^{-\text{pH}_{0,n}}\right)$	Normal hydrogen ion concentration in the cytoplasm
$[\text{lac}]_n$	m M	3	Normal concentration of lactate in the cytoplasm
$[\text{PCr}]_n$	m M	2.6	Normal concentration of phosphocreatine in cell cytoplasm
$[\text{P}]_n$	m M	$\frac{[\text{PCr}]_n}{[\text{PCr}]_n / [\text{P}_i]_n}$	The normal concentration of inorganic phosphate in the cytoplasm
$[\text{Py}]_n$	m M	0.1	Normal concentration of pyruvate ions in the cytoplasm
$\text{Cu}_{\text{A,frac}}$	dimensionless	0.67	Normal oxidised fraction of Cu_{A}

$\text{Cu}_{A,o,\text{init}}$	m M	$\text{Cu}_{A,o,n}$	Initial oxidized Cu_A
$\text{Cu}_{A,o,n}$	m M	$[\text{CCO}]_{\text{mit}} \text{Cu}_{A,\text{frac}}$	Normal oxidized Cu_A
$\text{Cu}_{A,\text{red},n}$	m M	0.01084	The resting amount of reduced cytochrome-c-oxidase
$a3_{\text{frac},n}$	dimensionless	$1 - \frac{\text{cyta}3_{r,n}}{[\text{CCO}]_{\text{mit}}}$	Normal oxidised fraction of cyt a3
$a3_{o,\text{init}}$	m M	$a3_{o,n}$	Initial oxidised cytochrome a3
$a3_{o,n}$	m M	$[\text{CCO}]_{\text{mit}} - \text{cyta}3_{r,n}$	Normal oxidised cytochrome a3
$V_{\text{blood},n}$	dimensionless	0.0325	Normal blood volume as a fraction of brain tissue volume
$[\text{a}3r]_{\text{init}}$	m M	$\text{cyta}3_{r,n}$	Initial reduced cytochrome a3
$\text{cyta}3_{r,n}$	m M	$\frac{\frac{f_n}{c_{k2}}}{P_a \text{CO}_{2,n} \frac{\exp(-c3 (\text{SaO}_{2,n} - \Delta p_{30}))}{1 + \exp(-c3 (\text{SaO}_{2,n} - \Delta p_{30}))}}$	Normal reduced cytochrome a3
$c3$	$\text{m}^{-1} \text{V}$	0.11	Parameter controlling the sensitivity of reaction 3 to PMF
$C_{\text{buff}i}$	dimensionless	0.022	Buffering capacity for protons in mitochondria
$C_{\text{buff}c}$	dimensionless	0.025	Buffering capacity for protons in cytoplasm
C_{cytc}	m V	-30	Redox potential minus standard redox potential for cyt c $Z \log \frac{C2^+}{C3^+}$
$C_{\text{cytc},n}$	m V	-30	Normal value of C_{cytc}
occ_{frac}	dimensionless	0.8	Fraction of arterial blood which flows through the carotid arteries under normal conditions

C_{im}	$\text{m M m}^{-1} \text{ V}$	0.00675	Capacitance of mitochondrial inner membrane
$C_{\text{NADH},n}$	m V	$\frac{Z}{2} \log_{10} \left(\frac{1}{[\text{NAD}]_n / [\text{NADH}]_n} \right)$	Normal value of C_{NADH}
C_v	mmHg^{-1}	0.047	Compliance of the veins (normalised)
CBF_n	$\text{ml m}^{-1} \text{ s}^{-1}$	0.008	Normal cerebral blood flow
CBFscale	cm	5000	Ratio between Vmca and CBF
$\Delta \text{oxCCO}_{\text{offset}}$	μM	0	An arbitrary baseline offset to the CCO signal (NIRS)
c_{k1}	$\text{m}^{-1} \text{ V}$	0.01	Parameter controlling sensitivity of $k1$ to PMF
c_{k2}	$\text{m}^{-1} \text{ V}$	0.02	Parameter controlling sensitivity of $k2$ to PMF
$\text{CMR}_{\text{gluc},n}$	dimensionless	0.0044	Normal rate of glucose metabolism for the brain
CMRO2_n	m M s^{-1}	0.02	The resting CMRO2 .
$L_{\text{CV},\text{frac}}$	dimensionless	1	A control parameter representing the action of complex V inhibitors
$[\text{CCO}]_{\text{mit}}$	m M	$\frac{[\text{CCO}]_{\text{tis}}}{\text{Vol}_{\text{mit}}}$	Concentration of cytochrome c oxidase in mitochondria
$[\text{CCO}]_{\text{tis}}$	m M	0.0022	Concentration of cytochrome c oxidase in tissue
D_{O2}	s^{-1}	$\frac{R_u}{[\text{O}_{2,c}]_n - P_a \text{CO}_{2,n}}$	Diffusion rate between capillaries and mitochondria.

$\Delta G_{1,n}$	m V	$p_1 \text{SaO}_{2,n} - 4 \left(E_{1,n} + \mathcal{E}_0(\text{cyt } a_3) \log_{10} \left(\frac{V_{\text{Arat}_n}}{\text{Cu}_{\Lambda,0,n}} \right) \right)$	Normal free energy associated with reaction 1
$\Delta G_{2,n}$	m V	$p_2 \text{SaO}_{2,n} - 4 \left(E_2 + \mathcal{E}_0(\text{cyt } a_3) \left(\log_{10} \left(\frac{\text{Cu}_{\Lambda,0,n}}{V_{\text{Arat}_n}} \right) - \log_{10} \left(\frac{\text{cyt}a_{3rn}}{a_{3o,n}^3} \right) \right) \right)$	Normal free energy associated with reaction 2
ΔG_n	J mol ⁻¹	$\Delta G^\circ + \mathcal{E}_0(\text{cyt } a_3) F \log_{10} (g_{p,n})$	Normal Gibbs free energy of ATP hydrolysis
$\Delta \text{Hbdiff}_{\text{offset}}$	μM	0	An arbitrary baseline offset to the HHb signal (NIRS)
$\Delta \text{HbO}_{2,\text{offset}}$	μM	0	An arbitrary baseline offset to the HbO ₂ signal (NIRS)
$\Delta \text{HbT}_{\text{offset}}$	μM	0	An arbitrary baseline offset to the HbT signal (NIRS)
$\Delta \text{HHb}_{\text{offset}}$	μM	0	An arbitrary baseline offset to the HHb signal (NIRS)
$\Delta p_{3,\text{corr}}$	m V	-25	Δp_{30} minus normal PMF
Δp_{30}	m V	$\text{SaO}_{2,n} + \Delta p_{3,\text{corr}}$	Value of PMF at which reaction 3 is maximally sensitive to PMF
$L_{CV,\text{max}}$	m V	$\frac{-\Delta G_n}{n_a F}$	A constant in the rate of complex V
Dp_n	m V	$\Delta \Psi_n + \mathcal{E}_0(\text{cyt } a_3) \Delta \text{pH}_n$	The resting value of the proton motive force.
dpH	dimensionless	0.001	A constant in the buffering relationship
ΔpH_n	dimensionless	$\text{pH}_{m,n} - \text{pH}_{o,n}$	The resting value of pH difference across mitochondrial inner membrane

$\Delta\Psi_{init}$	m V	$\Delta\Psi_n$	Initial value of mitochondrial inner membrane potential
$\Delta\Psi_n$	m V	145	Normal mitochondrial inner membrane potential
$E_{1,NADH,n}$	m V	$\mathcal{E}_0(\text{Cu}_A) - \mathcal{E}_0(\text{NADH}) + C_{NADH,n}$	Normal value of E1NADH
$E_{1,n}$	m V	$E_{1,NADH,n}$	The normal value of E_1
E_2	m V	$\mathcal{E}_0(\text{cyt a}_3) - \mathcal{E}_0(\text{Cu}_A)$	The energy provided by transfer of four electrons from Cu_A to to cyt a_3
$\mathcal{E}_0(\text{cyt a}_3)$	m V	350	Cyt a3 standard redox potential
$\mathcal{E}_0(\text{Cu}_A)$	m V	250	CuA standard redox potential
$\mathcal{E}_0(\text{NADH})$	m V	-320	NADH standard redox potential
EPP	dimensionless	$Pi_n + PCr_n + 2ATP_n + ADP_n$	Exchangeable phosphate pool
f_n	m M s ⁻¹	$\frac{CBF_n}{CBF_n}$	Normal resting rate of f1 and f2.
F	C m ⁻¹ mol	96.4853	Faraday constant
G_0	mmHg ⁻¹ s ⁻¹	$K_{G,0}r0^4$	Conductance of the supplying artery compartment
$G_{0,n}$	mmHg ⁻¹ s ⁻¹	$G_{0,rat}G_n$	Normal conductance of the supplying artery compartment
$G_{0,rat}$	dimensionless	10	Ratio between the conductance of the cerebral arteries and the supplying artery compartment
G_v	mmHg ⁻¹ s ⁻¹	$G_{VArat,n} G_n$	Conductance of the veins
$G_{VArat,n}$	dimensionless	4	Normal ratio of conductances between arteries and veins G_v/G_n (determines venous pressure).

$[\text{gluc}_c]$	m M	5.3		Concentration of glucose in the blood
$\text{glyc}_{a,n}$	dimensionless	$\frac{([\text{ADP}]_n)^2}{(k_{m,\text{glycA}})^2 + ([\text{ADP}]_n)^2}$		Term in the expression for normal glycolysis rate
$\text{glyc}_{g,n}$	dimensionless	$\frac{[\text{gluc}]_n}{k_{m,\text{glycG}} + [\text{gluc}]_n}$		Term in the expression for normal glycolysis rate
$\text{glyc}_{n,n}$	dimensionless	$\frac{(\text{NAD}_{\text{cytn}})^2}{(k_{m,\text{glycN}})^2 + (\text{NAD}_{\text{cytn}})^2}$		Term in the expression for normal glycolysis rate
$\text{glyc}_{p,n}$	dimensionless	$\frac{([\text{P}]_n)^2}{(k_{m,\text{glycP}})^2 + ([\text{P}]_n)^2}$		Term in the expression for normal glycolysis rate
G_n	mmHg ⁻¹ s ⁻¹	$\frac{\text{CBF}_n}{P_a - P_{vs}} \left(1 + \frac{1}{G_{0,\text{rat}}} + \frac{1}{G_{\text{VArat},n}} \right)$		Normal resistance of cerebral circulation
ΔG°	J mol ⁻¹	-30500		Standard Gibbs free energy of ATP hydrolysis
$g_{p,n}$	dimensionless	$\frac{[\text{ADP}]_n [\text{P}]_n}{[\text{ATP}]_n \times 1000}$		Normal phosphorylation potential
$G_{t,n}$	mmHg ⁻¹ s ⁻¹	$\frac{G_n G_{0,n} G_v}{G_n G_{0,n} + G_n G_v + G_v G_{0,n}}$		Normal value of the total Conductance of all blood vessel compartments
h_0	cm	0.003		Vascular wall thickness when radius is r_0
$\text{H}_{m,\text{init}}^+$	m M	$\text{H}_{m,n}^+$		Initial hydrogen ion concentration in mitochondria
$\text{H}_{m,n}^+$	m M	$10^{3-\text{pH}_{m,n}}$		Normal hydrogen ion concentration in mitochondria

h_n	cm	$\left([\text{Hbtot}_c]^2 + 2r_0 h_0 + h_0 h_0\right)^{\frac{1}{2}} - [\text{Hbtot}_c]$	Normal wall thickness of cerebral vessels
H_{on}	m M	$10^{3-\text{pH}_{\text{o,n}}}$	Normal hydrogen ion concentration in the cytoplasm
$\text{HbO}_{2\text{n}}$	μM	$\frac{V_{\text{a,n}} [\text{HbO}_{2,\text{a}}]_{\text{n}} + V_{\text{v,n}} [\text{HbO}_{2,\text{v}}]_{\text{n}}}{4} V_{\text{blood,n}} \times 1000$	Normal total oxygenated haemoglobin (NIRS)
k_{H,O_2}	m M mmHg ⁻¹	0.0014000	Constant setting relationship between oxygen saturation and oxygen concentration in artery
Hbt_n	μM	$\frac{(V_{\text{a,n}} + V_{\text{v,n}}) [\text{Hbtot}]_{\text{n}}}{4} V_{\text{blood,n}} \times 1000$	Normal total deoxygenated haemoglobin (NIRS)
I	dimensionless	3	The parameter which describes how strongly the AMP/ATP ratio inhibits the conversion of glucose to pyruvate
R_u	m M s ⁻¹	CBF_n	The resting rate of supply of oxygen to the mitochondria.
$k_{1,\text{n}}$	s ⁻¹	$\frac{f_n}{V_{\text{Arat}_n} - \frac{1}{K_{\text{eq}1,\text{n}}} \text{Cu}_{\text{A},\text{o},\text{n}}}$	The value of k_1 at normal Δp and NADH
$k_{2,\text{n}}$	m ⁻¹ M s ⁻¹	$\frac{f_n}{\text{Cu}_{\text{A},\text{o},\text{n}} a_{3\text{o},\text{n}} - \frac{1}{K_{\text{eq}2,\text{n}}} V_{\text{Arat}_n} \text{cyta}_{3\text{r},\text{n}}}$	Normal forward rate constant for reaction 2
c_{k2}	m ⁻¹ M s ⁻¹	$\frac{k_{3,0}}{\frac{\exp(-c3 (\text{SaO}_{2,\text{n}} - \Delta p_{30}))}{1 + \exp(-c3 (\text{SaO}_{2,\text{n}} - \Delta p_{30}))}}$	Rate constant for reaction 3
$k_{3,0}$	m ⁻¹ M s ⁻¹	2.5E + 5	An apparent second-order rate constant for reaction 3 at zero PMF

k_{AK}	$m^{-1} Ms^{-1}$	1055	The forward rate constant for the conversion of two molecules of ADP to one of ATP and one of AMP
Keq_{ADPATP}	dimensionless	$\frac{k_{AK}}{k_{AK}^-}$	Equilibrium constant for the conversion of ADP to ATP and AMP
$t_{12,ADPATP}$	s	0.000002	Halftime for the conversion of ADP to ATP and AMP
$T_{e,n}$	dimensionless	1	Control parameter allowing destruction of autoregulation
K_G	$mmHg^{-1} s^{-1} cm^{-4}$	$\frac{G_n}{\text{pow}([Hbtot_c], 4)}$	Constant of proportionality relating pressure drop to flow
K_{G0}	$mmHg^{-1} s^{-1} cm^{-4}$	$G_{0,n}$	Constant in relationship between normal conductance of supplying artery and its radius
k_{glut}	mM	6.2	Km for the transport of glucose in and out of the cell
k_{MCT}	mM	2	Km for the transport of lactate in and out of the cell.
f_n	$m^{-1} V$	0.038	Second constant controlling rate of L_{lk} of Δp .
k_{AK}^-	$m^{-1} Ms^{-1}$	379	The backward rate constant for the conversion of two molecules of ADP to one of ATP and one of AMP
k_{pl}^-	s^{-1}	$t_{1/2,pl}$	Rate of backwards reaction in the pyruvate lactate equilibrium

$K_{eq,PCr}$	$m^{-1} M$	$\frac{K_{eq,PCr}^*}{[H^+]_n}$	Equilibrium of the reaction in which phosphocreatine combines with ADP to give creatine and ATP
$K_{eq,PCr}^*$	dimensionless	166	Effective equilibrium constant for the reaction in which phosphocreatine combines with ADP to give creatine and ATP
$t_{1/2,PCr}$	s	0.00002	Halftime for the reaction in which phosphocreatine combines with ADP to give creatine and ATP
$t_{1/2,pl}$	s^{-1}	10	Time constant for pyruvate to lactate interconversion
K_σ	dimensionless	10	Parameter controlling sensitivity of σ_e to radius
k_{TCA_n}	$m M s^{-1}$	$\frac{1}{3} \frac{CBF_n}{CBF_n}$	Normal rate of the TCA cycle
$\Delta p_{3,corr}$	dimensionless	1	A parameter representing the action of uncouplers
k_{CV}	$m^{-1} V$	$\frac{-1}{SaO_{2,n} - L_{CV,max}} \log \left(\frac{1 - L_{CV,0}}{1 + r_{CV} L_{CV,0}} \right)$	A parameter controlling the sensitivity of complex V flux to driving force
$Keq_{1,n}$	dimensionless	$10^{\frac{-1}{E_0(cyta3)} \left(\frac{p_1 SaO_{2,n}}{4} - E_{1,n} \right)}$	Normal equilibrium constant for reaction 1
$Keq_{2,n}$	dimensionless	$10^{\frac{-1}{E_0(cyta3)} \left(\frac{p_2 SaO_{2,n}}{4} - E_2 \right)}$	Normal equilibrium constant for reaction 2

$K_{eq_{MAshut}}$	dimensionless	10	Equilibrium constant for the malate-aspartate shuttle
$k_{m,ATP}$	dimensionless	0.025	Km for ATP use as a fraction of normal ATP concentration .
$k_{m,glycA}$	m M	$k_{m,glycA,f} [ADP]_n$	Km for ADP in the caricature of glycolysis
$k_{m,glycA,f}$	dimensionless	0.2	Km for ADP in glycolysis as a fraction of normal ADP concentration
$k_{m,glycG}$	m M	0.05000	Km for glucose in the caricature of glycolysis
$k_{m,glycN}$	m M	$k_{m,glycN,f} [NAD]_n$	Km for NAD in the caricature of glycolysis
$k_{m,glycN,f}$	m M	0.2	Km for NAD in glycolysis as a fraction of normal NAD concentration
$k_{m,glycP}$	m M	$k_{m,glycP,f} [P]_n$	Km for inorganic phosphate in the caricature of glycolysis.
$k_{m,glycP,f}$	dimensionless	0.2	Km for inorganic phosphate in glycolysis as a fraction of normal phosphate concentration
km_{NAD}	m M	100000	Km for NAD in the TCA cycle as a fraction of the normal NAD concentration
$Km_{NAD,TCA}$	m M	$km_{NAD} [NAD]_n$	Km for NAD in the TCA cycle

km_{py}	m M	0.005	Km for pyruvate for the TCA cycle as a fraction of the normal pyruvate concentration
$Km_{Py,TCA}$	m M	$km_{py} [Py]_n$	Km for pyruvate in the TCA cycle
$k_{m,ATP}$	m M	0.025	
k_m	m M	$[ATP]_n k_{m,ATP}$	Km for ATP use
$k_{-1,0}$	s^{-1}	$\frac{f_n}{Keq_{1,n} VArat_n - Cu_{A,o,n}}$	Backward rate constant for reaction 1 at normal PMF
$kn1_n$	dimensionless	$\frac{f_n}{Keq_{1,n} VArat_n - Cu_{A,o,n}}$	The value of k1 at normal Δp and NADH
$k_{-2,n}$	$m^{-1} M s^{-1}$	$\frac{f_n}{Keq_{2,n} Cu_{A,o,n} a_{3,o,n} - VArat_n cyta3_{r,n}}$	Normal backward rate constant for reaction 2
$L_{CV,0}$	dimensionless	0.4	Normal complex V flux as a fraction of maximum possible flux
$L_{CV,n}$	$m M s^{-1}$	$L_n L_{CV,frac}$	Normal rate of protons reentering mitochondrial matrix
$L_{CV,frac}$	dimensionless	$1 - L_{lk,frac}$	Normal fraction of proton entry into mitochondria associated with ADP phosphorylation
$L_{CV,max}$	$m M s^{-1}$	$\frac{CBF_n}{L_{CV,0}}$	The maximum rate of proton flow through complex V.
L_{lk0}	$m M s^{-1}$	$\frac{CBF_n}{\exp(SaO_{2,n} f_n) - 1}$	First constant controlling rate of L_{lk} of Δp .

$L_{lk,frac}$	dimensionless	0.25	Normal fraction of proton entry into mitochondria which is via leak channels
L_{lkn}	$m M s^{-1}$	$L_{ln} L_{lk,frac}$	The resting flow of protons into the matrix via leak channels.
L_n	$m M s^{-1}$	$p_{tot} f_n$	The total flow of protons back into mitochondria
$[lac_c]$	$m M$	1	Capillary lactate concentration .
μ_{max}	dimensionless	1	Maximum value of mu
μ_{min}	dimensionless	-1	Minimum value of mu
μ_n	dimensionless	0	Normal value of mu
n_h	dimensionless	2.5	Hill coefficient for haemoglobin saturation
n_m	dimensionless	1.83	Exponent in the muscular tension relationship
n_a	dimensionless	4.33	Number of protons passing through Complex V for each ATP synthesised
NAD_{cytn}	$m M$	359	Normal concentration of NAD in the cytoplasm
$NADH_{cytn}$	dimensionless	50	Normal concentration of NADH in the cytoplasm
$[NADH]_n$	$m M$	$N_t - [NAD]_n$	Normal mitochondrial NADH concentration
$[NAD]_n$	$m M$	$\frac{N_t}{1 + \frac{1}{[NAD]_n/[NADH]_n}}$	Normal concentration of NAD in the mitochondria

$[\text{NAD}]_n / [\text{NADH}]_n$	dimensionless	9	Normal NAD/NADH ratio
N_t	m M	3	Total mitochondrial NAD + NADH concentration
$[\text{O}_2]_{\text{init}}$	m M	$[\text{O}_2]_n$	Initial oxygen concentration in mitochondria.
$[\text{O}_2]_n$	m M	0.024	Normal oxygen concentration in mitochondria.
$[\text{O}_{2,a}]$	m M	$\phi \left(\frac{SaO2sup}{1.0 - SaO2sup} \right)^{\frac{1}{n_h}}$	Arterial dissolved oxygen concentration
$[\text{O}_{2,c}]_{\text{init}}$	m M	$[\text{O}_{2,c}]_n$	Initial concentration of dissolved oxygen in the capillary.
$[\text{O}_{2,c}]_n$	m M	$[\text{O}_{2,c}]_{\text{init}} \text{pow} \left(\frac{ScO_{2,n}}{1 - ScO_{2,n}}, \frac{1}{n_h} \right)$	Normal concentration of dissolved oxygen in the capillary.
p_1	dimensionless	$p_{tot} - p_{23}$	The number of protons pumped by a red (reduction reaction)
p_2	dimensionless	4	Total protons pumped by reaction 2
p_{23}	dimensionless	8	Total protons pumped by reactions 2 and 3
p_3	dimensionless	$p_{23} - p_2$	Total protons pumped by reaction 3
$P_{1,n}$	mmHg	$\frac{P_{a2,n} + P_{v,n}}{2}$	Normal average blood pressure in vessels
P_a	mmHg	50	Arterial blood pressure
$P_{a2,n}$	mmHg	$\frac{G_{0,n} P_a + G_n P_{v,n}}{G_n + G_{0,n}}$	Normal arterial blood pressure at the start of the cerebral arteries

P_a	mmHg	50	Normal value of arterial blood pressure
p_{C1}	dimensionless	8	Total protons pumped by complex 1
p_{C3}	dimensionless	4	Total protons pumped by complex 3
P_{ic}	mmHg	4.5	Intracranial blood pressure
$P_{ic,n}$	mmHg	4.5	Normal intracranial blood pressure
p_{tot}	dimensionless	18.40	Total protons pumped by reactions 1, 2 and 3
$p_{tot,NADH}$	dimensionless	$p_{C1} + p_{C3} + p_{23}$	Total protons pumped when the reducing agent is NADH
$P_{v,n}$	mmHg	$\frac{G_{t,n}}{G_v} (P_a - P_{vs}) + P_{vs}$	Normal venous blood pressure
P_{vs}	mmHg	1.5	Pressure in the venous sinuses
P_aCO_2	mmHg	40	Arterial partial pressure of CO2
$P_aCO_{2,n}$	mmHg	40	Normal arterial partial pressure of CO2
PaO_2	mmHg	$\frac{[O_{2,a}]}{k_{H,O_2}}$	Partial pressure of oxygen in the arteries
$[PCr]_n / [Pi]_n$	dimensionless	2.73	Normal Pcr/Pi concentration in the cytoplasm. Set this way because this is often measured by MRS (although mitochondria/cytoplasm differences are ignored).
$pH_{m,n}$	dimensionless	8	Normal mitochondrial pH
$pH_{o,n}$	dimensionless	7	Normal extra-mitochondrial pH

ϕ	m M	0.036	Value of O2 at half maximal saturation
r_0	cm	$1 - r_{frac}r_{occ}$	Radius of the supplying artery compartment
r_0	cm	0.0126	A special radius in the elastic tension relationship
R_C	dimensionless	2.2	Parameter controlling sensitivity of η to P_aCO_2
R_O	dimensionless	1.5	Parameter controlling sensitivity of η to $[O_{2,c}]$
R_P	dimensionless	4	Parameter controlling sensitivity of η to P_a
R_u	dimensionless	0	parameter controlling sensitivity of η to u
r_{CV}	dimensionless	5	A parameter controlling the ratio of maximal to minimal rates of oxidative phosphorylation
r_{init}	cm	$[Hbtot_c]$	Initial radius of blood vessels
r_m	cm	0.027	Value of vessel radius giving maximum muscular tension
$[Hbtot_c]$	cm	0.0187	Normal radius of blood vessels normal radius of blood vessels
r_t	cm	0.018	Parameter in the muscular tension relationship

r_{frac}	dimensionless	$1 - (\text{sqrt}(1 - \text{occ}_{frac}))^{\frac{1}{2}}$	Fraction by which the radius of the supplying artery compartment has been reduced
r_{occ}	dimensionless	0	Fraction by which the radius of the carotid arteries has been reduced
$SaO_{2,n}$	dimensionless	0.96	Normal saturation of the arterial haemoglobin
SaO_2	dimensionless	0.96	Saturation of the arterial haemoglobin
$ScO_{2,n}$	dimensionless	$\frac{SaO_{2,n} + SvO_{2,n}}{2}$	Normal capillary oxygen saturation
σ_{coll}	mmHg	62.79	Value of pressure at which vessels collapse
σ_{e0}	mmHg	0.1425	Parameter in relationship determining σ_e
$\sigma_{e,n}$	mmHg	$\sigma_{e0} \left(\exp \left(\frac{K_{\sigma} ([Hbtot_c] - r_0)}{r_0} \right) - 1 \right) - \sigma_{coll}$	Normal elastic stress in vessel walls
$SvO_{2,n}$	dimensionless	$\frac{[HbO_{2,v}]_n}{[Hbtot]_n}$	Normal venous oxygen saturation
$\nu_{u,n}$	s	5	The time constant associated with v_{CO_2}
$T_{e,n}$	mmHg cm	$\sigma_{e,n} h_n$	Normal elastic tension in vessel walls
T_{max0}	mmHg cm	$\frac{T_{max,n}}{1 + T_{e,n} \mu_n}$	Tmax at normal mu
$T_{max,n}$	mmHg cm	$\frac{T_{m,n}}{\exp \left(-\text{pow} \left(\text{fabs} \left(\frac{[Hbtot_c] - r_m}{r_t - r_m} \right), n_m \right) \right)}$	Normal maximum muscular tension developed by circulation
$T_{m,n}$	mmHg cm	$(P_{1,n} - P_{ic,n}) [Hbtot_c] - T_{e,n}$	Normal muscular tension in vessel walls

$v_{u,n}$	s	20	The time constant associated with v_{O_2}
$v_{u,n}$	s	5	The time constant associated with v_{P_a}
$v_{u,n}$	s	0.5	The time constant associated with v_u
u	dimensionless	1	The representation of "demand" in the model.
u_n	dimensionless	1	Resting "demand"
$V_{\max,ATP}$	$m M s^{-1}$	$\left(\frac{L_{CVn} Vol_{mit}}{na} + 2.0CMR_{glucn} \right) (1.0 + km) u$	Vmax of ATP use
$v_{CO_2,n}$	mmHg	$P_aCO_{2,n}$	Normal value of v_{CO_2} (CO2 passed through a first order filter)
$V_{glucosein}$	dimensionless	$\frac{[gluc_c]}{k_{glut} + [gluc_c]}$	Rate term for glucose transported into the cell. This is a Michaelis-Menten term, but fixed because blood glucose concentration is fixed.
v_{glut}	m M	$\frac{CMR_{gluc,n}}{V_{glucosein} - \frac{[gluc]_n}{[gluc]_n + k_{glut}}}$	Vmax for glucose transport both in and out of the cell from the capillary.
V_{lacin}	dimensionless	$\frac{[lac_c]}{k_{MCT} + [lac_c]}$	Rate of lactate transport into the cell
v_{MCT}	$m M s^{-1}$	$\frac{2CMR_{gluc,n} - \frac{CBF_n}{3}}{\frac{[lac]_n [H^+]_n}{([lac]_n + k_{MCT})([H^+]_n + k_{MCT})} - V_{lacin}}$	
$v_{O_2,n}$	m M	$[O_{2,c}]_n$	Normal value of v_{O_2} (capillary O2 passed through a first order filter)
$v_{P_a,n}$	mmHg	$P_{a2,n}$	Normal value of v_{P_a} (ABP passed through a first order filter)

v_{TCA}	$m M s^{-1}$	$\frac{k_{TCA_n}}{[Py]_n [NAD]_n} (k_{m,tcaN} + [NAD]_n) (k_{m,tcaP} + [Py]_n)$	Vmax for the TCA cycle
$v_{u,n}$	dimensionless	$L_{CV,frac}$	Normal value of v_u (u passed through a first order filter)
V_{Arat_n}	dimensionless	3	The normal ratio of the volume of the veins to the volume of the arteries
$v_{glyc,n}$	$m M s^{-1}$	$\frac{CMR_{gluc,n}}{glyc_{g,n} glyc_{p,n} glyc_{a,n} glyc_{m}}$	Normal Vmax for glycolysis which is assumed to be modified by the ratio of AMP to ATP normal
$V_{a,n}$	dimensionless	$\frac{t_n}{1 + V_{Arat_n}}$	Normal arterial blood volume as a fraction of total blood volume
Vol_{mit}	dimensionless	0.067	Fraction of brain water which is mitochondria
$V_{t,n}$	dimensionless	1	Normal total blood volume
$V_{v,n}$	dimensionless	$t_n \frac{V_{Arat_n}}{1 + V_{Arat_n}}$	Normal venous volume
$[HHb_a]$	m M	$[Hbtot] (1 - SaO_2)$	Unsaturated arterial haemoglobin
$[HHb_a]_n$	m M	$[Hbtot]_n (1 - SaO_{2,n})$	Normal unsaturated arterial haemoglobin
$[HbO_{2,a}]$	m M	$[Hbtot] SaO_2$	Concentration of arterial oxy-haemoglobin.
$[HbO_{2,a}]_n$	m M	$[Hbtot]_n SaO_{2,n}$	Normal concentration of arterial oxy-haemoglobin.
$[HbO_{2,v}]_{init}$	m M	$[HbO_{2,v}]_n$	Initial concentration of venous oxy-haemoglobin.

$[\text{HbO}_{2,v}]_n$	m M	$\frac{\text{CBF}_n [\text{HbO}_{2,a}]_n - R_u}{\text{CBF}_n}$	Normal concentration of venous oxy-haemoglobin.
$[\text{HbO}_{2,a}]_n$	m M	$[\text{Hbtot}]_n$	Total haemoglobin concentration in the arteries and veins.
$[\text{Hbtot}]_n$	m M	5.4	Normal total haemoglobin concentration in the arteries and veins.
$[\text{HHb}_v]_n$	m M	$[\text{Hbtot}]_n - [\text{HbO}_{2,v}]_n$	Normal unsaturated venous haemoglobin
Z	m V	59.028	2.303*RT/F

A.3 BrainPiglet v.2.0.1

A.3.1 Overview

- 25 differential state variables
- 3 algebraic state variables
- 128 intermediate variables
- 338 parameters

A.3.2 Differential equations

$$\begin{aligned} \frac{d[\text{ADP}]}{dt} = & (k_{\text{PCr}}^- + [\text{ATP}] [\text{Cr}]) - k_{\text{ATP,Cv}} + 2 (k_{\text{AK}}^- + [\text{ATP}] [\text{AMP}]) - 2 (k_{\text{AK}} + [\text{ADP}]^2) \\ & + \frac{V_{\text{max,ATP}} [\text{ATP}]}{k_m + [\text{ATP}]} - (k_{\text{PCr}} + [\text{PCr}] [\text{ADP}] [\text{H}^+]) \\ & - 2 \frac{v_{\text{glyc}} [\text{ADP}]^2 [\text{P}_i]^2 [\text{gluc}] \text{NAD}_{\text{cyt}}^2}{(k_{m,\text{glycA}}^2 + [\text{ADP}]^2) (k_{m,\text{glycP}}^2 + [\text{P}_i]^2) (k_{m,\text{glycG}} + [\text{gluc}]) (k_{m,\text{glycN}}^2 + \text{NAD}_{\text{cyt}}^2)} \end{aligned} \quad (\text{A.59})$$

$$\frac{d[\text{AMP}]}{dt} = (k_{\text{AK}} + [\text{ADP}]^2) - (k_{\text{AK}}^- + [\text{ATP}] [\text{AMP}]) \quad (\text{A.60})$$

$$\begin{aligned} \frac{d[\text{ATP}]}{dt} = & k_{\text{ATP,Cv}} - (k_{\text{PCr}}^- + [\text{ATP}] [\text{Cr}]) - (k_{\text{AK}}^- + [\text{ATP}] [\text{AMP}]) + (k_{\text{AK}} + [\text{ADP}]^2) \\ & - \frac{V_{\text{max,ATP}} [\text{ATP}]}{k_m + [\text{ATP}]} + (k_{\text{PCr}} + [\text{PCr}] [\text{ADP}] [\text{H}^+]) \\ & + 2 \frac{v_{\text{glyc}} [\text{ADP}]^2 [\text{P}_i]^2 [\text{gluc}] \text{NAD}_{\text{cyt}}^2}{(k_{m,\text{glycA}}^2 + [\text{ADP}]^2) (k_{m,\text{glycP}}^2 + [\text{P}_i]^2) (k_{m,\text{glycG}} + [\text{gluc}]) (k_{m,\text{glycN}}^2 + \text{NAD}_{\text{cyt}}^2)} \end{aligned} \quad (\text{A.61})$$

$$\begin{aligned} \frac{d[\text{BiC}_{\text{cyt}}]}{dt} = & (k_{\text{Chi}} + [\text{CO}_{2,\text{cyt}}]) - (k_{\text{nChi}} + [\text{H}^+] [\text{BiC}_{\text{cyt}}]) - (k_{\text{BiCshut}} + [\text{BiC}_{\text{cyt}}]) \\ & + (k_{\text{nBiCshut}} + [\text{BiC}_{\text{mit}}]) \end{aligned} \quad (\text{A.62})$$

$$\begin{aligned} \frac{d[\text{CO}_{2,\text{cyt}}]}{dt} = & (k_{\text{nChi}} + [\text{H}^+] [\text{BiC}_{\text{cyt}}]) - (k_{\text{Chi}} + [\text{CO}_{2,\text{cyt}}]) + (k_{\text{CO}_2\text{shut}} + [\text{CO}_{2,\text{mit}}]) \\ & - k_{\text{CO}_2,\text{out}} - (k_{\text{CO}_2\text{shut}} + [\text{CO}_{2,\text{cyt}}]) \quad (\text{A.63}) \end{aligned}$$

$$\frac{d[\text{Cr}]}{dt} = (k_{\text{PCr}} + [\text{PCr}] [\text{ADP}] [\text{H}^+]) - (k_{\text{PCr}}^- + [\text{ATP}] [\text{Cr}]) \quad (\text{A.64})$$

$$\begin{aligned} \frac{d[\text{gluc}]}{dt} = & V_{\text{glucosein}} v_{\text{glut}} - \frac{v_{\text{glut}} [\text{gluc}]}{k_{\text{glut}} + [\text{gluc}]} \\ & - \frac{v_{\text{glyc}} [\text{ADP}]^2 [\text{P}_i]^2 [\text{gluc}] \text{NAD}_{\text{cyt}}^2}{(k_{m,\text{glycA}}^2 + [\text{ADP}]^2) (k_{m,\text{glycP}}^2 + [\text{P}_i]^2) (k_{m,\text{glycG}} + [\text{gluc}]) (k_{m,\text{glycN}}^2 + \text{NAD}_{\text{cyt}}^2)} \quad (\text{A.65}) \end{aligned}$$

$$\begin{aligned} \frac{d[\text{H}^+]}{dt} = & \frac{p_1 + 4}{\frac{R_{\text{Hic}}}{\text{CBF}_n}} f_1 - \frac{1}{R_{\text{Hic}}} (k_{\text{MAshut}} + [\text{H}^+] [\text{NAD}]) - \frac{1}{R_{\text{Hic}}} (k_{\text{nChi}} + [\text{H}^+] [\text{BiC}_{\text{cyt}}]) \\ & + \frac{1}{R_{\text{Hic}}} (k_{\text{Chi}} + [\text{CO}_{2,\text{cyt}}]) + \frac{1}{R_{\text{Hic}}} (k_{\text{PCr}}^- + [\text{ATP}] [\text{Cr}]) + \frac{1}{R_{\text{Hic}}} (k_{\text{pl}}^- + [\text{lac}] \text{NAD}_{\text{cyt}}) \\ & + \frac{1}{R_{\text{Hic}}} V_{\text{lacin}} v_{\text{MCT}} + \frac{p_2}{\frac{R_{\text{Hic}}}{\text{CBF}_n}} f_2 - \frac{1}{R_{\text{Hic}}} (k_{\text{pl}} + [\text{Py}] [\text{H}^+]) - \frac{1}{\frac{R_{\text{Hic}}}{\text{CBF}_n}} k_{\text{TCA}} - \frac{1}{\frac{R_{\text{Hic}}}{\text{CBF}_n}} L \\ & - \frac{1}{R_{\text{Hic}}} \frac{v_{\text{MCT}} [\text{lac}] [\text{H}^+]}{(k_{\text{MCT}} + [\text{lac}]) (k_{\text{MCT}} + [\text{H}^+])} + \frac{1}{R_{\text{Hic}}} (k_{\text{MAshut}}^- + \text{NAD}_{\text{cyt}} \text{H}_m^+) \\ & + \frac{4}{R_{\text{Hic}}} \frac{v_{\text{glyc}} [\text{ADP}]^2 [\text{P}_i]^2 [\text{gluc}] \text{NAD}_{\text{cyt}}^2}{(k_{m,\text{glycA}}^2 + [\text{ADP}]^2) (k_{m,\text{glycP}}^2 + [\text{P}_i]^2) (k_{m,\text{glycG}} + [\text{gluc}]) (k_{m,\text{glycN}}^2 + \text{NAD}_{\text{cyt}}^2)} \\ & - \frac{1}{R_{\text{Hic}}} (k_{\text{PCr}} + [\text{PCr}] [\text{ADP}] [\text{H}^+]) \quad (\text{A.66}) \end{aligned}$$

$$\begin{aligned} \frac{d[\text{lac}]}{dt} = & (k_{\text{pl}} + [\text{Py}] [\text{H}^+]) - (k_{\text{pl}}^- + [\text{lac}] \text{NAD}_{\text{cyt}}) \\ & - \frac{v_{\text{MCT}} [\text{lac}] [\text{H}^+]}{(k_{\text{MCT}} + [\text{lac}]) (k_{\text{MCT}} + [\text{H}^+])} + V_{\text{lacin}} v_{\text{MCT}} \quad (\text{A.67}) \end{aligned}$$

$$\begin{aligned} \frac{d[\text{BiC}_{\text{mit}}]}{dt} = & \frac{1}{\text{CBF}_n} (k_{\text{BiCshut}} + [\text{BiC}_{\text{cyt}}]) - \frac{1}{\text{CBF}_n} (k_{\text{nBiCshut}} + [\text{BiC}_{\text{mit}}]) \\ & - (k_{\text{nCHm}} + \text{H}_m^+ [\text{BiC}_{\text{mit}}]) + (k_{\text{CHm}} + [\text{CO}_{2,\text{mit}}]) \end{aligned} \quad (\text{A.68})$$

$$\begin{aligned} \frac{d[\text{CO}_{2,\text{mit}}]}{dt} = & 3k_{\text{TCA}} - \frac{1}{\text{CBF}_n} (k_{\text{CO2shut}} + [\text{CO}_{2,\text{mit}}]) + \frac{1}{\text{CBF}_n} (k_{\text{CO2shut}} + [\text{CO}_{2,\text{cyt}}]) \\ & + (k_{\text{nCHm}} + \text{H}_m^+ [\text{BiC}_{\text{mit}}]) - (k_{\text{CHm}} + [\text{CO}_{2,\text{mit}}]) \end{aligned} \quad (\text{A.69})$$

$$\begin{aligned} \frac{d[\text{P}_i]}{dt} = & \frac{V_{\text{max,ATP}} [\text{ATP}]}{k_m + [\text{ATP}]} - k_{\text{ATP,Cv}} \\ & - 2 \frac{v_{\text{glyc}} [\text{ADP}]^2 [\text{P}_i]^2 [\text{gluc}] \text{NAD}_{\text{cyt}}^2}{\left(k_{m,\text{glycA}}^2 + [\text{ADP}]^2\right) \left(k_{m,\text{glycP}}^2 + [\text{P}_i]^2\right) \left(k_{m,\text{glycG}} + [\text{gluc}]\right) \left(k_{m,\text{glycN}}^2 + \text{NAD}_{\text{cyt}}^2\right)} \end{aligned} \quad (\text{A.70})$$

$$\frac{d[\text{PCr}]}{dt} = (k_{\text{PCr}}^- + [\text{ATP}] [\text{Cr}]) - (k_{\text{PCr}} + [\text{PCr}] [\text{ADP}] [\text{H}^+]) \quad (\text{A.71})$$

$$\begin{aligned} \frac{d[\text{Py}]}{dt} = & \left(k_{\text{pl}}^- + [\text{lac}] \text{NAD}_{\text{cyt}}\right) - \left(k_{\text{pl}} + [\text{Py}] [\text{H}^+]\right) - \frac{1}{\text{CBF}_n} k_{\text{TCA}} \\ & + 2 \frac{v_{\text{glyc}} [\text{ADP}]^2 [\text{P}_i]^2 [\text{gluc}] \text{NAD}_{\text{cyt}}^2}{\left(k_{m,\text{glycA}}^2 + [\text{ADP}]^2\right) \left(k_{m,\text{glycP}}^2 + [\text{P}_i]^2\right) \left(k_{m,\text{glycG}} + [\text{gluc}]\right) \left(k_{m,\text{glycN}}^2 + \text{NAD}_{\text{cyt}}^2\right)} \end{aligned} \quad (\text{A.72})$$

$$\frac{d\text{Cu}_{\text{A,o}}}{dt} = 4f_2 - 4f_1 \quad (\text{A.73})$$

$$\frac{d\text{cyta}_{3r}}{dt} = 4f_2 - 4f_3 \quad (\text{A.74})$$

$$\frac{d\Delta\Psi}{dt} = \frac{p_2 f_2 + p_1 f_1 + p_3 f_3 - L}{C_{im}} \quad (\text{A.75})$$

$$\begin{aligned} \frac{dH_m^+}{dt} = & \frac{1}{R_{Hi} CBF_n} (k_{MAshut} + [H^+] [NAD]) - \frac{p_1 + \frac{5}{3}}{R_{Hi}} f_1 - \frac{p_2}{R_{Hi}} f_2 - \frac{p_3}{R_{Hi}} f_3 \\ & + \frac{4}{R_{Hi}} k_{TCA} + \frac{1}{R_{Hi}} L - \frac{1}{R_{Hi}} (k_{nCHm} + H_m^+ [BiCmit]) \\ & - \frac{1}{R_{Hi} CBF_n} (k_{MAshut}^- + NAD_{cyt} H_m^+) + \frac{1}{R_{Hi}} (k_{CHm} + [CO_{2,mit}]) \quad (A.76) \end{aligned}$$

$$\begin{aligned} \frac{d[NAD]}{dt} = & 2f_1 - \frac{1}{CBF_n} (k_{MAshut} + [H^+] [NAD]) - 5k_{TCA} \\ & + \frac{1}{CBF_n} (k_{MAshut}^- + NAD_{cyt} H_m^+) \quad (A.77) \end{aligned}$$

$$\begin{aligned} \frac{dNAD_{cyt}}{dt} = & (k_{MAshut} + [H^+] [NAD]) - (k_{pl}^- + [lac] NAD_{cyt}) + (k_{pl} + [Py] [H^+]) \\ & - (k_{MAshut}^- + NAD_{cyt} H_m^+) \\ & - 2 \frac{v_{glyc} [ADP]^2 [P_i]^2 [gluc] NAD_{cyt}^2}{(k_{m,glycA}^2 + [ADP]^2) (k_{m,glycP}^2 + [P_i]^2) (k_{m,glycG} + [gluc]) (k_{m,glycN}^2 + NAD_{cyt}^2)} \quad (A.78) \end{aligned}$$

$$\frac{d[O_2]}{dt} = \frac{1}{CBF_n} J_{O_2} - f_3 \quad (A.79)$$

$$\frac{dv_{CO_2}}{dt} = \frac{1}{v_{u,n}} (P_a CO_2 - v_{CO_2}) \quad (A.80)$$

$$\frac{dv_{O_2}}{dt} = \frac{1}{v_{u,n}} ([O_{2,c}] - v_{O_2}) \quad (A.81)$$

$$\frac{dv_{P_a}}{dt} = \frac{1}{v_{u,n}} (P_{a2} - v_{P_a}) \quad (A.82)$$

$$\frac{dv_u}{dt} = \frac{1}{v_{u,n}} (CBF - v_u) \quad (A.83)$$

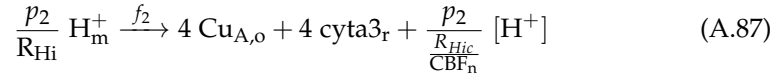
A.3.3 Algebraic equations

$$[\text{O}_{2,c}]_{\text{init}} \text{pow} \left(\frac{\text{ScO}_2}{1 - \text{ScO}_2}, \frac{1}{n_h} \right) - [\text{O}_{2,c}] = 0 \quad (\text{A.84})$$

$$T_e + T_m - (P_1 - P_{ic}) r = 0 \quad (\text{A.85})$$

$$\text{CBF} ([\text{HbO}_{2,a}] - [\text{HbO}_{2,v}]) - J_{\text{O}_2} = 0 \quad (\text{A.86})$$

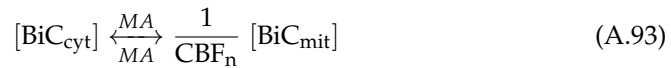
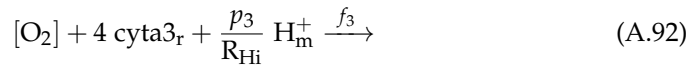
A.3.4 Chemical reactions



Mass Action kinetics are assumed for the forward reaction, with calculated rate term $k_{\text{AK}} + [\text{ADP}]^2$. Mass Action kinetics are assumed for the reverse reaction, with calculated rate term $k_{\text{AK}}^- + [\text{ATP}] [\text{AMP}]$.

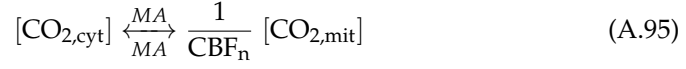


Michaelis-Menten kinetics are assumed, with calculated rate term $\frac{V_{\text{max,ATP}} [\text{ATP}]}{k_m + [\text{ATP}]}$.



Mass Action kinetics are assumed for the forward reaction, with calculated rate term $k_{\text{BiCshut}} + [\text{BiC}_{\text{cyt}}]$. Mass Action kinetics are assumed for the reverse reaction, with calculated rate term $k_{\text{BiCshut}}^- + [\text{BiC}_{\text{mit}}]$.





Mass Action kinetics are assumed for the forward reaction, with calculated rate term $k_{\text{CO}_2\text{shut}} + [\text{CO}_{2,\text{cyt}}]$. Mass Action kinetics are assumed for the reverse reaction, with calculated rate term $k_{\text{CO}_2\text{shut}} + [\text{CO}_{2,\text{mit}}]$.



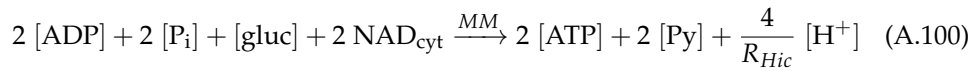
Mass Action kinetics are assumed for the forward reaction, with calculated rate term $k_{\text{CH}_m} + [\text{CO}_{2,\text{mit}}]$. Mass Action kinetics are assumed for the reverse reaction, with calculated rate term $k_{n\text{CH}_m} + \text{H}_m^+ [\text{BiC}_{\text{mit}}]$.



Mass Action kinetics are assumed for the forward reaction, with calculated rate term $k_{\text{CH}_i} + [\text{CO}_{2,\text{cyt}}]$. Mass Action kinetics are assumed for the reverse reaction, with calculated rate term $k_{n\text{CH}_i} + [\text{H}^+] [\text{BiC}_{\text{cyt}}]$.

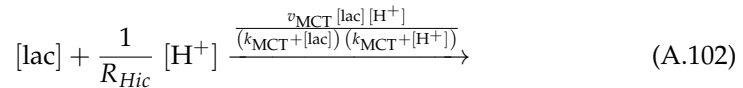
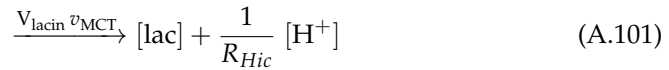


Michaelis-Menten kinetics are assumed, with calculated rate term $\frac{v_{\text{glut}} [\text{gluc}]}{k_{\text{glut}} + [\text{gluc}]}$.



Michaelis-Menten kinetics are assumed, with calculated rate term

$$\frac{v_{\text{glyc}} [\text{ADP}]^2 [\text{P}_i]^2 [\text{gluc}] \text{NAD}_{\text{cyt}}^2}{\left(k_{m,\text{glycA}}^2 + [\text{ADP}]^2\right) \left(k_{m,\text{glycP}}^2 + [\text{P}_i]^2\right) \left(k_{m,\text{glycG}} + [\text{gluc}]\right) \left(k_{m,\text{glycN}}^2 + \text{NAD}_{\text{cyt}}^2\right)}$$



Mass Action kinetics are assumed for the forward reaction, with calculated rate term $k_{MAshut} + [H^+] [NAD]$. Mass Action kinetics are assumed for the reverse reaction, with calculated rate term $k_{MAshut}^- + NAD_{cyt} H_m^+$.

$$\xrightarrow{J_{O_2}} \frac{1}{CBF_n} [O_2] \quad (A.104)$$

$$[PCr] + [ADP] + \frac{1}{R_{Hic}} [H^+] \xleftrightarrow{MA} [ATP] + [Cr] \quad (A.105)$$

Mass Action kinetics are assumed for the forward reaction, with calculated rate term $k_{PCr} + [PCr] [ADP] [H^+]$. Mass Action kinetics are assumed for the reverse reaction, with calculated rate term $k_{PCr}^- + [ATP] [Cr]$.

$$\frac{1}{\frac{R_{Hic}}{CBF_n}} [H^+] \xrightarrow{L} \frac{1}{R_{Hi}} H_m^+ \quad (A.106)$$

$$[Py] + \frac{1}{R_{Hic}} [H^+] \xleftrightarrow{MA} [lac] + NAD_{cyt} \quad (A.107)$$

Mass Action kinetics are assumed for the forward reaction, with calculated rate term $k_{pl} + [Py] [H^+]$. Mass Action kinetics are assumed for the reverse reaction, with calculated rate term $k_{pl}^- + [lac] NAD_{cyt}$.

$$\frac{1}{CBF_n} [Py] + 5 [NAD] + \frac{1}{\frac{R_{Hic}}{CBF_n}} [H^+] \xrightarrow{k_{TCA}} \frac{4}{R_{Hi}} H_m^+ + 3 [CO_{2,mit}] \quad (A.108)$$

A.3.5 State variables

Symbol	Units	Initialiser	Notes
[ADP]	m M	[ADP] _n	ADP concentration in cytoplasm and mitochondria
[AMP]	m M	[AMP] _n	AMP concentration in cytoplasm
[ATP]	m M	[ATP] _n	ATP concentration in cytoplasm and mitochondria
[BiC _{cyt}]	m M	[BiC _{cyt,n}]	The concentration of bicarbonate ions in the cytoplasm
[CO _{2,cyt}]	m M	[CO _{2,cyt,n}]	The concentration of dissolved carbon dioxide in the cytoplasm
[Cr]	m M	[Cr] _n	Creatine concentration in cytoplasm
[gluc]	m M	[gluc] _n	Concentration of glucose in the cytoplasm

$[H^+]$	m M	$[H^+]_n$	Concentration of hydrogen ions in the cytoplasm
$[lac]$	m M	$[lac]_n$	Concentration of lactate in the cytoplasm
$[BiC_{mit}]$	m M	$[BiC_{mit,n}]$	The concentration of bicarbonate ions in the mitochondria
$[CO_{2,mit}]$	m M	$[CO_{2,mit,n}]$	The concentration of dissolved carbon dioxide in the mitochondria
$[P_i]$	m M	$[P]_n$	Inorganic phosphate concentration in cytoplasm and mitochondria
$[PCr]$	m M	$[PCr]_n$	Phosphocreatine concentration in cytoplasm
$[Py]$	m M	$[Py]_n$	Concentration of pyruvate in the cytoplasm
$Cu_{A,o}$	m M	$Cu_{A,o,init}$	The concentration of oxidised cytochrome-c-oxidase
$cyta3_r$	m M	$[a3r]_{init}$	Concentration of reduced cyt a3 in mitochondria
$\Delta\Psi$	m V	$\Delta\Psi_{init}$	Mitochondrial inner membrane potential
H_m^+	m M	$H_{m,init}^+$	Concentration of hydrogen ions in mitochondria
$[NAD]$	m M	$[NAD]_n$	Concentration of NAD in the mitochondria
NAD_{cyt}	m M	NAD_{cytn}	Concentration of NAD in the cytoplasm
$[O_2]$	m M	$[O_2]_{init}$	The concentration of oxygen in the mitochondria
$[O_{2,c}]$	m M	$[O_{2,c}]_{init}$	The concentration of oxygen in the capillary.
r	cm	r_{init}	Typical radius of cerebral vessels
ν_{CO_2}	mmHg	$\nu_{CO_2,n}$	CO2 passed through a first order filter.
ν_{O_2}	m M	$\nu_{O_2,n}$	Capillary O2 passed through a first order filter.
ν_{P_a}	mmHg	$\nu_{P_a,n}$	Arterial blood pressure passed through a first order filter.

ν_u	dimensionless	$\nu_{u,n}$	The demand parameter u passed through a first order filter.
$[\text{HbO}_{2,v}]$	mM	$[\text{HbO}_{2,v}]_{\text{init}}$	The concentration of bound oxygen in the veins.

A.3.6 Intermediate variables

Symbol	Units	Expression	Notes
$\text{Cu}_{A,o}$	mM	$\mathcal{E}_0(\text{cyt } a_3) - \text{Cu}_{A,o}$	The concentration of reduced cytochrome-c-oxidase in the mitochondria.
AVR	dimensionless	$\frac{V_a}{V_v}$	Arterio-venous volume ratio
$\text{cyt}a_3_o$	mM	$\mathcal{E}_0(\text{cyt } a_3) - \text{cyt}a_3_r$	Concentration of oxidised cyt a3 in mitochondria
C_{0i}	dimensionless	$\frac{10^{-\text{pH}_m} - 10^{-\text{pH}_m - \text{dpH}}}{\text{dpH}}$	Natural buffering capacity for protons in mitochondria
C_{0ic}	dimensionless	$\frac{10^{-\text{pH}_o} - 10^{-\text{pH}_o - \text{dpH}}}{\text{dpH}}$	Natural buffering capacity for protons in the cytoplasm
C_{NADH}	mV	$\frac{\mathcal{E}_0(\text{cyt } a_3)}{2} \log_{10} \left(\frac{1}{[\text{NAD}]/[\text{NADH}]} \right)$	Redox potential minus standard redox potential for NADH at normal demand
CBF	$\text{ml m}^{-1} \text{s}^{-1}$	$G (P_{a2} - P_v)$	Cerebral blood flow
TOS	μM	$\Delta\text{oxCCO}_{\text{offset}} + 1000\text{CBF}_n (\text{Cu}_{A,o} - \text{VArat}_n)$	The expected CCO signal (as measured by NIRS)
CMRO_2	mM s^{-1}	$f_3 \text{CBF}_n$	Cerebral metabolic rate for oxygen
ΔG_1	mV	$p_1 \Delta p - 4 \left(E_1 + \mathcal{E}_0(\text{cyt } a_3) \log_{10} \left(\frac{\text{Cu}_{A,o}}{\text{Cu}_{A,o}} \right) \right)$	Free energy associated with reaction 1

ΔG_2	m V	$p_2 \Delta p$ $-4 \left(E_2 + \mathcal{E}_0(\text{cyt } a_3) \left(\log_{10} \left(\frac{\text{Cu}_{A,o}}{\text{Cu}_{A,o}} \right) - \log_{10} \left(\frac{\text{cyta}_3^r}{\text{cyta}_3^o} \right) \right) \right)$	Free energy associated with reaction 2
ΔG	J mol ⁻¹	$\Delta G^\circ + \mathcal{E}_0(\text{cyt } a_3) F \log_{10} (g_p)$	Gibbs free energy of ATP hydrolysis
ΔHbdiff	μM	$\Delta \text{Hbdiff}_{\text{offset}} + \Delta \text{HbO}_2 - \Delta \text{HHb}$	Change in Hbdiff (NIRS)
ΔHbO_2	μM	$\Delta \text{HbO}_{2,\text{offset}} + \text{HbO}_2 - \text{HbO}_{2n}$	Change in total oxygenated haemoglobin (NIRS)
ΔHbt	μM	$\Delta \text{HbT}_{\text{offset}} + \text{Hbt} - \text{Hbt}_n$	Change in total haemoglobin (NIRS)
ΔHHb	μM	$\Delta \text{HHb}_{\text{offset}} + \text{HHb} - \text{Hbt}_n$	Change in total deoxygenated haemoglobin (NIRS)
Δp	m V	$\Delta \Psi + \mathcal{E}_0(\text{cyt } a_3) \Delta \text{pH}$	The proton motive force across the mitochondrial inner membrane.
ΔpH	dimensionless	$\text{pH}_m - \text{pH}_o$	The pH difference across mitochondrial inner membrane
$E_{1,NADH}$	m V	$\mathcal{E}_0(\text{Cu}_A) - \mathcal{E}_0(\text{NADH}) + C_{\text{NADH}}$	E1 when the reducing substrate is NADH
E_1	m V	$E_{1,NADH}$	The energy provided by electron transfer to Cu _A
η	dimensionless	$R_P \left(\frac{v_{P_a}}{v_{P_a,n}} - 1 \right) + R_O \left(\frac{v_{O_2}}{v_{O_2,n}} - 1 \right) + R_U \left(1 - \frac{v_U}{v_{U,n}} \right) +$ $R_C \left(1 - \frac{v_{\text{CO}_2}}{v_{\text{CO}_2,n}} \right)$	Total autoregulatory stimuli
f_1	m M s ⁻¹	$k_1 \text{Cu}_{A,o} - k_{-1} \text{Cu}_{A,o}$	The rate at which Cu _A is reduced

f_2	m M s^{-1}	$k_2 \text{Cu}_{A,o} \text{cyt}a_3_o - k_{-2} \text{Cu}_{A,o} \text{cyt}a_3_r$	The rate at which Cu_A is oxidised and $\text{cyt} a_3$ reduced.
f_3	m M s^{-1}	$\frac{c_{k2} [\text{O}_2] \text{cyt}a_3_r \exp(-c_3 (\Delta p - \Delta p_{30}))}{1 + \exp(-c_3 (\Delta p - \Delta p_{30}))}$	The rate at which $\text{cyt} a_3$ is oxidised
G	$\text{mmHg}^{-1} \text{s}^{-1}$	$R_u \text{pow}(r, 4)$	Resistance of cerebral circulation
g_p	dimensionless	$\frac{[\text{ADP}] [\text{P}_i]}{[\text{ATP}] \times 1000}$	(Normalised) phosphorylation potential (or ADP/ATP ratio)
G_t	$\text{mmHg}^{-1} \text{s}^{-1}$	$\frac{G G_0 G_v}{G G_0 + G G_v + G_v G_0}$	The total conductance of the cerebral blood vessels
h	cm	$(\text{pow}(r, 2) + 2r_0 h_0 + h_0 h_0)^{\frac{1}{2}} - r$	Wall thickness of cerebral vessels
HbO_2	μM	$\frac{V_a [\text{HbO}_{2,a}] + V_v [\text{HbO}_{2,v}]}{4} V_{\text{blood},n} \times 1000$	Total oxygenated haemoglobin (NIRS)
Hbt	μM	$\frac{(V_a + V_v) [\text{HbO}_{2,a}]_n}{4} V_{\text{blood},n} \times 1000$	Total haemoglobin (NIRS)
HHb	μM	$\frac{V_a [\text{HHb}_a] + V_v [\text{HHb}_v]}{4} V_{\text{blood},n} \times 1000$	Total deoxygenated haemoglobin (NIRS)
J_{O_2}	m M s^{-1}	$J_{\text{O}_2,\text{min}}$	The rate at which oxygen is supplied to the mitochondria.
$J_{\text{O}_2,\text{min}}$	m M s^{-1}	$f_{\text{min}}(D_{\text{O}_2} ([\text{O}_{2,c}] - [\text{O}_2]), \text{CBF} [\text{HbO}_{2,a}])$	Rate at which oxygen is supplied to the mitochondria, minimum of diffusion rate and delivery rate
k_1	s^{-1}	$k_{1,0} \exp(-c_{k1} (\Delta p - \text{SaO}_{2,n}))$	Forward rate constant for reaction 1

$k_{1,0}$	s^{-1}	$\frac{k_{1,n} \frac{N_t}{1+[NAD]/[NADH]}}{[NADH]_n}$	Forward rate constant for reaction 1 at normal PMF
k_2	$m^{-1} M s^{-1}$	$k_{2,n} \exp(-c_{k2} (\Delta p - SaO_{2,n}))$	Forward rate constant for reaction 2
$k_{CO_2,out}$	dimensionless	$\frac{CBF_n [CO_{2,cyt}]}{[CO_{2,cyt,n}]}$	Rate at which CO2 moves out of the cell
k_{MAshut}	s^{-1}	$\frac{\frac{CBF_n NADH_{cyt}}{3}}{[NAD]_n [H^+]_n NADH_{cyt} - \frac{1}{K_{eqMAshut}} NAD_{cytn} H_{m,n}^+ NADH}$	Rate of forward reaction in the malate-aspartate shuttle
k_{MAshut}^-	s^{-1}	$\frac{\frac{k_{MAshut} NADH}{\mathit{mathrm}NADH_{cyt}}}{K_{eqMAshut}}$	Rate of backward reaction in the malate-aspartate shuttle
k_{PCr}^-	$m^{-1} M s^{-1}$	$\frac{\log(2)}{\left(K_{eq,PCr} \left([PCr]_n + [ADP]_n + \frac{[H^+]_n}{R_{Hic}}\right) + [Cr]_n + [ATP]_n\right) t_{1/2,PCr}}$	The backward rate of reaction for the reaction in which phosphocreatine combines with ADP to give creatine and ATP
k_{PCr}	$m^{-1} M s^{-1}$	$\frac{\log(2)}{\left([PCr]_n + [ADP]_n + \frac{[H^+]_n}{R_{Hic}} + \frac{[Cr]_n + [ATP]_n}{K_{eq,PCr}}\right) t_{1/2,PCr}}$	The forward rate of reaction for the reaction in which phosphocreatine combines with ADP to give creatine and ATP
k_{pl}	s^{-1}	$\frac{2CMR_{gluc,n} - \frac{CBF_n}{3} + k_{pl}^- [lac]_n NAD_{cytn} \mathit{mathrm}NADH_{cyt}}{[Py]_n [H^+]_n} \frac{\mathit{mathrm}NADH_{cyt}}{NADH_{cytn}}$	Rate of forward reaction in the pyruvate lactate equilibrium
k_{TCA}	$m M s^{-1}$	$\frac{v_{TCA} [Py] [NAD]}{(k_{m,tcaN} + [NAD]) (k_{m,tcaP} + [Py])}$	Rate of the TCA cycle

$k_{ATP,CV}$	$m M s^{-1}$	$\frac{L_{CV} CBF_n}{n_a}$	Rate of ATP synthesis by Complex V
Keq_1	dimensionless	$pow \left(10, \frac{-1}{\mathcal{E}_0(\text{cyt } a_3)} \left(\frac{p_1 \Delta p}{4} - E_1 \right) \right)$	Equilibrium constant for reaction 1
Keq_2	dimensionless	$pow \left(10, \frac{-1}{\mathcal{E}_0(\text{cyt } a_3)} \left(\frac{p_2 \Delta p}{4} - E_2 \right) \right)$	Equilibrium constant for reaction 2
k_{-1}	s^{-1}	$\frac{k_1}{Keq_1}$	Backward rate constant for reaction 1
k_{-2}	$m^{-1} M s^{-1}$	$\frac{k_2}{Keq_2}$	Backward rate constant for reaction 2
L	$m M s^{-1}$	$L_{CV} + L_{lk}$	The rate at which protons reenter the mitochondrial matrix
L_{CV}	$m M s^{-1}$	$\frac{L_{CV,frac} L_{CV,max} (1 - \exp(-\theta))}{1 + r_{CV} \exp(-\theta)}$	The rate at which protons reenter the mitochondrial matrix associated with ADP phosphorylation
L_{lk}	$m M s^{-1}$	$\Delta p_{3,corr} f_n (\exp(\Delta p f_n) - 1)$	The rate at which protons reenter the mitochondrial matrix through leak channels
μ	dimensionless	$\frac{\mu_{min} + \mu_{max} \exp(\eta)}{1 + \exp(\eta)}$	Total autoregulatory stimuli filtered through sigmoidal function
NADH	m M	$N_t - [NAD]$	Concentration of NADH in the mitochondria mitochondrial NADH concentration
NADH _{cyt}	m M	$NAD_{cytn} + NADH_{cytn} - NAD_{cyt}$	Concentration of NADH in the cytoplasm

$[\text{NAD}]/[\text{NADH}]$	dimensionless	$\frac{[\text{NAD}]}{[\text{NADH}]}$	NAD/NADH ratio
NTP/EPP	dimensionless	$\frac{[\text{ATP}]}{[\text{ATP}]}$	NTP/EPP calculation
P_1	mmHg	$\frac{EPP}{P_{a2} + P_v}$	Average blood pressure in vessels
P_{a2}	mmHg	$\frac{G_0 P_a + G P_v}{G + G_0}$	The pressure at the start of the cerebral artery compartment
P_v	mmHg	$\frac{G_t}{G_v} (P_a - P_{vs}) + P_{vs}$	Venous blood pressure
pH_m	dimensionless	$-\log_{10} \left(\frac{[\text{H}^+]_m}{1000} \right)$	Mitochondrial pH
pH_o	dimensionless	$-\log_{10} \left(\frac{[\text{H}^+]_o}{1000} \right)$	Cytoplasmic pH
r_{buffi}	dimensionless	$\frac{C_{\text{buffi}}}{C_{0i}}$	Buffering capacity for protons in mitochondria
r_{buffic}	dimensionless	$\frac{C_{\text{buffic}}}{C_{0ic}}$	Buffering capacity for protons in the cytoplasm
R_{Hi}	dimensionless	r_{buffi}	Relative mitochondrial volume for protons
R_{Hic}	dimensionless	r_{buffic}	Relative cytoplasmic volume for protons
ScO_2	dimensionless	$\frac{\text{SaO}_2 + \text{SvO}_2}{2}$	Capillary oxygen saturation
σ_e	mmHg	$\sigma_{e0} \left(\exp \left(\frac{K_\sigma (r - r_0)}{r_0} \right) - 1 \right) - \sigma_{coll}$	Elastic stress in vessel walls
SvO_2	dimensionless	$\frac{[\text{HbO}_{2,v}]}{[\text{HbO}_{2,a}]_n}$	Venous oxygen saturation

T_e	mmHg cm	$\sigma_e h$	Elastic tension in vessel walls
T_m	mmHg cm	$T_{\max} \exp \left(-\text{pow} \left(\text{fabs} \left(\frac{r - r_m}{r_t - r_m} \right), n_m \right) \right)$	Muscular tension in vessel walls
θ	dimensionless	$k_{CV} \left(\Delta p + \frac{\mathcal{E}_0(\text{cyt a}_3)}{n_a} \log_{10} \left(\frac{g_p}{g_{p,n}} \right) - L_{CV,\max} \right)$	Driving force for complex V
TOS	dimensionless	$\frac{100 \left(\frac{\text{pow} \left(\frac{r}{[\text{Hbtot}_c]}, 2 \right)}{\text{pow} \left(\frac{r}{[\text{Hbtot}_c]}, 2 \right) + \frac{V_v}{V_{a,n}}} [\text{HbO}_{2,a}] + \frac{\frac{V_v}{V_{a,n}}}{\text{pow} \left(\frac{r}{[\text{Hbtot}_c]}, 2 \right) + \frac{V_v}{V_{a,n}}} [\text{HbO}_{2,v}] \right)}{[\text{HbO}_{2,a}]_n}$	Tissue Oxygenation index.
v_{glyc}	m M s^{-1}	$\frac{v_{\text{glyc},n} (I + 1)}{1 + I \frac{[\text{ATP}]_n}{[\text{ATP}]_n} \frac{[\text{AMP}]_n}{[\text{AMP}]_n}}$	Vmax for glycolysis Vmax for glycolysis
V_{mca}	cm s^{-1}	CBF CBFscale	The velocity of blood in the middle cerebral artery
V_a	dimensionless	$V_{a,n} \text{pow} \left(\frac{r}{[\text{Hbtot}_c]}, 2 \right)$	arterial blood volume as a fraction of normal total blood volume
V_t	dimensionless	$V_a + V_v$	Normalised total blood volume
V_v	dimensionless	$V_{v,n} + C_v (P_v - P_{v,n})$	Venous blood volume as a fraction of total blood volume
$[\text{HHb}_v]$	m M	$[\text{HbO}_{2,a}]_n - [\text{HbO}_{2,v}]$	The concentration of deoxy-haemoglobin in the veins.

A.3.7 Parameters

Symbol	Units	Initialiser	Notes
$[ADP]_n$	m M	0.012	The normal concentration of ADP in the cytoplasm
$[AMP]_n$	m M	$\frac{K_{eq,ADPATP} \text{pow} ([ADP]_n, 2)}{[ATP]_n}$	Normal AMP concentration in cytoplasm
$[ATP]_n$	m M	1.2	The normal concentration of ATP in the cytoplasm
$[BiC_{cyt,n}]$	m M	$\frac{0.95k_{CH,eq} [CO_{2,cyt,n}]}{[H^+]_n}$	The normal concentration of bicarbonate ions in the cytoplasm
$[CO_{2,cyt,n}]$	m M	$PtCO_2 n k_{H,CO_2,t}$	The normal concentration of dissolved carbon dioxide in the cytoplasm
$[Cr]_n$	m M	$\frac{K_{eq,PCr}^* [ADP]_n [PCr]_n}{[ATP]_n}$	Normal concentration of creatine in cytoplasm
$[gluc]_n$	m M	1.2	Normal cellular concentration of glucose
$[H^+]_n$	m M	$1000 \text{pow} (10, -pH_{o,n})$	Normal hydrogen ion concentration in the cytoplasm
$[lac]_n$	m M	3	Normal concentration of lactate in the cytoplasm
$[BiC_{mit,n}]$	m M	$\frac{k_{CH,eq} [CO_{2,mit,n}]}{H_{m,n}^+}$	The normal concentration of bicarbonate ions in the mitochondria

$[\text{CO}_{2,\text{mit},n}]$	m M	$1.2[\text{CO}_{2,\text{cyt},n}]$	The normal concentration of dissolved carbon dioxide in the mitochondria
$[\text{PCr}]_n$	m M	2.6	Normal concentration of phosphocreatine in cell cytoplasm
$[\text{P}]_n$	m M	$\frac{[\text{PCr}]_n}{[\text{PCr}]_n/[\text{P}_i]_n}$	The normal concentration of inorganic phosphate in the cytoplasm
$[\text{Py}]_n$	m M	0.1	Normal concentration of pyruvate ions in the cytoplasm
$\text{Cu}_{\text{A,frac},n}$	dimensionless	0.67	Normal oxidised fraction of Cu_{A}
$\text{Cu}_{\text{A,o,init}}$	m M	$\text{Cu}_{\text{A,o},n}$	Initial oxidized Cu_{A}
$\text{Cu}_{\text{A,o},n}$	m M	$[\text{CCO}]_{\text{mit}} \text{Cu}_{\text{A,frac},n}$	Normal oxidized Cu_{A}
$\text{Cu}_{\text{A,r},n}$	m M	$[\text{CCO}]_{\text{mit}} - \text{Cu}_{\text{A,o},n}$	The resting amount of reduced cytochrome-c-oxidase
$\text{a3}_{\text{frac},n}$	dimensionless	$1 - \frac{\text{cyta3}_{\text{r},n}}{[\text{CCO}]_{\text{mit}}}$	Normal oxidised fraction of cyt a3
$\text{a3}_{\text{o,init}}$	m M	$\text{a3}_{\text{o},n}$	Initial oxidised cytochrome a3
$\text{a3}_{\text{o},n}$	m M	$[\text{CCO}]_{\text{mit}} - \text{cyta3}_{\text{r},n}$	Normal oxidised cytochrome a3
$V_{\text{blood},n}$	dimensionless	0.0325	Normal blood volume as a fraction of brain tissue volume
$[\text{a3r}]_{\text{init}}$	m M	$\text{cyta3}_{\text{r},n}$	Initial reduced cytochrome a3
$\text{cyta3}_{\text{r},n}$	m M	$\frac{\frac{f_n}{c_{k2}}}{P_a \text{CO}_{2,n} \frac{\exp(-c3(\text{SaO}_{2,n} - \Delta p_{30}))}{1 + \exp(-c3(\text{SaO}_{2,n} - \Delta p_{30}))}}$	Normal reduced cytochrome a3
$c3$	$\text{m}^{-1} \text{V}$	0.11	Parameter controlling the sensitivity of reaction 3 to PMF

C_{buffi}	dimensionless	0.022	Buffering capacity for protons in mitochondria
C_{buffic}	dimensionless	0.025	Buffering capacity for protons in the cytoplasm
occ_{frac}	dimensionless	0.8	Fraction of arterial blood which flows through the carotid arteries under normal conditions
C_{im}	$mM m^{-1} V$	0.00675	Capacitance of mitochondrial inner membrane
C_{im0}	dimensionless	0.00675	Normal value of C_{NADH}
$C_{NADH,n}$	mV	$\frac{\epsilon_0(\text{cyt } a_3)}{2} \log_{10} \left(\frac{1}{\frac{[NAD]_n}{[NADH]_n}} \right)$	
C_v	$mmHg^{-1}$	0.047	Compliance of the veins (normalised)
CBF_n	$ml m^{-1} l s^{-1}$	0.008	Normal cerebral blood flow
CBF_{scale}	cm	5000	Ratio between V_{mca} and CBF
$\Delta oxCCO_{offset}$	μM	0	An arbitrary baseline offset to the CCO signal (NIRS)
c_{k1}	$m^{-1} V$	0.01	Parameter controlling sensitivity of k_1 to PMF
c_{k2}	$m^{-1} V$	0.02	Parameter controlling sensitivity of k_2 to PMF
$CMR_{gluc,n}$	dimensionless	0.0044	Normal rate of glucose metabolism for the brain
$CMRO2_n$	$mM s^{-1}$	0.02	The resting $CMRO_2$.
$L_{CV,frac}$	dimensionless	1	A control parameter representing the action of complex V inhibitors

$[\text{CCO}]_{\text{mit}}$	m M	$\frac{[\text{CCO}]_{\text{tis}}}{\text{Vol}_{\text{mit}}}$	Concentration of cytochrome c oxidase in mitochondria
$[\text{CCO}]_{\text{tis}}$	m M	0.0022	Concentration of cytochrome c oxidase in tissue
D_{O_2}	s^{-1}	$\frac{R_u}{[\text{O}_{2,c}]_n - P_a \text{CO}_{2,n}}$	Diffusion rate between capillaries and mitochondria.
$\Delta G_{1,n}$	m V	$p_1 \text{SaO}_{2,n} - 4 \left(E_{1,n} + \mathcal{E}_0(\text{cyt } a_3) \log_{10} \left(\frac{\text{VArat}_n}{\text{Cu}_{A,o,n}} \right) \right)$	Normal free energy associated with reaction 1
$\Delta G_{2,n}$	m V	$p_2 \text{SaO}_{2,n} - 4 \left(E_2 + \mathcal{E}_0(\text{cyt } a_3) \left(\log_{10} \left(\frac{\text{Cu}_{A,o,n}}{\text{VArat}_n} \right) - \log_{10} \left(\frac{\text{cyt}a_{3rn}}{a_{3o,n}^3} \right) \right) \right)$	Normal free energy associated with reaction 2
ΔG_n	J mol^{-1}	$\Delta G^\circ + \mathcal{E}_0(\text{cyt } a_3) F \log_{10} (g_{p,n})$	Normal Gibbs free energy of ATP hydrolysis
$\Delta \text{Hbdiff}_{\text{offset}}$	μM	0	An arbitrary baseline offset to the HHb signal (NIRS)
$\Delta \text{HbO}_{2,\text{offset}}$	μM	0	An arbitrary baseline offset to the HbO ₂ signal (NIRS)
$\Delta \text{HbT}_{\text{offset}}$	μM	0	An arbitrary baseline offset to the HbT signal (NIRS)
$\Delta \text{HHb}_{\text{offset}}$	μM	0	An arbitrary baseline offset to the HHb signal (NIRS)
$\Delta p_{3,\text{corr}}$	m V	-25	
Δp_{30}	m V	$\text{SaO}_{2,n} + \Delta p_{3,\text{corr}}$	Value of PMF at which reaction 3 is maximally sensitive to PMF

$L_{CV,max}$	m V	$\frac{-\Delta G_n}{n_a F}$	A constant in the rate of complex V
Δp_n	m V	$\Delta \Psi_n + \mathcal{E}_0(\text{cyt } a_3) \Delta \text{pH}_n$	The resting value of the proton motive force.
dpH	dimensionless	0.001	A constant in the buffering relationship
ΔpH_n	dimensionless	$\text{pH}_{m,n} - \text{pH}_{o,n}$	The resting value of pH difference across mitochondrial inner membrane
$\Delta \Psi_{init}$	m V	$\Delta \Psi_n$	Initial value of mitochondrial inner membrane potential
$\Delta \Psi_n$	m V	145	Normal mitochondrial inner membrane potential
$E_{1,NADH,n}$	m V	$\mathcal{E}_0(\text{Cu}_A) - \mathcal{E}_0(\text{NADH}) + C_{NADH,n}$	Normal value of E1NADH
$E_{1,n}$	m V	$E_{1,NADH,n}$	The normal value of E_1
E_2	m V	$\mathcal{E}_0(\text{cyt } a_3) - \mathcal{E}_0(\text{Cu}_A)$	The energy provided by transfer of four electrons from Cu_A to to cyt a3
$\mathcal{E}_0(\text{cyt } a_3)$	m V	350	Cyt a3 standard redox potential
$\mathcal{E}_0(\text{Cu}_A)$	m V	250	Cu_A standard redox potential
$\mathcal{E}_0(\text{NADH})$	m V	-320	NADH standard redox potential
EPP	dimensionless	$Pi_n + PCr_n + 2ATP_n + ADP_n$	Exchangeable phosphate pool
f_n	m M s ⁻¹	$\frac{CBF_n}{CBF_n}$	Normal resting rate of f1 and f2.
F	C m ⁻¹ mol	96.4853	Faraday constant
G_0	mmHg ⁻¹ s ⁻¹	$K_{G,0} r_0^4$	Conductance of the supplying artery compartment

$G_{0,n}$	$\text{mmHg}^{-1} \text{s}^{-1}$	$G_{0,\text{rat}} G_n$	Normal conductance of the supplying artery compartment
$G_{0,\text{rat}}$	dimensionless	10	Ratio between the conductance of the cerebral arteries and the supplying artery compartment
G_v	$\text{mmHg}^{-1} \text{s}^{-1}$	$G_{\text{VArat},n} G_n$	Conductance of the veins
$G_{\text{VArat},n}$	dimensionless	4	Normal ratio of conductances between arteries and veins G_v/G_n (determines venous pressure) .
$[\text{gluc}_c]$	m M	5.3	Concentration of glucose in the blood
$\text{glyc}_{a,n}$	dimensionless	$\frac{([\text{ADP}]_n)^2}{(k_{m,\text{glycA}})^2 + ([\text{ADP}]_n)^2}$	Term in the expression for normal glycolysis rate
$\text{glyc}_{g,n}$	dimensionless	$\frac{[\text{gluc}]_n}{k_{m,\text{glycG}} + [\text{gluc}]_n}$	Term in the expression for normal glycolysis rate
glyc_{nn}	dimensionless	$\frac{(\text{NAD}_{\text{cytn}})^2}{(k_{m,\text{glycN}})^2 + (\text{NAD}_{\text{cytn}})^2}$	Term in the expression for normal glycolysis rate
$\text{glyc}_{p,n}$	dimensionless	$\frac{([\text{P}]_n)^2}{(k_{m,\text{glycP}})^2 + ([\text{P}]_n)^2}$	Term in the expression for normal glycolysis rate
G_n	$\text{mmHg}^{-1} \text{s}^{-1}$	$\frac{\text{CBF}_n}{P_a - P_{vs}} \left(1 + \frac{1}{G_{0,\text{rat}}} + \frac{1}{G_{\text{VArat},n}} \right)$	Normal resistance of cerebral circulation
ΔG°	J mol^{-1}	-30500	Standard Gibbs free energy of ATP hydrolysis

$g_{p,n}$	dimensionless	$\frac{[\text{ADP}]_n [\text{P}]_n}{[\text{ATP}]_n \times 1000}$	Normal phosphorylation potential
$G_{t,n}$	$\text{mmHg}^{-1} \text{s}^{-1}$	$\frac{G_n G_{0,n} G_v}{G_n G_{0,n} + G_n G_v + G_v G_{0,n}}$	Normal value of the total conductance of all blood vessel compartments
h_0	cm	0.003	Vascular wall thickness when radius is r_0
$H_{m,\text{init}}^+$	m M	$H_{m,n}^+$	Initial hydrogen ion concentration in mitochondria
$H_{m,n}^+$	m M	$10^{3-\text{pH}_{m,n}}$	Normal hydrogen ion concentration in mitochondria
h_n	cm	$\left(([\text{Hbtot}_c])^2 + 2r_0 h_0 + h_0 h_0 \right)^{\frac{1}{2}} - [\text{Hbtot}_c]$	Normal wall thickness of cerebral vessels
$H_{\text{cyt},n}$	m M	$10^{3-\text{pH}_{o,n}}$	Normal hydrogen ion concentration in the cytoplasm
$\text{HbO}_{2,n}$	μM	$\frac{V_{a,n} [\text{HbO}_{2,a}]_n + V_{v,n} [\text{HbO}_{2,v}]_n}{4} V_{\text{blood},n} \times 1000$	Normal total oxygenated haemoglobin (NIRS)
Hbt_n	μM	$\frac{(V_{a,n} + V_{v,n}) [\text{Hbtot}]_n}{4} V_{\text{blood},n} \times 1000$	Normal total haemoglobin (NIRS)
$henry_{\text{CO}_2}$	dimensionless	0.030000	Solubility of CO ₂ in tissue
$k_{\text{H},\text{CO}_2,t}$	m M mmHg ⁻¹	0.038000	Constant setting relationship between carbon dioxide saturation and carbon dioxide concentration in tissue
k_{H,O_2}	m M mmHg ⁻¹	0.0014000	Constant setting relationship between oxygen saturation and oxygen concentration in artery

Hbt _n	μM	$\frac{V_{a,n} [\text{HHb}_a]_n + V_{v,n} [\text{HHb}_v]_n}{4} V_{\text{blood},n} \times 1000$	Normal total deoxygenated haemoglobin (NIRS)
I	dimensionless	3	normal total deoxygenated haemoglobin (NIRS) The parameter which describes how strongly the AMP/ATP ratio inhibits the conversion of glucose to pyruvate
R _u	m M s ⁻¹	CBF _n	The resting rate of supply of oxygen to the mitochondria.
k _{1,n}	s ⁻¹	$\frac{f_n}{V_{\text{Arat}_n} - \frac{1}{K_{\text{eq1},n}} \text{Cu}_{\text{A},\text{o},n}}$	The value of k ₁ at normal Δp and NADH
k _{2,n}	m ⁻¹ M s ⁻¹	$\frac{f_n}{\text{Cu}_{\text{A},\text{o},n} a_{3,\text{o},n} - \frac{1}{K_{\text{eq2},n}} V_{\text{Arat}_n} \text{cyta}_{3,\text{r},n}}$	Normal forward rate constant for reaction 2
c _{k2}	m ⁻¹ M s ⁻¹	$\frac{k_{3,0}}{\frac{\exp(-c_3 (\text{SaO}_{2,n} - \Delta p_{30}))}{1 + \exp(-c_3 (\text{SaO}_{2,n} - \Delta p_{30}))}}$	Rate constant for reaction 3 rate constant for reaction 3
k _{3,0}	m ⁻¹ M s ⁻¹	2.5E + 5	An apparent second-order rate constant for reaction 3 at zero PMF
k _{AK}	m ⁻¹ M s ⁻¹	1055	The forward rate constant for the conversion of two molecules of ADP to one of ATP and one of AMP.
K _{eqADPATP}	dimensionless	$\frac{k_{\text{AK}}}{k_{\text{AK}}^-}$	equilibrium constant for the conversion of ADP to ATP and AMP equilibrium constant for the conversion of ADP to ATP and AMP

$t_{1/2,ADPATP}$	s	0.000002	Halftime for the conversion of ADP to ATP and AMP
$T_{e,n}$	dimensionless	1	Control parameter allowing destruction of autoregulation
$k_{BiCshut}$	$ml \cdot s^{-1}$	$\frac{\log(2.0)}{t_{1/2,BiCshut} \left(1 + \frac{1.0}{Vol_{mit} Keq_{BiCshut}}\right)}$	The rate of transfer of bicarbonate ions from cytoplasm to mitochondria
$Keq_{BiCshut}$	dimensionless	$\frac{HCO_{3,mit}^-}{HCO_{3,cyt}^-}$	Equilibrium constant for the transport of bicarbonate ions between mitochondria and cytoplasm
$t_{1/2,BiCshut}$	dimensionless	2200	The half time for the transport of bicarbonate ions between mitochondria and cytoplasm
$k_{CH,eq}$	dimensionless	0.00079000	
Keq_{CHi}	dimensionless	$\frac{H_{cyt,n}^+ HCO_{3,cyt}^-}{CO_{2,cyt,n}}$	Equilibrium constant for the production and dissociation of carbonic acid in the cytoplasm
Keq_{CHm}	dimensionless	$\frac{H_{m,n}^+ HCO_{3,mit}^-}{CO_{2,mit,n}}$	Equilibrium constant for the production and dissociation of carbonic acid in the mitochondria
k_{CHi}	s^{-1}	$\frac{\log(2.0)}{t_{1/2,CHi} (1.0 + H_{cyt,n}^+ / Keq_{CHi})}$	The rate of conversion of CO ₂ to bicarbonate and protons in cytoplasm
$t_{1/2,CHi}$	dimensionless	3.2	Halftime for the production of carbonic acid in cell cytoplasm

k_{CHm}	s^{-1}	$\frac{\log(2.0)}{t_{1/2,\text{CHm}}(1.0 + H_{m,n}^+/\text{Keq}_{\text{CHm}})}$	The rate of conversion of CO_2 to bicarbonate and protons in mitochondria
$t_{1/2,\text{CHm}}$	dimensionless	25	Halftime for the production of carbonic acid in the mitochondria
$k_{\text{CO}_2\text{out}}$	$\text{ml} \cdot \text{s}^{-1}$	$\frac{\text{CMRO}_{2n} \text{CO}_{2,\text{cyt}}}{\text{CO}_{2,\text{cyt},n}}$	The rate at which CO_2 moves out of the cell
$k_{\text{CO}_2\text{shut}}$	$\text{ml} \cdot \text{s}^{-1}$	$\frac{\text{CMRO}_{2n}}{\text{CO}_{2,\text{mit},n} - \text{CO}_{2,\text{cyt},n}}$	The rate of transfer of CO_2 between mitochondria to cytoplasm
K_G	$\text{mmHg}^{-1} \text{s}^{-1} \text{cm}^{-4}$	$\frac{G_n}{([\text{Hbtot}_c])^4}$	Constant of proportionality relating pressure drop to flow
K_{G0}	$\text{mmHg}^{-1} \text{s}^{-1} \text{cm}^{-4}$	$G_{0,n}$	Constant in relationship between normal conductance of supplying artery and its radius
k_{glut}	mM	6.2	km for the transport of glucose in and out of the cell
k_{MCT}	mM	$10^{-k_{\text{lac},ph}}$	km for the transport of lactate in and out of the cell.
$k_{\text{lac},ph}$	dimensionless	7	Constant in Km for the transport of lactate
f_n	$\text{m}^{-1} \text{V}$	0.038	Second constant controlling rate of L_{lk} of Δp .
k_{AK}^-	$\text{m}^{-1} \text{M} \text{s}^{-1}$	379	The backward rate constant for the conversion of two molecules of ADP to one of ATP and one of AMP

$k_{nBiCshut}$	$ml \cdot s^{-1}$	$\frac{\log(2.0)}{t_{1/2,BiCshut}(K_{eqBiCshut} + 1.0/Vol_{mit})}$	The rate of transfer of bicarbonate ions from mitochondria to cytoplasm
k_{nCHi}	$mM^{-1} \cdot s^{-1}$	$\frac{\log(2.0)}{t_{1/2,CHi}(H_{cyt,n} + K_{eqCHi})}$	The backward rate in the conversion of CO ₂ to bicarbonate and protons in cytoplasm
k_{nCHm}	$mM^{-1} \cdot s^{-1}$	$\frac{\log(2.0)}{t_{1/2,CHm}(H_{m,n} + K_{eqCHm})}$	The backward rate in the conversion of CO ₂ to bicarbonate and protons in mitochondria
k_{pl}^-	s^{-1}	$t_{1/2,pl}$	Rate of backwards reaction in the pyruvate lactate equilibrium
$K_{eq,PCr}$	$m^{-1} M$	$\frac{K_{eq,PCr}^*}{[H^+]_n}$	Equilibrium of the reaction in which phosphocreatine combines with ADP to give creatine and ATP
$K_{eq,PCr}^*$	dimensionless	166	Effective equilibrium constant for the reaction in which phosphocreatine combines with ADP to give creatine and ATP
$t_{1/2,PCr}$	s	0.00002	Halftime for the reaction in which phosphocreatine combines with ADP to give creatine and ATP
$t_{1/2,pl}$	s^{-1}	10	Time constant for pyruvate to lactate interconversion
K_{σ}	dimensionless	10	Parameter controlling sensitivity of σ_e to radius

k_{TCA_n}	m M s^{-1}	$\frac{1}{3} \frac{\text{CBF}_n}{\text{CBF}_n}$	Normal rate of the TCA cycle
$\Delta p_{3,\text{corr}}$	dimensionless	1	A parameter representing the action of uncouplers
k_{CV}	$\text{m}^{-1} \text{V}$	$\frac{-1}{\text{SaO}_{2,n} - L_{CV,\text{max}}} \log \left(\frac{1 - L_{CV,0}}{1 + r_{CV} L_{CV,0}} \right)$	A parameter controlling the sensitivity of complex V flux to driving force
$\text{Keq}_{1,n}$	dimensionless	$10^{\frac{-1}{Z} \left(\frac{p_1 \text{SaO}_{2,n}}{4} - E_{1,n} \right)}$	Normal equilibrium constant for reaction 1
$\text{Keq}_{2,n}$	dimensionless	$10^{\frac{-1}{Z} \left(\frac{p_2 \text{SaO}_{2,n}}{4} - E_2 \right)}$	Normal equilibrium constant for reaction 2
$\text{Keq}_{\text{MAshut}}$	dimensionless	10	Equilibrium constant for the malate-aspartate shuttle
$k_{m,\text{ATP}}$	dimensionless	0.025	Km for ATP use as a fraction of normal ATP concentration.
$k_{m,\text{glycA}}$	m M	$k_{m,\text{glycA},f} [\text{ADP}]_n$	Km for ADP in the caricature of glycolysis
$k_{m,\text{glycA},f}$	dimensionless	0.2	Km for ADP in glycolysis as a fraction of normal ADP concentration
$k_{m,\text{glycG}}$	m M	0.05000	Km for glucose in the caricature of glycolysis
$k_{m,\text{glycN}}$	m M	$k_{m,\text{glycN},f} [\text{NAD}]_n$	Km for NAD in the caricature of glycolysis
$k_{m,\text{glycN},f}$	m M	0.2	Km for NAD in glycolysis as a fraction of normal NAD concentration

$k_{m,\text{glycP}}$	m M	$k_{m,\text{glycP},f} [\text{P}]_n$	Km for inorganic phosphate in the car- icature of glycolysis.
$k_{m,\text{glycP},f}$	dimensionless	0.2	Km for inorganic phosphate in glycol- ysis as a fraction of normal phosphate concentration
km_{NAD}	m M	100000	Km for NAD in the tca cycle as a frac- tion of the normal NAD concentration
$\text{Km}_{\text{NAD},\text{TCA}}$	m M	$\text{km}_{\text{NAD}} [\text{NAD}]_n$	Km for NAD in the TCA cycle
km_{Py}	m M	0	Km for pyruvate for the tca cycle as a fraction of the normal pyruvate con- centration
$\text{Km}_{\text{Py},\text{TCA}}$	m M	$\text{km}_{\text{Py}} [\text{Py}]_n$	Km for pyruvate in the TCA cycle
$k_{m,\text{ATP}}$	m M	0	Km for ATP for the tca cycle as a frac- tion of the normal ATP concentration
k_m	m M	$[\text{ATP}]_n k_{m,\text{ATP}}$	Km for ATP use
$k_{-1,0}$	s^{-1}	$\frac{f_n}{\text{Keq}_{1,n} \text{VArat}_n - \text{Cu}_{\text{A},0,n}}$	Backward rate constant for reaction 1 at normal PMF
$kn1_n$	dimensionless	$\frac{f_n}{\text{Keq}_{1,n} \text{VArat}_n - \text{Cu}_{\text{A},0,n}}$	The value of k1 at normal Δp and NADH
$k_{-2,n}$	$\text{m}^{-1} \text{M s}^{-1}$	$\frac{f_n}{\text{Keq}_{2,n} \text{Cu}_{\text{A},0,n} \text{a}_{3,0,n} - \text{VArat}_n \text{cyt}_{3,r,n}}$	Normal backward rate constant for re- action 2
	m M	0.005	Explicit Km for O2 for reaction 3
$L_{\text{CV},0}$	dimensionless	0.4	Normal complex V flux as a fraction of maximum possible flux

$L_{CV,frac}$	dimensionless	$1 - L_{lk,frac}$	Normal fraction of proton entry into mitochondria associated with ADP phosphorylation
$L_{CV,max}$	$m M s^{-1}$	$\frac{CBF_n}{L_{CV,0}}$	The maximum rate of proton flow through complex V.
L_{CVn}	$m M s^{-1}$	$L_n L_{CV,frac}$	The resting flow of protons into the matrix through complex V
f_n	$m M s^{-1}$	$\frac{CBF_n}{\exp(SaO_{2,n} f_n) - 1}$	First constant controlling rate of L_{lk} of Δp .
$L_{lk,frac}$	dimensionless	0.25	Normal fraction of proton entry into mitochondria which is via leak channels
L_{lkn}	$m M s^{-1}$	$L_n L_{lk,frac}$	The resting flow of protons into the matrix via leak channels.
L_n	$m M s^{-1}$	$p_{tot} f_n$	The total flow of protons back into mitochondria
$[lac_c]$	$m M$	1	Capillary lactate concentration
μ_{max}	dimensionless	1	Maximum value of mu
μ_{min}	dimensionless	-1	Minimum value of mu
μ_n	dimensionless	0	Normal value of mu
n_h	dimensionless	2.5	Hill coefficient for haemoglobin saturation
n_m	dimensionless	1.83	Exponent in the muscular tension relationship

n_a	dimensionless	4.33	Number of protons passing through Complex V for each ATP synthesised
NAD_{cytn}	m M	359	Normal concentration of NAD in the cytoplasm
$NADH_{\text{cytn}}$	dimensionless	50	Normal concentration of NADH in the cytoplasm
$[NADH]_n$	m M	$N_t - [NAD]_n$	Normal mitochondrial NADH concentration
$[NAD]_n$	m M	$\frac{N_t}{1 + \frac{1}{[NAD]_n/[NADH]_n}}$	Normal concentration of NAD in the mitochondria
$[NAD]_n/[NADH]_n$	dimensionless	9	Normal NAD/NADH ratio
N_t	m M	3	Total mitochondrial NAD + NADH concentration
$[O_2]_{\text{init}}$	m M	$[O_2]_n$	Initial oxygen concentration in mitochondria.
$[O_2]_n$	m M	0.024	Normal oxygen concentration in mitochondria.
$[O_{2,a}]$	m M	$\phi \left(\frac{SaO_2sup}{1.0 - SaO_2sup} \right)^{\frac{1}{n_h}}$	Arterial dissolved oxygen concentration
$[O_{2,c}]_{\text{init}}$	m M	$[O_{2,c}]_n$	Initial concentration of dissolved oxygen in the capillary.
$[O_{2,c}]_n$	m M	$[O_{2,c}]_{\text{init}} \left(\frac{ScO_{2,n}}{1 - ScO_{2,n}} \right)^{\frac{1}{n_h}}$	Normal concentration of dissolved oxygen in the capillary.

p_1	dimensionless	$p_{tot} - p_{23}$	The number of protons pumped by a red (reduction reaction)
p_2	dimensionless	4	Total protons pumped by reaction 2
p_{23}	dimensionless	8	Total protons pumped by reactions 2 and 3
p_3	dimensionless	$p_{23} - p_2$	Total protons pumped by reaction 3
$P_{1,n}$	mmHg	$\frac{P_{a2,n} + P_{v,n}}{2}$	Normal average blood pressure in vessels
P_a	mmHg	50	Arterial blood pressure
$P_{a2,n}$	mmHg	$\frac{G_{0,n} P_a + G_n P_{v,n}}{G_n + G_{0,n}}$	Normal arterial blood pressure at the start of the cerebral arteries
P_a	mmHg	50	Normal value of arterial blood pressure
p_{C1}	dimensionless	8	Total protons pumped by complex 1
p_{C3}	dimensionless	4	Total protons pumped by complex 3
P_{ic}	mmHg	4.5	Intracranial blood pressure
$P_{ic,n}$	mmHg	4.5	Normal intracranial blood pressure
p_{tot}	dimensionless	18.40	Total protons pumped by reactions 1, 2 and 3
$p_{tot,NADH}$	dimensionless	$p_{C1} + p_{C3} + p_{23}$	Total protons pumped when the reducing agent is NADH
$P_{v,n}$	mmHg	$\frac{G_{t,n}}{G_v} (P_a - P_{vs}) + P_{vs}$	Normal venous blood pressure
P_{vs}	mmHg	1.5	Pressure in the venous sinuses
$P_a\text{CO}_2$	mmHg	40	Arterial partial pressure of CO2

$P_a\text{CO}_{2,n}$	mmHg	40	Normal arterial partial pressure of CO ₂
$P_a\text{O}_2$	mmHg	$\frac{[\text{O}_{2,a}]}{k_{\text{H},\text{O}_2}}$	Partial pressure of oxygen in the arteries
$[\text{PCr}]_n / [\text{Pi}]_n$	dimensionless	2.73	Normal Pcr/Pi concentration in the cytoplasm. Set this way because this is often measured by MRS (although mitochondria/cytoplasm differences are ignored).
$\text{pH}_{m,n}$	dimensionless	8	Normal mitochondrial pH
$\text{pH}_{o,n}$	dimensionless	7	Normal cytoplasmic pH
ϕ	m M	0.036	Value of O ₂ at half maximal saturation
$P_t\text{CO}_{2n}$	dimensionless	54.000	Partial pressure of CO ₂ in tissue
r_0	cm	$1 - r_{\text{frac}}r_{\text{occ}}$	Radius of the supplying artery compartment
r_0	cm	0.0126	A special radius in the elastic tension relationship
R_C	dimensionless	2.2	Parameter controlling sensitivity of η to $P_a\text{CO}_2$
R_O	dimensionless	1.5	Parameter controlling sensitivity of η to $[\text{O}_{2,c}]$
R_P	dimensionless	4	Parameter controlling sensitivity of η to P_a
R_u	dimensionless	0	Parameter controlling sensitivity of η to u

r_{CV}	dimensionless	5	A parameter controlling the ratio of maximal to minimal rates of oxidative phosphorylation
r_{init}	cm	$[Hbtot_c]$	Initial radius of blood vessels
r_m	cm	0.027	Value of vessel radius giving maximum muscular tension
$[Hbtot_c]$	cm	0.0187	Normal radius of blood vessels normal radius of blood vessels
r_t	cm	0.018	Parameter in the muscular tension relationship
r_{frac}	dimensionless	$1 - (1 - occ_{frac})^{\frac{1}{2}}$	Fraction by which the radius of the supplying artery compartment has been reduced
r_{occ}	dimensionless	0	Fraction by which the radius of the carotid arteries has been reduced
$SaO_{2,n}$	dimensionless	0.96	Normal saturation of the arterial haemoglobin
SaO_2	dimensionless	0.96	Saturation of the arterial haemoglobin
$ScO_{2,n}$	dimensionless	$\frac{SaO_{2,n} + SvO_{2,n}}{2}$	Normal capillary oxygen saturation
σ_{coll}	mmHg	62.79	Value of pressure at which vessels collapse
σ_{e0}	mmHg	0.1425	Parameter in relationship determining σ_e
$\sigma_{e,n}$	mmHg	$\sigma_{e0} \left(\exp \left(\frac{K_\sigma ([Hbtot_c] - r_0)}{r_0} \right) - 1 \right) - \sigma_{coll}$	Normal elastic stress in vessel walls

SvO_{2n}	dimensionless	$\frac{[HbO_{2,v}]_n}{[Hbtot]_n}$	Normal venous oxygen saturation
$\nu_{u,n}$	s	5	The time constant associated with ν_{CO_2} the time constant associated with ν_{CO_2}
$T_{e,n}$	mmHg cm	$\sigma_{e,n} h_n$	Normal elastic tension in vessel walls
T_{max0}	mmHg cm	$\frac{T_{max,n}}{1 + T_{e,n} \mu_n}$	Tmax at normal μ
$T_{max,n}$	mmHg cm	$\frac{T_{m,n}}{\exp\left(-\text{pow}\left(\text{fabs}\left(\frac{[Hbtot_c] - r_m}{r_t - r_m}\right), n_m\right)\right)}$	Normal maximum muscular tension developed by circulation
$T_{m,n}$	mmHg cm	$(P_{1,n} - P_{ic,n}) [Hbtot_c] - T_{e,n}$	Normal muscular tension in vessel walls
$\nu_{u,n}$	s	20	Tthe time constant associated with ν_{O_2}
$\nu_{u,n}$	s	5	The time constant associated with ν_{P_i}
$\nu_{u,n}$	s	0.5	The time constant associated with ν_u
u	dimensionless	1	The representation of "demand" in the model.
u_n	dimensionless	1	Resting "demand"
$V_{max,ATP}$	$m M s^{-1}$	$\left(\frac{LCV_n Vol_{mit}}{na} + 2.0CMR_{glucn}\right) (1.0 + km) u$	Vmax of ATP use
$\nu_{CO_2,n}$	mmHg	$P_aCO_{2,n}$	normal value of ν_{CO_2} (CO2 passed through a first order filter)
$V_{glucosein}$	dimensionless	$\frac{[gluc_c]}{k_{glut} + [gluc_c]}$	Rate term for glucose transported into the cell. This ia a michaelis menten term, but fixed because blood glucose concentration is fixed.

v_{glut}	m M	$\frac{CMR_{gluc,n}}{V_{glucosein} - \frac{[gluc]_n}{[gluc]_n + k_{glut}}}$	Vmax for glucose transport both in and out of the cell from the capillary. .
V_{lacin}	dimensionless	$\frac{[lac_c]}{k_{MCT} + [lac_c]}$	Rate of lactate transport into the cell
v_{MCT}	m M s ⁻¹	$\frac{2CMR_{gluc,n} - \frac{CBF_n}{3}}{\frac{[lac]_n [H^+]_n}{([lac]_n + k_{MCT})([H^+]_n + k_{MCT})} - V_{lacin}}$	
$v_{O_2,n}$	m M	$\frac{[O_{2,c}]_n}{[O_{2,c}]_n}$	Normal value of v_{O_2} (capillary O2 passed through a first order filter)
$v_{P_a,n}$	mmHg	$P_{a2,n}$	Normal value of v_{P_a} (Arterial blood pressure passed through a first order filter)
v_{TCA}	m M s ⁻¹	$\frac{k_{TCA_n}}{[Py]_n [NAD]_n} (k_{m,tcaN} + [NAD]_n) (k_{m,tcaP} + [Py]_n)$	Vmax for the TCA cycle
$v_{u,n}$	dimensionless	$L_{CV,frac}$	normal value of v_u (u passed through a first order filter)
V_{Arat_n}	dimensionless	3	The normal ratio of the volume of the veins to the volume of the arteries
$v_{glyc,n}$	m M s ⁻¹	$\frac{CMR_{gluc,n}}{glyc_{g,n} glyc_{p,n} glyc_{a,n} glyc_{nn}}$	Normal Vmax for glycolysis which is assumed to be modified by the ratio of AMP to ATP normal
$V_{a,n}$	dimensionless	$\frac{t_n}{1 + V_{Arat_n}}$	Normal arterial blood volume as a fraction of total blood volume
Vol_{mit}	dimensionless	0.067	Fraction of brain water which is mitochondria
$V_{t,n}$	dimensionless	1	Normal total blood volume

$V_{v,n}$	dimensionless	$t_n \frac{V_{Arat_n}}{1 + V_{Arat_n}}$	Normal venous volume
$[HHb_a]$	m M	$[Hbtot] (1 - SaO_2)$	Unsaturated arterial haemoglobin
$[HHb_a]_n$	m M	$[Hbtot]_n (1 - SaO_{2,n})$	Normal unsaturated arterial haemoglobin
$[HbO_{2,a}]$	m M	$[Hbtot] SaO_2$	Concentration of arterial oxy-haemoglobin.
$[HbO_{2,a}]_n$	m M	$[Hbtot]_n SaO_{2,n}$	Normal concentration of arterial oxy-haemoglobin.
$[HbO_{2,v}]_{init}$	m M	$[HbO_{2,v}]_n$	Initial concentration of venous oxy-haemoglobin.
$[HbO_{2,v}]_n$	m M	$\frac{CBF_n [HbO_{2,a}]_n - R_u}{CBF_n}$	Normal concentration of venous oxy-haemoglobin.
$[HbO_{2,a}]_n$	m M	$[Hbtot]_n$	Total haemoglobin concentration in the arteries and veins.
$[Hbtot]_n$	m M	5.4	Normal total haemoglobin concentration in the arteries and veins.
$[HHb_v]_n$	m M	$[Hbtot]_n - [HbO_{2,v}]_n$	Normal unsaturated venous haemoglobin
Z	m V	59.028	2.303*RT/F

A.4 BrainPiglet v2.1

A.4.1 Overview

- 26 differential state variables
- 3 algebraic state variables
- 131 intermediate variables
- 338 parameters

A.4.2 Differential equations

$$\begin{aligned} \frac{d[\text{ADP}]}{dt} = & (k_{\text{PCr}}^- + [\text{ATP}] [\text{Cr}]) - k_{\text{ATP,Cv}} + V_{pp} + 2 (k_{\text{AK}}^- + [\text{ATP}] [\text{AMP}]) \\ & - 2 \left(k_{\text{AK}} + [\text{ADP}]^2 \right) + \frac{V_{\text{max,ATP}} [\text{ATP}]}{k_m + [\text{ATP}]} - (k_{\text{PCr}} + [\text{PCr}] [\text{ADP}] [\text{H}^+]) \\ & - 2 \frac{v_{\text{glyc}} [\text{ADP}]^2 [\text{Pi}]^2 [\text{gluc}] \text{NAD}_{\text{cyt}}^2}{\left(k_{m,\text{glycA}}^2 + [\text{ADP}]^2 \right) \left(k_{m,\text{glycP}}^2 + [\text{Pi}]^2 \right) \left(k_{m,\text{glycG}} + [\text{gluc}] \right) \left(k_{m,\text{glycN}}^2 + \text{NAD}_{\text{cyt}}^2 \right)} \end{aligned} \quad (\text{A.109})$$

$$\frac{d[\text{AMP}]}{dt} = \left(k_{\text{AK}} + [\text{ADP}]^2 \right) - \left(k_{\text{AK}}^- + [\text{ATP}] [\text{AMP}] \right) \quad (\text{A.110})$$

$$\begin{aligned} \frac{d[\text{ATP}]}{dt} = & k_{\text{ATP,Cv}} - \left(k_{\text{PCr}}^- + [\text{ATP}] [\text{Cr}] \right) - V_{pp} - \left(k_{\text{AK}}^- + [\text{ATP}] [\text{AMP}] \right) \\ & + 2 \frac{v_{\text{glyc}} [\text{ADP}]^2 [\text{Pi}]^2 [\text{gluc}] \text{NAD}_{\text{cyt}}^2}{\left(k_{m,\text{glycA}}^2 + [\text{ADP}]^2 \right) \left(k_{m,\text{glycP}}^2 + [\text{Pi}]^2 \right) \left(k_{m,\text{glycG}} + [\text{gluc}] \right) \left(k_{m,\text{glycN}}^2 + \text{NAD}_{\text{cyt}}^2 \right)} \\ & + \left(k_{\text{AK}} + [\text{ADP}]^2 \right) - \frac{V_{\text{max,ATP}} [\text{ATP}]}{k_m + [\text{ATP}]} + \left(k_{\text{PCr}} + [\text{PCr}] [\text{ADP}] [\text{H}^+] \right) \end{aligned} \quad (\text{A.111})$$

$$\begin{aligned} \frac{d[\text{BiC}_{\text{cyt}}]}{dt} = & \left(k_{\text{Chi}} + [\text{CO}_{2,\text{cyt}}] \right) - \left(k_{\text{nChi}} + [\text{H}^+] [\text{BiC}_{\text{cyt}}] \right) \\ & - \left(k_{\text{BiCshut}} + [\text{BiC}_{\text{cyt}}] \right) + \left(k_{\text{nBiCshut}} + [\text{BiC}_{\text{mit}}] \right) + V_{\text{NaBiC}} \end{aligned} \quad (\text{A.112})$$

$$\begin{aligned} \frac{d[\text{CO}_{2,\text{cyt}}]}{dt} = & (k_{\text{nChi}} + [\text{H}^+] [\text{BiC}_{\text{cyt}}]) - (k_{\text{Chi}} + [\text{CO}_{2,\text{cyt}}]) + (k_{\text{CO}_2\text{shut}} + [\text{CO}_{2,\text{mit}}]) \\ & - k_{\text{CO}_2,\text{out}} - (k_{\text{CO}_2\text{shut}} + [\text{CO}_{2,\text{cyt}}]) \quad (\text{A.113}) \end{aligned}$$

$$\frac{d[\text{Cr}]}{dt} = (k_{\text{PCr}} + [\text{PCr}] [\text{ADP}] [\text{H}^+]) - (k_{\text{PCr}}^- + [\text{ATP}] [\text{Cr}]) \quad (\text{A.114})$$

$$\begin{aligned} \frac{d[\text{gluc}]}{dt} = & V_{\text{glucosein}} v_{\text{glut}} - \frac{v_{\text{glut}} [\text{gluc}]}{k_{\text{glut}} + [\text{gluc}]} \\ & - \frac{v_{\text{glyc}} [\text{ADP}]^2 [\text{P}_i]^2 [\text{gluc}] \text{NAD}_{\text{cyt}}^2}{(k_{m,\text{glycA}}^2 + [\text{ADP}]^2) (k_{m,\text{glycP}}^2 + [\text{P}_i]^2) (k_{m,\text{glycG}} + [\text{gluc}]) (k_{m,\text{glycN}}^2 + \text{NAD}_{\text{cyt}}^2)} \quad (\text{A.115}) \end{aligned}$$

$$\begin{aligned} \frac{d[\text{H}^+]}{dt} = & \frac{p_1 + 4}{\frac{R_{\text{Hic}}}{\text{CBF}_n}} f_1 - \frac{1}{R_{\text{Hic}}} (k_{\text{MAshut}} + [\text{H}^+] [\text{NAD}]) - \frac{1}{R_{\text{Hic}}} (k_{\text{nChi}} + [\text{H}^+] [\text{BiC}_{\text{cyt}}]) \\ & + \frac{1}{R_{\text{Hic}}} (k_{\text{Chi}} + [\text{CO}_{2,\text{cyt}}]) + \frac{1}{R_{\text{Hic}}} (k_{\text{PCr}}^- + [\text{ATP}] [\text{Cr}]) + \frac{1}{R_{\text{Hic}}} (k_{\text{pl}}^- + [\text{lac}] \text{NAD}_{\text{cyt}}) \\ & + \frac{p_2}{\frac{R_{\text{Hic}}}{\text{CBF}_n}} f_2 - \frac{1}{R_{\text{Hic}}} (k_{\text{pl}} + [\text{Py}] [\text{H}^+]) - \frac{1}{\frac{R_{\text{Hic}}}{\text{CBF}_n}} L - \frac{1}{R_{\text{Hic}}} \frac{v_{\text{MCT}} [\text{lac}] [\text{H}^+]}{(k_{\text{MCT}} + [\text{lac}]) (k_{\text{MCT}} + [\text{H}^+])} \\ & + \frac{1}{R_{\text{Hic}}} V_{\text{lacin}} v_{\text{MCT}} + \frac{1}{R_{\text{Hic}}} (k_{\text{MAshut}}^- + \text{NAD}_{\text{cyt}} \text{H}_m^+) - \frac{1}{R_{\text{Hic}}} i_{\text{NHE}} - \frac{1}{\frac{R_{\text{Hic}}}{\text{CBF}_n}} k_{\text{TCA}} \\ & + \frac{4}{R_{\text{Hic}}} \frac{v_{\text{glyc}} [\text{ADP}]^2 [\text{P}_i]^2 [\text{gluc}] \text{NAD}_{\text{cyt}}^2}{(k_{m,\text{glycA}}^2 + [\text{ADP}]^2) (k_{m,\text{glycP}}^2 + [\text{P}_i]^2) (k_{m,\text{glycG}} + [\text{gluc}]) (k_{m,\text{glycN}}^2 + \text{NAD}_{\text{cyt}}^2)} \\ & - \frac{1}{R_{\text{Hic}}} (k_{\text{PCr}} + [\text{PCr}] [\text{ADP}] [\text{H}^+]) \quad (\text{A.116}) \end{aligned}$$

$$\begin{aligned} \frac{d[\text{lac}]}{dt} = & (k_{\text{pl}} + [\text{Py}] [\text{H}^+]) - (k_{\text{pl}}^- + [\text{lac}] \text{NAD}_{\text{cyt}}) \\ & - \frac{v_{\text{MCT}} [\text{lac}] [\text{H}^+]}{(k_{\text{MCT}} + [\text{lac}]) (k_{\text{MCT}} + [\text{H}^+])} + V_{\text{lacin}} v_{\text{MCT}} \quad (\text{A.117}) \end{aligned}$$

$$\begin{aligned} \frac{d[\text{BiC}_{\text{mit}}]}{dt} = & \frac{1}{\text{CBF}_n} (k_{\text{BiCshut}} + [\text{BiC}_{\text{cyt}}]) - \frac{1}{\text{CBF}_n} (k_{n\text{BiCshut}} + [\text{BiC}_{\text{mit}}]) \\ & - (k_{n\text{CHm}} + \text{H}_m^+ [\text{BiC}_{\text{mit}}]) + (k_{\text{CHm}} + [\text{CO}_2, \text{mit}]) \quad (\text{A.118}) \end{aligned}$$

$$\begin{aligned} \frac{d[\text{CO}_2, \text{mit}]}{dt} = & 3k_{\text{TCA}} - \frac{1}{\text{CBF}_n} (k_{\text{CO}_2\text{shut}} + [\text{CO}_2, \text{mit}]) + \frac{1}{\text{CBF}_n} (k_{\text{CO}_2\text{shut}} + [\text{CO}_2, \text{cyt}]) \\ & + (k_{n\text{CHm}} + \text{H}_m^+ [\text{BiC}_{\text{mit}}]) - (k_{\text{CHm}} + [\text{CO}_2, \text{mit}]) \quad (\text{A.119}) \end{aligned}$$

$$\frac{d[\text{Na}]}{dt} = k_{\text{Na}} + i_{\text{NHE}} - 3V_{pp} + V_{\text{NaBiC}} \quad (\text{A.120})$$

$$\begin{aligned} \frac{d[\text{P}_i]}{dt} = & V_{pp} - k_{\text{ATP}, \text{Cv}} + \frac{V_{\text{max}, \text{ATP}} [\text{ATP}]}{k_m + [\text{ATP}]} \\ & - 2 \frac{v_{\text{glyc}} [\text{ADP}]^2 [\text{P}_i]^2 [\text{gluc}] \text{NAD}_{\text{cyt}}^2}{(k_{m, \text{glycA}}^2 + [\text{ADP}]^2) (k_{m, \text{glycP}}^2 + [\text{P}_i]^2) (k_{m, \text{glycG}} + [\text{gluc}]) (k_{m, \text{glycN}}^2 + \text{NAD}_{\text{cyt}}^2)} \quad (\text{A.121}) \end{aligned}$$

$$\frac{d[\text{PCr}]}{dt} = (k_{\text{PCr}}^- + [\text{ATP}] [\text{Cr}]) - (k_{\text{PCr}} + [\text{PCr}] [\text{ADP}] [\text{H}^+]) \quad (\text{A.122})$$

$$\begin{aligned} \frac{d[\text{Py}]}{dt} = & (k_{\text{pl}}^- + [\text{lac}] \text{NAD}_{\text{cyt}}) - (k_{\text{pl}} + [\text{Py}] [\text{H}^+]) - \frac{1}{\text{CBF}_n} k_{\text{TCA}} \\ & + 2 \frac{v_{\text{glyc}} [\text{ADP}]^2 [\text{P}_i]^2 [\text{gluc}] \text{NAD}_{\text{cyt}}^2}{(k_{m, \text{glycA}}^2 + [\text{ADP}]^2) (k_{m, \text{glycP}}^2 + [\text{P}_i]^2) (k_{m, \text{glycG}} + [\text{gluc}]) (k_{m, \text{glycN}}^2 + \text{NAD}_{\text{cyt}}^2)} \quad (\text{A.123}) \end{aligned}$$

$$\frac{d\text{Cu}_{\text{A}, \text{o}}}{dt} = 4f_2 - 4f_1 \quad (\text{A.124})$$

$$\frac{d\text{cyta}_{3\text{r}}}{dt} = 4f_2 - 4f_3 \quad (\text{A.125})$$

$$\frac{d\Delta\Psi}{dt} = \frac{p_2 f_2 + p_1 f_1 + p_3 f_3 - L}{C_{im}} \quad (\text{A.126})$$

$$\begin{aligned} \frac{dH_m^+}{dt} = & \frac{1}{R_{Hi} CBF_n} (k_{MAshut} + [H^+] [NAD]) - \frac{p_1 + \frac{5}{3}}{R_{Hi}} f_1 - \frac{p_2}{R_{Hi}} f_2 - \frac{p_3}{R_{Hi}} f_3 + \frac{4}{R_{Hi}} k_{TCA} \\ & + \frac{1}{R_{Hi}} L - \frac{1}{R_{Hi}} (k_{nCHm} + H_m^+ [BiC_{mit}]) - \frac{1}{R_{Hi} CBF_n} (k_{MAshut}^- + NAD_{cyt} H_m^+) \\ & + \frac{1}{R_{Hi}} (k_{CHm} + [CO_{2,mit}]) \quad (\text{A.127}) \end{aligned}$$

$$\begin{aligned} \frac{d[NAD]}{dt} = & 2f_1 - \frac{1}{CBF_n} (k_{MAshut} + [H^+] [NAD]) \\ & - 5k_{TCA} + \frac{1}{CBF_n} (k_{MAshut}^- + NAD_{cyt} H_m^+) \quad (\text{A.128}) \end{aligned}$$

$$\begin{aligned} \frac{dNAD_{cyt}}{dt} = & (k_{MAshut} + [H^+] [NAD]) - (k_{pl}^- + [lac] NAD_{cyt}) + (k_{pl} + [Py] [H^+]) \\ & - (k_{MAshut}^- + NAD_{cyt} H_m^+) \\ & - 2 \frac{v_{glyc} [ADP]^2 [P_i]^2 [gluc] NAD_{cyt}^2}{(k_{m,glucA}^2 + [ADP]^2) (k_{m,glucP}^2 + [P_i]^2) (k_{m,glucG} + [gluc]) (k_{m,glucN}^2 + NAD_{cyt}^2)} \quad (\text{A.129}) \end{aligned}$$

$$\frac{d[O_2]}{dt} = \frac{1}{CBF_n} J_{O_2} - f_3 \quad (\text{A.130})$$

$$\frac{dv_{CO_2}}{dt} = \frac{1}{v_{u,n}} (P_a CO_2 - v_{CO_2}) \quad (\text{A.131})$$

$$\frac{dv_{O_2}}{dt} = \frac{1}{v_{u,n}} ([O_{2,c}] - v_{O_2}) \quad (\text{A.132})$$

$$\frac{dv_{P_a}}{dt} = \frac{1}{v_{u,n}} (P_{a2} - v_{P_a}) \quad (\text{A.133})$$

$$\frac{dv_u}{dt} = \frac{1}{v_{u,n}} (CBF - v_u) \quad (\text{A.134})$$

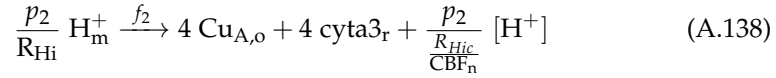
A.4.3 Algebraic equations

$$[\text{O}_{2,c}]_{\text{init}} \text{pow} \left(\frac{\text{ScO}_2}{1 - \text{ScO}_2}, \frac{1}{n_h} \right) - [\text{O}_{2,c}] = 0 \quad (\text{A.135})$$

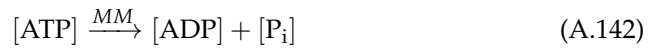
$$T_e + T_m - (P_1 - P_{ic}) r = 0 \quad (\text{A.136})$$

$$\text{CBF} ([\text{HbO}_{2,a}] - [\text{HbO}_{2,v}]) - J_{\text{O}_2} = 0 \quad (\text{A.137})$$

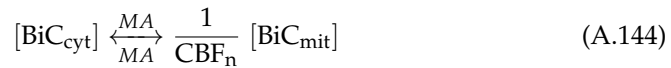
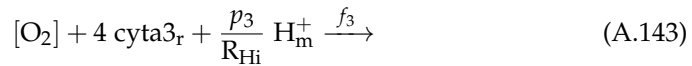
A.4.4 Chemical reactions



Mass Action kinetics are assumed for the forward reaction, with calculated rate term $k_{\text{AK}} + [\text{ADP}]^2$. Mass Action kinetics are assumed for the reverse reaction, with calculated rate term $k_{\text{AK}}^- + [\text{ATP}] [\text{AMP}]$.

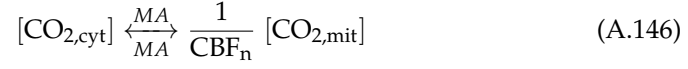


Michaelis-Menten kinetics are assumed, with calculated rate term $\frac{V_{\text{max,ATP}} [\text{ATP}]}{k_m + [\text{ATP}]}$.



Mass Action kinetics are assumed for the forward reaction, with calculated rate term $k_{\text{BiCshut}} + [\text{BiC}_{\text{cyt}}]$. Mass Action kinetics are assumed for the reverse reaction, with calculated rate term $k_{\text{BiCshut}}^- + [\text{BiC}_{\text{mit}}]$.





Mass Action kinetics are assumed for the forward reaction, with calculated rate term $k_{\text{CO}_2\text{shut}} + [\text{CO}_{2,\text{cyt}}]$. Mass Action kinetics are assumed for the reverse reaction, with calculated rate term $k_{\text{CO}_2\text{shut}} + [\text{CO}_{2,\text{mit}}]$.



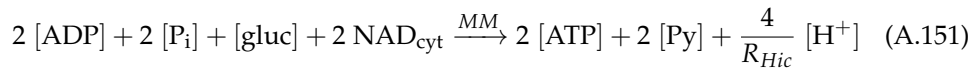
Mass Action kinetics are assumed for the forward reaction, with calculated rate term $k_{\text{CH}_m} + [\text{CO}_{2,\text{mit}}]$. Mass Action kinetics are assumed for the reverse reaction, with calculated rate term $k_{\text{nCH}_m} + \text{H}_m^+ [\text{BiC}_{\text{mit}}]$.



Mass Action kinetics are assumed for the forward reaction, with calculated rate term $k_{\text{CH}_i} + [\text{CO}_{2,\text{cyt}}]$. Mass Action kinetics are assumed for the reverse reaction, with calculated rate term $k_{\text{nCH}_i} + [\text{H}^+] [\text{BiC}_{\text{cyt}}]$.

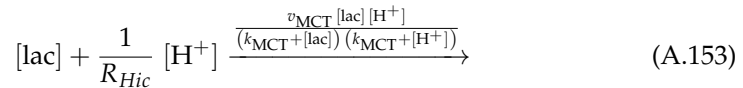
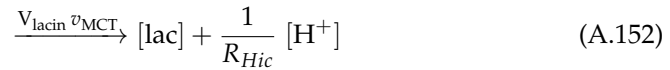


Michaelis-Menten kinetics are assumed, with calculated rate term $\frac{v_{\text{glut}} [\text{gluc}]}{k_{\text{glut}} + [\text{gluc}]}$.



Michaelis-Menten kinetics are assumed, with calculated rate term

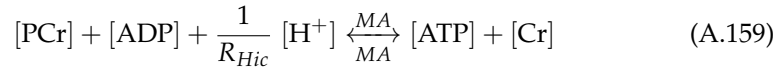
$$\frac{v_{\text{glyc}} [\text{ADP}]^2 [\text{P}_i]^2 [\text{gluc}] \text{NAD}_{\text{cyt}}^2}{\left(k_{m,\text{glycA}}^2 + [\text{ADP}]^2\right) \left(k_{m,\text{glycP}}^2 + [\text{P}_i]^2\right) \left(k_{m,\text{glycG}} + [\text{gluc}]\right) \left(k_{m,\text{glycN}}^2 + \text{NAD}_{\text{cyt}}^2\right)}$$



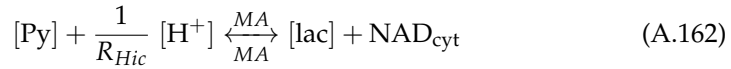
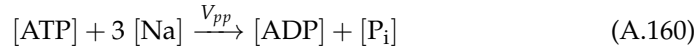
Mass Action kinetics are assumed for the forward reaction, with calculated rate term $k_{MAshut} + [H^+] [NAD]$. Mass Action kinetics are assumed for the reverse reaction, with calculated rate term $k_{MAshut}^- + NAD_{cyt} H_m^+$.



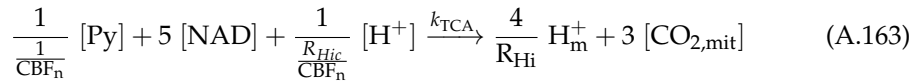
Mass Action kinetics are assumed, with calculated rate term k_{Na} .



Mass Action kinetics are assumed for the forward reaction, with calculated rate term $k_{PCr} + [PCr] [ADP] [H^+]$. Mass Action kinetics are assumed for the reverse reaction, with calculated rate term $k_{PCr}^- + [ATP] [Cr]$.



Mass Action kinetics are assumed for the forward reaction, with calculated rate term $k_{pl} + [Py] [H^+]$. Mass Action kinetics are assumed for the reverse reaction, with calculated rate term $k_{pl}^- + [lac] NAD_{cyt}$.



A.4.5 State variables

Symbol	Units	Initialiser	Notes
[ADP]	m M	[ADP] _n	ADP concentration in cytoplasm and mitochondria
[AMP]	m M	[AMP] _n	AMP concentration in cytoplasm
[ATP]	m M	[ATP] _n	ATP concentration in cytoplasm and mitochondria
[BiC _{cyt}]	m M	[BiC _{cyt,n}]	The concentration of bicarbonate ions in the cytoplasm
[CO _{2,cyt}]	m M	[CO _{2,cyt,n}]	The concentration of dissolved carbon dioxide in the cytoplasm
[Cr]	m M	[Cr] _n	Creatine concentration in cytoplasm
[gluc]	m M	[gluc] _n	Concentration of glucose in the cytoplasm
[H ⁺]	m M	[H ⁺] _n	Concentration of hydrogen ions in the cytoplasm
[lac]	m M	[lac] _n	Concentration of lactate in the cytoplasm
[BiC _{mit}]	m M	[BiC _{mit,n}]	The concentration of bicarbonate ions in the mitochondria
[CO _{2,mit}]	m M	[CO _{2,mit,n}]	The concentration of dissolved carbon dioxide in the mitochondria
[Na]	m M	[Na] _n	The concentration of sodium in the cytoplasm
[P _i]	m M	[P] _n	Inorganic phosphate concentration in cytoplasm and mitochondria
[PCr]	m M	[PCr] _n	phosphocreatine concentration in cytoplasm
[Py]	m M	[Py] _n	Concentration of pyruvate in the cytoplasm
Cu _{A,o}	m M	Cu _{A,o,init}	The concentration of oxidised cytochrome-c-oxidase
cyta3 _r	m M	[a3r] _{init}	Concentration of reduced cyt a3 in mitochondria
ΔΨ	m V	ΔΨ _{init}	Mitochondrial inner membrane potential

H_m^+	m M	$H_{m,init}^+$	Concentration of hydrogen ions in mitochondria
[NAD]	m M	[NAD] _n	Concentration of NAD in the mitochondria
NAD _{cyt}	m M	NAD _{cytn}	Concentration of NAD in the cytoplasm
[O ₂]	m M	[O ₂] _{init}	The concentration of oxygen in the mitochondria
[O _{2,c}]	m M	[O _{2,c}] _{init}	The concentration of oxygen in the capillary.
r	cm	r_{init}	Typical radius of cerebral vessels
ν_{CO_2}	mmHg	$\nu_{CO_2,n}$	CO ₂ passed through a first order filter.
ν_{O_2}	m M	$\nu_{O_2,n}$	Capillary O ₂ passed through a first order filter.
ν_{P_a}	mmHg	$\nu_{P_a,n}$	Arterial blood pressure passed through a first order filter.
ν_u	dimensionless	$\nu_{u,n}$	The demand parameter u passed through a first order filter.
[HbO _{2,v}]	m M	[HbO _{2,v}] _{init}	The concentration of bound oxygen in the veins.

A.4.6 Intermediate variables

Symbol	Units	Expression	Notes
$\text{Cu}_{A,o}$	mM	$\mathcal{E}_0(\text{cyt } a_3) - \text{Cu}_{A,o}$	The concentration of reduced cytochrome-c-oxidase in the mitochondria.
AVR	dimensionless	$\frac{V_a}{V_v}$	Arterio-venous volume ratio
$\text{cyt}a_3_o$	mM	$\mathcal{E}_0(\text{cyt } a_3) - \text{cyt}a_3_r$	Concentration of oxidised cyt a3 in mitochondria
C_{0i}	dimensionless	$\frac{10^{-\text{pH}_m} - 10^{-\text{pH}_m - \text{dpH}}}{\text{dpH}}$	Natural buffering capacity for protons in mitochondria
C_{0ic}	dimensionless	$\frac{10^{-\text{pH}_o} - 10^{-\text{pH}_o - \text{dpH}}}{\text{dpH}}$	Natural buffering capacity for protons in the cytoplasm
C_{NADH}	mV	$\frac{\mathcal{E}_0(\text{cyt } a_3)}{2} \log_{10} \left(\frac{1}{[\text{NAD}]/[\text{NADH}]} \right)$	Redox potential minus standard redox potential for NADH at normal demand
CBF	$\text{ml m}^{-1} \text{s}^{-1}$	$G (P_{a2} - P_v)$	Cerebral blood flow
ΔoxCCO	μM	$\Delta\text{oxCCO}_{\text{offset}} + 1000\text{CBF}_n (\text{Cu}_{A,o} - \text{VArat}_n)$	The expected CCO signal (as measured by NIRS)
CMRO_2	mM s^{-1}	$f_3 \text{CBF}_n$	Cerebral metabolic rate for oxygen
ΔG_1	mV	$p_1 \Delta p - 4 \left(E_1 + \mathcal{E}_0(\text{cyt } a_3) \log_{10} \left(\frac{\text{Cu}_{A,o}}{\text{Cu}_{A,o}} \right) \right)$	Free energy associated with reaction 1

ΔG_2	m V	$p_2 \Delta p$ $-4 \left(E_2 + \mathcal{E}_0(\text{cyt } a_3) \left(\log_{10} \left(\frac{\text{Cu}_{A,o}}{\text{Cu}_{A,o}} \right) - \log_{10} \left(\frac{\text{cyta}_3^r}{\text{cyta}_3^o} \right) \right) \right)$	Free energy associated with reaction 2
ΔG	J mol ⁻¹	$\Delta G^\circ + \mathcal{E}_0(\text{cyt } a_3) F \log_{10} (g_p)$	Gibbs free energy of ATP hydrolysis
ΔHbdiff	μM	$\Delta \text{Hbdiff}_{\text{offset}} + \Delta \text{HbO}_2 - \Delta \text{HHb}$	Change in Hbdiff (NIRS)
ΔHbO_2	μM	$\Delta \text{HbO}_{2,\text{offset}} + \text{HbO}_2 - \text{HbO}_{2n}$	Change in total oxygenated haemoglobin (NIRS)
ΔHbt	μM	$\Delta \text{HbT}_{\text{offset}} + \text{Hbt} - \text{Hbt}_n$	Change in total haemoglobin (NIRS)
ΔHHb	μM	$\Delta \text{HHb}_{\text{offset}} + \text{HHb} - \text{Hbt}_n$	Change in total deoxygenated haemoglobin (NIRS)
Δp	m V	$\Delta \Psi + \mathcal{E}_0(\text{cyt } a_3) \Delta \text{pH}$	The proton motive force across the mitochondrial inner membrane.
ΔpH	dimensionless	$\text{pH}_m - \text{pH}_o$	The pH difference across mitochondrial inner membrane
$\Delta \Psi_{\text{rate}}$	dimensionless	$\frac{p_2 f_2 + p_1 f_1 + p_3 f_3 - L}{C_{im}}$	Rate of change of mitochondrial inner membrane potential
$E_{1,NADH}$	m V	$\mathcal{E}_0(\text{Cu}_A) - \mathcal{E}_0(\text{NADH}) + C_{\text{NADH}}$	E1 when the reducing substrate is NADH
E_1	m V	$E_{1,NADH}$	The energy provided by electron transfer to Cu _A
η	dimensionless	$R_P \left(\frac{v_{P_a}}{v_{P_a,n}} - 1 \right) + R_O \left(\frac{v_{O_2}}{v_{O_2,n}} - 1 \right) + R_u \left(1 - \frac{v_u}{v_{u,n}} \right) + R_C \left(1 - \frac{v_{\text{CO}_2}}{v_{\text{CO}_2,n}} \right)$	Total autoregulatory stimuli

f_1	m M s^{-1}	$k_1 \text{Cu}_{A,o} - k_{-1} \text{Cu}_{A,o}$	The rate at which Cu_A is reduced
f_2	m M s^{-1}	$k_2 \text{Cu}_{A,o} \text{cyta3}_o - k_{-2} \text{Cu}_{A,o} \text{cyta3}_r$	The rate at which Cu_A is oxidised and cyt a3 reduced.
f_3	m M s^{-1}	$\frac{c_{k2} [\text{O}_2] \text{cyta3}_r \exp(-c3 (\Delta p - \Delta p_{30}))}{1 + \exp(-c3 (\Delta p - \Delta p_{30}))}$	The rate at which cyt a3 is oxidised
G	$\text{mmHg}^{-1} \text{s}^{-1}$	$R_u \text{pow}(r, 4)$	Resistance of cerebral circulation
g_p	dimensionless	$\frac{[\text{ADP}] [\text{P}_i]}{[\text{ATP}] \times 1000}$	(Normalised) phosphorylation potential (or ADP/ATP ratio)
G_t	$\text{mmHg}^{-1} \text{s}^{-1}$	$\frac{G G_0 G_v}{G G_0 + G G_v + G_v G_0}$	The total conductance of the cerebral blood vessels
h	cm	$(\text{pow}(r, 2) + 2r_0 h_0 + h_0 h_0)^{\frac{1}{2}} - r$	Wall thickness of cerebral vessels
HbO_2	μM	$\frac{V_a [\text{HbO}_{2,a}] + V_v [\text{HbO}_{2,v}]}{4} V_{\text{blood},n} \times 1000$	Total oxygenated haemoglobin (NIRS)
Hbt	μM	$\frac{(V_a + V_v) [\text{HbO}_{2,a}]_n}{4} V_{\text{blood},n} \times 1000$	Total haemoglobin (NIRS)
HHb	μM	$\frac{V_a [\text{HHb}_a] + V_v [\text{HHb}_v]}{4} V_{\text{blood},n} \times 1000$	Total deoxygenated haemoglobin (NIRS)
i_{NHE}	dimensionless	$\frac{V_{\text{maxNHE}} ([\text{Na}]_n - [\text{Na}])}{K_{\text{mNHE}} + [\text{Na}]_n - [\text{Na}]} \frac{1}{1 + \exp(\text{NapH} (\text{pH}_o - 6.7))}$	Rate of the sodium-hydrogen exchanger
J_{O_2}	m M s^{-1}	$J_{\text{O}_2,\text{min}}$	The rate at which oxygen is supplied to the mitochondria.
$J_{\text{O}_2,\text{min}}$	m M s^{-1}	$f_{\text{min}} (D_{\text{O}_2} ([\text{O}_{2,c}] - [\text{O}_2]), \text{CBF} [\text{HbO}_{2,a}])$	Rate at which oxygen is supplied to the mitochondria, minimum of diffusion rate and delivery rate

k_1	s^{-1}	$k_{1,0} \exp(-c_{k1} (\Delta p - SaO_{2,n}))$	Forward rate constant for reaction 1
$k_{1,0}$	s^{-1}	$\frac{k_{1,n} \frac{N_t}{1 + [NAD]/[NADH]}}{[NADH]_n}$	Forward rate constant for reaction 1 at normal PMF
k_2	$m^{-1} M s^{-1}$	$k_{2,n} \exp(-c_{k2} (\Delta p - SaO_{2,n}))$	Forward rate constant for reaction 2
$k_{CO_2,out}$	dimensionless	$\frac{CBF_n [CO_{2,cyt}]}{[CO_{2,cyt,n}]}$	Rate at which CO2 moves out of the cell
k_{MAshut}	s^{-1}	$\frac{\frac{CBF_n NADH_{cyt}}{3}}{[NAD]_n [H^+]_n NADH_{cyt} - \frac{1}{K_{eqMAshut}} NAD_{cyt,n} H_{m,n}^+ NADH}$	Rate of forward reaction in the malate-aspartate shuttle
k_{Na}	$ml \cdot s^{-1}$	$([Na]_n - [Na])$	Rate constant for the diffusion of sodium ions between the extracellular space and the cytoplasm
k_{MAshut}^-	s^{-1}	$\frac{\frac{k_{MAshut} NADH}{NADH_{cyt}}}{K_{eqMAshut}}$	Rate of backward reaction in the malate-aspartate shuttle
k_{PCr}^-	$m^{-1} M s^{-1}$	$\frac{\log(2)}{\left(K_{eq,PCr} \left([PCr]_n + [ADP]_n + \frac{[H^+]_n}{K_{Hic}} \right) + [Cr]_n + [ATP]_n \right) t_{1/2,PCr}}$	The backward rate of reaction for the reaction in which phosphocreatine combines with ADP to give creatine and ATP

k_{PCr}	$m^{-1} M s^{-1}$	$\frac{\log(2)}{\left([\text{PCr}]_n + [\text{ADP}]_n + \frac{[\text{H}^+]_n}{R_{Hic}} + \frac{[\text{Cr}]_n + [\text{ATP}]_n}{K_{eq,PCr}}\right)} t_{1/2,PCr}$	The forward rate of reaction for the reaction in which phosphocreatine combines with ADP to give creatine and ATP
k_{pl}	s^{-1}	$\frac{2\text{CMR}_{gluc,n} - \frac{\text{CBF}_n}{3} + k_{pl}^- [\text{lac}]_n \text{NAD}_{cytn}}{[\text{Py}]_n [\text{H}^+]_n} \frac{\text{NADH}_{cyt}}{\text{NADH}_{cytn}}$	Rate of forward reaction in the pyruvate lactate equilibrium
k_{TCA}	$m M s^{-1}$	$\frac{v_{TCA} [\text{Py}] [\text{NAD}]}{(k_{m,tcaN} + [\text{NAD}]) (k_{m,tcaP} + [\text{Py}])}$	Rate of the TCA cycle
$k_{ATP,CV}$	$m M s^{-1}$	$\frac{L_{CV} \text{CBF}_n}{n_a}$	Rate of ATP synthesis by Complex V
Keq_1	dimensionless	$\text{pow}\left(10, \frac{-1}{\mathcal{E}_0(\text{cyt } a_3)} \left(\frac{p_1 \Delta p}{4} - E_1\right)\right)$	Equilibrium constant for reaction 1
Keq_2	dimensionless	$\text{pow}\left(10, \frac{-1}{\mathcal{E}_0(\text{cyt } a_3)} \left(\frac{p_2 \Delta p}{4} - E_2\right)\right)$	Equilibrium constant for reaction 2
k_{-1}	s^{-1}	$\frac{k_1}{\text{Keq}_1}$	Backward rate constant for reaction 1
k_{-2}	$m^{-1} M s^{-1}$	$\frac{k_2}{\text{Keq}_2}$	Backward rate constant for reaction 2
L	$m M s^{-1}$	$L_{CV} + L_{lk}$	The rate at which protons reenter the mitochondrial matrix
L_{CV}	$m M s^{-1}$	$\frac{L_{CV,frac} L_{CV,max} (1 - \exp(-\theta))}{1 + r_{CV} \exp(-\theta)}$	The rate at which protons reenter the mitochondrial matrix associated with ADP phosphorylation

L_{lk}	m M s^{-1}	$\Delta p_{3,\text{corr}} f_n (\exp(\Delta p f_n) - 1)$	The rate at which protons reenter the mitochondrial matrix through leak channels
μ	dimensionless	$\frac{\mu_{\min} + \mu_{\max} \exp(\eta)}{1 + \exp(\eta)}$	Total autoregulatory stimuli filtered through sigmoidal function
NADH	m M	$N_t - [\text{NAD}]$	Concentration of NADH in the mitochondria
NADH _{cyt}	m M	$\text{NAD}_{\text{cytn}} + \text{NADH}_{\text{cytn}} - \text{NAD}_{\text{cyt}}$	Concentration of NADH in the cytoplasm
$[\text{NAD}]/[\text{NADH}]$	dimensionless	$\frac{[\text{NAD}]}{[\text{NADH}]}$	NAD/NADH ratio
NTP/EPP	dimensionless	$\frac{[\text{ATP}]}{[\text{ADP}]}$	NTP/EPP calculation
P_1	mmHg	$\frac{EPP}{P_{a2} + P_v}$	Average blood pressure in vessels
P_{a2}	mmHg	$\frac{G_0 P_a + G P_v}{G + G_0}$	The pressure at the start of the cerebral artery compartment
P_v	mmHg	$\frac{G_t}{G_v} (P_a - P_{vs}) + P_{vs}$	Venous blood pressure
pH _m	dimensionless	$-\log_{10} \left(\frac{[\text{H}^+]_m}{1000} \right)$	Mitochondrial pH
pH _o	dimensionless	$-\log_{10} \left(\frac{[\text{H}^+]_o}{1000} \right)$	Cytoplasmic pH
r_{buffi}	dimensionless	$\frac{C_{\text{buffi}}}{C_{0i}}$	Buffering capacity for protons in mitochondria
r_{buffic}	dimensionless	$\frac{C_{\text{buffic}}}{C_{0ic}}$	Buffering capacity for protons in the cytoplasm

R_{Hi}	dimensionless	r_{buffi}	Relative mitochondrial volume for protons
R_{Hic}	dimensionless	r_{buffic}	Relative cytoplasmic volume for protons
ScO_2	dimensionless	$\frac{SaO_2 + SvO_2}{2}$	Capillary oxygen saturation
σ_e	mmHg	$\sigma_{e0} \left(\exp \left(\frac{K_\sigma (r - r_0)}{r_0} \right) - 1 \right) - \sigma_{coll}$	Elastic stress in vessel walls
SvO_2	dimensionless	$\frac{[HbO_{2,v}]}{[HbO_{2,a}]_n}$	Venous oxygen saturation
T_e	mmHg cm	$\sigma_e h$	Elastic tension in vessel walls
T_m	mmHg cm	$T_{max} \exp \left(-\text{pow} \left(\text{fabs} \left(\frac{r - r_m}{r_t - r_m} \right), n_m \right) \right)$	Muscular tension in vessel walls
T_{max}	mmHg cm	$T_{max0} (1 + T_{e,n} \mu)$	Maximum muscular tension developed by circulation
θ	dimensionless	$k_{CV} \left(\Delta p + \frac{\mathcal{E}_0(\text{cyt } a_3)}{n_a} \log_{10} \left(\frac{g_p}{g_{p,n}} \right) - L_{CV,max} \right)$	Driving force for complex V
TOS	dimensionless	$100 \left(\frac{\text{pow} \left(\frac{r}{[Hb_{tot,c}]} , 2 \right)}{\text{pow} \left(\frac{r}{[Hb_{tot,c}]} , 2 \right) + \frac{V_v}{V_{a,n}}} [HbO_{2,a}] + \frac{\frac{V_v}{V_{a,n}}}{\text{pow} \left(\frac{r}{[Hb_{tot,c}]} , 2 \right) + \frac{V_v}{V_{a,n}}} [HbO_{2,v}] \right)$	Tissue Oxygenation index.
v_{glyc}	$m M s^{-1}$	$\frac{v_{glyc,n} (I + 1)}{1 + I \frac{[ATP]}{[ATP]_n} \frac{[AMP]_n}{[AMP]}}$	Vmax for glycolysis
$Vmca$	$cm s^{-1}$	$CBF CBF_{scale}$	The velocity of blood in the middle cerebral artery
V_a	dimensionless	$V_{a,n} \left(\frac{r}{[Hb_{tot,c}]} \right)^2$	Arterial blood volume as a fraction of normal total blood volume

V_t	dimensionless	$V_a + V_v$	Normalised total blood volume
V_v	dimensionless	$V_{v,n} + C_v (P_v - P_{v,n})$	Venous blood volume as a fraction of total blood volume
$[\text{HHb}_v]$	mM	$[\text{HbO}_{2,a}]_n - [\text{HbO}_{2,v}]$	The concentration of deoxy-haemoglobin in the veins.

A.4.7 Parameters

Symbol	Units	Initialiser	Notes
$[ADP]_n$	m M	0.012	The normal concentration of ADP in the cytoplasm
$[AMP]_n$	m M	$\frac{K_{eq,ADPATP} \text{pow} ([ADP]_n, 2)}{[ATP]_n}$	Normal AMP concentration in cytoplasm normal AMP concentration in cytoplasm
$[ATP]_n$	m M	1.2	The normal concentration of ATP in the cytoplasm
$[BiC_{cyt,n}]$	m M	$\frac{0.95k_{CH,eq} [CO_{2,cyt,n}]}{[H^+]_n}$	The normal concentration of bicarbonate ions in the cytoplasm
$[CO_{2,cyt,n}]$	m M	$PtCO_2n k_{H,CO_2,t}$	The normal concentration of dissolved carbon dioxide in the cytoplasm
$[Cr]_n$	m M	$\frac{K_{eq,PCr}^* [ADP]_n [PCr]_n}{[ATP]_n}$	Normal concentration of creatine in cytoplasm
$[gluc]_n$	m M	1.2	Normal cellular concentration of glucose
$[H^+]_n$	m M	$1000\text{pow} (10, -pH_{o,n})$	Normal hydrogen ion concentration in the cytoplasm
$[lac]_n$	m M	3	Normal concentration of lactate in the cytoplasm
$[BiC_{mit,n}]$	m M	$\frac{k_{CH,eq} [CO_{2,mit,n}]}{H_{m,n}^+}$	The normal concentration of bicarbonate ions in the mitochondria

$[\text{CO}_{2,\text{mit},n}]$	m M	$1.2[\text{CO}_{2,\text{cyt},n}]$	The normal concentration of dissolved carbon dioxide in the mitochondria
$[\text{Na}]_n$	mM	15	The normal concentration of sodium in the cytoplasm
$[\text{PCr}]_n$	m M	2.6	normal concentration of phosphocreatine in cell cytoplasm
$[\text{P}]_n$	m M	$\frac{[\text{PCr}]_n}{[\text{PCr}]_n / [\text{P}_i]_n}$	The normal concentration of inorganic phosphate in the cytoplasm
$[\text{Py}]_n$	m M	0.1	Normal concentration of pyruvate ions in the cytoplasm
$\text{Cu}_{\text{A},\text{o},\text{frac}}$	dimensionless	0.67	Normal oxidised fraction of Cu_A
$\text{Cu}_{\text{A},\text{o},\text{init}}$	m M	$\text{Cu}_{\text{A},\text{o},n}$	Initial oxidized Cu_A
$\text{Cu}_{\text{A},\text{o},n}$	m M	$[\text{CCO}]_{\text{mit}} \text{Cu}_{\text{A},\text{o},\text{frac}}$	Normal oxidized Cu_A
$\text{Cu}_{\text{A},\text{r},n}$	m M	$[\text{CCO}]_{\text{mit}} - \text{Cu}_{\text{A},\text{o},n}$	The resting amount of reduced cytochrome-c-oxidase
$\text{a}3_{\text{frac},n}$	dimensionless	$1 - \frac{\text{cyta}3_{\text{r},n}}{[\text{CCO}]_{\text{mit}}}$	Normal oxidised fraction of cyt a3
$\text{a}3_{\text{o},\text{init}}$	m M	$\text{a}3_{\text{o},n}$	Initial oxidised cytochrome a3
$\text{a}3_{\text{o},n}$	m M	$[\text{CCO}]_{\text{mit}} - \text{cyta}3_{\text{r},n}$	Normal oxidised cytochrome a3
$[\text{a}3\text{r}]_{\text{init}}$	m M	$\text{cyta}3_{\text{r},n}$	Initial reduced cytochrome a3
$\text{cyta}3_{\text{r},n}$	m M	$\frac{\frac{f_n}{c_{k2}}}{P_a \text{CO}_{2,n}}$	Normal reduced cytochrome a3
$c3$	$\text{m}^{-1} \text{V}$	$\frac{\exp(-c3 (\text{SaO}_{2,n} - \Delta p_{30}))}{1 + \exp(-c3 (\text{SaO}_{2,n} - \Delta p_{30}))}$	Parameter controlling the sensitivity of reaction 3 to PMF

C_{buffi}	dimensionless	0.022	Buffering capacity for protons in mitochondria
C_{buffic}	dimensionless	0.025	Buffering capacity for protons in the cytoplasm
occ_{frac}	dimensionless	0.8	Fraction of arterial blood which flows through the carotid arteries under normal conditions
C_{im}	$mM m^{-1} V$	0.00675	Capacitance of mitochondrial inner membrane
$C_{NADH,n}$	mV	$\frac{\mathcal{E}_0(\text{cyt } a_3)}{2} \log_{10} \left(\frac{1}{[\text{NAD}]_n / [\text{NADH}]_n} \right)$	normal value of C_{NADH}
C_v	$mmHg^{-1}$	0.047	Compliance of the veins (normalised)
CBF_n	$ml m^{-1} l s^{-1}$	0.008	Normal cerebral blood flow
CBF_{scale}	cm	5000	Ratio between V_{mca} and CBF
$\Delta oxCCO_{offset}$	μM	0	An arbitrary baseline offset to the CCO signal (NIRS)
c_{k1}	$m^{-1} V$	0.01	Parameter controlling sensitivity of k1 to PMF
c_{k2}	$m^{-1} V$	0.02	Parameter controlling sensitivity of k2 to PMF
$CMR_{gluc,n}$	dimensionless	0.0044	Normal rate of glucose metabolism for the brain
$CMRO2_n$	$mM s^{-1}$	0.02	The resting CMRO2.
$L_{CV,frac}$	dimensionless	1	A control parameter representing the action of complex V inhibitors

$[\text{CCO}]_{\text{mit}}$	m M	$\frac{[\text{CCO}]_{\text{tis}}}{\text{Vol}_{\text{mit}}}$	Concentration of cytochrome c oxidase in mitochondria
$[\text{CCO}]_{\text{tis}}$	m M	0.0022	Concentration of cytochrome c oxidase in tissue
D_{O_2}	s^{-1}	$\frac{R_u}{[\text{O}_{2,c}]_n - P_a \text{CO}_{2,n}}$	Diffusion rate between capillaries and mitochondria.
$\Delta G_{1,n}$	m V	$p_1 \text{SaO}_{2,n} - 4 \left(E_{1,n} + \mathcal{E}_0(\text{cyt } a_3) \log_{10} \left(\frac{\text{VArat}_n}{\text{Cu}_{A,o,n}} \right) \right)$	Normal free energy associated with reaction 1
$\Delta G_{2,n}$	m V	$p_2 \text{SaO}_{2,n} - 4 \left(E_2 + \mathcal{E}_0(\text{cyt } a_3) \left(\log_{10} \left(\frac{\text{Cu}_{A,o,n}}{\text{VArat}_n} \right) - \log_{10} \left(\frac{\text{cyt}a_3 r_n}{a_{3,o,n}} \right) \right) \right)$	Normal free energy associated with reaction 2
ΔG_n	J mol^{-1}	$\Delta G^\circ + \mathcal{E}_0(\text{cyt } a_3) F \log_{10} (g_{p,n})$	Normal Gibbs free energy of ATP hydrolysis
$\Delta \text{Hbdiff}_{\text{offset}}$	μM	0	An arbitrary baseline offset to the HHb signal (NIRS)
$\Delta \text{HbO}_{2,\text{offset}}$	μM	0	An arbitrary baseline offset to the HbO ₂ signal (NIRS)
$\Delta \text{HbT}_{\text{offset}}$	μM	0	An arbitrary baseline offset to the HbT signal (NIRS)
$\Delta \text{HHb}_{\text{offset}}$	μM	0	An arbitrary baseline offset to the HHb signal (NIRS)
$\Delta p_{3,\text{corr}}$	m V	-25	
Δp_{30}	m V	$\text{SaO}_{2,n} + \Delta p_{3,\text{corr}}$	Value of PMF at which reaction 3 is maximally sensitive to PMF

$L_{CV,max}$	m V	$\frac{-\Delta G_n}{n_a F}$	A constant in the rate of complex V
Δp_n	m V	$\Delta \Psi_n + \mathcal{E}_0(\text{cyt } a_3) \Delta \text{pH}_n$	The resting value of the proton motive force.
dpH	dimensionless	0.001	A constant in the buffering relationship
ΔpH_n	dimensionless	$\text{pH}_{m,n} - \text{pH}_{o,n}$	The resting value of pH difference across mitochondrial inner membrane
$\Delta \Psi_{init}$	m V	$\Delta \Psi_n$	Initial value of mitochondrial inner membrane potential
$\Delta \Psi_n$	m V	145	Normal mitochondrial inner membrane potential
$E_{1,NADH,n}$	m V	$\mathcal{E}_0(\text{Cu}_A) - \mathcal{E}_0(\text{NADH}) + C_{NADH,n}$	Normal value of E1NADH
$E_{1,n}$	m V	$E_{1,NADH,n}$	The normal value of E_1
E_2	m V	$\mathcal{E}_0(\text{cyt } a_3) - \mathcal{E}_0(\text{Cu}_A)$	The energy provided by transfer of four electrons from Cu_A to to cyt a3
$\mathcal{E}_0(\text{cyt } a_3)$	m V	350	Cyt a3 standard redox potential
$\mathcal{E}_0(\text{Cu}_A)$	m V	250	
$\mathcal{E}_0(\text{NADH})$	m V	-320	NADH standard redox potential
EPP	dimensionless	$Pi_n + PCr_n + 2ATP_n + ADP_n$	Exchangeable phosphate pool
f_n	m M s ⁻¹	$\frac{CBF_n}{CBF_n}$	Normal resting rate of f1 and f2.
F	C m ⁻¹ mol	96.4853	Faraday constant
G_0	mmHg ⁻¹ s ⁻¹	$K_{G,0} r_0^4$	Conductance of the supplying artery compartment

$G_{0,n}$	$\text{mmHg}^{-1} \text{s}^{-1}$	$G_{0,\text{rat}} G_n$	Normal conductance of the supplying artery compartment
$G_{0,\text{rat}}$	dimensionless	10	Ratio between the conductance of the cerebral arteries and the supplying artery compartment
G_v	$\text{mmHg}^{-1} \text{s}^{-1}$	$G_{\text{VArat},n} G_n$	Conductance of the veins
$G_{\text{VArat},n}$	dimensionless	4	Normal ratio of conductances between arteries and veins G_v/G_n (determines venous pressure)
$[\text{gluc}_c]$	m M	5.3	Concentration of glucose in the blood
$\text{glyc}_{a,n}$	dimensionless	$\frac{([\text{ADP}]_n)^2}{(k_{m,\text{glycA}})^2 + ([\text{ADP}]_n)^2}$	Term in the expression for normal glycolysis rate
$\text{glyc}_{g,n}$	dimensionless	$\frac{[\text{gluc}]_n}{k_{m,\text{glycG}} + [\text{gluc}]_n}$	Term in the expression for normal glycolysis rate
glyc_{nn}	dimensionless	$\frac{(\text{NAD}_{\text{cytn}})^2}{(k_{m,\text{glycN}})^2 + (\text{NAD}_{\text{cytn}})^2}$	Term in the expression for normal glycolysis rate
$\text{glyc}_{p,n}$	dimensionless	$\frac{([\text{P}]_n)^2}{(k_{m,\text{glycP}})^2 + ([\text{P}]_n)^2}$	Term in the expression for normal glycolysis rate
G_n	$\text{mmHg}^{-1} \text{s}^{-1}$	$\frac{\text{CBF}_n}{P_a - P_{vs}} \left(1 + \frac{1}{G_{0,\text{rat}}} + \frac{1}{G_{\text{VArat},n}} \right)$	Normal resistance of cerebral circulation
ΔG°	J mol^{-1}	-30500	Standard Gibbs free energy of ATP hydrolysis

$g_{p,n}$	dimensionless	$\frac{[\text{ADP}]_n [\text{P}]_n}{[\text{ATP}]_n \times 1000}$	Normal phosphorylation potential
$G_{t,n}$	$\text{mmHg}^{-1} \text{s}^{-1}$	$\frac{G_n G_{0,n} G_v}{G_n G_{0,n} + G_n G_v + G_v G_{0,n}}$	Normal value of the total conductance of all blood vessel compartments
h_0	cm	0.003	Vascular wall thickness when radius is r_0
$\text{H}_{m,\text{init}}^+$	m M	$\text{H}_{m,n}^+$	Initial hydrogen ion concentration in mitochondria
$\text{H}_{m,n}^+$	m M	$10^{3-\text{pH}_{m,n}}$	Normal hydrogen ion concentration in mitochondria
h_n	cm	$\left(([\text{Hbtot}_c])^2 + 2r_0 h_0 + h_0 h_0 \right)^{\frac{1}{2}} - [\text{Hbtot}_c]$	Normal wall thickness of cerebral vessels
$H_{\text{cyt},n}$	dimensionless	$10^{3-\text{pH}_{o,n}}$	Normal hydrogen ion concentration in cytoplasm
$\text{HbO}_{2,n}$	μM	$\frac{V_{a,n} [\text{HbO}_{2,a}]_n + V_{v,n} [\text{HbO}_{2,v}]_n}{4} V_{\text{blood},n} \times 1000$	Normal total oxygenated haemoglobin (NIRS)
Hbt_n	μM	$\frac{(V_{a,n} + V_{v,n}) [\text{Hbtot}]_n}{4} V_{\text{blood},n} \times 1000$	Normal total haemoglobin (NIRS)
$henry_{\text{CO}_2}$	dimensionless	0.030000	Solubility of CO2 in tissue
$k_{\text{H},\text{CO}_2,t}$	m M mmHg ⁻¹	0.038000	Constant setting relationship between carbon dioxide saturation and carbon dioxide concentration in tissue
k_{H,O_2}	m M mmHg ⁻¹	0.0014000	Constant setting relationship between oxygen saturation and oxygen concentration in artery

Hbt_n	μM	$\frac{V_{a,n} [HHb_a]_n + V_{v,n} [HHb_v]_n}{4} V_{\text{blood},n} \times 1000$	Normal total deoxygenated haemoglobin (NIRS)
I	dimensionless	3	The parameter which describes how strongly the AMP/ATP ratio inhibits the conversion of glucose to pyruvate
R_u	m M s^{-1}	CBF_n	The resting rate of supply of oxygen to the mitochondria.
$k_{1,n}$	s^{-1}	$\frac{f_n}{VArat_n - \frac{1}{K_{eq1,n}} Cu_{A,o,n}}$	The value of k_1 at normal Δp and NADH
$k_{2,n}$	$\text{m}^{-1} \text{M s}^{-1}$	$\frac{f_n}{Cu_{A,o,n} a_{3,o,n} - \frac{1}{K_{eq2,n}} VArat_n cyta_{3,r,n}}$	Normal forward rate constant for reaction 2
c_{k2}	$\text{m}^{-1} \text{M s}^{-1}$	$\frac{k_{3,0}}{\frac{\exp(-c3(SaO_{2,n} - \Delta p_{30}))}{1 + \exp(-c3(SaO_{2,n} - \Delta p_{30}))}}$	Rate constant for reaction 3
$k_{3,0}$	$\text{m}^{-1} \text{M s}^{-1}$	$2.5E + 5$	an apparent second-order rate constant for reaction 3 at zero PMF
k_{AK}	$\text{m}^{-1} \text{M s}^{-1}$	1055	The forward rate constant for the conversion of two molecules of ADP to one of ATP and one of AMP
Keq_{ADPATP}	dimensionless	$\frac{k_{AK}}{k_{AK}^-}$	Equilibrium constant for the conversion of ADP to ATP and AMP
$t_{12,ADPATP}$	s	0.000002	Halftime for the conversion of ADP to ATP and AMP
$T_{e,n}$	dimensionless	1	Control parameter allowing destruction of autoregulation

k_{BiCshut}	$\text{ml} \cdot \text{s}^{-1}$	$\frac{\log(2.0)}{t_{1/2,\text{BiCshut}} \left(1 + \frac{1.0}{\text{Vol}_{\text{mit}} \text{Keq}_{\text{BiCshut}}}\right)}$	The rate of transfer of bicarbonate ions from cytoplasm to mitochondria
$\text{Keq}_{\text{BiCshut}}$	dimensionless	$\frac{\text{HCO}_{3,\text{mit}}^-}{\text{HCO}_{3,\text{cyt}}^-}$	Equilibrium constant for the transport of bicarbonate ions between mitochondria and cytoplasm
$t_{1/2,\text{BiCshut}}$	dimensionless	2200	The half time for the transport of bicarbonate ions between mitochondria and cytoplasm
$k_{\text{CH,eq}}$	dimensionless	0.00079000	Equilibrium constant for the production and dissociation of carbonic acid at normal concentrations
Keq_{CHi}	dimensionless	$\frac{H_{\text{cyt},n}^+ \text{HCO}_{3,\text{cyt}}^-}{\text{CO}_{2,\text{cyt},n}}$	Equilibrium constant for the production and dissociation of carbonic acid in the cytoplasm
Keq_{CHm}	dimensionless	$\frac{H_{m,n}^+ \text{HCO}_{3,\text{mit}}^-}{\text{CO}_{2,\text{mit},n}}$	Equilibrium constant for the production and dissociation of carbonic acid in the mitochondria
k_{CHi}	s^{-1}	$\frac{\log(2.0)}{t_{1/2,\text{CHi}} (1.0 + H_{\text{cyt},n}^+ / \text{Keq}_{\text{CHi}})}$	The rate of conversion of CO_2 to bicarbonate and protons in cytoplasm
$t_{1/2,\text{CHi}}$	dimensionless	3.2	Halftime for the production of carbonic acid in cell cytoplasm
k_{CHm}	s^{-1}	$\frac{\log(2.0)}{t_{1/2,\text{CHm}} (1.0 + H_{m,n}^+ / \text{Keq}_{\text{CHm}})}$	The rate of conversion of CO_2 to bicarbonate and protons in mitochondria

$t_{1/2,CHm}$	dimensionless	25	Halftime for the production of carbonic acid in the mitochondria
k_{CO2out}	$ml \cdot s^{-1}$	$\frac{CMRO2_n CO_{2,cyt}}{CO_{2,cyt,n}}$	The rate at which CO ₂ moves out of the cell
$k_{CO2shut}$	$ml \cdot s^{-1}$	$\frac{CMRO2_n}{CO_{2,mit,n} - CO_{2,cyt,n}}$	The rate of transfer of CO ₂ between mitochondria to cytoplasm
K_G	$mmHg^{-1} s^{-1} cm^{-4}$	$\frac{G_n}{([Hbtot_c])^4}$	Constant of proportionality relating pressure drop to flow
K_{G0}	$mmHg^{-1} s^{-1} cm^{-4}$	$G_{0,n}$	Constant in relationship between normal conductance of supplying artery and its radius
k_{glut}	m M	6.2	Km for the transport of lactate in and out of the cell.
k_{MCT}	m M	$10^{-k_{lac,ph}}$	
$k_{lac,ph}$	dimensionless	7	Constant in Km for the transport of lactate
f_n	$m^{-1} V$	0.038	Second constant controlling rate of L_{lk} of Δp .
k_{AK}^-	$m^{-1} Ms^{-1}$	379	The backward rate constant for the conversion of two molecules of ADP to one of ATP and one of AMP
$k_{nBiCshut}$	$ml \cdot s^{-1}$	$\frac{\log(2.0)}{t_{1/2,BiCshut} (Keq_{BiCshut} + 1.0/Vol_{mit})}$	The rate of transfer of bicarbonate ions from mitochondria to cytoplasm

k_{nCHi}	$\text{mM}^{-1} \cdot \text{s}^{-1}$	$\frac{\log(2.0)}{t_{1/2,CHi}(H_{cyt,n} + K_{eqCHi})}$	The backward rate in the conversion of CO_2 to bicarbonate and protons in cytoplasm
k_{nCHm}	$\text{mM}^{-1} \cdot \text{s}^{-1}$	$\frac{\log(2.0)}{t_{1/2,CHm}(H_{m,n} + K_{eqCHm})}$	The backward rate in the conversion of CO_2 to bicarbonate and protons in mitochondria
k_{pl}^-	s^{-1}	$t_{1/2,pl}$	Rate of backwards reaction in the pyruvate lactate equilibrium
$K_{eq,PCr}$	$\text{m}^{-1} \text{M}$	$\frac{K_{eq,PCr}^*}{[H^+]_n}$	Equilibrium of the reaction in which phosphocreatine combines with ADP to give creatine and ATP
$K_{eq,PCr}^*$	dimensionless	166	Effective equilibrium constant for the reaction in which phosphocreatine combines with ADP to give creatine and ATP
$t_{1/2,PCr}$	s	0.00002	Halftime for the reaction in which phosphocreatine combines with ADP to give creatine and ATP
$t_{1/2,pl}$	s^{-1}	10	Time constant for pyruvate to lactate interconversion
K_σ	dimensionless	10	Parameter controlling sensitivity of σ_e to radius
k_{TCA_n}	mM s^{-1}	$\frac{1 \text{ CBF}_n}{3 \text{ CBF}_n}$	Normal rate of the TCA cycle

$\Delta p_{3,corr}$	dimensionless	1	A parameter representing the action of uncouplers
k_{CV}	$m^{-1} V$	$\frac{-1}{SaO_{2,n} - L_{CV,max}} \log \left(\frac{1 - L_{CV,0}}{1 + r_{CV} L_{CV,0}} \right)$	Parameter controlling the sensitivity of complex V flux to driving force
$Keq_{1,n}$	dimensionless	$10^{\frac{-1}{\varepsilon_0(cyta3)} \left(\frac{p_1 SaO_{2,n}}{4} - E_{1,n} \right)}$	Normal equilibrium constant for reaction 1
$Keq_{2,n}$	dimensionless	$10^{\frac{-1}{\varepsilon_0(cyta3)} \left(\frac{p_2 SaO_{2,n}}{4} - E_2 \right)}$	Normal equilibrium constant for reaction 2
Keq_{MAshut}	dimensionless	10	Equilibrium constant for the malate-aspartate shuttle
$k_{m,ATP}$	dimensionless	0.025	Km for ATP use as a fraction of normal ATP concentration
$k_{m,glycA}$	m M	$k_{m,glycA,f} [ADP]_n$	Km for ADP in the caricature of glycolysis
$k_{m,glycA,f}$	dimensionless	0.2	Km for ADP in glycolysis as a fraction of normal ADP concentration
$k_{m,glycG}$	m M	0.05000	Km for glucose in the caricature of glycolysis
$k_{m,glycN}$	m M	$k_{m,glycN,f} [NAD]_n$	Km for NAD in the caricature of glycolysis
$k_{m,glycN,f}$	m M	0.2	Km for NAD in glycolysis as a fraction of normal NAD concentration

$k_{m,glycP}$	m M	$k_{m,glycP,f} [P]_n$	Km for inorganic phosphate in the caricature of glycolysis.
$k_{m,glycP,f}$	dimensionless	0.2	Km for inorganic phosphate in glycolysis as a fraction of normal phosphate concentration
Km_{KATPA}	mM	1.4	Km for intracellular ATP for the sodium potassium pump
Km_{KATPNa}	mM	20	Km for intracellular sodium for the sodium potassium pump
Km_{NaBiC}	mM	10.4	Km for the sodium bicarbonate co-transporter
Km_{NHE}	mM	33	Km for the sodium hydrogen exchanger
km_{NAD}	m M	100000	Km for NAD in the tca cycle as a fraction of the normal NAD concentration
$Km_{NAD,TCA}$	m M	$km_{NAD} [NAD]_n$	Km for NAD in the TCA cycle
km_{py}	m M	0	Km for pyruvate for the tca cycle as a fraction of the normal pyruvate concentration
$Km_{Py,TCA}$	m M	$km_{py} [Py]_n$	Km for pyruvate in the TCA cycle
k_m	m M	$[ATP]_n k_{m,ATP}$	Km for ATP use
$k_{-1,0}$	s^{-1}	$\frac{f_n}{Keq_{1,n} VArat_n - Cu_{A,o,n}}$	Backward rate constant for reaction 1 at normal PMF
$kn1_n$	dimensionless	$\frac{f_n}{Keq_{1,n} VArat_n - Cu_{A,o,n}}$	

$k_{-2,n}$	$m^{-1} M s^{-1}$	$\frac{f_n}{K_{eq2,n} C_{uA,o,n} a_{3o,n} - V_{Arat,n} cyta_{3r,n}}$	Normal backward rate constant for reaction 2
$L_{CV,0}$	dimensionless	0.4	Normal complex V flux as a fraction of maximum possible flux
$L_{CV,frac}$	dimensionless	$1 - L_{lk,frac}$	Normal fraction of proton entry into mitochondria associated with ADP phosphorylation
$L_{CV,max}$	$m M s^{-1}$	$\frac{CBF_n}{L_{CV,0}}$	The maximum rate of proton flow through complex V.
L_{CVn}	$m M s^{-1}$	$L_n L_{CV,frac}$	The resting flow of protons into the matrix through complex V
f_n	$m M s^{-1}$	$\frac{CBF_n}{\exp(SaO_{2,n} f_n) - 1}$	First constant controlling rate of L_{lk} of Δp .
$L_{lk,frac}$	dimensionless	0.25	Normal fraction of proton entry into mitochondria which is via leak channels
L_{lkn}	$m M s^{-1}$	$L_n L_{lk,frac}$	The resting flow of protons into the matrix via leak channels.
L_n	$m M s^{-1}$	$p_{tot} f_n$	The total flow of protons back into mitochondria
$[lac_C]$	$m M$	1	Capillary lactate concentration
μ_{max}	dimensionless	1	Maximum value of mu
μ_{min}	dimensionless	-1	Minimum value of mu
μ_n	dimensionless	0	Normal value of mu

n_h	dimensionless	2.5	Hill coefficient for haemoglobin saturation
n_m	dimensionless	1.83	Exponent in the muscular tension relationship
n_a	dimensionless	4.33	Number of protons passing through Complex V for each ATP synthesised
NAD_{cytn}	m M	359	Normal concentration of NAD in the cytoplasm
$\text{NADH}_{\text{cytn}}$	dimensionless	50	Normal concentration of NADH in the cytoplasm
$[\text{NADH}]_n$	m M	$N_t - [\text{NAD}]_n$	Normal mitochondrial NADH concentration
$[\text{NAD}]_n$	m M	$\frac{N_t}{1 + \frac{1}{[\text{NAD}]_n/[\text{NADH}]_n}}$	Normal concentration of NAD in the mitochondria
$[\text{NAD}]_n/[\text{NADH}]_n$	dimensionless	9	Normal NAD/NADH ratio
N_t	m M	3	Total mitochondrial NAD + NADH concentration
NapH	dimensionless	1	Parameter controlling the sensitivity of the sodium hydrogen exchanger to cytoplasmic pH
$[\text{O}_2]_{\text{init}}$	m M	$[\text{O}_2]_n$	Initial oxygen concentration in mitochondria.
$[\text{O}_2]_n$	m M	0.024	Normal oxygen concentration in mitochondria.

$[O_{2,a}]$	m M	$\phi \left(\frac{SaO2sup}{1.0 - SaO2sup} \right)^{\frac{1}{n_h}}$	Arterial dissolved oxygen concentration
$[O_{2,c}]_{init}$	m M	$[O_{2,c}]_n$	Initial concentration of dissolved oxygen in the capillary.
$[O_{2,c}]_n$	m M	$[O_{2,c}]_{init} \text{ pow} \left(\frac{ScO_{2,n}}{1 - ScO_{2,n}}, \frac{1}{n_h} \right)$	Normal concentration of dissolved oxygen in the capillary.
p_1	dimensionless	$p_{tot} - p_{23}$	The number of protons pumped by ared (reduction reaction)
p_2	dimensionless	4	Total protons pumped by reaction 2
p_{23}	dimensionless	8	Total protons pumped by reactions 2 and 3
p_3	dimensionless	$p_{23} - p_2$	Total protons pumped by reaction 3
$P_{1,n}$	mmHg	$\frac{P_{a2,n} + P_{v,n}}{2}$	Normal average blood pressure in vessels
P_a	mmHg	50	Arterial blood pressure
$P_{a2,n}$	mmHg	$\frac{G_{0,n} P_a + G_n P_{v,n}}{G_n + G_{0,n}}$	Normal arterial blood pressure at the start of the cerebral arteries
P_a	mmHg	50	Normal value of ABP Normal value of ABP
p_{C1}	dimensionless	8	Total protons pumped by complex 1
p_{C3}	dimensionless	4	Total protons pumped by complex 3
P_{ic}	mmHg	4.5	Intracranial blood pressure
$P_{ic,n}$	mmHg	4.5	Normal intracranial blood pressure

p_{tot}	dimensionless	18.40	Total protons pumped by reactions 1, 2 and 3
$p_{tot,NADH}$	dimensionless	$p_{C1} + p_{C3} + p_{23}$	Total protons pumped when the reducing agent is NADH
$P_{v,n}$	mmHg	$\frac{G_{t,n}}{G_v} (P_a - P_{vs}) + P_{vs}$	Normal venous blood pressure
P_{vs}	mmHg	1.5	Pressure in the venous sinuses
P_aCO_2	mmHg	40	Arterial partial pressure of CO ₂
$P_aCO_{2,n}$	mmHg	40	Normal arterial partial pressure of CO ₂
PaO_2	mmHg	$\frac{[O_{2,a}]}{k_{H,O_2}}$	Partial pressure of oxygen in the arteries
$[PCr]_n/[Pi]_n$	dimensionless	2.73	Normal Pcr/Pi concentration in the cytoplasm. Set this way because this is often measured by MRS (although mitochondria/cytoplasm differences are ignored).
$pH_{m,n}$	dimensionless	8	Normal mitochondrial pH
$pH_{o,n}$	dimensionless	7	Normal extra-mitochondrial pH
$[O_{2,c}]_{init}$	m M	0.036	Value of O ₂ at half maximal saturation
P_tCO_{2n}	dimensionless	54	Partial pressure of CO ₂ in tissue
r_0	cm	$1 - r_{frac}r_{occ}$	Radius of the supplying artery compartment
r_0	cm	0.0126	A special radius in the elastic tension relationship

R_C	dimensionless	2.2	Parameter controlling sensitivity of η to $P_a\text{CO}_2$
R_O	dimensionless	1.5	Parameter controlling sensitivity of η to $[\text{O}_{2,c}]$
R_P	dimensionless	4	Parameter controlling sensitivity of η to P_a
R_u	dimensionless	0	Parameter controlling sensitivity of η to u
r_{CV}	dimensionless	5	A parameter controlling the ratio of maximal to minimal rates of oxidative phosphorylation
r_{init}	cm	$[\text{Hbtot}_c]$	Initial radius of blood vessels
r_m	cm	0.027	Value of vessel radius giving maximum muscular tension
$[\text{Hbtot}_c]$	cm	0.0187	Normal radius of blood vessels normal radius of blood vessels
r_t	cm	0.018	Parameter in the muscular tension relationship
r_{frac}	dimensionless	$1 - (1 - \text{occ}_{frac})^{\frac{1}{2}}$	Fraction by which the radius of the supplying artery compartment has been reduced
r_{occ}	dimensionless	0	Fraction by which the radius of the carotid arteries has been reduced
$\text{SaO}_{2,n}$	dimensionless	0.96	Normal saturation of the arterial haemoglobin

SaO ₂	dimensionless	0.96	Saturation of the arterial haemoglobin
ScO _{2,n}	dimensionless	$\frac{SaO_{2,n} + SvO_{2,n}}{2}$	Normal capillary oxygen saturation
σ_{coll}	mmHg	62.79	Value of pressure at which vessels collapse
σ_{e0}	mmHg	0.1425	Parameter in relationship determining σ_e
$\sigma_{e,n}$	mmHg	$\sigma_{e0} \left(\exp \left(\frac{K_\sigma ([Hbtot_c] - r_0)}{r_0} \right) - 1 \right) - \sigma_{coll}$	Normal elastic stress in vessel walls
SvO _{2,n}	dimensionless	$\frac{[HbO_{2,v}]_n}{[Hbtot]_n}$	Normal venous oxygen saturation
$\nu_{u,n}$	s	5	The time constant associated with ν_{CO_2}
$T_{e,n}$	mmHg cm	$\sigma_{e,n} h_n$	Normal elastic tension in vessel walls
T_{max0}	mmHg cm	$\frac{T_{max,n}}{1 + T_{e,n} \mu_n}$	Tmax at normal mu
$T_{max,n}$	mmHg cm	$\frac{T_{m,n}}{\exp \left(-\text{pow} \left(\text{fabs} \left(\frac{[Hbtot_c] - r_m}{r_t - r_m} \right), n_m \right) \right)}$	Normal maximum muscular tension developed by circulation
$T_{m,n}$	mmHg cm	$(P_{1,n} - P_{ic,n}) [Hbtot_c] - T_{e,n}$	Normal muscular tension in vessel walls
$\nu_{u,n}$	s	20	The time constant associated with ν_{O_2}
$\nu_{u,n}$	s	5	The time constant associated with ν_{P_a}
$\nu_{u,n}$	s	0.5	The time constant associated with ν_u
u	dimensionless	1	The representation of "demand" in the model.
u_n	dimensionless	1	Resting "demand"

$V_{\max,ATP}$	$m M s^{-1}$	$\left(\frac{L_{CVn} Vol_{mit}}{na} + 2.0CMR_{glucn} \right) (1.0 + km) u$	Vmax of ATP use
$v_{CO_2,n}$	mmHg	$P_aCO_{2,n}$	Normal value of v_{CO_2} (CO2 passed through a first order filter)
$V_{glucosein}$	dimensionless	$\frac{[gluc_c]}{k_{glut} + [gluc_c]}$	Rate term for glucose transported into the cell. This is a michaelis menten term, but fixed because blood glucose concentration is fixed.
v_{glut}	m M	$\frac{CMR_{gluc,n}}{V_{glucosein} - \frac{[gluc]_n}{[gluc]_n + k_{glut}}}$	Vmax for glucose transport both in and out of the cell from the capillary.
V_{lacin}	dimensionless	$\frac{[lac_c]}{k_{MCT} + [lac_c]}$	Rate of lactate transport into the cell
v_{MCT}	$m M s^{-1}$	$\frac{2CMR_{gluc,n} - \frac{CBF_n}{3}}{\frac{[lac]_n [H^+]_n}{([lac]_n + k_{MCT})([H^+]_n + k_{MCT})} - V_{lacin}}$	
$v_{O_2,n}$	m M	$\frac{[O_{2,c}]_n}{[O_{2,c}]_n}$	Normal value of v_{O_2} (capillary O2 passed through a first order filter)
$v_{P_a,n}$	mmHg	$P_{a2,n}$	Normal value of v_{P_a} (Arterial blood pressure passed through a first order filter)
v_{TCA}	$m M s^{-1}$	$\frac{k_{TCA_n}}{[Py]_n [NAD]_n} (k_{m,tcaN} + [NAD]_n) (k_{m,tcaP} + [Py]_n)$	Vmax for the TCA cycle
v_u,n	dimensionless	$L_{CV,frac}$	normal value of v_u (u passed through a first order filter)
V_{Arat_n}	dimensionless	3	The normal ratio of the volume of the veins to the volume of the arteries

$v_{glyc,n}$	$m M s^{-1}$	$\frac{CMR_{gluc,n}}{glyc_{g,n} glyc_{p,n} glyc_{a,n} glyc_{nn}}$	Normal Vmax for glycolysis which is assumed to be modified by the ratio of AMP to ATP
$V_{max_{NaBiC}}$	$mM \cdot ml \cdot s^{-1}$	0.001	Vmax for the sodium bicarbonate co-transporter
$V_{max_{NHE}}$	$mM \cdot ml \cdot s^{-1}$	0.02	Vmax for the sodium hydrogen exchanger
$V_{a,n}$	dimensionless	$\frac{t,n}{1 + VArat_n}$	Normal arterial blood volume as a fraction of total blood volume
Vol_{mit}	dimensionless	0.067	Fraction of brain water which is mitochondria
$V_{t,n}$	dimensionless	1	Normal total blood volume
$V_{v,n}$	dimensionless	$t,n \frac{VArat_n}{1 + VArat_n}$	Normal venous volume
$[HHb_a]$	m M	$[Hbtot] (1 - SaO_2)$	Unsaturated arterial haemoglobin
$[HHb_a]_n$	m M	$[Hbtot]_n (1 - SaO_{2,n})$	Normal unsaturated arterial haemoglobin
$[HbO_{2,a}]$	m M	$[Hbtot] SaO_2$	Concentration of arterial oxy-haemoglobin.
$[HbO_{2,a}]_n$	m M	$[Hbtot]_n SaO_{2,n}$	Normal concentration of arterial oxy-haemoglobin.
$[HbO_{2,v}]_{init}$	m M	$[HbO_{2,v}]_n$	Initial concentration of venous oxy-haemoglobin.
$[HbO_{2,v}]_n$	m M	$\frac{CBF_n [HbO_{2,a}]_n - R_u}{CBF_n}$	Normal concentration of venous oxy-haemoglobin.

$[\text{HbO}_{2,a}]_n$	m M	$[\text{Hbtot}]_n$	Total haemoglobin concentration in the arteries and veins.
$[\text{Hbtot}]_n$	m M	5.4	Normal total haemoglobin concentration in the arteries and veins.
$[\text{HHb}_v]_n$	m M	$[\text{Hbtot}]_n - [\text{HbO}_{2,v}]_n$	Normal unsaturated venous haemoglobin
Z	m V	59.028	$2.303 \cdot RT/F$

Bibliography

The World Health Report 2005 make every mother and child count. Technical report, World Health Organisation, Geneva, Switzerland, 2005. URL http://www.kfshrc.edu.sa/annals/articles/25_6/25-6_516-517.pdf.

OpenCell, 2009. URL <https://www.cellml.org/tools/opencell>.

MATLAB R2013a, 2013.

Agulhon, C., Petravicz, J., McMullen, A. B., Sweger, E. J., Minton, S. K., Taves, S. R., Casper, K. B., Fiacco, T. a., and McCarthy, K. D. What is the role of astrocyte calcium in neurophysiology? *Neuron*, 59(6):932–46, September 2008. ISSN 1097-4199. doi: 10.1016/j.neuron.2008.09.004. URL <http://www.ncbi.nlm.nih.gov/pubmed/18817732>.

Akiba, T., Alpern, R. J., Eveloff, J., Calamina, J., and Warnock, D. G. Electrogenic sodium/bicarbonate cotransport in rabbit renal cortical basolateral membrane vesicles. *The Journal of clinical investigation*, 78(6):1472–8, December 1986. ISSN 0021-9738. doi: 10.1172/JCI112738. URL <http://www.ncbi.nlm.nih.gov/pubmed/423898><http://www.pubmedcentral.nih.gov/articlerender.fcgi?artid=423898&tool=pmcentrez&rendertype=abstract>.

Akiba, T., Rocco, V. K., and Warnock, D. G. Parallel adaptation of the rabbit renal cortical sodium/proton antiporter and sodium/bicarbonate cotransporter in metabolic acidosis and alkalosis. *The Journal of clinical investigation*, 80(2):308–15, August 1987. ISSN 0021-9738. doi: 10.1172/JCI113074. URL <http://www.pubmedcentral.nih.gov/articlerender.fcgi?artid=442239&tool=pmcentrez&rendertype=abstract>.

- Alastruey, J., Moore, S. M., Parker, K. H., David, T., Peiró, J., and Sherwin, S. J. Reduced modelling of blood flow in the cerebral circulation: Coupling 1-D, 0-D and cerebral auto-regulation models. *International Journal for Numerical Methods in Fluids*, 56(8):1061–1067, March 2008. ISSN 02712091. doi: 10.1002/flid.1606. URL <http://doi.wiley.com/10.1002/flid.1606>.
- Almaas, R., Pytte, M., Lindstad, J. K., Wright, M., Saugstad, O. D., Pleasure, D., and Rootwelt, T. Acidosis has opposite effects on neuronal survival during hypoxia and reoxygenation. *Journal of Neurochemistry*, 84(5):1018–1027, February 2003. ISSN 00223042. doi: 10.1046/j.1471-4159.2003.01593.x. URL <http://doi.wiley.com/10.1046/j.1471-4159.2003.01593.x>.
- Altman, D. I., Powers, W. J., Perlman, J. M., Herscovitch, P., Volpe, S. L., and Volpe, J. J. Cerebral blood flow requirement for brain viability in newborn infants is lower than in adults. *Annals of neurology*, 24(2):218–26, August 1988. ISSN 0364-5134. doi: 10.1002/ana.410240208. URL <http://www.ncbi.nlm.nih.gov/pubmed/3263081>.
- Amess, P. N., Penrice, J., Cady, E. B., Lorek, A., Wylezinska, M., Cooper, C. E., D'Souza, P., Tyszczyk, L., Thoresen, M., Edwards, A. D., Wyatt, J. S., and Reynolds, E. O. Mild hypothermia after severe transient hypoxia-ischemia reduces the delayed rise in cerebral lactate in the newborn piglet. *Pediatric research*, 41(6):803–8, June 1997. ISSN 0031-3998. doi: 10.1203/00006450-199706000-00002. URL <http://www.ncbi.nlm.nih.gov/pubmed/9167192>.
- Anderson, A. W., Marois, R., Colson, E. R., Peterson, B. S., Duncan, C. C., Ehrenkranz, R. A., Schneider, K. C., Gore, J. C., and Ment, L. R. Neonatal auditory activation detected by functional magnetic resonance imaging. *Magnetic resonance imaging*, 19(1):1–5, January 2001. ISSN 0730-725X. URL <http://www.ncbi.nlm.nih.gov/pubmed/11295339>.
- Aoyagi, T. Pulse oximetry: its invention, theory, and future. *Journal of anesthesia*, 17(4):259–66, January 2003. ISSN 0913-8668. doi: 10.1007/s00540-003-0192-6. URL <http://www.ncbi.nlm.nih.gov/pubmed/14625714>.
- Aubert, A. and Costalat, R. Compartmentalization of brain energy metabolism between glia and neurons: insights from mathematical mod-

- eling. *Glia*, 1279(April 2006):1272–1279, 2007. doi: 10.1002/glia. URL <http://onlinelibrary.wiley.com/doi/10.1002/glia.20360/full>.
- Aubert, A., Costalat, R., and Valabrègue, R. Modelling of the coupling between brain electrical activity and metabolism. *Acta biotheoretica*, 49(4): 301–26, January 2001. ISSN 0001-5342. URL <http://www.ncbi.nlm.nih.gov/pubmed/11804241>.
- Aubert, A. and Costalat, R. A Model of the Coupling between Brain Electrical Activity, Metabolism, and Hemodynamics: Application to the Interpretation of Functional Neuroimaging. *NeuroImage*, 17(3):1162–1181, November 2002. ISSN 10538119. doi: 10.1006/nimg.2002.1224. URL <http://linkinghub.elsevier.com/retrieve/pii/S1053811902912243>.
- Aubert, A. and Costalat, R. Interaction between astrocytes and neurons studied using a mathematical model of compartmentalized energy metabolism. *Journal of cerebral blood flow and metabolism : official journal of the International Society of Cerebral Blood Flow and Metabolism*, 25(11):1476–90, November 2005. ISSN 0271-678X. doi: 10.1038/sj.jcbfm.9600144. URL <http://www.ncbi.nlm.nih.gov/pubmed/15931164>.
- Austin, T., Shanmugalingam, S., and Clarke, P. To cool or not to cool? Hypothermia treatment outside trial criteria. *Archives of disease in childhood. Fetal and neonatal edition*, 98(5):F451–3, September 2013. ISSN 1468-2052. doi: 10.1136/archdischild-2012-302069. URL <http://www.ncbi.nlm.nih.gov/pubmed/22820487>.
- Azzopardi, D., Wyatt, J. S., Cady, E. B., Delpy, D. T., Baudin, J., Stewart, a. L., Hope, P. L., Hamilton, P. a., and Reynolds, E. O. Prognosis of newborn infants with hypoxic-ischemic brain injury assessed by phosphorus magnetic resonance spectroscopy. *Pediatric research*, 25(5):445–51, May 1989. ISSN 0031-3998. doi: 10.1203/00006450-198905000-00004. URL <http://www.ncbi.nlm.nih.gov/pubmed/2717259>.
- Azzopardi, D. V., Strohm, B., Edwards, a. D., Dyet, L., Halliday, H. L., Juszczak, E., Kapellou, O., Levene, M., Marlow, N., Porter, E., Thoresen, M., Whitelaw, A., and Brocklehurst, P. Moderate hypothermia to treat perinatal asphyxial encephalopathy. *The New England journal of medicine*, 361(14):1349–58, October 2009. ISSN 1533-4406. doi:

10.1056/NEJMoa0900854. URL <http://www.ncbi.nlm.nih.gov/pubmed/19797281>.

Babbs, C. F. Oscillometric measurement of systolic and diastolic blood pressures validated in a physiologic mathematical model. *Biomedical engineering online*, 11(1):56, January 2012. ISSN 1475-925X. doi: 10.1186/1475-925X-11-56. URL <http://www.pubmedcentral.nih.gov/articlerender.fcgi?artid=3541069&tool=pmcentrez&rendertype=abstract>.

Bainbridge, A., Tachtsidis, I., Faulkner, S., Price, D., Zhu, T., Baer, E., Broad, K. D., Thomas, D. L., Cady, E. B., Robertson, N. J., and Golay, X. Brain mitochondrial oxidative metabolism during and after cerebral hypoxia-ischemia studied by simultaneous phosphorus magnetic-resonance and broadband near-infrared spectroscopy. *NeuroImage*, pages 1–11, August 2013. ISSN 1095-9572. doi: 10.1016/j.neuroimage.2013.08.016. URL <http://www.ncbi.nlm.nih.gov/pubmed/23959202>.

Bale, G., Mitra, S., Meek, J., Robertson, N., and Tachtsidis, I. A new broadband near-infrared spectroscopy system for in-vivo measurements of cerebral cytochrome-c-oxidase changes in neonatal brain injury. *Biomedical optics express*, 5(10):3450–66, October 2014. ISSN 2156-7085. doi: 10.1364/BOE.5.003450. URL <http://www.pubmedcentral.nih.gov/articlerender.fcgi?artid=4206316&tool=pmcentrez&rendertype=abstract>.

Banaji, M. The BRAINCIRC model: Modelling the Human Brain Circulation, 2005. URL <http://www.medphys.ucl.ac.uk/braincirc/>.

Banaji, M. A generic model of electron transport in mitochondria. *Journal of theoretical biology*, 243(4):501–16, December 2006. ISSN 0022-5193. doi: 10.1016/j.jtbi.2006.07.006. URL <http://www.ncbi.nlm.nih.gov/pubmed/16938312>.

Banaji, M., Tachtsidis, I., Delpy, D., and Baigent, S. A physiological model of cerebral blood flow control. *Mathematical biosciences*, 194(2):125–73, April 2005. ISSN 0025-5564. doi: 10.1016/j.mbs.2004.10.005. URL <http://www.ncbi.nlm.nih.gov/pubmed/15854674>.

- Banaji, M., Mallet, A., Elwell, C. E., Nicholls, P., and Cooper, C. E. A model of brain circulation and metabolism: NIRS signal changes during physiological challenges. *PLoS computational biology*, 4(11): e1000212, November 2008. ISSN 1553-7358. doi: 10.1371/journal.pcbi.1000212. URL <http://www.pubmedcentral.nih.gov/articlerender.fcgi?artid=2573000&tool=pmcentrez&rendertype=abstract>.
- Barker, R. and Cicchetti, F. *Neuroanatomy and Neuroscience at a Glance*. Wiley, 4th edition, 2012. ISBN 978-0-470-65768-3.
- Barkovich, A. J. MR imaging of the neonatal brain. *Neuroimaging clinics of North America*, 16(1):117–35, viii–ix, February 2006. ISSN 1052-5149. doi: 10.1016/j.nic.2005.10.003. URL <http://www.ncbi.nlm.nih.gov/pubmed/16543088>.
- Bartocci, M., Winberg, J., Ruggiero, C., Bergqvist, L. L., Serra, G., and Lagercrantz, H. Activation of olfactory cortex in newborn infants after odor stimulation: a functional near-infrared spectroscopy study. *Pediatric research*, 48(1):18–23, July 2000. ISSN 0031-3998. doi: 10.1203/00006450-200007000-00006. URL <http://www.ncbi.nlm.nih.gov/pubmed/10879795>.
- Bazin, J.-E., Constantin, J.-M., and Gindre, G. [Laboratory animal anaesthesia: influence of anaesthetic protocols on experimental models]. *Annales françaises d'anesthésie et de réanimation*, 23(8):811–8, August 2004. ISSN 0750-7658. doi: 10.1016/j.annfar.2004.05.013. URL <http://www.ncbi.nlm.nih.gov/pubmed/15345253>.
- Beard, D. A biophysical model of the mitochondrial respiratory system and oxidative phosphorylation. *PLoS computational biology*, 1(4), 2005. doi: 10.1371/journal.pcbi.0010036. URL <http://dx.plos.org/10.1371/journal.pcbi.0010036>.
- Beard, D. a. Modeling of oxygen transport and cellular energetics explains observations on in vivo cardiac energy metabolism. *PLoS computational biology*, 2(9):e107, September 2006. ISSN 1553-7358. doi: 10.1371/journal.pcbi.0020107. URL <http://www.pubmedcentral.nih.gov/articlerender.fcgi?artid=1570176&tool=pmcentrez&rendertype=abstract>.

- Bertholdo, D., Watcharakorn, A., and Castillo, M. Brain Proton Magnetic Resonance Spectroscopy. *Am Soc Neuroradiology*, 1980. URL <http://www.ajnr.org/site/fellows/files/MRS-chapter-Castillo.pdf>.
- Beutler, E. and Waalen, J. The definition of anemia: what is the lower limit of normal of the blood hemoglobin concentration? *Blood*, 107(5):1747–50, March 2006. ISSN 0006-4971. doi: 10.1182/blood-2005-07-3046. URL <http://www.pubmedcentral.nih.gov/articlerender.fcgi?artid=1895695&tool=pmcentrez&rendertype=abstract>.
- Biallas, M., Trajkovic, I., Hagmann, C., Scholkmann, F., Jenny, C., Holper, L., Beck, A., and Wolf, M. Multimodal recording of brain activity in term newborns during photic stimulation by near-infrared spectroscopy and electroencephalography. *Journal of biomedical optics*, 17(8):086011–1, August 2012. ISSN 1560-2281. doi: 10.1117/1.JBO.17.8.086011. URL <http://www.ncbi.nlm.nih.gov/pubmed/23224198>.
- Black, J. Drugs from emasculated hormones: the principle of syntopic antagonism. *Bioscience reports*, 24(4-5):302–22, 2005. ISSN 0144-8463. doi: 10.1007/s10540-005-2736-5. URL <http://www.ncbi.nlm.nih.gov/pubmed/16134017>.
- Brown, D. W., Hadway, J., and Lee, T.-Y. Near-infrared spectroscopy measurement of oxygen extraction fraction and cerebral metabolic rate of oxygen in newborn piglets. *Pediatric research*, 54(6):861–7, December 2003. ISSN 0031-3998. doi: 10.1203/01.PDR.0000090928.93045.BE. URL <http://www.ncbi.nlm.nih.gov/pubmed/12930911>.
- Cady, E., Dawson, M. J., and Hope, P. Non-invasive investigation of cerebral metabolism in newborn infants by phosphorus nuclear magnetic resonance spectroscopy. *The Lancet*, (May):1–4, 1983. URL <http://www.sciencedirect.com/science/article/pii/S0140673683919062>.
- Cady, E. B., Iwata, O., Bainbridge, A., Wyatt, J. S., and Robertson, N. J. Phosphorus magnetic resonance spectroscopy 2 h after perinatal cerebral hypoxia-ischemia prognosticates outcome in the newborn piglet. *Journal of neurochemistry*, 107(4):1027–35, November 2008. ISSN 1471-4159. doi: 10.1111/j.1471-4159.2008.05662.x. URL <http://www.ncbi.nlm.nih.gov/pubmed/18786177>.

- Caldwell, M., Hapuarachchi, T., Highton, D., Elwell, C., Smith, M., and Tachtsidis, I. BrainSignals Revisited: Simplifying a Computational Model of Cerebral Physiology. *PloS one*, 10(5): e0126695, January 2015. ISSN 1932-6203. doi: 10.1371/journal.pone.0126695. URL <http://www.pubmedcentral.nih.gov/articlerender.fcgi?artid=4427507&tool=pmcentrez&rendertype=abstract>.
- Casey, J. R., Grinstein, S., and Orlowski, J. Sensors and regulators of intracellular pH. *Nature reviews. Molecular cell biology*, 11(1):50–61, January 2010. ISSN 1471-0080. doi: 10.1038/nrm2820. URL <http://www.ncbi.nlm.nih.gov/pubmed/19997129>.
- Cavaglia, M., Dombrowski, S. M., Drazba, J., Vasani, a., Bokesch, P. M., and Janigro, D. Regional variation in brain capillary density and vascular response to ischemia. *Brain research*, 910(1-2):81–93, August 2001. ISSN 0006-8993. URL <http://www.ncbi.nlm.nih.gov/pubmed/11489257>.
- Chudler, E. Brain Facts and Figures. URL <http://faculty.washington.edu/chudler/facts.html>.
- Cloutier, M., Bolger, F. B., Lowry, J. P., and Wellstead, P. An integrative dynamic model of brain energy metabolism using in vivo neurochemical measurements. *Journal of computational neuroscience*, 27(3):391–414, December 2009. ISSN 1573-6873. doi: 10.1007/s10827-009-0152-8. URL <http://www.ncbi.nlm.nih.gov/pubmed/19396534>.
- Cooper, C. E. and Springett, R. Measurement of cytochrome oxidase and mitochondrial energetics by near-infrared spectroscopy. *Philosophical transactions of the Royal Society of London. Series B, Biological sciences*, 352(1354):669–76, June 1997. ISSN 0962-8436. doi: 10.1098/rstb.1997.0048. URL <http://www.pubmedcentral.nih.gov/articlerender.fcgi?artid=1691958&tool=pmcentrez&rendertype=abstract>.
- Cooper, C. E., Cope, M., Quaresima, V., Ferrari, M., Nemoto, E., Springett, R., Matcher, S., Amess, P., Penrice, J., Tyszczyk, L., Wyatt, J., and Delpy, D. T. Measurement of cytochrome oxidase redox state by near infrared spectroscopy. *Advances in experimental medicine and biology*, 413:63–73, January 1997. ISSN 0065-2598. URL http://www.medphys.ucl.ac.uk/research/borg/pdf/cooper_aemb_1997.pdf<http://www.ncbi.nlm.nih.gov/pubmed/9238486>.

- Cooper, C. E. Nitric oxide and cytochrome oxidase: substrate, inhibitor or effector? *Trends in biochemical sciences*, 27(1):33–9, January 2002. ISSN 0968-0004. URL <http://www.ncbi.nlm.nih.gov/pubmed/11796222>.
- Cooper, R. J., Hebden, J. C., O'Reilly, H., Mitra, S., Michell, a. W., Everdell, N. L., Gibson, a. P., and Austin, T. Transient haemodynamic events in neurologically compromised infants: a simultaneous EEG and diffuse optical imaging study. *NeuroImage*, 55(4):1610–6, April 2011. ISSN 1095-9572. doi: 10.1016/j.neuroimage.2011.01.022. URL <http://www.ncbi.nlm.nih.gov/pubmed/21255658>.
- Corbett, R. J., Laptook, a. R., and Nunnally, R. L. The use of the chemical shift of the phosphomonoester P-31 magnetic resonance peak for the determination of intracellular pH in the brains of neonates., November 1987. ISSN 0028-3878. URL <http://www.ncbi.nlm.nih.gov/pubmed/3670615>.
- Courchesne, E., Pierce, K., Schumann, C. M., Redcay, E., Buckwalter, J. a., Kennedy, D. P., and Morgan, J. Mapping early brain development in autism. *Neuron*, 56(2):399–413, October 2007. ISSN 0896-6273. doi: 10.1016/j.neuron.2007.10.016. URL <http://www.ncbi.nlm.nih.gov/pubmed/17964254>.
- Crambert, G., Hasler, U., Beggah, a. T., Yu, C., Modyanov, N. N., Horisberger, J. D., Lelièvre, L., and Geering, K. Transport and pharmacological properties of nine different human Na, K-ATPase isozymes. *The Journal of biological chemistry*, 275(3):1976–86, January 2000. ISSN 0021-9258. URL <http://www.ncbi.nlm.nih.gov/pubmed/10636900>.
- Cuellar, A. A., Lloyd, C. M., Nielsen, P. F., Bullivant, D. P., Nickerson, D. P., and Hunter, P. J. An Overview of CellML 1.1, a Biological Model Description Language. *SIMULATION*, 79(12):740–747, December 2003. ISSN 0037-5497. doi: 10.1177/0037549703040939. URL <http://sim.sagepub.com/cgi/doi/10.1177/0037549703040939>.
- Currie, S., Hadjivassiliou, M., Craven, I. J., Wilkinson, I. D., Griffiths, P. D., and Hoggard, N. Magnetic resonance spectroscopy of the brain. *Postgraduate medical journal*, 89(1048):94–106, February 2013. ISSN 1469-0756. doi: 10.1136/postgradmedj-2011-130471. URL <http://www.ncbi.nlm.nih.gov/pubmed/23014671>.

- Czosnyka, M., Harris, N. G., Pickard, J. D., and Piechnik, S. CO₂ cerebrovascular reactivity as a function of perfusion pressure a modelling study. *Acta Neurochirurgica*, 121(3-4):159–165, September 1993. ISSN 0001-6268. doi: 10.1007/BF01809269. URL <http://link.springer.com/article/10.1007/BF01809269><http://link.springer.com/10.1007/BF01809269>.
- de Lima Santos, H. and Ciancaglini, P. Kinetic characterization of Na,K-ATPase from rabbit outer renal medulla: properties of the ($\alpha\beta$)₂ dimer. *Comparative Biochemistry and Physiology Part B: Biochemistry and Molecular Biology*, 135(3):539–549, July 2003. ISSN 10964959. doi: 10.1016/S1096-4959(03)00139-8. URL <http://linkinghub.elsevier.com/retrieve/pii/S1096495903001398>.
- DeCharms, R. C. Applications of real-time fMRI. *Nature reviews. Neuroscience*, 9(9):720–9, September 2008. ISSN 1471-003X. doi: 10.1038/nrn2414. URL <http://www.ncbi.nlm.nih.gov/pubmed/18714327>.
- Easa, D. Noninvasive Intracranial Pressure Measurement in the Newborn. *American Journal of Diseases of Children*, 137(4):332, April 1983. ISSN 0002-922X. doi: 10.1001/archpedi.1983.02140300014004. URL <http://archpedi.jamanetwork.com/article.aspx?doi=10.1001/archpedi.1983.02140300014004>.
- Edvinsson, L., Mackenzie, E. T., and McCulloch, J. *Cerebral blood flow and metabolism*. Raven Press, 1992. ISBN 0-88167-918-6.
- Edwards, A. D., Wyatt, J. S., Richardson, C., Delpy, D. T., Cope, M., and Reynolds, E. O. Cotside measurement of cerebral blood flow in ill newborn infants by near infrared spectroscopy. *Lancet*, 2(8614):770–1, October 1988. ISSN 0140-6736. URL <http://www.sciencedirect.com/science/article/pii/S014067368892418X><http://www.ncbi.nlm.nih.gov/pubmed/2901613>.
- Edwards, A. D., Wyatt, J. S., and Thoresen, M. Treatment of hypoxic-ischaemic brain damage by moderate hypothermia. *Archives of disease in childhood. Fetal and neonatal edition*, 78(2):F85–8, March 1998. ISSN 1359-2998. URL <http://www.pubmedcentral.nih.gov/articlerender.fcgi?artid=1720772&tool=pmcentrez&rendertype=abstract>.

- Edwards, A., Yue, X., Squier, M., Thoresen, M., Cady, E., Penrice, J., Cooper, C., Wyatt, J., Reynolds, E., and Mehmet, H. Specific Inhibition of Apoptosis after Cerebral Hypoxia-Ischemia by Moderate Post-Insult Hypothermia. *Biochemical and Biophysical Research Communications*, 217(3):1193–1199, December 1995. ISSN 0006291X. doi: 10.1006/bbrc.1995.2895. URL <http://linkinghub.elsevier.com/retrieve/pii/S0006291X85728951>.
- Ellsworth, M. a., Lang, T. R., Pickering, B. W., and Herasevich, V. Clinical data needs in the neonatal intensive care unit electronic medical record. *BMC medical informatics and decision making*, 14(1):92, January 2014. ISSN 1472-6947. doi: 10.1186/1472-6947-14-92. URL <http://www.ncbi.nlm.nih.gov/pubmed/25341847>.
- Elwell, C. E., Cope, M., Edwards, A. D., Wyatt, J. S., Delpy, D. T., and Reynolds, E. O. Quantification of adult cerebral hemodynamics by near-infrared spectroscopy. *Journal of applied physiology (Bethesda, Md. : 1985)*, 77(6):2753–60, December 1994. ISSN 8750-7587. URL <http://www.ncbi.nlm.nih.gov/pubmed/7896617>.
- Elwell, C. E., Owen-Reece, H., Wyatt, J. S., Cope, M., Reynolds, E. O., and Delpy, D. T. Influence of respiration and changes in expiratory pressure on cerebral haemoglobin concentration measured by near infrared spectroscopy. *Journal of cerebral blood flow and metabolism : official journal of the International Society of Cerebral Blood Flow and Metabolism*, 16(2):353–7, March 1996. ISSN 0271-678X. doi: 10.1097/00004647-199603000-00022. URL <http://www.ncbi.nlm.nih.gov/pubmed/8594069>.
- Elwell, C. E., Henty, J. R., Leung, T. S., Austin, T., Meek, J. H., Delpy, D. T., and Wyatt, J. S. Measurement of CMRO₂ in neonates undergoing intensive care using near infrared spectroscopy. *Advances in experimental medicine and biology*, 566:263–8, January 2005. ISSN 0065-2598. doi: 10.1007/0-387-26206-7_35. URL http://link.springer.com/chapter/10.1007/0-387-26206-7_35<http://www.ncbi.nlm.nih.gov/pubmed/16594161>.
- Fuster, D., Moe, O. W., and Hilgemann, D. W. Steady-state function of the ubiquitous mammalian Na/H exchanger (NHE1) in relation to dimer coupling models with 2Na/2H stoichiometry. *The Journal of general physiology*, 132(4):465–80, October 2008. ISSN 1540-7748. doi: 10.1085/jgp.

200810016. URL <http://www.pubmedcentral.nih.gov/articlerender.fcgi?artid=2553392&tool=pmcentrez&rendertype=abstract>.

Gavaghan, D., Coveney, P. V., and Kohl, P. The virtual physiological human: tools and applications I. *Philosophical transactions. Series A, Mathematical, physical, and engineering sciences*, 367(1895):1817–21, May 2009. ISSN 1364-503X. doi: 10.1098/rsta.2009.0070. URL <http://www.ncbi.nlm.nih.gov/pubmed/19380313>.

Gjedde, A. Cerebral Blood Flow Change in Arterial Hypoxemia Is Consistent with Negligible Oxygen Tension in Brain Mitochondria. *NeuroImage*, 17(4):1876–1881, December 2002. ISSN 10538119. doi: 10.1006/nimg.2002.1272. URL <http://linkinghub.elsevier.com/retrieve/pii/S1053811902912723>.

Grant, P. E., Roche-Labarbe, N., Surova, A., Themelis, G., Selb, J., Warren, E. K., Krishnamoorthy, K. S., Boas, D. A., and Franceschini, M. A. Increased cerebral blood volume and oxygen consumption in neonatal brain injury. *Journal of cerebral blood flow and metabolism : official journal of the International Society of Cerebral Blood Flow and Metabolism*, 29(10):1704–13, October 2009. ISSN 1559-7016. doi: 10.1038/jcbfm.2009.90. URL <http://www.pubmedcentral.nih.gov/articlerender.fcgi?artid=2762197&tool=pmcentrez&rendertype=abstract>.

Greisen, G. Cerebral blood flow in preterm infants during the first week of life. *Acta paediatrica Scandinavica*, 75(1):43–51, January 1986. ISSN 0001-656X. URL <http://www.ncbi.nlm.nih.gov/pubmed/2420149>.

Greisen, G. Autoregulation of cerebral blood flow in newborn babies. *Early human development*, 2005. doi: 10.1016/j.earlhumdev.2005.03.005. URL <http://www.sciencedirect.com/science/article/pii/S0378378205000630>.

Gujar, S. Magnetic resonance spectroscopy. *Journal of neuro-ophthamology*, 25(3):217–226, 2005. URL http://journals.lww.com/jneuro-ophthamology/Abstract/2005/09000/Magnetic_Resonance_Spectroscopy.15.aspx.

Gunawardena, J. Models in biology: ‘accurate descriptions of our pathetic thinking’. *BMC biology*, 12:29, January 2014. ISSN 1741-7007. doi:

10.1186/1741-7007-12-29. URL <http://www.pubmedcentral.nih.gov/articlerender.fcgi?artid=4005397&tool=pmcentrez&rendertype=abstract>.

Gutenkunst, R. N., Waterfall, J. J., Casey, F. P., Brown, K. S., Myers, C. R., and Sethna, J. P. Universally sloppy parameter sensitivities in systems biology models. *PLoS computational biology*, 3(10): 1871–78, October 2007. ISSN 1553-7358. doi: 10.1371/journal.pcbi.0030189. URL <http://www.pubmedcentral.nih.gov/articlerender.fcgi?artid=2000971&tool=pmcentrez&rendertype=abstract>.

Haefner, J. W. *Modeling Biological Systems Principles and Applications*. Springer Science+Business Media, Inc., 2005. ISBN 9780387250120.

Hairer, E. and Wanner, G. *Solving Ordinary Differential Equations II*, volume 14 of *Springer Series in Computational Mathematics*. Springer Berlin Heidelberg, Berlin, Heidelberg, 1996. ISBN 978-3-642-05220-0. doi: 10.1007/978-3-642-05221-7. URL <http://link.springer.com/10.1007/978-3-642-05221-7>.

Hartwig, V., Giovannetti, G., Vanello, N., Lombardi, M., Landini, L., and Simi, S. Biological effects and safety in magnetic resonance imaging: a review. *International journal of environmental research and public health*, 6(6): 1778–98, June 2009. ISSN 1660-4601. doi: 10.3390/ijerph6061778. URL <http://www.pubmedcentral.nih.gov/articlerender.fcgi?artid=2705217&tool=pmcentrez&rendertype=abstract>.

Heep, A., Scheef, L., Jankowski, J., Born, M., Zimmermann, N., Sival, D., Bos, A., Gieseke, J., Bartmann, P., Schild, H., and Boecker, H. Functional magnetic resonance imaging of the sensorimotor system in preterm infants. *Pediatrics*, 123(1):294–300, January 2009. ISSN 1098-4275. doi: 10.1542/peds.2007-3475. URL <http://www.ncbi.nlm.nih.gov/pubmed/19117895>.

Helbig, H., Korbmacher, C., Berweck, S., Kühner, D., and Wiederholt, M. Kinetic properties of Na⁺/H⁺ exchange in cultured bovine pigmented ciliary epithelial cells. *Pflügers Archiv : European journal of physiology*, 412 (1-2):80–5, July 1988. ISSN 0031-6768. doi: 10.1007/BF00583734. URL <http://www.ncbi.nlm.nih.gov/pubmed/3174387>.

- Helmy, M. M., Tolner, E. a., Vanhatalo, S., Voipio, J., and Kaila, K. Brain alkalosis causes birth asphyxia seizures, suggesting therapeutic strategy. *Annals of neurology*, 69(3):493–500, March 2011. ISSN 1531-8249. doi: 10.1002/ana.22223. URL <http://www.ncbi.nlm.nih.gov/pubmed/21337602>.
- Helmy, M. M., Ruusuvuori, E., Watkins, P. V., Voipio, J., Kanold, P. O., and Kaila, K. Acid extrusion via blood-brain barrier causes brain alkalosis and seizures after neonatal asphyxia. *Brain : a journal of neurology*, 135 (Pt 11):3311–9, November 2012. ISSN 1460-2156. doi: 10.1093/brain/aww257. URL <http://www.pubmedcentral.nih.gov/articlerender.fcgi?artid=3501974&tool=pmcentrez&rendertype=abstract>.
- Hucka, M., Finney, A., Sauro, H. M., Bolouri, H., Doyle, J. C., Kitano, H., Arkin, A. P., Bornstein, B. J., Bray, D., Cornish-Bowden, A., Cuel-lar, A. A., Dronov, S., Gilles, E. D., Ginkel, M., Gor, V., Goryanin, I. I., Hedley, W. J., Hodgman, T. C., Hofmeyr, J.-H., Hunter, P. J., Juty, N. S., Kasberger, J. L., Kremling, A., Kummer, U., Le Novère, N., Loew, L. M., Lucio, D., Mendes, P., Minch, E., Mjolsness, E. D., Nakayama, Y., Nelson, M. R., Nielsen, P. F., Sakurada, T., Schaff, J. C., Shapiro, B. E., Shimizu, T. S., Spence, H. D., Stelling, J., Takahashi, K., Tomita, M., Wagner, J., and Wang, J. The systems biology markup language (SBML): a medium for representation and exchange of biochemical network models. *Bioinformatics (Oxford, England)*, 19(4):524–31, March 2003. ISSN 1367-4803. URL <http://www.ncbi.nlm.nih.gov/pubmed/12611808>.
- Hunter, P. J. and Borg, T. K. Integration from proteins to organs: the Physiome Project. *Nature reviews. Molecular cell biology*, 4(3):237–43, March 2003. ISSN 1471-0072. doi: 10.1038/nrm1054. URL <http://www.ncbi.nlm.nih.gov/pubmed/12612642>.
- Huwaldt, J. A. and Steinhorst, S. Plot Digitizer. URL <http://plotdigitizer.sourceforge.net/>.
- Hyder, F., Kida, I., Behar, K. L., Kennan, R. P., Maciejewski, P. K., and Rothman, D. L. Quantitative functional imaging of the brain: towards mapping neuronal activity by BOLD fMRI. *NMR in biomedicine*, 14(7-8):413–31, 2001. ISSN 0952-3480. doi: 10.1002/nbm.733. URL <http://www.ncbi.nlm.nih.gov/pubmed/11746934>.

- Hyder, F., Shulman, R. G., and Rothman, D. L. A model for the regulation of cerebral oxygen delivery. *Journal of applied physiology (Bethesda, Md. : 1985)*, 85(2):554–64, August 1998. ISSN 8750-7587. URL <http://www.ncbi.nlm.nih.gov/pubmed/9688733>.
- Iliff, J. J., Wang, M., Zeppenfeld, D. M., Venkataraman, A., Plog, B. a., Liao, Y., Deane, R., and Nedergaard, M. Cerebral arterial pulsation drives paravascular CSF-interstitial fluid exchange in the murine brain. *The Journal of neuroscience : the official journal of the Society for Neuroscience*, 33(46):18190–9, November 2013. ISSN 1529-2401. doi: 10.1523/JNEUROSCI.1592-13.2013. URL <http://www.pubmedcentral.nih.gov/articlerender.fcgi?artid=3866416&tool=pmcentrez&rendertype=abstract>.
- Jelfs, B., Banaji, M., Tachtsidis, I., Cooper, C. E., and Elwell, C. E. Modelling noninvasively measured cerebral signals during a hypoxemia challenge: steps towards individualised modelling. *PloS one*, 7(6):e38297, January 2012. ISSN 1932-6203. doi: 10.1371/journal.pone.0038297. URL <http://www.pubmedcentral.nih.gov/articlerender.fcgi?artid=3367969&tool=pmcentrez&rendertype=abstract>.
- Jessen, N. A., Munk, A. S. F., Lundgaard, I., and Nedergaard, M. The Glymphatic System: A Beginner’s Guide. *Neurochemical research*, May 2015. ISSN 1573-6903. doi: 10.1007/s11064-015-1581-6. URL <http://www.ncbi.nlm.nih.gov/pubmed/25947369>.
- Jones, E., Oliphant, T., Peterson, P., and ... SciPy: Open Source Scientific Tools for Python. URL <http://www.scipy.org/>.
- Jopling, J., Henry, E., Wiedmeier, S. E., and Christensen, R. D. Reference ranges for hematocrit and blood hemoglobin concentration during the neonatal period: data from a multihospital health care system. *Pediatrics*, 123(2):e333–7, February 2009. ISSN 1098-4275. doi: 10.1542/peds.2008-2654. URL <http://www.ncbi.nlm.nih.gov/pubmed/19171584>.
- Jung, A., Faltermeier, R., Rothoerl, R., and Brawanski, A. A mathematical model of cerebral circulation and oxygen supply. *Journal of mathematical biology*, 51(5):491–507, November 2005. ISSN 0303-6812. doi: 10.1007/s00285-005-0343-5. URL <http://www.ncbi.nlm.nih.gov/pubmed/16195926>.

- Karen, T., Morren, G., Haensse, D., Bauschatz, A. S., Bucher, H. U., and Wolf, M. Hemodynamic response to visual stimulation in newborn infants using functional near-infrared spectroscopy. *Human brain mapping*, 29(4): 453–60, April 2008. ISSN 1065-9471. doi: 10.1002/hbm.20411. URL <http://www.ncbi.nlm.nih.gov/pubmed/17525986>.
- Kendall, G. S., Hristova, M., Zbarsky, V., Clements, A., Peebles, D. M., Robertson, N. J., and Raivich, G. Distribution of pH changes in mouse neonatal hypoxic-ischaemic insult. *Developmental neuroscience*, 33(6):505–18, January 2011. ISSN 1421-9859. doi: 10.1159/000333850. URL <http://www.ncbi.nlm.nih.gov/pubmed/22343485>.
- Kirilina, E., Jelzow, A., Heine, A., Niessing, M., Wabnitz, H., Brühl, R., Ittermann, B., Jacobs, A. M., and Tachtsidis, I. The physiological origin of task-evoked systemic artefacts in functional near infrared spectroscopy. *NeuroImage*, 61(1):70–81, May 2012. ISSN 1095-9572. doi: 10.1016/j.neuroimage.2012.02.074. URL <http://www.pubmedcentral.nih.gov/articlerender.fcgi?artid=3348501&tool=pmcentrez&rendertype=abstract>.
- Kodali, B. S. Capnography outside the operating rooms. *Anesthesiology*, 118(1):192–201, January 2013. ISSN 1528-1175. doi: 10.1097/ALN.0b013e318278c8b6. URL <http://www.ncbi.nlm.nih.gov/pubmed/23221867>.
- Korzeniewski, B. Regulation of ATP supply during muscle contraction: theoretical studies. *The Biochemical journal*, 330 (Pt 3):1189–95, March 1998. ISSN 0264-6021. URL <http://www.biochemj.org/bj/330/bj3301189.htmhttp://www.pubmedcentral.nih.gov/articlerender.fcgi?artid=1219260&tool=pmcentrez&rendertype=abstract>.
- Korzeniewski, B. and Froncisz, W. An extended dynamic model of oxidative phosphorylation. *Biochimica et biophysica acta*, 1060(2):210–23, October 1991. ISSN 0006-3002. URL <http://www.ncbi.nlm.nih.gov/pubmed/1657162>.
- Korzeniewski, B. and Zoladz, J. a. A model of oxidative phosphorylation in mammalian skeletal muscle. *Biophysical chemistry*, 92(1-2):17–34, August 2001. ISSN 0301-4622. URL <http://www.ncbi.nlm.nih.gov/pubmed/11527576>.

- Kozberg, M. G., Chen, B. R., DeLeo, S. E., Bouchard, M. B., and Hillman, E. M. C. Resolving the transition from negative to positive blood oxygen level-dependent responses in the developing brain. *Proceedings of the National Academy of Sciences of the United States of America*, 110(11): 4380–5, March 2013. ISSN 1091-6490. doi: 10.1073/pnas.1212785110. URL <http://www.pnas.org/content/110/11/4380.short><http://www.pubmedcentral.nih.gov/articlerender.fcgi?artid=3600493&tool=pmcentrez&rendertype=abstract>.
- Lawn, J., Shibuya, K., and Stein, C. No cry at birth: global estimates of intrapartum stillbirths and intrapartum-related neonatal deaths. *Bulletin of the World Health Organization*, 83(6):409–17, June 2005. ISSN 0042-9686. doi: /S0042-96862005000600008. URL <http://www.pubmedcentral.nih.gov/articlerender.fcgi?artid=2626256&tool=pmcentrez&rendertype=abstract>.
- Lawn, J. E., Lee, A. C. C., Kinney, M., Sibley, L., Carlo, W. a., Paul, V. K., Pattinson, R., and Darmstadt, G. L. Two million intrapartum-related stillbirths and neonatal deaths: where, why, and what can be done? *International journal of gynaecology and obstetrics: the official organ of the International Federation of Gynaecology and Obstetrics*, 107 Suppl:S5–18, S19, October 2009. ISSN 1879-3479. doi: 10.1016/j.ijgo.2009.07.016. URL <http://www.ncbi.nlm.nih.gov/pubmed/19815202>.
- Lee, J.-m., Grabb, M. C., Zipfel, G. J., and Choi, D. W. Tissue responses to ischemia Brain tissue responses to ischemia. *The Journal of Clinical Investigation*, 106(6):723–731, 2000.
- Levene, M. I. Cool treatment for birth asphyxia, but what's next? *Archives of disease in childhood. Fetal and neonatal edition*, 95(3):F154–7, May 2010. ISSN 1468-2052. doi: 10.1136/adc.2009.165738. URL <http://www.ncbi.nlm.nih.gov/pubmed/20444808>.
- Lind, N. M., Moustgaard, A., Jelsing, J., Vajta, G., Cumming, P., and Hansen, A. K. The use of pigs in neuroscience: modeling brain disorders. *Neuroscience and biobehavioral reviews*, 31(5):728–51, January 2007. ISSN 0149-7634. doi: 10.1016/j.neubiorev.2007.02.003. URL <http://www.ncbi.nlm.nih.gov/pubmed/17445892>.

- Linninger, A. A., Xenos, M., Sweetman, B., Ponkshe, S., Guo, X., and Penn, R. A mathematical model of blood, cerebrospinal fluid and brain dynamics. *Journal of mathematical biology*, 59(6):729–59, December 2009. ISSN 1432-1416. doi: 10.1007/s00285-009-0250-2. URL <http://www.ncbi.nlm.nih.gov/pubmed/19219605>.
- Lloyd-Fox, S., Blasi, a., and Elwell, C. E. Illuminating the developing brain: the past, present and future of functional near infrared spectroscopy. *Neuroscience and biobehavioral reviews*, 34(3):269–84, March 2010. ISSN 1873-7528. doi: 10.1016/j.neubiorev.2009.07.008. URL <http://www.ncbi.nlm.nih.gov/pubmed/19632270>.
- Lloyd-Fox, S., Blasi, A., Elwell, C. E., Charman, T., Murphy, D., and Johnson, M. H. Reduced neural sensitivity to social stimuli in infants at risk for autism. *Proceedings. Biological sciences / The Royal Society*, 280(1758):20123026, May 2013. ISSN 1471-2954. doi: 10.1098/rspb.2012.3026. URL <http://www.pubmedcentral.nih.gov/articlerender.fcgi?artid=3619456&tool=pmcentrez&rendertype=abstract>.
- Lo, C.-J., Leake, M. C., and Berry, R. M. Fluorescence measurement of intracellular sodium concentration in single *Escherichia coli* cells. *Biophysical journal*, 90(1):357–65, January 2006. ISSN 0006-3495. doi: 10.1529/biophysj.105.071332. URL <http://www.pubmedcentral.nih.gov/articlerender.fcgi?artid=1367033&tool=pmcentrez&rendertype=abstract>.
- Lobo, N., Yang, B., Rizvi, M., and Ma, D. Hypothermia and xenon: novel noble guardians in hypoxic-ischemic encephalopathy? *Journal of neuroscience research*, 91(4):473–8, April 2013. ISSN 1097-4547. doi: 10.1002/jnr.23178. URL <http://www.ncbi.nlm.nih.gov/pubmed/23335252>.
- Lodygensky, G. A., Inder, T. E., and Neil, J. J. Application of magnetic resonance imaging in animal models of perinatal hypoxic-ischemic cerebral injury. *International journal of developmental neuroscience : the official journal of the International Society for Developmental Neuroscience*, 26(1):13–25, February 2008. ISSN 0736-5748. doi: 10.1016/j.ijdevneu.2007.08.018. URL <http://www.sciencedirect.com/science/article/pii/S0736574807001189>[http:](http://)

[//www.pubmedcentral.nih.gov/articlerender.fcgi?artid=2277321&tool=pmcentrez&rendertype=abstract](http://www.pubmedcentral.nih.gov/articlerender.fcgi?artid=2277321&tool=pmcentrez&rendertype=abstract).

Logothetis, N. K. What we can do and what we cannot do with fMRI. *Nature*, 453(7197):869–78, June 2008. ISSN 1476-4687. doi: 10.1038/nature06976. URL <http://www.ncbi.nlm.nih.gov/pubmed/18548064>.

Longo, L. D. and Packianathan, S. Hypoxia-ischaemia and the developing brain: hypotheses regarding the pathophysiology of fetal-neonatal brain damage. *British journal of obstetrics and gynaecology*, 104(6):652–62, June 1997. ISSN 0306-5456. URL <http://www.ncbi.nlm.nih.gov/pubmed/9197867>.

Lorek, a., Takei, Y., Cady, E. B., Wyatt, J. S., Penrice, J., Edwards, a. D., Peebles, D., Wylezinska, M., Owen-Reece, H., and Kirkbride, V. Delayed (“secondary”) cerebral energy failure after acute hypoxia-ischemia in the newborn piglet: continuous 48-hour studies by phosphorus magnetic resonance spectroscopy. *Pediatric research*, 36(6):699–706, December 1994. ISSN 0031-3998. URL <http://www.ncbi.nlm.nih.gov/pubmed/7898977>.

Lossec, G., Lebreton, Y., Hulin, J. C., Fillaut, M., and Herpin, P. Age-related changes in oxygen and nutrient uptake by hindquarters in newborn pigs during cold-induced shivering. *Experimental physiology*, 83(6): 793–807, November 1998. ISSN 0958-0670. URL <http://www.ncbi.nlm.nih.gov/pubmed/9782189>.

Lou, H. C., Lassen, N. A., and Friis-Hansen, B. Impaired autoregulation of cerebral blood flow in the distressed newborn infant. *The Journal of pediatrics*, 94(1):118–21, January 1979. ISSN 0022-3476. URL <http://www.ncbi.nlm.nih.gov/pubmed/758388>.

Malamateniou, C., Adams, M. E., Srinivasan, L., Allsop, J. M., Counsell, S. J., Cowan, F. M., Hajnal, J. V., and Rutherford, M. a. The anatomic variations of the circle of Willis in preterm-at-term and term-born infants: an MR angiography study at 3T. *AJNR. American journal of neuroradiology*, 30(10): 1955–62, November 2009. ISSN 1936-959X. doi: 10.3174/ajnr.A1724. URL <http://www.ncbi.nlm.nih.gov/pubmed/19643922>.

Meek, J. H., Tyszczuk, L., Elwell, C. E., and Wyatt, J. S. Low cerebral blood flow is a risk factor for severe intraventricular haemorrhage. *Archives of*

Disease in Childhood - Fetal and Neonatal Edition, 81(1):F15–F18, July 1999. ISSN 1359-2998. doi: 10.1136/fn.81.1.F15. URL <http://fn.bmj.com/cgi/doi/10.1136/fn.81.1.F15>.

Meek, J. H., Firbank, M., Elwell, C. E., Atkinson, J., Braddick, O., and Wyatt, J. S. Regional hemodynamic responses to visual stimulation in awake infants. *Pediatric research*, 43(6):840–3, June 1998. ISSN 0031-3998. doi: 10.1203/00006450-199806000-00019. URL <http://dx.doi.org/10.1203/00006450-199806000-00019><http://www.ncbi.nlm.nih.gov/pubmed/9621996>.

Mehmet, H., Yue, X., Squier, M., and Lorek, A. Increased apoptosis in the cingulate sulcus of newborn piglets following transient hypoxia-ischaemia is related to the degree of high energy phosphate depletion. *Neuroscience ...*, 181:121–125, 1994. URL <http://www.sciencedirect.com/science/article/pii/0304394094905746>.

Mitra, S., Bale, G., Meek, J., Mathieson, S., Kendall, G., Robertson, N. J., and Tachtsidis, I. In vivo Measurement of Cerebral Mitochondrial Metabolism using Broadband Near Infrared Spectroscopy following Neonatal Stroke. *Advances in experimental medicine and biology (Accepted for publication)*, 2015.

Moroz, T., Banaji, M., Robertson, N. J., Cooper, C. E., and Tachtsidis, I. Computational modelling of the piglet brain to simulate near-infrared spectroscopy and magnetic resonance spectroscopy data collected during oxygen deprivation. *Journal of the Royal Society, Interface / the Royal Society*, January 2012. ISSN 1742-5662. doi: 10.1098/rsif.2011.0766. URL <http://www.ncbi.nlm.nih.gov/pubmed/22279158>.

Moroz, T., Hapuarachchi, T., Bainbridge, A., Price, D., Cady, E., Baer, E., Tachtsidis, I., Broad, K., Ezzati, M., Robertson, N. J., Thomas, D., Golay, X., and Cooper, C. E. Modelling blood flow and metabolism in the piglet brain during hypoxia-ischaemia: simulating brain energetics. *Advances in experimental medicine and biology*, 789:339–44, January 2013. ISSN 0065-2598. doi: 10.1007/978-1-4614-7411-1_45. URL <http://www.ncbi.nlm.nih.gov/pubmed/23852513>.

Morris, M. D. Factorial Sampling Plans for Preliminary Computational Experiments. *Technometrics*, 33(2):161, May 1991. ISSN 00401706. doi: 10.

2307/1269043. URL <http://www.jstor.org/stable/1269043?origin=crossref>.

Narins, S. C., Park, E. H., Ramakrishnan, R., Garcia, F. U., Diven, J. N., Balin, B. J., Hammond, C. J., Sodam, B. R., Smith, P. R., and Abedin, M. Z. Functional characterization of Na(+)/H(+) exchangers in primary cultures of prairie dog gallbladder. *The Journal of membrane biology*, 197(2): 123–34, January 2004. ISSN 0022-2631. doi: 10.1007/s00232-003-0647-6. URL <http://www.ncbi.nlm.nih.gov/pubmed/15014914>.

Nascimento, M. C. V. A., Xavier, C. C., and Goulart, E. M. A. Arterial blood pressure of term newborns during the first week of life. *Brazilian journal of medical and biological research = Revista brasileira de pesquisas médicas e biológicas / Sociedade Brasileira de Biofísica ... [et al.]*, 35(8):905–11, August 2002. ISSN 0100-879X. URL <http://www.ncbi.nlm.nih.gov/pubmed/12185382>.

Northington, F. J. Brief update on animal models of hypoxic-ischemic encephalopathy and neonatal stroke. *ILAR journal / National Research Council, Institute of Laboratory Animal Resources*, 47(1):32–8, January 2006. ISSN 1084-2020. URL <http://www.ncbi.nlm.nih.gov/pubmed/16391429>.

Orlowski, P., Chappell, M., Park, C. S., Grau, V., and Payne, S. Modelling of pH dynamics in brain cells after stroke. *Interface Focus*, 1(3):408–416, March 2011. ISSN 2042-8898. doi: 10.1098/rsfs.2010.0025. URL <http://rsfs.royalsocietypublishing.org/cgi/doi/10.1098/rsfs.2010.0025>.

Orlowski, P., O'Neill, D., Grau, V., Ventikos, Y., and Payne, S. Modelling of the physiological response of the brain to ischaemic stroke. *Interface focus*, 3(2):20120079, April 2013. ISSN 2042-8898. doi: 10.1098/rsfs.2012.0079. URL <http://rsfs.royalsocietypublishing.org/content/3/2/20120079.shorhttp://www.pubmedcentral.nih.gov/articlerender.fcgi?artid=3638479&tool=pmcentrez&rendertype=abstract>.

Paus, T., Collins, D. L., Evans, a. C., Leonard, G., Pike, B., and Zijdenbos, a. Maturation of white matter in the human brain: a review of magnetic resonance studies. *Brain research bulletin*, 54(3):255–66, February 2001. ISSN 0361-9230. URL <http://www.ncbi.nlm.nih.gov/pubmed/11287130>.

- Pejovic, B., Peco-Antic, A., and Marinkovic-Eric, J. Blood pressure in non-critically ill preterm and full-term neonates. *Pediatric nephrology (Berlin, Germany)*, 22(2):249–57, February 2007. ISSN 0931-041X. doi: 10.1007/s00467-006-0311-3. URL <http://www.ncbi.nlm.nih.gov/pubmed/17053885>.
- Penrice, J., Lorek, A., Cady, E. B., Amess, P. N., Wylezinska, M., Cooper, C. E., D'Souza, P., Brown, G. C., Kirkbride, V., Edwards, A. D., Wyatt, J. S., and Reynolds, E. O. Proton magnetic resonance spectroscopy of the brain during acute hypoxia-ischemia and delayed cerebral energy failure in the newborn piglet. *Pediatric research*, 41(6):795–802, June 1997. ISSN 0031-3998. doi: 10.1203/00006450-199706000-00001. URL <http://www.ncbi.nlm.nih.gov/pubmed/9167191>.
- Perlman, J. M. Summary proceedings from the neurology group on hypoxic-ischemic encephalopathy. *Pediatrics*, 117(3 Pt 2):S28–33, March 2006. ISSN 1098-4275. doi: 10.1542/peds.2005-0620E. URL <http://www.ncbi.nlm.nih.gov/pubmed/16777819>.
- Petroff, O. a., Prichard, J. W., Behar, K. L., Alger, J. R., den Hollander, J. a., and Shulman, R. G. Cerebral intracellular pH by 31P nuclear magnetic resonance spectroscopy., June 1985. ISSN 0028-3878. URL <http://www.ncbi.nlm.nih.gov/pubmed/7816318>.
- Pettegrew, J. and Withers, G. Considerations for brain pH assessment by 31 P NMR. *Magnetic resonance ...*, 6:135–142, 1988. URL <http://www.sciencedirect.com/science/article/pii/0730725X88904432>.
- Plog, B. a., Dashnaw, M. L., Hitomi, E., Peng, W., Liao, Y., Lou, N., Deane, R., and Nedergaard, M. Biomarkers of Traumatic Injury Are Transported from Brain to Blood via the Glymphatic System. *Journal of Neuroscience*, 35(2):518–526, January 2015. ISSN 0270-6474. doi: 10.1523/JNEUROSCI.3742-14.2015. URL <http://www.jneurosci.org/cgi/doi/10.1523/JNEUROSCI.3742-14.2015>.
- Polin, R. A., Fox, W. W., and Abman, S. H. *Fetal and Neonatal Physiology, 4th edition*, volume 41. Saunders, fourth edition, January 2010. ISBN 978-1-4160-3479-7.

- Powell, M. J. D. An efficient method for finding the minimum of a function of several variables without calculating derivatives. *The Computer Journal*, 7(2):155–162, February 1964. ISSN 0010-4620. doi: 10.1093/comjnl/7.2.155. URL <http://comjnl.oxfordjournals.org/content/7/2/155.abstract>.
- Rehncrona, S., Rosén, I., and Siesjö, B. K. Excessive cellular acidosis: an important mechanism of neuronal damage in the brain? *Acta physiologica Scandinavica*, 110(4):435–7, December 1980. ISSN 0001-6772. doi: 10.1111/j.1748-1716.1980.tb06692.x. URL <http://onlinelibrary.wiley.com/doi/10.1111/j.1748-1716.1980.tb06692.x/abstract><http://www.ncbi.nlm.nih.gov/pubmed/7234448>.
- Robertson, N. J. and Wyatt, J. S. The magnetic resonance revolution in brain imaging: impact on neonatal intensive care. *Archives of disease in childhood. Fetal and neonatal edition*, 89(3):F193–7, May 2004. ISSN 1359-2998. URL <http://www.pubmedcentral.nih.gov/articlerender.fcgi?artid=1721681&tool=pmcentrez&rendertype=abstract>.
- Robertson, N. J., Cox, I. J., Cowan, F. M., Counsell, S. J., Azzopardi, D., and Edwards, A. D. Cerebral intracellular lactic alkalosis persisting months after neonatal encephalopathy measured by magnetic resonance spectroscopy. *Pediatric research*, 46(3):287–96, September 1999. ISSN 0031-3998. doi: 10.1203/00006450-199909000-00007. URL <http://www.ncbi.nlm.nih.gov/pubmed/10473043>.
- Robertson, N. J., Cowan, F. M., Cox, I. J., and Edwards, A. D. Brain alkaline intracellular pH after neonatal encephalopathy. *Annals of neurology*, 52(6): 732–42, December 2002. ISSN 0364-5134. doi: 10.1002/ana.10365. URL <http://www.ncbi.nlm.nih.gov/pubmed/12447926>.
- Robertson, N. J., Kato, T., Bainbridge, A., Chandrasekaran, M., Iwata, O., Kapetanakis, A., Faulkner, S., Cheong, J., Iwata, S., Hristova, M., Cady, E., and Raivich, G. Methyl-isobutyl amiloride reduces brain Lac/NAA, cell death and microglial activation in a perinatal asphyxia model. *Journal of neurochemistry*, 124(5):645–57, March 2013. ISSN 1471-4159. doi: 10.1111/jnc.12097. URL <http://www.ncbi.nlm.nih.gov/pubmed/23171224>.
- Robertson, N., Nakakeeto, M., and Hagmann, C. Therapeutic hypothermia for birth asphyxia in low-resource settings: a pilot randomised controlled

- trial. *The Lancet*, pages 801–803, 2008. URL [http://www.thelancet.com/journals/lancet/article/PIIS0140-6736\(08\)61329-X](http://www.thelancet.com/journals/lancet/article/PIIS0140-6736(08)61329-X).
- Roche-Labarbe, N., Fenoglio, A., Radhakrishnan, H., Kocienski-Filip, M., Carp, S. a., Dubb, J., Boas, D. a., Grant, P. E., and Franceschini, M. A. Somatosensory evoked changes in cerebral oxygen consumption measured non-invasively in premature neonates. *NeuroImage*, 85 Pt 1:279–86, January 2014. ISSN 1095-9572. doi: 10.1016/j.neuroimage.2013.01.035. URL <http://www.ncbi.nlm.nih.gov/pubmed/23370052>.
- Rosenberg, A. A. Cerebral blood flow and O₂ metabolism after asphyxia in neonatal lambs. *Pediatric research*, 20(8):778–82, August 1986. ISSN 0031-3998. doi: 10.1203/00006450-198608000-00016. URL <http://www.ncbi.nlm.nih.gov/pubmed/3737291>.
- Roth, S. C., Edwards, a. D., Cady, E. B., Delpy, D. T., Wyatt, J. S., Azzopardi, D., Baudin, J., Townsend, J., Stewart, a. L., and Reynolds, E. O. Relation between cerebral oxidative metabolism following birth asphyxia, and neurodevelopmental outcome and brain growth at one year. *Developmental medicine and child neurology*, 34(4):285–95, April 1992. ISSN 0012-1622. URL <http://www.ncbi.nlm.nih.gov/pubmed/1572514>.
- Rutherford, M. MRI of the Neonatal Brain. *MRI of the NEonatal Brain*, 9:1–18, 2002. URL <http://scholar.google.com/scholar?hl=en&btnG=Search&q=intitle:MRI+of+the+neonatal+brain#0>.
- Saltelli, A., Tarantola, S., and Chan, K. P-S. A Quantitative Model-Independent Method for Global Sensitivity Analysis of Model Output. *Technometrics*, 41(1):39, February 1999. ISSN 00401706. doi: 10.2307/1270993. URL <http://www.jstor.org/stable/1270993?origin=crossref>.
- Saltelli, A., Tarantola, S., Campolongo, F., and Ratto, M. *Sensitivity analysis in practice: a guide to assessing scientific models*. John Wiley and Sons, 2004. ISBN 0470870931. URL http://books.google.com/books?hl=en&lr=&id=NsAVmohPNpQC&oi=fnd&pg=PR5&dq=Sensitivity+Analysis+in+Practice:+A+Guide+to+Assessing+Scientific+Models&ots=0QqASZTOAV&sig=Xy3xzRvvtHZJq-BGDPP_TFy5QIEhttp://books.google.com/books?hl=en&lr=&id=NsAVmohPNpQC&oi=fnd&pg=PR5&dq=Sensitivity+analysis+

[in+practice:+a+guide+to+assessing+scientific+models&ots=0QqASZT1sW&sig=EGQQMaY0-k6xOP4LqUS0m0AnFf0.](#)

Scholkmann, F. Figure. (*reproduced with permission*), 2014.

Scholkmann, F., Kleiser, S., Metz, A. J., Zimmermann, R., Mata Pavia, J., Wolf, U., and Wolf, M. A review on continuous wave functional near-infrared spectroscopy and imaging instrumentation and methodology. *NeuroImage*, 85 Pt 1:6–27, January 2014. ISSN 1095-9572. doi: 10.1016/j.neuroimage.2013.05.004. URL <http://www.ncbi.nlm.nih.gov/pubmed/23684868>.

Seghier, M. L., Lazeyras, F., Zimine, S., Maier, S. E., Hanquinet, S., Delavelle, J., Volpe, J. J., and Huppi, P. S. Combination of event-related fMRI and diffusion tensor imaging in an infant with perinatal stroke. *NeuroImage*, 21(1):463–472, January 2004. ISSN 10538119. doi: 10.1016/j.neuroimage.2003.09.015. URL <http://linkinghub.elsevier.com/retrieve/pii/S1053811903005640>.

Shadid, M., Moison, R., Steendijk, P., Hiltermann, L., Berger, H. M., and van Bel, F. The effect of antioxidative combination therapy on post hypoxic-ischemic perfusion, metabolism, and electrical activity of the newborn brain. *Pediatric research*, 44(1):119–24, July 1998. ISSN 0031-3998. doi: 10.1203/00006450-199807000-00019. URL <http://www.ncbi.nlm.nih.gov/pubmed/9667381>.

Shah, P., Ohlsson, A., and Perlman, M. Hypothermia to treat neonatal hypoxic ischemic encephalopathy: systematic review. *Archives of pediatrics & adolescent medicine*, 161(10):951–958, 2007. URL <http://aapgrandrounds.aappublications.org/content/19/1/3.shorthhttp://archpedi.ama-assn.org/cgi/reprint/161/10/951.pdf>.

Siesjo, B. *Brain Energy Metabolism*. {John Wiley and Sons Ltd}, 1978. ISBN 0471995150. URL <http://www.citeulike.org/group/160/article/1473537>.

Simpson, I., Carruthers, A., and Vannucci, S. Supply and demand in cerebral energy metabolism: the role of nutrient transporters. ...*Blood Flow & Metabolism*, 27(11):1766–1791, 2007. URL <http://www.nature.com/jcbfm/journal/v27/n11/abs/9600521a.html>.

- Singh, H., Cooper, R. J., Wai Lee, C., Dempsey, L., Edwards, A., Brigadoi, S., Airantzis, D., Everdell, N., Michell, A., Holder, D., Hebden, J. C., and Austin, T. Mapping cortical haemodynamics during neonatal seizures using diffuse optical tomography: a case study. *NeuroImage. Clinical*, 5:256–65, January 2014. ISSN 2213-1582. doi: 10.1016/j.nicl.2014.06.012. URL <http://www.pubmedcentral.nih.gov/articlerender.fcgi?artid=4141980&tool=pmcentrez&rendertype=abstract>.
- Smye, S. W. and Clayton, R. H. Mathematical modelling for the new millennium: medicine by numbers. *Medical engineering & physics*, 24(9):565–74, November 2002. ISSN 1350-4533. URL <http://www.ncbi.nlm.nih.gov/pubmed/12376043>.
- Soares, D. P. and Law, M. Magnetic resonance spectroscopy of the brain: review of metabolites and clinical applications. *Clinical radiology*, 64(1):12–21, January 2009. ISSN 1365-229X. doi: 10.1016/j.crad.2008.07.002. URL <http://www.ncbi.nlm.nih.gov/pubmed/19070693>.
- Solas, A.-B., Munkeby, B. H., and Saugstad, O. D. Comparison of short- and long-duration oxygen treatment after cerebral asphyxia in newborn piglets. *Pediatric research*, 56(1):125–31, July 2004. ISSN 0031-3998. doi: 10.1203/01.PDR.0000128978.90201.1D. URL <http://www.ncbi.nlm.nih.gov/pubmed/15128930>.
- Soul, J. S., Taylor, G. a., Wypij, D., Duplessis, a. J., and Volpe, J. J. Noninvasive detection of changes in cerebral blood flow by near-infrared spectroscopy in a piglet model of hydrocephalus. *Pediatric research*, 48(4):445–9, October 2000. ISSN 0031-3998. doi: 10.1203/00006450-200010000-00005. URL <http://www.ncbi.nlm.nih.gov/pubmed/11004233>.
- Springett, R., Newman, J., Cope, M., and Delpy, D. T. Oxygen dependency and precision of cytochrome oxidase signal from full spectral NIRS of the piglet brain. *American journal of physiology. Heart and circulatory physiology*, 279(5):H2202–9, November 2000. ISSN 0363-6135. URL <http://www.ncbi.nlm.nih.gov/pubmed/11045954>.
- Springett, R., Sakata, Y., and Delpy, D. T. Precise measurement of cerebral blood flow in newborn piglets from the bolus passage of indocyanine green. *Physics in medicine and biology*, 46(8):2209–25, August 2001. ISSN 0031-9155. URL <http://www.ncbi.nlm.nih.gov/pubmed/11512620>.

- Steiner, L. A. and Andrews, P. J. D. Monitoring the injured brain: ICP and CBF. *British journal of anaesthesia*, 97(1):26–38, July 2006. ISSN 0007-0912. doi: 10.1093/bja/ael110. URL <http://www.ncbi.nlm.nih.gov/pubmed/16698860>.
- Sturmfels, B. Can biology lead to new theorems? *Annual report of the Clay Mathematics Institute*, 2005. URL http://www2.maths.ox.ac.uk/cmi/library/annual_report/ar2005/05report_featurearticle.pdf.
- Tachtsidis, I., Bainbridge, A., Faulkner, S., Price, D., Powell, E., Thomas, D., Cady, E., Robertson, N., and Golay, X. In-Vivo Measurements of Brain Haemodynamics and Energetics using Multimodal Spectroscopy in Perinatal Hypoxia-Ischaemia. In *Biomedical Optics and 3-D Imaging*, page JM3A.27, Washington, D.C., 2012. OSA. ISBN 978-1-55752-942-8. doi: 10.1364/BIOMED.2012.JM3A.27. URL <http://www.opticsinfobase.org/abstract.cfm?URI=BIOMED-2012-JM3A.27>.
- Thayyil, S., Chandrasekaran, M., Taylor, A., Bainbridge, A., Cady, E. B., Chong, W. K. K., Murad, S., Omar, R. Z., and Robertson, N. J. Cerebral magnetic resonance biomarkers in neonatal encephalopathy: a meta-analysis. *Pediatrics*, 125(2):e382–95, February 2010. ISSN 1098-4275. doi: 10.1542/peds.2009-1046. URL <http://www.ncbi.nlm.nih.gov/pubmed/20083516>.
- Thompson, R. F. *The Brain: A Neuroscience Primer*. W. H. Freeman and Company, third edition, 2000. ISBN 978-0716732266.
- Thoresen, M., Penrice, J., Lorek, a., Cady, E. B., Wylezinska, M., Kirkbride, V., Cooper, C. E., Brown, G. C., Edwards, a. D., and Wyatt, J. S. Mild hypothermia after severe transient hypoxia-ischemia ameliorates delayed cerebral energy failure in the newborn piglet. *Pediatric research*, 37(5):667–70, May 1995. ISSN 0031-3998. doi: 10.1203/00006450-199505000-00019. URL <http://www.ncbi.nlm.nih.gov/pubmed/7603788>.
- Tichauer, K. M., Brown, D. W., Hadway, J., Lee, T.-Y., and St Lawrence, K. Near-infrared spectroscopy measurements of cerebral blood flow and oxygen consumption following hypoxia-ischemia in newborn piglets. *Journal of applied physiology (Bethesda, Md. : 1985)*, 100(3):850–7, March 2006. ISSN 8750-7587. doi: 10.1152/jappphysiol.00830.2005. URL <http://www.ncbi.nlm.nih.gov/pubmed/16293704>.

- Tisdall, M., Tachtsidis, I., Leung, T., Elwell, C. E., and Smith, M. Near infrared spectroscopic quantification of changes in the concentration of oxidized cytochrome oxidase in the healthy human brain. *Journal of Biomedical Optics*, 2007.
- Tisdall, M. M. and Smith, M. Multimodal monitoring in traumatic brain injury: current status and future directions. *British journal of anaesthesia*, 99(1):61–7, July 2007. ISSN 0007-0912. doi: 10.1093/bja/aem143. URL <http://www.ncbi.nlm.nih.gov/pubmed/17548431>.
- Transtrum, M. K., Machta, B. B., and Sethna, J. P. Why are Nonlinear Fits to Data so Challenging? *Physical Review Letters*, 104(6):060201, February 2010. ISSN 0031-9007. doi: 10.1103/PhysRevLett.104.060201. URL <http://link.aps.org/doi/10.1103/PhysRevLett.104.060201>.
- Transtrum, M. K., Machta, B. B., and Sethna, J. P. Geometry of nonlinear least squares with applications to sloppy models and optimization. *Physical Review E*, 83(3):036701, March 2011. ISSN 1539-3755. doi: 10.1103/PhysRevE.83.036701. URL <http://link.aps.org/doi/10.1103/PhysRevE.83.036701>.
- Trescher, W. H., Ishiwa, S., and Johnston, M. V. Brief post-hypoxic-ischemic hypothermia markedly delays neonatal brain injury. *Brain & development*, 19(5):326–38, July 1997. ISSN 0387-7604. URL <http://www.ncbi.nlm.nih.gov/pubmed/9253485>.
- Tsuji, M., Naruse, H., Volpe, J., and Holtzman, D. Reduction of cytochrome aa3 measured by near-infrared spectroscopy predicts cerebral energy loss in hypoxic piglets. *Pediatric research*, 37(3):253–9, March 1995. ISSN 0031-3998. doi: 10.1203/00006450-199503000-00001. URL <http://www.ncbi.nlm.nih.gov/pubmed/7784131>.
- Tyszczuk, L., Meek, J., Elwell, C., and Wyatt, J. S. Cerebral blood flow is independent of mean arterial blood pressure in preterm infants undergoing intensive care. *Pediatrics*, 102(2 Pt 1):337–41, August 1998. ISSN 0031-4005. URL <http://www.ncbi.nlm.nih.gov/pubmed/9685435>.
- Uria-Avellanal, C. and Robertson, N. J. Na(+)/H (+) Exchangers and Intracellular pH in Perinatal Brain Injury. *Translational stroke research*, 5(1): 79–98, February 2014. ISSN 1868-601X. doi: 10.1007/s12975-013-0322-x.

URL <http://www.pubmedcentral.nih.gov/articlerender.fcgi?artid=3913853&tool=pmcentrez&rendertype=abstract>.

Ursino, M. and Lodi, C. a. A simple mathematical model of the interaction between intracranial pressure and cerebral hemodynamics. *Journal of applied physiology (Bethesda, Md. : 1985)*, 82(4):1256–69, April 1997. ISSN 8750-7587. URL <http://www.ncbi.nlm.nih.gov/pubmed/9104864>.

Ursino, M. and Lodi, C. Interaction among autoregulation, CO₂ reactivity, and intracranial pressure: a mathematical model. *American Journal of Physiology-Heart ...*, 1998. URL <http://ajpheart.physiology.org/content/274/5/H1715.short>.

van Kooij, B. J. M., Hendrikse, J., Benders, M. J. N. L., de Vries, L. S., and Groenendaal, F. Anatomy of the circle of Willis and blood flow in the brain-feeding vasculature in prematurely born infants. *Neonatology*, 97(3):235–41, January 2010. ISSN 1661-7819. doi: 10.1159/000253754. URL <http://www.ncbi.nlm.nih.gov/pubmed/19887852>.

Vatov, L., Kizner, Z., Ruppin, E., Meilin, S., Manor, T., and Mayevsky, A. Modeling brain energy metabolism and function: a multiparametric monitoring approach. *Bulletin of mathematical biology*, 68(2):275–91, February 2006. ISSN 0092-8240. doi: 10.1007/s11538-005-9008-1. URL <http://www.ncbi.nlm.nih.gov/pubmed/16794931>.

Vaz, A. I. F. and Vicente, L. N. A particle swarm pattern search method for bound constrained global optimization. *Journal of Global Optimization*, 39(2):197–219, February 2007. ISSN 0925-5001. doi: 10.1007/s10898-007-9133-5. URL <http://link.springer.com/10.1007/s10898-007-9133-5>.

Vaz, A. and Vicente, L. PSwarm: A hybrid solver for linearly constrained global derivative-free optimization. *Optimization Methods & Software*, pages 1–22, 2009. URL <http://www.tandfonline.com/doi/abs/10.1080/10556780902909948>.

Verhagen, E. a., Van Braeckel, K. N. J. a., van der Veere, C. N., Groen, H., Dijk, P. H., Hulzebos, C. V., and Bos, A. F. Cerebral oxygenation is associated with neurodevelopmental outcome of preterm children at age 2 to 3years. *Developmental medicine and child neurology*, (May 2006):

- 1–7, November 2014. ISSN 1469-8749. doi: 10.1111/dmcn.12622. URL <http://www.ncbi.nlm.nih.gov/pubmed/25382744>.
- Verma, P. K., Panerai, R. B., Rennie, J. M., and Evans, D. H. Grading of cerebral autoregulation in preterm and term neonates. *Pediatric neurology*, 23(3):236–42, September 2000. ISSN 0887-8994. URL <http://www.ncbi.nlm.nih.gov/pubmed/11033287>.
- Volpe, J. *Neurology of the Newborn*, volume 1. Saunders, fifth edit edition, 2008. URL <http://books.google.com/books?hl=en&lr=&id=RiPpQyaH7DIC&oi=fnd&pg=PP1&dq=Neurology+of+the+Newborn&ots=DNPmnhqDgi&sig=r9sh3QNh5Usy6mEd2PV0E-sS12s>.
- Vutskits, L. Cerebral blood flow in the neonate. *Paediatric anaesthesia*, 24(1):22–9, January 2014. ISSN 1460-9592. doi: 10.1111/pan.12307. URL <http://www.ncbi.nlm.nih.gov/pubmed/24238074>.
- Wakabayashi, S., Fafournoux, P., Sardet, C., and Pouysségur, J. The Na⁺/H⁺ antiporter cytoplasmic domain mediates growth factor signals and controls “H(+)-sensing”. *Proceedings of the National Academy of Sciences of the United States of America*, 89(6):2424–8, March 1992. ISSN 0027-8424. URL <http://www.pubmedcentral.nih.gov/articlerender.fcgi?artid=48670&tool=pmcentrez&rendertype=abstract>.
- Ward, K. R. and Yealy, D. M. End-tidal carbon dioxide monitoring in emergency medicine, Part 1: Basic principles. *Academic emergency medicine : official journal of the Society for Academic Emergency Medicine*, 5(6):628–36, June 1998. ISSN 1069-6563. URL <http://www.ncbi.nlm.nih.gov/pubmed/9660292>.
- Waterfall, J., Casey, F., Gutenkunst, R., Brown, K., Myers, C., Brouwer, P., Elser, V., and Sethna, J. Sloppy-Model Universality Class and the Vandermonde Matrix. *Physical Review Letters*, 97(15):150601, October 2006. ISSN 0031-9007. doi: 10.1103/PhysRevLett.97.150601. URL <http://link.aps.org/doi/10.1103/PhysRevLett.97.150601>.
- Wigner, E. The unreasonable effectiveness of mathematics in the natural sciences. *Communications in Pure and Applied Mathematics*, 13(1), 1960. URL http://link.springer.com/chapter/10.1007/978-3-642-78374-6_41.

- Williams, G. D. and Smith, M. B. Application of the accurate assessment of intracellular magnesium and pH from the 31P shifts of ATP to cerebral hypoxia-ischemia in neonatal rat. *Magnetic resonance in medicine : official journal of the Society of Magnetic Resonance in Medicine / Society of Magnetic Resonance in Medicine*, 33(6):853–7, June 1995. ISSN 0740-3194. URL <http://www.ncbi.nlm.nih.gov/pubmed/7651125>.
- Williamson, D. H., Lund, P., and Krebs, H. a. The redox state of free nicotinamide-adenine dinucleotide in the cytoplasm and mitochondria of rat liver. *The Biochemical journal*, 103(2):514–27, May 1967. ISSN 0264-6021. URL <http://www.pubmedcentral.nih.gov/articlerender.fcgi?artid=1270436&tool=pmcentrez&rendertype=abstract>.
- Wong, F. Y., Leung, T. S., Austin, T., Wilkinson, M., Meek, J. H., Wyatt, J. S., and Walker, A. M. Impaired autoregulation in preterm infants identified by using spatially resolved spectroscopy. *Pediatrics*, 121(3):e604–11, March 2008. ISSN 1098-4275. doi: 10.1542/peds.2007-1487. URL <http://www.ncbi.nlm.nih.gov/pubmed/18250118>.
- Worley, A., Fabrizi, L., Boyd, S., and Slater, R. Multi-modal pain measurements in infants. *Journal of neuroscience methods*, 205(2):252–7, April 2012. ISSN 1872-678X. doi: 10.1016/j.jneumeth.2012.01.009. URL <http://www.pubmedcentral.nih.gov/articlerender.fcgi?artid=3465552&tool=pmcentrez&rendertype=abstract>.
- Wray, S., Cope, M., Delpy, D. T., Wyatt, J. S., and Reynolds, E. O. Characterization of the near infrared absorption spectra of cytochrome aa3 and haemoglobin for the non-invasive monitoring of cerebral oxygenation. *Biochimica et biophysica acta*, 933(1):184–92, March 1988. ISSN 0006-3002. URL <http://www.ncbi.nlm.nih.gov/pubmed/2831976>.
- Wyatt, J. S., Cope, M., Delpy, D. T., Richardson, C. E., Edwards, a. D., Wray, S., and Reynolds, E. O. Quantitation of cerebral blood volume in human infants by near-infrared spectroscopy. *Journal of applied physiology (Bethesda, Md. : 1985)*, 68(3):1086–91, March 1990. ISSN 8750-7587. URL <http://www.ncbi.nlm.nih.gov/pubmed/2341336>.
- Yager, J. Y. and Ashwal, S. Animal models of perinatal hypoxic-ischemic brain damage. *Pediatric neurology*, 40(3):156–67, March 2009. ISSN 0887-

8994. doi: 10.1016/j.pediatrneurol.2008.10.025. URL <http://www.ncbi.nlm.nih.gov/pubmed/19218028>.

Yu, T., Lloyd, C. M., Nickerson, D. P., Cooling, M. T., Miller, A. K., Garny, A., Terkildsen, J. R., Lawson, J., Britten, R. D., Hunter, P. J., and Nielsen, P. M. F. The Physiome Model Repository 2. *Bioinformatics (Oxford, England)*, 27(5):743–4, March 2011. ISSN 1367-4811. doi: 10.1093/bioinformatics/btq723. URL <http://www.ncbi.nlm.nih.gov/pubmed/21216774>.

Zahler, R., Zhang, Z. T., Manor, M., and Boron, W. F. Sodium kinetics of Na,K-ATPase alpha isoforms in intact transfected HeLa cells. *The Journal of general physiology*, 110(2):201–13, August 1997. ISSN 0022-1295. doi: 0022-1295/97/08/201/13. URL <http://www.pubmedcentral.nih.gov/articlerender.fcgi?artid=2233788&tool=pmcentrez&rendertype=abstract>.

Zaramella, P., Freato, F., Amigoni, a., Salvadori, S., Marangoni, P., Suppiej, a., Suppiej, a., Schiavo, B., and Chiandetti, L. Brain auditory activation measured by near-infrared spectroscopy (NIRS) in neonates. *Pediatric research*, 49(2):213–9, February 2001. ISSN 0031-3998. doi: 10.1203/00006450-200102000-00014. URL <http://www.ncbi.nlm.nih.gov/pubmed/11158516>.

Zimmermann, B. B., Roche-Labarbe, N., Surova, A., Boas, D. A., Wolf, M., Grant, P. E., and Franceschini, M. A. The confounding effect of systemic physiology on the hemodynamic response in newborns. *Advances in experimental medicine and biology*, 737:103–9, January 2012. ISSN 0065-2598. doi: 10.1007/978-1-4614-1566-4_16. URL <http://link.springer.com/10.1007/978-1-4614-1566-4http://www.pubmedcentral.nih.gov/articlerender.fcgi?artid=3386795&tool=pmcentrez&rendertype=abstract>.